Randall Allemang  *Editor*

# Topics in Modal Analysis II, Volume 8

Proceedings of the 32nd IMAC, A Conference and Exposition on Structural Dynamics, 2014

SEM

Springer

# Conference Proceedings of the Society for Experimental Mechanics Series

*Series Editor*

Tom Proulx
Society for Experimental Mechanics, Inc.,
Bethel, CT, USA

Randall Allemang
Editor

# Topics in Modal Analysis II, Volume 8

Proceedings of the 32nd IMAC, A Conference and Exposition on Structural Dynamics, 2014

Springer

*Editor*
Randall Allemang
University of Cincinnati
Cincinnati, OH, USA

# Preface

*Topics in Modal Analysis II, Volume 8* represents one of the eight volumes of technical papers presented at the 32nd IMAC, A Conference and Exposition on Structural Dynamics, 2014, organized by the Society for Experimental Mechanics, and held in Orlando, Florida, February 3–6, 2014. The full proceedings also include volumes on Dynamics of Coupled Structures; Nonlinear Dynamics; Model Validation and Uncertainty Quantification; Dynamics of Civil Structures; Structural Health Monitoring; Special Topics in Structural Dynamics; and Topics in Modal Analysis I.

Each collection presents early findings from experimental and computational investigations on an important area within structural dynamics. *Topics in Modal Analysis II* represents papers on enabling technologies for modal analysis measurements such as sensors and instrumentation and applications of modal analysis in specific application areas. Topics in this volume include:

Finite element techniques
Modal parameter identification
Modal testing methods
Shock and vibration

The organizers would like to thank the authors, presenters, session organizers, and session chairs for their participation in this track.

Cincinnati, OH, USA                                                                                  Randall Allemang

# Contents

# Chapter 1
# Integrating Multiple Algorithms in Autonomous Modal Parameter Estimation

**R.J. Allemang and A.W. Phillips**

**Abstract** Recent work with autonomous modal parameter estimation has shown great promise in the quality of the modal parameter estimation results when compared to results from experienced user interaction using traditional methods. Current research with the Common Statistical Subspace Autonomous Mode Identification (CSSAMI) procedure involves the integration of multiple modal parameter estimation algorithms into the autonomous procedure. The current work uses possible solutions from different traditional methods like Polyreference Time Domain (PTD), Eigensystem Realization Algorithm (ERA) and Polyreference Frequency Domain (PFD) that are combined in the autonomous procedure to yield one consistent set of modal parameter solutions. This final, consistent set of modal parameters is identifiable due to the combination of temporal information (the complex modal frequency) and the spatial information (the modal vectors) in a Z domain state vector of relatively high order (5–10). Since this Z domain state vector has the complex modal frequency and the modal vector as embedded content, sorting consistent estimates from hundreds or thousands of possible solutions is now relatively trivial based upon the use of a state vector involving spatial information.

## Nomenclature

| | |
|---|---|
| $N_i$ | Number of inputs |
| $N_o$ | Number of outputs |
| $N_S$ | Short dimension size |
| $N_L$ | Long dimension size |
| $N$ | Number of vectors in cluster |
| $\omega_i$ | Discrete frequency (rad/s) |
| $[H(\omega_i)]$ | FRF matrix ($N_o \times N_i$) |
| $r$ | Mode number |
| $\lambda_r$ | S domain polynomial root |
| $\lambda_r$ | Complex modal frequency (rad/s) |
| $\lambda_r$ | $\sigma_r + j\omega_r$ |
| $\sigma_r$ | Modal damping |
| $\omega_r$ | Damped natural frequency |
| $z_r$ | Z domain polynomial root |
| $\{\psi_r\}$ | Base vector (modal vector) |
| $\{\phi_r\}$ | Pole weighted base vector (state vector) |

R.J. Allemang (✉) • A.W. Phillips
Structural Dynamics Research Laboratory, Department of Mechanical and Materials Engineering, College of Engineering and Applied Science, University of Cincinnati, Cincinnati, OH 45221-0072, USA
e-mail: Randall.Allemang@UC.EDU

## 1.1 Introduction

The desire to estimate modal parameters automatically, once a set or multiple sets of test data are acquired, has been a subject of great interest for more than 40 years. Even in the 1960s, when modal testing was limited to analog test methods, several researchers were exploring the idea of an automated test procedure for determining modal parameters [1–3]. Today, with the increased memory and compute power of current computers used to process test data, an automated or autonomous, modal parameter estimation procedure is entirely possible and is being evaluated by numerous researchers and users.

Before proceeding with a discussion of how multiple modal parameter estimation algorithms can be combined into autonomous modal parameter estimation, some discussion of the current autonomous modal parameter estimation procedure is required. In general, autonomous modal parameter estimation refers to an automated procedure that is applied to a modal parameter estimation algorithm so that no user interaction is required once the process is initiated. This typically involves setting a number of parameters or thresholds that are used to guide the process in order to exclude solutions that are not acceptable to the user. When the procedure finishes, a set of modal parameters is identified that can then be reduced or expanded if necessary. The goal is that no further reduction, expansion or interaction with the process will be required.

For the purposes of further discussion, the autonomous modal parameter estimation procedure is simply an efficient mechanism for sorting a very large number of solutions into a final set of solutions that satisfies a set of criteria and thresholds that are acceptable to the user. When multiple modal parameter estimation algorithms are combined into a single autonomous procedure, this yields more estimates of the modal parameters which contribute to a statistically more significant result. Currently, the user of autonomous modal parameter estimation is assumed to be very experienced and is using autonomous modal parameter estimation as a sophisticated tool to highlight the most likely solutions based upon statistics. The experienced user will realize that the final solutions may include unrealistic solutions or non-optimal solutions and further evaluation will be required.

## 1.2 Background

In order to discuss the impact and use of multiple modal parameter estimation algorithms in autonomous modal parameter estimation, the importance of spatial information to the solution procedure is critical. Therefore, some background is needed to clarify terminology and methodology. This background has been provided in previous papers [4–7] and will only be highlighted here in terms of spatial information, modal parameter estimation and autonomous modal parameter estimation.

### 1.2.1 Spatial Information

Spatial information, with respect to experimental modal parameter estimation, refers to the vector information and dimension associated with the inputs and outputs of the experimental test. Essentially, this represents the locations of the sensors in the experimental test. It is important to recognize that an experimental test should always include multiple inputs and outputs in order to clearly estimate different modal vectors and to resolve modal vectors when the complex natural frequencies are close, what is called repeated or pseudo-repeated roots.

Since the data matrix, normally involving frequency response functions (FRF) or impulse response functions (IRF), is considered to be symmetric or reciprocal, the data matrix can be transposed, switching the effective meaning of the row and column index with respect to the physical inputs and outputs.

$$[H\left(\omega_i\right)]_{N_o \times N_i} = [H\left(\omega_i\right)]^{T}_{N_i \times N_o} \tag{1.1}$$

Since many modal parameter estimation algorithms are developed on the basis of either the number of inputs ($N_i$) or the number of outputs ($N_o$), assuming that one or the other is larger based upon test method, some nomenclature conventions are required for ease of further discussion. In terms of the modal parameter estimation algorithms, it is more important to recognize whether the algorithm develops the solution on the basis of the larger ($N_L$) of $N_i$ or $N_o$, or the smaller ($N_S$) of $N_i$ or $N_o$, dimension of the experimental data. For this reason, the terminology of *long* (larger of $N_i$ or $N_o$) dimension or *short* (smaller of $N_i$ or $N_o$) dimension is easier to understand without confusion.

Therefore, the nomenclature of the number of outputs ($N_o$) and number of inputs ($N_i$) has been replaced by the length of the long dimension of the data matrix ($N_L$) and the length of the short dimension ($N_S$) regardless of which dimension refers to the physical output or input. This means that the above reciprocity relationship can be restated as:

$$[H(\omega_i)]_{N_L \times N_S} = [H(\omega_i)]_{N_S \times N_L}^T \tag{1.2}$$

Note that the reciprocity relationships embedded in Eqs. 1.1 and 1.2 are a function of the common degrees of freedom (DOFs) in the short and long dimensions. If there are no common DOFs, there are no reciprocity relationships and the data requirement for modern modal parameter estimation algorithms (multiple references) will not be met. Nevertheless, the importance of Eqs. 1.1 and 1.2 is that the dimensions of the FRF matrix can be transposed as needed to fit the requirement of specific modal parameter estimation algorithms. This impacts the size of the square matrix coefficients in the matrix coefficient, polynomal equation and the length of the associated modal (base) vector.

### 1.2.2  Autonomous Modal Parameter Estimation

The interest in automatic modal parameter estimation methods has been documented in the literature since at least the mid 1960s when the primary modal method was the analog, force appropriation method [1–3]. Following that early work, there has been a continuing interest in autonomous methods that, in most cases, have been procedures that are formulated based upon a specific modal parameter estimation algorithm like the Eigensystem Realization Algorithm (ERA), the Polyreference Time Domain (PTD) algorithm or more recently the Polyreference Least Squares Complex Frequency (PLSCF) algorithm (which thebasis of the commercial version of the PLSCF, the PolyMAX $^{®}$ method and the rational fraction polynomial algorithm with Z-domain generalized frequency (RFP-z)) [8]. A relatively complete list of autonomous and semi-autonomous procedures that have been reported can be found in a recent paper [4].

Each of these past procedures have shown some promise but have not yet been widely adopted. In many cases, the procedure focused on a single modal parameter estimation algorithm and did not develop a general procedure. Most of the past procedural methods focused on modal frequency (pole) density but depended on limited modal vector data to identify correlated solutions. Currently, due to increased computational speed and availability of memory, procedural methods can be developed that were beyond the computational scope of available hardware only a few years ago. These methods do not require any initial thresholding of the solution sets and rely upon correlation of the vector space of hundreds or thousands of potential solutions as the primary identification tool.

The discussion in the following sections of the use of multiple modal parameter estimation algorithms in autonomous modal parameter estimation is based upon recent implementation and experience with an autonomous modal parameter estimation procedure referred to as the Common Statistical Subspace Autonomous Mode Identification (CSSAMI) method. The strategy of the CSSAMI autonomous method is to use a default set of parameters and thresholds to allow for all possible solutions from a given data set. This strategy allows for some poor estimates to be identified as well as the good estimates. The philosophy of this approach is that it is easier for the user to evaluate and eliminate poor estimates compared to trying to find additional solutions. The reader is directed to a series of previous papers in order to get an overview of the methodology and to view application results for several cases [4–7].

Note that much of the background of the CSSAMI method is based upon the Unified Matrix Polynomial Algorithm (UMPA) [8]. This means that this method can be applied to both low and high order methods with short or long dimension modal (base) vectors. This also means that most commercial algorithms could take advantage of this procedure. Note that high order, matrix coefficient polynomials normally have coefficient matrices of a dimension that is based upon the short dimension of the data matrix, $N_S$. In these cases, it may be useful to solve for the complete, unscaled or scaled, modal vector of the large dimension, $N_L$. This will extend the temporal-spatial information in the modal (base) vector so that the vector will be more sensitive to change. This characteristic is what gives the CSSAMI autonomous method a robust ability to distinguish between computational and structural modal parameters.

### 1.2.3  Pole Weighted Modal Vectors

The key to estimating the modal parameters utilizing the CSSAMI autonomous procedure is formulating clusters of pole weighted modal vectors, or state vectors, from the estimates of modal parameters that are represented in a consistency diagram. These state vectors are formed from the modal vector estimates found as the consistency diagram is developed.

**Fig. 1.1** Eighth order,
pole-weighted vector (state
vector) example
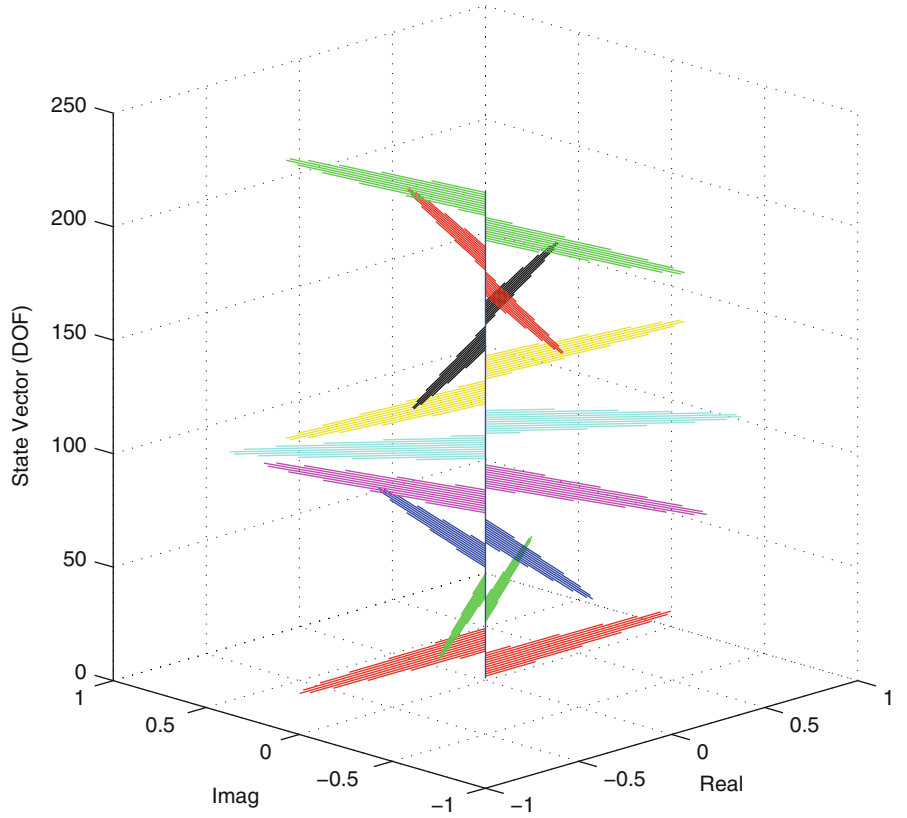


When comparing modal (base) vectors, at either the short or the long dimension, a pole weighted vector can be constructed independent of the original algorithm used to estimate the poles and modal (base) vectors. For a given order k of the pole weighted vector, the modal (base) vector and the associated pole can be used to formulate the pole weighted vector as follows:

$$\{\phi\}_r = \begin{Bmatrix} \lambda_r^k\{\psi\}_r \\ \cdot \\ \cdot \\ \cdot \\ \lambda_r^2\{\psi\}_r \\ \lambda_r^1\{\psi\}_r \\ \lambda_r^0\{\psi\}_r \end{Bmatrix}_r \qquad \{\phi\}_r = \begin{Bmatrix} z_r^k\{\psi\}_r \\ \cdot \\ \cdot \\ \cdot \\ z_r^2\{\psi\}_r \\ z_r^1\{\psi\}_r \\ z_r^0\{\psi\}_r \end{Bmatrix}_r \qquad (1.3)$$

While the above formulation (on the left) is possible, this form would be dominated by the high order terms if actual frequency units are utilized. Generalized frequency concepts (frequency normalization or Z domain mapping) are normally used to minimize this issue by using the Z domain form ($z_r$) of the complex modal frequency ($\lambda_r$) as shown above (on the right). The Z domain form of the complex natural frequency is developed as follows:

$$z_r = e^{\pi^*(\lambda_r/\Omega_{\max})} \qquad (1.4)$$

$$z_r^m = e^{m^*\pi^*(\lambda_r/\Omega_{\max})} \qquad (1.5)$$

In the above equations, $\Omega_{\max}$ can be chosen as needed to cause the positive and negative roots to wrap around the unit circle in the Z domain without overlapping (aliasing). Normally, $\Omega_{\max}$ is taken to be five percent larger than the largest frequency (absolute value of the complex frequency) identified in the roots of the matrix coefficient polynomial.

Figures 1.1 and 1.2 are graphical representations of the pole weighted vector (state vector) defined in Eq. 1.3. In this example, the modal (base) vector (at the bottom of Fig. 1.1) is a real-valued normal mode that looks like one period of a

**Fig. 1.2** Eighth order, pole-weighted vector (state vector) example—Top view
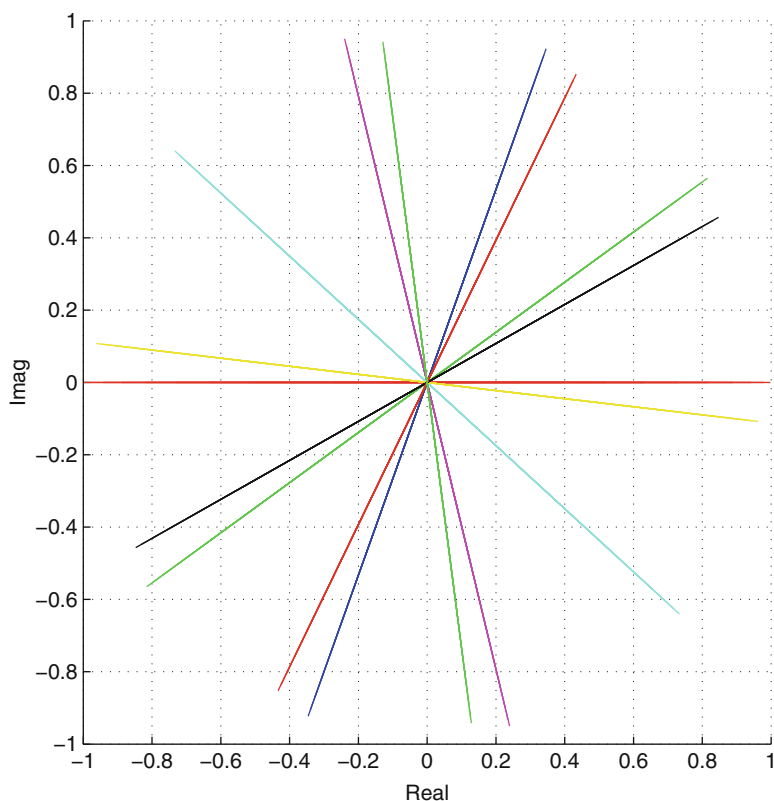


sine wave. The successive higher orders, up to order eight, are shown in different colors moving up the vertical axis of this figure. The effect of scaling of the modal (base) vector by the higher powers of the Z domain frequency value causes the base vector to rotate in the real and imaginary space. Figure 1.2 shows the rotation affect clearly. Note that the choice of the order (k) of the pole weighted vector, therefore, just generates additional length and rotation in the pole weighted vector and gives varying sensitivity to comparisons between estimates. Futhermore, note that the choice of order (k) is independent of algorithm. State vectors are a natural part of the numerical formulation for all modal parameter estimation algorithms but this pole weighted vector (state vector), which looks similar, can be formed independently once the modal (base) vector is estimated and, thus, is not constrained by the algorithm. The choice of the order of the pole weighted vector (k) will depend upon the length of the modal (base) vector and is under continuing study at present.

Since the magnitude of the Z domain frequency value is unity, there is no magnitude weighting involved. This rotation gives a method for a single vector to represent the modal (base) vector shape together with the complex-valued frequency. With respect to sorting and separating modal vectors that have similar shapes but different frequencies or similar frequencies but different modal vector shapes, this becomes a powerful parameter, together with modal vector correlation tools like the modal assurance criterion (MAC), for modal parameter estimation and for autonomous modal parameter estimation.

## 1.3 Multi-algorithm, Extended Consistency Diagrams

Consistency diagrams, historically called stability diagrams, have almost always been utilized and developed for a specific modal parameter estimation algorithm. As such the numerical implementation can be different as a function of basis dimension ($N_S$ or $N_L$), model order and/or subspace iteration. This would make it very hard to combine different algorithms into a single consistency diagram. However, every algorithm, at the point of the numerical implementation of the consistency diagram, has multiple sets of complex modal frequency and complex-valued modal vectors. The modal vectors may be of different length ($N_S$ or $N_L$) as a function of algorithm. This potential mismatch in modal (base) vector length can be solved by restricting the long dimension to the DOFs of the short dimension or, more preferably, adding an extra step in the solution procedure to estimate the missing portion of the long dimension vectors, extending them from the short dimension DOFs to the long dimension DOFs. The latter approach is used in the following two figures as an example of *extended consistency*
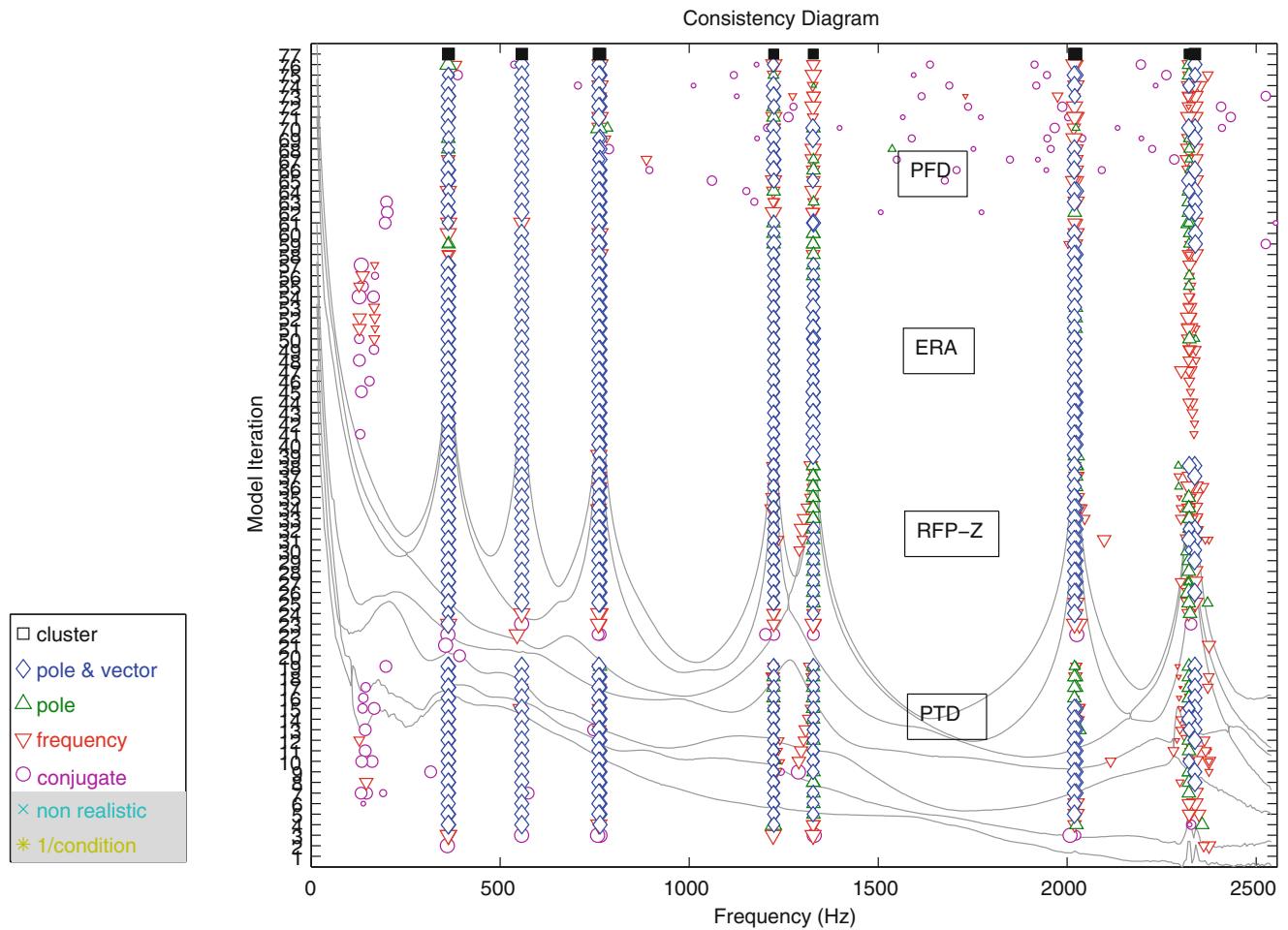
**Fig. 1.3** Extended consistency diagram—Conventional version

*diagrams* based upon multiple modal parameter estimation algorithms. In these examples, the results from the individual algorithms are simply stacked into the extended consistency diagram with common sorting and evaluation settings. It should be noted that the order of the stacking of the different algorithms will affect the look of the consistency diagram but the CSSAMI autonomous procedure uses all of the estimated parameters and pays no attention to the sequential ordering and stability calculation involved in the consistency diagram.

The data used for this, and all following examples in this paper, is FRF data taken from an impact test of a steel disc supported in a pseudo free-free boundary condition. The steel disc is approximately 2 cm. thick and 86 cm. in diameter with several small holes through the disc. The center area of the disc (diameter of approximately 25 cm.) has a thickness of approximately 6 cm. There are seven reference accelerometers and measured force inputs from an impact hammer are applied to thirty-six locations, including next to the seven reference accelerometers. The frequency resolution of the data is 5 Hz. While the disc is not as challenging as some industrial data situations that contain more noise or other complicating factors like small nonlinearities, the disc has a number of pseudo-repeated roots spaced well within the 5 Hz frequency resolution and a mix of close modes involving repeated and non-repeated roots which are very challenging. Based upon the construction of the disc, real-valued, normal modes can be expected and the inability to resolve these modes can be instructive relative to both modal parameter estimation algorithm and autonomous procedure performance. For the interested reader, a number of realistic examples are shown in other past papers including FRF data from an automotive structure and a bridge structure [4, 7].

Figure 1.3 is an example of using a conventional, sequential sorting procedure involving criteria for frequency, damping and modal vector consistency.

Figure 1.4 is an example using a pole weighted vector (state vector) method of producing a similar consistency diagram. In this example, every estimate from every matrix coefficient polynomial solution from every algorithm is converted into a pole weighted vector of a specific order, in this case tenth order. Then, the consistency diagram is developed by using vector
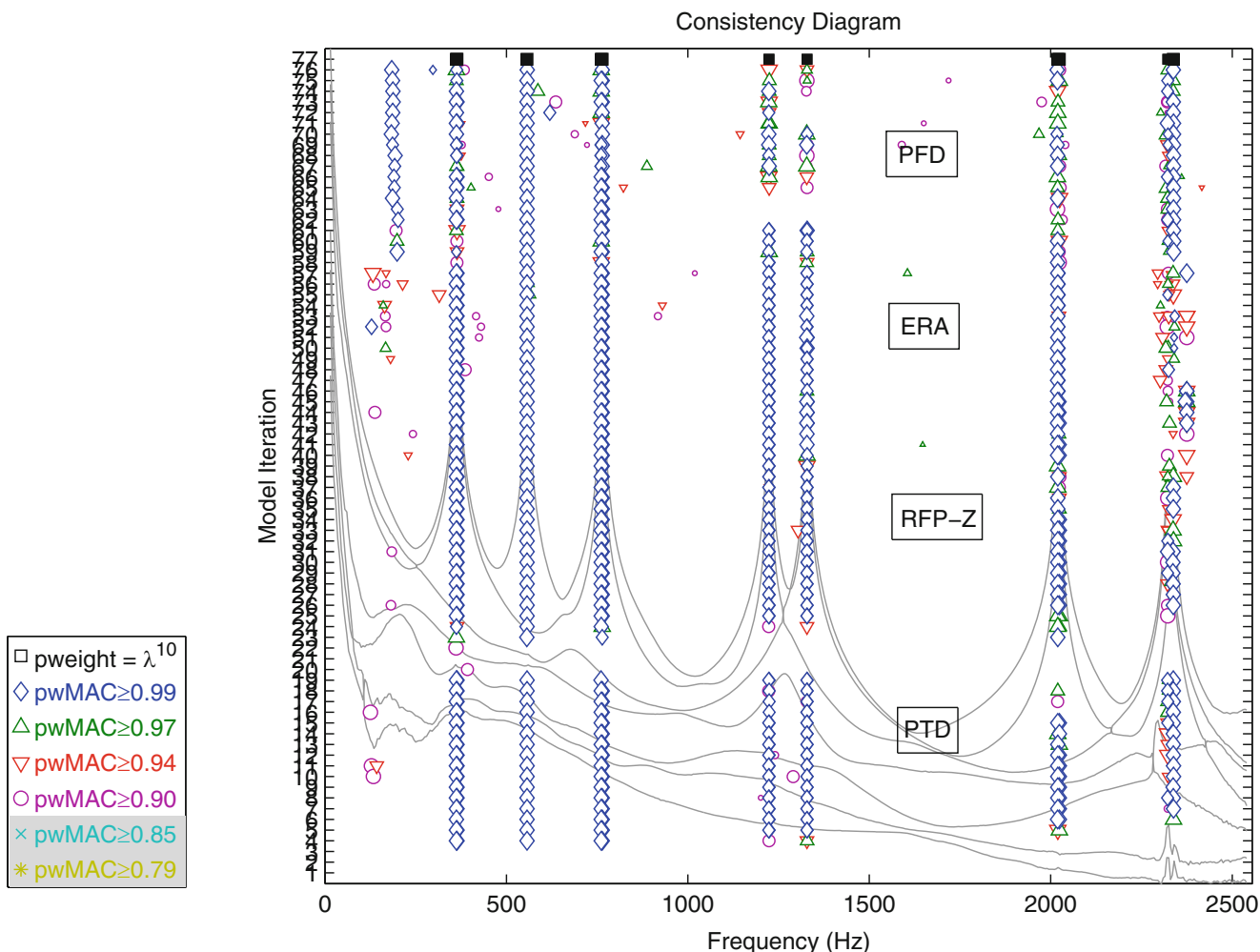
**Fig. 1.4** Extended consistency diagram—Pole weighted MAC version

correlation methods (MAC) to identify consistency. A similar set of symbols, as those used in Fig. 1.3, are used to define increased levels of consistency as numerical solutions are added.

Both methods work very well but the implementation of Fig. 1.4 is computationally easier and not subject to a frequency drift in the symbol path that can occur in the conventional implementation shown in Fig. 1.1. Note that the solid square symbols at the top of both consistency diagrams represent the solution found from the CSSAMI autonomous modal parameter estimation procedure applied to the information represented by each consistency diagram.

Note that all of the above algorithms are using the same matrix polynomial equation normalization procedure which tends to yield clear consistency diagrams. Each consistency diagram can yield twice as many estimates of the desired modal parameters if both low and high matrix coefficient normalizations are utilized. This is also under current study.

## 1.4 Autonomous Modal Parameter Estimation with Extended Consistency Diagrams

The CSSAMI autonomous procedure utilizes all solutions indicated by a symbol in the consistency diagram. If some symbols are not present, it means the user has decided not to view solutions identified by those symbols. This provides a way to remove solutions from the autonomous procedure that are clearly not reasonable. However, experience with the CSSAMI autonomous procedure has shown that some solutions that are often eliminated by users in an attempt to have a clear consistency diagram are often statistically consistent and useful.

Figure 1.5 shows the solutions that are included in the autonomous procedure. The graphical representation on the left represents a MAC matrix involving the pole weighted vectors for all possible solutions from Fig. 1.3. The graphical
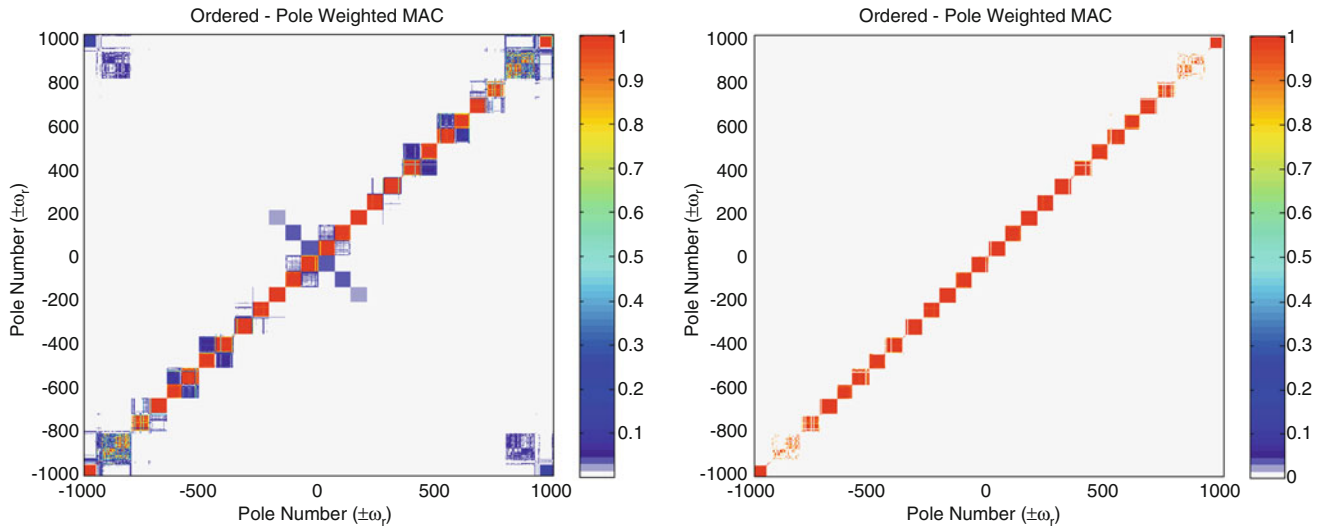
**Fig. 1.5** Pole weighted MAC of all consistency diagram solutions—Before and after threshold applied

representation on the right represents the pole weighted vectors that remain after threshold and cluster size limitations are imposed. Each cluster that remains is evaluated, cluster by cluster, independently to estimate the best modal frequency and modal vector from that cluster. Note that both the positive frequency and negative frequency (complex conjugate) roots are included and identified separately as clusters. Figure 1.5 represents nearly 1,000 solution estimates spanning four different algorithms and 19 different solutions form each algorithm.

Once the final set of modal parameters, along with their associated statistics, is obtained, quality can be assessed by many methods that have been used in the past. The most common example is to perform comparisons between the original measurements and measurements synthesized from the modal parameters. Another common example is to look at physical characteristics of the identified parameters such as reasonableness of frequency and damping values, normal mode characteristics in the modal vectors, and appropriate magnitude and phasing in the modal scaling. Other evaluations that may be helpful are unweighted and weighted modal assurance criterion (MAC) evaluation of the independence of the complete modal vector set, mean phase correlation (MPC) of each vector or any other method available. Naturally, since a significant number of pole weighted vectors are used in a cluster to identify the final modal parameters, traditional statistics involving mean and standard deviation are now available.

## 1.5  Summary and Future Work

With the advent of more computationally powerful computers and sufficient memory, it has become practical to evaluate sets of solutions involving hundreds or thousands of modal parameter estimates and to extract the common information from those sets. If multiple modal parameter estimation algorithms can be combined into a single autonomous procedure, the statistics related to the common modal parameter estimation become even more meaningful. In most experimental cases studied so far, autonomous procedures give very acceptable results, in some cases superior results, in a fraction of the time required for an experienced user to get the same result.

Future work will involve evaluating alternate numerical methods for combining algorithms into a single consistency diagram (equation normalization, order of the pole weighted vector, etc.) and as well as modal vector solution methods for identifying the best causal results (Do we get a normal mode when we expect a normal mode?). Numerical solution methods that identify both real-valued modal vectors (normal modes) and complex-valued modal vectors, when appropriate, would be truly autonomous.

However, it is important to reiterate that the use of these autonomous procedures or *wizard* tools by users with limited experience is probably not yet appropriate. Such tools are most appropriately used by users with the experience to accurately judge the quality of the parameter solutions identified.

# References

1. Hawkins FJ (1965) An automatic resonance testing technique for exciting normal modes of vibration of complex structures. In: Symposium IUTAM, "Progres Recents de la Mecanique des Vibrations Lineaires", pp. 37–41
2. Hawkins FJ (1967) GRAMPA—An automatic technique for exciting the principal modes of vibration of complex structures. Royal Aircraft Establishment, RAE-TR-67-211
3. Taylor GA, Gaukroger DR, Skingle CW (1967) MAMA—A semi-automatic technique for exciting the principal modes of vibration of complex structures. Aeronautical Research Council, ARC-R/M-3590, 20pp
4. Allemang RJ, Brown DL, Phillips AW (2010) Survey of modal techniques applicable to autonomous/semi-autonomous parameter identification. In: Proceedings of international conference on noise and vibration engineering (ISMA), Katholieke Universiteit Leuven, Belgium, 42pp
5. Phillips AW, Allemang RJ, Brown DL (2011) Autonomous modal parameter estimation: methodology. In: Proceedings of international modal analysis conference (IMAC), 22pp
6. Allemang RJ, Phillips AW, Brown DL (2011) Autonomous modal parameter estimation: statistical considerations. In: Proceedings of international modal analysis conference (IMAC), 17pp
7. Brown DL, Allemang RJ, Phillips AW (2011) Autonomous modal parameter estimation: application examples. In: Proceedings of international modal analysis conference (IMAC), 26pp
8. Allemang RJ, Phillips AW (2004) The unified matrix polynomial approach to understanding modal parameter estimation: an update. In: Proceedings of international conference on noise and vibration engineering (ISMA)

# Chapter 2
# Effects of Magneto-Mechanical Coupling on Structural Modal Parameters

**M. Kirschneck, D.J. Rixen, Henk Polinder, and Ron van Ostayen**

**Abstract** Structures that are exposed to a magnetic field experience magnetic forces. As these forces are geometry dependent they vary with the displacement of the structure that can result in an additional stiffness. Furthermore eddy currents induced by the movement of the structure can lead to an increased dissipation resulting in a higher damping value for the mechanical part of the system. This paper introduces calculation techniques for predicting these effects and validates them with measurements done on a simple set up in the lab.

**Keywords** Modal parameter identification • Magneto-mechanical coupling • Monolithic eigenvalue problem

## 2.1 Introduction

All ferro-magnetic objects, that are exposed to a magnetic field, experiences local forces. For an object at rest in a magnetic field these local forces cancel each other out and the net force on the object is zero. But when the magnetic field is such that the local forces do not balance each other out the object experiences a net force. In such a case the magnetic force has an effect on the mechanics of the system. At the same time the change of geometry due to movement will affect the magnetic field. These kind of systems are called two way magneto-mechanically coupled systems. In such as system the dynamical behavior of can be altered compared to its behavior without that coupling. This also has an impact on the modal parameters that the system displays under no coupling conditions. Certain configurations and geometries contribute to the impact of the effect of the magneto-mechanical coupling. In this paper such a system is introduced and it is shown how the change on modal parameters can be simulated and predicted.

There has been extensive research on magneto-mechanical systems. In fact many transducer that transforms electric energy to mechanic energy or the other way around, i.e. electric machines, are magneto-mechanical coupled systems. Therefore the research on magneto-mechanical coupled systems began by the discovery of forces due to electric currents and their mentioning by Maxwell [7].

In light weight structures the opposing aims of making a structure as stiff as possible and as light as possible is commonly found. For these kind of structures that are exposed to magnetic fields, the exact knowledge of the dynamics of the structure might be crucial. The knowledge might allow to reduce the weight of the structure further. The same is true for electric machines that operate in places where weight reduction is essential. The rotors and stators of these machines are exposed to magnetic fields while being required to be as stiff and as light as possible. Applications can be found in electric cars or large off-shore direct-drive wind turbines.

---

M. Kirschneck (✉) • R. van Ostayen
Faculty of Mechanical, Maritime and Materials Engineering, Delft University of Technology, Stevinweg 1,
2628 CN Delft, The Netherlands
e-mail: m.kirschneck@tudelft.nl

D.J. Rixen
Faculty of Mechanical Engineering, Technical University of Munich, Boltzmannstr. 15, 85748 München, Germany

H. Polinder
Faculty of Electrical Engineering Mathematics and Computer Science, Delft University of Technology,
Stevinweg 1, 2628 CN Delft, The Netherlands

Recent research on dynamics of magneto-mechanical coupled system concentrated on one way coupled formulations [4, 8, 9]. The reason for this is that 3D magnetic calculations are expensive and are avoided unless absolutely necessary. Research on 3D two way coupled problems has been done but not applied to modal analysis [2].

## 2.2 The Test Setup

The test set up consists of a stator yoke, two permanent magnets and a flexible beam. Figure 2.1 shows a photo of the test set up and a 3D schematic of it. The coil that can be seen in the picture was not used for the experiments. The stator yoke is fixed to the table by clamps. The flexible beam is fixed to a table that can be moved. This construction allows to move the front part of the beam in and out of the air gap of the stator yoke. The two permanent magnets are located in the air gap and create the magnetic field that passively interacts with the structural dynamics (Table 2.1). Because neither the stator yoke nor the beam are slotted eddy currents are possible in the system and heat dissipation can occur.

### 2.2.1 Emerging Effects

The beam is constructed in such a way that the first bending frequency in one direction is much lower than in the other directions. The bending mode shown in Fig. 2.1b will decrease the air gap length on one side of the beam while it is increased on the other side of the beam. This will change the magnetic field in the air gap. Due to fringe effects the magnetic flux density will rise on the side where the air gap length is reduced and diminish where the air gap lengthened. The resulting magnetic force that acts on the beam and pulls the beam in both air gaps towards the yoke will also change. Because the force does not depend linearly on the air gap length but is proportional to $1/l$, where $l$ is the air gap length, the forces will no longer even each other out and the beam will see a force pulling it in the same direction as the displacement. From a dynamical point of view this can be seen as an additional negative stiffness that is introduced into the system when the beam oscillates. As a result the oscillation frequency of the first bending mode will decrease.

Additionally the time changing magnetic field will induce eddy currents in the stator yoke counter acting the change of the magnetic field. The result is that the peak of the magnetic field has a short delay compared to the peak of the displacement.
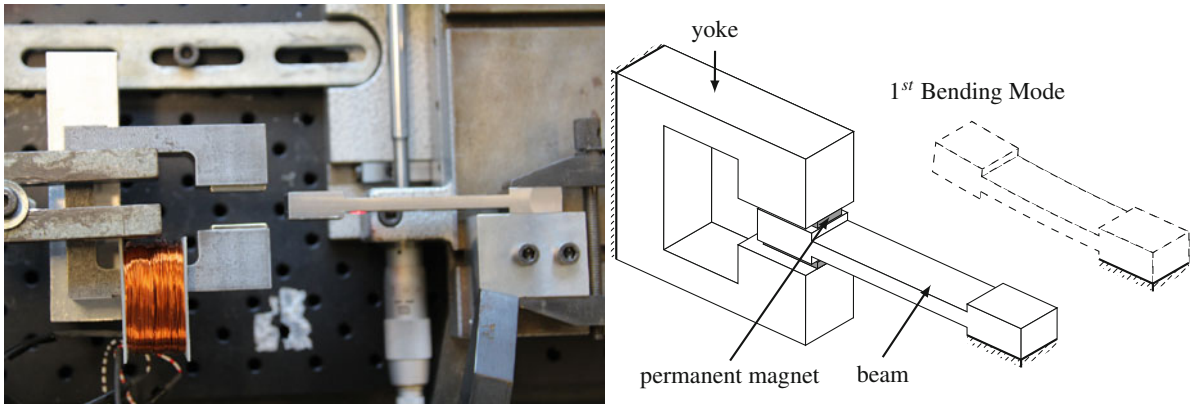


**Fig. 2.1** The test rig used for measurements

**Table 2.1** Specification of permanent magnets as documented by the suppliers (if documented)

| Property | Value |
| --- | --- |
| Height | 2 mm |
| Length | 20 mm |
| Width | 10 mm |
| Remanence flux density | 1.32–1.37 T |
| Coercity | 860–995 $\frac{kA}{m}$ |
| Relative permeability | 1.056–1.26 |
| Conductivity | 5882–9090.9 $\frac{S}{m}$ |

The force acting on the beam is therefore smaller while it moves away from the equilibrium position than when it moves towards it. This slows the oscillation down resulting in an increased damping. However the force is not linearly dependent on the velocity of the beam. This distorts the oscillation behavior of the beam slightly.

### 2.2.2 Mathematical Description of the System

The system consists of two domains: the mechanical structural dynamics of the beam and the magnetic field. It is therefore necessary to use a coupled model of these two physics to describe it completely [6]. The mechanical system can be described as a second order system

$$\rho \ddot{u}_i + \frac{\partial \sigma_{ij}}{\partial x_j} + f_{i,ext} = 0 \tag{2.1}$$

where $\sigma$ denotes the stress tensor and $f_{ext}$ the external force. The magnetic field can be described by the magnetic vector potential $\mathbf{A}$

$$\nabla \times \frac{1}{\mu} \nabla \times \mathbf{A} = -\gamma \frac{\partial \mathbf{A}}{\partial t} + \frac{1}{\mu} \nabla \times \mathbf{B}_r \tag{2.2}$$

where $\mu$ represents the permeability of the material, $\mathbf{B}_r$ the remanence flux density of the magnets and $\gamma$ the conductivity of the material.

Both parts of the system can store energy. Assuming a conservative system the energy between the mechanical system and the magnetic domain can be exchanged in both directions. The total energy in the system can therefore be calculated by

$$W = W_{mech} + W_{mag} = W_{kin} + W_{pot} + W_{mag}$$

This can be seen as a potential energy for small displacements (the magnetic potential is not defined for all points in the domain due to singularities at corners. However as long as the integration path does not encircle such a singularity the energy is conservative.) As stated in [5] the change of the magnetic field energy can be described by

$$dW_{mag} = i \, d\lambda + f_{mag} du \tag{2.3}$$

where $\lambda$ is the flux linkage, $i$ the currents in any eventual coils, $f_{mag}$ the magnetic force and $u$ the displacement. In this system however we can ignore the first term on the right hand side as there are no coils present. Extending this kind of analysis to the whole system it can be concluded that the only ways of energy entering or leaving the system is by means of external forces $f_{ext}$, coils, mechanical friction and ohmic losses.

$$dW = d \cdot \dot{u} + \gamma \cdot i_{eddy} + i_{coil} d\lambda + f_{ext} \cdot du \tag{2.4}$$

the above mentioned energy exchange by force $f_{mag} \cdot du$ becomes in this case an internal energy conversion from the magnetic domain to the mechanical domain and vis versa. It can be seen from (2.3) the magnetic force can be calculated using the principle of virtual work

$$f_{mag} = \frac{\partial W_{mag}}{\partial \mathbf{u}} \tag{2.5}$$

### 2.2.3 Parameter Identification

In order to determine the magnet properties of the steal used for beam and yoke impedance measurements were conducted. The permeability of metals depends on the manufacturing process. Therefore it is hard to predict this property beforehand. However, this property can be determined by measuring the impedance of a coil winded around the beam or the yoke. This property depends mainly on the conductivity of the material and the permeability. For structural steal that is used in this case the conductivity is roughly known. Therefore the impedance can be used to approximate the permeability.

By simulating the same system in a 3D FEM program the permeability of the material can be estimated. Figure 2.2 shows the comparison between the measured values for the inductance and resistance and the calculated values for different permeabilities and conductivities of the iron material. The instrument used was lacking the capability to measure below a frequency of 20 Hz. It is presumed that due to the skin effect in the iron the inductance drops rapidly for some frequencies
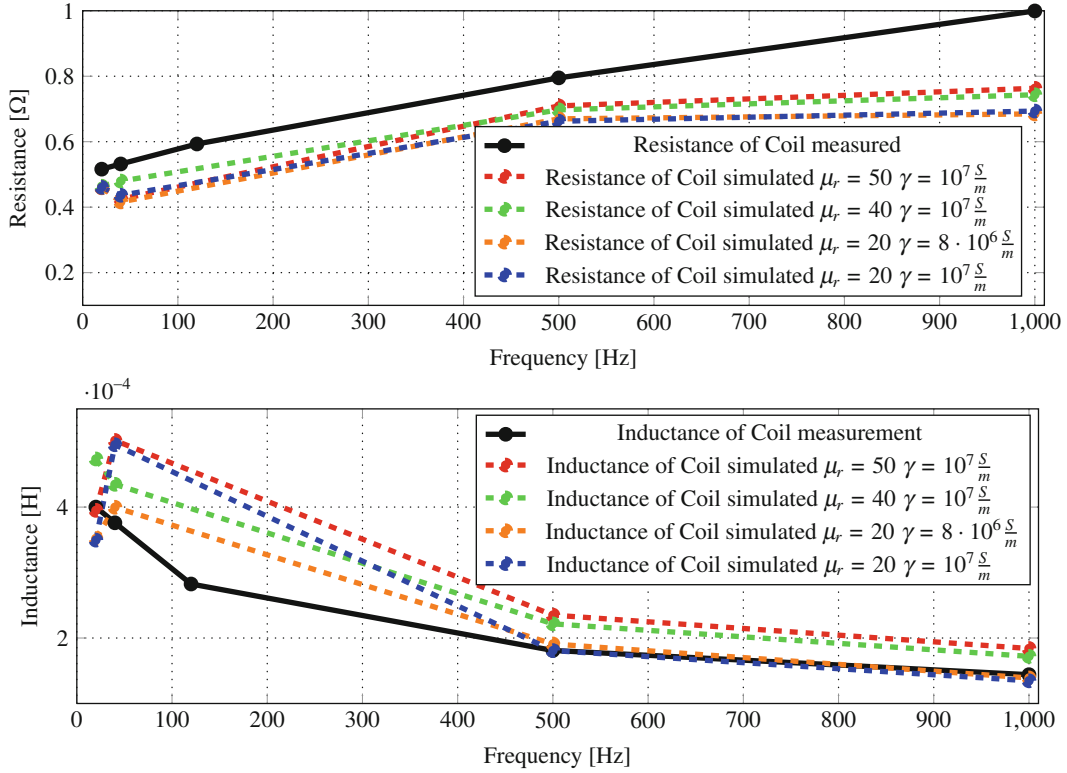
**Fig. 2.2** Impedance measurements of the stator yoke

below 20 Hz. Being able to measure this drop at very low frequencies would increase the impact of different permeability and conductivity values on the inductance leading to a more accurate determination of the material properties. At the frequencies measured it can be seen in Figs. 2.3 and 2.2 that the variation of the values has little effect on the inductance making a property identification difficult.

It should also be noted that the devices used has a higher accuracy at higher frequencies. At 20 Hz the error is around 1% of the measured. Therefore it is more important to properly fit the measured data to the simulated one at higher frequencies (Table 2.2).

## 2.3   3D FEM Model

Above it was discussed that the oscillation are not linear oscillation but slightly distorted. However, in the computer model the assumption is made that the coupled system oscillates linearly around the equilibrium position.

In order to calculate the eigenparameters of this model a monolithic formulation is necessary as it has been done in [3], in [10] for electro-mechanical coupling and in [1] for piezo elements. A 3D analysis of the magnetic field is necessary because the change in magnetic field density can only be predicted accurately by taking the fringe effects around the edges of the magnets and the beam into account. A 2D model would neglect parts of the edges of the system and hence also part of the fringe effects. As a result the calculated change of magnetic force density due to the movement of the geometry that depends on the magnetic flux density would also be underestimated in a 2D model. This would lead to an underestimation of the effect of interest too.

The FEM formulation for the uncoupled system can be looked up in literature [6, 15]. The derivation can be started from the energy of the system and by derivation with respect to the dofs $\mathbf{q}_u$ the stiffness and mass matrices for the uncoupled system can be derived. The continuous function $\mathbf{A(x)}$ and $\mathbf{u(x)}$ are approximated by the shape functions $\mathbf{N(x)}$ and the degrees of freedom $\mathbf{q} = [\mathbf{q}_u \mathbf{q}_A]$ of the discrete system.

$$\mathbf{u} = \mathbf{N(x)} \cdot \mathbf{q}_u$$

$$\mathbf{A} = \mathbf{N(x)} \cdot \mathbf{q}_A$$
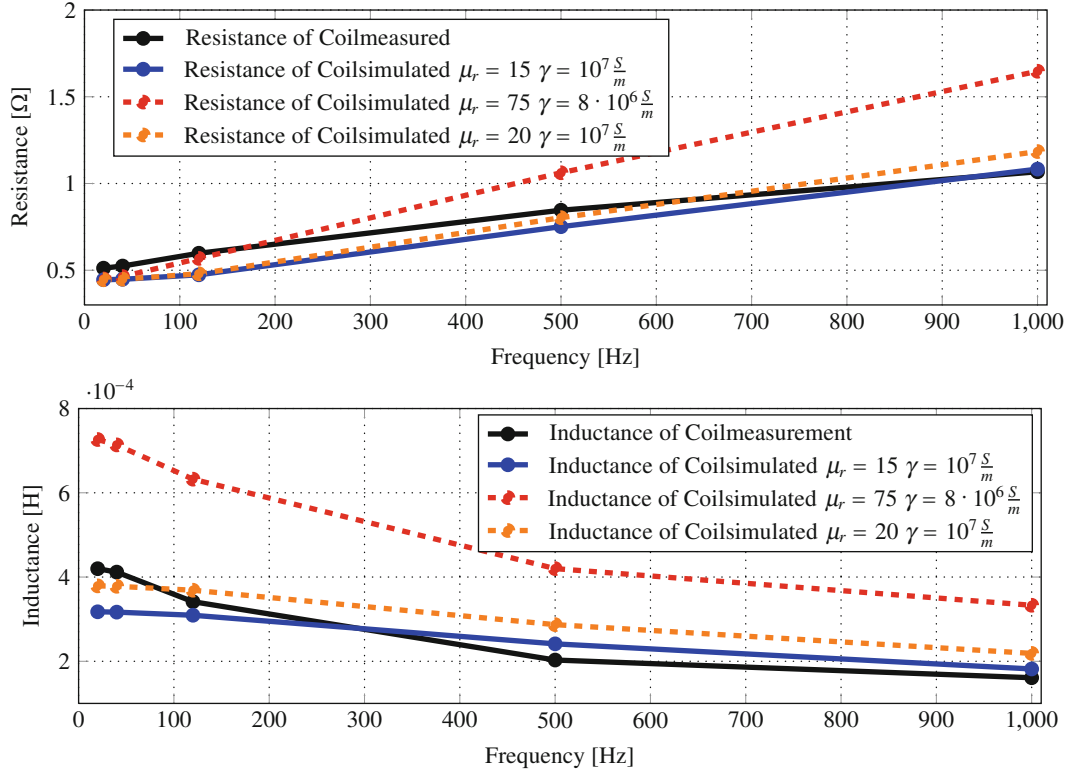
**Fig. 2.3** Impedance measurements of the beam

**Table 2.2** Chosen parameters for the models

| Property | Value |
|---|---|
| Remanence flux density | 1.32 T |
| Relative permeability | 1.06 |
| Conductivity | $0.6 \cdot 10^6 \ \frac{S}{m}$ |
| Relative permitivity | $1 \ \frac{F}{m}$ |
| Properties of stator-yoke | |
| Conductivity | $10^7 \ \frac{S}{m}$ |
| Relative permitivity | $1 \frac{F}{m}$ |
| Relative permeability | 20 |
| Properties of beam | |
| Conductivity | $10^7 \ \frac{S}{m}$ |
| Relative permitivity | $1 \frac{F}{m}$ |
| Relative permeability | 20 |
| Mass matrix Rayleig damping coefficient | 40 |
| Stiffness matrix Rayleig damping coefficient | $6 \cdot 10^{-6}$ |

Applying these approximations to the energies we can derive the matrices for the discrete system.

$$\mathbf{K}_{uu} = \frac{\partial^2 W_{pot}}{\partial \mathbf{q}_u^2} = \frac{\partial^2}{\partial \mathbf{q}_u^2} \frac{1}{2} \int_\Omega \mathbf{u}^T \mathbf{C} \mathbf{u} d\Omega \tag{2.6}$$

with **C** being the material stiffness matrix which is constant assuming a linear elastic material and a first order finite element.

The Mass matrix can be calculated by taking the second derivative of the kinetic energy with respect to the acceleration of the displacement

$$\mathbf{M}_u = \frac{\partial^2 W_{kin}}{\partial \dot{\mathbf{q}}_u^2} = \frac{\partial^2}{\partial \dot{\mathbf{q}}_u^2} \frac{1}{2} \int_\Omega \dot{\mathbf{u}}^T \rho \dot{\mathbf{u}} d\Omega \tag{2.7}$$

Rayleigh damping was used to approximate the damping behavior of the beam. The coefficients of the Rayleigh damping $\alpha$ and $\beta$ were determined by measuring the damping ratio of the system without any interaction with the magnetic field. It was assumed that the damping ratio is the same for 417 Hz and 370 Hz. The Rayleigh damping coefficients were tuned in a 3D FEM model without any magnetic coupling until the measured damping ratio for the two frequencies was reached.

$$\mathbf{D}_u = \alpha \mathbf{M}_u + \beta \mathbf{K}_{uu} \tag{2.8}$$

The magnetic stiffness matrix was calculated in the same way as the mechanical stiffness matrix. Instead of the potential energy the magnetic energy was used.

$$\mathbf{K}_{AA} = \frac{\partial^2 W_{mag}}{\partial \mathbf{q}_A^2} \int_\Omega (\nabla \times \mathbf{A})^T \frac{1}{\mu} (\nabla \times \mathbf{A}) d\Omega \tag{2.9}$$

the magnetic mass matrix $\mathbf{M}_A$ can be calculated out of the source term $\gamma \frac{\partial \mathbf{A}}{\partial t}$ using the Galerkin method.

$$\mathbf{M}_A = \frac{\partial^2}{\partial \mathbf{q}_A \partial \dot{\mathbf{q}}_A} \int_\Omega \mathbf{A}^T \gamma \dot{\mathbf{A}} d\Omega \tag{2.10}$$

For the calculation of the magnetic force vector $\mathbf{F}_{mag}$ the Maxwell stress tensor $T$ was used [11,12,14]. This tensor is derived from the principle of virtual work that can be derived from (2.3). It can be shown analog to [10] that the magnetic force can be calculated by

$$\mathbf{F}_{mag} = \frac{\partial}{\partial \mathbf{q}_u} \int_\Omega (\nabla \times \mathbf{A})^T \frac{1}{\mu} (\nabla \times \mathbf{A}) d\Omega \tag{2.11}$$

The magnetic force represents the first coupling (in this case from the magnetic domain to the mechanical domain). Due to the distortion of the domain caused by the displacement $\mathbf{u}$ the magnetic stiffness and mass matrix as well as the magnetic force vector depend on the displacement $\mathbf{u}$. For the magnetic stiffness and mass matrix this dependency is crucial because this dependency will cause a coupling between the mechanical displacement and the magnetic field.

With these matrices we can formulate the non linear set of equations that describe the coupled system.

$$\mathbf{M}_{uu} \cdot \ddot{\mathbf{q}}_u + \mathbf{D}_{uu} \cdot \dot{\mathbf{q}}_u + \mathbf{K}_{uu} \cdot \mathbf{q}_u = \mathbf{F}_{ext} + \mathbf{F}_{mag}(\mathbf{q}_u, \mathbf{q}_A) \tag{2.12}$$

$$\mathbf{M}_{\mathbf{A}}(\mathbf{q}_u) \cdot \dot{\mathbf{q}}_A + \mathbf{K}_{\mathbf{AA}}(\mathbf{q}_u) \cdot \mathbf{q}_A = \mathbf{J}_{ext} + \frac{1}{\mu}(\nabla \times \mathbf{B}_r)$$

Each physics for themselves is linear. Coupling the two physical domains will cause the complete set of PDEs to become non linear. Therefore in order to do a modal analysis they need to be linearized. As the oscillation of interest is around the undeformed configuration of the structure and the static magnetic field generated by the permanent magnets, the linearization point is given by those to states.

For such a linearization point (2.12) can be transformed into a linear monolithic system of equations:

$$\underbrace{\begin{bmatrix} \mathbf{M}_u & 0 \\ 0 & 0 \end{bmatrix}}_{\mathbf{M}} \begin{bmatrix} \ddot{\mathbf{q}}_u \\ \ddot{\mathbf{q}}_A \end{bmatrix} + \underbrace{\begin{bmatrix} \mathbf{D}_u & 0 \\ 0 & \mathbf{M}_A \end{bmatrix}}_{\mathbf{D}} \begin{bmatrix} \dot{\mathbf{q}}_u \\ \dot{\mathbf{q}}_A \end{bmatrix} + \underbrace{\begin{bmatrix} \mathbf{K}_{uu} & \mathbf{K}_{uA} \\ \mathbf{K}_{Au} & \mathbf{K}_{AA} \end{bmatrix}}_{\mathbf{K}} \underbrace{\begin{bmatrix} \mathbf{q}_u \\ \mathbf{q}_A \end{bmatrix}}_{\mathbf{q}} = \underbrace{\begin{bmatrix} \mathbf{F}_{ext} \\ \mathbf{J}_{ext} + \mathbf{L}_{PM} \end{bmatrix}}_{\mathbf{L}} \tag{2.13}$$

The coupling matrices $\mathbf{K}_{uA}$ and $\mathbf{K}_{Au}$ can be derived from the magnetic force and therefore from the energy stored in the magnetic field.

$$\mathbf{K}_{uA} = \frac{\partial \mathbf{F}_{mag}}{\partial \mathbf{q}_A} = \frac{\partial}{\partial \mathbf{q}_A} \left( \frac{\partial}{\partial \mathbf{q}_u} W_{mag} \right) = \frac{\partial}{\partial \mathbf{q}_u} \left( \frac{\partial}{\partial \mathbf{q}_A} W_{mag} \right) = \frac{\partial}{\partial \mathbf{q}_u} (\mathbf{J}_{int}) = \mathbf{K}_{Au} \tag{2.14}$$

Looking at Eq. (2.14) it can be assumed that the total stiffness matrix is symmetric. However, in the FEM code used for the simulation the stiffness coupling matrix $\mathbf{K}_{uA}$ is derived in another way which ruins this symmetry.

Using the Maxwell stress tensor $\mathbf{T}$ the specific magnetic force acting on a structure can be computed by

$$\mathbf{f}_{mag} = \nabla \cdot \mathbf{T} = \nabla \cdot \left( \mathbf{H} \mathbf{B}^T - \mathbf{I} \frac{\mathbf{H} \cdot \mathbf{B}}{\mu} \right) \tag{2.15}$$

where $\mathbf{I}$ denotes the identity matrix. The force acting on a whole domain can therefore be represented by the integral of the specific force on that domain

$$\mathbf{F}_{mag} = \int_{\Omega} \mathbf{f}_{mag} \mathrm{d}\Omega = \int_{\Omega} \nabla \cdot \mathbf{T} \mathrm{d}\Omega \qquad (2.16)$$

Using the divergence theorem we can write this integral as an integral over the surface of the domain $\partial\Omega$

$$\mathbf{F}_{mag} = \int_{\partial\Omega} \mathbf{n} \cdot \mathbf{T}(\mathbf{A}) \mathrm{d}\partial\Omega \qquad (2.17)$$

where $\mathbf{n}$ is the normal vector pointing outwards of the domain boundary. For a domain where the gradient of the magnetic field throughout the domain is almost zero the magnetic forces created within the domain are negligible. This is an assumption that holds for iron because the permeability of that iron is so high that the resulting gradients of the magnetic field are small compared to the gradients at its surface. In that case only the forces on the surface of the domain contribute to the total magnetic force. Therefore the projection of the magnetic forces from within the domain on its surface is negligible and therefore the therm $\mathbf{n} \cdot \mathbf{T}$ actually represents the local stress on the surface of the domain.

Starting the derivation of the stiffness matrix with (2.17) yields a different matrix than the derivation starting with (2.11). The same result has been discovered in [13] for electro-static field forces.

Starting from (2.17) we can the derive the coupling matrix $\mathbf{K}_{uA}$

$$\mathbf{K}_{uA} = \frac{\partial}{\partial \mathbf{q}_A} \int_{\partial\Omega} \mathbf{n} \cdot \mathbf{T}(\mathbf{A}) \mathrm{d}\partial\Omega \qquad (2.18)$$

The matrices formulated in (2.13) can be rewritten in the quadratic eigenvalue problem:

$$\left(\mathbf{K} + j \cdot \lambda_r \mathbf{D} - \lambda_r^2 \mathbf{M}\right) \mathbf{q}_r = 0 \qquad (2.19)$$

where $\mathbf{q}_r$ represent the eigenvector and $\lambda_r$ the eigenvalues. Solving this eigenvalue problem yields the modes and resonance frequencies of the coupled system.

## 2.4  Measurements

Using a laser doppler vibrometer (LDV) hammering tests where conducted to measure the frequency and damping behavior of the first bending mode of the beam. These measurements where done in three different positions of the beam: completely out of the air gap, completely inserted in the air gap and half way inserted in the air gap. The modal parameters where evaluated by fitting a decaying sinusoidal function to the data using a least square evaluation.

$$\underset{y_0,\, \omega_n,\, \zeta}{\text{minimize}} \left( \sum_t (x(t) - y(t - t_0))^2 \right) \quad \text{for } t \in [t_0, t_0 + \Delta t] \qquad (2.20)$$

$$\text{with} \quad y(t) = y_0 \cdot e^{-2\pi \omega_n (\zeta + \sqrt{\zeta^2 - 1})}$$

where $\zeta$, $\omega_n$ and $y_0$ are the parameters to identify. $I$ is the cost function and $x(t)$ the measurement data. The measured data $x(t)$ and the decaying sinusoidal function $y(t)$ are aligned by setting $x(t_0) = max(x(t))$ and choosing an arbitrary length $\Delta t$. The measured parameters are shown in Table 2.3.

**Table 2.3** Simulation results and measurements

| | 3d-Model | | Measurement | |
|---|---|---|---|---|
| | Frequency | Damping | Frequency | Damping |
| No EM coupling | 417.1 Hz | $\zeta = 1.66\%$ | 417 Hz | $\zeta = 1.66\%$ |
| With EM coupling | 371.7 Hz | $\zeta = 3.32\%$ | 370 Hz | $\zeta = 3.6\%$ |
| Half EM coupling | 387.1 Hz | $\zeta = 2.62\%$ | 384.6 Hz | $\zeta = 2.25\%$ |

## 2.5 Results

The measurements show clearly a trend towards more damping and a lower system in the system than before. Table 2.3 shows the simulated and measured eigenfrequencies and damping ratios of the system. For the case where the beam is completely inserted in the air gap, the frequency change is over estimated by the 3D model while the damping is underestimated. Considering that the system introduced is not linear the expected agreement with the linear 3D model cannot be perfect. It was shown that it is possible to do a approximation using the linearized set of equations and a linear modal analysis.

## 2.6 Conclusion and Outlook

A monolithic eigenvalue formulation for magneto-mechanical coupled problems was introduced. It could be shown that a 3D FEM model using this formulation can predict the eigenbehavior of magneto-mechanical coupled systems. Although the measured data deviates slightly from the simulated data it is clear that the effects of interest are qualitatively correctly predicted by the model.

In future research the demonstrated methods will be applied to wind turbine generators in order to allow a coupled modal analysis of the system and to analyze to what extend the structural dynamics are influenced by the magnetic field.

## References

1. Allik H, Hughes TJR (1970) Finite element method for piezoelectric vibration. Int J Numer Meth Eng 2(2):151–157
2. Belahcen A (2005) Magnetoelastic coupling in rotating electrical machines. IEEE Trans Magn 41(5):1624–1627
3. Belahcen A (2006) Vibrations of rotating electrical machines due to magnetomechanical coupling and magnetostriction. IEEE Trans Magn 42(4):971–974
4. Furlan M, Cernigoj A, Boltezar M (2003) A coupled electromagnetic-mechanical-acoustic model of a DC electric motor. COMPEL: Int J Comput Math Electr Electron Eng 22(4):1155–1165
5. Herbert Woodson JRM (1968) Electromechanical dynamics. Wiley, New York
6. Kaltenbacher M (2007) Numerical simulation of mechatronic sensors and actuators. Springer, New York
7. Maxwel JC (1865) A dynamical theory of the electromagnetic field
8. Pellerey P, Lanfranchi V, Friedrich G (2012a) Coupled numerical simulation between electromagnetic and structural models. Influence of the supply harmonics for synchronous machine vibrations. IEEE Trans Magn 48(2):983–986
9. Pellerey P, Lanfranchi V, Friedrich G (2012b) Coupled numerical simulation between electromagnetic and structural models. Influence of the supply harmonics for synchronous machine vibrations. IEEE Trans Magn 48(2):983–986
10. Rochus V, Rixen DJ, Golinval J-C (2006) Monolithic modelling of electro-mechanical coupling in micro-structures. Int J Numer Method Eng 65(4):461–493
11. Sanchez-Grandia R, Vives-Fos R, Aucejo-Galindo V (2006) Magnetostatic Maxwell's tensors in magnetic media applying virtual works method from either energy or co-energy. Eur Phys J Appl Phys 35(01):61–68
12. Sanchez Grandia R, Aucejo Galindo V, Usieto Galve A, Vives Fos R (2008) General formulation for magnetic forces in linear materials and permanent magnets. IEEE Trans Magn 44(9):2134–2140
13. Stephan H (2010) Modeling strategies for electro - mechanical microsystems with uncertainty quantification door. PhD thesis
14. Vandevelde L (2001) A survey of magnetic force distributions based on different magnetization models and on the virtual work principle. IEEE Trans Magn 37(5):3405–3409
15. Zienkiewicz OC, Taylor RL, Zhu JZ (2005) The finite element method: its basis and fundamentals, vol 1 of The finite element method. Elsevier Butterworth-Heinemann

# Chapter 3
# Extraction of Modal Parameters of Micromachined Resonators in Higher Modes

**AVSS Prasad, K.P. Venkatesh, Navakanta Bhat, and Rudra Pratap**

**Abstract** In this paper, a micro machined resonator is fabricated using SOI MUMPs process. A total of 50 out-of-plane mode shapes and their corresponding modal parameters (resonant frequency and damping) are extracted. With the applied voltage, due to joule heating, natural frequency ($f_n$) and Quality (Q) factor change. This can be effectively used for tuning the resonator. A detailed modal analysis is carried out using an FEM simulator to compute the modal parameters across all the modes and results are within 5% of the data measured using a Laser Vibrometer. Q is estimated using the half-power point approach for the first 42 modes. It is also observed that Q goes up by a factor > 2 for modes beyond 27, as only a portion of the structure contributes to modal displacement. At higher voltages, thermal softening is observed due to local heating which results in structure behaving like a coupled resonator. Under these conditions, peak splitting is observed. This structure can be used in different sensor and actuator applications depending on the mode of operation.

**Keywords** SOIMUMPs • Natural frequency • Damping • Higher modes • Modal parameters • Thermal softening

## 3.1 Introduction

Micromachined resonators have potential applications in RF-MEMS, clock oscillators, resonant sensors such as biological mass detectors, optical communication systems, displays, barcode readers and biomedical imaging systems [1–3]. The actuation mode used for a given device depends on the target application. There are several actuation schemes that are proposed and they can be classified into electrostatic, piezoelectric, electromagnetic and electrothermal types [4]. The response of a resonator to any actuation mechanism depends on two important characteristics of the resonator—it's resonant frequency and quality factor [5]. It is an easy task to estimate resonant frequencies using numerical tools. However, it is very challenging to experimentally capture the higher modes of vibration of the resonator as the amplitude of vibrations reduces drastically in higher modes.

A resonator can be used in a variety of applications depending on the mode shape and resonant frequency. For example an electrothermal actuator can be used as an accelerometer in the first mode and as a micro mirror in second and third modes [1]. So it is essential to determine resonant frequencies and mode shapes which dictate the suitability of their application. Many researchers are exploring ways to capture higher modes of vibration. Liang-chia chen [6] reported data till seventh mode of vibrations for an AFM cantilever. Mitchell [7] in early 1998 has reported data for a macro scale plate (with dimensions $18 \times 18 \times \frac{1}{8}$ in) upto the ninth normal mode. Venkatesh [1] was successful in capturing the first 28 modes of electrothermal actuator using a microsystem analyzer.

The current study is partly motivated by a need to explore higher modes of vibration in MEMS devices for sensing purposes. In devices constructed using high Q materials like silicon, most of the damping in oscillations is due to squeeze film effects [8–10]. It has been reported in the literature [2] that it is possible to reduce this kind of damping and increase the Q factor of MEMS resonators by exciting them in higher modes. During this study, it is found that we are able to easily capture high modes of oscillations because the vibrating structure is of micro scale.

AVSS Prasad • K.P. Venkatesh • N. Bhat • R. Pratap (✉)
Centre for Nano Science and Engineering, Indian Institute of Science, Bangalore, India 560012

Department Mechanical of Engineering, Indian Institute of Science, Bangalore, India 560012
e-mail: pavss@ece.iisc.ernet.in; venkyrp@mecheng.iisc.ernet.in; navakant@ece.iisc.ernet.in; pratap@mecheng.iisc.ernet.in

**Fig. 3.1** Image of
micromachined electrothermal
actuator
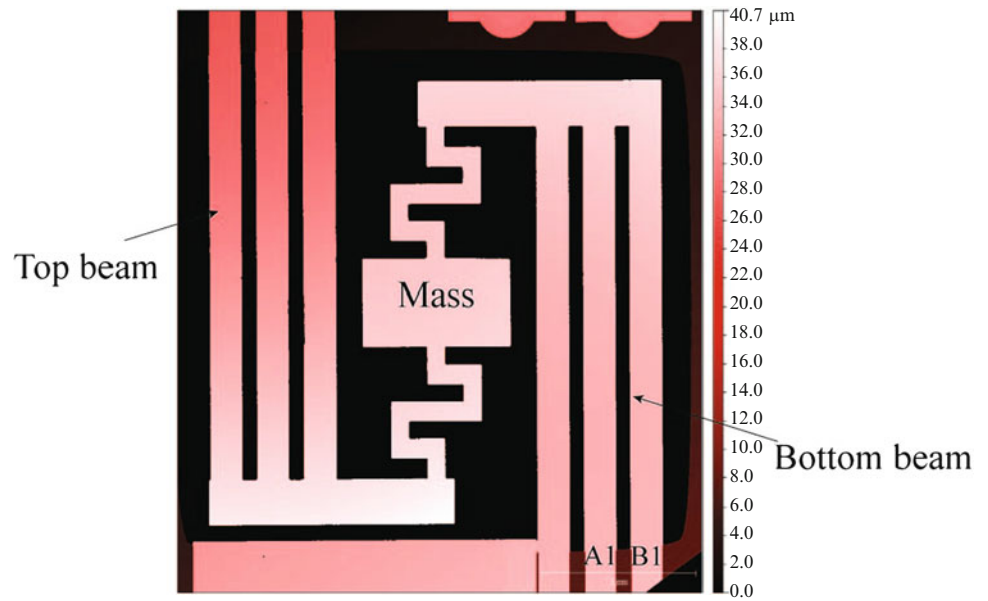


**Table 3.1** Mechanical and
physical parameters of the
electrothermal actuator

| Parameter | Value |
|---|---|
| Length of straight beams connecting to the substrate, $L$ | $3{,}500\,\mu$m |
| Width of straight beams connecting to the substrate, $w$ | $200\,\mu$m |
| Thickness of structure, $t$ | $25\,\mu$m |
| Proof mass size | $200 \times 200\,\mu\text{m}^2$ |
| Young's modulus, $E$ | 130 GPa |
| Poisson ratio, $\nu$ | 0.22 |
| Density, $\rho$ | $2{,}300\,\text{kg/m}^3$ |
| Co-efficient of thermal expansion, $\alpha$ | $2.33 \times 10^{-6}/°\text{C}$ |

In this study we used a MEMS resonator (a electrothermal acutator) fabricated using SOI MUMPs process [11] from MEMSCAP. Structure of the fabricated device is shown in Fig. 3.1. This structure consists of a proof mass suspended by a set of meandering beams. These meanders are connected to the substrate by means of a set of straight beams that are anchored on one side. For ease of probing, contact pads are provided on these straight beams at the end, where they are anchored on the substrate. Table 3.1 provides the details of geometric and material properties of the structure used in simulations.

In our experiments with this resonator, we could capture up to 50 out-of-plane modes with single excitation. FEM based numerical simulations have confirmed that the captured mode shapes and the measured frequencies are very close to the theoretically predicted values. Details of experiments and numerical simulations, carried out, are discussed in the subsequent sections.

## 3.2 Theory

In this section we outline the numerical and experimental procedures that are used to calculate the natural frequency of the resonator.

### 3.2.1 Functional Description

This structure can be operated by applying potential between any two pads. In this study, voltage is applied between the pads A1 and B1. Physically all the pads are anchored on the substrate and therefore from thermal point of view all pads will be at the ambient temperature. Rest of the structure is floating in a cavity of 400 μm. As the applied voltage is increased, due to joule heating, temperature of the beam tends to increase. The actual temperature distribution depends on electrical

**Fig. 3.2** Working principle of
laser doppler vibrometer
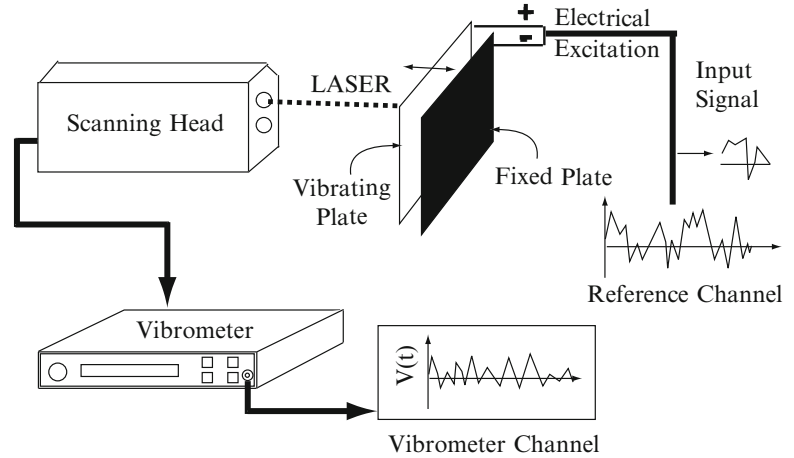


conductivity, thermal conductivity, convection, radiation properties and their dependency on temperature. As temperature goes up, beams tend to become softer and therefore reduced stiffness. By virtue of the design, temperature along the beam of interest will not be uniform and also localized heating is expected.

### 3.2.2   Numerical Procedure

Modal analysis of the structure is carried out using commercially available finite-element simulator, ANSYS [12]. The numerical computation of natural frequencies and the mode shapes involves different steps. First, the geometric modelling is done using CoventorWare, a MEMS specific design tool. For geometric modeling, one has to give the mask data and fabrication steps required in realizing the 3D structure. The generated 3D model is imported into ANSYS and the structure is meshed with 50,000 eight-noded brick elements, and zero-displacement and zero rotation boundary conditions are applied on the substrate. Modal analysis is carried out to estimate the eigen values and eigen vectors of the structure. Natural frequencies and the corresponding mode shapes for all out-of-plane modes are extracted in the post processing step.

### 3.2.3   Experimental Procedure

The working principle of the setup is schematically shown in Fig. 3.2. The experimentation involves electrical excitation (say $V_{input} = V_{dc} + V_{ac}$) that causes the suspended structure to vibrate. The laser spot from the interferometer in the scanning head is positioned on a scan point on the object by means of mirrors and is scattered back. The back scattered laser light interferes with the reference beam in the scanning head. A photo detector records the interference. A decoder in the vibrometer provides a voltage which is proportional to the velocity of the scanned point parallel to the measurement beam. The voltage is digitized and processed as the vibrometer signal [4, 13]. The output signal can be obtained as velocity or displacement signal using the velocity or the displacement decoder.

In the device under investigation, due to peltier effect, hot and cold junctions are formed when voltage applied between two pads. Due to thermal expansion, the structure tends to bend. Upon application of a sinusoidal signal, structure starts to vibrate about its equilibrium position. To experimentally capture the modal parameters (resonant frequency and damping) of the structure, a pseudorandom signal of voltage $V_{dc} + V_{ac}$ is applied during the experimentation. After averaging the FRF of the output signal over 50 times, we determine the resonant frequency of the structure using the frequency response curve, and the corresponding mode shapes are obtained from presentation mode of the vibrometer.

## 3.3   Results and Discussion

We now present the results of the numerical and experimental studies. In contrast to such studies at macroscales, we used experimental results here to validate the numerical results since the finite element model of the structure is likely to have more errors due to uncertainties in material properties and geometric parameters.

**Fig. 3.3** Frequency response of electrothermal actuator
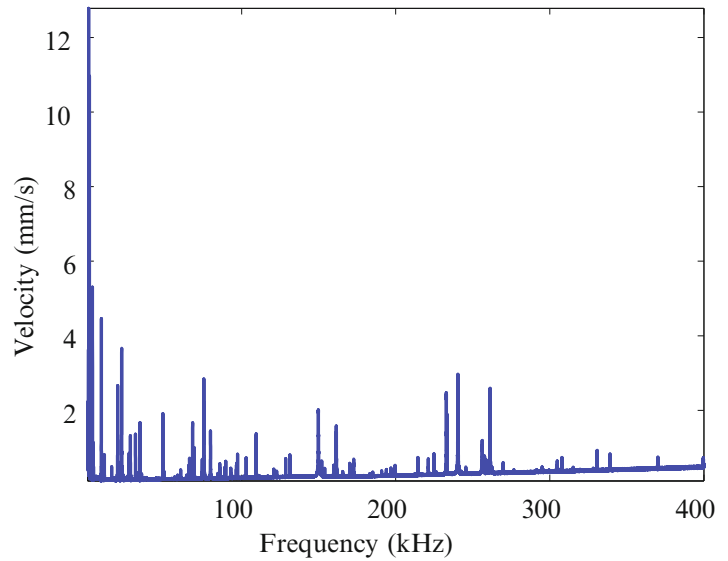


**Table 3.2** Comparison between experimental and numerical results

| Mode No. | $f_{exp}$ (kHz) | $f_{Num}$ (kHz) | % error $\left| \frac{f_{exp} - f_{num}}{f_{exp}} \right| \times 100$ | Mode No. | $f_{exp}$ (kHz) | $f_{Num}$ (kHz) | % error $\left| \frac{f_{exp} - f_{Num}}{f_{exp}} \right| \times 100$ |
|---|---|---|---|---|---|---|---|
| 1 | 3.17 | 3.1634 | 0.21 | 26 | 161.27 | 159.57 | 1.05 |
| 2 | 3.67 | 3.5704 | 2.71 | 27 | 168.15 | 161.32 | 4.06 |
| 3 | 8.91 | 8.9503 | 0.45 | 28 | 169.97 | 163.98 | 3.52 |
| 4 | 10.88 | 11.01 | 1.19 | 29 | 172.4 | 172.47 | 0.04 |
| 5 | 19.48 | 18.96 | 2.67 | 30 | 184.95 | 182.95 | 1.08 |
| 6 | 22.05 | 21.567 | 2.19 | 31 | 199.7 | 198.25 | 0.73 |
| 7 | 26.91 | 26.881 | 0.11 | 32 | 201.89 | 200.36 | 0.76 |
| 8 | 27.67 | 27.727 | 0.21 | 33 | 217.16 | 215.62 | 0.71 |
| 9 | 30.8 | 30.48 | 1.04 | 34 | 218.54 | 217.49 | 0.48 |
| 10 | 32.8 | 31.338 | 4.46 | 35 | 221.16 | 219.39 | 0.80 |
| 11 | 33.8 | 33.66 | 0.41 | 36 | 224.98 | 219.39 | 2.48 |
| 12 | 48.77 | 48.111 | 1.35 | 37 | 225.21 | 227.91 | 1.20 |
| 13 | 68.07 | 67.689 | 0.56 | 38 | 226.64 | 229.7 | 1.35 |
| 14 | 69.02 | 71.986 | 4.30 | 39 | 232.82 | 231.47 | 0.58 |
| 15 | 75.41 | 73.26 | 2.85 | 40 | 236.67 | 235.75 | 0.39 |
| 16 | 79.71 | 78.113 | 2.00 | 41 | 240.51 | 236.98 | 1.47 |
| 17 | 86.2 | 84.085 | 2.45 | 42 | 242.74 | 246.6 | 1.59 |
| 18 | 87.86 | 85.293 | 2.92 | 43 | 256 | 247.47 | 3.33 |
| 19 | 89.14 | 87.624 | 1.70 | 44 | 257.6 | 255.65 | 0.76 |
| 20 | 92.84 | 90.556 | 2.46 | 45 | 258.66 | 255.93 | 1.06 |
| 21 | 96.39 | 94.437 | 2.03 | 46 | 261.12 | 259.99 | 0.43 |
| 22 | 102.66 | 101.57 | 1.06 | 47 | 274.23 | 273 | 0.45 |
| 23 | 109.22 | 106.7 | 2.31 | 48 | 295 | 295.17 | 0.06 |
| 24 | 150.01 | 147.87 | 1.43 | 49 | 304.86 | 303.12 | 0.57 |
| 25 | 153.03 | 149.95 | 2.01 | 50 | 308.77 | 305.53 | 1.05 |

### 3.3.1 Natural Frequency

Figure 3.3 shows the frequency response of the structure. Natural frequency is estimated from the frequency response using peak picking approach. Table 3.2 provides the experimental and numerical values of natural frequencies for the first 50 out-of-plane modes of the resonator. It was noticed that error is within 5% of the experimentally obtained results across all the modes. The corresponding mode shapes are shown in Fig. 3.4.
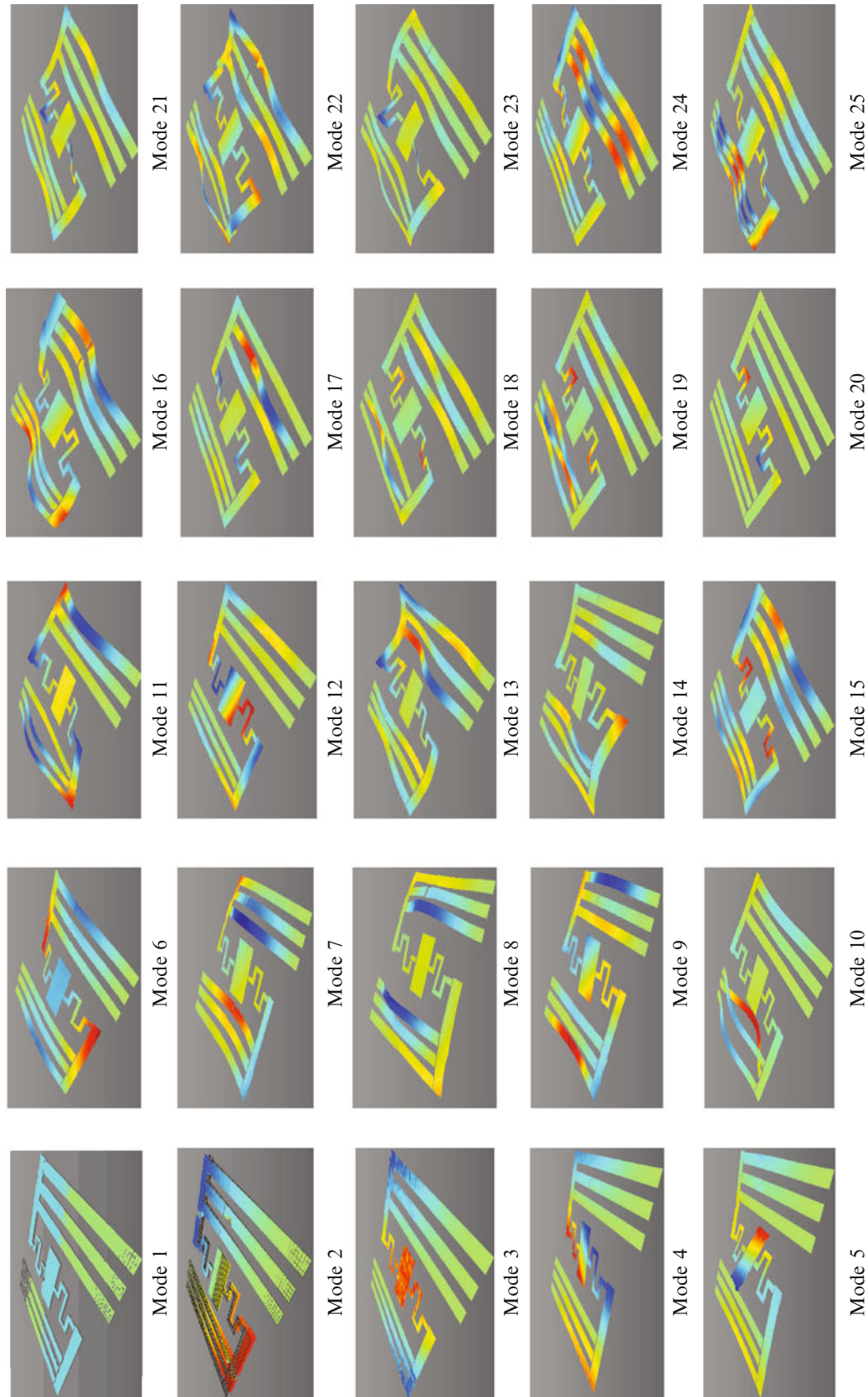
**Fig. 3.4** Modeshapes of electrothermal actuator

Mode 46

Mode 47

Mode 48

Mode 49

Mode 50

Mode 41

Mode 42

Mode 43

Mode 44

Mode 45

Mode 36

Mode 37

Mode 38

Mode 39

Mode 40

Mode 31

Mode 32

Mode 33

Mode 34

Mode 35

Mode 26

Mode 27

Mode 28

Mode 29

Mode 30
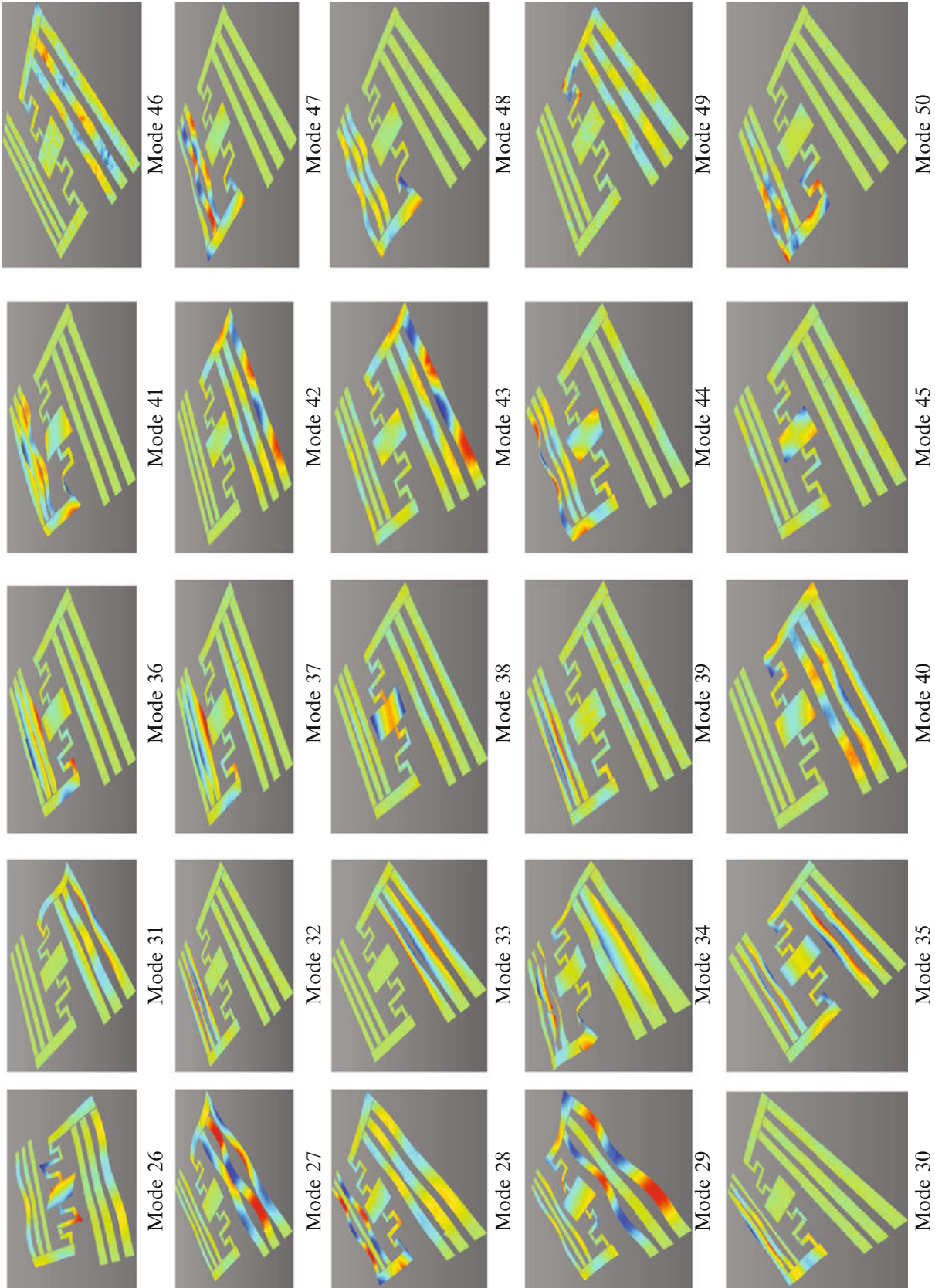
**Fig. 3.4** (continued)

**Fig. 3.5** Quality factor of the MEMS actuator in several modes
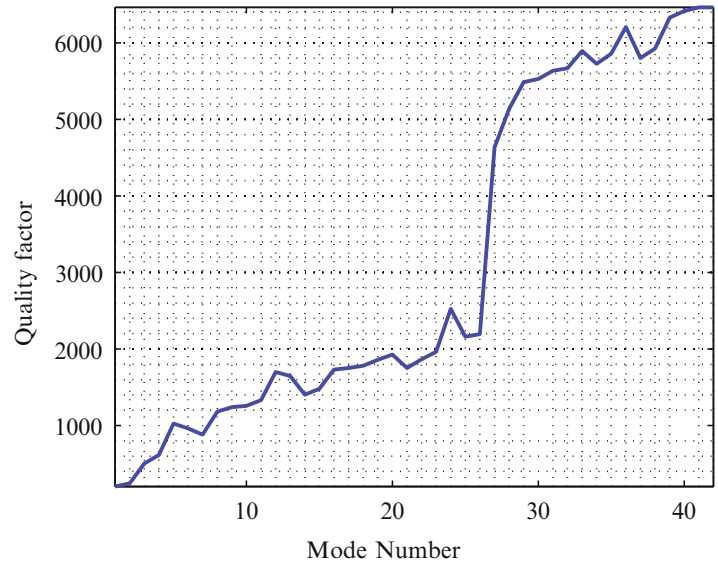


**Fig. 3.6** Power law relationship of quality factor with natural frequency
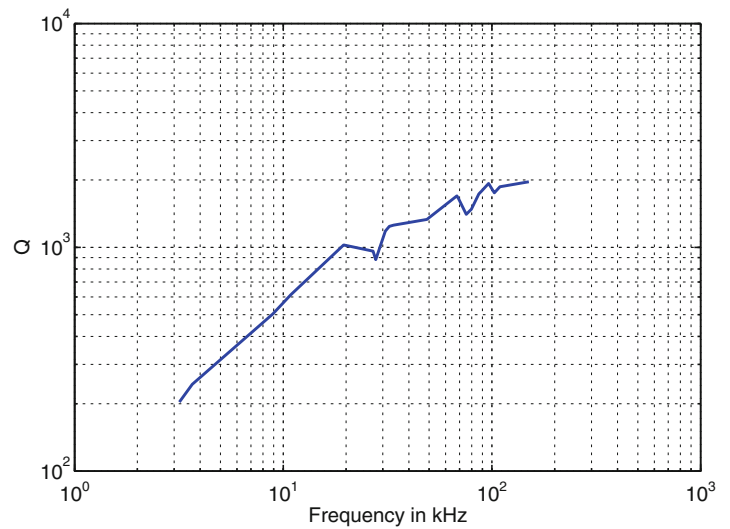
### 3.3.2  Damping

Quality factor (a measure of damping) is estimated from the frequency response using half power point approach, given by

$$Q = \frac{f_n}{(f_1 - f_2)} \tag{3.1}$$

where $f_n$ is the natural frequency and $f_1$ *and* $f_2$ are the 3dB frequencies. Figure 3.5 shows the Q factor distribution across several modes of the structure. It can be noticed that Q factor is fairly high for microstructure (1,000s), in comparison to its macro counterparts. It can also be seen that Q factor goes up by a factor > 2 after 27th mode, which can be attributed to the fact that only a portion of the structure is contributing to modal displacement. Figure 3.6 shows the variation of Q factor with the natural frequency. Using MATLAB, curve fitting is done to derive an empirical relation between the two and the same is found to be a power relation. To be specific, $Q \propto f_n^{1.25}$.

**Fig. 3.7** Frequency response
with different DC potentials
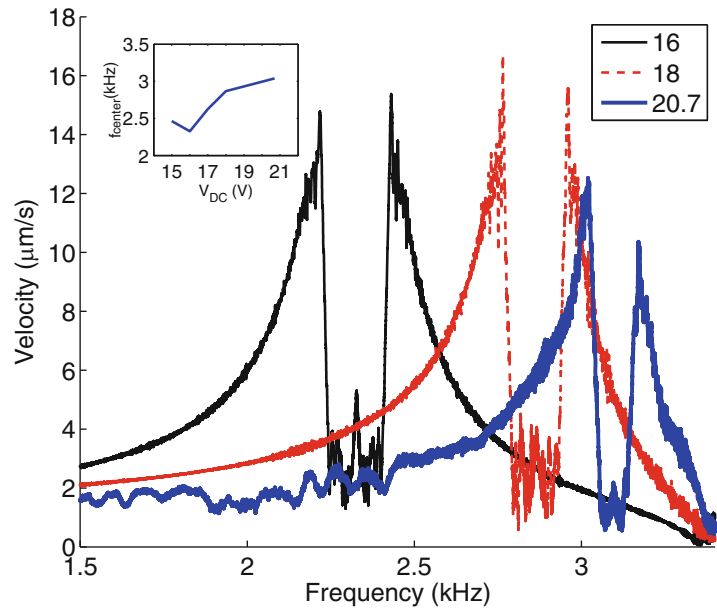


**Fig. 3.8** Temperature profile
along the structure
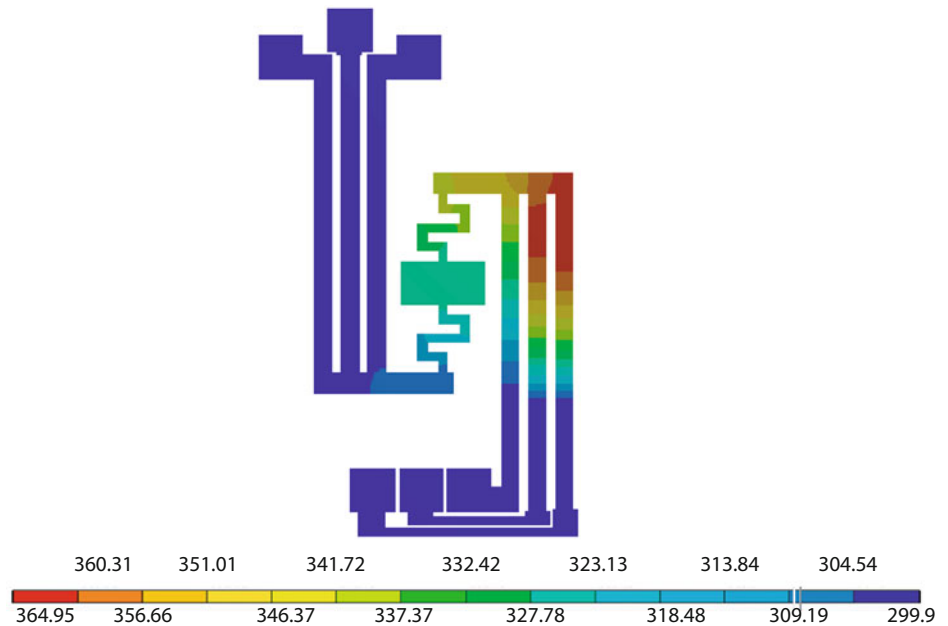


### 3.3.3 *Influence of Loading*

The fabricated thermal actuator is characterized by applying varying potentials ($V_{DC} + V_{AC}$). With varying DC bias voltage, resonant frequency was found to be changing due to thermal dependent softening of the beams [14]. For example, natural frequency measured is varying between 3.1 and 2.9 KHz, when $V_{DC}$ is swept from 3 to 12V and $V_{AC}$ is of 5V. Figure 3.7 shows the frequency response for higher values of DC voltage (greater than 13V). We observe that for $V_{DC} \geq 13$, the frequency response starts splitting into an equivalent response of a system with two coupled resonators. At higher voltages, one can see two effects (a) increase in the resonant frequency with temperature and (b) peak splitting. Increase in frequency is due to the fact that the effective mass of the spring is reducing due to excessive softening of the spring. As these results are very repeatable and consistent, one can change the bias voltage to tune the resonant frequency of a given structure.

Figure 3.8 gives temperature profile along the length of the beam for a given applied voltage. It is evident from this figure that there is a huge temperature gradient along the beam. Also, beam tends to become very hot in a localized fashion. From the temperature distribution point of view, temperature is low at the bend due to the fact that there is an additional thermal

mass that leads to more thermal conduction. These results can be used to design structures where one can create hot spots at the required locations along the length of the beam. It is also observed that the adjacent beams gain higher temperature due to convection effect.

## 3.4   Conclusion

We have experimentally determined 50 modes of out-of-plane vibrations of a MEMS resonator. Experimentally measured frequencies are compared with the numerically computed values (using Ansys). Good correlation is observed between the two and percentage error is less than 5%. This work shows that micro resonators can be easily excited in fairly higher modes, in contrast to their macro counterparts. The accuracy of results shows that the simulation models can be used for analysis of these structures and their suitability for different applications.

We have successfully extracted damping for the first 42 modes of vibration of the fabricated structure. It was noticed that quality factor increases by a factor $> 2$ for modes beyond 27. Same can be used in several applications involving high Q applications, such as biological mass detectors. Our experiments show change in natural frequency and Q factor with the applied bias voltage due to joule heating. This particular characteristic can be used to control different design parameters ($f_n$, Q factor). This can be achieved by generating controlled hot spots that lead to softening of the spring.

## References

1. Venkatesh KP, Pratap R (2009) Capturing higher modes of vibration of micromachined resonators. J Phys Conf 181:1–8,
2. Ashok Kumar P (2007) Analytical numerical and experimental studies of fluid damping in MEMS devices. Ph.D. thesis, Indian Institute of Science, Bangalore, India
3. Marc Madou J (1997) Fundamentals of microfabrication. CRC Press, Boca Raton, FL
4. POLYTEC, Advanced measurements by light http://www.polytec.com
5. Singiresu SR (1995) Mechanical vibrations. Wesley Publishing, New York
6. Chen L-C, et al. (2006) High bandwidth dynamic full-field profilometry for nano-scale charecterization of MEMS. J Phys 48:1058–1062
7. Mitchell LD, et al (1998) An emerging trend in experimental dynamics: merging of laser based three dimensional structural imaging and modal analysis. J. Sound Vib 211(3):323–333
8. Pratap R et al (2007) Squeeze-film effects in MEMS devices. J Indian Inst Sci 87:75:94
9. Kwok P (1999) Fluid effects in vibrating micromachined structures. Master's thesis, Massachusetts Institute of Technology, Cambridge
10. Bao MH (2000) Handbook of sensors and actuators. Elsevier, Amsterdam
11. MEMSCAP, SOIMUMPS multi user MEMS process http://www.memsrus.com/nc-mumps.soi.html
12. ANSYS, Finite element solver for multiphysics problems http://www.ansys.com/
13. Ozdoganlar OB et al (2005) Experimental modal analysis for microelectromechanical systems. J Exp Mech 45:498–506
14. Kimberly LT et al (1998) Five parametric resonances in a microelectromechanical system. Nature 396:149–152

# Chapter 4
# Normalization of Experimental Modal Vectors to Remove Modal Vector Contamination

**A.W. Phillips and R.J. Allemang**

**Abstract** When modal vectors are estimated from measured frequency response function (FRF) data, some amount of contamination in terms of random and bias errors is always present. The sources of these errors may be the experimental data acquisition process (calibration inconsistencies, averaging limitations, leakage errors, etc.) or due to limitations of the modal parameter estimation methods (mismatch between measured FRF data and the model form). These random and bias errors include uncertainty in complex magnitude about the central axis of the modal vector as well as rotation of the central axis. In a number of practical applications, particularly those involving close modal frequencies, the contamination of a modal vector will often have a significant influence from the modal vector that is near in frequency. In these situations, the numerical procedure for estimating the final, scaled modal vector, in terms of residue, generally involves a linear estimation method that, with MIMO FRF data, utilizes a weighted least squares solution procedure. This numerical solution process is reviewed and a real normalization of the weighting vectors used for estimating each modal vector in the MIMO FRF case is shown to reduce the contamination from nearby modal vectors. Theoretical evaluations for both proportional and non-proportional analytical cases are evaluated, as well as, results for a real application with pseudo-repeated modal frequencies and associated modal vectors that has historically demonstrated the problem.

**Keywords** Residue estimation • Modal vector contamination • Modal participation weighting • MAC • Modal vector estimation

## Nomenclature

| | |
|---|---|
| $N_i$ | Number of inputs |
| $N_o$ | Number of outputs |
| $N_S$ | Short dimension size |
| $N_L$ | Long dimension size |
| $\lambda_r$ | Complex modal frequency (rad/sec) |
| $\lambda_r$ | $\sigma_r + j\,\omega_r$ |
| $\sigma_r$ | Modal damping |
| $\omega_r$ | Damped natural frequency |
| r | Mode number |
| $\omega_i$ | Discrete frequency (rad/sec) |
| $[H(\omega_i)]$ | FRF matrix ($N_o \times N_i$) |
| Apqr | Residue for response DOF p, input DOF q, mode r |
| MAC | Modal assurance criterion |
| riMAC | MAC (real versus imaginary) |
| riwMAC | Weighted MAC (real versus imaginary) |

A.W. Phillips (✉) • R.J. Allemang
Structural Dynamics Research Laboratory, Department of Mechanical and Materials Engineering, College of Engineering and Applied Science, University of Cincinnati, Cincinnati, OH 45221-0072, USA
e-mail: Allyn.Phillips@UC.EDU

## 4.1  Introduction

As modal parameter estimation has evolved over the last 40 years or so, the way that modal vectors are estimated from experimental data has changed, as well. Although the technological advances from single measurement modal parameter estimation to autonomous multiple input, multiple output (MIMO) modal parameter estimation has resulted in improved estimates, the recent developments in autonomous parameter estimation methods has revealed that, while the random errors are reduced, these estimates may still contain small amounts of bias contamination from nearby modes. The results of this contamination are slightly complex estimates of the modal vectors when normal modal vectors are anticipated. The challenge for the analyst is how to deal with this contamination.

In testing situations where modal vectors show some contamination, the problem is often ignored or eliminated through a real normalization procedure of the final modal vectors. Frequently, this process is justified because the contamination appears to be dominantly random. However, when the contamination is biased, this justification becomes uncertain. Even with the most sophisticated modal parameter estimation algorithms and numerical procedures, the form of the contamination will often be biased to look like a nearby mode. This indicates that, while the estimated modal vectors may satisfy whatever algorithm and numerical procedures are being utilized, the estimated modal vectors still contain characteristics that can be perceived as non-physical.

## 4.2  Background

The estimation of modal vectors in modern modal parameter estimation algorithms normally involves a two-step process. In the first step, the modal participation vectors, $\{L\}_r$, are estimated from the eigenvectors of a companion matrix, formulated on the basis of either the short dimension, $N_S$, or the long dimension, $N_L$, of the measured FRF data matrix. Then in a second step, the corresponding modal vectors, $\{\psi\}_r$, are found from a weighted least squares set of linear equations involving the selected modal frequencies and modal participations from the eigenvalues and eigenvectors of the companion matrix. In modern algorithms, due to the available speed and memory of modern computers used in testing and data analysis, these two steps are often combined, in what appears to the user, as a single step.

The following sections review the relevant theoretical concepts and equations required for discussing the estimation of final, scaled modal vectors. The final scaled modal vectors are often presented as the residues of the partial fraction model of the MIMO FRF data matrix [1]. Alternatively, the final, scaled modal vectors can be presented as a vector proportional to the residue vector with associated modal scaling, such as Modal A ($M_{A_r}$).

### 4.2.1  Modal Vectors from Weighted Estimation of Residues

The equations that relate the complex modal frequencies, complex modal vectors, complex-valued modal participation vectors and residue vectors to the FRF data are well-known and are restated in the following equations for discussion purposes [1]:

*Single Reference*:

$$H_{pq}(\omega) = \sum_{r=1}^{N} \frac{A_{pqr}}{j\omega - \lambda_r} + \frac{A_{pqr}^*}{j\omega - \lambda_r^*} \tag{4.1}$$

*Multiple Reference*:

$$[H(\omega)] = \sum_{r=1}^{N} \frac{[A_r]}{j\omega - \lambda_r} + \frac{[A_r^*]}{j\omega - \lambda_r^*} = \sum_{r=1}^{2N} \frac{[A_r]}{j\omega - \lambda_r} \tag{4.2}$$

$$[H(\omega)]_{N_L \times N_S} = [L]_{N_L \times 2N} \left[ \frac{1}{j\omega - \lambda_r} \right]_{2N \times 2N} [\psi]_{2N \times N_S}^T \tag{4.3}$$

$$[H(\omega)]_{N_S \times N_L} = [L]_{N_S \times 2N} \left[ \frac{1}{j\omega - \lambda_r} \right]_{2N \times 2N} [\psi]_{2N \times N_L}^T \tag{4.4}$$

**Auto–MAC of Reference File**

| Mode Freq. (Hz) | 362.56 | 363.87 | 557.05 | 761.23 | 764.16 | 1222.98 | 1224.05 | 1328.03 | 1328.82 | 2019.30 | 2023.81 | 2322.02 | 2322.48 | 2338.06 |
|---|---|---|---|---|---|---|---|---|---|---|---|---|---|---|
| 2338.06 | 0.00 | 0.00 | 0.15 | 0.00 | 0.00 | 0.00 | 0.00 | 0.00 | 0.00 | 0.00 | 0.00 | 0.00 | 0.00 | 1.00 |
| 2322.48 | 0.05 | 0.04 | 0.00 | 0.00 | 0.00 | 0.00 | 0.00 | 0.00 | 0.00 | 0.00 | 0.00 | 0.27 | 1.00 | 0.00 |
| 2322.02 | 0.03 | 0.05 | 0.00 | 0.00 | 0.00 | 0.00 | 0.00 | 0.00 | 0.00 | 0.00 | 0.00 | 1.00 | 0.27 | 0.00 |
| 2023.81 | 0.00 | 0.00 | 0.00 | 0.00 | 0.00 | 0.00 | 0.00 | 0.00 | 0.00 | 0.00 | 1.00 | 0.00 | 0.00 | 0.00 |
| 2019.30 | 0.00 | 0.00 | 0.00 | 0.00 | 0.00 | 0.00 | 0.00 | 0.00 | 0.00 | 1.00 | 0.00 | 0.00 | 0.00 | 0.00 |
| 1328.82 | 0.00 | 0.00 | 0.00 | 0.00 | 0.00 | 0.00 | 0.00 | 0.09 | 1.00 | 0.00 | 0.00 | 0.00 | 0.00 | 0.00 |
| 1328.03 | 0.00 | 0.00 | 0.00 | 0.00 | 0.00 | 0.00 | 0.00 | 1.00 | 0.09 | 0.00 | 0.00 | 0.00 | 0.00 | 0.00 |
| 1224.05 | 0.00 | 0.00 | 0.00 | 0.00 | 0.00 | 0.06 | 1.00 | 0.00 | 0.00 | 0.00 | 0.00 | 0.00 | 0.00 | 0.00 |
| 1222.98 | 0.00 | 0.00 | 0.00 | 0.00 | 0.00 | 1.00 | 0.06 | 0.00 | 0.00 | 0.00 | 0.00 | 0.00 | 0.00 | 0.00 |
| 764.16 | 0.00 | 0.00 | 0.00 | 0.00 | 1.00 | 0.00 | 0.00 | 0.00 | 0.00 | 0.00 | 0.00 | 0.00 | 0.00 | 0.00 |
| 761.23 | 0.00 | 0.00 | 0.00 | 1.00 | 0.00 | 0.00 | 0.00 | 0.00 | 0.00 | 0.00 | 0.00 | 0.00 | 0.00 | 0.00 |
| 557.05 | 0.00 | 0.00 | 1.00 | 0.00 | 0.00 | 0.00 | 0.00 | 0.00 | 0.00 | 0.00 | 0.00 | 0.00 | 0.00 | 0.15 |
| 363.87 | 0.02 | 1.00 | 0.00 | 0.00 | 0.00 | 0.00 | 0.00 | 0.00 | 0.00 | 0.00 | 0.00 | 0.05 | 0.04 | 0.00 |
| 362.56 | 1.00 | 0.02 | 0.00 | 0.00 | 0.00 | 0.00 | 0.00 | 0.00 | 0.00 | 0.00 | 0.00 | 0.03 | 0.05 | 0.00 |
| −362.56 | 0.97 | 0.00 | 0.00 | 0.00 | 0.00 | 0.00 | 0.00 | 0.00 | 0.00 | 0.00 | 0.00 | 0.04 | 0.06 | 0.00 |
| −363.87 | 0.00 | 0.99 | 0.00 | 0.00 | 0.00 | 0.00 | 0.00 | 0.00 | 0.00 | 0.00 | 0.00 | 0.06 | 0.05 | 0.00 |
| −557.05 | 0.00 | 0.00 | 1.00 | 0.00 | 0.00 | 0.00 | 0.00 | 0.00 | 0.00 | 0.00 | 0.00 | 0.00 | 0.00 | 0.15 |
| −761.23 | 0.00 | 0.00 | 0.00 | 1.00 | 0.00 | 0.00 | 0.00 | 0.00 | 0.00 | 0.00 | 0.00 | 0.00 | 0.00 | 0.00 |
| −764.16 | 0.00 | 0.00 | 0.00 | 0.00 | 1.00 | 0.00 | 0.00 | 0.00 | 0.00 | 0.00 | 0.00 | 0.00 | 0.00 | 0.00 |
| −1222.98 | 0.00 | 0.00 | 0.00 | 0.00 | 0.00 | 0.94 | 0.00 | 0.00 | 0.00 | 0.00 | 0.00 | 0.00 | 0.00 | 0.00 |
| −1224.05 | 0.00 | 0.00 | 0.00 | 0.00 | 0.00 | 0.00 | 0.93 | 0.00 | 0.00 | 0.00 | 0.00 | 0.00 | 0.00 | 0.00 |
| −1328.03 | 0.00 | 0.00 | 0.00 | 0.00 | 0.00 | 0.00 | 0.00 | 0.92 | 0.00 | 0.00 | 0.00 | 0.00 | 0.00 | 0.00 |
| −1328.82 | 0.00 | 0.00 | 0.00 | 0.00 | 0.00 | 0.00 | 0.00 | 0.00 | 0.90 | 0.00 | 0.00 | 0.00 | 0.00 | 0.00 |
| −2019.30 | 0.00 | 0.00 | 0.00 | 0.00 | 0.00 | 0.00 | 0.00 | 0.00 | 0.00 | 1.00 | 0.00 | 0.00 | 0.00 | 0.00 |
| −2023.81 | 0.00 | 0.00 | 0.00 | 0.00 | 0.00 | 0.00 | 0.00 | 0.00 | 0.00 | 0.00 | 1.00 | 0.00 | 0.00 | 0.00 |
| −2322.02 | 0.04 | 0.06 | 0.00 | 0.00 | 0.00 | 0.00 | 0.00 | 0.00 | 0.00 | 0.00 | 0.00 | 0.81 | 0.01 | 0.00 |
| −2322.48 | 0.06 | 0.05 | 0.00 | 0.00 | 0.00 | 0.00 | 0.00 | 0.00 | 0.00 | 0.00 | 0.00 | 0.01 | 0.66 | 0.00 |
| −2338.06 | 0.00 | 0.00 | 0.15 | 0.00 | 0.00 | 0.00 | 0.00 | 0.00 | 0.00 | 0.00 | 0.00 | 0.00 | 0.00 | 1.00 |

*Y-axis: Mode Frequency, Hz — X-axis: Mode Frequency, Hz — Color scale: MAC Value (0 to 1)*

**Fig. 4.1**  MAC of modal vectors and conjugate modal vectors

where:

$$A_{pqr} = L_{pr}\psi_{qr} \quad \text{OR} \quad A_{pqr} = \frac{\psi_{pr}\psi_{qr}}{M_{A_r}} \tag{4.5}$$

In the above equations, and particularly in Eq. 4.5, it should be noted that the residue should be purely imaginary for a normal mode case utilizing displacement over force FRF data. For the anticipated normal mode situation, there is no constraint on the numerical characteristics of either the modal participation coefficient or the modal vector coefficient individually as long as the product of these two terms yields the correct residue characteristic.

### 4.2.2  Modal Assurance Criterion

The traditional modal assurance criterion (MAC) computation [2], restated in Eq. 4.1, is widely used in modal parameter estimation and structural dynamics [3–6] to sort the numerous possible solutions of modal vectors from either modeling or experiment.

$$\text{MAC}_{cd} = \frac{\left| \{\psi_c\}^H \{\psi_d\} \right|^2}{\{\psi_c\}^H \{\psi_c\} \{\psi_d\}^H \{\psi_d\}} = \frac{\{\psi_c\}^H \{\psi_d\} \{\psi_d\}^H \{\psi_c\}}{\{\psi_c\}^H \{\psi_c\} \{\psi_d\}^H \{\psi_d\}} \tag{4.6}$$

Once modal vectors are estimated in any modal parameter estimation procedure, the MAC computation is often utilized to evaluate the quality of the solutions. This begins with an evaluation of the MAC between all of the modal vectors in the final set to ascertain whether the modal set is an independent set of vectors. This often involves the modal vectors associated with the conjugate poles. Since the conjugate poles and vectors are estimated separately, if non-conjugate relationships exist between the associated modal vector estimates (between the modal vector for a pole and the modal vector of the conjugate pole), the MAC between these two vectors will not be unity as expected. A number of users have noted that this often correlates with modal vectors that are exhibiting some unexpected characteristics or contamination.

Figure 4.1 is a graphical representation of this situation. While the MAC values are acceptable, the comparisons between modal vectors and the associated conjugate modal vectors do exhibit slightly lowered consistency or correlation.

Unlike the historical approach to estimation of the modal vectors, many recent modal parameter estimation algorithms, including the autonomous procedures, are based upon numerical processing methods like singular value decomposition (SVD). The solutions that are identified, based upon the data associated with a cluster of estimates of the same modal vector, have no direct physical or causal constraint. An example of a physical or causal constraint would be the expectation of real-valued, normal modes for systems where no expectation of non-proportional damping is likely. SVD methods will identify the most dominant unitary (orthogonal and unit length) vectors in a cluster, yielding a complex-valued vector in general. Experience has shown that when modes are very close in frequency with minimal spatial resolution, the complex-valued vectors will still show significant independence.

However, when these complex-valued vectors are examined closely, the non-dominant portion of the complex-valued vector often correlates very highly with one or more nearby modal vectors. This can be examined by several variants of the MAC calculation and the weighted MAC calculation. This is discussed in the next section and is the subject of a companion paper associated with this work [7].

#### 4.2.2.1 Special Forms of the Modal Assurance Criterion

To understand the nature of the possible modal vector contamination in a complex-valued modal vector, three conventional MAC calculations can be performed (1) between the real parts of the modal vectors and the complex-valued modal vectors (rMAC), (2) between the imaginary parts of the modal vectors and the complex-valued modal vectors (iMAC) and (3) between the real parts of the modal vectors and the imaginary parts of the modal vectors (riMAC). These three MAC calculations and the interpretation of these MAC values will be sensitive to the rotation and normalization of the complex-valued modal vector estimates. The following use and discussion assumes that the complex-valued modal vectors have been rotated so that the central axis of the complex-valued modal vector is centered on the real axis. These three MAC computations identify (1) that the real part of the modal vector is the dominant part of the complex-valued modal vector (rMAC), (2) that the imaginary part of the modal vector is the dominant part of the complex-valued modal vector (iMAC) and (3) that the real and imaginary parts of the modal vector are, or are not, related to one another. All MAC computations in this case are, as always, bounded from zero to one. If near normal modes are expected, (1) the rMAC should be close to one, (2) the iMAC should be close to zero and (3) the riMAC should also be close to zero. Note in the following definitions, complex-valued modal vectors c and d can again be any of the modal vectors that the user wishes to include in the evaluation.

$$\text{rMAC}_{cd} = \frac{\left(\text{Re}\{\psi_c\}^H\right) \{\psi_d\} \ \{\psi_d\}^H \left(\text{Re}\{\psi_c\}\right)}{\left(\text{Re}\{\psi_c\}^H\right) \left(\text{Re}\{\psi_c\}\right) \ \{\psi_d\}^H \left\{\psi_d\right\}} \tag{4.7}$$

$$\text{iMAC}_{cd} = \frac{\left(\text{Im}\{\psi_c\}^H\right) \{\psi_d\} \ \{\psi_d\}^H \left(\text{Im}\{\psi_c\}\right)}{\left(\text{Im}\{\psi_c\}^H\right) \left(\text{Im}\{\psi_c\}\right) \ \{\psi_d\}^H \left\{\psi_d\right\}} \tag{4.8}$$

$$\text{riMAC}_{cd} = \frac{\left(\text{Re}\{\psi_c\}^H\right) \left(\text{Im}\{\psi_d\}\right) \ \left(\text{Im}\{\psi_d\}\right)^H \left(\text{Re}\{\psi_c\}\right)}{\left(\text{Re}\{\psi_c\}^H\right) \left(\text{Re}\{\psi_c\}\right) \ \left(\text{Im}\{\psi_d\}^H\right) \left(\text{Im}\{\psi_d\}\right)} \tag{4.9}$$

The above MAC evaluations identify whether, and how, the contamination of a complex-valued modal vector is related to another of the identified modal vectors. However, the MAC computation is normalized to unity vector length, vector by vector, for the vectors used in the calculation. A weighted MAC can be used to determine the degree or scale of the contamination. The following three definitions of the weighting for each of the above MAC calculations limits the associated MAC value to a fraction of the zero to one scale. If near normal modes are expected, (1) the weighting and rwMAC should be close to one, (2) the weighting and iwMAC should be close to zero and (3) the combined weighting and riwMAC should also be close to zero. Note in the following definitions, complex-valued modal vectors c and d can again be any of the modal vectors that the user wishes to include in the evaluation.

$$\text{rwMAC}_{cd} = \text{rW}_c \times \text{rMAC}_{cd} \quad \text{where} \quad \text{rW}_c = \frac{\left(\text{Re}\{\psi_c\}^H\right) \left(\text{Re}\{\psi_c\}\right)}{\{\psi_c\}^H \ \{\psi_c\}} \tag{4.10}$$

$$\text{iwMAC}_{cd} = \text{iW}_c \times \text{iMAC}_{cd} \quad \text{where} \quad \text{iW}_c = \frac{\left( \text{Im}\{\psi_c\}^H \right) \left( \text{Im}\{\psi_c\} \right)}{\{\psi_c\}^H \{\psi_c\}} \tag{4.11}$$

$$\text{riwMAC}_{cd} = \text{rW}_c \times \text{iW}_d \times \text{riMAC}_{cd} \tag{4.12}$$

### 4.2.3   Modal Vector Contamination: Simple Example

For the following example, the presentation is illustrative of the nature and appearence of the complex modal vector contamination. It is not a rigorous definition of the specific form and source of contamination that results from the solution of the companion matrix.

For the basic partial fraction model, the numerator or residue will be a purely imaginary number for the case of a normal mode, assuming that the FRF is in displacement over force form. The residue for all modes in the summation will also be plus/minus purely imaginary numbers.

$$\{H(\omega)\} = \sum_{r=1}^{2N} \frac{\{A\}_r}{j\omega - \lambda_r} \tag{4.13}$$

Assuming that the numerical solution procedure does not completely eliminate the estimate of one residue from the next, the question is then, *what will be the nature of the contamination?* For mode r, the residue $A_{pqr}$ for a particular measurement $H_{pq}$ will be a purely imaginary number but, if there is contamination coming from the next mode higher (or lower) in frequency, this will alter the desired residue $A_{pqr}$, adding both real and imaginary contamination coming from mode s in the following way:

$$\left\{\widehat{A}\right\}_r = \{A\}_r + \frac{\{A\}_s}{j\omega_r - \lambda_s} = \{A\}_r + \frac{\{A\}_s}{\sigma_s + j(\omega_r - \omega_s)} \tag{4.14}$$

Even if the nearby residue is also purely imaginary, the contamination of the $A_{pqr}$ will be biased in both the real and imaginary part by a contribution that is proportional to the nearby mode. Due to the magnitude of the imaginary part of $A_{pqr}$ this contribution may not be noticeable but, as the real part of the residue $A_{pqr}$ should be zero, the contamination of the real part of the residue will be quite noticeable. This was demonstrated in two recent papers [7, 11] and the form of this contamination has been known for some time [8].

## 4.3   Normalization of the Modal Weighting (Participation) Vector

Identifying the potential contamination of modal vectors is helpful to the thorough understanding of modal parameter estimation algorithms and autonomous procedures, as well as, being instructive for potential removal of the contamination. If some sort of real normalization is desirable (to match up well with an undamped, analytical model, for example), understanding of the contamination that is being removed is a prerequisite to any procedure. Random contamination may simply be ignored, smoothed or averaged out, but if the contamination is related to nearby modes, it may indicate that the modal parameter estimation may need further evaluation or that more data from additional reference DOFs is required.

### 4.3.1   Central Axis Rotation

In order to establish a uniform procedure for normalizing the modal participation vector which will be used as the weighting vector when estimating modal vectors from MIMO FRF data, each potentially complex valued vector must first be rotated to an orientation where the dominant information of the vector in complex space is aligned with the real axis. This is required since the vector is the result of the solution of an eigenvalue-eigenvector problem involving the complex-valued MIMO FRF data.

Given an original (contaminated) modal participation vector for mode r, a central axis rotation method is utilized to determine the dominant axes. These dominant axes can be identified via the singular value decomposition of the relationship between the real part, $\{L_R\}_r$, and imaginary part, $\{L_I\}_r$, of the modal participation vector for mode r as follows:

$$[U, \Sigma, V] = \text{svd}\left([\{L_I\}_r\ \{L_R\}_r]^T\ [\{L_I\}_r\ \{L_R\}_r]\right) \tag{4.15}$$

Recognize that this decomposition is an attempt to locate the two dominant axes of a 2-D ellipse that encompasses the modal participation vector data in the complex plane. Following the decomposition, the central axis angle is estimated using the true (four quadrant) arctangent of the right singular vector relationship. Note that, regardless of the number of DOF positions represented in the modal vector, the right singular vector matrix will always be two by two in dimension representing the 2-D characteristics of the ellipse.

$$\overline{\phi}_r = \tan^{-1}\left(\frac{V_{22}}{-V_{12}}\right) \tag{4.16}$$

After identifying the central axis angle, the original complex vector is rotated by multiplying by the complex rotational phasor.

$$\left\{\widehat{L}\right\}_r = \left(\cos\left(\overline{\phi}_r\right) - j\sin\left(\overline{\phi}_r\right)\right)\{L\}_r \tag{4.17}$$

This rotation and normalization procedure assures that the resulting vector is dominantly real, based upon all of the vector information, rather than a single DOF that is chosen arbitrarily (for example, rather than selecting the DOF associated with the largest modal vector coefficient).

### 4.3.2 Modal Vector Complexity

Modal vector complexity is often defined in terms of mean phase deviation as an indication of how the phase deviates from 0 ° and/or 180 °. This definition allows some ambiguity in what is meant by a *complex mode*. It may simply mean that the elements of the estimated modal vector contain complex values. For this case, the elements of the modal vector may be rotated by an angle in the complex plane, but are otherwise colinear. Or it may mean that the modal vector contains complex values that cannot be made real by a simple comple phasor rotation. For this case, the modal coefficients are not all colinear in the complex plane. For this development, it is the second definition that is used.

The mean phase deviation (MPD$_r$) for modal vector r has been defined historically as a number between zero and unity where zero represents a real valued modal vector (normal mode) and where unity represents a complex valued modal vector with no recognizable dominant real or imaginary characteristic, once an attempt has been made to rotate the vector to a dominant central axis position. This fraction is often multipled by 100 to represent the precentage of complex valued modal vector characteristics. In terms of the definitions utilized in the previous section, assuming that the modal vector has already been rotated to its most dominant real orientation, the MPD$_r$ is defined as the norm of the imaginary part of the rotated vector divided by the norm of the real part of the rotated vector, as shown in Eq. 4.18. Thus, the MPD$_r$ gives a dispersion ratio around the central axis of the rotated modal vector bounded between zero and one.

*Mean Phase Deviation* (MPD$_r$):

Once the MPD$_r$ is defined in terms of the fraction between zero and unity, the associated mean phase correlation for modal vector r is defined as in Eq. 4.19.

$$\text{MPD}_r = \frac{\left\|\left\{\widehat{\psi}_I\right\}_r\right\|}{\left\|\left\{\widehat{\psi}_R\right\}_r\right\|} \tag{4.18}$$

*Mean Phase Correlation* (MPC$_r$):

$$\text{MPC}_r = 1 - \text{MPD}_r \tag{4.19}$$

The mean phase correlation can then be interpreted as an indicator of normalcy; from a purely normal mode (1.0) to a purely complex mode (0.0).

### 4.3.3  Proposed New Methodology

The proposed new methodology involves a real normalization of the modal participation vectors, $\{L_{pr}\}$, that are used as the weighting factors in the corresponding estimates of the modal vectors $\{\psi_{qr}\}$. No limitation or normalization is placed upon the modal vectors $\{\psi_{qr}\}$. In this way, the final residue vector $\{A_{pqr}\}$ is still estimated as a completely complex valued vector as noted in Eq. 4.5. The real normalization of the modal participation vectors $\{L_{pr}\}$ currently is implemented by dropping the imaginary part of the modal participation vectors $\{L_{pr}\}$ after the vectors have been rotated to the most dominant central axis as defined in Eqs. 4.15–4.17.

This simple procedure does not eliminate complex-valued modal vectors when they exist due to non-proportional damping but shows dramatic improvement in the estimation of the residue vectors when the structure is thought to satisfy the conditions of proportional damping (normal modes). In these cases, the product of the modal participation vectors and the modal vectors, as noted in Eq. 4.5, yields residues that are very close to purely imaginary vectors as would be expected for the normal mode case involving displacement over force FRF data. The next two sections demonstrate these characteristics. The academic example shows that the real normalization of the modal participation vectors has no negative effects on the estimation of the expected final modal vectors while the practical example indicates that for a case where modal contamination has been noted, the real normalization of the modal participation vectors greatly reduces this observed phenomena.

## 4.4  15 DOF Analytical Example

A 15 DOF analytical example is used to generate a set of MIMO FRFs with known properties to be certain that the real normalization procedure gives expected results in the two cases. Three different cases were utilized to perform this evaluation. Case I involved a proportionally damped model, Case II involved a non-proportionally damped model (5 % complexity) and Case III involved a non-proportionally damped model (20 % complexity).

To clarify the three cases in terms of the previous modal vector complexity concepts, the percentage of non-proportional damping (NPD) utilized the $MPD_r$ as a descriptor metric, multiplied times 100 to give the result in percentage form. For proportional damping (PD) used in Case I, the $MPD_r$ for the vectors was essentially zero when a small amount of random noise was included. For Case II where the non-proportional damping is described as 5 % NPD, the complexity of the analytical vectors was nominally around 5 % MPD. For Case III where the non-proportional damping is described as 20 % NPD, the complexity of the analytical vectors was nominally around 20 % MPD. For comparison, a 100 % NPD would be 100 % MPD implying that the vector is completely complex and there is no central vector at all.

The comparison of the three cases is presented in Fig. 4.2. The left column is the real weighting and the right column is the complex weighting for each case. As can be noted, no significant difference exists between the cases. A comparison of the resultant estimated poles and vectors with the MCK analytical values reveals that the estimation of complex vectors using real weighting is essentially the same, differing only by very small amounts that can be related to the random noise that has been added to the synthesized FRF data.

The conclusion that can be drawn from Fig. 4.2, as well as inspecting the final modal frequencies and modal vectors that are estimated from these consistency diagrams, is that the real normalization of the modal participation vector that is used as a weighting vector appears to have no impact on getting the correct modal vector, regardless of proportional or non-proportional damping.

## 4.5  C-Plate Example

The data used for the following section is MIMO FRF data taken from an impact test of a steel disc supported in a pseudo free-free boundary condition. The steel disc is approximately 2 cm thick and 86 cm in diameter with several small holes through the disc. The center area of the disc (diameter of approximately 25 cm) has a thickness of approximately 6 cm. There
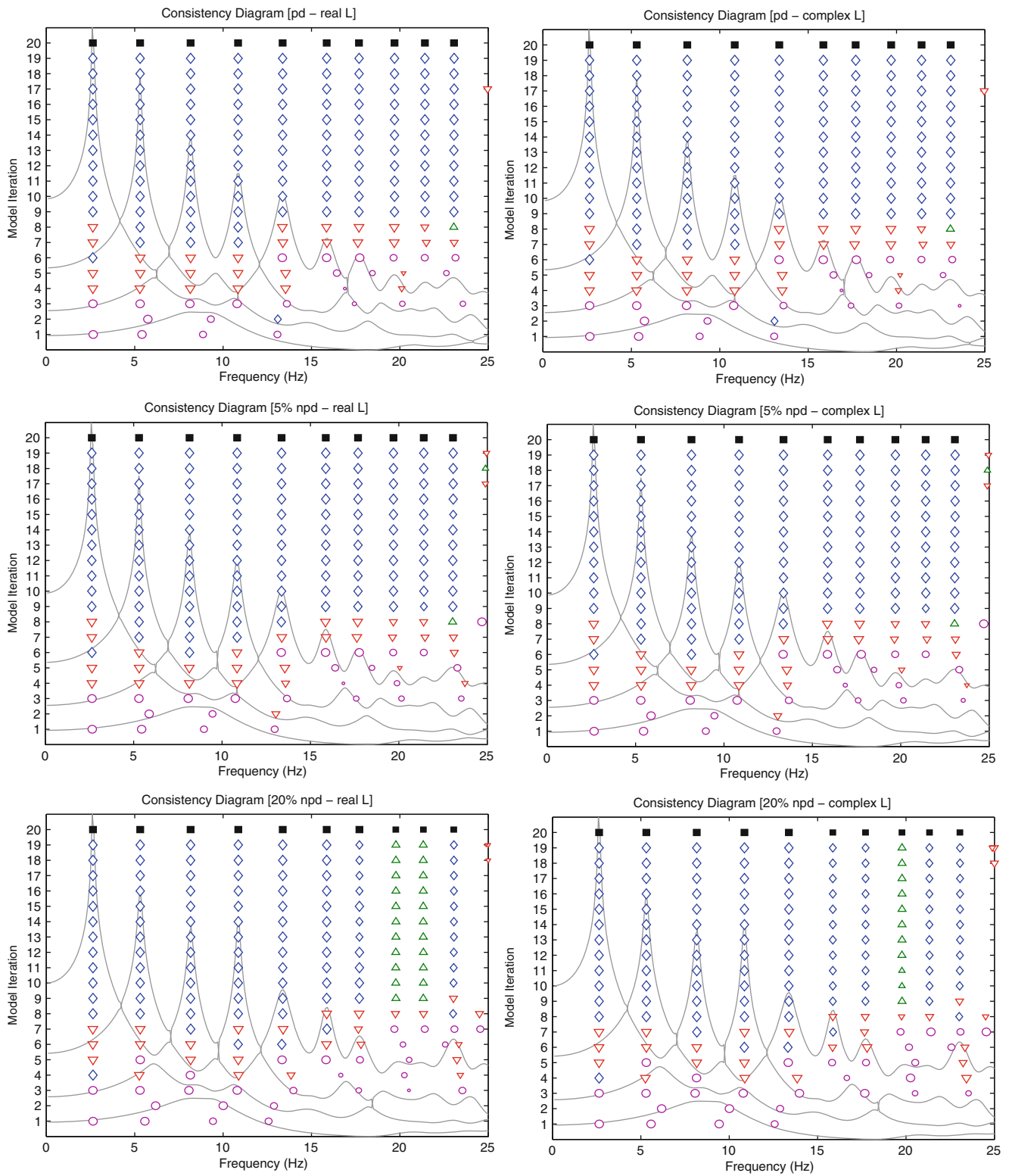
**Fig. 4.2** 15 DOF consistency diagram, real and complex weighting, proportional and non-proportional damping
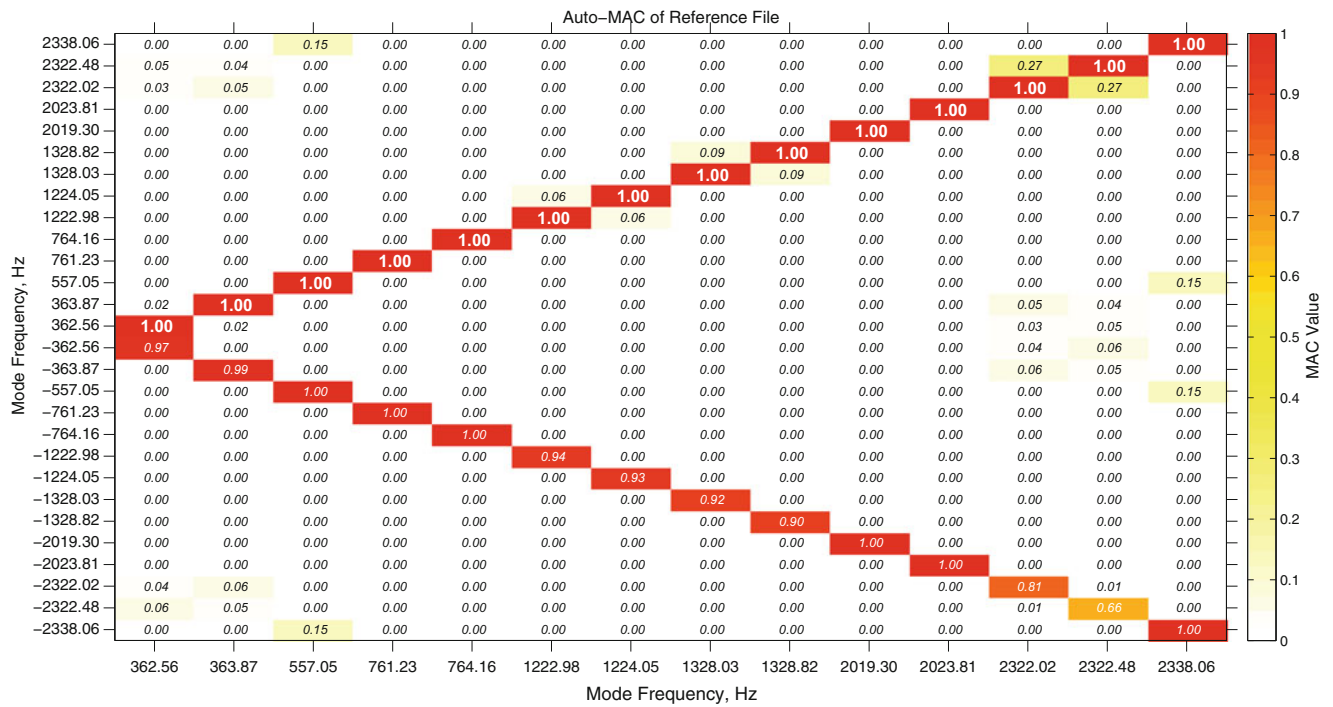
Auto–MAC of Reference File

| Mode Frequency, Hz | 362.56 | 363.87 | 557.05 | 761.23 | 764.16 | 1222.98 | 1224.05 | 1328.03 | 1328.82 | 2019.30 | 2023.81 | 2322.02 | 2322.48 | 2338.06 |
|---|---|---|---|---|---|---|---|---|---|---|---|---|---|---|
| 2338.06 | 0.00 | 0.00 | 0.15 | 0.00 | 0.00 | 0.00 | 0.00 | 0.00 | 0.00 | 0.00 | 0.00 | 0.00 | 0.00 | 1.00 |
| 2322.48 | 0.05 | 0.04 | 0.00 | 0.00 | 0.00 | 0.00 | 0.00 | 0.00 | 0.00 | 0.00 | 0.00 | 0.27 | 1.00 | 0.00 |
| 2322.02 | 0.03 | 0.05 | 0.00 | 0.00 | 0.00 | 0.00 | 0.00 | 0.00 | 0.00 | 0.00 | 0.00 | 1.00 | 0.27 | 0.00 |
| 2023.81 | 0.00 | 0.00 | 0.00 | 0.00 | 0.00 | 0.00 | 0.00 | 0.00 | 0.00 | 0.00 | 1.00 | 0.00 | 0.00 | 0.00 |
| 2019.30 | 0.00 | 0.00 | 0.00 | 0.00 | 0.00 | 0.00 | 0.00 | 0.00 | 0.00 | 1.00 | 0.00 | 0.00 | 0.00 | 0.00 |
| 1328.82 | 0.00 | 0.00 | 0.00 | 0.00 | 0.00 | 0.00 | 0.00 | 0.09 | 1.00 | 0.00 | 0.00 | 0.00 | 0.00 | 0.00 |
| 1328.03 | 0.00 | 0.00 | 0.00 | 0.00 | 0.00 | 0.00 | 0.00 | 1.00 | 0.09 | 0.00 | 0.00 | 0.00 | 0.00 | 0.00 |
| 1224.05 | 0.00 | 0.00 | 0.00 | 0.00 | 0.00 | 0.06 | 1.00 | 0.00 | 0.00 | 0.00 | 0.00 | 0.00 | 0.00 | 0.00 |
| 1222.98 | 0.00 | 0.00 | 0.00 | 0.00 | 0.00 | 1.00 | 0.06 | 0.00 | 0.00 | 0.00 | 0.00 | 0.00 | 0.00 | 0.00 |
| 764.16 | 0.00 | 0.00 | 0.00 | 0.00 | 1.00 | 0.00 | 0.00 | 0.00 | 0.00 | 0.00 | 0.00 | 0.00 | 0.00 | 0.00 |
| 761.23 | 0.00 | 0.00 | 0.00 | 1.00 | 0.00 | 0.00 | 0.00 | 0.00 | 0.00 | 0.00 | 0.00 | 0.00 | 0.00 | 0.00 |
| 557.05 | 0.00 | 0.00 | 1.00 | 0.00 | 0.00 | 0.00 | 0.00 | 0.00 | 0.00 | 0.00 | 0.00 | 0.00 | 0.00 | 0.15 |
| 363.87 | 0.02 | 1.00 | 0.00 | 0.00 | 0.00 | 0.00 | 0.00 | 0.00 | 0.00 | 0.00 | 0.00 | 0.05 | 0.04 | 0.00 |
| 362.56 | 1.00 | 0.02 | 0.00 | 0.00 | 0.00 | 0.00 | 0.00 | 0.00 | 0.00 | 0.00 | 0.00 | 0.03 | 0.05 | 0.00 |
| −362.56 | 0.97 | 0.00 | 0.00 | 0.00 | 0.00 | 0.00 | 0.00 | 0.00 | 0.00 | 0.00 | 0.00 | 0.04 | 0.06 | 0.00 |
| −363.87 | 0.00 | 0.99 | 0.00 | 0.00 | 0.00 | 0.00 | 0.00 | 0.00 | 0.00 | 0.00 | 0.00 | 0.06 | 0.05 | 0.00 |
| −557.05 | 0.00 | 0.00 | 1.00 | 0.00 | 0.00 | 0.00 | 0.00 | 0.00 | 0.00 | 0.00 | 0.00 | 0.00 | 0.00 | 0.15 |
| −761.23 | 0.00 | 0.00 | 0.00 | 1.00 | 0.00 | 0.00 | 0.00 | 0.00 | 0.00 | 0.00 | 0.00 | 0.00 | 0.00 | 0.00 |
| −764.16 | 0.00 | 0.00 | 0.00 | 0.00 | 1.00 | 0.00 | 0.00 | 0.00 | 0.00 | 0.00 | 0.00 | 0.00 | 0.00 | 0.00 |
| −1222.98 | 0.00 | 0.00 | 0.00 | 0.00 | 0.00 | 0.94 | 0.00 | 0.00 | 0.00 | 0.00 | 0.00 | 0.00 | 0.00 | 0.00 |
| −1224.05 | 0.00 | 0.00 | 0.00 | 0.00 | 0.00 | 0.00 | 0.93 | 0.00 | 0.00 | 0.00 | 0.00 | 0.00 | 0.00 | 0.00 |
| −1328.03 | 0.00 | 0.00 | 0.00 | 0.00 | 0.00 | 0.00 | 0.00 | 0.92 | 0.00 | 0.00 | 0.00 | 0.00 | 0.00 | 0.00 |
| −1328.82 | 0.00 | 0.00 | 0.00 | 0.00 | 0.00 | 0.00 | 0.00 | 0.00 | 0.90 | 0.00 | 0.00 | 0.00 | 0.00 | 0.00 |
| −2019.30 | 0.00 | 0.00 | 0.00 | 0.00 | 0.00 | 0.00 | 0.00 | 0.00 | 0.00 | 1.00 | 0.00 | 0.00 | 0.00 | 0.00 |
| −2023.81 | 0.00 | 0.00 | 0.00 | 0.00 | 0.00 | 0.00 | 0.00 | 0.00 | 0.00 | 0.00 | 1.00 | 0.00 | 0.00 | 0.00 |
| −2322.02 | 0.04 | 0.06 | 0.00 | 0.00 | 0.00 | 0.00 | 0.00 | 0.00 | 0.00 | 0.00 | 0.00 | 0.81 | 0.01 | 0.00 |
| −2322.48 | 0.06 | 0.05 | 0.00 | 0.00 | 0.00 | 0.00 | 0.00 | 0.00 | 0.00 | 0.00 | 0.00 | 0.01 | 0.66 | 0.00 |
| −2338.06 | 0.00 | 0.00 | 0.15 | 0.00 | 0.00 | 0.00 | 0.00 | 0.00 | 0.00 | 0.00 | 0.00 | 0.00 | 0.00 | 1.00 |

Mode Frequency, Hz

MAC Value

**Fig. 4.3** C-Plate MAC of modal vectors and conjugate modal vectors—Complex weighting

are seven reference accelerometers and measured force inputs from an impact hammer are applied to thirty-six locations, including next to the seven reference accelerometers. The frequency resolution of the data is 5 Hz. While the disc is not as challenging as some industrial data situations that contain more noise or other complicating factors like small nonlinearities, the disc has a number of pseudo-repeated roots spaced well within the 5 Hz frequency resolution and a mix of close modes involving repeated and non-repeated roots which are very challenging. Based upon the construction of the disc, real-valued, normal modes can be expected and the inability to resolve these modes can be instructive relative to both modal parameter estimation algorithm and autonomous procedure performance. For the interested reader, a number of realistic examples are shown in other past papers including FRF data from an automotive structure and a bridge structure [9, 10].
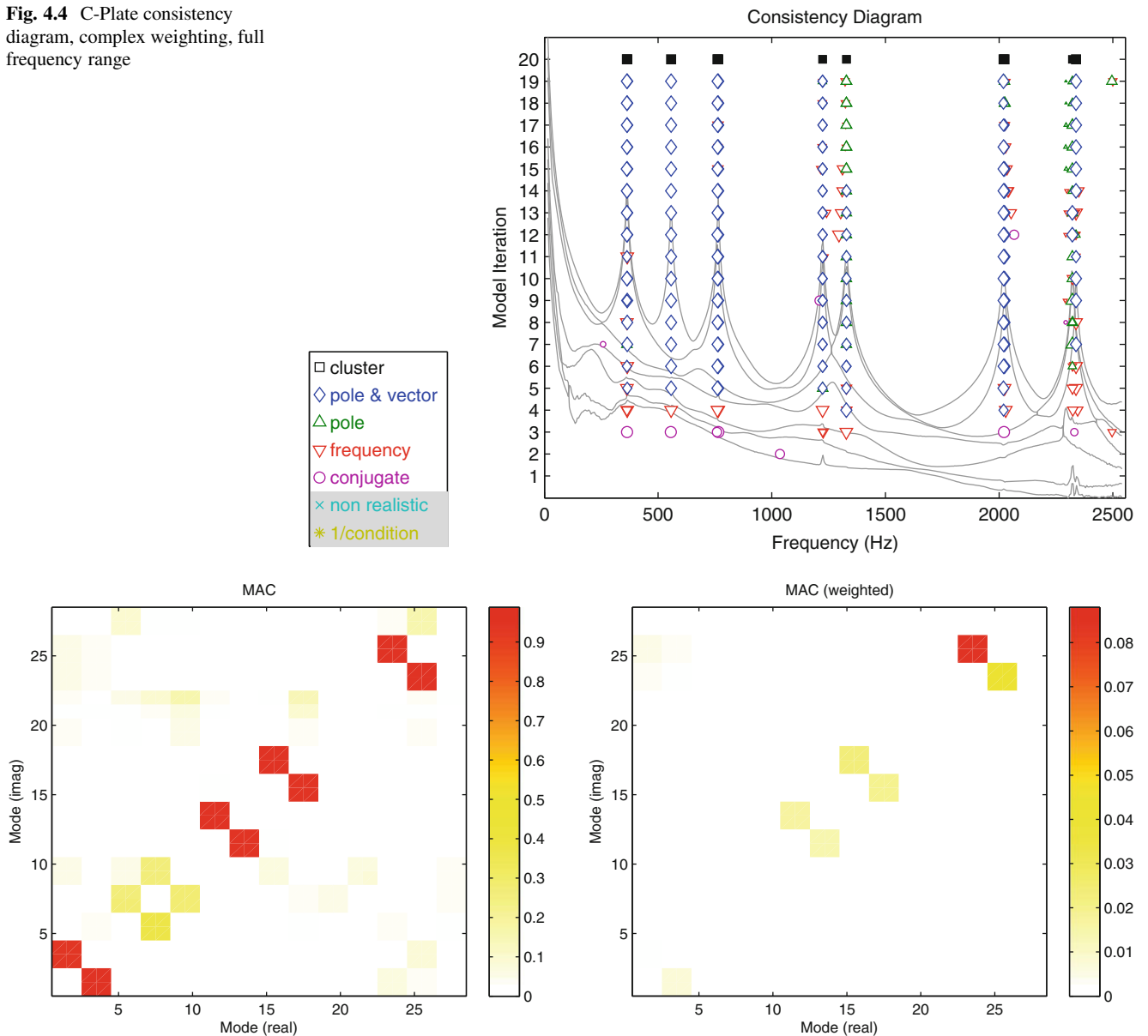
### 4.5.1 C-Plate Example: Estimates with Complex Weighting

For this example, the entire frequency range from 200 to 2,500 Hz was fit by the Rational Fraction Polynomial Algorithm with Z-frequency weighting (RFP-Z) in a single parameter estimation run using traditional complex participation weighting. The CSSAMI autonomous modal parameter estimation procedure was utilized to remove user bias from the selected results [9–11] using the same input parameters to the RFP-Z algorithm and the CSSAMI procedure. The following results are similar regardless of the base modal parameter estimation algorithm chosen.

It can be observed in the MAC plot (Fig. 4.3) that there exists a coupling contamination between the 2,300 Hz repeated root modes. This is further revealed by the symbols in the consistency diagram (Fig. 4.4) where the green delta symbol indicates that no stable pole and vector was identifed. In addition, the small size of the symbol indicates that the vector that has been found is significantly complex-valued. Using the weighted and unweighted versions of the riMAC (Fig. 4.5), it is evident that each of the repeated root pairs has some contamination from its twin. Finally, expanding the region of the consistency diagram around the 2,300 Hz modal pair (Fig. 4.6), it is clear that while a consistent frequency and damping are identified, there is no consistent modal vector identified from iteration to iteration.

While this solution represents the theoretical concept of generalized weighting vectors for each mode that can be complex-valued, the results for this case yield solutions that are slightly non-physical when the nature of the structure under test is considered.

**Fig. 4.4** C-Plate consistency diagram, complex weighting, full frequency range



**Fig. 4.5** C-Plate, complex weighting, riMAC and riwMAC

## 4.5.2 C-Plate Example: Estimates with Real Weighting

For this example, the entire frequency range from 200 to 2,500 Hz was again fit by the Rational Fraction Polynomial Algorithm with Z-frequency weighting (RFP-Z) in a single parameter estimation run. The final results were again determined from the CSSAMI autonomous procedure. All conditions match the modal parameter estimation process used in the last section. This time, however, instead of using the complex valued modal participation vectors as weighting vectors, real normalization of the modal participation vector (first rotated to its dominant central axis) was used to generated real-valued weighting vectors.

Dramatically improved results can be observed in the following figures. It can be observed in the MAC plot (Fig. 4.7) that the coupling contamination between the 2,300 Hz repeated root modes has been eliminated. Further, it can be observed that the cross MAC between each vector and its complex conjugate is also improved. This improvement is further revealed by the

**Fig. 4.6** C-Plate consistency diagram, complex weighting, 2,315–2,345 Hz range
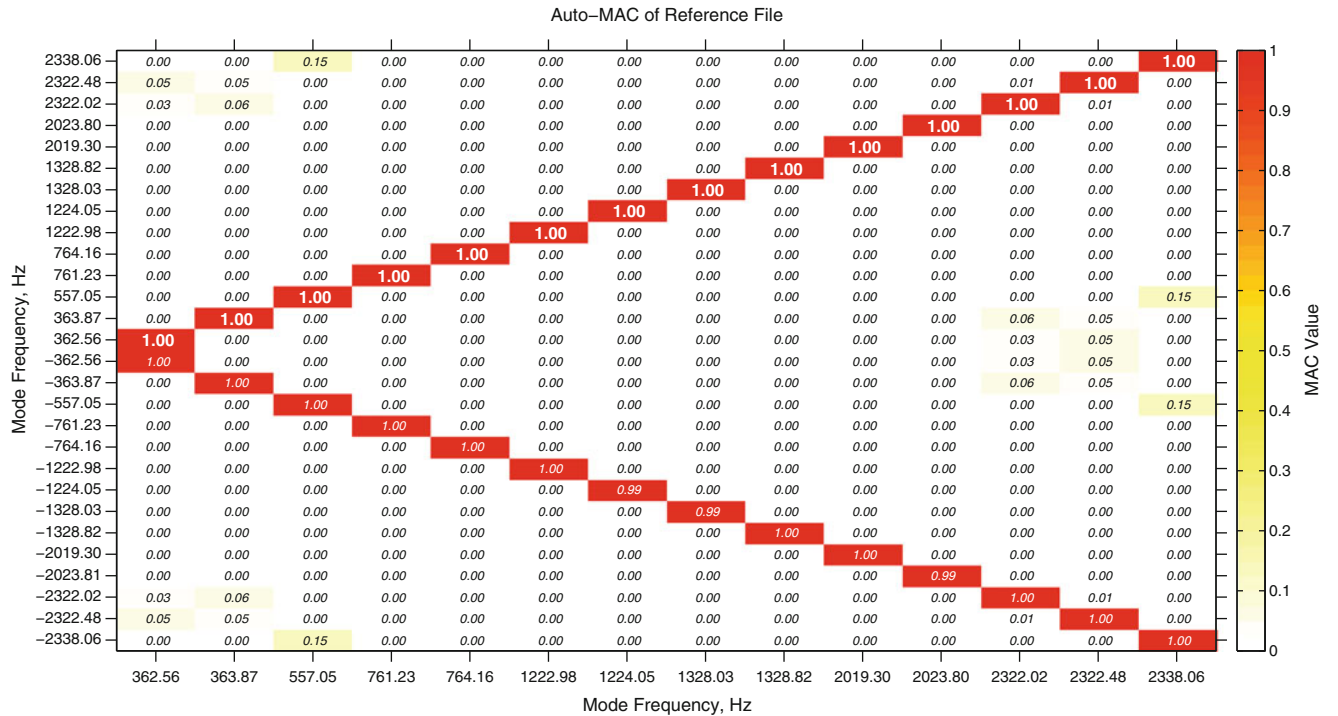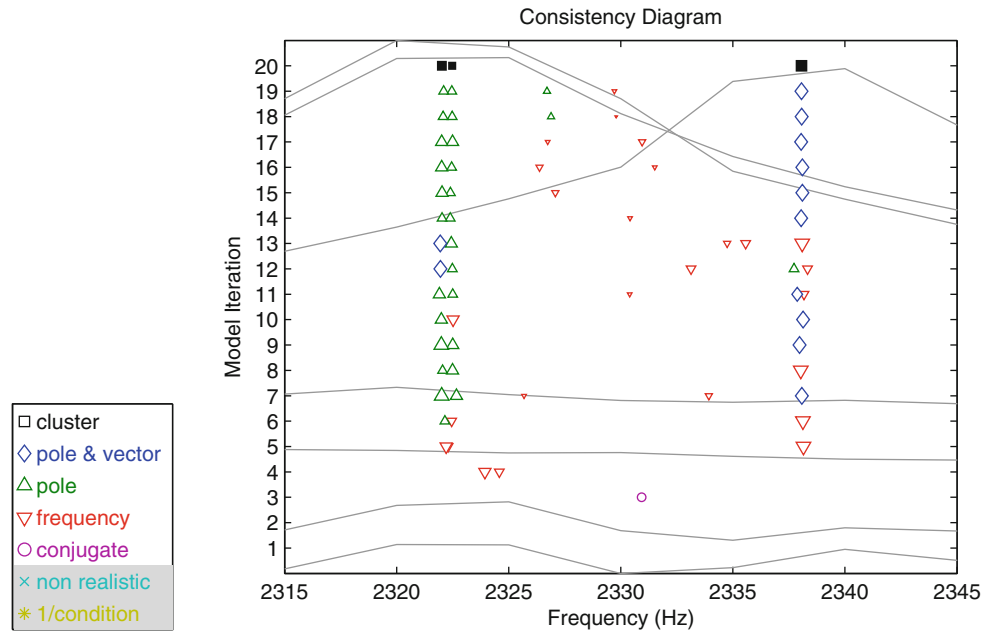


**Fig. 4.7** MAC of modal vectors and conjugate modal vectors—Real weighting

symbols in the consistency diagram (Fig. 4.8). Whereas before the symbols indicated a complex-valued, inconsistent modal vector, in this case, the large blue diamonds indicate a consistent, nearly normal mode. The nearly two orders of magnitude change in the weighted riMAC (Fig. 4.9), also indicates the significant reduction in contamination. Finally, expanding the region of the consistency diagram around the 2,300 Hz modal pair (Fig. 4.10), it is clear that both the pole and the modal vector are identified consistently from iteration to iteration.

**Fig. 4.8** C-Plate consistency
diagram, real weighting, full
frequency range
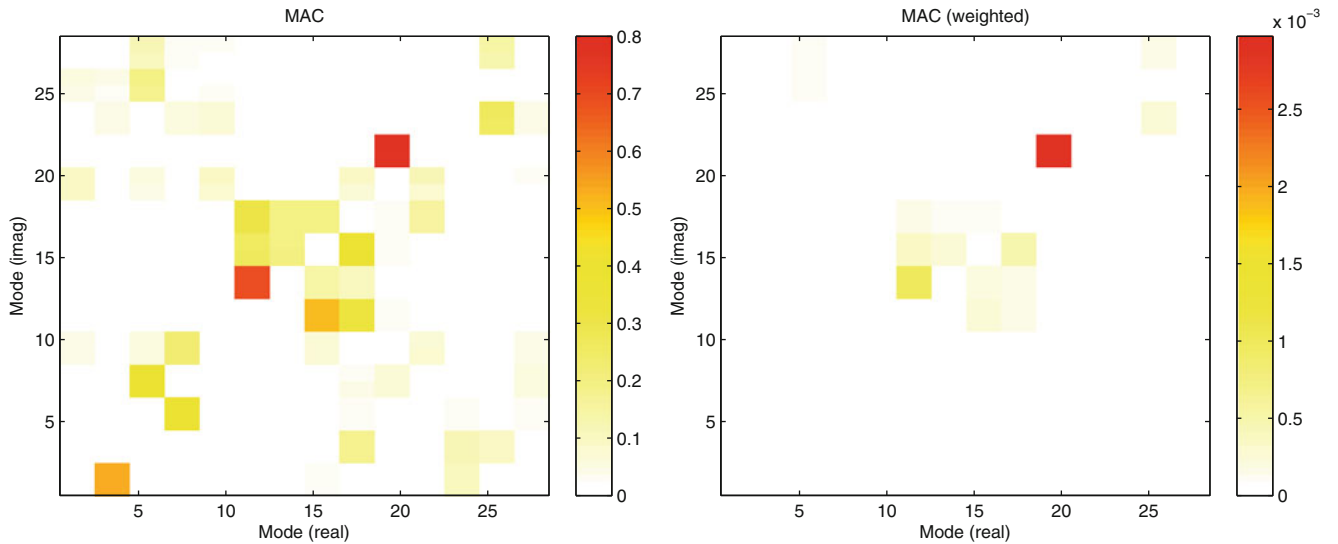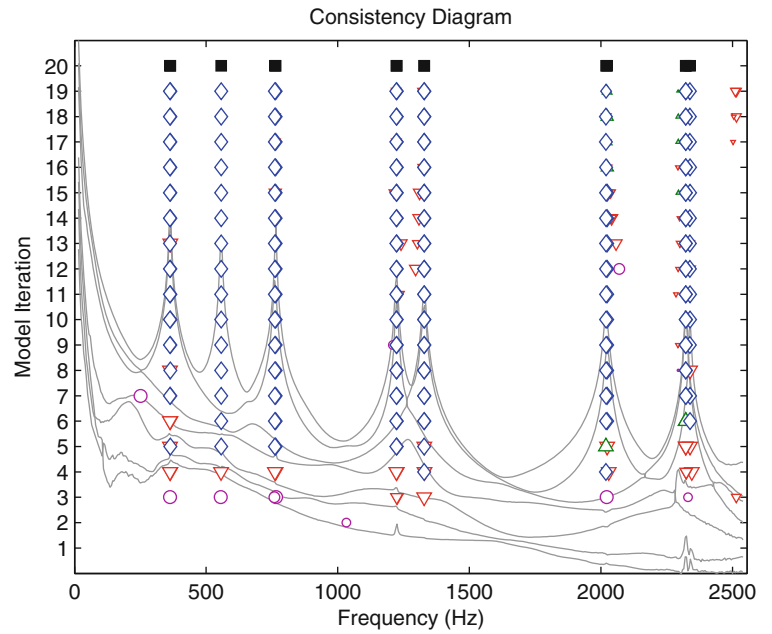




**Fig. 4.9** C-Plate, real weighting, riMAC and riwMAC

## 4.6  Summary and Future Work

A relatively simple change to the weighting vectors used in the weighted estimation of the residues for each mode has dramatically improved the results with little to no observable negative effects. For the examples chosen, the use of central vector rotation and real normalization of the modal participation vectors appears to improve the quality and characteristics of the final, scaled modal vectors (residues) significantly.

Future work will involve alternative numerical methods for decoupling the contaminated modal vectors and a more rigorous evaluation of the source of contamination derived from the companion matrix solution with the goal of eliminating the contamination earlier in the parameter estimation process. A more complete understanding of why this technique works so well is still needed.

**Fig. 4.10** C-Plate consistency
diagram, real weighting,
2,315–2,345 Hz range
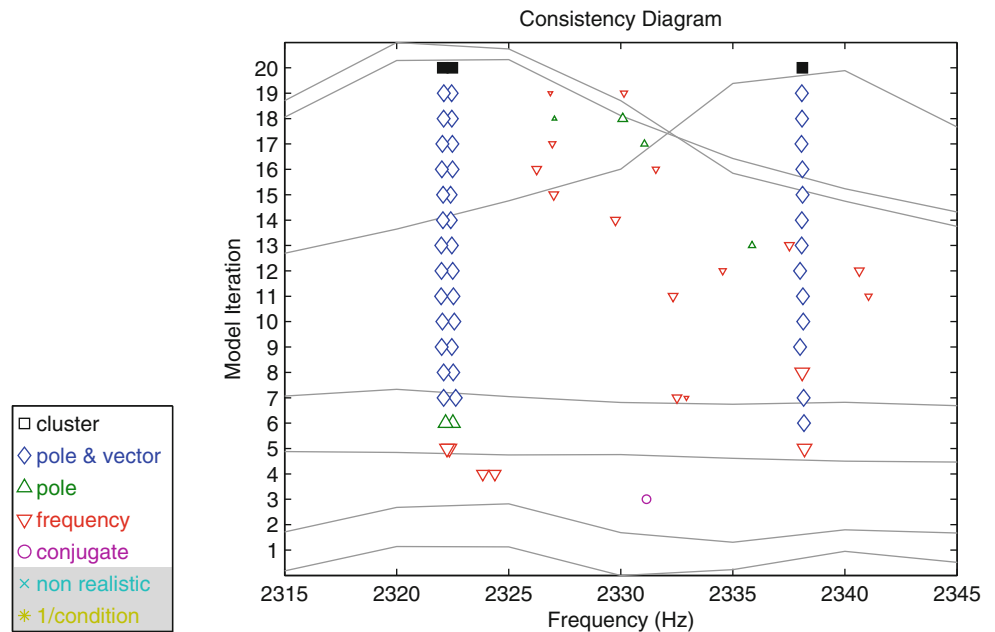


# References

1. Allemang RJ, Phillips AW (2004) The unified matrix polynomial approach to understanding modal parameter estimation: an update. In: Proceedings of international conference on noise and vibration engineering (ISMA)
2. Allemang RJ, Brown DL (1982) A correlation coefficient for modal vector analysis. In: Proceedings of international modal analysis conference, pp. 110–116
3. Heylen W (1990) Extensions of the modal assurance criterion. J Vib Acoust 112:468–472
4. Lallement G, Kozanek J (1999) Comparison of vectors and quantification of their complexity. In: Proceedings of international modal analysis conference, pp. 785–790
5. Allemang RJ (2002) The modal assurance criterion (MAC): twenty years of use and abuse. In: Proceedings of international modal analysis conference, pp. 397–405
6. Allemang RJ (2003) The modal assurance criterion (MAC): twenty years of use and abuse. Sound Vib Mag 37(8):14–23
7. Allemang RJ, Phillips AW (2014) Un-weighted and weighted versions of the modal assurance criterion (MAC) for evaluation of modal vector contamination. In: Proceedings of international modal analysis conference (IMAC), 8 pp
8. Deblauwe F, Allemang RJ (1986) A possible origin of complex modal vectors. In: Proceedings of 11th international seminar on modal analysis (ISMA), Katholieke Universiteit Leuven, Belgium, 10 pp
9. Phillips AW, Allemang RJ, Brown DL (2011) Autonomous modal parameter estimation: methodology. In: Proceedings of international modal analysis conference (IMAC), 22 pp
10. Allemang RJ, Phillips AW, Brown DL (2011) Autonomous modal parameter estimation: statistical considerations. In: Proceedings of international modal analysis conference (IMAC), 17 pp
11. Allemang RJ (2013) Spatial information in autonomous modal parameter estimation. Invited keynote paper, International conference on structural engineering dynamics (ICEDyn 2013), Sesimbra, Portugal, 18pp

# Chapter 5
# Effective Use of Scanning Laser Doppler Vibrometers for Modal Testing

**Ben Weekes and David Ewins**

**Abstract**  Vibration measurement using a scanning laser Doppler vibrometer (SLDV) has a number of advantages over the use of accelerometers: setup is rapid, the sensor is non-contacting, and many more measurement points can be acquired in a given testing period. Use of SLDVs can therefore drastically reduce concerns of spatial aliasing, and makes identification of local modes simple. However, effective use of SLDVs for modal analysis can be difficult given that line-of-sight between the SLDV head and tested surface must be maintained, and so significant parts of the structure may be unrepresented in the analysis. This has been addressed in recent trials of hybrid accelerometer/SLDV test geometries applied to aerospace structures, in which a relatively sparse accelerometer array is combined with detailed SLDV inspections of local regions. In these trial inspections a number of difficulties particular to combining the respective test geometries, and then matching the combined test geometry to an FE model, were experienced and solutions developed. Also discussed are the effects of acquiring 'pockets' of SLDV data with many measurement points that can bias the metrics on which experimental modal analysis and model updating procedures are based. In this paper, effective use of the SLDV as a tool for modal analysis and model updating is explored in some detail.

**Keywords**  SLDV • Laser • Vibrometry • Modal analysis • Model updating

## 5.1  Introduction

### 5.1.1  Scope of Paper

This paper is intended to aid the reader in deciding whether SLDV would be beneficial for their application of experimental modal analysis, and in learning how to use the SLDV effectively. Operating principles for SLDV in general are reviewed, then use of the SLDV in modal analysis, followed by a case study which shows how model updating results can be affected.

### 5.1.2  Introduction to SLDVs

Laser Doppler vibrometers (LDVs) are a type of optical interferometer which measure velocity at a point on a surface by detection of the Doppler shift of light—a phenomenon in which back-scattered (or reflected) light is frequency shifted if the emitting/reflecting body is moving relative to the source/viewer of the light. The laser notionally emits light of a single frequency, and so by mixing the returned light with a reference monochromatic light source on a photo-detector, a beat signal which can be measured with an extremely high accuracy is produced. The demodulated output takes the form of a voltage proportional to the measured velocity. As an optical sensor, there are a number of differences in the application of LDV compared to transducers which are attached to a test-piece. First, it must be noted that the laser potentially exists in

B. Weekes (✉) • D. Ewins
University of Bristol, Queen's Building, University Walk, Bristol BS8 1TR, UK
e-mail: b.weekes@bristol.ac.uk

a different inertial frame to the test-piece, i.e., relative vibration of either the LDV or the test-piece will be detected. This can be problematic since the LDV is usually mounted to a tripod which contacts the floor, whilst in a modal test the test-piece is often isolated on soft suspension. There are also potential optical issues; adequate laser light must be returned to the photo-detector for the demodulation electronics to function else a 'drop-out' wherein the outputted velocity signal becomes a spurious and strongly negative occurs. This issue is compounded by the issue of laser speckle [1, 2]; surfaces which are optically rough (i.e., non-specular) will see the laser light incident upon the surface self-interfere, which given the highly monochromatic and coherent content causes localised bright and dark regions. The speckle pattern observed is a spatial phenomenon, and so the usual means to achieve a measurement when a dark speckle is incident upon the photo-detector is simply to fractionally move the laser spot such that a brighter part of the speckle pattern is then incident upon the sensor.

SLDVs are LDVs with the addition of a pair of scanning mirrors and typically also a video feed. For each test configuration a calibration is performed such that the laser spot can be located on the surface of the test-piece by interaction with the video feed. The scanning mirrors allow the laser to be steered, moving the measurement location. However, there must be line-of-sight between the mirrors and all desired measurement locations, limiting the scope of the test that can be performed by a single SLDV head in a single location. It is possible to use additional mirrors to expand the possible area of inspection, but movement of the mirrors will be also be measured. Note that multi-laser vibrometer systems are a subject of developmental interest [3].

SLDVs, like LDVs, comprise a single sensor, and so although data can be acquired at many locations, the measurements are sequential. The apparent time-saving from use of SLDVs and the increase in the number of measurements which can be taken are by virtue of how rapidly an SLDV can be set up compared to an array of physically-attached transducers and their associated wiring. Since the SLDV measurement is sequential, the full excitation signal must be repeated at each measurement location (with repeat measurements as necessary), and so for the SLDV measurement locations to be compared the test should either be repeatable, or statistically rigorous.

## 5.2   Use of SLDVs in Modal Analysis

A flow chart for a typical modal analysis is given in Fig. 5.1, showing the often iterative nature of the validation process. Virtual testing (or pre-test) comprises test strategy and test plan, which can be summarised as '*what test?*' and '*how?*' [4]. A finite element (FE) model is used to aid test planning to help define specific aspects of the test, particularly regarding optimal locations for degrees of freedom (DOFs) for the frequency bandwidth of interest. An experimental modal analysis (EMA) is performed as prescribed by the test plan, for which a modal solution is calculated. Given that the FE model used to generate the test plan is not validated, it is unsurprising that the modal analysis may fail to adequately describe the dynamics of the structure, and so a new test plan and further experimental analysis may be required. Once an acceptable modal solution is believed to have been found the FE model can be correlated against the EMA and attempts can be made to update the model. Again, the model updating process can fail if the model cannot be reconciled with the experimental data, requiring revisions to be made to the model structure, which in turn may show some deficiency in the EMA. Once a model which accurately approximates the observed dynamics of the part or structure has been found and successfully updated the model can be considered valid, and can be used in rigorous predictive analyses which would be too expensive to perform experimentally.

The SLDV is a transducer which yields data much like an accelerometer (albeit measuring velocity, not acceleration), but as discussed above a successful modal analysis demands a 'complete' dataset. The SLDV allows many measurement locations to be captured, but redundant capture may not benefit modal analysis. In this Section test planning for SLDVs is discussed, and the fundamental line-of-sight limitation is addressed by use of a combination of SLDV and accelerometers. Also discussed is how to combine and import these hybrid datasets into existing modal analysis software.

### 5.2.1   Changes to Test Design

The differences between performing an ad-hoc experimental analysis and an EMA can be somewhat subtle, but are informed by the ultimate use for the data. In Fig. 5.2 the models through which the data move are shown schematically; measurements capture responses to an input, from which data a modal description (solution) is found. The FE model is a spatial description of the test article, from which a modal solution can also be found, allowing the EMA and FE data to be correlated and model updating to be performed. The EMA and FE datasets are fundamentally mismatched since the EMA will typically comprise tens to hundreds of DOFs, whilst the FE model could easily comprise many thousands to millions of DOFs—most often, the

**Fig. 5.1** Schematic of modal analysis, showing flow from virtual testing to a validated model, with the contributions from the model and experimental analysis (*green* and *blue*, respectively) (Color figure online)
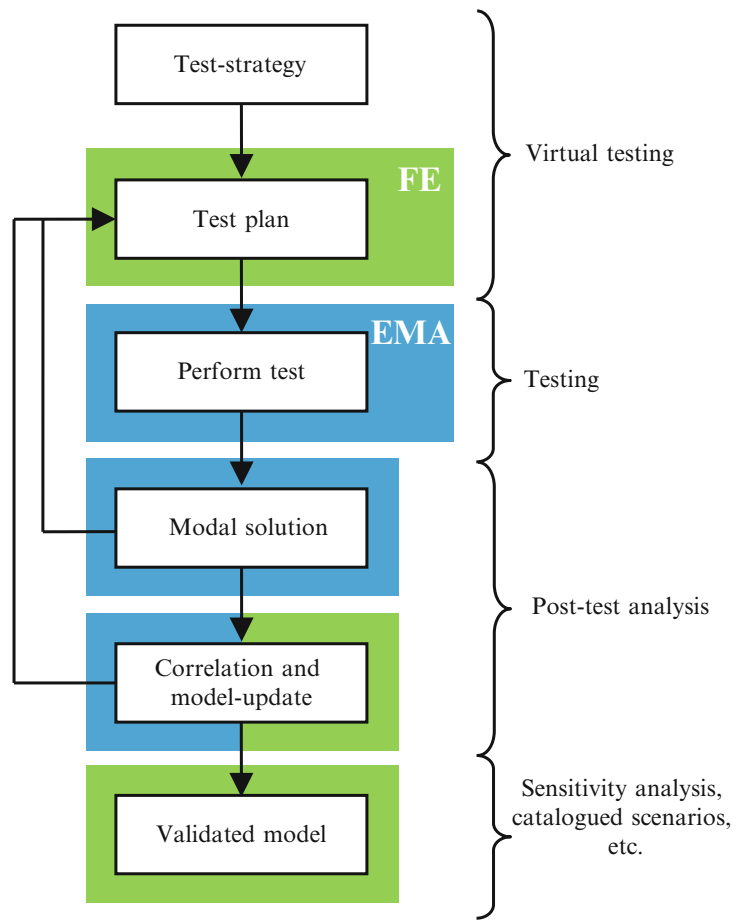


**Fig. 5.2** Schematic of modal analysis models
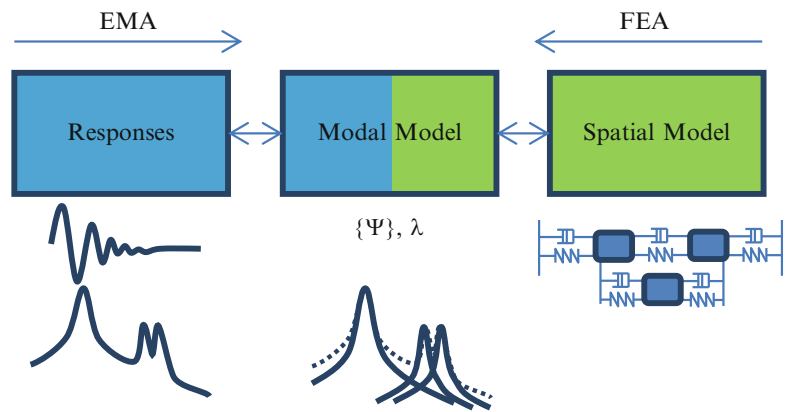


FE model is reduced to match the EMA rather than interpolation/extrapolation to expand the EMA dataset. When updating the model, the EMA geometry defines the reduced FE geometry, i.e., the number, orientation and distribution of the degrees of freedom. The test plan for the EMA is therefore more nuanced than an ad-hoc experiment-only analysis of vibration, with a complete modal description usually sought such that the system equations are not under-determined. Hence, use of virtual testing wherever possible to guide the experiment. However, there is some difficulty in creating a practical SLDV test geometry using virtual test tools because of the additional constraint in measurement locations required to maintain line-of-sight. Further, once a realisable SLDV test geometry has been created in the virtual test software, it is difficult to then perform measurements at the prescribed measurement locations without resorting to manually programming the locations at length. Without further development of tools to ease this process of creating and performing a SLDV test based on a pre-test, the speed advantage of SLDVs is limited. An alternative approach would be to simply define many measurement locations such that there is no concern of spatial aliasing between modes; the pre-test and test geometries need not be identical in

this case if sufficiently many measurement locations are defined. The limitation of this approach is that a single view-point of the laser will for non-2D (i.e., non-planar) test objects often fail to adequately capture the dynamics of the structure, necessitating supplementary transducers to provide additional DOFs out of the line-of-sight of the SLDV. The caveat in the use of additional transducers in such a manner is that the metrics on which the correlation is based will (by default) be significantly weighted by the many SLDV points, and so the relative weight of the supplementary DOFs (which are clearly of importance to be warranted) is reduced.

The capture of many non-coincident measurement locations by SLDV inherently increases capture of local modes. The identification of local modes is usually an advantage of using the SLDV, since it is often desirable to update the model based only on the lower order global modes, discarding the modes identified as local. This is because the low-order global modes are more likely to be a structural concern, and local modes often feature only subassemblies, which are likely to be subject to a boundary condition comprised of joints which are difficult to model (and therefore likely to be updated in a spurious way, to the detriment of the more important global modes). In the model updating process the model is iteratively updated multiple times, making it easier to discard the EMA local modes and rely upon the FE local modes not correlating against the EMA global modes and therefore not affecting the model update.

### 5.2.2   Import of SLDV Data: The Universal File Format

Modal analysis of structures which behave in a strongly linear manner is highly developed, with a number of software suites available in which to perform capture[1] and analysis[2] of the relevant data. However, these capture suites tend to require an array of transducers such that concurrent capture can be performed at all DOFs. Since capture is performed on discrete transducers by means of a simple voltage input, these systems can easily accommodate various transducers such as accelerometers and strain gauges. Such software suites currently lack the means to acquire data from SLDVs, which is unsurprising since interfacing with SLDVs requires calibration of the scanning mirrors to the video feed (test specific), defining the scan geometry on the video feed, measurement sequencing, etc., with the bespoke hardware/software giving interfacing difficulties. The software which comes with SLDV systems is usually adequate to perform a test and to review the results as FRFs, ODSs and sometimes as mode shapes, damping values, etc., but for more detailed analyses it is often desirable to output the captured time-histories or FRF data to perform the modal analysis in proven modal analysis software.

#### 5.2.2.1   Origin of the Universal File Format

The standard means of conveying modal test data is the universal file format (often .unv, .uff, .asc), an ASCII (i.e., text) based format defined by the Structural Dynamics Research Corporation (SDRC) [5] in the late 1960s and early 1970s to permit transfer of data between early computer design and test systems. Such is the legacy of the format that the data fields are typified by 80 character limits to fit 80 column punch card records. As an ASCII-based format, the files can be opened with any text editor, and with the formatting guide the files can be understood by a human operator.

#### 5.2.2.2   Important UFF Datasets for Modal Analysis

Universal files comprise datasets of various types [5]. There is provision for time history and FRF data in dataset type 58, and mode shape data in dataset type 55. Also present in universal files are datasets containing the header information (metadata), units, geometry, and coordinate systems. In exporting data from one software package to another using universal files it is often necessary to adjust the data manually if there is some disparity between the universal file interpretations for the software packages. Despite the supposed standardisation offered by the format, there is some ambiguity and variation in how the UFF interpreters are written, e.g., translation and rotation matrices may be defined to map from global to local coordinate systems, or vice versa. There are also legacy dataset types which can lead to difficulties with incomplete support, e.g., geometry dataset type 2,411 vs. type 15. Units are often imported incorrectly, especially in the case of units of acceleration, e.g., $g$, instead of mm/s$^2$ when the units dataset specifies SI units. The author has found cases of FRF plots scaled correctly in the modal

---

[1]e.g.: LMS Test.Lab, DataPhysics SignalCalc, M + P International SmartOffice.

[2]e.g.: LMS Test.Lab, DataPhysics SignalCalc, Spectral Dynamics STAR Modal, HDM nCode, M + P International SmartOffice.

analysis software since the SI units in the axes labels were taken from the universal file, whilst subsequent processing of the data in the same software package assumed units in $g$. Depending on the tools available in the modal analysis software and the permitted access to the underlying data, error-checking the imported data can be difficult.

#### 5.2.2.3  UFF and SLDV

The strength of the universal file format is its widespread use and the relative simplicity in directly interrogating the files when troubleshooting. However, when dealing with many DOFs (as is typical for SLDV data) the files can become unwieldy and difficult to edit. The files can also become large, although the more recent binary dataset 58b can reduce file sizes. There is no fundamental incompatibility between UFF files and SLDV data: the difficulties stem from managing the increased amount of data from the multitude of SLDV measurement points and in combining datasets from various capture systems of supporting transducers (see Sect. 2.3).

### 5.2.3  Management of Hybrid Datasets

As is described in the case study below (Sect. 3), the authors have tended to use hybrid accelerometer-plus-SLDV datasets. This requires some management of the respective accelerometer and SLDV datasets, which are generated by two different capture systems. As such, both datasets have their own node numbering and coordinate systems, and capture different temporal derivatives. Additional complexity is often incurred since most SLDV systems lack range-finding, and so assume all measurement points lie on a plane, with the measurement perpendicular to the plane (see Sect. 2.4). A simple program was written to combine the datasets, taking the following approach:
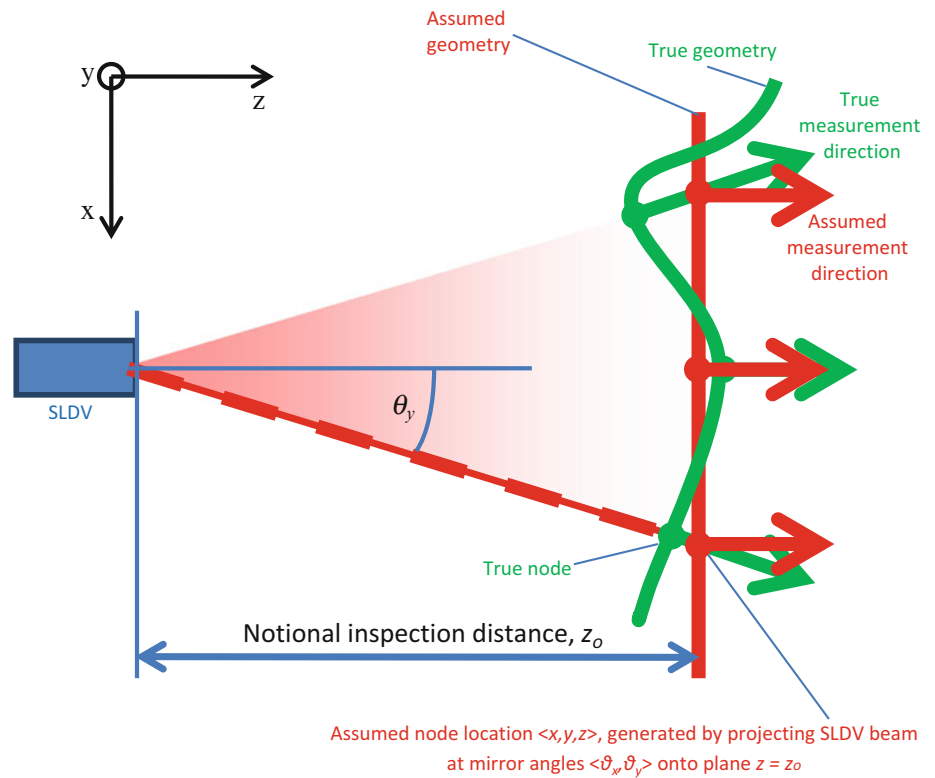
1. Take an accelerometer coordinate system as the master (often there is only one), and by means of three or more reference points common to both datasets, map the SLDV coordinates into the accelerometer system (e.g., using [6]).
2. Define local coordinate systems for all SLDV points to reorient each measurement axis to the incident angle of the laser. This requires the assumption that the test-piece is relatively planar, and an approximate location for the SLDV. This assumption is acceptable when the stand-off between the SLDV and test-piece is large relative to the geometric complexity of the test object in the stand-off direction.
3. Scale the velocity FRF data to acceleration by factor of $j\omega$.
4. Append SLDV data to accelerometer data, correcting node numbering (and associated references such as coordinate systems, driving point(s), etc.).

The UFF output of this bespoke software required some options regarding definition of the coordinate systems, units, and legacy UFF dataset formats depending on the modal analysis software which was to interpret the data, as discussed in Sect. 2.2. There remain some residual issues with the combined data, concerning the specific frequency resolution—the dissimilar capture hardware can give mismatches in the available sampling rates, clock, and buffer sizes. Some modal solvers can solve for such dissimilar frequency abscissa, although they rely upon resampling the data which may induce tangible error. Mismatched frequency abscissa can potentially see a single mode represented as multiple modes with nominally the same mode shape, separated by one or more discrete frequency increment. Ultimately, the ideal is to build a capture tool which unifies clocks, excitation bandwidth and sample frequencies.

### 5.2.4  Matching SLDV Test Geometries to FE Models

Accelerometer and SLDV geometries are typically generated by different means. The accelerometer array is located by the considered, deliberate act of attaching individual physical transducers to the test-piece. The SLDV measurement 'grid' is usually defined by drawing scan objects on the calibrated video feed, adding single measurement points, line sections, or polygons to cover areas. For large objects viewed on a relatively low resolution video feed, the spatial accuracy with which a measurement point can be placed can be noticeably coarse. In the case of scan objects which cover areas, the actual measurement points are usually set to comprise a number of key points around the perimeter of the object, with a number of measurement points in the enclosed area, typically uniformly spaced (rectangular grid, tessellated triangles, etc.) with respect to the pixels of the video feed. Unless the SLDV has the facility for range-finding, the two-dimensional geometry defined

**Fig. 5.3** Schematic of assumptions in a typical SLDV test geometry without range-finding



Assumed node location <x,y,z>, generated by projecting SLDV beam at mirror angles <$\vartheta_x$,$\vartheta_y$> onto plane $z = z_0$

**Fig. 5.4** Schematic showing (**a**) typical FEA/EMA node-point pairing, (**b**) a simple, improved FEA/EMA node-point pairing method for SLDV data
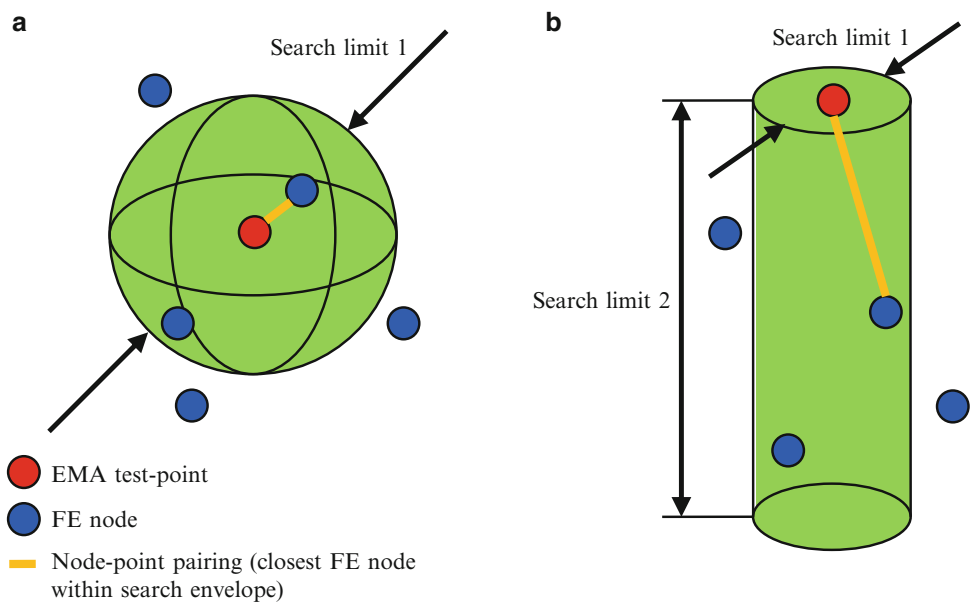


by the pixels in the video feed is the only geometry information available, and is often converted into units of measurement by simple scaling. Since the geometry lacks a depth dimension, the geometry is limited to a plane (Fig. 5.3). Further, the velocity measurement is typically considered to be perpendicular to the plane, rather than along the laser beam axis. This places limitations on the test design since the assumption that the velocity is out of plane could lead to significant inaccuracy in a model correlation.

An accelerometer array geometry is usually fitted to the FE model most easily by simple minimum distance (Fig. 5.4a). There are often small errors in the matching process due to mismatches between the FE and EMA geometries, which are typically corrected more easily for accelerometers simply because there are usually fewer accelerometer measurement points.

Since the SLDV data is usually from a single viewpoint, a simple projection along one axis is typically adequate to match the SLDV data to an FE model, although correction of the measurement angle is necessary if the SLDV measurement axis was deflected significantly.

## 5.3 Case Study

The UB100X is a University of Bristol test assembly which was designed to represent a highly simplified helicopter tail cone with wing (Fig. 5.5). The parts of the assembly considered in this paper are UB100X-B (component B), a box structure which represents a simplified helicopter tail-cone, and UB100X-C (component C), which represents a wing attached by four interference-fit pin joints to UB100X-B. Component B was welded together from aluminium plate, and has a number of features: large holes in two opposite faces, heavy flanges at one end, and brackets for attachment of component C. Component C is simply an aluminium plate with the corresponding brackets to component B. The brackets are bolted rigidly to the structure.

### 5.3.1 Virtual Testing and Experimental Analysis

The assembled box and wing structure was to be tested using a combination of accelerometers and SLDV, but given the difficulty in representing SLDV measurement locations with current virtual test tools it was decided to consider only the accelerometers, and to supplement the accelerometer array with an SLDV test geometry using operator judgement. First, component B was considered in the virtual test software without the wing (component C) attached, on the premise that the SLDV can easily measure many points on the attached wing (and usefully the SLDV avoids adding mass and damping to the wing). Component B was considered in isolation to avoid the confusion of the many aliased modes that would result in the B + C configuration with no degrees of freedom (DOFs) on component C. However, it is acknowledged that this is not ideal since the modes of B will differ somewhat from the modes of component B with component C attached.[3] The FE mesh comprised TET10 elements, and was generated automatically from a CAD model using MSC PATRAN. Using automated DOF placement it was found extremely difficult to place the DOFs for both unique determination of modes and for human visualisation of the modes, with the software tending to cluster the available DOFs at one end of the box (Fig. 5.6a). This test geometry is also found to be difficult to copy onto the genuine structure, and it would be easy to make an error in attaching, wiring and cataloguing the accelerometers since the test geometry is non-intuitive to the operator. This automated placement was achieved using an oft-used means of automatically placing a large number of DOFs (here, 80) using normalised modal displacement (NMD), and then reducing the number of DOFs (here, to 25) by considering the effect on the MAC. A test



**Fig. 5.5** Composite photograph showing the inspiration for the UB100X structure—the AgustaWestland 159 'Wildcat' tail cone and wing

Component C

Component B

---
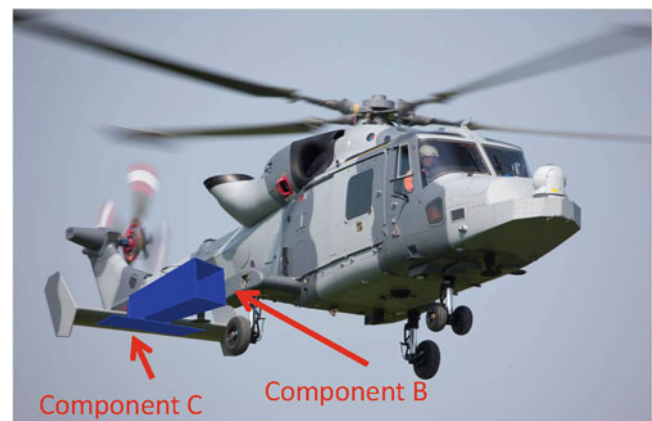
[3]Note also that it was observed in experimental data taken on the box without the wing, that the model upon which the virtual test was based did not behave with as much symmetry about the longitudinal axis as the genuine article, which explains some of the difficulty with the virtual test. Tests on the box structure alone are omitted here for brevity, but it is noteworthy that the box-only model could not be validated for updating, whilst the B + C model was adequate for updating.
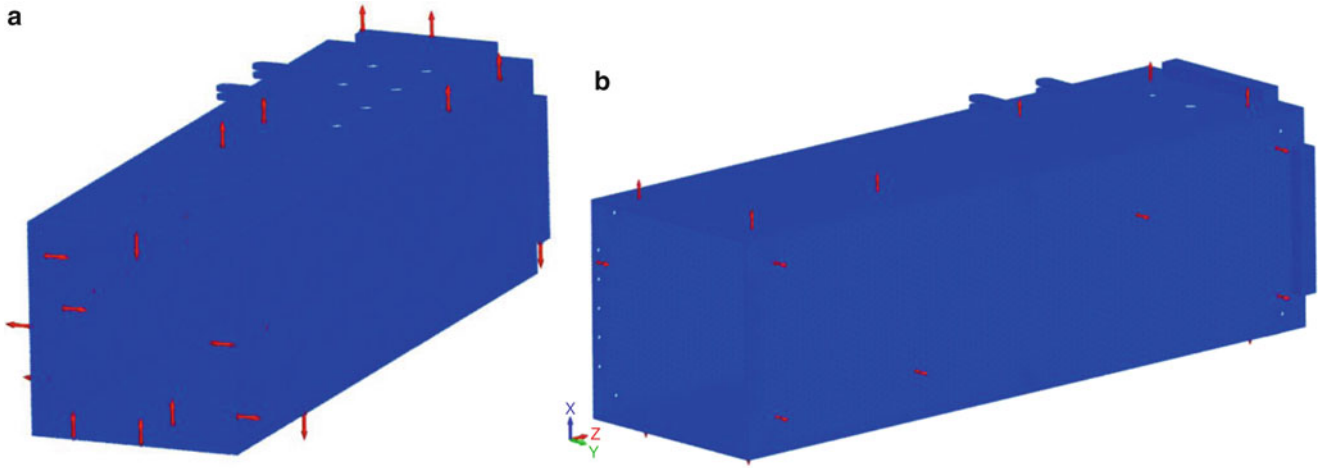
**Fig. 5.6** UB100X-B accelerometer test geometry from (**a**) automated DOF placement using normalised modal displacement and DOF reduction using MAC, (**b**) operator intuition
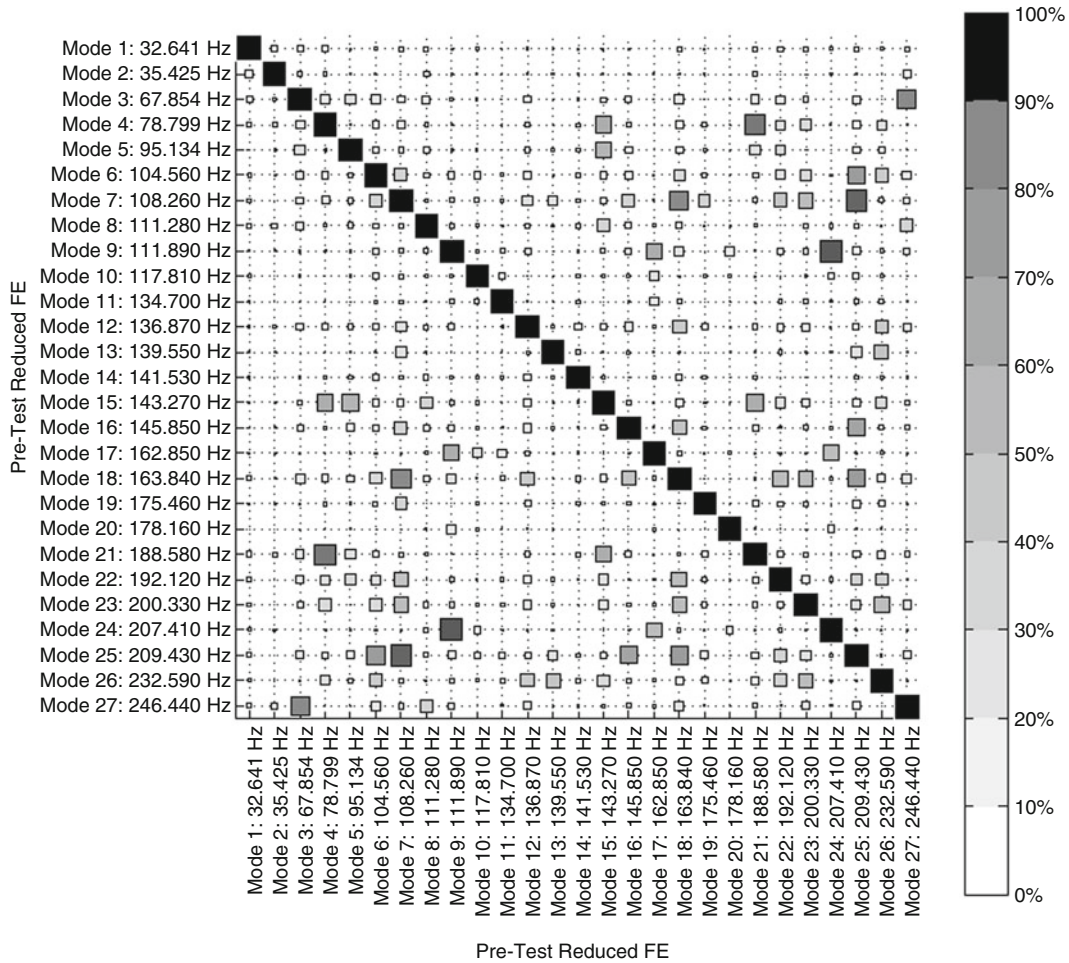


**Fig. 5.7** AutoMAC matrix for the prototype test geometry on UB100X-B shown in Fig. 5.6b

geometry with the same pattern of DOFs applied to each panel surface was manually-defined in the virtual test software, as shown in Fig. 5.6b. This geometry was found to give minimal aliasing of the mode shapes over the frequency range 0–250 Hz (see autoMAC matrix, Fig. 5.7), and the modes which correlate due to aliasing are observed to occur at dissimilar frequencies.

**Fig. 5.8** Photograph of experimental setup
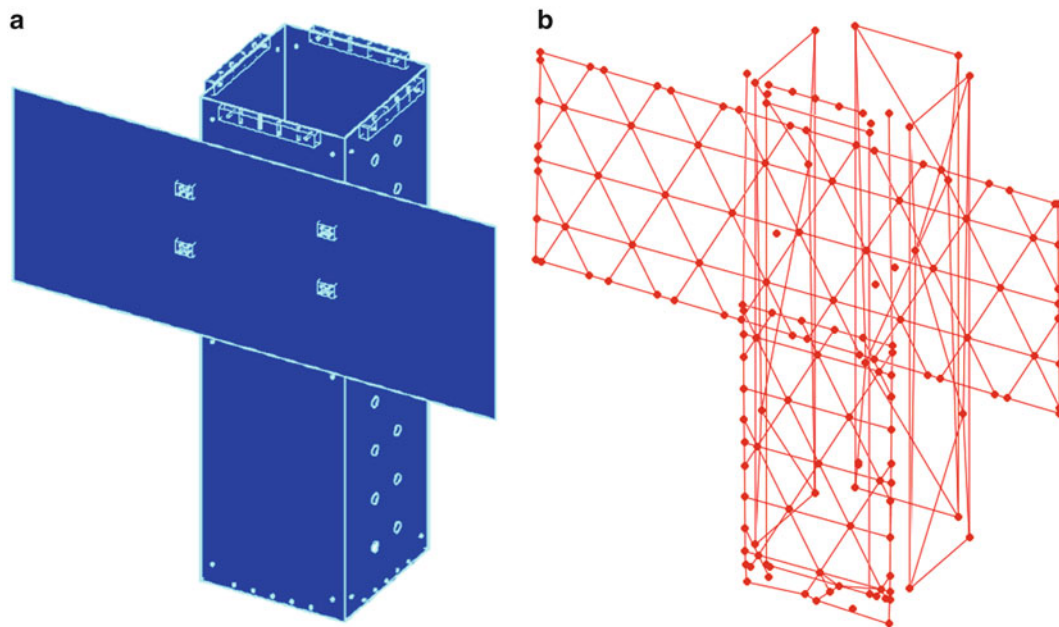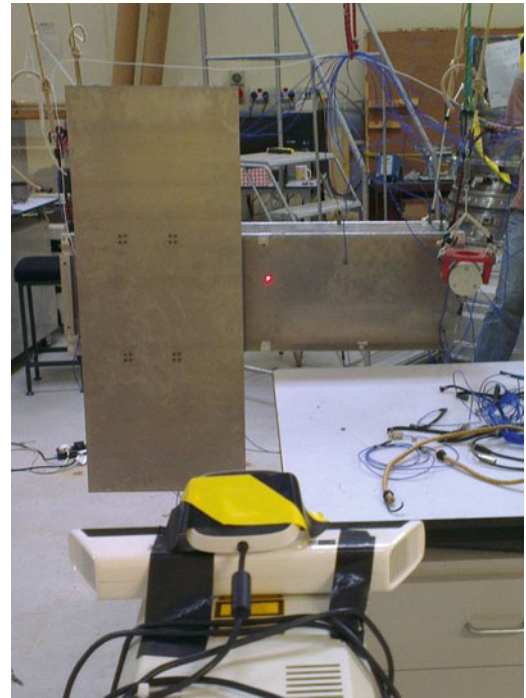




**Fig. 5.9** Test structure UB100X components B and C, (**a**) FE model, (**b**) EMA test geometry

The complete UB100X B + C model was meshed, again from a CAD model using TET10 elements in MSC PATRAN, with the pin-joints considered rigid (i.e., the whole assembly was effectively monolithic). The experimental analysis was performed using a Polytec PSV-300 SLDV system and a LMS SCADAS to control the accelerometer capture. A photograph of the experimental configuration is given in Fig. 5.8. The experiment was performed using a single exciter, which was a necessary concession to the capabilities of the SLDV system (although note that newer systems can perform MIMO). The combined accelerometer and SLDV test geometry can be seen in Fig. 5.9. An autoMAC matrix for an a posteriori reduction of the FE model using the test geometry points is given in Fig. 5.10. This autoMAC matrix is observed to be largely well-conditioned, although there are some significant off-diagonal terms. Examples of the aliased modes are given in Fig. 5.11, typified by similar behaviour on the faces which the SLDV can observe, but various symmetric and non-symmetric shapes on
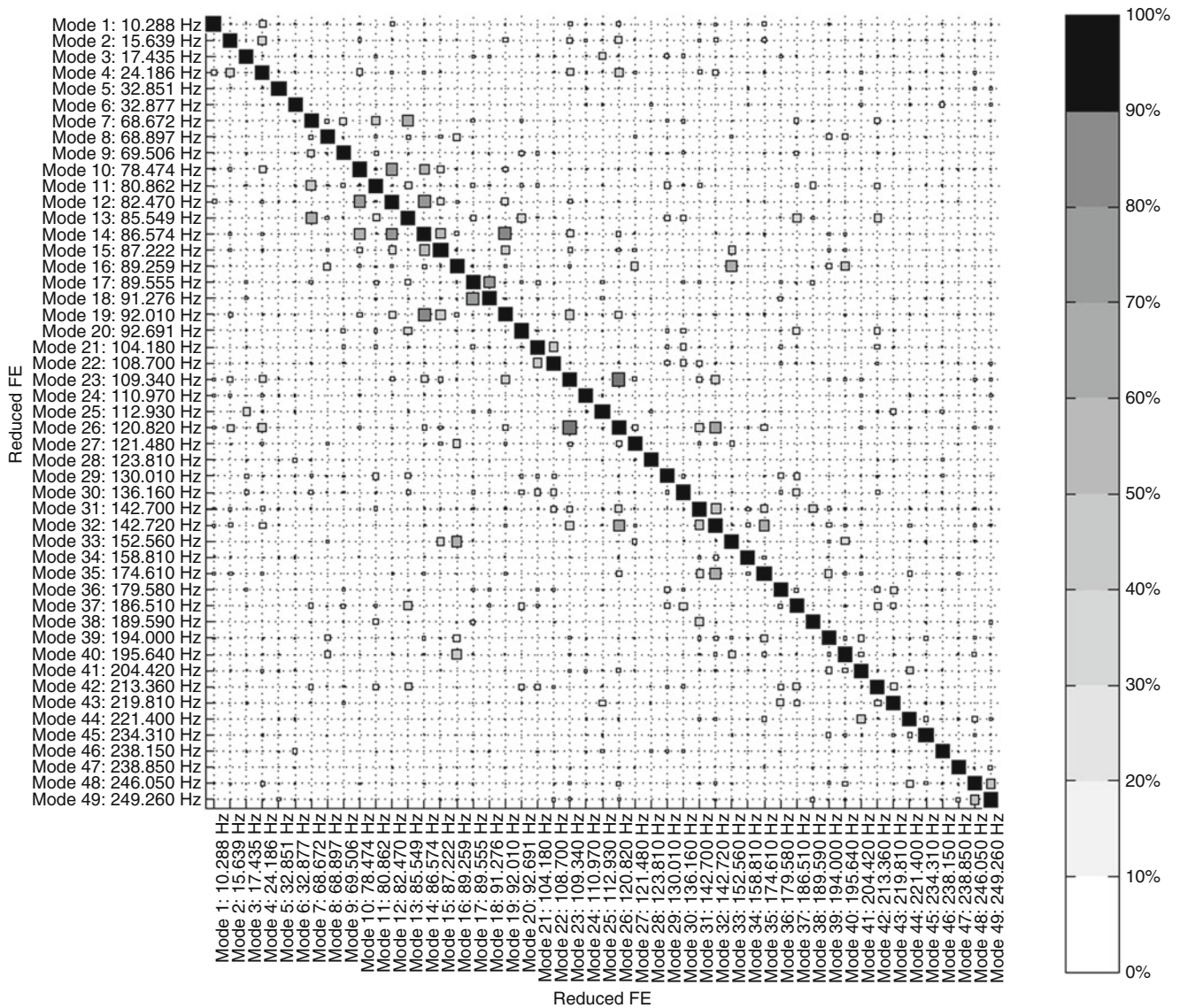
**Fig. 5.10** A posteriori autoMAC matrix for the UB100X-B + C model shown in Fig. 5.9a, reduced using the EMA points in Fig. 5.9b

the faces of the box section that the SLDV could not observe. Note that with better integration of SLDV into the virtual test, this autoMAC matrix could have been found a priori and a better-informed test performed. The SLDV was approximately perpendicular to the areas on which it measured (the wing, and some of one face of the box section) largely as a convenience to aid assimilation of the datasets (Sect. 2), but a location of the SLDV head which also gave a view of the top of the box would have significantly reduced the instances of aliased modes.

### 5.3.2 Experimental Modal Analysis and Model Correlation

The experimental SLDV and accelerometer FRF data were combined in a bespoke MathWorks MATLAB program, performing the functions described in Sect. 2.3 and outputting a master universal file. The combined dataset was imported once more into LMS Test.Lab, and a modal solution found. The experimental mode shapes were exported, again as a universal file, into DDS FEMtools for correlation and model updating.

Despite the relative simplicity of the component B + C model and the previous poor results from a component B-only correlation, the correlation between the test data and non-updated model were observed to be mostly extremely good, albeit
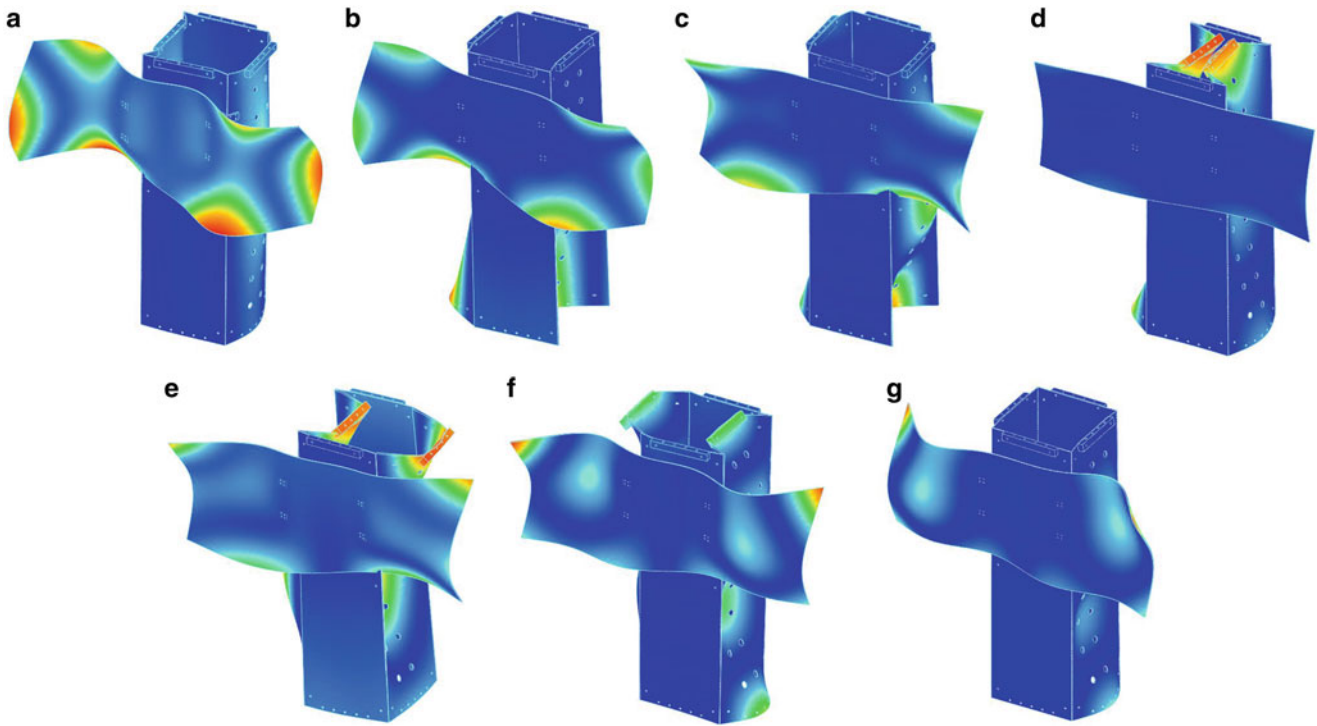
**Fig. 5.11** (**a–g**) FE modes 10, 12, 14, 15, 19, 23, 26, respectively. These FE modes are given as examples of the high off-diagonal mode pairs in the autoMAC matrix in Fig. 5.10. The reduced geometry which aliased these mode shapes is given in Fig. 5.9b, from which it is clear that whilst the SLDV allows adequate description of these high-order mode shapes on the wing, critically, the sides of the box are inadequately characterised

with some high off-diagonal terms in the MAC matrix (Fig. 5.12) caused by aliasing of modes in areas the SLDV could not measure. The FE and EMA modes were paired based on a minimum MAC of 50 %, with no repeated pairings (i.e., each mode could only be paired once) and no restriction between the difference in frequency of the modes. This relative lack of constraint and relatively low minimum MAC is acknowledged to be potentially sub-optimal, but it can be instructive to see how well the FE and EMA agree with minimal intervention.

The UB100X B + C structure was observed to exhibit effectively no local modes; the box has inherent symmetries, and as a welded assembly is assumed to have a fairly uniform mechanical impedance (i.e., distributed stiffness). Additionally, considered individually both the box and wing feature many modes in the frequency range of interest (0–250 Hz), and so it is unsurprising that when considered as a system (B attached to C) that all modes see some participation from both components. In the case of the UB100X B + C assembly, the lack of local modes instead saw the spatial resolution advantage of the SLDV translated into being able to match a large number of EMA global modes to the FE, namely 20 pairs.

### 5.3.3 Model Updating

In order to explore the influence of the SLDV measurements on the model updating process, multiple model updates were trialled with the complete EMA dataset, and a reduced EMA dataset representative of the spatial resolution which could be reasonably achieved with accelerometers. In the reduced EMA dataset there were six SLDV DOFs left on the wing (corners plus mid-points), which gave a total of 31 DOFs (which including a force reference on the driving point would populate a 32 channel acquisition system). The model updating was performed in several different ways, as is often the case when trying to understand the sensitivity of a model to changes in parameters, as explained under Sects. 3.3.1 and 3.3.2. The common settings between all updates were mass-density ($\rho$) and Young's modulus (E) were parameterised, with no constraint on the amount they could be varied. The responses were a target mass, and to optimise the frequencies and MAC for the paired modes. Updating was stopped when the correlation criterion fell below a certain level, or no improvement was seen between model iterations.
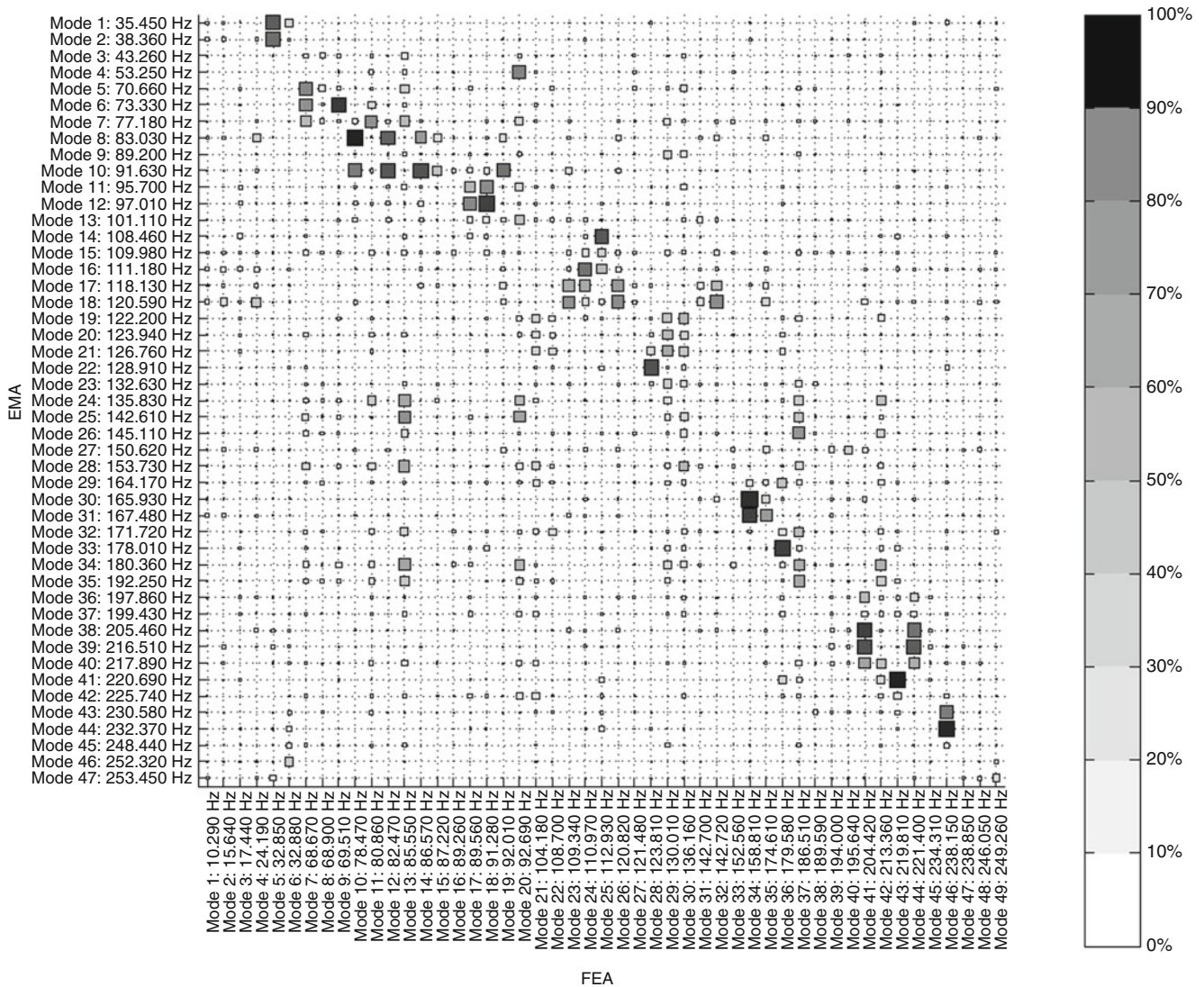
**Fig. 5.12** FEA/EMA MAC Matrix for the UB100X B + C structure before model updating

### 5.3.3.1 Model Updating Using Global Parameters of Component Subsets

The first updating method which was trialled was to define subsets of the B + C structure, then allow the parameters (density and Young's modulus) to vary globally for each subset. The subsets are shown in Fig. 5.13. The idea behind this parameterisation was to identify which components of the model were not representative of the real structure. The structure was fabricated from sheet and billet aluminium, and so it seems implausible that these properties should vary much locally, excepting at joints. There remains a question over the properties of the welds, but these do appear to be of a very high quality and so are assumed to be similar to the parent aluminium structure. This means of parameterisation is appealing because if such a model update can be validated the component parts of the model are each described by a single material, and not many materials per component.

The results from the updating are given in Table 5.1. The effect of reducing the number of measurement points on the structure was significant, with the complete dataset strongly altering the properties of the wing (component C), the welds, and the flanges, whilst the reduced dataset saw the strong alteration of the welds, the brackets and the pins. The results for the reduced dataset appear more plausible since it identifies the joints between the wing and box section. The complete dataset saw the mass of the wing more than double (with the increase in stiffness presumably compensating for the otherwise reduced resonant frequencies), which is highly unrealistic.

**Fig. 5.13** FE model of components B (box section) and C (wing), broken into subsets: wing (component C), brackets, pins, welds, flanges, bulk (remainder of component B). Parameter updating for density and Young's modulus based on allowing individual materials for each of these subsets are given in Table 5.1
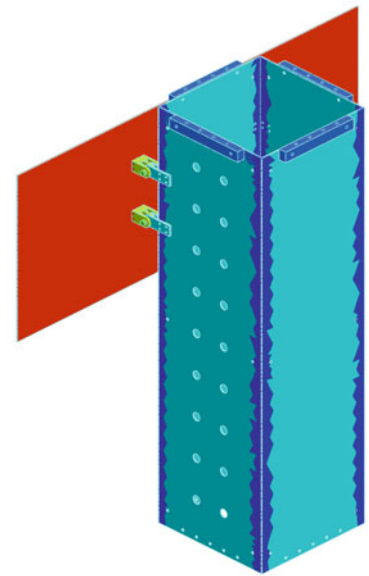


**Table 5.1** Values for density and Young's modulus after model updating based on component subsets

|  |  | $\rho$ | $\Delta\rho/\rho$ (%) | E | $\Delta E/E$ (%) |
|---|---|---|---|---|---|
|  | *Starting values* | *2,700* | – | *6.90E + 10* | – |
| Complete dataset | Component B (bulk) | 2,556 | −5.33 | 7.06E + 10 | 2.32 |
|  | **Component C** | 6,303 | **133.44** | 1.17E + 11 | **69.86** |
|  | **Welds** | 298 | **−88.96** | 4.89E + 10 | −29.13 |
|  | Brackets | 2,764 | 2.37 | 9.16E + 10 | 32.75 |
|  | Pins | 2,785 | 3.15 | 8.80E + 10 | 27.54 |
|  | **Flanges** | 2,059 | −23.74 | 5.40E + 09 | **−92.17** |
| Reduced dataset | Component B (bulk) | 2,885 | 6.85 | 6.99E + 10 | 1.30 |
|  | Component C | 1,883 | −30.26 | 5.84E + 10 | −15.36 |
|  | **Welds** | 1,670 | **−38.15** | 3.56E + 10 | **−48.41** |
|  | **Brackets** | 10,911 | **304.11** | 4.44E + 09 | **−93.57** |
|  | **Pins** | 3,459 | 28.11 | 1.20E + 11 | **73.48** |
|  | Flanges | 2,836 | 5.04 | 7.15E + 10 | 3.62 |

The complete EMA dataset and a reduced version of the same dataset were considered

### 5.3.3.2 Model Updating Using Local Parameters

A second round of updating was performed, this time allowing local parameterisation for all FE nodes. In Figs. 5.14 and 5.15 the updated model is shown for the complete and reduced datasets, respectively. As was observed in the updating using global parameters on subsets of the model (Sect. 3.3.1), the updating results vary significantly for the complete and reduced datasets. Whilst the results from the two datasets bear a resemblance, the reduced dataset sees greater local variation and contrast in the density and Young's modulus parameters. This is particularly apparent on the wing section, in which the Young's modulus map sees strong increases around all four attachment points to the box section. 'Shadows' of the paired modes are apparent in the local variations of the parameters, and given that different numbers of modes could be paired for the two datasets this accounts for some of the difference in the updating results.

A further model update was performed, taking the updated models from Sect. 3.3.1, and then allowing local parameterisation as described above. The underlying idea was that the first round of updating using global parameters of subsets should have given a better model to start from, with the local updating then requiring fewer iterations and less strong local variation of the parameters to converge. Again, the model updating was performed twice, first on the complete and secondly on the reduced datasets, with the results shown in Figs. 5.16 and 5.17, respectively. This two-stage approach appears to have lessened the amount of local updating on component B, although component C appears much the same, with the patterns in the maps of density and Young's modulus both seeming to indicate some deficiency in the modelling of the joints. The two-stage approach applied to the reduced dataset yielded results different to both local-only updating of the complete dataset (Fig. 5.14), and local-only updating on the reduced dataset (Fig. 5.15). The strong and well-defined updates around the component C joints in the local-only update of the reduced model are not as clear, and there is more local variation of the parameters on the sides of component B.
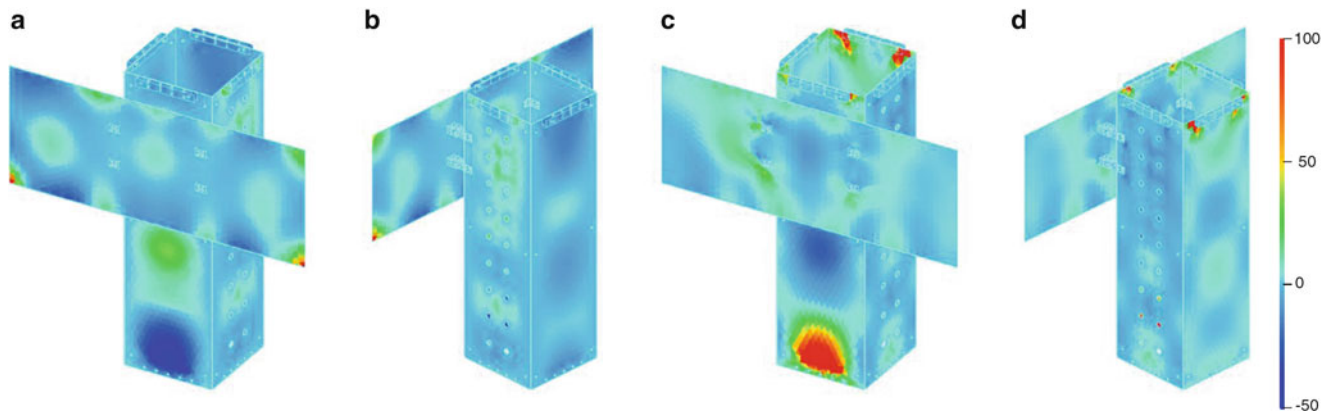
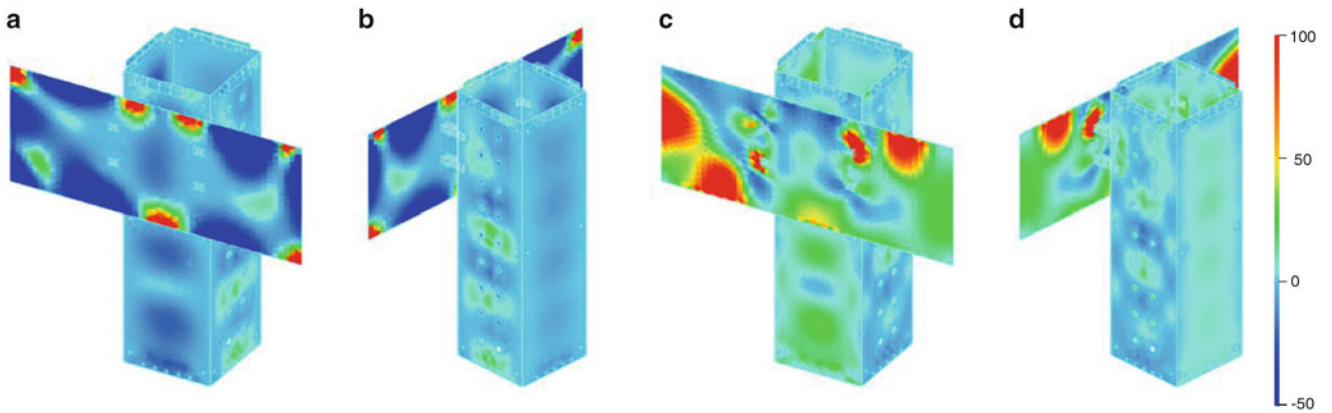**Fig. 5.14** UB100X model after update using local parameters. Change in: (**a**, **b**) density; (**c**, **d**) Young's modulus
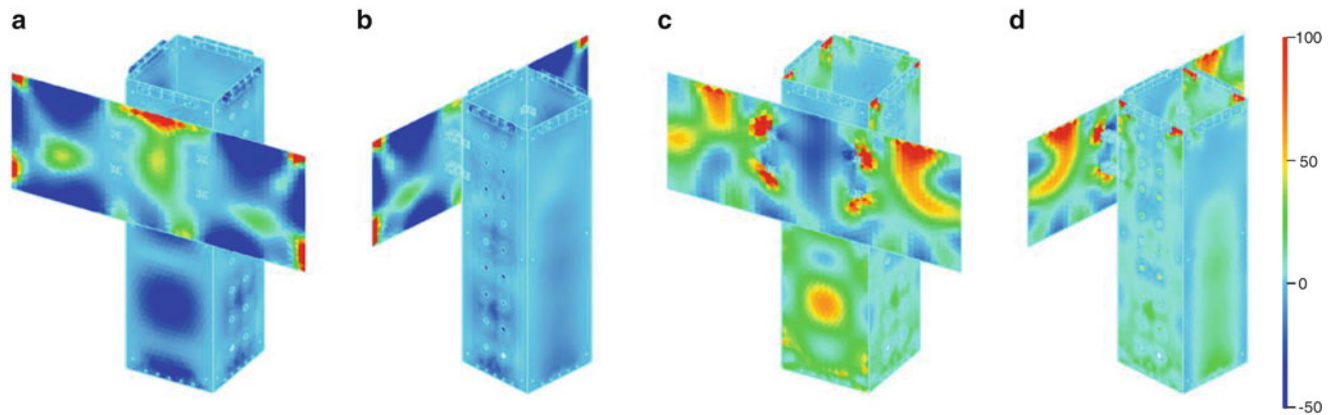


**Fig. 5.15** UB100X model after update using local parameters on the reduced test geometry. Change in: (**a**, **b**) density; (**c**, **d**) Young's modulus
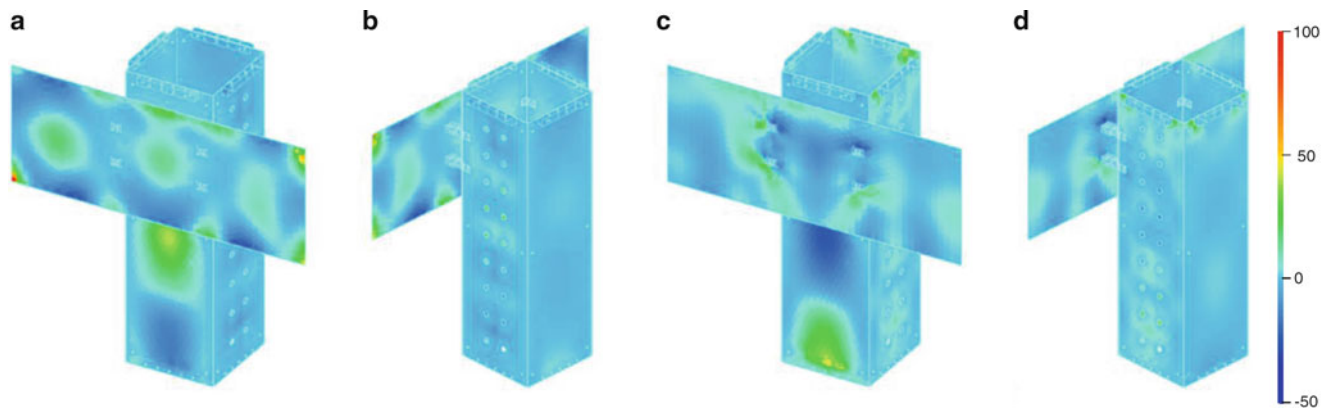


**Fig. 5.16** UB100X model after update using global subsets, then local parameters. Change in: (**a**, **b**) density; (**c**, **d**) Young's modulus

The natural frequencies for the paired modes for each of the updating trials discussed in this paper are given for the complete and reduced datasets in Fig. 5.18. From this plot it is clear that the mode pairing for the complete dataset (blue points) is better than for the reduced dataset (red points). This is not surprising, since the reduced dataset gives an increase in instances of aliased modes. Note that a restriction was placed on the frequency difference allowed in mode pairing for the reduced dataset (no greater than 50 %), while no restriction on frequency was necessary for the complete dataset. The lower numbers of paired modes for the reduced dataset, and higher numbers of spurious pairings strongly supports the use of SLDV in this application. The small number of poor mode shape pairings observed with the complete dataset may have been improved by locating the SLDV in a different position relative to the test-structure such that multiple faces of component B could be observed.

**Fig. 5.17** UB100X model after update using global subsets, then local parameters on the reduced test geometry. Change in: (**a**, **b**) density; (**c**, **d**) Young's modulus
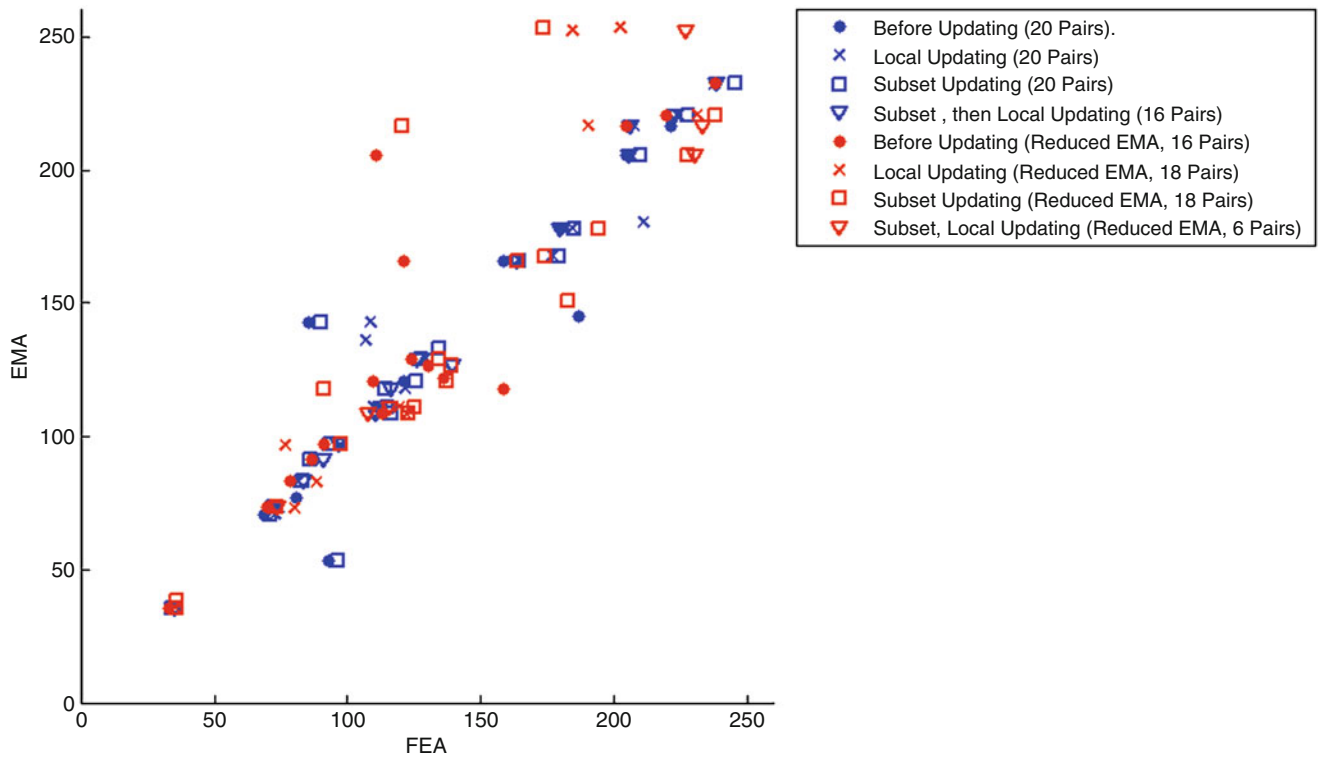


**Fig. 5.18** Frequency-frequency plot for paired mode shapes (MAC ≥ 50 %). No restriction on frequency difference was set for the complete dataset, whilst a maximum frequency difference of 50 % was set for the reduced dataset to minimise pairing of aliased modes

## 5.4 Conclusions

In this paper, various means of performing modal testing using SLDVs were discussed, with particular attention to the challenges encountered in importing measured data into existing modal analysis software packages. A case study of the application of a hybrid SLDV and accelerometer test geometry was demonstrated, and the correlation with a basic FE model through to high order modes was shown to be extremely good. The SLDV was shown to be a useful tool for modal analysis, although the line-of-sight limitation of such a device when trying to characterise the structural dynamics of a three-dimensional structure must be considered. Development of virtual testing tools to optimise use of SLDV is highly desirable and would significantly increase the benefit in the use of SLDVs for modal analysis.

Various model updating trials were detailed including use of a reduced number of degrees of freedom. It was shown that the use of many degrees of freedom increased the number of model and test mode shapes which could be paired, and reduced

instances of spatial aliasing. The updated model was clearly affected by the change in the number of degrees of freedom, although the merit in the increased number of measurement locations is difficult to qualify and is likely application-specific. Interpretation of results from model updating is often difficult, and the model updating process itself will—for better or worse—converge towards a solution based solely on the parameters, responses and metric for correlation defined by the operator. However, the option to match the response of the finite element model to an experimental measurement at a greater number of locations as afforded by use of SLDV often appears appealing.

## References

1. Rothberg S (2006) Numerical simulation of speckle noise in laser vibrometry. Appl Opt 45:4523–4533
2. Sraric M, Allen M (2009) Experimental investigation of the effect of speckle noise on continuous scan laser doppler vibrometer measurements. In: *IMAC XXVII*, Orlando, FL
3. AIVELA (2012) Ancona
4. Ewins D (2000) Modal testing 2. Research Studies Press Ltd., Hertfordshire
5. University of Cincinnati, SDRL, "Universal File Formats for Modal Analysis Testing," [Online]. Available http://www.sdrl.uc.edu/universal-file-formats-for-modal-analysis-testing-1/universal-file-formats-for-modal-analysis-testing.
6. Arun KS, Huang TS, Blostein SD (1987) Least-squares fitting of two 3D point sets. IEEE Trans Pattern Anal Mach Intell 9(5):698–700

# Chapter 6
# Precise Frequency Domain Algorithm of Half Spectrum and FRF

**J.M. Liu, W.D. Zhu, M. Ying, S. Shen, and Y.F. Xu**

**Abstract** In operational modal analysis, the half spectrum is needed. Its corresponding time wave is the half part of correlating function with positive time delay. In classic modal analysis, the frequency response function (FRF) is needed. Its corresponding time wave is the unit impulse response function (UIRF). In current commercial modal analysis software, the frequency domain algorithm is used to compute half spectrum or FRF first. For algorithm of frequency domain based on FFT, its computation speed is very high, but there are errors caused by the periodic assumption of FFT both for half spectrum and FRF. For algorithm of time domain, the half part of correlating function with positive time delay or the UIRF are computed directly with the best preciseness, but the computation speed is slow and unpractical. The precise frequency domain algorithm put forward here is still based on FFT, with innovation in computing mode. The half spectrum computed out by the new algorithm, can reach the same precise as the time domain algorithm but the computation speed level is similar to traditional frequency domain algorithm. To compute the FRF, let the length of output wave be two times of input data wave, the length of unit impulse wave corresponding to FRF is the same as the input data wave. By this way, the errors caused by periodic assumption of FFT can be totally eliminated both for impact exciting and continuous exciting. For continuous exciting, the initial response is needed to be considered. This consideration can be fulfilled by a few times iteration. The precise of FRF by new algorithm is very close to time domain algorithm. The computation speed of the new algorithm is accelerated more than ten times comparing with the algorithm of time domain. A new coherence function definition, which is suitable for half spectrum, for FRF of the traditional algorithm and new algorithm in frequency domain, as well as for FRF of algorithm in time domain, is introduced. It can be used to evaluate the preciseness of FRF and half spectrum. For impact test, if only the data of one impact is available, the value of traditional coherence function is one in all the spectrum lines, without any physical meaning, but the value of new coherence function will still reflect the ratio of signal to noise in each spectrum lines.

**Keywords** Half spectrum • FRF • Algorithm of frequency domain • Coherence function

## 6.1 Introduction

In OMA operational modal analysis, the half spectrum is needed. Its corresponding time wave is the half part of correlating function with positive time delay [1]. The tradition algorithm of half spectrum is in frequency domain, for below steps:

(1) Computing cross spectrum.
(2) By IFFT transforming the cross spectrum to obtain the correlating function coefficients.
(3) Throw away the part of negative time delay, FFT transform the part with positive time delay to obtain the half spectrum.

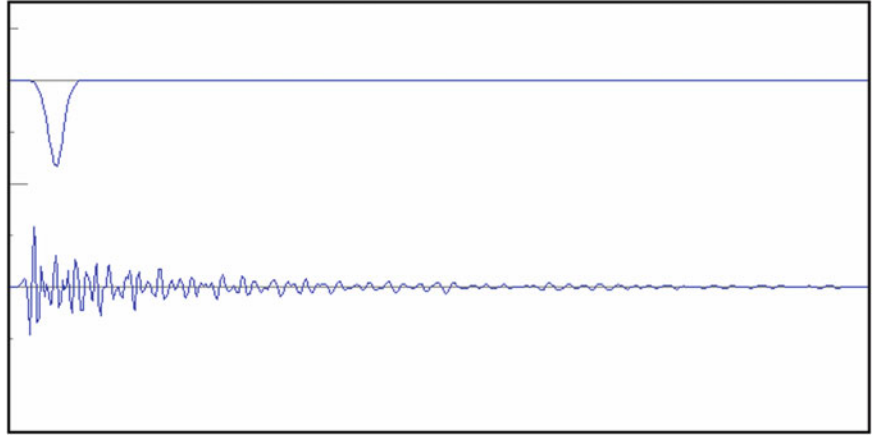J.M. Liu (✉) • M. Ying • S. Shen
China Orient Institute of Noise and Vibration, Beijing 100085, China
e-mail: Liujm@coinv.com

W.D. Zhu • Y.F. Xu
University of Maryland, Baltimore, MD 20250, USA

**Fig. 6.1** Exciting and response
wave
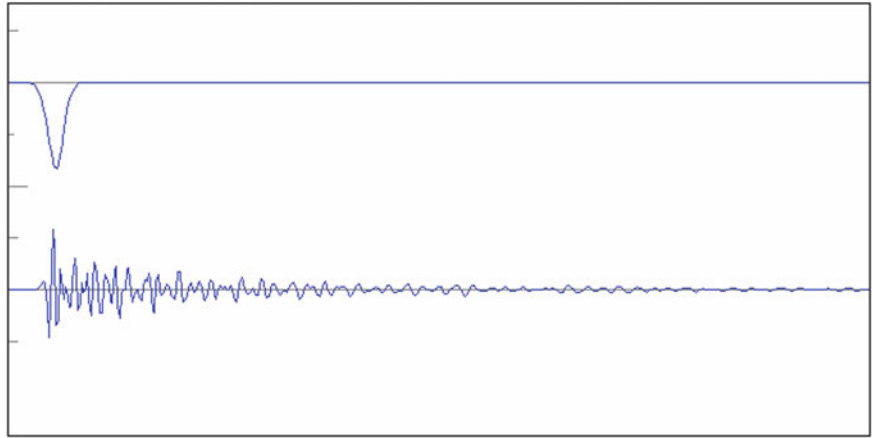


**Fig. 6.2** The response wave is
been moved ahead m point



When input wave $X(r)$ is known ($r = 0, 1, 2, \ldots, L-1$) and output wave $Y(r)$ is also known, $r = 0, 1, 2, \ldots, L+N-1$, the correlating function with positive time delay is defined as

$$R_{xy}(m) = \frac{1}{L}\sum_{r=0}^{L-1} X(r)Y(r+m) \tag{6.1}$$

$m = 0, 1, 2, \ldots, N-1$

Here the point number of output wave must be greater than input wave with $N$ points, to ensure the result of computation is correct.

For one time averaging, $L = N$.

With algorithm in frequency domain, FFT point number is $N$, the length of input wave and output wave both are $N$ points, correlating function coefficients of $m = -N/2, \ldots, -2, -1, 0, 1, 2, \ldots, N/2 - 1$ can be computed out. Only the points of positive time delay, from 0 to $N/2$, that is $m = 0, 1, 2, \ldots, N/2 - 1$ are used to obtain half spectrum. Among $N/2$ points of coefficients, when $r + m \geq N$, $Y(r+m)$ is not exist, because of FFT periodic assumption, it is replaced by $Y(r+m-N)$. In this way, the error will be produced. The error varies with different m value. When $m = 0$, there is no error. When $m = 1$, in the sum of $N$ products, only one product is incorrect. With $m$ increasing, the number of incorrect products will also increase.

For impact exciting, in traditional algorithm of frequency, the length of input wave is the same as output wave, equals to FFT points number for each averaging. The length of UIRF also equals to FFT points number. This computation mode does not in accordance with real condition. If the length of exciting wave is N point, and the length of UIRF is also N point, 2 N points of response wave will be produced. Thus for each averaging, the reasonable computation mode should be 2 N points of response wave and N points of impact wave to obtain UIRF of N points.

Here one example is given to show the defect of equal length computation mode. In Fig. 6.1, the above part is exciting wave of N points, the below part is the response wave of N points. For real structure, the response is always produced after exciting force. The real structure can be called "cause and outcome" system [2]. For test modal analysis, all the test objects are "cause and outcome" system. If the response wave is being moved ahead $m$ points, illustrated as Fig. 6.2, the response

**Fig. 6.3** The theoretical response wave (below part is after above part)
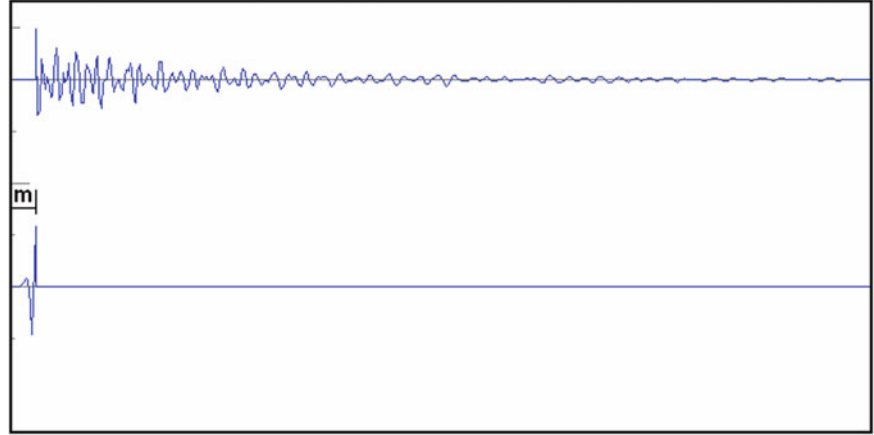


will produced before exciting force, this kind of system does not exist in real world. By equal length mode with one time averaging, the FRF and UIRF of Fig. 6.2 can be obtained, the value of coherence function in all spectrum lines are one, no abnormal signal will be displayed. The impact wave of N points and UIRF of N points will produce response wave of 2 N points, illustrated as Fig. 6.3. In Fig. 6.3, in above part 0 to 1,023 points of response wave are displayed, in below part 1,024 to 2,047 points of response wave are displayed. In above part, the first m points are all 0. In below part, there are wave in first m points, which is the same as the first m points of response wave in the Fig. 6.2. It can be proved theoretically that the UIRF of Fig. 6.2 is the UIRF of Fig. 6.1 moving ahead m points [3]. In the process, the points of negative time are moved to the end of UIRF because of periodic assumption. In the unequal length mode, the Fig. 6.2 can be found abnormal by the new coherence function. When losing point error happened because of hardware defect, the phenomena similar to Fig. 6.2 may appear. In traditional equal length mode, this kind error can't be found.

For continuous exciting, in the traditional equal length mode, the initial response wave is not considered. By changing computation mode and iteration, the initial response wave can be considered and the preciseness of FRF can be improved greatly.

## 6.2  Precise Frequency Domain Algorithm

### 6.2.1  Half Spectrum

By improving the traditional frequency algorithm, precise half spectrum can be obtained.

(1) Computing averaged cross spectrum first. In each averaging, input data is N points of input wave adding N points 0, output data is 2 N points of output wave. Averaging times is obtained by total points' number of data divided by N and minus 1, the FFT number is 2 N. The averaged process can be looked as traditional frequency algorithm, the FFT number is 2 N and overlap coefficient is 50 %. In each averaging, there are 2 N points of input data and output data, the last N points of input data are set to zero.

(2) IFFT transforms the averaged cross spectrum, obtain the correlating coefficients.

(3) Throw away the part of negative delayed time, the left coefficients that are the part of positive delayed time, should be multiplied by two and proceeds N points FFT transform. The precise half spectrum will be obtained.

For each averaging, FFT number is 2N, for $X(r)$, only when $r = 0, 1, 2, \ldots, N-1$, there is data, the other points' value is The correlating coefficient of positive delayed time obtained by above algorithm is:

$$R_{xy}(m) = \frac{1}{2N} \sum_{r=0}^{N-1} X(r) Y(r+m) \tag{6.2}$$

$m = 0, 1, 2, \ldots, N-1$

Because when $r = 0, 1, 2, \ldots, N-1$, $r+m < 2N$, $Y(r+m)$ exist, thus there is no error in the correlating coefficient of positive delayed time. Each coefficient should be multiplied by two.

New algorithm can be looked as traditional algorithm with overlap coefficient 50 %, the back half of input data set to 0, obtain the correlating coefficient of positive time delay. Each coefficient times two. The result is the same as direct computation in time domain.

If in traditional algorithm with overlap coefficient 50 %, the first half of input data set to 0, obtain the correlating coefficient of negative time delay. Each coefficient times two. The result is the same as direct computation in time domain.

To obtain the whole coefficients, two times of computation are needed, the positive time delay and negative time delay will be computed separately. The preciseness is the same as direct computation in time domain.

In present, there is no definition of coherence function of half spectrum.

With new algorithm, the coherence function can be defined to evaluate the preciseness of half spectrum.

The averaged coefficient $\overline{R}_{xy}(m)$ obtained by new algorithm can be look as directly computed out in time domain by total data, with the best preciseness. For each averaging, the one time averaging coefficient $_kR_{xy}(m)$ can be obtained, here k is kth averaging. The error of one time coefficient is

$$_k e_{xy}(m) = {_k}R_{xy}(m) - \overline{R}_{xy}(m) \tag{6.3}$$

By these error series, obtain the power spectrum $_kP_e(f)$.

Averaged error power spectrum is

$$P_e(f) = \frac{1}{n}\sum_{k=1}^{n} {_k}P_e(f) \tag{6.4}$$

Here $n$ is averaging times.

By FFT transform of $\overline{R}_{xy}(m)$, obtain the power spectrum $P_{xy}(f)$, $f = i * SF/N$, Here $i = 0, 1, 2, \ldots, N/2$, $SF$ is sampling frequency, the coherence function is defined as

$$\gamma^2(f) = P_{xy}(f)/\left(P_e(f) + P_{xy}(f)\right) \tag{6.5}$$

When averaging time is one, for new algorithm, $P_e(f) = 0$, all the coherence function value is one. For tradition frequency domain algorithm, $P_e(f) \neq 0$ even averaging times is one.

### 6.2.2 Impact Test

For each impact, input data length is N, adding N points 0, let the length be 2 N.

For the response wave, the data length is 2 N, or N points adding N points 0. The second method is suitable for previous saved data. For the adding N points 0 it is assumed that the response wave is decried to 0. If response wave does not decried enough in position N, the input and output data need adding negative exponent window at the same time, after parameters identification completed, correct the damping ratio [4].

First FRF is computed with traditional method, the FFT number is 2 N. When FRF obtained, IFFT transform of FRF, obtain the UIRF of 2 N points. Throw away the backward N points. Proceeding FFT transform to the forward N points, obtain the FRF amplitude and phase.

For each impact the exciting signal of N points, convolve with UIRF of N points, the theoretical response wave of 2 N points can be obtained. The computing process can be accelerated by FFT, that is, the exciting data and UIRF both adding N points 0, obtain the spectrum of FFT with 2 N points. IFFT of the product of two spectrums will obtain the theoretical response wave of 2 N points [2]. Here the product of two spectrums is not the same as cross spectrum, in cross spectrum, the input data spectrum will be conjugated.

When response wave have added 0, comparing the forward N points with the theoretical response wave, obtain the error series of N points. When response wave have not added 0, comparing the 2 N points with the theoretical response wave, obtain the error series of 2 N points. To measured response wave and error series with FFT transform of N point, obtain averaged power spectrum of $P_y(f)$ and error power spectrum $P_e(f)$, $f = i * SF/N$, here $i = 0, 1, 2, \ldots, N/2$, $SF$ is sampling frequency, the coherence function is defined as

$$\gamma^2(f) = P_y(f)/\left(P_e(f) + P_y(f)\right) \tag{6.6}$$

For one time averaging, the coherence function value is still meaningful.

The preciseness of FRF evaluation can be reflected by fitting coefficient

$$fit = y_{rms} / \sqrt{e_{rms}^2 + y_{rms}^2} \qquad (6.7)$$

The greater is the value, the better.

Where $y_{rms}$ and $e_{rms}$ are roots of mean square of measured response wave and error series separately.

The error coefficient is defined as

$$error = e_{rms} / y_{rms} \qquad (6.8)$$

It can also be used to reflect the FRF evaluation preciseness, the smaller is the value, the better.

The relationship of fitting coefficient with error coefficient is

$$fit = \frac{1}{\sqrt{1 + error^2}} \qquad (6.9)$$

The relationship of fitting index with coherence function is

$$fit = \sqrt{\sum P_y(f) / \left( \sum P_y(f) / \gamma^2(f) \right)} \qquad (6.10)$$

Where $\sum$ means the sum of all the spectrum lines. If $\sum$ means only part of the spectrum lines, the fitting coefficient of part frequency domain district can be obtained by Eq. 6.10.

## 6.2.3  Continuous Exciting

For continuous exciting of MIMO test, the least square deconvolution algorithm of time domain, to obtain the UIRF first, is best in preciseness [3]. But the computation time is very long. The iteration algorithm of time domain is put forward in our previous paper [3] which is suitable for short data. The iteration algorithm of frequency domain is put forward in our previous paper [5] which is suitable for long data. These two algorithms can reach or very close to the best preciseness, but the computation time is greatly shortened by hundred or thousand times comparing to the least square deconvolution algorithm of time domain.

## 6.3  Examples

### 6.3.1  Precise Half Spectrum and Coherence Function

Figures 6.4 and 6.5 is one measured point half spectrum of one bridge modal test, Shanghai Lufu Arch Bridge [6]. The half spectrum is computed out by the precise frequency domain algorithm. The measured point and reference point both measures the horizontal vibration. The sampling frequency is 10 Hz. In Fig. 6.4, averaged times is four, the data length for analysis is 5*1,024 = 5,120 points, sampling time is 512 s. In Fig. 6.5, averaged times is eight, the data length for analysis is 9*1,024 = 9,216 points, sampling time is 922 s. There are three curves in each figure, above is amplitude of half spectrum with log style, middle is the phase of half spectrum, bellow is the coherence function. The difference of three curves in Figs. 6.4 and 6.5 is small.

The coherence function is computed according to Eq. 6.5. It is different to the coherence function of traditional cross power spectrum, is decided only by the cross coefficients of positive delayed time. In Figs. 6.4 and 6.5, the fit coefficient is calculated with Eq. 6.10.

Figures 6.6 and 6.7 is traditional cross power spectrum of same measured point and reference point with averaged times four and eight separately.
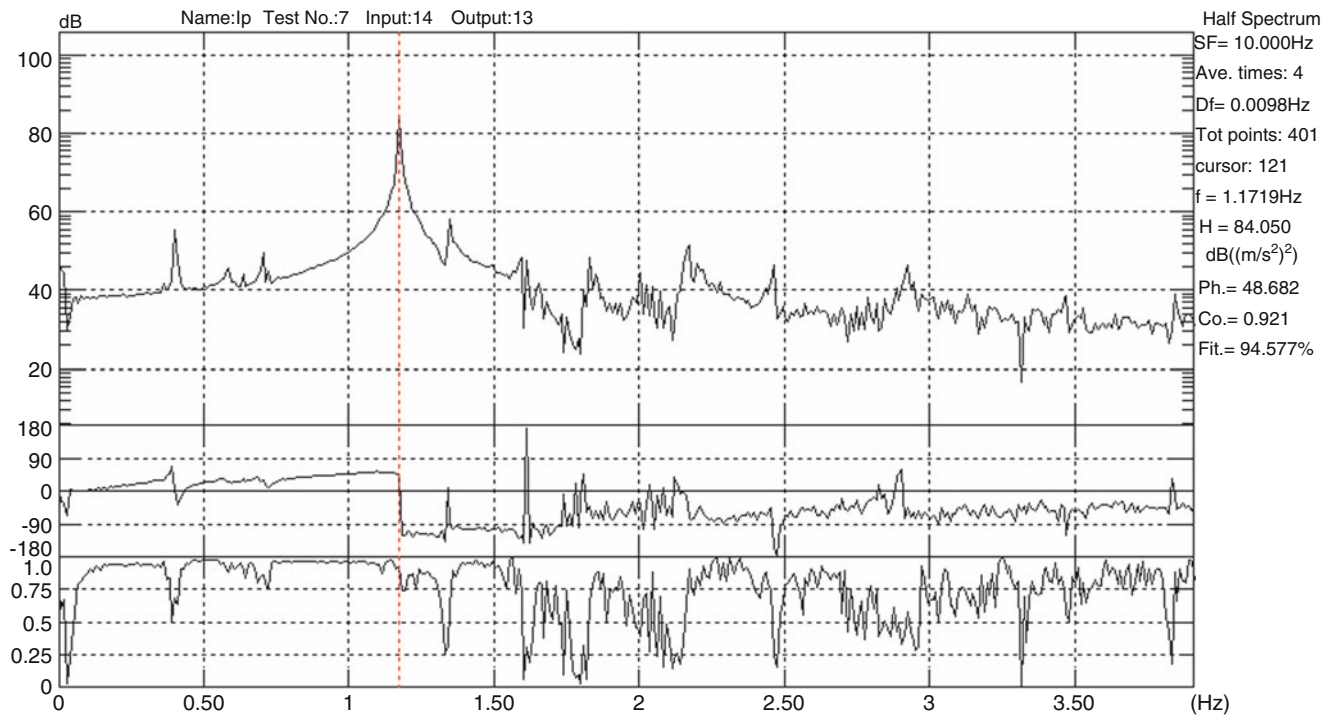
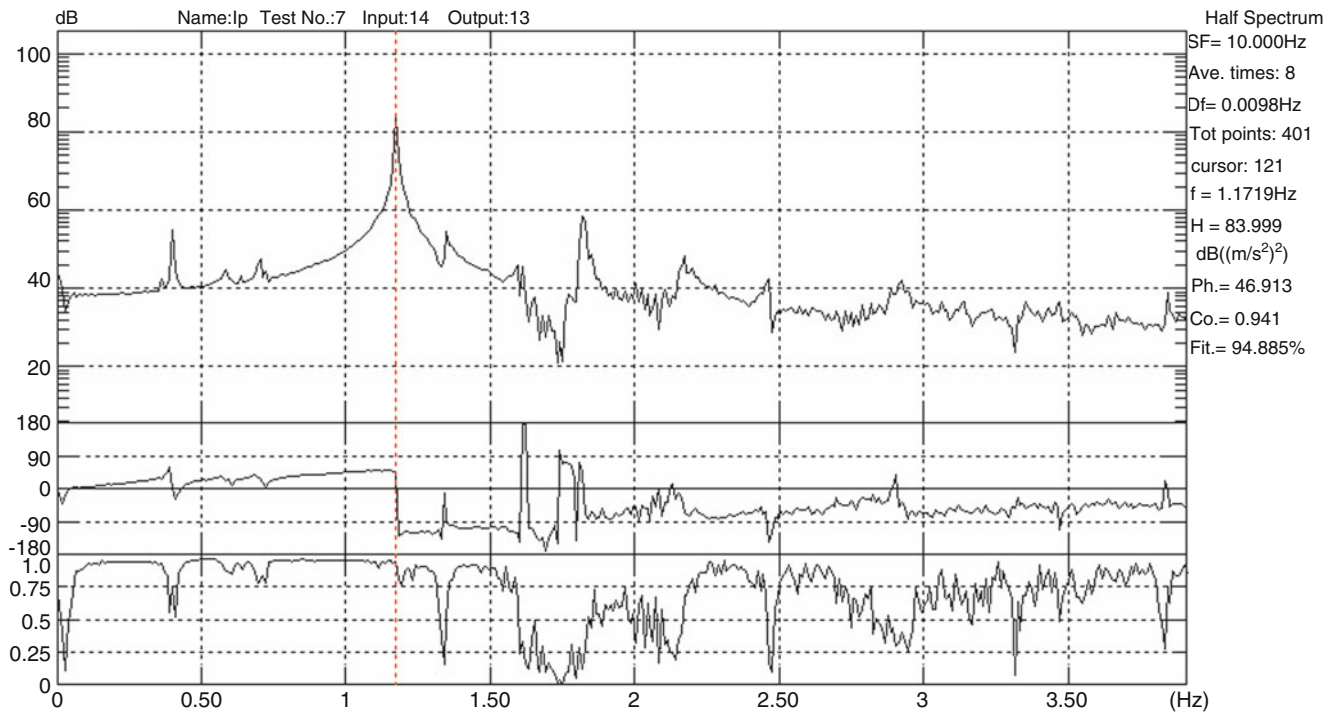**Fig. 6.4** Half spectrum of averaged four times



**Fig. 6.5** Half spectrum of averaged eight times

## 6.3.2 Impact Test and Coherence Function

An educational beam with both ends pinned connection, is illustrated as Fig. 6.8, to obtain the FRF between point A and point B with impact test method.
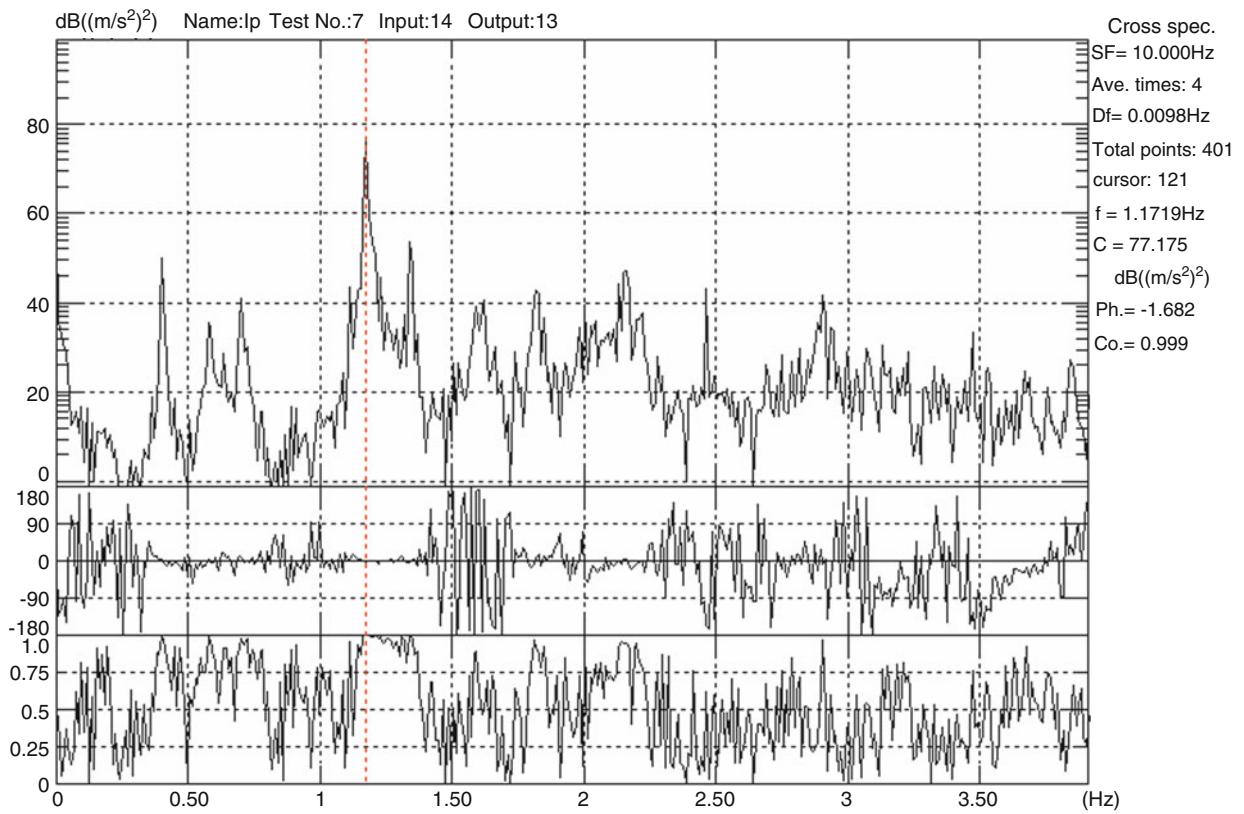
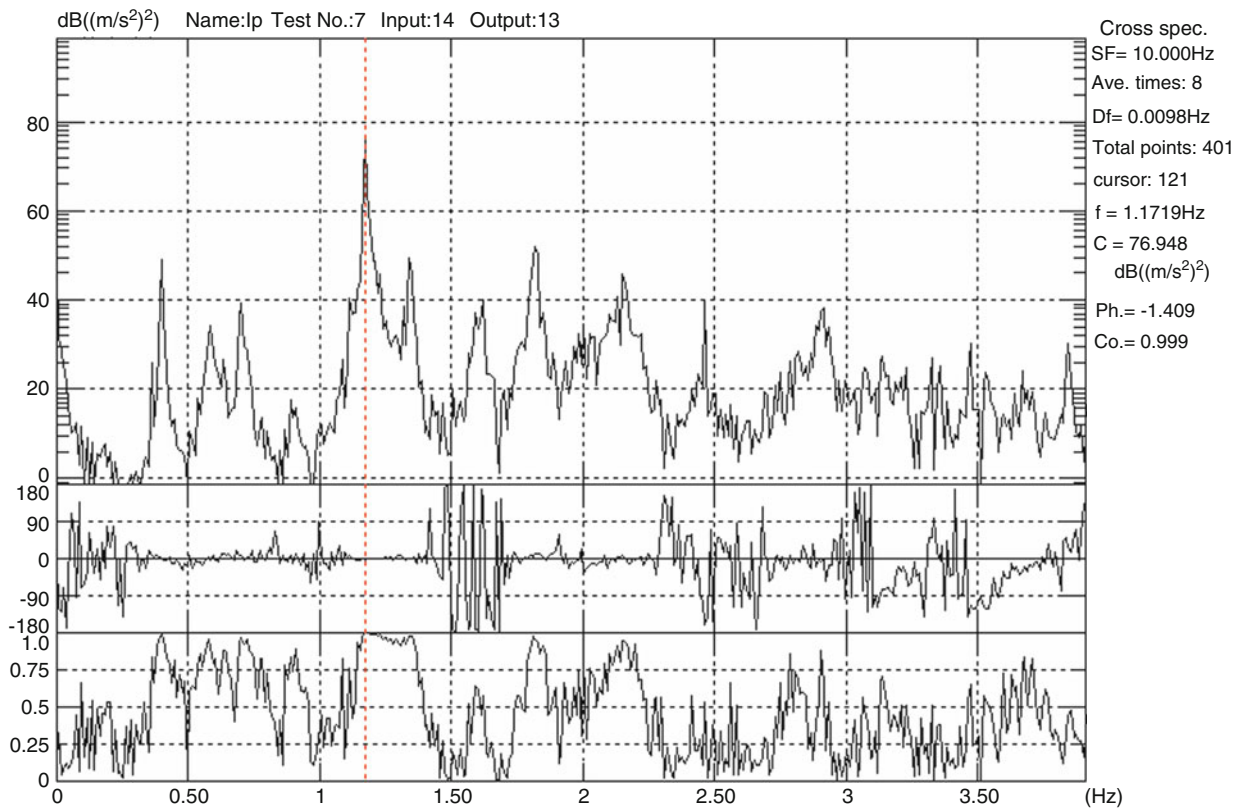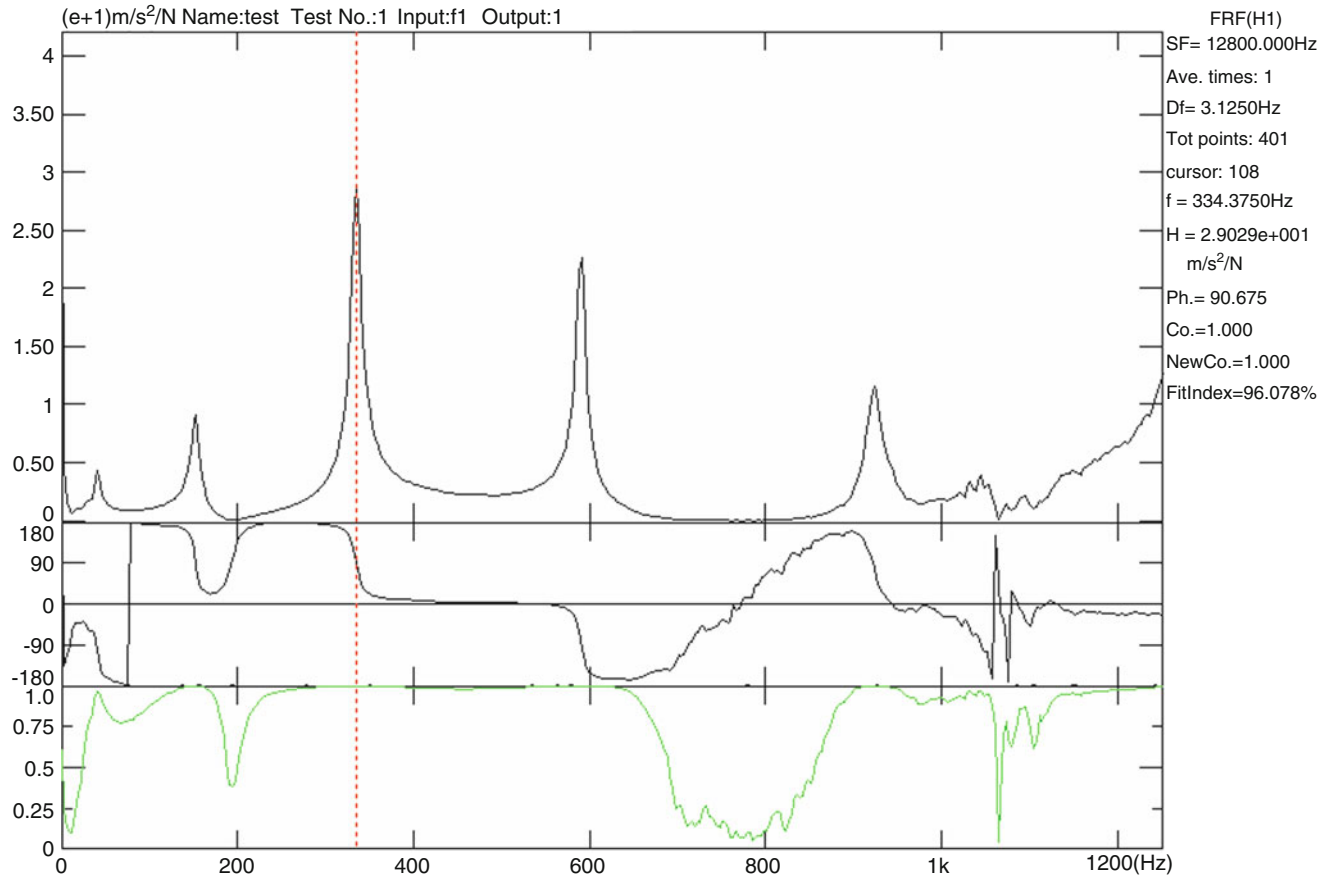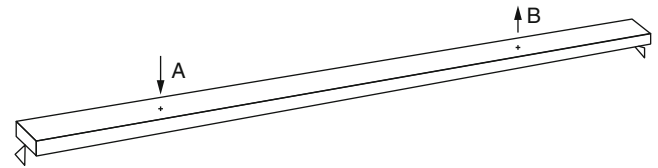**Fig. 6.6** Cross power spectrum of averaged four times



**Fig. 6.7** Cross power spectrum of averaged eight times

**Fig. 6.8** Exciting point and
response point





**Fig. 6.9** FRF and new coherence function with one time averaging

Exciting point is A, for harmer to knock in vertical direction. Accelerometer is fixed in point B for measuring vertical direction. Five times impacting are recorded. The sampling frequency is 12,800 Hz, FFT point number is 4,096. The analyzing frequency range is 0 to 1,250 Hz. The analysis result is illustrated as Figs. 6.9, 6.10, 6.11, 6.12, and 6.13 with different averaging times. In the figure, the above part is FRF amplitude with log style, middle part is FRF phase, below part is coherence function and new coherence function (green color).

With new coherence function definition, only one impact will obtain the stable coherence function, so the impact times can be greatly reduced. Furthermore, the new coherence function has clearer engineering meaning than tradition coherence function. Let's assume in one test, the sampling length is too short in one impact, which will cause serious leakage in FRF calculation. But in the traditional coherence function, the serious leakage can't be reflected. With new coherence function, only by one time averaging, the serious leakage will be reflected.

The traditional coherence function can't reflect the leakage caused by too short of sampling length of one impact, the leakage is reduced by adding negative exponent window, the exponent window index is decided according to analyzer's experience.
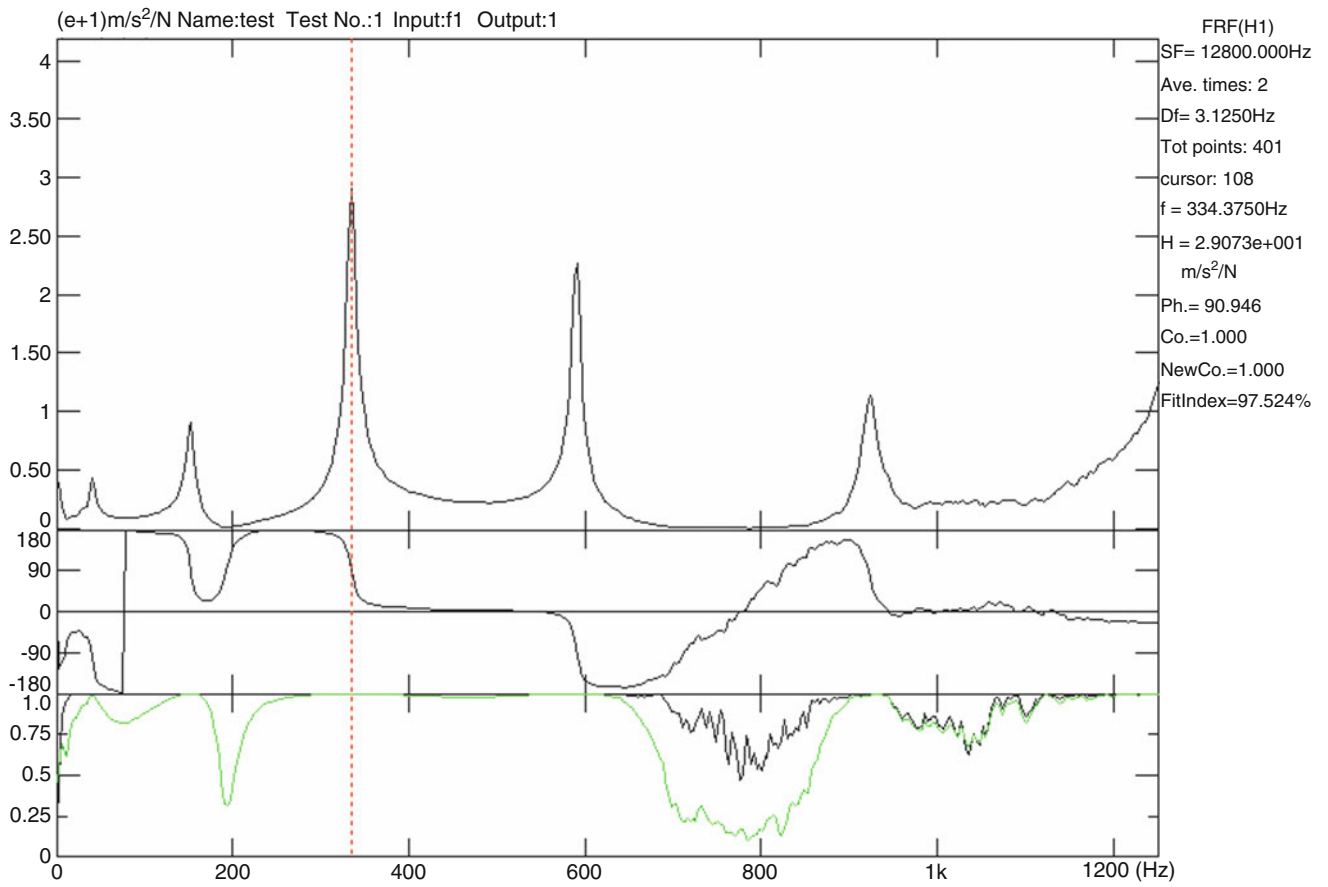
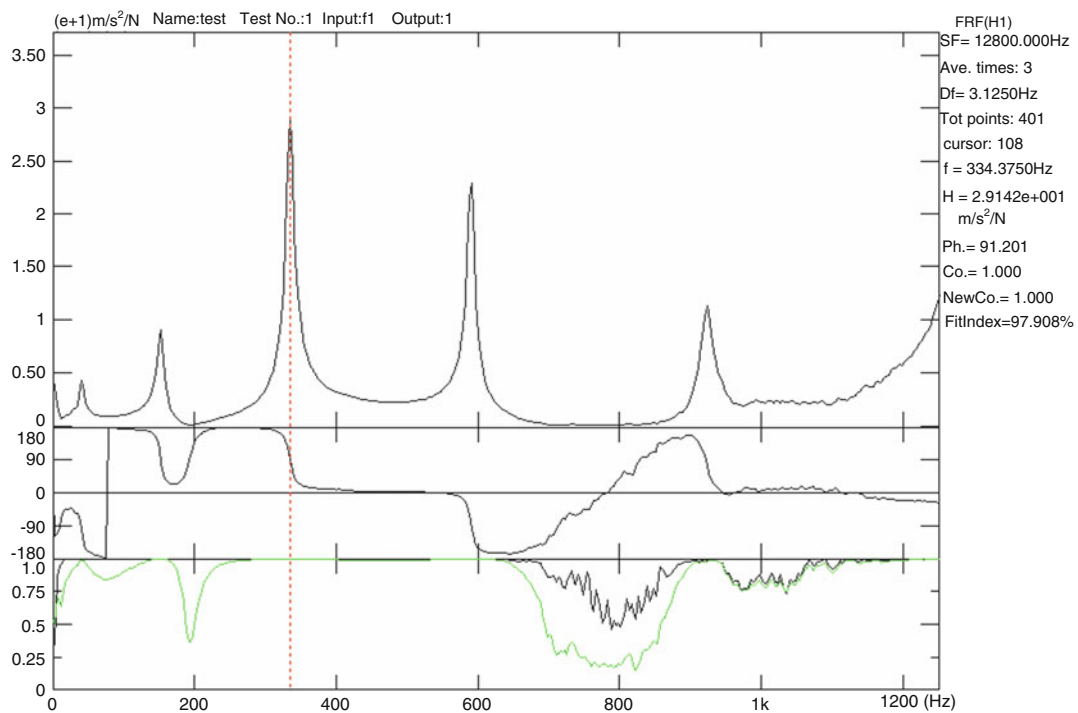**Fig. 6.10** FRF and new coherence function with two times averaging



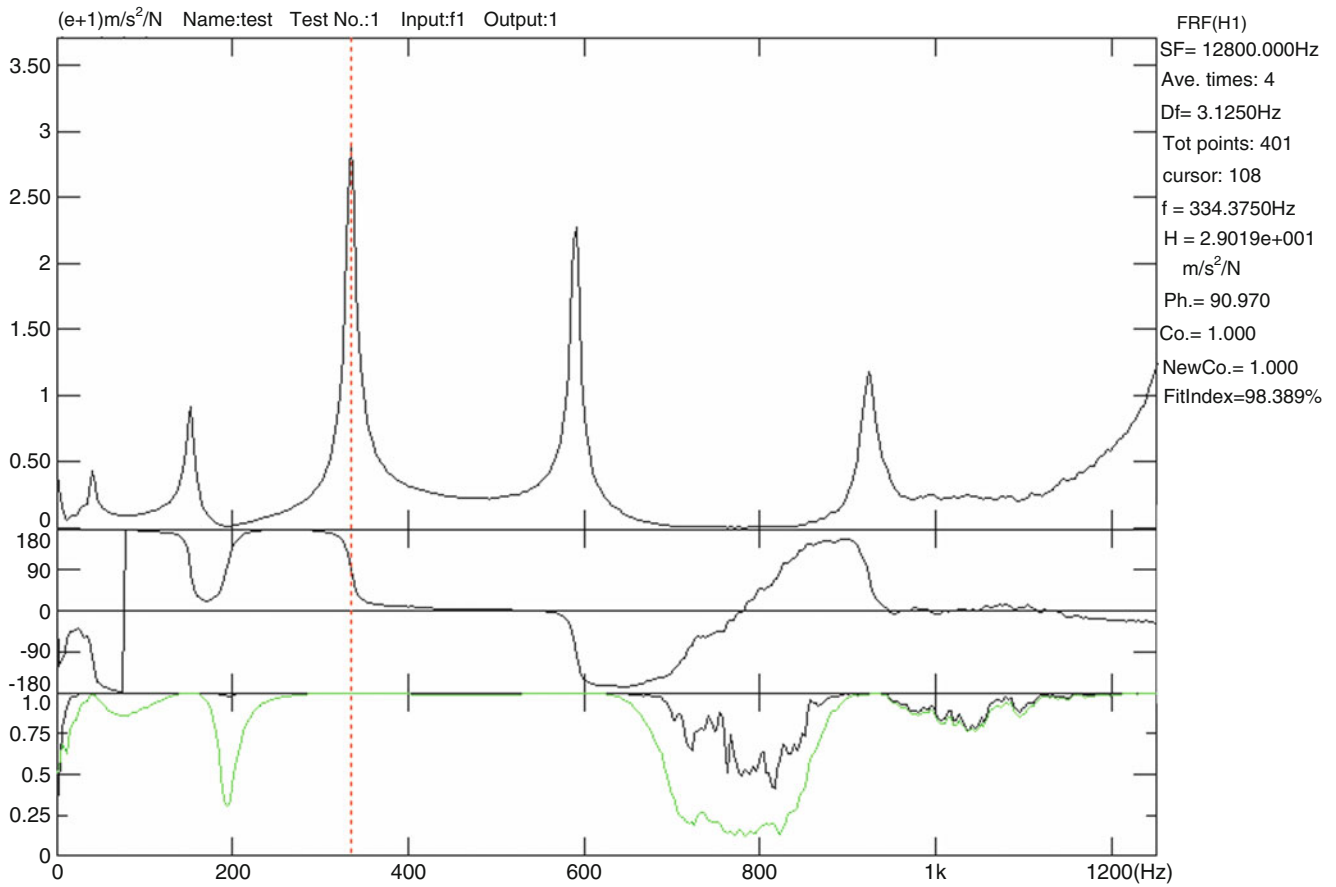**Fig. 6.11** FRF and new coherence function with three times averaging

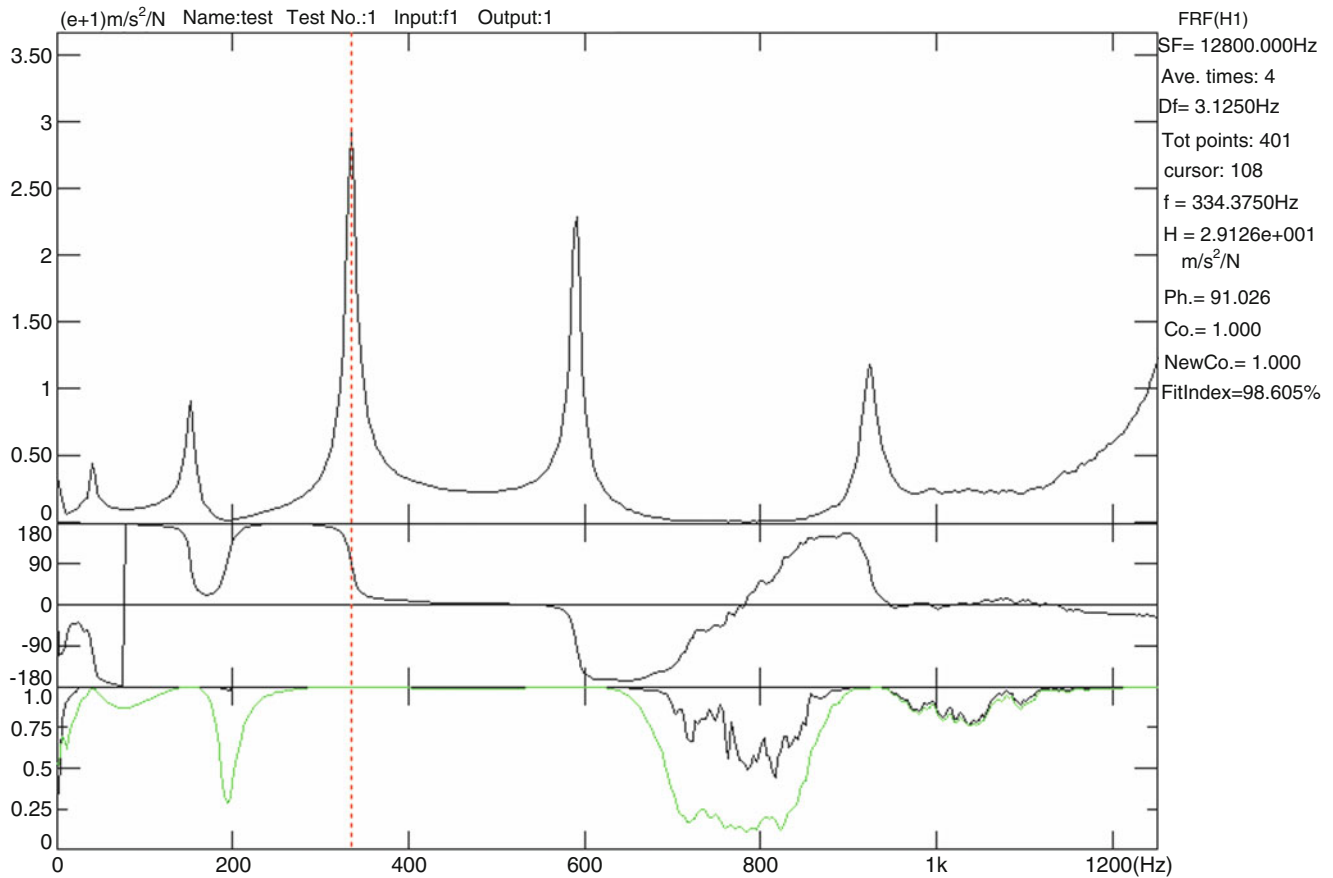**Fig. 6.12** FRF and new coherence function with four times averaging

## 6.4 Conclusions

The half spectrum obtained by the new algorithm of frequency domain is best in preciseness, which is the same as computed directly by time domain, with the computation speed of traditional frequency domain algorithm. The coherence function can be used to evaluate the ratio of signal to noise at different spectrum lines.

For impact test, the computation mode introduced here can avoid the error caused by the periodic assumption. Even for one time averaging the coherence function can still reflect the ratio of signal to noise and leakage at different spectrum lines. The traditional coherence function can't reflect the leakage even that it is serious. With the new coherence function, the impact test averaging times can reduced to one, the test time can be greatly reduced. The coherence function is often used as weighting coefficients of modal parameters identification algorithm in frequency domain, the new coherence function has clearer engineering meaning than tradition coherence function, by using new coherence function as weighting coefficients, the modal parameters identification algorithm will also be improved.

For continuous exciting of MIMO test, the iteration algorithm of time domain and frequency domain can be used to consider the initial response influence. The iteration algorithm of time domain is suitable for short data. The iteration algorithm of frequency domain is suitable for long data. The coherence function definition is similar to impact test.

For both impact test and continuous exciting, the new coherence function can be used to evolve the quantified FRF total preciseness.

**Fig. 6.13** FRF and new coherence function with five times averaging

# References

1. Pierro E, Mucchi E, Soria L, Vecchio A (2009) On the vibro-acoustical operational modal analysis of a helicopter cabin. Mech Syst Signal Pr 23(4):1205–1217
2. Chen PQ (2004) Digital signal processing tutorial. Tsinghua University Publishing Company, Beijing, pp 104–108
3. Liu JM, Zhu WD, Lu QH, Ren GX (2011) An efficient iterative algorithm for accurately calculating impulse response functions in modal testing. J Vib Acoust 133(6). doi: 10.1115/1.4005221
4. Fladung W, Rost R (1997) Application and correction of the exponential window for frequency response functions. Mech Syst Signal Pr 11(1):23–36
5. Liu JM, Zhu WD, Ying M, Shen S (2013) Fast precise algorithm of computing FRF by considering initial response. Proceedings of the SEM IMAC XXXI Conference, Los Angeles, CA
6. Zhang GY, Liu JM (2008) Measurement of Lupu arch bridge vibration characteristics. J Vib Shock (China) 27(9):167–170

# Chapter 7
# Identification of a Time-Varying Beam Using Hilbert Vibration Decomposition

**M. Bertha and J.C. Golinval**

**Abstract**  The present work is concerned by modal identification of time-varying systems. For this purpose, a method based on instantaneous frequency identification and synchronous demodulation is used to extract modal components from recorded signals. The proposed method of iterated sifting process is based on the Hilbert Vibration Decomposition (HVD) technique which is used to extract the instantaneous dominant vibrating component at each iteration. A source separation preprocessing step is introduced to treat multiple degree-of-freedom systems in an optimal way. Sources are used as reference signals to get a single instantaneous frequency of each mode for the demodulation on all the channels. The algorithm is presented and is applied to numerical simulation of a randomly excited time-varying structure for illustration purpose. The investigated structure is made up of a beam on which a non-negligible mass is traveling. The variable location of the mass results in changes in modal parameters.

**Keywords**  Modal identification • Time-varying systems • Instantaneous modal parameters • Hilbert transform • Signal decomposition

## 7.1  Introduction

During the last decade, a lot of new processing techniques appeared in the field of modal identification of time-varying systems. The Hilbert-Huang transform (HHT) introduced by Huang et al. in [1] is a powerful and highly adaptive technique able to deal with non-stationary signals. First, the use of the Empirical Mode Decomposition (EMD) method results in a set of so-called Intrinsic Mode Functions (IMFs) which are ideally mono-component signals. Then the instantaneous frequency and instantaneous amplitude of each IMF are obtained by use of the Hilbert transform.

More recently, the Hilbert Vibration Method (HVD) proposed by Feldman [2] was introduced with the ambition of being more accurate than the EMD method. In the following, the HVD method will serve as a basis for the developments reported in the present paper.

The paper is organized as follows. First the main ideas of the EMD and HVD methods are recalled and their practical limitations are highlighted. Then a description of the proposed method is presented along with its application on synthetic responses of a randomly excited time-varying system. The system considered here consists in a beam simply supported at its both ends on which a non-negligible mass is moving. Finally, a conclusion and some words on future work close the paper.

## 7.2  The Hilbert-Huang Transform as a Tool to Compute Instantaneous Properties of Multi-Component Signals

The Hilbert-Huang transform works in two steps: (1) the signal is decomposed in IMFs using the EMD and (2) the instantaneous properties of the IMFs are extracted using the Hilbert transform.

M. Bertha (✉) • J.C. Golinval
Department of Aerospace and Mechanical Engineering, University of Liège, Liège, Belgium
e-mail: mathieu.bertha@ulg.ac.be; jc.golinval@ulg.ac.be

### 7.2.1   The Empirical Mode Decomposition as Sifting Process

The main idea of the HHT method is to sift the processed signal by successively removing slow oscillations from the signal using the EMD method. Practically, the EMD method works by first identifying all the minima and maxima in the signal. With the minima and maxima, the lower and upper envelopes of the signal are calculated by use of cubic-spline fitting, respectively. The mean of the lower and upper envelopes is a slowly oscillating function which is removed from the original signal. The process is then repeated until the remaining signal has the following two properties [1]:

- the difference between the number of extrema and zero crossing is maximum 1,
- the local mean value of the lower and upper envelope of the signal is zero.

When these two conditions are fulfilled, the component is considered as an IMF and is extracted from the original signal. The process is iterated until it is not possible anymore to extract an IMF.

Once all useful IMFs are extracted, their instantaneous characteristics are calculated by use of the Hilbert transform.

### 7.2.2   The Hilbert Transform and the Analytic Signal for the Extraction of Instantaneous Characteristics

Let $x(t)$ be a real-valued signal. Its Hilbert transform $\mathcal{H}(x)$ is defined as the convolution product between the signal and $h(t) = \frac{1}{\pi t}$:

$$y(t) = \mathcal{H}(x) = \frac{1}{\pi} \, \text{p.v.} \int_{-\infty}^{+\infty} \frac{x(\tau)}{t - \tau} \, d\tau \tag{7.1}$$

The Cauchy principal value of the integral has to be taken to solve this improper integral because of the singularity occurring for $\tau = t$.

A (non-exhaustive) list of properties of the Hilbert transform are given hereafter:

**Inverse transform:** $\mathcal{H}(\mathcal{H}(x)) = -x$ which implies that $\mathcal{H}^{-1} = -\mathcal{H}$;

**Differentiation:** the ($kth$-)derivative of the Hilbert transform is the Hilbert transform of the ($kth$-)derivative $\frac{\lceil^k}{\lceil t^k} [d(x)] = \mathcal{H}\left(\frac{\lceil^k x}{\lceil t^k}\right)$;

**The Bedrosian's theorem [3]:** the Bedrosian's theorem states that if a signal $x(t)$ is a product of two components; one slowly and the other fast varying, then the Hilbert transform of $x(t)$ is equal to the slowly varying function times the Hilbert transform of the fast varying one. So, if $f(t)$ and $g(t)$ represent the slowly and fast varying functions and $x(t) = f(t) g(t)$, then $\mathcal{H}(x(t)) = f(t) \mathcal{H}(g(t))$. The separation condition between slow and fast parts is that the Fourier spectra of $f$ and $g$ must not overlap.

By adding to the real-valued signal its Hilbert transform multiplied by the imaginary units, an analytic signal $z(t)$ is formed:

$$z(t) = x(t) + i\mathcal{H}(x(t)). \tag{7.2}$$

In this form, the signal can now be seen as a rotating phasor in the complex plane characterized at each time instant by an amplitude $A(t)$ and a phase angle $\phi(t)$:

$$z(t) = x(t) + i\mathcal{H}(x(t))$$
$$= A(t) e^{i\,\phi(t)}. \tag{7.3}$$

The instantaneous amplitude and phase are extracted directly from the analytic signal by the amplitude and argument calculations of $z$:

$$A(t) = |z(t)|; \tag{7.4}$$

$$\phi(t) = \angle z(t); \tag{7.5}$$

and the instantaneous angular frequency of the signal is then obtained by time differentiation of the phase angle

$$\omega(t) = \frac{d\phi(t)}{dt} \tag{7.6}$$

In the case of a multi-component signal, the instantaneous amplitude and frequency obtained are those of the resultant signal (vector summation of each phasor). In that way, the amplitude of the signal is always lower or equal than the sum of the amplitudes of each component (triangle inequality) and the instantaneous frequency may be negative. This latter point occurs when the resultant phasor rotates backwards in the complex plane. Such a negative frequency has no physical meaning.

The HVD method presented in the next section uses the analytic form of the signal to split it into its mono-component parts.

## 7.3 The Hilbert Vibration Decomposition Method

The Hilbert Vibration Decomposition method presented by M. Feldman [2] is an iterative algorithm that exploits the analytic form to extract the dominant vibration component from a signal. The method is based on the fact that if we observe the phase (or frequency) of the analytic form of a multi-component signal, its global evolution is driven by the dominant mono-component (the one with the highest amplitude) of the signal. The other components appear as oscillations around the phase (frequency) of the dominant mode. It can be shown [2] that the latter oscillation parts vanishes when integrated over the time. To isolate the dominant mode component present in the signal the phase (or frequency) is low-pass filtered. Finally, the component corresponding to the dominant mode is extracted from the signal using a synchronous demodulation based on the phase (or frequency) of the dominant mode. Once the dominant component is extracted, the whole process is repeated on the remaining components.

## 7.4 Drawbacks of the HHT and HVD Methods

For some multi-component signals the EMD and HVD methods may fail to sift properly all their constitutive mono-component signals. As recalled in Sect. 7.2.1 the EMD method extracts at each step the mono-component with the fastest oscillations. In Sect. 7.3 we saw that the HVD method extracts components from highest to lowest amplitudes. This implies that if the constitutive mono-component signals cross themselves in frequency or if the component with the highest frequency vanishes, the EMD method will not be able anymore to follow this component and will jump to the component having the new highest frequency. Similarly, if components cross themselves in amplitude the HVD method will always extract the component with the highest instantaneous amplitude.

To illustrate this problem, let us consider a simple two degree-of-freedom system which is made time-variant by introducing a time-dependent stiffness. The system is shown in Fig. 7.1 and its properties are listed hereafter:
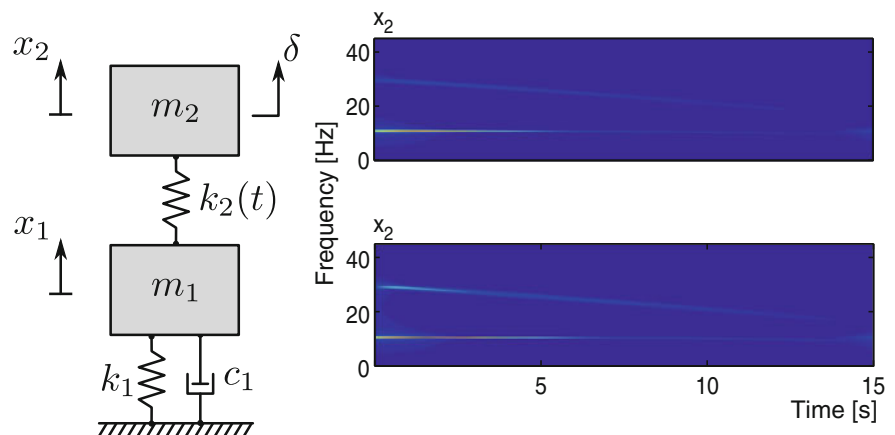


**Fig. 7.1** Two degree-of-freedom time-varying system with time-frequency plots of its time responses
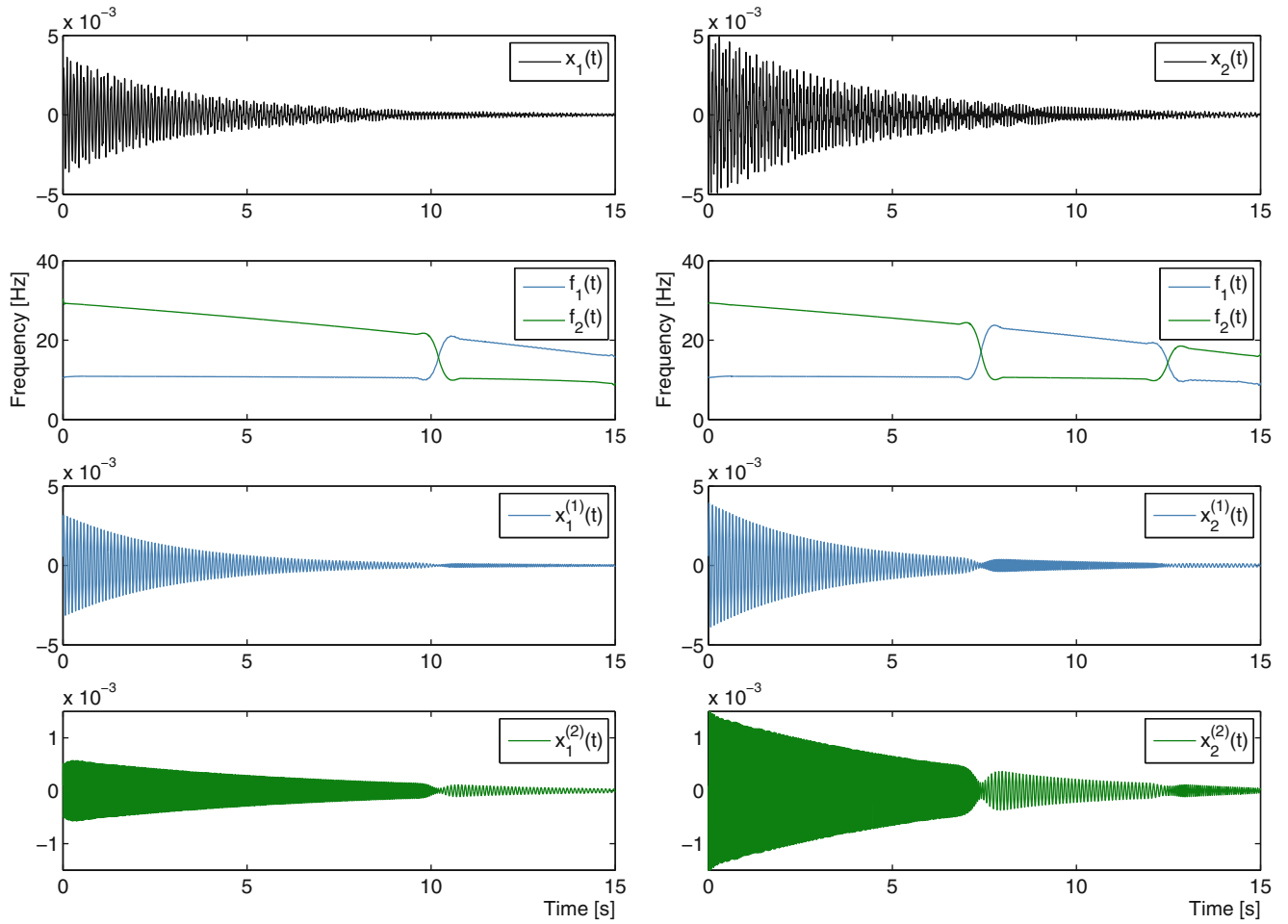
**Fig. 7.2** Time responses and extracted instantaneous frequencies and components. *First row*: time response of each DoF. *Second row*: identified instantaneous frequencies for each DoF. *Third and fourth rows*: components corresponding to the identified instantaneous frequencies

- $m_1 = 3$ kg;
- $m_2 = 1$ kg;
- $k_1 = 20{,}000$ N/m;
- $k_2 = 25{,}000 \searrow 5{,}000$ N/m (linear decrease in the time span);
- $c_1 = 3$ Ns/m.

The system is submitted to an impulse at DoF $x_2$ and the response of the whole system is simulated during 15 s. A standard Newmark integration scheme was used for the time integration in which the stiffness matrix is updated at each time step to take into account the dependence of $k_2$ with respect to the time.

Applying the standard HVD method on the two channels separately leads to some undesirable behavior. Each time one intrinsic component becomes dominant in the signal, the method follows it and a mode switching phenomenon occurs during the extraction process. Moreover, as it can be seen in Fig. 7.2, the mode switching does not occur at the same time on each channel, which makes the correction of these switches more difficult. When the frequency curve jumps from one mode to the other, the corresponding demodulated component also follows this jump.

## 7.5 Modified Hilbert Vibration Decomposition Method

### 7.5.1 Addition of a Source Separation Step to Avoid Mode Switching

In signal processing, source separation methods are used to recover initial signals, the sources, from a set of recorded signals which are mixtures of the initial sources. A large variety of methods exist trying to separate them as much as possible based on decorrelation, independence or other probabilistic properties. One can cite, among others, the Principal Component Analysis (PCA) (also known as Proper Orthogonal Decomposition (POD) or Karhunen-Loève transform (KLT)), the Smooth Orthogonal Decomposition (SOD), the Independent Component Analysis (ICA) and the Second-Order Blind Source Identification (SOBI). Some of these techniques have been already used in the field of structural dynamics as for example POD [4], SOD [5] and SOBI [6].

In the present work, the application of a source separation method will help to overcome the previously cited limitations of the HVD method. When several responses recorded on the structure under test are available, the source separation will highlight a particular mode in each identified source. Then, applying the standard steps of the HVD method on the sources rather than directly on the recorded signals will reduce the risk of frequency or amplitude crossing between different modes.

As an example, the identification of the system described in Sect. 7.4 was performed again using separated sources (given by the SOD method in the present case) as references for the instantaneous phase identification. As it is observed in Fig. 7.3, this procedure leads to well decomposed components. Furthermore, while in the previous identification we get four frequency curves (two instantaneous frequencies for each channel), we have this time only two instantaneous frequencies for the whole system, one frequency curve per mode.
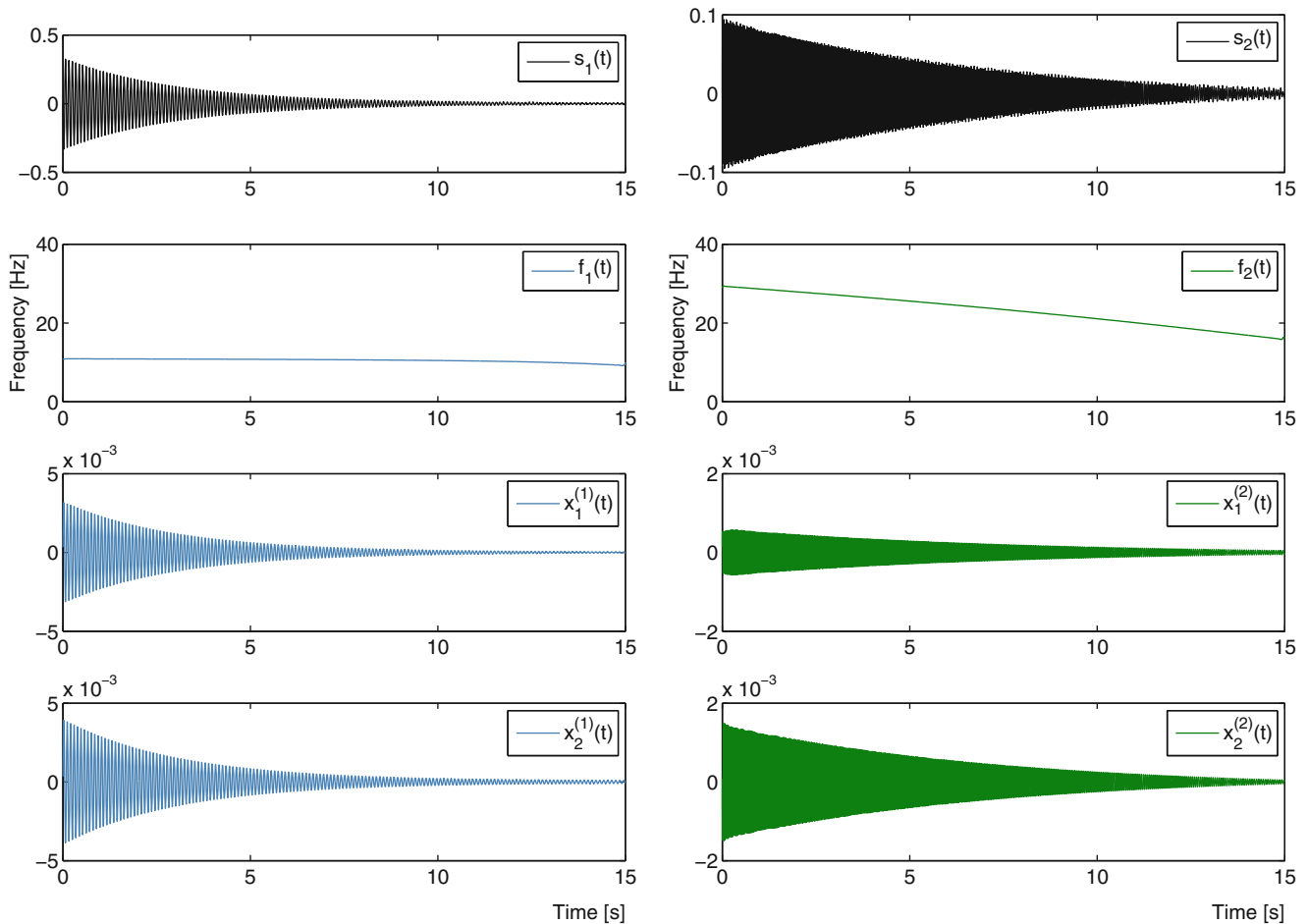


**Fig. 7.3** Source separation step introduced in the algorithm. *First row*: separated sources. *Second row*: identified instantaneous frequency for each source. *Third and fourth rows*: components corresponding to the identified instantaneous frequencies for each DoF

### 7.5.2 Instantaneous Phase/Frequency and Mode Deflection Shapes Calculation

Once the source separation method has generated a set of different sources, the Hilbert transform is applied on the first one. The unwrapped phase of the dominant source is computed taking the phase angle of the analytic signal and removing all the $2\pi$ radians jumps. At this stage the phase curve contains the phase evolution of the dominant mode plus some deviations due to other modes and noise. In the original HVD method, the next steps would be to differentiate the phase to get the instantaneous frequency and low-pass it. In the present approach, we choose to work directly on the phase signal so that the low-pass filter step becomes a trend detection step. For that purpose, several techniques exist such as the Hodrick-Prescott filter [7].

To make a long story short, let us recall that the Hodrick-Prescott filter models the signal (the unwrapped phase $\phi(t)$ in our case) at the summation of a trend $\tau$, oscillatory components $c$ and noise $\nu$:

$$\phi(t) = \tau(t) + c(t) + \nu(t) \tag{7.7}$$

The goal of the filter is to find the optimal trend $\tau$ that minimizes the following objective function:

$$\min_\tau \left[ \sum_{t=1}^{T} (\phi_t - \tau_t)^2 + \lambda \sum_{t=2}^{T-1} ((\tau_{t+1} - \tau_t) - (\tau_t - \tau_{t-1}))^2 \right], \tag{7.8}$$

$\lambda$ being a smoothing parameter. This objective function is a trade-off between two parts. The first term of (7.8) penalizes large variations of the signal around the trend while the second term is a smoothing function penalizing too fast variations of the trend.

Finally a Vold-Kalman filter (VKF) [8] is used instead of synchronous demodulation for its ability of extracting simultaneously a set of mono-components. The Vold-Kalman filter is a technique able to recover from a signal the component(s) $x_k(t)$ corresponding to the phase(s) $\phi_k(t)$. The model used for the signal under interest is a summation of components and noise

$$x(t) = \sum_k \underbrace{a_k(t)\, e^{i\,\phi_k(t)}}_{x_k(t)} + \nu(t) \tag{7.9}$$

in which $a_k(t)$ is the complex amplitude of the $k$th component $x_k(t)$ and $\nu(t)$ is the noise in the signal.

The way to recover the components $x_k(t)$ is based on the minimization of two equations. First the *data equation*

$$x(t) - \sum_k a_k(t)\, e^{i\,\phi_k(t)} = \delta(t) \tag{7.10}$$

in which the error $\delta(t)$ should be minimal. The second one is the *structural equation* ensuring the smoothness of the solution using the difference operator $\nabla^{p+1}$ applied on $a_k(t)$

$$\nabla^{p+1} a_k(t) = \varepsilon_k(t), \tag{7.11}$$

where $\varepsilon_k(t)$ should also be minimized.

All the complex amplitudes $a_k(t)$ are computed in a least square sense considering these two set of equations. Now making a parallelism between Eq. (7.9) and modal expansion, we can equate the complex amplitude of the component $k$ from (7.9) to the unscaled time-varying component in the $k^{th}$ mode of vibration.

$$\text{Vold} - \text{Kalman filter}: \boldsymbol{x}(t) = \sum_k \boldsymbol{a_k}(t)\ e^{i\,\phi_k(t)}$$
$$\updownarrow \qquad \updownarrow$$
$$\text{Modal expansion}: \boldsymbol{x}(t) = \sum_k \boldsymbol{V_k}(t)\ \eta_k(t)$$

The full algorithm of the method is illustrated in a block diagram in Fig. 7.4.

**Fig. 7.4** Flow chart of the
method
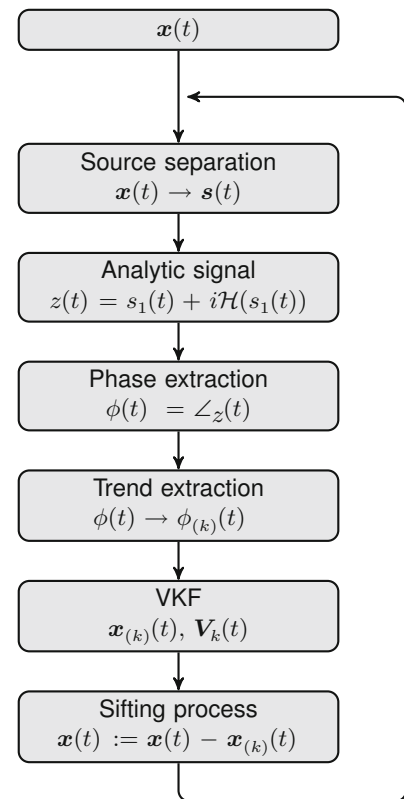


## 7.6   Numerical Application

The numerical application considered in this study consists of a beam on which a moving mass is traveling. The beam is 2 m-long and is simply supported at both ends; two random external force excitations are applied in the vertical and lateral directions at a quarter of the total length of the beam. Five equally spaced measurement points are selected to record the time response of the beam in the vertical and lateral directions. A mass of 3 kg travels the whole beam in 60 s during which the external forces are applied. The response of the system is computed using the LMS-Samcef Mecano [9] software in which a slider element is used to make the connection between the beam and the lumped mass. The measured time responses are sampled at a rate of 1,000 Hz and to better simulate a real measurement process, a normally distributed noise is added on each signal with a signal-to-noise ratio of 1 %. The simulated system and the measurement set-up are illustrated in Fig. 7.5. The properties of the system are the following:

- Beam length: $l = 2$ m
- Beam cross section 80 mm (width) $\times$ 20 mm (height)
- Density: $\rho = 2{,}700$ kg/m$^3$
- Young's modulus: $E = 70{,}000$ MPa
- Poisson's ration: 0.33
- Moving mass: 3 kg
- Pinned connections: $x(0) = y(0) = z(0) = x(l) = y(l) = z(l) = 0$

The eigenfrequencies of the beam subsystem are listed in Table 7.1 with their corresponding mode-shapes.

Using cross correlation between time signals, it can be verified that the responses in the lateral and vertical directions are completely separated, so that the two sets of measurements can be treated separately. In Fig. 7.6 wavelet spectra of the response of the first node in both lateral Fig. 7.6a and vertical Fig. 7.6b directions are shown. In this figure, the white dashed lines correspond to the natural frequencies of the beam subsystem (when the mass is located on one support, before beginning its motion). It can be observed that, for a given mode, the natural frequency decreases as the mass is moving and comes back to its initial value every time the mass passes upon a vibration node. This is due to the fact that the additional inertia force

**Fig. 7.5** Beam travelled by the moving mass
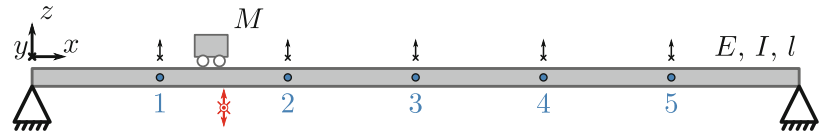


**Table 7.1** Modal parameters of the simply supported beam only (LTI system)

| Mode Nbr. | Frequency (Hz) | Mode shape |
|---|---|---|
| Mode 1 | 11.54 | First vertical bending |
| Mode 2 | 46.05 | First lateral bending |
| Mode 3 | 46.15 | Second vertical bending |
| Mode 4 | 103.74 | Third vertical bending |
| Mode 5 | 182.72 | Second lateral bending |
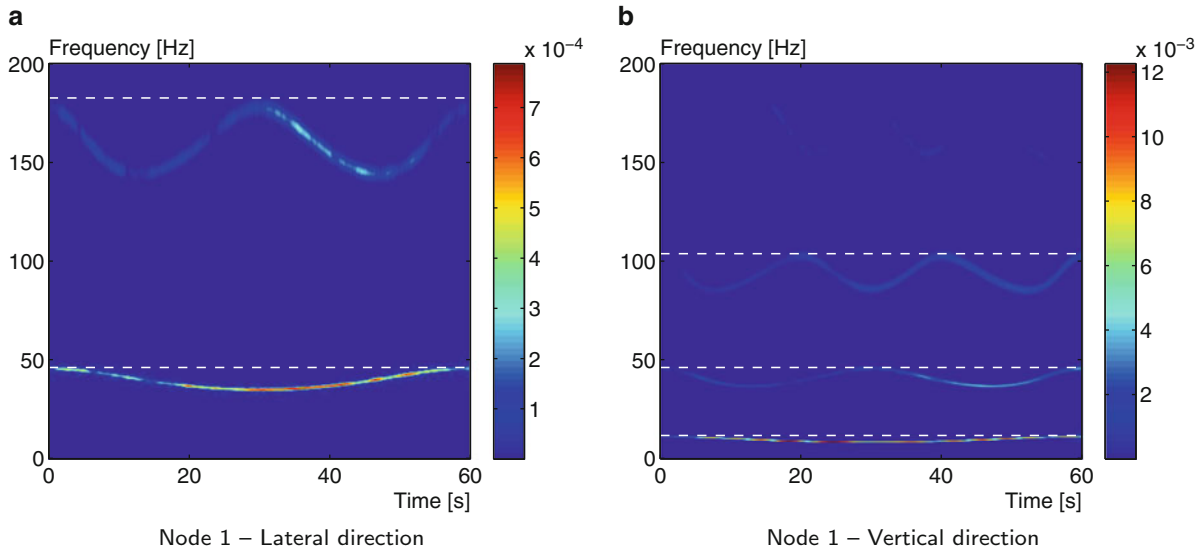


**Fig. 7.6** Wavelet spectra of two degrees of freedom. The time varying behaviour of the structure is clearly visible. (**a**) Node 1—Lateral direction. (**b**) Node 1—Vertical direction

induced by the moving mass does not produce any work on that mode at this time. Conversely, when the mass is located at an anti-node of vibration for a particular mode, the inertia effect is maximum and produces the maximum decay in frequency for that mode.
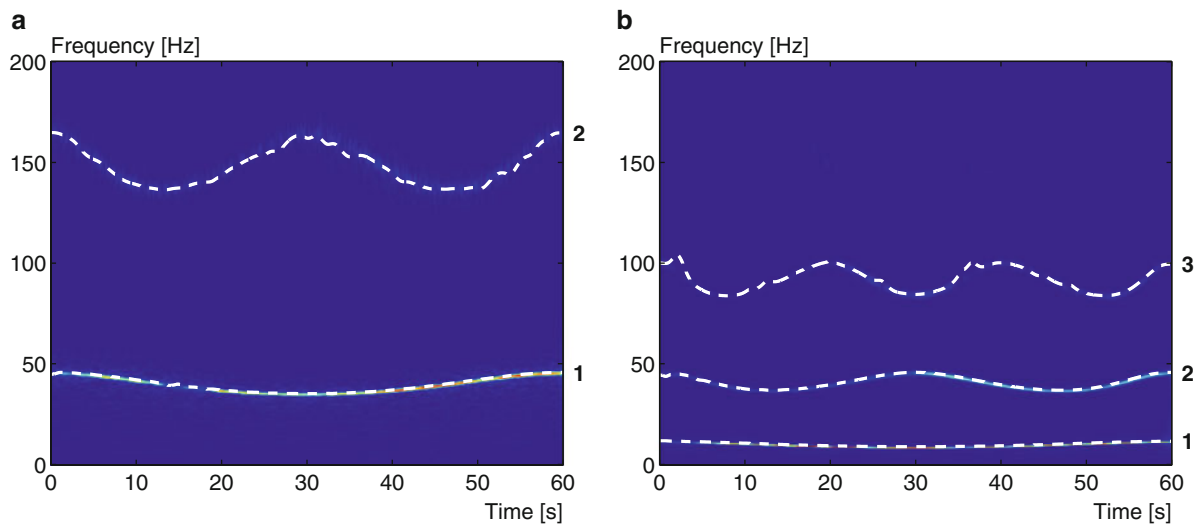
### 7.6.1 Identification of Instantaneous Frequencies

The algorithm proposed in Fig. 7.4 is now applied on each set of recorded signals. Based on the time-frequency plots Fig. 7.6a,b it is chosen to extract two modes from the set of lateral measurements and three modes from the vertical ones.

The evolution of the five identified instantaneous frequencies are shown using white dashed curves in Fig. 7.7a,b for the lateral and vertical modes respectively. Wavelet spectra of node 1 are used in the background of the plots and it can be seen that the identified instantaneous frequencies match very well the highest amplitude in the spectra.

### 7.6.2 Component Extraction and Calculation of Mode Deflection Shapes

Once that the instantaneous eigenfrequencies are well identified, the next step is to extract the intrinsic components corresponding to each frequency in all the channels. This is done by the use of the Vold-Kalman filter and results in a set of mono-components and complex amplitudes. Referring to (7.9), these complex amplitudes are used as unscaled instantaneous mode-shapes.

**Fig. 7.7** Identified instantaneous frequencies. (Numbers on the right of each time-frequency plot indicates the sequence of the modes extraction.) (**a**) Instantaneous frequencies of lateral bending modes. (**b**) Instantaneous frequencies of vertical bending modes

For seek of illustration, the three first vertical bending modes obtained at three different times are given in Fig. 7.8 along with the mode-shapes of the beam subsystem. Note that the lateral bending modes show the same behavior but are not reported here. In the first row of Fig. 7.8, the considered time is 15 s. At this time, the mass is located at a quarter of the length of the beam, which corresponds to an anti-node of vibration for the second mode. As seen in Fig. 7.8b, the second mode is highly perturbed by the moving mass.

In Fig. 7.8f,h, the deformed shapes corresponding to modes 3 and 2 at 20 and 30 s respectively are shown. In both configurations, the mass is located at a node of vibration for the considered mode and the instantaneous mode-shape is similar to the corresponding mode-shape of the beam subsystem.

Finally, Fig. 7.8a,d,g reveal that the first bending mode is not very sensitive to the presence of the moving mass.

From the set of identified instantaneous mode-shapes, it is possible to perform a correlation with the mode-shapes of the beam subsystem using the classical modal assurance criterion (MAC). As the instantaneous modes are identified at each time step, the time dimension has to be taken into account. So for each time step, the MAC matrix between the identified mode-shapes and the mode-shapes from the finite element analysis (FEA) of the beam subsystem is reshaped in a column vector. In Fig. 7.9, the instantaneous MAC values are shown between identified bending modes in the lateral Fig. 7.9a and vertical Fig. 7.9b directions respectively.

The previously observed perturbations of the mode-shapes due to the presence of the moving mass at vibration nodes or anti-nodes are also visible in Fig. 7.9a,b. As for the identified instantaneous frequencies, the time-varying MAC values drop periodically when the mass is passing on an antinode of vibration and come back close to unity when the mass is passing on a node of vibration.

## 7.7  Conclusion

In this paper, two well known techniques (the HHT and the HVD methods) used for non-stationary signal decomposition were considered and their limitations in the case of crossing frequencies or amplitudes of intrinsic components were highlighted. As these methods work on single signals, it was shown that, in the case of a multiple degree-of-freedom system, applying them separately on each channel can lead to non-unique frequency curves and consequently to non-corresponding demodulated components on all the channels. To alleviate this problem, a source separation technique was introduced into the algorithm of the original HVD method. It was shown that both limitations were removed as a single frequency curve was calculated for each mode. Thanks to the better estimation of the instantaneous frequencies, mono-components and instantaneous mode-shapes were calculated.
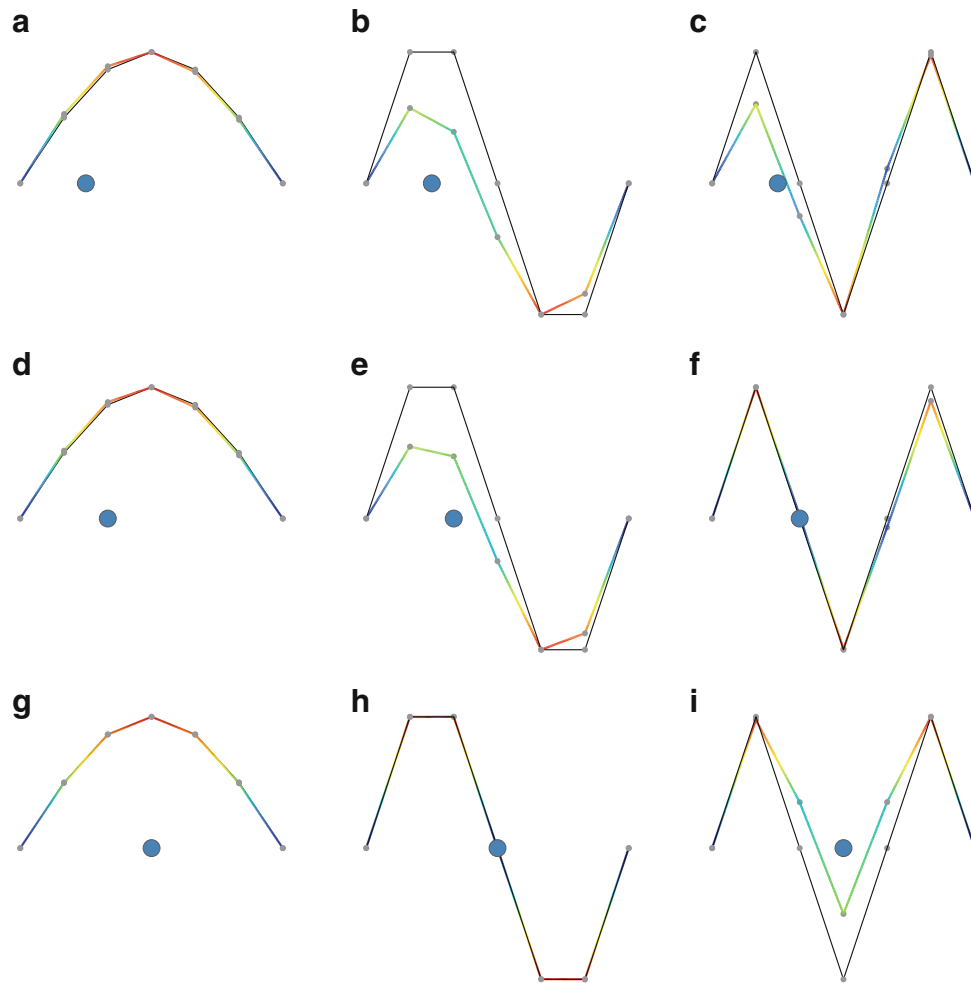
**Fig. 7.8** Plots of the vertical bending mode-shapes at three times: 15, 20 and 30 s. The mode-shapes of the beam subsystem are plotted in *black* and the instantaneous mode-shapes of the time-varying system in *color*. The *blue dot* shows the location of the mass for the three considered times. (**a**) Mode 1—$t = 15$ s. (**b**) Mode 2—$t = 15$ s. (**c**) Mode 3—$t = 15$ s. (**d**) Mode 1—$t = 20$ s. (**e**) Mode 2—$t = 20$ s. (**f**) Mode 3—$t = 20$ s. (**g**) Mode 1—$t = 30$ s. (**h**) Mode 2—$t = 30$ s. (**i**) Mode 3—$t = 30$ s
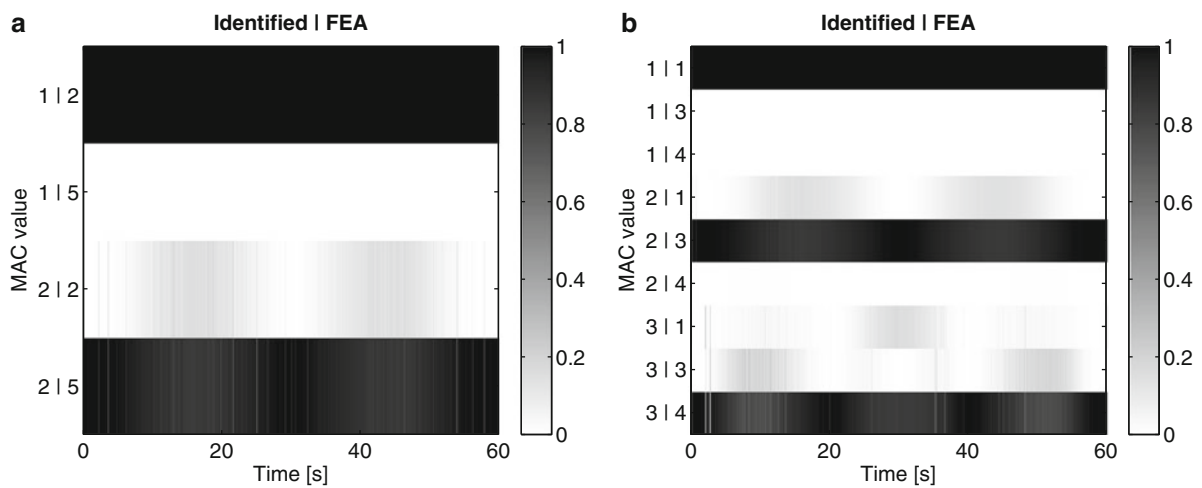


**Fig. 7.9** Modified MAC matrix to take the time variability into account. (**a**) Lateral bending modes. (**b**) Vertical bending modes

# References

1. Huang NE, Shen Z, Long SR, Wu MC, Shih HH, Zheng Q, Yen N-C, Tung CC, Liu HH (1998) The empirical mode decomposition and the Hilbert spectrum for nonlinear and non-stationary time series analysis. Proc Roy Soc A Math Phys Eng Sci 454(1971):903–995
2. Feldman M (2011) Hilbert transform applications in mechanical vibration. Wiley, Chichester
3. Bedrosian E (1963) A product theorem for Hilbert transforms. Proc IEEE 51(5):868–869
4. Kerschen G, Golinval J (2002) Physical interpretation of the proper orthogonal modes using the singular value decomposition. J Sound Vib 249(5):849–865
5. Chelidze D, Zhou W (2006) Smooth orthogonal decomposition-based vibration mode identification. J Sound Vib 292(3–5):461–473
6. Poncelet F, Kerschen G, Golinval J-C, Verhelst D (2007) Output-only modal analysis using blind source separation techniques. Mech Syst Signal Proc 21(6):2335–2358
7. Alexandrov T, Bianconcini S, Dagum EB, Maass P, McElroy TS (2012) A review of some modern approaches to the problem of trend extraction. Econometric Reviews 31(6):593–624 http://ideas.repec.org/a/taf/emetrv/v31y2012i6p593-624.html
8. Feldbauer C, Höldrich R (2000) Realization of a Vold-Kalman tracking filter - a least squares problem. Proceedings of the COST G-6 Conference on Digital Audio Effects (DAFX-00) No. 8, pp. 8–11, Verona, Italy
9. SAMCEF Mecano http://www.lmsintl.com/?sitenavid=8435E5BB-C04D-49AB-B72A-9CB01D6FD9DB

# Chapter 8
# Recovery of Operational Deflection Shapes from Noise-Corrupted Measurement Data from CSLDV: Comparison Between Polynomial and Mode Filtering Approaches

P. Castellini, P. Chiariotti, E.P. Tomasini, M. Martarelli, D. Di Maio, B. Weekes, and D.J. Ewins

**Abstract** Continuous Scanning LDV measurement methods allow estimates to be made of high spatial density vibration deflection shapes (ODSs) in very short testing times. The correct reconstruction of the ODS depends on the quality of the acquired data. Speckle and other types of noise, usually resulting from surface treatment of the specimen can be detrimental in this recovery process.

This paper presents a comparison between two alternative methods for recovering ODSs from CSLDV data. The well-known method is based on the fact that the amplitude modulated response can be processed by calculating the peak amplitudes and phases of the spectral sidebands and, eventually, the deflection shapes can be calculated by conversion of these peak amplitudes into polynomial coefficients. The second method exploits the idea that, if the mode shapes of the structure under test are known a priori, e.g. from a numerical model or from an analytical formulation, it is possible to settle a procedure that searches for similarities between those known mode shapes (the candidate mode shapes) and ODSs that actually modulate the CSLDV signal. This procedure can be considered a pattern matching technique that is able to identify the resonance frequency related to each ODS and the mode shapes that better match with ODSs excited making it possible to filter out the uncorrelated noise.

Both methods have been applied to data acquired from measurements on the tailcone of a Lynx helicopter, which contained levels of noise disrupting the correct peak amplitudes data processing. Comparison with step-scan results was done in order to have a reference technique and to understand how optical noise issues could affect the measurement.

**Keywords** CSLDV • Speckle noise • Mode matching techniques • Tailcone helicopter vibration • Experimental modal analysis

## 8.1 Introduction

This paper presents a research work focussed on Continuous Scanning LDV measurement methods applied to a tail cone of a helicopter. The initial objective was to be able to reconstruct from a single time record acquired by using straight line continuous scan method several Operational Deflection Shapes (ODSs). It was demonstrated that continuous scanning technology is capable of acquiring information of more than one ODS inside a single time record and therefore cancelling the need of designing a grid of measurement points [1]. The application of this technology gave promising results on a simple cantilever specimen but when applied to a real test structure then it was soon evident the level of SNR of the LDV was causing several problems for the post-processing of the acquired time data. The test structure available in Bristol University, and presented in this paper, is a Lynx helicopter which has got a military matt coating. That was cause of poor signal quality

P. Castellini (✉) • P. Chiariotti • E.P. Tomasini
Università Politecnica delle Marche, Brecce Bianche, 60131 Ancona, Italy
e-mail: p.castellini@univpm.it

M. Martarelli
Università degli Studi e-Campus, Isimbardi, Novedrate, CO, Italy
e-mail: m.martarelli@univpm.it

D. Di Maio • B. Weekes • D.J. Ewins
University of Bristol, University walk, Bristol BS8 1TR, UK

for the LDV and, in fact, step scanning measurement method had to be performed by taping a grid of measurement points over the tail cone of the helicopter. The reconstruction of ODSs from CSLDV multi-tonal approach were not that bad for the first few modes but quite poor for the other selected for this experimental exercise. Based on the assumption that response mode are measured but information calculated from some sidebands corrupt the ODS reconstruction a different post-processing approach is adopted and presented in this paper.

CSLDV data processing methods are based on targeted FFT for the recovering of sideband spectra related to ODSs modulating the LDV output. However the method requires to operate with really good quality measurement data which can be compensated only by the experience of the experimentalist who recognises the sideband spectra from the noise. However, in presence of low SNR the typical sideband spectra are merged into the noise floor and therefore mode shapes can be hardly recovered. To overcome this problem, when mode shapes are known from a priori knowledge, for instance from a numerical/analytical model, those mode shapes can be taken as candidate mode shapes and a pattern matching-like procedure applied to estimate the resonance frequencies of the structure under test. The procedure searches for similarities between the candidate mode shapes and the ODS modulating the time history measured by the CSLDV technique. A time domain approach for the recovery of the resonance frequencies of a beam has been described in [2]. In that work only simulated measurement data have been taken into consideration. However, unlike the time domain approach the extraction of the mode shapes from CSLDV data can be performed in frequency domain. In that case the pattern matching is not based on actual mode shapes but on sideband spectra. A detailed description of the algorithm is given in [3]. In this paper the application of this technique to a complex test case is shown and the results obtained compared with the ones achieved with the conventional CSLDV method.

## 8.2 Measurement of ODSs of LINX Tail Cone Using CSLDV

An experimental attempt on a real component, by using the presented measurement approach, is applied to a tail cone of a helicopter, as shown in Fig. 8.1. The helicopter is a LYNX model which is stored in the dynamic laboratory of BLADE (University of Bristol) and it used for several vibration experiments. The aim of this section is to attempt the use of continuous scanning and multi-tonal excitation waveforms to aircraft structures like the LYNX.

### 8.2.1 Step Scanning Method

The tail cone was tested so as to obtain the mode shapes and natural frequencies. These could be used for generating the multi-tonal excitation waveforms for the continuous scanning method and for comparing the measured ODS at the
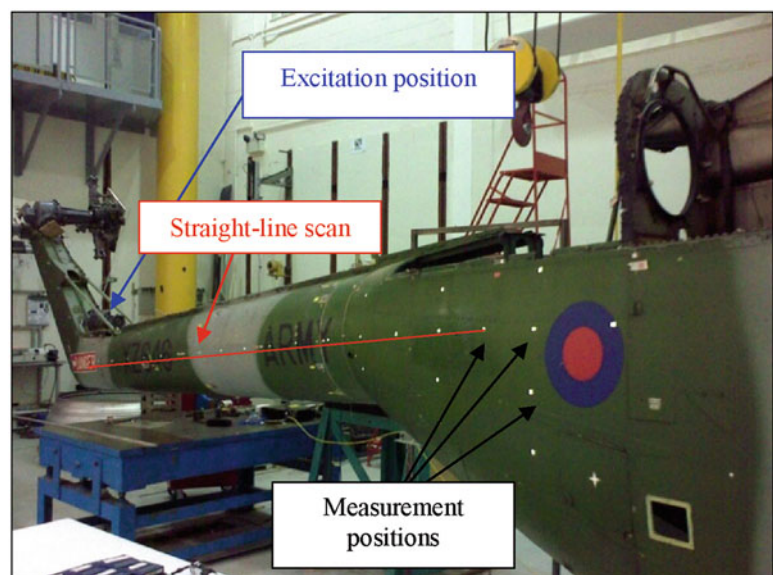


**Fig. 8.1** Tail cone of LINX helicopter and measurement setup
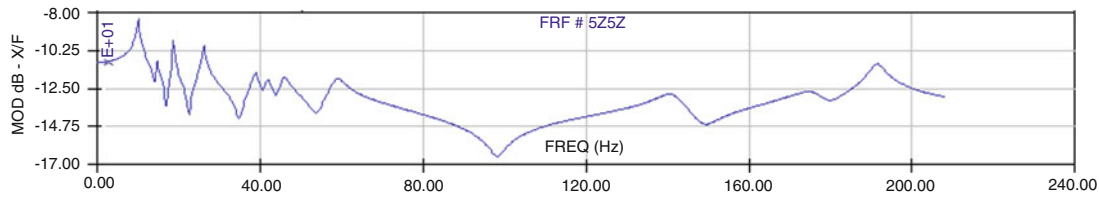
**Fig. 8.2** Example of FRF measured from the Lynx on a reflective tape

**Table 8.1** Natural frequencies and loss factor measured from tail cone (step scanning method)

|  | Mode-2 | Mode-3 | Mode-4 | Mode-5 | Mode-6 | Mode-7 | Mode-8 |
|---|---|---|---|---|---|---|---|
| Natural Frequency [Hz] | 14.64 | 18.79 | 26.18 | 38.95 | 41.84 | 45.76 | 58.83 |
| Loss factor [%] | 2.5 | 0.9 | 1.9 | 3.2 | 3.5 | 3.8 | 4.8 |

resonances. Before proceeding with the measurements, the tail cone was marked using reflective tapes, white square patches, as it can be seen in Fig. 8.1. An electromagnetic shaker was attached, opposite the scanned area, by the gear box shown by a blue arrow in Fig. 8.1. That position was merely chosen to excite the lateral modes of the tail cone and this paper is not aiming to identify pure modes of the tail cone. The helicopter was supported using inner tyre tubes for achieving "free-free" supporting conditions.

This procedure was needed in order to improve the LDV signal quality because of the matt green paint. A broadband excitation, using chirp waveform, was produced in a frequency bandwidth of 500 Hz and within which several modes were measured, as shown in Fig. 8.2. The first order modes were selected after modal analysis, as reported in Table 8.1, and mode shapes are reported in Fig. 8.3.

## 8.2.2 Investigation of Stepped Scan and Continuous Scan Signals

This section reports some insights gathered from the LDV output time signals when it was used as either as stepped or continuous scanning mode. In order to better-understand how the velocity signal output from the velocity decoder varies when the laser-spot is stationary or moving on a test surface, an illustrative qualitative study is now given. The tested SLDV system was a Polytec PSV-300 SLDV, trained upon the Lynx tail as previously described. The velocity output and a reference signal from the force transducer (conditioned by a Kistler 5134) were acquired simultaneously using the Polytec system. The tail was excited at 39.5 Hz, and all combinations of the following scenarios were tested:

1. With/without retro-reflective tape.
2. Stationary/moving spot.
3. With/without tracking filter.

In Fig. 8.4 200 cycles of the velocity output are plotted directly against the force reference—the signal is qualitatively evaluated by simply considering deviation from the underlying closed form (an approximately elliptical parametric function of time). In each of the sub-Figures in Figs. 8.4, 8.5, and 8.6 the laser spot was stationary, with the top sub-Figures taken on retro-reflective tape and the bottom sub-Figures taken on the bare Lynx paint; the left sub-Figures without the tracking filter and the right sub-Figures with the tracking filter. For the stationary spot on retro-reflective tape the signal is observed to be of a high quality. Without the retro-reflective tape there is a slight reduction in signal quality, which worsens with use of the tracking filter. Spectra for some of the above data are given in Fig. 8.5. It is clear that the noise floor increases for all frequencies between the stationary spot and moving spot cases. Although this example is merely qualitative, the conclusions are clear:

1. Signal quality is reduced by 'on the fly' measurement.
2. Use of retro-reflective tape is preferred when practicable.
3. Use of the tracking filter should be restricted to already high-quality signals—the tracking filter can increase periodic noise components.

Figure 8.6 shows 8 s of LDV output signal measured for a scan rate of 0.1 Hz. It is clear to see that the signal quality is not that great and so some spectral sidebands can be corrupted by noise.
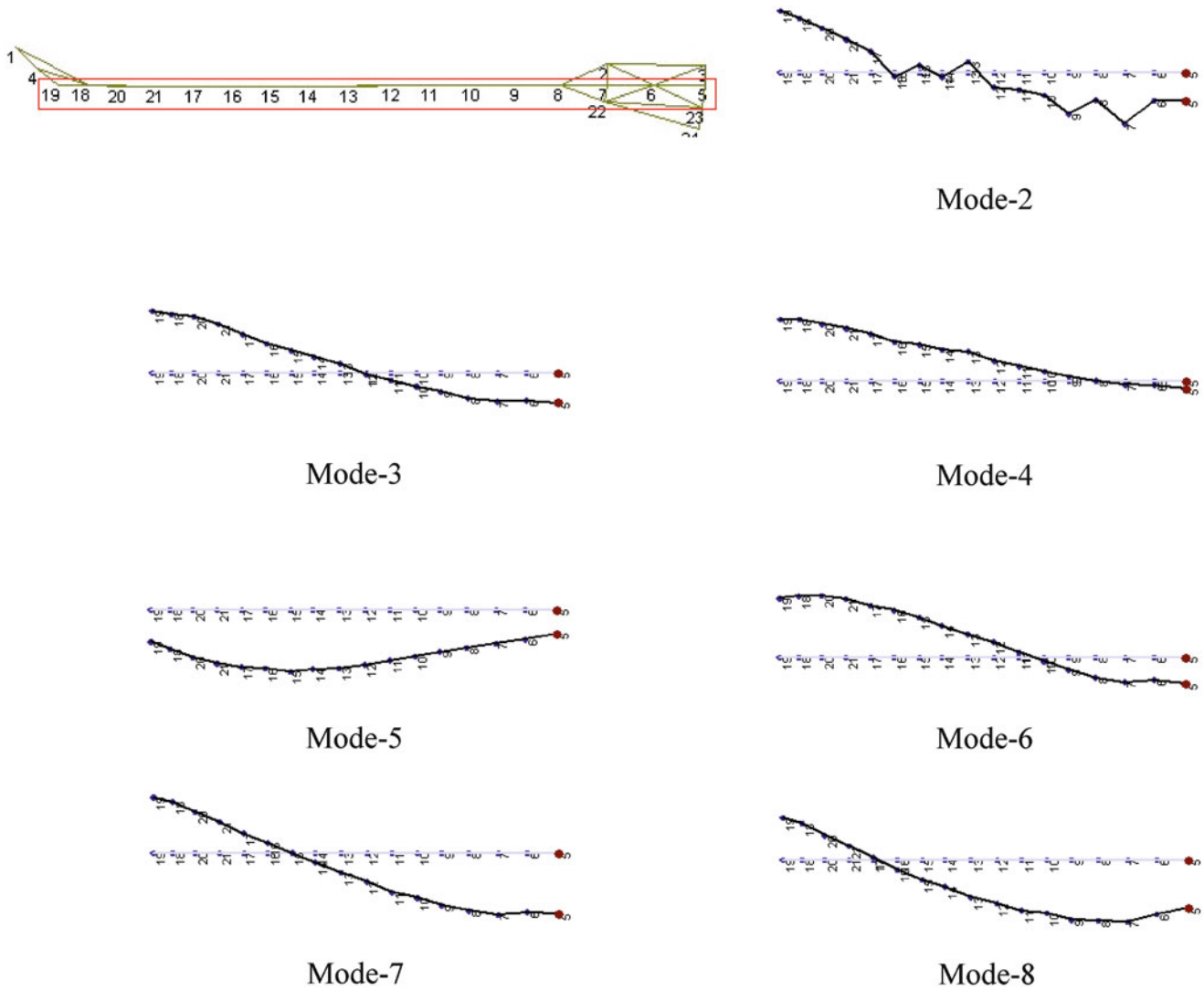
**Fig. 8.3** Mode shapes of the tail cone obtained by modal analysis (step scanning method); tail cone top view

### 8.2.3 Continuous Scanning LDV Method

In this paragraph the CSLDV method is illustrated. This experiment was designed so as to perform a straight-line scan along the tail cone, as shown by a red line in Fig. 8.1. Hence, the scanning laser was then used in continuous mode rather than stepped one. Having obtained the natural frequencies a multi-tonal excitation waveform could be built using the natural frequencies, as reported in Table 8.2.

A straight-line was scanned along the tail cone across some of the measurement points used for the step scanning measurements. Four sets of measurements were produced on the tail cone using three different scan rates for scanning the line and these are reported in Table 8.3.

Seven ODSs, as reported in Fig. 8.7, were reconstructed from the CSLDV time histories; amplitude and measurement positions were scaled between −1 and 1 to simplify the comparison.

### 8.2.4 Mode Matching Analysis

Results from processing the CSLDV data measured on the Linx Tail cone using the mode matching approach are discussed in this paragraph.

**Fig. 8.4** 200 cycles of output from a force transducer on the exciter versus output from the laser vibrometer for (*top-left*) retro-reflective tape, tracking filter disabled; (*top-right*) retro-reflective tape, tracking filter enabled; (*bottom-left*) bare Lynx surface, tracking filter disabled; (*bottom-right*) bare Lynx surface, tracking filter enabled
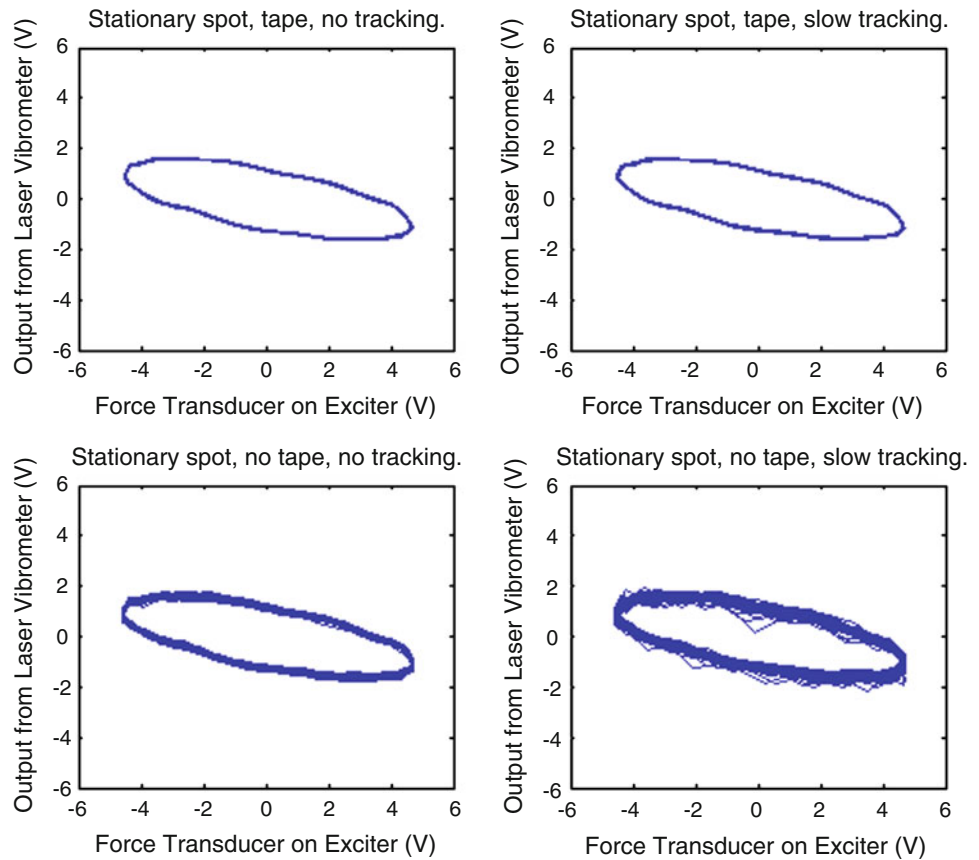


Since a comprehensive numerical model of the Linux tail was not available at the time of the analysis the mode shapes calculated from the step scanning were taken as reference to build up the set of candidate mode shapes. It was decided to use only the real part of the selected mode shapes. The set of candidate mode shapes in reported in Fig. 8.2. The plot shows that some modes are quite similar to each other in terms of shape: this is mainly due to the fact that the tail represents a quite small section of the whole helicopter structure, and therefore differences in terms of global modes cannot be appreciated. It can be expected the pattern-matching algorithm will suffer on separating mode shapes characterised by this level of similarity. Modes from the step scanning were thus curve-fitted in order to extract the corresponding polynomials. In such a way it is possible to collect a set of kernels that represents the sideband patterns that should be present, if correctly excited and measured, within the CSLDV spectrum.

Figure 8.8 shows the shape of such kernels (gray stars) superimposed to the CSLDV spectrum (black line) in the frequency range where each mode is expected. The columns of Fig. 8.8 refer to the different tests performed (from Test#1 to Test#4). Looking at the CSLDV spectrum for the different tests, it is clear that the signal quality worsens from Test#1 to Test#4. This is due to several factors, among whom an important role is played by the presence of periodic speckle noise. Moreover the superposition of sidebands related to adjacent modes contributes to further spoil the CSLDV spectrum.

The mode shapes recovered for each test are reported in Table 8.4 where the thick represents they are correctly found.

The technique demonstrates to be quite robust to the noise, being able to recognize modes also on Test#3 and Test#4, where the CSLDV spectrum gets more difficult to be analyzed because of noise. On the other hand, the algorithm fails in recovery modes from V to VII simply because the kernels extracted from the step scanning test do not correspond to the sideband patterns that are effectively present on the CSLDV spectrum. This can be due to the not perfect matching between the step scanning acquisition and the continuous scanning one. Indeed, if the scanning line is not perfectly aligned with the grid of points of the step scanning measurement, the two measurements can highlight different mode shapes. This happens, for instance, if we consider the role played by torsional modes on the measurements: the line scan cannot distinguish between bending and torsional modes of the tail, but modes contribute differently depending on the portion of the tail that is scanned.
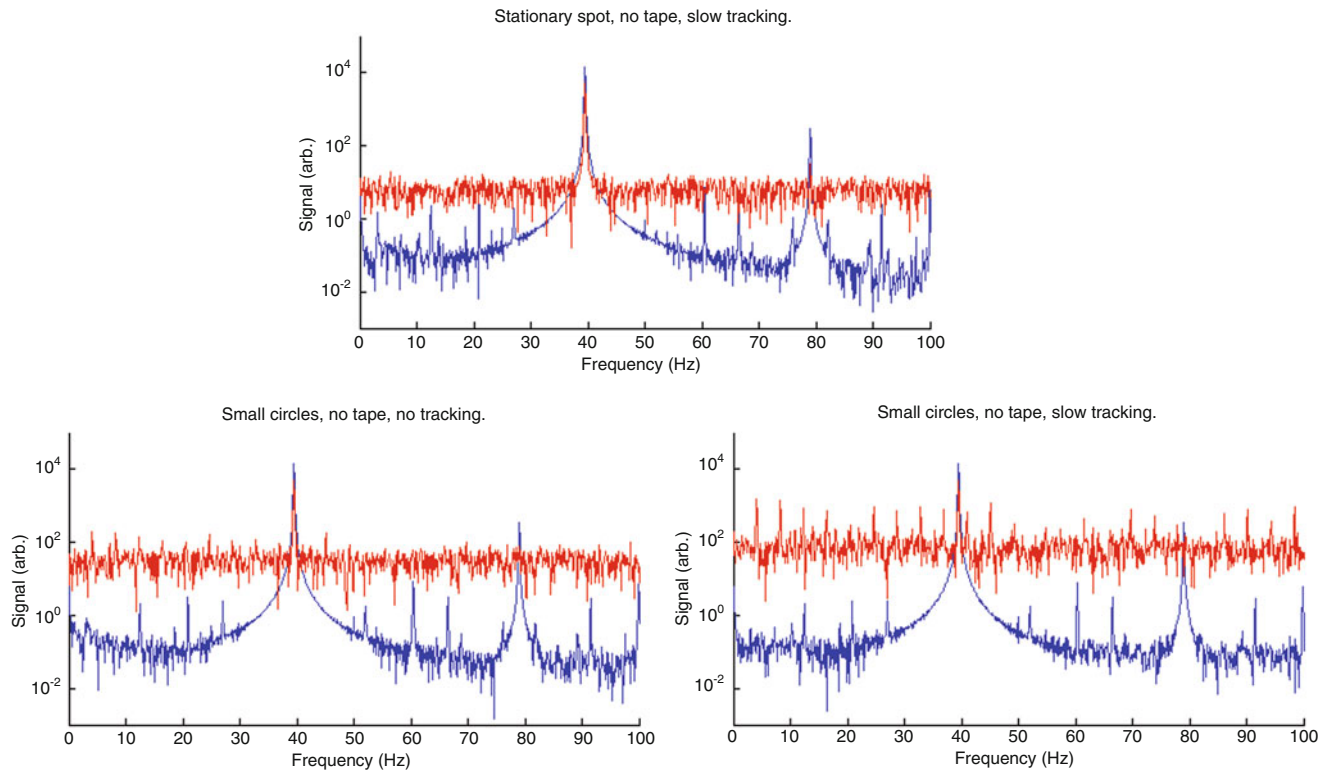
**Fig. 8.5** Spectra showing unscaled force transducer output (*blue*) and vibrometer output (*red*) for: (*top*) stationary measurement spot, tracking filter on; (*middle*) moving measurement spot, tracking filter off; (*bottom*) moving measurement spot, tracking filter on. In all cases above the measurement was taken on the painted surface of the Lynx
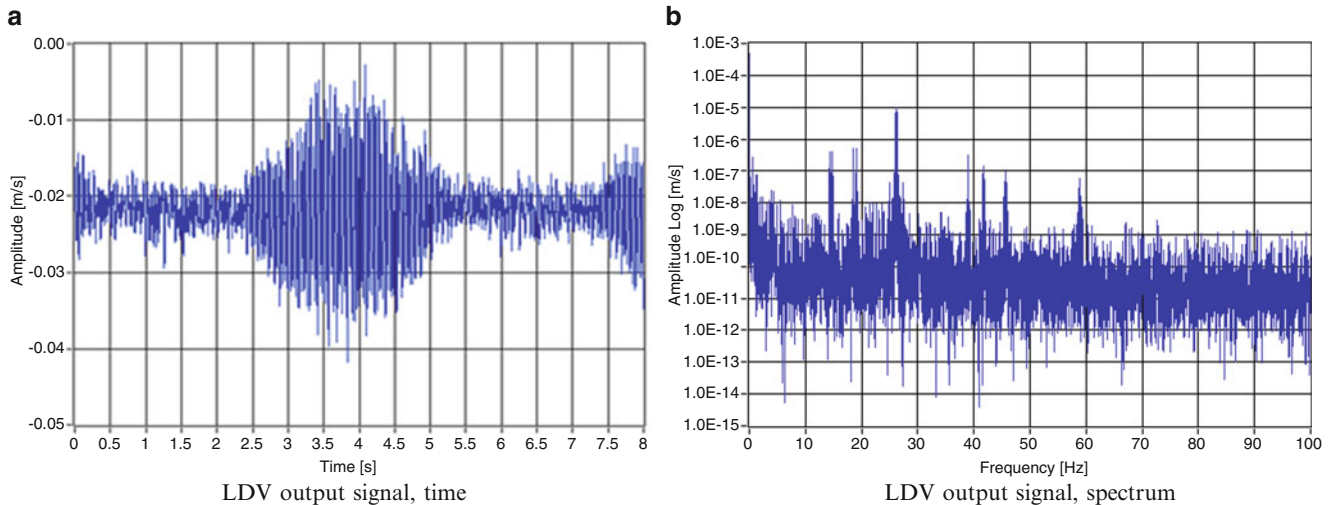


**Fig. 8.6** LDV output signal measured on the tail cone using Continuous Scan method and multi-tonal excitation waveform

## 8.3    Conclusions

This paper presents an experimental work performed on the tail cone of the Lynx helicopter which is available at University of Bristol. Modal testing was performed on the test structure using two measurement methods: stepped and continuous scanning methods. The paper aimed to demonstrate that (i) continuous scanning can perform measurements on a specimen without using surface treatments and that (ii) in presence of poor signal quality the deflection shapes can still be recovered

**Table 8.2** Components of multi tonal excitation waveform for performing continuous scanning measurement

|  | Mode-2 Tone-1 | Mode-3 Tone-2 | Mode-4 Tone-3 | Mode-5 Tone-4 | Mode-6 Tone-5 | Mode-7 Tone-6 | Mode-8 Tone-7 |
|---|---|---|---|---|---|---|---|
| Frequency (Hz) | 14.6 | 18.8 | 26.2 | 38.9 | 41.8 | 45.7 | 58.8 |

**Table 8.3** Measurement parameters for CSLDV method

|  | Scan rate(Hz) | Acquisition time(s) | Sampling rate(Sample/s) | Number of Sample(Sample) |
|---|---|---|---|---|
| Test-1 | 0.2 | 60 | 1,000 | 60,000 |
| Test-2 | 0.1 | 100 | 1,000 | 100,000 |
| Test-3 | 1.1 | 31.429 | 1,000 | 31,429 |
| Test-4 | 1.1 | 20 | 1,000 | 20,000 |
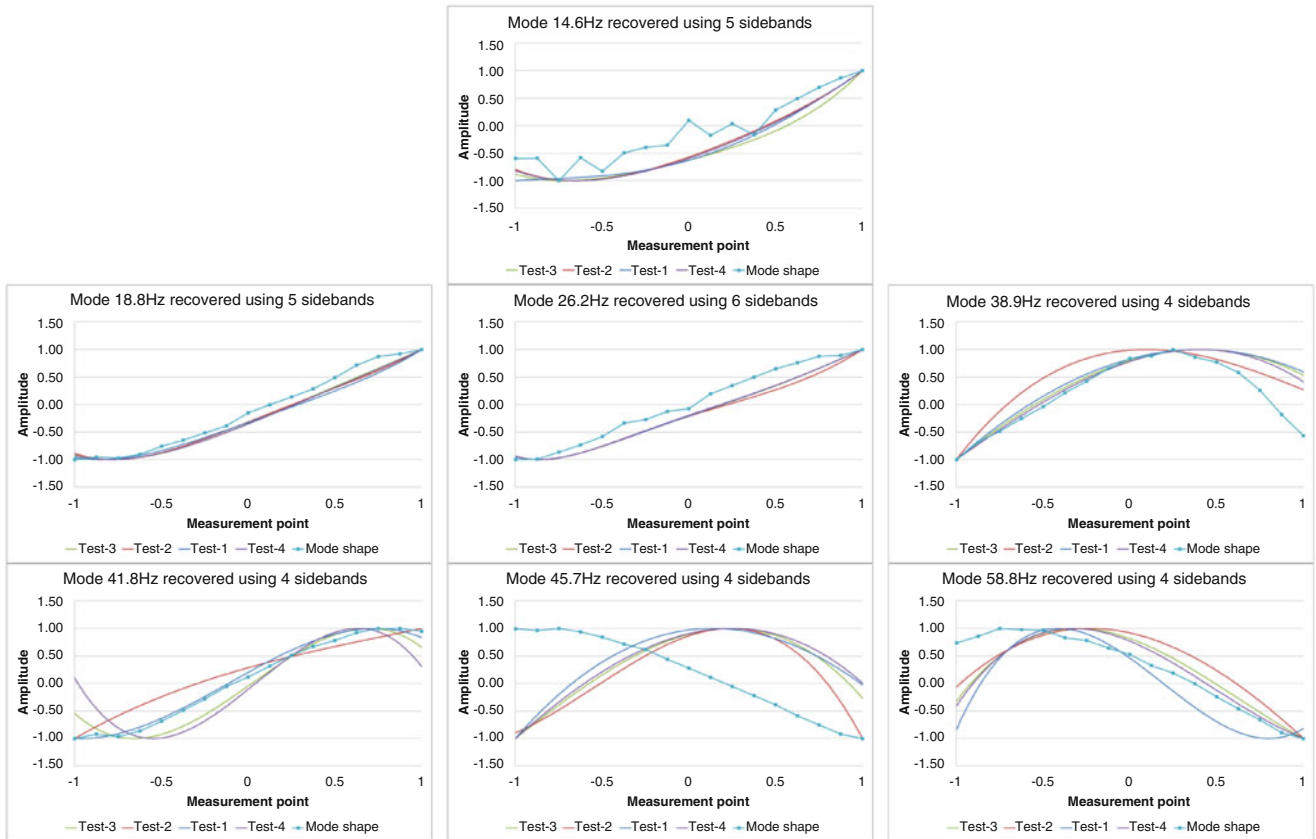


**Fig. 8.7** Comparison between ODSs and mode shapes (CSLDV vs. Stepped)

either by using spectral harmonic coefficients or by mode matching. The measurements were performed using multi-tonal excitation waveforms so as to demonstrate that continuous scanning can actually record in one single time record information of many response modes, instead of capturing many FRFs measurements.

The results demonstrated that ODSs can be recovered and some of those can be compared quite well with the mode shapes obtained from the stepped scan method. It also showed that the mode matching is an important method for recovering ODSs from LDV time signals which can present high level of noise. Unfortunately, the lack of an FE model of the tail cone of the helicopter was preventing to use clean mode shapes for comparisons.

Fig. 8.8 Candidate mode shapes obtained by the numerical model
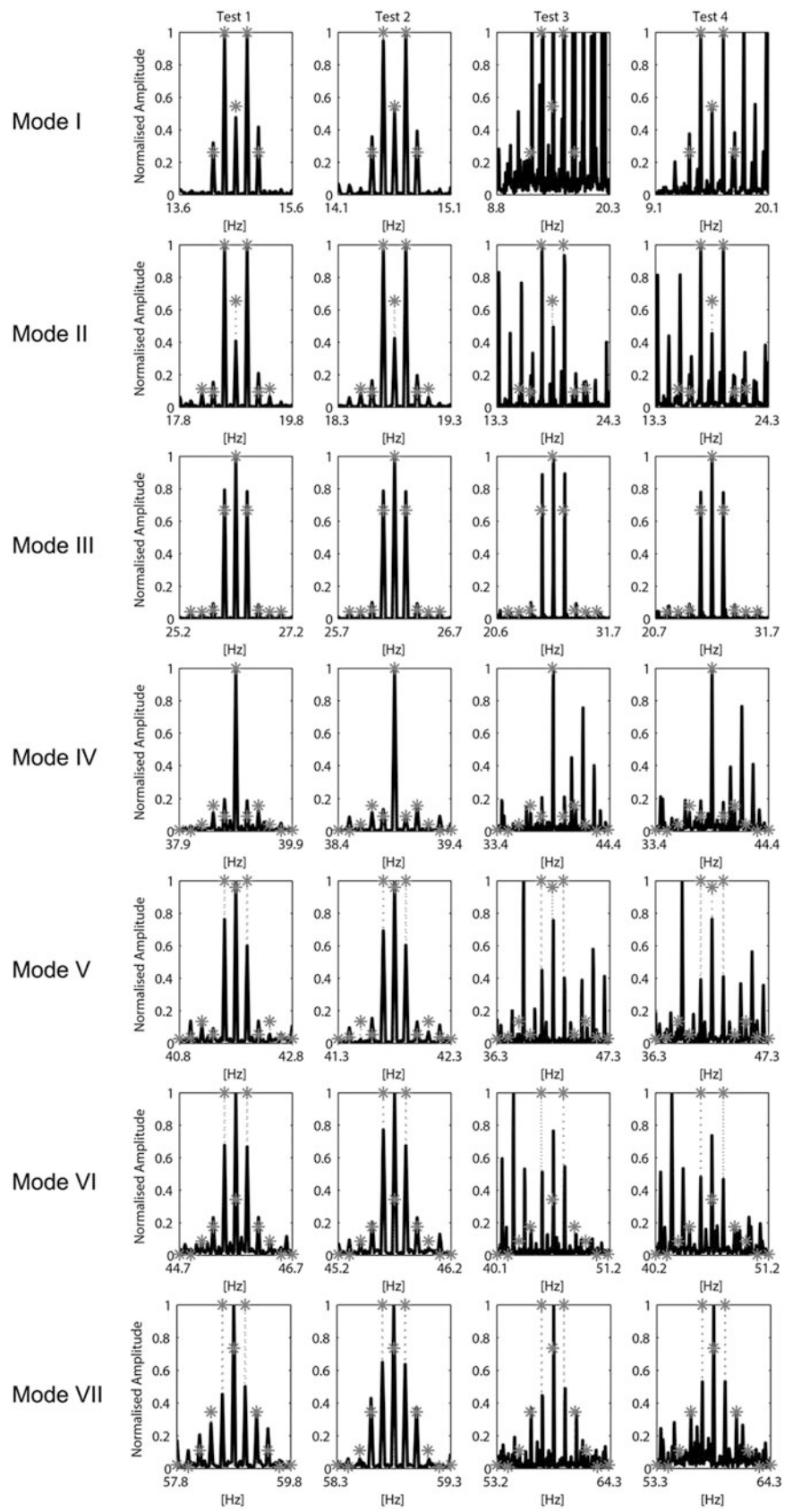
**Table 8.4** Recovered ($\checkmark$) and not recovered ($\times$) mode shapes by mode matching algorithm

|          | Test #1 | Test #2 | Test #3 | Test #4 |
|----------|---------|---------|---------|---------|
| Mode I   | $\checkmark$ | $\checkmark$ | $\times$ | $\checkmark$ |
| Mode II  | $\checkmark$ | $\checkmark$ | $\checkmark$ | $\checkmark$ |
| Mode III | $\checkmark$ | $\checkmark$ | $\checkmark$ | $\checkmark$ |
| Mode IV  | $\checkmark$ | $\checkmark$ | $\checkmark$ | $\checkmark$ |
| Mode V   | $\times$ | $\times$ | $\times$ | $\times$ |
| Mode VI  | $\times$ | $\times$ | $\times$ | $\times$ |
| Mode VII | $\times$ | $\times$ | $\times$ | $\times$ |

# References

1. Di Maio D, Ewins DJ (2011) Continuous scan, a method for performing modal testing using meaningful measurement parameters, part I. Mech Syst Signal Process 25:3027–3042
2. Castellini P, Chiariotti P, Martarelli M (2013) Mode filtering of continuous scanning laser doppler vibration data, special topics in structural dynamics, vol 6. Proceedings of the 31st IMAC, A conference on structural dynamics, Series 43, doi: 10.1007/978-1-4614-6546-1
3. Chiariotti P, Castellini P, Martarelli M (2014) Recovery of mode shapes from continuous scanning laser doppler vibration data: a mode matching frequency domain approach. Proceedings of the 32nd IMAC, A conference on structural dynamics

# Chapter 9
# Exploiting Imaging Techniques to Overcome the Limits of Vibration Testing in High Excitation Level Conditions

**M. Martarelli, P. Castellini, P. Chiariotti, and E.P. Tomasini**

**Abstract** Traditional vibration testing procedures fail when extremely high excitation levels are reached. On the other hands, large displacements are well suitable to be analysed by imaging techniques based on high-speed cameras.

This work aims at identifying the exploitability of imaging techniques for output-only experimental modal analysis, the so-called Operational Modal Analysis (OMA). Mode shapes evaluated from image-extracted Frequency Response Functions (FRFs) have been compared with mode shapes extracted from mobility FRFs measured by Laser Doppler Vibrometry. The test has been performed on a simple structure showing large displacements but using excitation levels that made it possible to still consider Laser Doppler Vibrometry the reference technique. Once assessed that, even at limited excitation levels, results from the two approaches are similar, the validity of the image-based approach in high excitation level tests can be derived accordingly. Sensitivity to image processing parameters, as spatial resolution and averaging, has been evaluated quantitatively exploiting the Modal Assurance Criterion (MAC) to correlate the mode shapes from the image-based approach with those extracted exploiting Laser Doppler Vibrometry.

**Keywords** Vision system • Scanning laser doppler vibrometry • Operational modal analysis • High displacement measurement • Image processing

## 9.1 Introduction

With the increasing interest on vibration monitoring and structural behaviour characterisation of large and heavy structures, as for instance bridges or wind turbines, conventional vibration testing techniques have to deal with operational high displacements which can saturate the sensor measurement range. Such circumstance can occur also when components work under extremely high excitation levels, as for instance landing gears, which operates in non-linear conditions. In these cases, typical instrumentation can range from contact sensors (e.g. accelerometers attached to the structure) to non-contact measurement systems, as radar [1] or lidar [2].

A valid alternative, which is recently gaining more and more interest for its versatility, is represented by measurements based on imaging techniques [3–5]. Cameras technology has done lots of progresses within the last years and today's imaging measurement systems are characterised by high resolution and accuracy also in dynamic condition. For this reason image processing-based measurement techniques are gaining importance in diverse application fields, from health care to quality control, from fluid dynamics to structural dynamics. If considered within the structural vibration field, it should be recalled that cameras record the displacement of the structure. When dealing with large displacements, especially in the low frequency range, this is certainly an advantage rather than measuring the vibration velocity/acceleration of the structure under test. The high resolution standards that have been reached by camera's developers make the imaging approach close to a full-field

M. Martarelli (✉)
Università degli Studi e-Campus, Via Isimbardi, Novedrate, CO, Italy
e-mail: m.martarelli@univpm.it

P. Castellini • P. Chiariotti • E.P. Tomasini
Università Politecnica delle Marche, Via Brecce Bianche, Ancona 60131, Italy

measurement technique. The negative effects of a too coarse resolution, which can be a possibility when framing a large structure subjected to large displacements, can be minimized, choosing the correct optics, but not completely avoided. This probably represents the main drawback of the image-based approach.

However, apart from this, image-based measurement systems present other practical characteristics that make them good candidates for Operational Modal Analysis (OMA). First of all these techniques are non-invasive and this avoid to struggle in placing sensors and long cables on the structure. Data Acquisition systems are less expensive as well, since there is no need to manage several channels. Information gathered from the measurement points are synchronous and, by properly placing the cameras, different directions of vibration can be assessed. In this scenario, a question that still needs to be discussed is related to how performances of these systems and the coupled imaging processing strategies affect the final results in OMA.

The performances of an imaging system based on a high-speed camera, when used for OMA on a lightweight beam subject to large displacement, are compared to those of a Laser Doppler Vibrometry based measurement system. Laser Doppler Vibrometer (LDV) is considered as the reference technique in this application, even though in conventional OMA measurements accelerometers are considered the reference sensors, because the structure under test is a lightweight beam, and it would have been misleading to use accelerometers, mainly because of the mass loading effect.

The main task of the paper is therefore to discuss advantages and limits of an image-based approach in relation to the vibratory characteristics of the structure and to present an exhaustive analysis of the OMA results in dependence to different image processing strategies and parameters, e.g. spatial resolution and averaging. The paper is organized as follows. The two test set-ups (the camera-based one and the LDV one) are described at first in Sect. 2. Data processing is then discussed in Sect. 3. Results from the two measurement approaches are reported in Sect. 4 where their dependence from different image processing approaches is discussed.

## 9.2 Camera-Based and LDV-Based Tests Set-Up

Experiments were performed on a thin steel beam excited along its thickness direction by an electro-dynamic shaker. The measurement set-up is shown in Fig. 9.1. The steel beam was observed by a Scanning LDV (SLDV) from the top and by a high-speed camera from the side. Back illumination was used to improve the quality of the image acquired. That illumination was realised by a halogen lamp and a frosted glass placed in between the lamp and the beam. The camera was aligned in order to observe the object under test in backlight lighting. This camera set-up makes it possible to observe bending modes as vertical motion of the beam shadow and torsional modes as variation of the local thickness of the beam shadow.

The acquisition sensor was a 14 bit CMOS sensor of 4.3 Mpixel ($2,400 \times 1,800$). The data rate of 2 Gpx/s guaranteed a frame rate of 480 fps at full frame and 4,000 fps at $1,520 \times 64$ pixels. At this frame rate the CMOS embedded memory of 3 GB made it possible to record a video up to 4 s long. Figure 9.2 reports a sample of the beam installed on the shaker as seen by the camera point of view. The red box displays the Area of Interest (AoI) that was actually framed and recorded by the camera.

The reference vibration measurement was performed by a SLDV over a grid of $61 \times 5$ points on the beam top surface, see Fig. 9.3. The input force was measured by a force sensor PCB Model 208C01 attached to the beam via a stiff push-rod. The reference FRF data set was acquired on a frequency range of 2 kHz, with a resolution of 1.25 Hz.
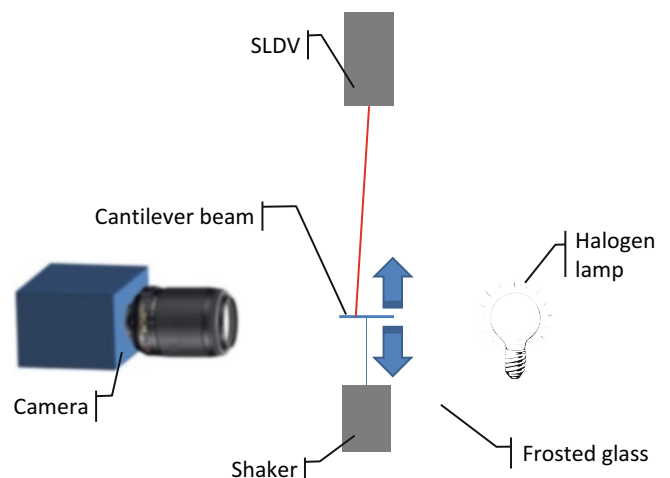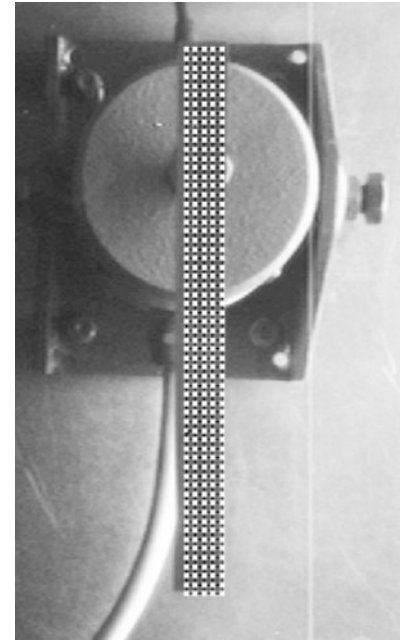


**Fig. 9.1** Dynamic test rig for both the image acquisition and the SLDV reference one

**Fig. 9.2** Camera framing on the steel beam



**Fig. 9.3** SLDV measurement grid



## 9.3   Image Processing Method

The image sequence recorded by the camera was processed in order to extract the displacement of the beam. Each frame was analyzed independently. A set of vertical sections of the image were considered across the beam front view framed by the camera and grey level fluctuations were extracted on each section. In order to evaluate the sensitivity of the modal analysis results to spatial resolution two data sets have been extracted from the image: one with poor spatial resolution (61 sections) and the other one with better spatial resolution (1,220 sections). In addition, the data set with better resolution was exploited to test the sensitivity to spatial averaging. Ten and twenty consecutive sections of the 1,220 sections data set were averaged together in order to reduce the measurement noise and to attenuate the pixel-lock effect that occurs when an image edge transits from a pixel line to another one. This effect is due to the digital nature of the CMOS sensor, and it can be significantly reduced by averaging when the edge line is tilted with respect to the image reference system, allowing rather accurate sub-pixels interpolation. Since edges can be distinguished as sharp discontinuity of the grey level, they have been extracted by searching the maximum of the grey level profile first derivative. This process also makes it possible to reach a sub-pixel resolution. An example of the process on a single section is shown in Fig. 9.4. Square boxes represent found edges, respectively the upper and the lower ones. This option of extracting the two beam edges was considered with the aim of averaging the upper and lower profile. The averaging will bring two positive effects on the image processing:

- a further increase of the noise rejection,
- a cancellation of torsional modes.

In fact, when working with back light lighting, the average of the upper and lower edge should give the motion of the neutral axis of the beam, i.e. to show only bending modes, while the difference between upper and lower edge should be sensitive to torsional modes. In the presented case, torsional modes should not be excited in the structure, and averaging upper and lower edge position helps in mitigating eventual torsional modes residues still vibrating.
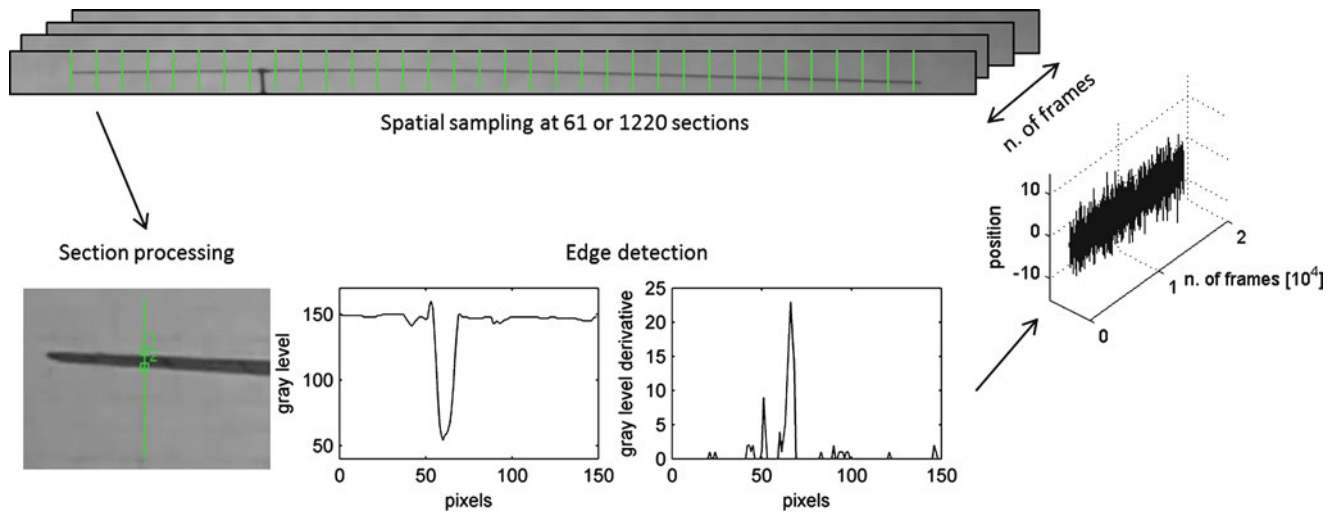
**Fig. 9.4** Image processing flow-chart

## 9.4 Analysis of Results

The sensitivity of OMA to the different image processing strategies is presented here. OMA was performed on the image data considering the spectra referenced to the driving point. For simplicity this transfer function is called hereafter FRF. The modal analysis algorithm exploited was the Polymax [6]. Results from standard EMA (experimental Modal Analysis) on SLDV data are considered as the reference data. Comparison with the reference data set was at first performed in terms of spatially averaged FRFs. Once assessed the compatibility of the two measurement data sets in terms of FRFs, the analysis was moved to mode shapes.

### 9.4.1 Sensitivity to Spatial Resolution

Sensitivity to the spatial resolution was considered at first. The FRFs obtained by spatially averaging the FRFs extracted on each data set are compared in Fig. 9.5, while mode shapes are reported and compared in Fig. 9.6. When looking at FRFs, it can be noticed that the SNR (Signal to Noise Ratio) of data obtained from the vision system is worse than the SNR that characterises the SLDV data. The increase in spatial resolution makes the quality of modal data worse, as it is evident from the mode shapes plotted in Fig. 9.6. This effect is even clearer in high frequency modes.

### 9.4.2 Sensitivity to Spatial Averaging

The effect of the spatial averaging starting from the set of 1,220 points is reported in Figs. 9.7 and 9.8 respectively in terms of spatially averaged FRFs and extracted mode shapes. The spatial average increases the SNR as highlighted by both the FRFs and the mode shapes.

### 9.4.3 Sensitivity to Edge Effects

The effect of the spatial averaging considering both the upper and lower section of the beam profile in the image is shown in Figs. 9.9 and 9.10. As expected, the average influences the high frequency modes. This is even clearer on the 8th mode. This behavior can be justified by the fact that the 8th mode shape is mostly torsional and the averaging process cancels it out.

**Fig. 9.5** FRF sum for the three different data set: SLDV, image data sampled with 61 points and image data sampled with 1,220 points
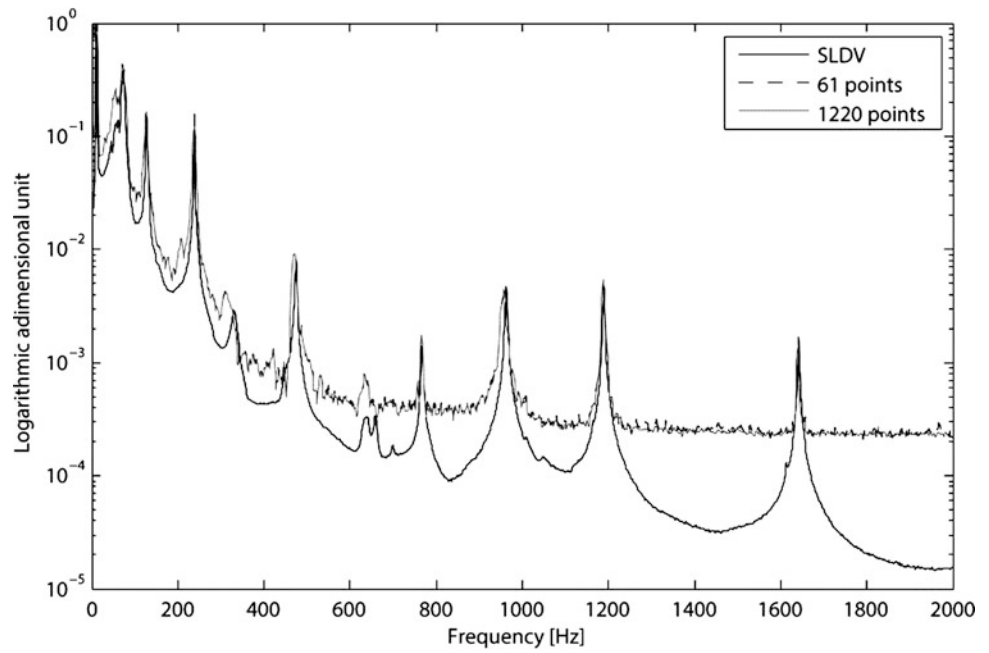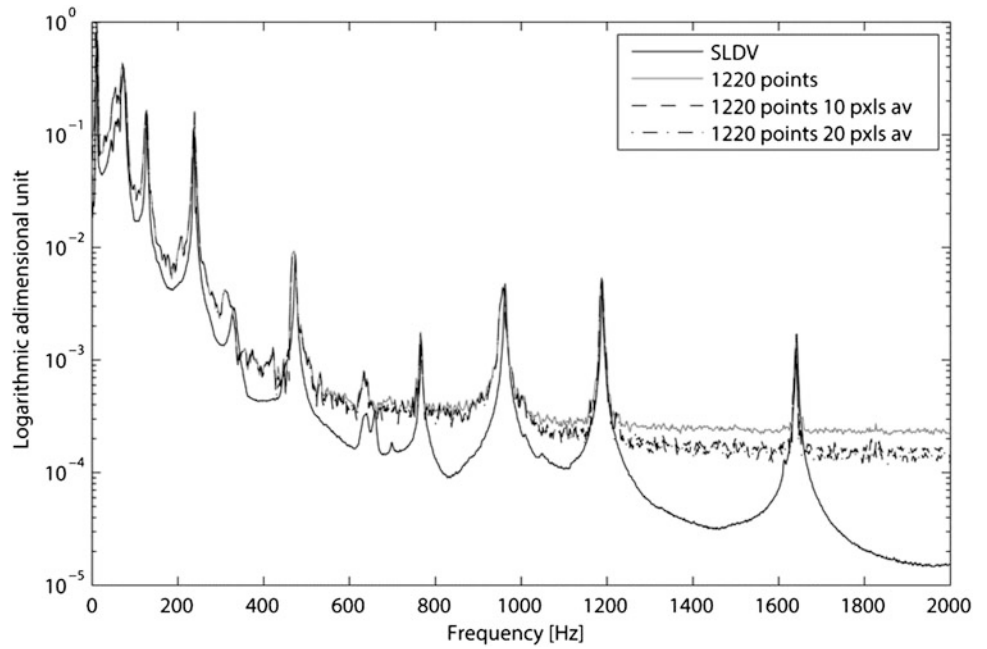


**Fig. 9.6** Mode shapes for the three different data set: SLDV, image data sampled with 61 points and image data sampled with 1,220 points
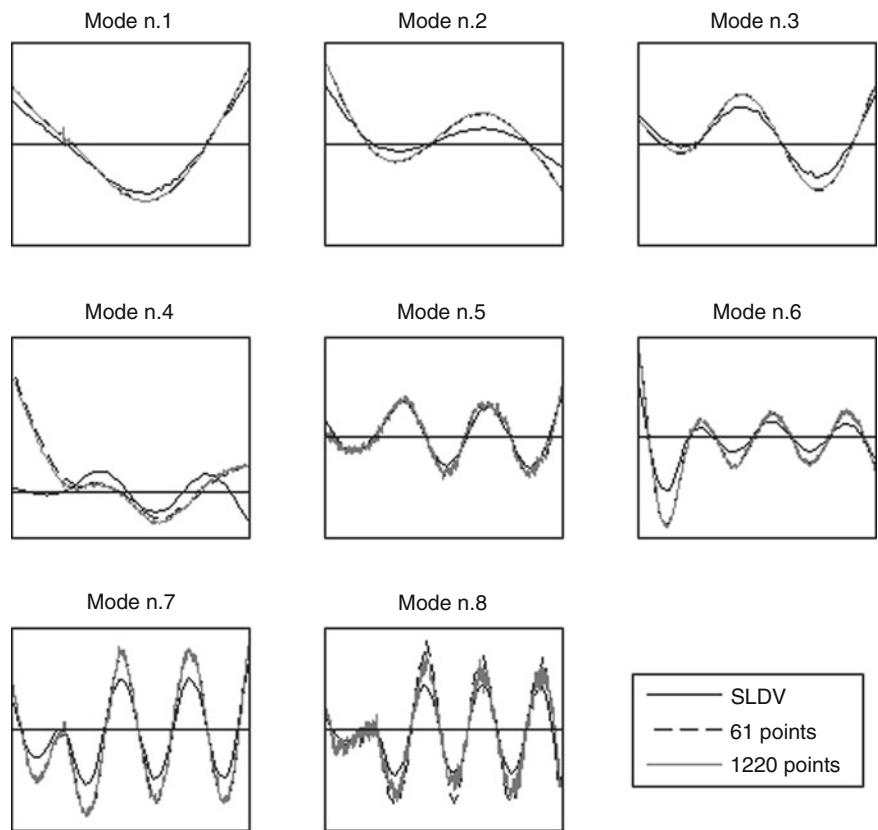


   The natural frequencies estimated with the different processing strategies are reported in Table 9.1. The maximum variation is contained within 1.09 Hz: this is a value that can be considered intrinsic in the uncertainty of the modal analysis algorithms.

   A quantitative comparison between mode shapes estimated with the different processing strategies can be given by exploiting the Modal Assurance Criterion (MAC), shown in Fig. 9.11. This plot reports the trend of the MAC values for all the mode shapes except the 4th one. That mode indeed has a low MAC value (an average of 4.15 for all the image

**Fig. 9.7** FRF sum for the four different data set: SLDV, image data sampled with 1,220 points and image data sampled with 1,220 points averaged over 10 points (122 points), image data sampled with 1,220 points averaged over 20 points (61 points)
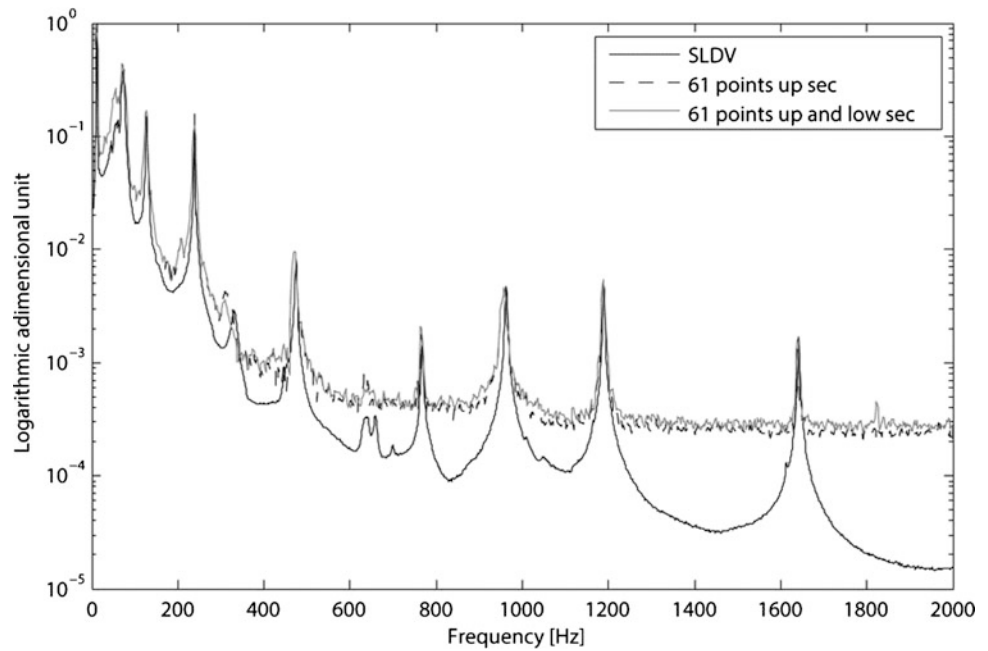


**Fig. 9.8** Mode shapes for the four different data set: SLDV, image data sampled with 1,220 points and image data sampled with 1,220 points averaged over 10 points (122 points), image data sampled with 1,220 points averaged over 20 points (61 points)
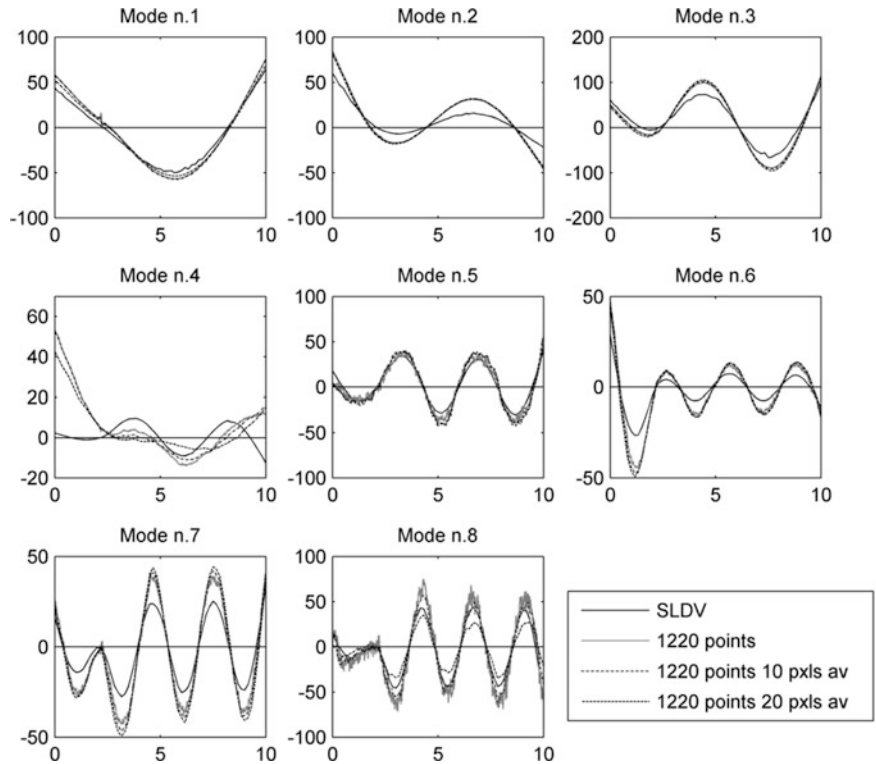


processing strategies) since the mode shape extracted from the vision system data is manifestly uncorrelated with the one obtained from the SLDV FRF set (see Figs. 9.6, 9.8, and 9.10). The improvement in terms of spatial resolution (from 61 to 1,220 points) worsens the correlation (the configuration with 1,220 points has the lowest MAC level, at least in the medium-high frequency range). However, if combined with the averaging process, the better resolved approach (1,220 points) shows the highest MAC level.

**Fig. 9.9** FRF sum for the four different data set: SLDV, image data sampled with 61 points on the upper section and image data sampled with 61 points, average of the upper and lower profile



**Fig. 9.10** Mode shapes for the four different data set: SLDV, image data sampled with 61 points on the upper section and image data sampled with 61 points, average of the upper and lower profile
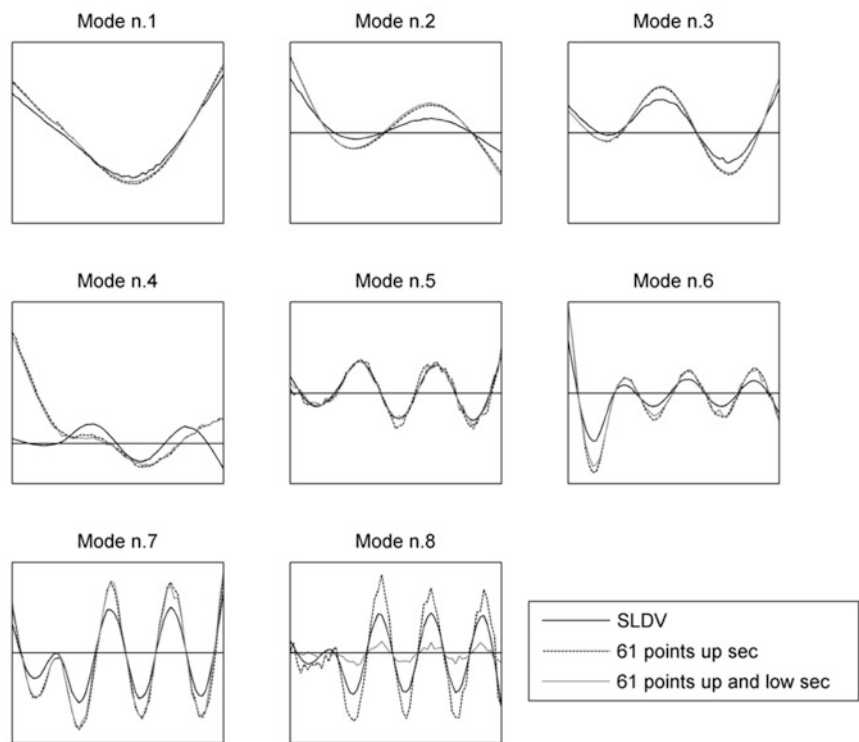


## 9.5   Conclusion

This paper aimed at discussing the suitability of image-based measurement techniques for providing valid data for Operational Modal Analysis. This is an important aspect to be analysed, since LDV-based methods fail when extremely high excitation levels, and therefore also high displacements, are reached. The study has been conducted on a simplified test rig by comparing the outputs of standard LDV-based EMA and the outputs of OMA, when OMA is performed on data extracted from a high speed camera. Despite this work aims at proposing the image-based approach as a valid alternative in high excitation levels tests, measurements presented referred to excitation levels where LDV could still be considered

**Table 9.1** Natural frequencies estimated for the different processing strategies

| SLDV (Hz) | Camera(Hz) 61 points upper profile | 61 points upper and lower profile | 1,220 points | 1,220 points 10 pixels average (122 points) | 1,220 points 20 pixels average (61 points) | Mean | Standard deviation |
|---|---|---|---|---|---|---|---|
| 74.73 | 76.04 | 75.01 | 75.64 | 75.38 | 76.29 | 75.67 | 0.51 |
| 129.32 | 126.10 | 126.07 | 126.11 | 126.07 | 126.08 | 126.09 | 0.02 |
| 240.62 | 238.02 | 237.99 | 238.03 | 238.07 | 238.08 | 238.04 | 0.04 |
| 474.47 | 467.52 | 467.08 | 467.53 | 468.58 | 468.79 | 467.90 | 0.74 |
| 767.63 | 764.91 | 763.09 | 765.05 | 765.28 | 765.03 | 764.67 | 0.89 |
| 966.78 | 956.91 | 956.85 | 956.81 | 956.72 | 956.68 | 956.80 | 0.09 |
| 1,191.91 | 1,187.60 | 1,186.80 | 1,187.71 | 1,187.44 | 1,187.30 | 1,187.37 | 0.35 |
| 1,643.61 | 1,640.76 | 1,639.10 | 1,640.98 | 1,641.27 | 1,642.08 | 1,640.84 | 1.09 |



**Fig. 9.11** MAC value—SLDV mode shapes taken as reference
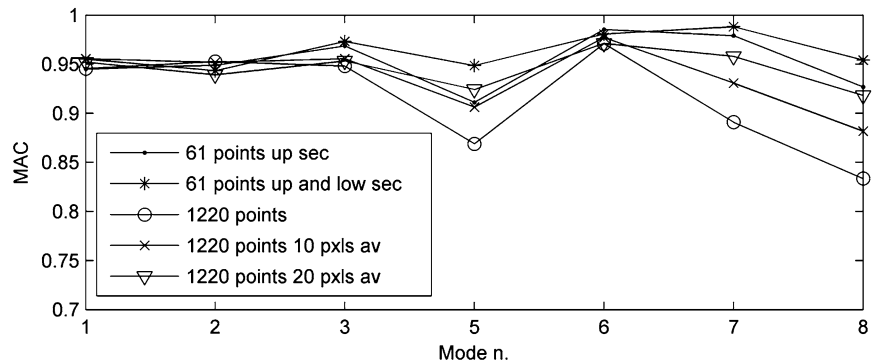
the reference technique. However, if the method succeeds in giving comparable results in low excitation level condition, the scalability to high excitation levels should be in favour of the image-based approach. Effects of different processing strategies have been discussed. The comparison with standard EMA results has been performed in terms of both Modal Assurance Criterion and SNR. The main drawbacks of the vision system can be recognised in the fact that the camera is sensitive to the target displacement: when the vibration frequency increases, the displacement can fall to values lower than system resolution and the SNR decreases significantly. In addition, in the Back Light Lighting setup used in this paper, it is not possible to observe correctly torsional mode shapes. Depending from the image processing strategy different situations can be obtained. If only upper (or lower) edge is extracted torsional modes are mixed up with bending ones. If upper and lower edges are extracted their average allows to reject torsional modes while their difference enhances torsional modes, although those modes are buried in the noise.

# References

1. Gentile C (2010) Radar-based measurement of deflections on bridges and large structures. Eur J Environ Civ Eng 14(4). doi:10.1080/19648189.2010.9693238
2. Guéguen P, Jolivet V, Michel C, Schveitzer AS (2010) Comparison of velocimeter and coherent Lidar measurements for building frequency assessment. B Earthq Eng 8(2):327–338
3. Javad JB, Lundstrom T, Niezrecki C, Avitabile P (2013) Measuring the dynamics of operating helicopter rotors and wind turbines using 3D digital stereophotogrammetry. 69th annual forum proceedings—AHS international, vol 3. p 2250–2256
4. Lundstrom T, Baqersad J, Niezrecki C, Avitabile P (2012) Using high-speed stereophotogrammetry techniques to extract shape information from wind turbine/rotor operating data (Conference Paper). 30th IMAC, A conference on structural dynamics, vol 6. Jacksonville, p 269–275
5. Busca G, Cigada A, Mazzoleni P, Tarabini M, Zappa E (2013) Static and dynamic monitoring of bridges by means of vision-based measuring system. Conference proceedings of the society for experimental mechanics series, vol 3. P 83–92
6. El-Kafafy M, Guillaume P, Peeters B (2013) Modal parameter estimation by combining stochastic and deterministic frequency-domain approaches. Mech Syst Signal Pr 35:52–68

# Chapter 10
# An Experimental Modal Channel Reduction Procedure Using a Pareto Chart

**William H. Semke, Kaci J. Lemler, and Milan Thapa**

**Abstract**  This paper's focus is on an experimental sensor placement procedure developed to assist in placing accelerometers in critical locations for modal testing. The procedure is an efficient method to reduce the number of channels for a full modal analysis. A candidate set of measurements are taken at select locations using a non-contact tool and then evaluated using a Pareto chart to obtain a reduced set of sensor locations. The Pareto chart identifies the points that have the largest response to an input excitation based on participation. These points correspond to the locations of the largest contributing modal data based upon their statistical significance. Thus, the experimental procedure aids in the efficient placement of accelerometers. Most contemporary channel reduction techniques rely on analytical models and simulations to aid in sensor placement, but are lacking without these preliminary analyses. To illustrate the effectiveness, the experimental channel reduction technique is applied on a small unmanned aerial vehicle and compared to finite element simulations.

**Keywords**  Modal analysis • Unmanned aerial vehicle • Sensor placement • Pareto chart • ModalVIEW

## 10.1    Introduction

Modal analysis is the study of the vibration modes and natural frequencies of a structure and is essential to a full understanding of a structure's vibration characteristics. Channel reduction is an important topic in modal analysis. With every extraneous channel there are associated costs. These costs include an extra sensor and the time spent installing, indexing and logging the sensor as well as processing and analyzing the data obtained from said sensor [1]. Because of this, it is important to use as few channels as possible while still keeping enough to identify the modes of the structure [2]. A key point in channel reduction is sensor location selection.

Several methods for identifying important locations for sensors have been developed. One common method is to use a finite element model in which sensor sets are found which maximize the ability to observe modes while constraining each sensor to contribute unique information [3]. Another method selects sensor locations that make the corresponding target mode shape partitions as linearly independent as possible while maximizing the signal strength of the target modal responses within the sensor data [4]. Yet another method uses a genetic algorithm to identify sensor locations by starting with a relatively small number of possible final locations and evolving these locations to the best set [5]. There is also a method that locates sensors at the maximum response position of an orthogonal sequence of vectors [6]. An efficient computational method to create an optimal sensor configuration using a Pareto approach has been demonstrated to be effective in structural identification [7]. However, the majority of the methods require extensive finite element modeling, algorithm development, mathematical modeling or a combination thereof. Therefore, it was desired to develop a relatively quick and easy, non-contact, experimental method with which to identify important sensor locations for existing complex systems that are difficult and time consuming to model.

The method presented here uses a Pareto chart to identify important sensor locations from an initial experimental test set, thus eliminating extensive structural modeling. This experimental procedure was shown to be effective in structural

W.H. Semke (✉) • K.J. Lemler • M. Thapa
Unmanned Aircraft Systems Engineering Laboratory, College of Engineering and Mines,
University of North Dakota, Grand Forks, ND 58202, USA
e-mail: william.semke@engr.und.edu

testing by Lemler and Semke [8]. A laser vibrometer is a suitable tool to use to acquire the initial measurements of the candidate set of locations because of its mobility and its capability to gather vibration data in a non-contact manner. Laser vibrometers measure surface motion using the Doppler shift concept to measure the velocity of surface vibration [9]. Multi-point laser vibrometers have been used for several years for modal analysis but they have not been used for quickly and efficiently identifying important sensor locations. A test was performed in which a single beam laser vibrometer was used to measure the velocity at several locations of the surface of a structure under excitation. These values were then used to identify locations of high interaction.

The important sensor locations were identified from the laser vibrometer values using a Pareto chart. Pareto charts are a statistical tool used to identify the variables that are the most significant [10]. This tool has been used in many different fields including identification of the most effective plasma processing variable that would impact the porosity of an aluminum oxide coating and for a sustainability root cause analysis method for chemical/energy production systems [11]. The Pareto chart was originally developed for use in the field of economics, and studies employing the Pareto chart can be found in the fields of natural and social sciences as well as physical sciences [12]. The use of a Pareto chart to identify significant sensor locations in modal analysis is illustrated through a case study on a small unmanned aerial system (UAS).

## 10.2 Theory

The Pareto principle, which states that 80 % of the effects are caused by 20 % of the causes, was based off of the observation by Vilfredo Pareto that 80 % of the wealth in Italy belonged to 20 % of the population. This principle led to the introduction of Pareto charts in the field of quality control. A Pareto chart is a vertical bar graph in which the relative frequency of each of the events is plotted in decreasing order from left to right. A line, representing the cumulative total, is then plotted on top of the bars. Pareto charts are used to determine the most significant aspects of a body of information by quickly and easily identifying which elements have the most effect [13]. Resources can then be used on the important aspects and not wasted on trivial aspects.

The Pareto principle has been shown to identify the locations for effective modal analyses measurements. The recommended testing procedure when using the sensor location identification method is outlined as follows. First, the structure should be mounted in a test rig so that it is in the desired modal configuration for the modal test. This can be free-free, fixed, or different boundary conditions. An excitation source and type then needs to be decided upon and installed. This could be a shaker with random or sinusoidal excitation, an impact hammer, or other such device. The same excitation device should be used for both the sensor location identification method and the modal test. The excitation device should also be installed in the same location and direction for both tests. The location(s) should be such that all of the modes of the structure are excited. Next, a grid pattern needs to be laid out on the structure at which to take measurements. The density and locations of the grid points need to be decided upon carefully as this is a critical part of the test. The density, especially, can affect the results of the sensor location identification test. All of the potential sensor locations can then be quickly and efficiently scanned for a full structure evaluation. This is accomplished by taking and recording measurements of the motion at each of the grid points. This data can then be processed to produce the Root Mean Square (RMS) values of the voltage at each point. A laser vibrometer is a good tool to use in this step as it is a quick, non-contact way of obtaining measurements but other tools, such as an accelerometer, can be used as well. The next step is to construct a Pareto chart to see which of the measured locations experience the largest relative amplitude under the excitation. An appropriate Pareto level then needs to be decided upon to identify the cutoff point in the Pareto chart. This information is then used to identify the significant locations at which to place sensors. These significant locations can then be instrumented with accelerometers and a full modal analysis can be performed. The modal analysis yields Frequency Response Functions (FRFs) from which the natural frequencies and mode shapes can be extracted. These values can then be analyzed to understand the modal characteristics of the structure. In summary, the basic procedure for implementing the sensor placement technique using a Pareto chart is as follows:

1. Install the test specimen in an appropriate mount for the test conditions desired.
2. Create a grid pattern of candidate sensor locations.
3. Excite the structure and record the dynamics response at each candidate position.
4. Calculate the RMS amplitude at all positions.
5. Construct a Pareto chart of all the candidate position RMS values.
6. Establish an appropriate Pareto level that captures the desired structural responses.
7. Instrument the reduced sensor set.
8. Conduct a complete modal analysis of the structure.

## 10.3   Test Description

Several tests were performed using the sensor location identification method at different levels of channel reduction and the results were compared to a base test to analyze which setups still captured all of the necessary information. The tests were performed on the Super Hauler UAS produced by Bruce Tharpe Engineering. The Super Hauler is constructed of plywood, balsa wood and Monokote and has a 3.7 m wingspan and a dry weight of 22 kg [14]. As outlined in the basic procedure, Step 1 was to isolate the Super Hauler by suspending it on bungee cords in a test rig so that all the wheels were 3.2 cm off of the ground. This setup simulates a free-free boundary condition for modal testing [15]. The instrumented Super Hauler in the test rig can be seen in Fig. 10.1. The laser vibrometer that was used for the tests was a Polytech OFV 2601 Laser Vibrometer Controller with a Polytech CLV Laser Unit and a Polytech CLV 700 Laser Head. The laser vibrometer was mounted on a stand and directed to measure the vibration of the aircraft. The candidate locations for preliminary testing were chosen (Step 2) and are shown in Fig. 10.2. All measurements were in the vertical direction except for the two on the vertical stabilizer which were in the horizontal direction.

Step 3 was to excite the Super Hauler using a small shaker and collect the data. The shaker used was the Mini SmartShaker™ with an integrated power amplifier from The Modal Shop Inc. The shaker was attached to the aircraft through the use of a suction cup. The shaker was set to random excitation with the amplitude set to an appropriate excitation level, in this test case it was 30 % of the maximum gain setting on the amplifier. The amplitude of excitation is chosen to provide sufficient excitation for a strong signal while small enough not to damage the shaker or aircraft. A signal-to-noise ratio of greater than $+5$ dB is desired, which typically produces consistent results from multiple tests.

It is recommended that, when using this method, the response is measured at grid points over the entire structure. However, this method is very sensitive to grid size since it can't distinguish if it is repeatedly capturing the same mode and so, if the grid is too fine, it could identify multiple points as significant that all correspond to the same response. Therefore, good candidate measurement locations are critical in using this method. The grid needs to be fine enough that all of the modes of interest (i.e. bending, torsion) are captured but not so fine that the same behavior is captured by several locations. A good candidate grid can be established from the structural response of similar structures, finite element results, or previous experience. However, additional points to those that are deemed potentially significant should be included as there could be unexpected participating modes. This method can help capture these unexpected modes that occur due to complex structural interactions



**Fig. 10.1** The Super Hauler Unmanned Aerial Vehicle in the test rig while instrumented with accelerometers. The airframe is approximately 3.7 m long and 3.1 m wide



**Fig. 10.2** Excitation (*blue*) and measurement (*red*) locations for laser vibrometer tests
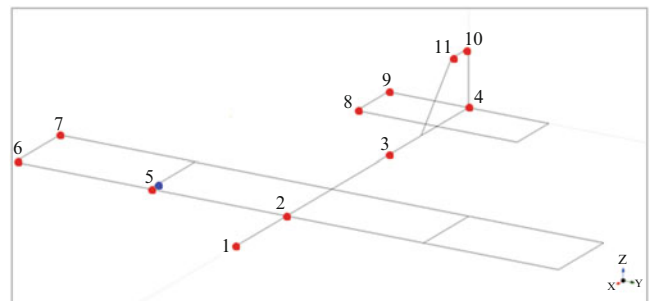
or complex structural response. For example, for the airframe example, a midpoint location on the wing must be included or the model cannot predict any nodes along the length of the wing, thereby failing to capture higher order wing bending. To capture wing and tail torsional modes, points on the leading edge and the trailing edge are necessary. In general, the number of candidate locations in any direction determines the order of the polynomial of the shape function in that direction. The best fit shape function is at maximum one order less than the number of nodes. Therefore, the proper number of candidate nodes in orthogonal directions must be chosen to capture all the potential modes of interest. Sound judgment is required to limit the number of candidate locations while still capturing all the motion of interest. This balance helps streamline the procedure to make it most efficient, but the process is valid for any number of candidate locations.

## 10.4   Results

The first step in the test procedure was to move the laser vibrometer to a measurement location and focus the laser to get a strong, clear signal. Next, the shaker was activated to vibrate the aircraft with random excitation. LabVIEW Signal Express was used to record the data from the vibrometer over a ten second period and export it to an Excel worksheet. These steps were repeated until three sets of data were gathered from each measurement location.

Voltage measurements were taken by the laser vibrometer at the selected test location and the Root Mean Square (RMS) of the amplitude was found at each point. A representative RMS value for each measurement location was then found by calculating the average of three RMS values from the three data sets at each location, per Step 4 of the basic procedure. The average RMS values can be seen in Fig. 10.3.

Figure 10.3 was created using Minitab with 95 % confidence intervals. It can be seen that the nodes are distinctly different and the relatively small size of the error bars indicate that the tests are repeatable.

Once the average RMS values were calculated, the Pareto chart statistical method was used to select the important nodes at which accelerometers need to be placed, as indicated in Step 5. The Pareto chart method was applied to this test by first assuming all of the motion of the aircraft was captured by the measured locations. The average RMS values were then ordered from largest to smallest and the individual percentages of the total were calculated. These percentages were then summed to find a running cumulative percentage of the total aircraft motion captured. These results were then graphed and are shown in Fig. 10.4. The average RMS values for each of the locations are shown in Table 10.1. A thorough screening of potential sensor locations must be conducted to help ensure that all the motion of interest is captured. The use of a laser vibrometer makes this process effective due to the efficiency of collecting data.

This chart and table can be used to determine which locations should be measured (Step 6). To capture 75 % of the measured motion, nodes 5, 6 and 7, which are the nodes on the wings, should be instrumented. Alternatively, to capture 90 % of the measured motion of the aircraft, nodes 8 and 9 on the horizontal stabilizer would have to be instrumented as well. To capture even more motion, nodes 10 and 11 on the vertical stabilizer could be instrumented as well to bring the measured motion up to 95 %.
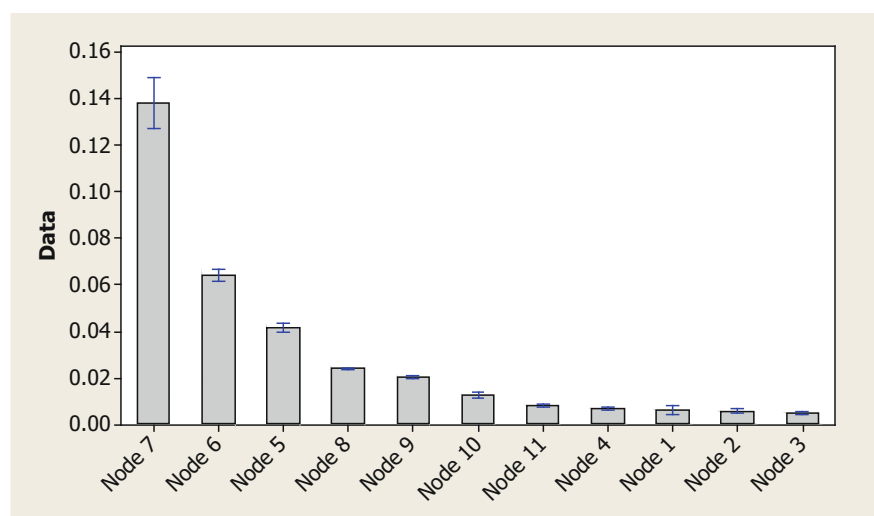


**Fig. 10.3**  Average RMS values for laser vibrometer measurement locations with 95 % confidence intervals

**Fig. 10.4** Pareto chart for the laser vibrometer test
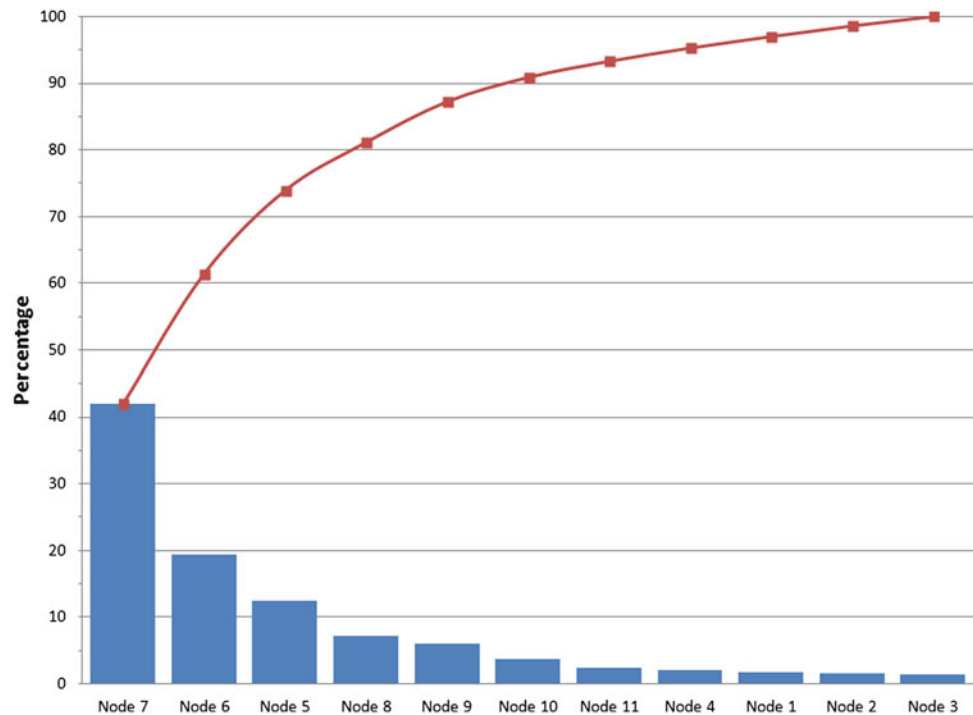


**Table 10.1** Data used to create the Pareto chart

| Location | Avg RMS | % of total | Cum % |
|---|---|---|---|
| Node 7 | 0.1382 | 42 | 42 |
| Node 6 | 0.0640 | 19 | 61 |
| Node 5 | 0.0412 | 13 | 74 |
| Node 8 | 0.0239 | 7 | 81 |
| Node 9 | 0.0201 | 6 | 87 |
| Node 10 | 0.0120 | 4 | 91 |
| Node 11 | 0.0080 | 2 | 93 |
| Node 4 | 0.0065 | 2 | 95 |
| Node 1 | 0.0057 | 2 | 97 |
| Node 2 | 0.0053 | 2 | 99 |
| Node 3 | 0.0046 | 1 | 100 |
| Total | 0.3294 | | |

## 10.5   Modal Testing

A modal analysis was performed to investigate the validity of the sensor location identification method, to illustrate the different sensor set results (Step 7). Four tests were performed with different levels of instrumentation. These tests included a base test with sensors placed at each measurement location from the laser vibrometer test, a test corresponding to the 95 % Pareto level, one corresponding to 90 % and one corresponding to 75 %. The accelerometer locations for each of the tests can be seen in Fig. 10.5. All of the accelerometers were mounted to measure acceleration in the Z direction except for the ones on the vertical stabilizer, which were mounted to measure in the Y direction.

The final step (Step 8) was to conduct a complete modal analysis of the structure. The aircraft was excited at several different locations, all in the Z direction, that are identified by the red dots in Fig. 10.6 and a load cell was attached in line with the shaker's stinger to measure input force.

The accelerometers and excitation devices were routed through a National Instruments data acquisition board that was connected directly to a computer. Data capture and analysis was performed using ModalVIEW, software designed specifically for modal testing and analysis. The natural frequencies presented are the average of eight tests. These eight tests are comprised of two tests at each of the four excitation locations.

The measurement type was set to FRF-EMA in ModalVIEW for an experimental modal analysis. The sampling rate was left at the default of 1651.61 Hz with the resolution set to 0.1 Hz. The shaker was activated so that the Super Hauler
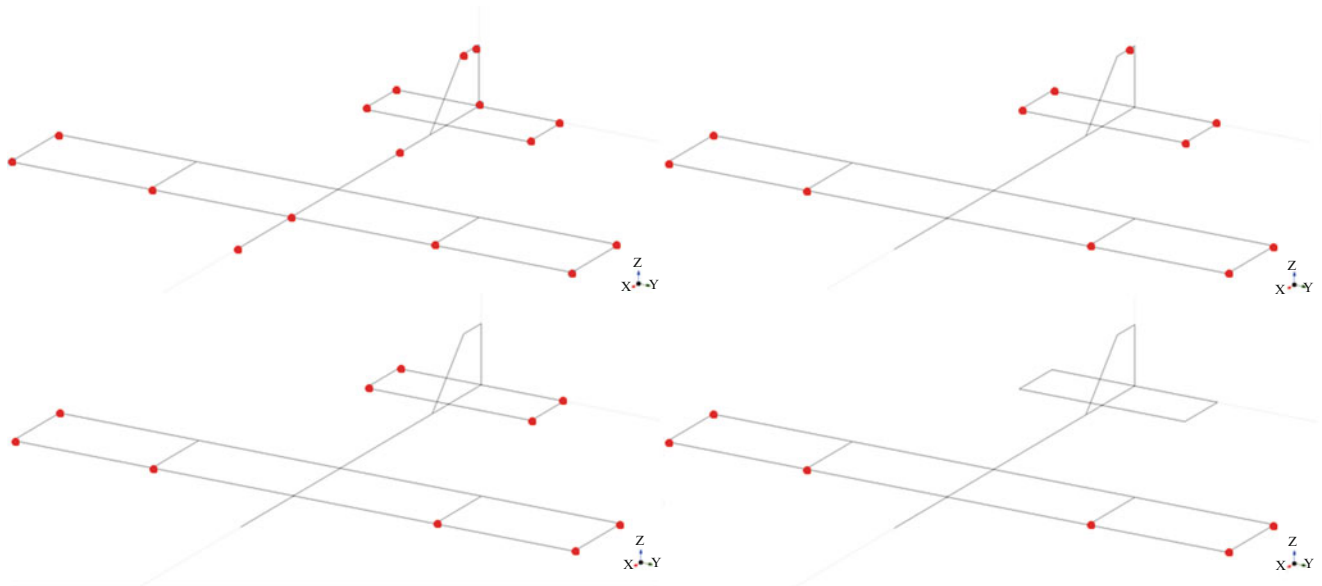
**Fig. 10.5** Clockwise from top left: base test, 95 % test, 75 % test, 90 % test

**Fig. 10.6** Shaker excitation locations
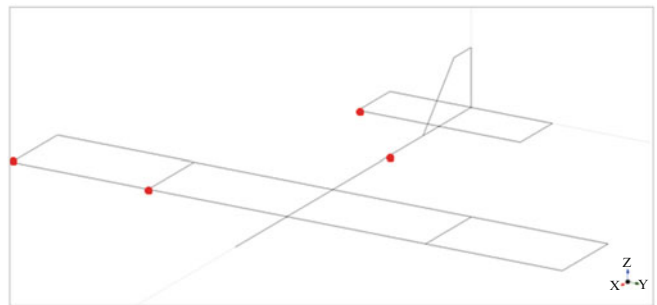


**Table 10.2** Summary of natural frequencies for the experimental modal analysis

| Base | 95 % | 90 % | 75 % | Description |
|---|---|---|---|---|
| 12.4 | 12.4 | 12.4 | 12.4 | Mode 1 wing bending |
| 17.3 | 17.5 | 17.5 | 17.5 | Tail torsion, antisymmetric wingtip bending |
| 20.8 | 20.8 | 20.8 | 21.0 | Wingtip, wing, tail, HS, VS torsion, wingtip bending |
| 26.7 | 26.0 | 26.0 | 25.9 | Wing torsion, slight HS bending |
| 28.9 | 28.2 | 28.1 | 28.1 | Symmetric wing torsion |
| 30.2 | 30.8 | 30.8 | 30.7 | Antisymmetric wingtip bending, tail wag |
| 33.8 | 36.5 | 36.1 | – | HS, VS torsion |
| 39.9 | 39.7 | 39.8 | 39.8 | HS bend/torsion, mode 2 wing bending, VS torsion |
| 45.0 | 44.9 | 44.9 | 44.7 | Mode 2 wing bending, HS bend/torsion, VS torsion |

was excited with random excitation. ModalVIEW was then prompted to record data from the accelerometers and when ModalVIEW was done sampling the shaker was turned off. This was repeated so that two data sets were gathered at each excitation location.

Once all of the vibration data was gathered, analysis was performed using ModalVIEW. The FRFs generated were analyzed and a list of natural frequencies was created. ModalVIEW was then used to build a model of the Super Hauler. The accelerometers were assigned to their respective nodes and degrees of freedom. The modal response of the structure can be animated illustrating the motion of each mode shape at its natural frequency. A summary of the natural frequencies found in the tests can be seen in Table 10.2 and the corresponding mode shapes can be seen in Fig. 10.7.

It can be seen that all of the natural frequencies that were observed in the base model were also observed in the 95 % test. However, as would make sense from the channels that were removed, any motion in the fuselage was undetectable using the 95 % data. Since there was relatively little activity in the fuselage when compared to the rest of the structure, the inability to observe that motion is fairly insignificant. This test only uses 11 sensors versus 16 sensors for the base test resulting in a 31 % reduction in sensors.
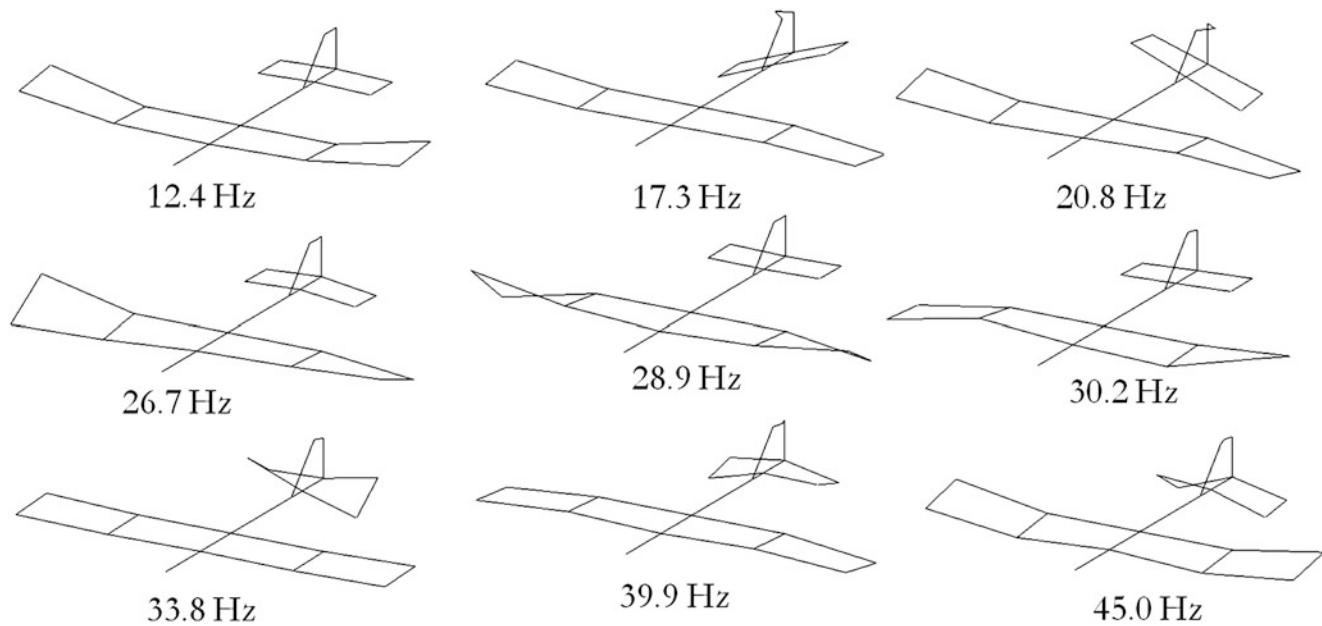
**Fig. 10.7** Mode shapes and frequencies obtained from the experimental modal testing on the UAS

The 90 % test also captured all of the natural frequencies that were seen in the base model. However, any motion in the fuselage or vertical stabilizer was undetectable using the 90 % data. The inability to observe this motion could be acceptable since the fuselage and vertical stabilizer don't experience much motion and all of the modes were detected. This test uses 10 sensors versus 16, resulting in a 38 % reduction in sensors.

The 75 % test captured almost all of the natural frequencies that were seen in the base model, missing one mode at 33.8 Hz. However, any motion in the fuselage or tail was undetectable in this test. The inability to detect a mode at 33.8 Hz can be traced to this fact since that mode consists of horizontal and vertical stabilizer motion. This lack of important information leads to the conclusion that this is too much channel reduction and that all of the important surfaces of the aircraft should be instrumented. This test uses 6 sensors versus 16, resulting in a 63 % reduction in sensors.

It can be seen that, according to this test, 90 % of the motion should be captured by sensors if all of the modes are to be recognized. The values chosen in this case were chosen because they coincide with the significant structural components of the aircraft while resulting in nearly a 40 % reduction in required channels. Since the correct level is case dependent, this value should be left to user discretion.

## 10.6   Finite Element Modeling

A finite element model was made of the UAV to simulate the dynamic behavior of the aircraft and to find the natural frequencies and mode shapes. ANSYS was used for the modeling where the wings and tail sections were meshed with plate elements and the fuselage with beam elements. The meshed model is shown in Fig. 10.8. In this simple model the wings and tail are constructed of plate elements of constant thickness and composition while the beam elements are a hollow tube with constant wall thickness and composition. The actual composition of the aircraft is much more complex. For example the wings are made of multiple ribs of wood with spars running through them and are covered with a plastic film while the fuselage is made of truss segments connected to plywood sheets. While this structure is very complex, the simplified FE model illustrates much the same behavior with far less modeling effort.

A modal analysis was performed on the structure in a free configuration to identify the natural frequencies and mode shapes of the structure, summaries of the results are shown in Table 10.3 and Fig. 10.9. The number of elements used was varied to assess the influence on mode shapes and frequencies and it was observed that adding more degrees of freedom to this model did not change the results significantly. It was found that reducing the number of beam elements used did eliminate any fuselage bending, resulting only in wing and tail motion.

**Fig. 10.8** Finite element model of the Super Hauler UAS meshed with shells and beams
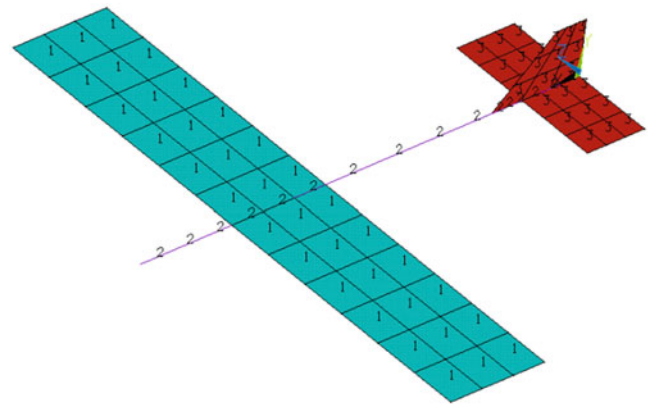


**Table 10.3** Summary of natural frequencies for the numerical analysis

| Freq (Hz) | Description |
|---|---|
| 12.8 | Mode 1 wing bending |
| 17.0 | Tail torsion, antisymmetric wingtip bending |
| 19.7 | Tail horizontal wag |
| 20.8 | Tail vertical wag |
| 43.4 | Mode 2 wing bending, tail torsion |



12.8 Hz                17.0 Hz                19.7 Hz

20.8 Hz                43.4 Hz
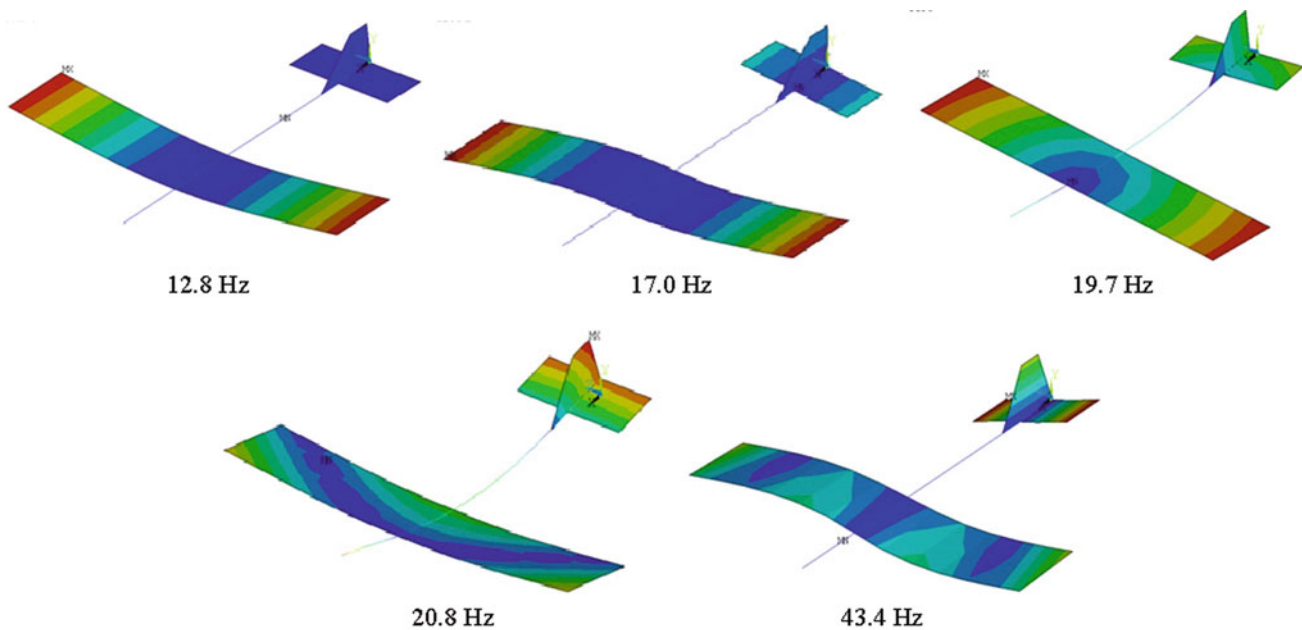
**Fig. 10.9** Mode shapes and frequencies obtained from the experimental modal testing on the UAS

The results for many of the modes of vibration were consistent between the FE results and the experimental results. The first two modes of both the experimental and simulated methods had excellent correlation in both shape and frequency. The first mode showed bending in the wings in the same direction and the second mode produced bending of the wings in opposite directions and tail torsion, much as was found in the experimental testing. These two modes are also the most significant participators in the motion of the system as they contain over 99 % of the effective mass of the system. In looking at the channel reduction procedure, the nodes identifies as being the most significant are all strong participants in the first two mode shapes. Very good correlation was also observed around 45 Hz, which is Mode 9 in the experimental results and Mode 5 in the numerical. It is believed that more detailed modeling of the aircraft would result in even better correlation with these and other modes. In more detailed analyses done to date of the wing sections with the ribs and spars, the onset of torsional modes was identified at frequencies around 30 Hz. These were not observed in the simplified model. This seems reasonable as a plate has greatly increased torsional resistance than a series of ribs connected by spars. However, the simple model does indeed capture much of the dynamics of the airframe.

## 10.7   Conclusion

A novel modal sensor location identification method was shown to provide a quick, relatively simple, non-contact experimental way to determine important sensor locations through the use of a Pareto chart. A laser vibrometer was used to measure the response at several locations along the aircraft and the RMS values were calculated. A Pareto chart was used to identify which of these locations are important to instrument by identifying which locations contribute to most of the motion experienced by the aircraft. This method would be most effectively used by measuring the motion at several locations on the structure and placing sensors at the nodes that capture a certain percentage of the motion that was measured. This provides the user with the flexibility to choose the percentage of motion that is important for that structure.

A study was done on channel reduction and three tests with different levels of channel reduction were performed and analyzed. While maintaining the ability to detect the modes of interest, the number of channels used was reduced from 16 channels down to 10 channels, which is a 38 % reduction in channels. This reduction not only saves money by using less sensors and supporting equipment, but also saves time that would have been spent on data collection and analysis on the extra channels.

Finite element simulations were conducted that also demonstrated the ability to simulate mode shapes and natural frequencies. Relatively simple models of complex systems can generate accurate modal results. The nodes identified by the channel evaluation tool also correspond to the locations of large modal participation in the FE results. Over 99 % of the effective mass of the system is captured in the first two modes, which correspond to the nodal locations with the highest participation found in the experimental study.

In addition, this experimental procedure can be used in conjunction with numerical simulations for model validation and other sensor placement optimization techniques. The procedure also can augment the evaluation and assessment of their structural behavior of previously constructed structures. Future utilization and expansion of the methodology presented includes the correlation of the Pareto chart method to other sensor placement techniques. Also, studies providing additional guidelines for candidate sensor locations could improve the efficacy of the method. In general, this purely experimental procedure provides an effective method for enhanced modal analysis and can serve as a supplement to the procedures currently engaged in by the modal analysis community.

## References

1. Fleming GA, Buehrle RD (1998) Modal analysis of an aircraft fuselage panel using experimental and finite-element techniques. In: 3rd international conference on vibration measurements by laser techniques SPIE 3411, vol 1. Anacona, Italy, p 537–549
2. Carne TG, Dohrmann CR (1995) A modal test design strategy for model correlation. In: 13th international modal analysis conference (IMAC-XIII), Nashville, TN
3. Stephan C (2011) Sensor placement for modal identification. Mech Syst Signal Pr 27:461–470
4. Kammer DC, Tinker ML (2004) Optimal placement of triaxial accelerometers for modal vibration tests. Mech Syst Signal Pr 18:29–41
5. Stabb M, Blelloch P (1995) A genetic algorithm for optimally selecting accelerometer locations. In: 13th international modal analysis conference (IMAC-XIII), Nashville, TN
6. Balmes E (2005) Orthogonal maximum sequence sensor placements algorithms for modal tests, expansion and visibility. In: 23rd international modal analysis conference (IMAC-XXIII), Orlando, FL
7. Papadimitriou C (2005) Pareto optimal sensor locations for structural identification. Comput Meth Appl Mech Eng 194(12):1655–1673
8. Lemler KJ, Semke WH (2013) Application of modal testing and analysis techniques on a sUAV. In: 31st international modal analysis conference (IMAC-XXXI), Garden Grove, CA
9. Jenal RB, Staszewski WJ, Klepka A, Uhl T (2010) Structural damage detection using laser vibrometers. In: 2nd international symposium on NDT in aerospace, Hamburg, Germany
10. Keshri AK, Patel R, Agarwal A (2010) Comprehensive process maps to synthesize high density plasma sprayed aluminum oxide composite coatings with varying carbon nanotube content. Surf Coat Tech 205:690–702
11. Jayswal A, Li X, Zanwar A, Lou HH, Huang Y (2011) A sustainability root cause analysis methodology and its application. Comput Chem Eng 35:2786–2798
12. Heyde CC, Seneta E (2001) Statisticians of the centuries. Springer, New York
13. Lawson JS, Erjavec J (2001) Modern statistics for engineering and quality improvement. Duxbury Press, Pacific Grove, CA

14. Lemler KJ, Semke WH (2012) Structural analysis of the effects of wing payload pods on small UAS. In: 30th international modal analysis conference (IMAC-XXX), Jacksonville, FL, p 515–523
15. Perinpanayagam S, Ewins DJ (2003) Free-free, fixed or other test boundary conditions for the best modal test? In: 21st international modal analysis conference (IMAC-XXI), Kissimmee, FL

# Chapter 11
# Unique Isolation Systems to Protect Equipment in Navy Shock Tests

**Herb LeKuch, Kevork Kayayan, and Neil Donovan**

**Abstract** Shock Tech Seamount ™ elastomer isolation systems have successfully enabled many electronic systems to be shock qualified for Navy shipboard installations. The Seamount ™ (Tall Arch) isolator is well known in Navy applications for its effective shock and vibration protection of commercial electronic equipment (COTS). This paper reviews the Seamount's unique arch design and its controlled shock response including acceleration time history measurements, shock response spectrum (SRS) and Fourier analysis from different Mil-S-901D barge tests. We describe the isolators and the results of a series of Navy barge tests involving two candidate isolation systems (tested with dummy loaded racks) followed by test of a fully populated rack. Measured vertical response was 20–25 G's; the shock input ranged from 40 to 75 G's. SRS analysis showed substantial reduction of pseudo velocities (PV) levels to less than 70 ips at the mid to higher frequencies of equipment versus 100–120 ips at the same frequencies of the input shock spectrum.

**Keywords** Seamount • Mil-S-901D • Shock isolation • SRS • Electronic rack

## 11.1 Introduction

Navy electronic systems are often installed in isolated racks for protection from severe shock and vibration. Figure 11.1 shows a 901D LLC isolated rack and display console. The isolation system is designed to substantially reduce the dynamic forces at the equipment, and control the relative movement of the enclosure* during the shock event. Large racks are usually deck mounted. Isolators are widely separated at the base of the rack and combined with stabilizer mounts for stability of the unit to off-axis loads. This external isolation design typically has four to six mounts at the base of the rack and two or more as stabilizers at the top, rear of the rack. Vertical motion is mainly controlled by the base mounts in compression/tension. The orientation and combination of stabilizers and base mounts control pitch, sway and lateral motions of the rack. Internally isolated racks are also available from 901D that are hard mounted and require no bulkhead support.

The purpose of the isolation system is to attenuate the shock loads in the load path between the ship and the equipment. The primary objective is to reduce the peak G's to levels that COTS equipment can withstand. Allowable limits are based on equipment design specifications; experience suggests that 20–25 G's (or less) is an acceptable level for most electronics. Recent work by Shocktech/901D has also focused on the frequency content of the shock and the pseudo velocities (PV) at critical frequencies of the equipment in the region of 50–150 Hz [1].

• the terms—rack, enclosure and cabinet are used interchangeably.

Figure 11.2 shows several isolated electronic racks and other equipment mounted to the test deck within the barge. The deck is characterized as 8 Hz or 14 Hz (or other frequency) depending on the requirements of the test specification It replicates the installation of the cabinet on-board ship. For this unit, there were four base mounts and two stabilizers. The welded fixture bolts to the deck and is for attachment of the stabilizers at the upper, rear of the rack. Response accelerometers are installed

H. LeKuch (✉) • K. Kayayan • N. Donovan
Shock Tech Inc., Route 59, Monsey, NY 10952, USA
e-mail: hlekuch@pipeline.com

**Fig. 11.1** 901D LLC isolated
rack and display console



**Fig. 11.2** Examples of
equipment mounted to the test
deck



on the rack. Input is measured on the deck near the fixture. Velocity and displacement-time are calculated by integration of the acceleration time history. Physical measurements of the deflection of the isolators and/or relative movement of the rack are often made using clay cones, or equivalent, that 'squash' in shock.

## 11.2 Seamount Isolators

Identified by its unique tall arch shape, Seamounts exhibit large deflection capabilities in all directions [2, 3]. The isolators are molded at Shock Tech's facilities in Monsey, NY. Repeated load cycling tests have verified the mount's durability and accurate shock control. The proprietary elastomer compound used in the mount is a compressible, moderately well damped neoprene having a predictable rate of strain energy dissipation and nominal temperature variation [4]. Three mounts are shown in Fig. 11.3. Dimensions of each are 7 inches high, 8 inches wide and 4.5 inches deep. A large range of stiffness can be achieved in each direction by modifying the configuration and contour of the arch. To a vertical shock, energy control is mainly accomplished by buckling of the mount in compression and extension in tension. In the lateral directions, the mount undergoes off-axis deformation of its arch shape and progressive shear of the elastomer material. Tension, shear and roll exhibit nearly linear stiffness. Damping is strain dependent but usually accounted for as a velocity dependent force in shock calculations. Dynamic stiffness is greater than static stiffness by a measured factor. There are several families of Seamounts including thin wall and thin wall versions—Fig. 11.4. The half-arch mount is used with light loads and in 901D internally isolated racks.

As noted, shock attenuation effectiveness of the isolator is a function of the rate of energy absorption and dissipation in elastic deformation of isolator shape and material. By modifying these factors, the stiffness and hysteresis curves can be shifted and/or modified for more energy capacity and load carrying capability in limited space. The stiffness rate is strongly influenced by the transition from bearing on the column-like section to 'ovalizing' of the arch. There is also a close relationship of the durometer of the elastomer compound and mount stiffness. The Seamount is modular; multiple isolators

**Fig. 11.3** Three Seamount
examples
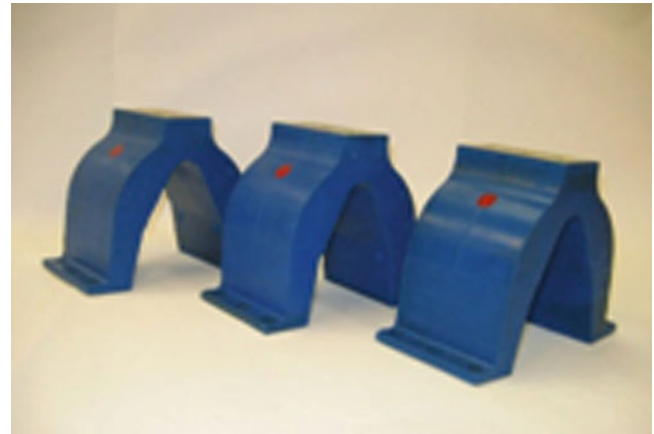


**Fig. 11.4** Examples of thin wall
and half-arch mounts



can be grouped for heavier loads. Features of the mounts are contoured wall construction, constant cross section in the buckling region, defined engineering characteristics including moderate damping, and broad temperature extremes. Using the Seamount for all ship's decks (universal shipboard application regardless of deck frequency) is a principal objective of the Seamount design.

### 11.2.1   Description of the Isolator

The Seamounts are designed for nearly constant force resistance in compression—the direction usually experiencing the greatest shock in barge test. Its buckling design produces bilinear stiffening in compression over the first third of stroke and softening over larger amplitude deflection. Figure 11.5 shows the load cycle in compression for three cycles. Load range is 125–300 lbs per mount, stiffness related to the durometer of the elastomer compound, four load increments, high stroke efficiency of 0.55 (defined as the ratio of maximum free displacement to isolator height), a nominal 15 year service life, and rated at 5–6 Hz shock response frequency. Mounts can be oriented and positioned to support the unit in any direction. The compression to lateral stiffness ratio is approximately 2:1, tension is nearly linear to 200–250 % extension, then yields but without a well defined value.

   Molded with custom formulated synthetic elastomer, durometer 40–75 Shore A scale, high resilience—excellent return to original position after the load is removed, dynamic to static stiffness 1.25–2 depending on elastomer compound, good tensile strength in excess of ship service conditions, temperature range 30–120 deg F at ±25 % stiffness variation,−20 deg F to 150 deg F at 35 % variation, stable over large deflections, repeatable use and consistent results, extremely rugged and durable.

## 11.3   Family of Seamounts

Ranging from 75 lbs to over 300 lbs static load rating, the isolators differ mostly in wall thickness and contour at the mid-height buckling region. Table 11.1 is a comparison of mounts. The mounts can be modified with different elastomers having well defined damping characteristics to 30–35 % of critical damping. Production mounts are normally at 12–17 % damping factor. Compression stiffness exhibits a softening curve, lateral (roll and shear) and tension are essentially linear over their

**Fig. 11.5** Typical load deflection (LD) data
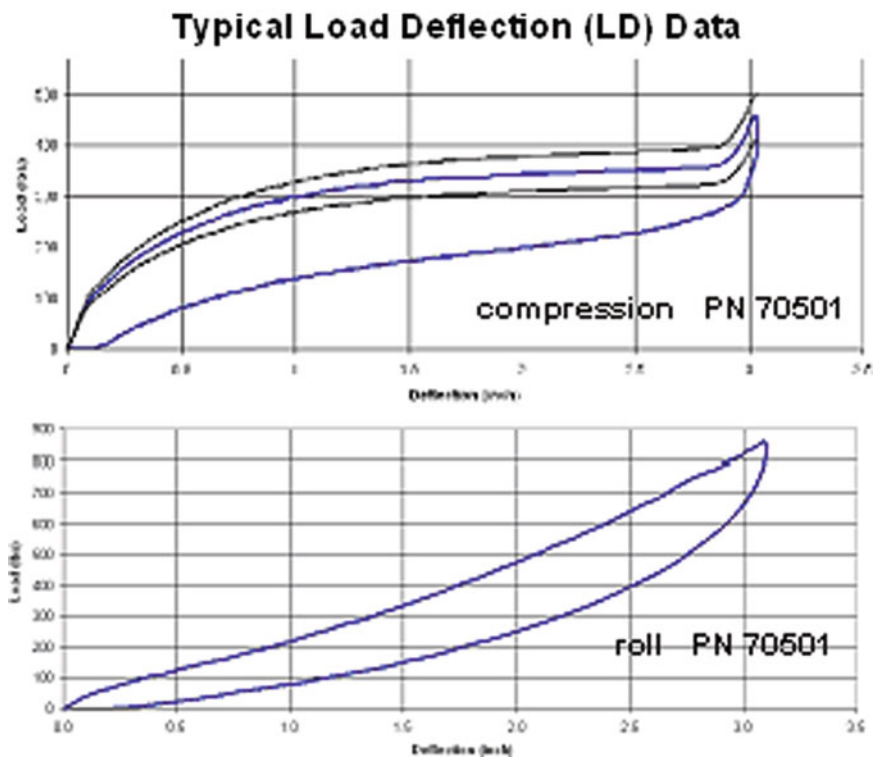


**Table 11.1** Comparison of Seamounts

|          |   | Load range (lbs) | Primary function | Natural frequency (Hz) | Shock frequency (Hz) |
|----------|---|------------------|------------------|------------------------|----------------------|
| Light    |   | 75–275           | Shock            | 6–7                    | 5–7                  |
| Moderate |   | 100–250          | Shock            | 7–8                    | 5–7                  |
| Heavy    |   | 100–300          | Shock            | 7–10                   | 5–7                  |

full stroke. Seamounts are stable over their entire vertical stroke to nearly 4.5 inches compression and tension, 3.5 inches in roll and shear.

## 11.4  Barge Test Program

### 11.4.1  Dummy Loaded Isolated Racks

Using dummy loaded racks, a series of barge shock tests were conducted with 901D LLC open frame racks and Seamount shock isolation system (base and stabilizer mounts) from Shock Tech Inc. These were evaluation tests to measure the shock attenuation of each isolation system and to select one of the two candidate designs for future use with a populated enclosure. The test installation is shown in Figs. 11.6 and 11.7. The rack is basically a formed metal construction, bolted assembly from among 901D's standard designs, PN 100-CA-1318. Door and panels were removed. Stacked steel plates were substituted for the equipment and the distribution of weight approximated that of the populated rack which would be tested at a later time. The welded fixture at the side of the rack was for use in measuring side displacement and sway of the rack during shock. The magnitude of the barge shock is subject to a number of variables including explosive charge, water temperature, weight of equipment on the deck and location of the input accelerometer, In consecutive shots from the same standoff distance, acceleration input readings can vary by ±20 to 25 %.

**Fig. 11.6** Test installation rack
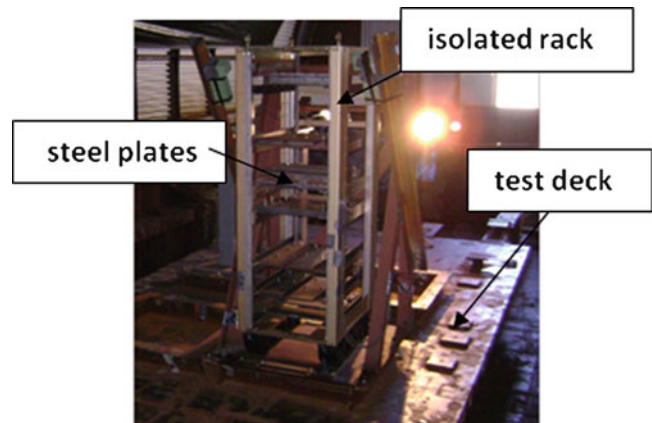


**Fig. 11.7** Test installation on barge.
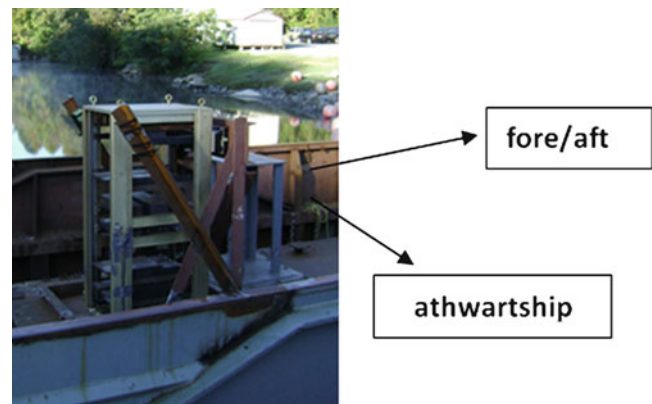


Two isolation systems were tested. They were similar having six mounts at the base but stiffer stabilizer mounts for configuration (2). Base isolators were two PN 70776–65 at the front, two PN 70776–55 midway and two PN 2100013–4 at the rear. Soft system stabilizers were two PN 2100031–00. Configuration 2 stabilizers were two PN 2100063–4 and two PN 2100031–00. Isolation mounts exhibit 'buckling' type stiffness characteristics in compression and nearly linear stiffness in tension, roll and shear. The total dummy load weighed 1,250 lbs (875 lbs steel plates and 375 lbs rack and mounts). Its, CG approximately 14.4 inches from the front of the rack and 30.1 inches above its base. Performance was based primarily on peak G's, relative displacement and visual inspection of the rack. More recently the acceleration time histories, Fourier spectrum, and pseudo velocity shock spectrum's (PV) were compared for evaluation of shock severity.

## 11.5   Test Series

Testing was conducted in accordance with Mil-S-90D guidelines using the extended floating shock platform (EFSP). The EFSP is a standard 16-foot by 28-foot FSP that has been extended by adding an 18-foot section. Testing was conducted using Navy standard 60-pound HBX-1 charges suspended at a depth of 24 feet below the surface of the water and at a 20-foot standoff from the barge.

The dummy loaded rack with isolation configuration 1 (soft stabilizers) was tested in shot 1. Configuration 2 (stiff stabilizers) was tested in shot 2. Both shots on the 8 Hz deck. Shots 3 and 4 were on the 14 Hz deck, isolation system configuration 2. The rack was instrumented with six accelerometers and one displacement sensor. An accelerometer on the deck measured deck acceleration in the vertical direction. No athwartship or fore/aft input measurements were made. Accelerometers are shown in Figs. 11.8, 11.9, and 11.10. Foam blocks measured the rack's maximum side motion.
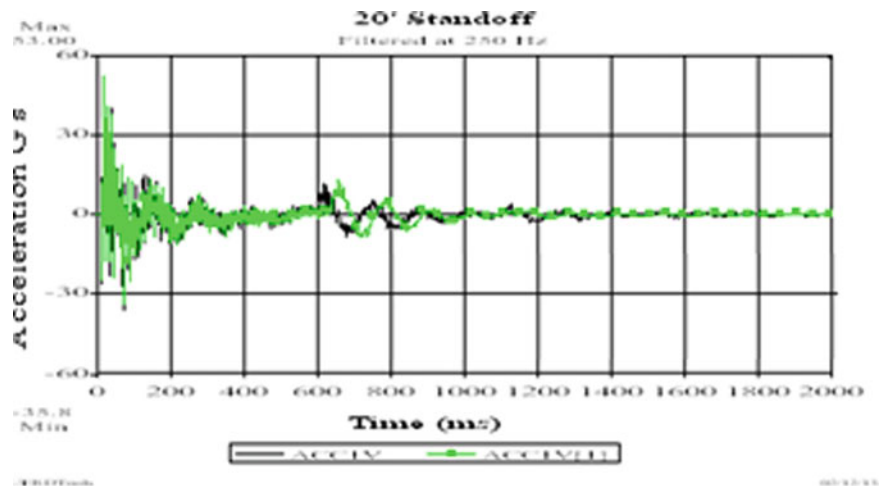
**Fig. 11.8** Accelerometer
locations mid height, front
column of rack



**Fig. 11.9** Accelerometer
locations top, rear - near
stabilizer mounts
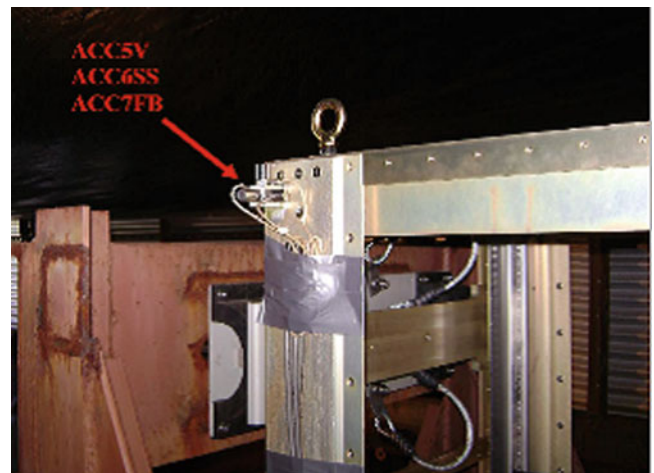


**Fig. 11.10** Accel



## 11.5.1  Shock Severity: Acceleration and Pseudo Velocity (PV)

A common method to evaluate the effectiveness of one isolation system versus another is to compare the shock attenuation of the two designs (Attenuation Ratio = Peak response G's/Peak input G's). This can be confusing when there is a significant contribution of high acceleration spikes extremely short duration) in the time-histories. To augment the acceleration method, we compared SRS levels particularly at the mid frequency region where COTS electronics are sometimes damaged.

**Table 11.2**

| | Dummy loaded isolated racks | | Summary of results | | | | | | |
|---|---|---|---|---|---|---|---|---|---|
| Test | Shot | | Input | Response | Response | Response | Response | Response | Response |
| | | | 1V | 2V | 3SS | 4FB | 5V | 6SS | 7FB |
| 8 Hz deck | 1 Config (1) | G's | 53 | 18.5 | 21.5 | 13.8 | 19.7 | 9.4 | 9.8 |
| | | PV ips-80 Hz | | 12 | 16 | 10 | 18 | 9 | 9 |
| | | PV ips-120 Hz | | 20 | 48 | 30 | 22 | 26 | 16 |
| 8 Hz deck | 2 Config (2) | G's | 50.6 | 21.9 | 30.6 | 25.2 | 25.1 | 18.6 | 17.9 |
| | | PV ips-80 Hz | | 22 | 34 | 23 | 19 | 8 | 11 |
| | | PV ips-120 Hz | | 24 | 97 | 66 | 16 | 41 | 26 |
| 14 Hz deck | 3 Config (2) | G's | 37.3 | 24 | 34.2 | 19.1 | 28 | 20.2 | 20.3 |
| | | PV ips-80 Hz | | 11 | 46 | 2 | 37 | 26 | 23 |
| | | PV ips-120 Hz | | 20 | 49 | 25 | 25 | 43 | 20 |
| 14 Hz deck | 4 Config (2) | G's | 42.6 | 24 | 26.9 | 17.3 | 30.6 | 11.5 | 34.4 |
| | | PV ips-80 Hz | | 20 | 36 | 28 | 46 | 16 | 29 |
| | | PV ips-120 Hz | | 28 | 38 | 19 | 25 | 20 | 22 |
| 14 Hz deck | Populated rack | G's | 69.5 | 19.8 | | | | | |

Gaberson [5, 6] noted that the PV level is proportional to maximum stress and that this is the damage factor, not acceleration. Based on the literature, a PV threshold of 100 ips is often used for shock design of structures. In general, 100 ips is considered severe, 80 ips moderate and 60 ips as not-damaging. This may be relatively simple to calculate for standard shapes. However when the equipment is more complex such as chassis, components, and PC boards, the PV threshold is thought to be lower and we used 60 ips as a guideline in our comparison of isolation. In other words, one design could be preferred over another if it exhibited a greater AR *and* lower PV levels in the region of interest. Relative displacement of the rack is important too. Did the isolated unit remain within allowable limits and do the isolators exhibit permanent offset? Typical damage of COTS electronics are solder fractures at electrical connections to components on the PC board and pull-out of inserts in thin wall chassis. It is an especially complex problem if there is dynamic coupling between the rack, equipment chassis and its components.

### 11.5.2   Analysis of Measured Data

UERDTools [7] software (available from the US Navy Carderock) was used to analyze accelerometer data. This integrated software package enabled easy comparison along with clear display plots of measured acceleration, SRS and FFT content. Test data had been pre-filtered at 250 Hz by the test lab in accordance with Navy practice. Peak accelerations are shown in the time-history plots. SRS plots were made at a 5 % damping factor. Data from the input and mid-height accelerometers are shown (1 V, 2 V, 3SS, 4FB). Accelerometer measurements from a second set of accelerometers on the test rack (accel 5 V, 6SS, 7FB) are comparable to the first set. Results are summarized in Table 11.2. It should be noted that the input shock was measured only in the vertical direction therefore an attenuation ratio (response g's/input g's) can be determined only in this direction. In general, input accelerations in the athwartship and fore/aft directions are approximately 40–60 % of vertical shock.

## 11.6   Survey of Barge Test Shock Results: Acceleration—Time, SRS, Fourier Analysis

### 11.6.1   8 Hz Deck Measurements

**Input (1 V)—vertical**—located on the barge deck near to the rack. Acceleration measurements in the vertical direction are nearly the same for both isolation configurations (50.6–53 G's). The general appearance shows a fundamental shock pulse of moderate peak amplitude with 'G' spikes superimposed on the main pulse. The predominant frequency is 7.8 Hz as would be expected with the 8 Hz deck. There is also a prominence at 5–6 Hz that is likely the isolation system frequency in the
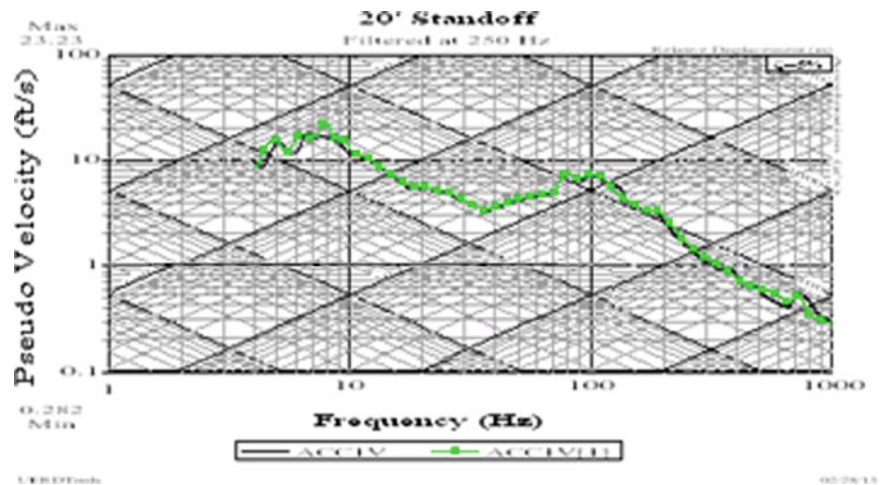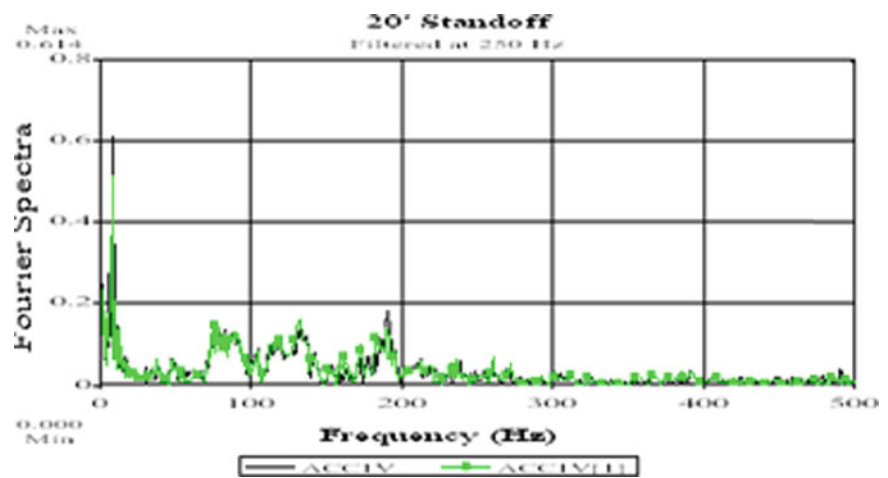
**Fig. 11.11** SRS



**Fig. 11.12** FFT



vertical direction. The Fourier spectrum (FFT) also shows the main frequency of nearly 8 Hz. Contributions of the higher frequencies are exhibited in the 50–200 Hz region of the FFT. The basic form of the SRS is a positive 'rise' peaked at 8 Hz, then decreasing with nearly constant negative slope, ramping up with a rise in PV levels in the 70–120 Hz region and declining again afterwards—Figs. 11.10, 11.11, and 11.12.

**Response (2 V)—vertical**—located mid height of the rack on its right outer column. It is a measure of the response in the vertical direction and reflects the shock reduction across the isolation system. Comparing it to (1 V) is the ratio of shock attenuation achieved with each configuration. Configuration (1), the softer system, shows a peak of 18.5 G's versus an input of 53 G's and a relatively smooth PV curve with only a minor rise in the 70–120 Hz region. In terms of PV, there is nearly a 70 % reduction compared to (1 V) in the same frequency region. The FFT spectrum shows the 8 Hz predominant frequency and very little energy content at the higher frequencies. Configuration (2), stiffer stabilizers, measures 21.9 peak G's versus an input of 50.64 G's. Its SRS and Fourier spectrum are very similar to configuration 1. There appears to be only a small difference in vertical response; vertical shock isolation effectiveness of each configuration is excellent (Figs. 11.13, 11.14, and 11.15).

**Response (3SS)—side to side direction**—the presence of higher frequencies is more pronounced than in the vertical response. Peak G's measure 30.6 G's, configuration (2) versus 20.4 G's configuration (1). The sharp peaks are attributed to high frequency effects. High PV content, configuration (2) is also evident in the 70–120 Hz region reaching nearly 96 ips in the form of a rounded second rise centered at about 110 Hz. It corresponds to the high frequency, high amplitude FFT spectrum over the same frequency region. The source of the high frequency vibrations is uncertain but a contributor may be the cantilevering effect and structural ringing of the four-column stiffened frame of the rack. The dummy loaded rack is basically a relatively tall, open structure having a narrow footprint in the side direction. The dummy loads are groups of steel plates bolted to the rack at the columns at several levels. Because of the column's structural design, mid-height bending is more pronounced in the side directions than front/back. PV shows a declining slope and is less than 70 ips for
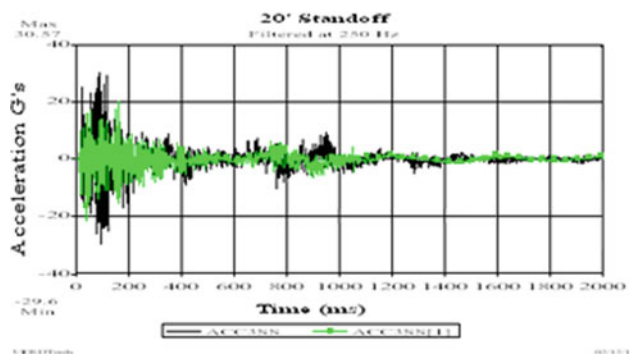
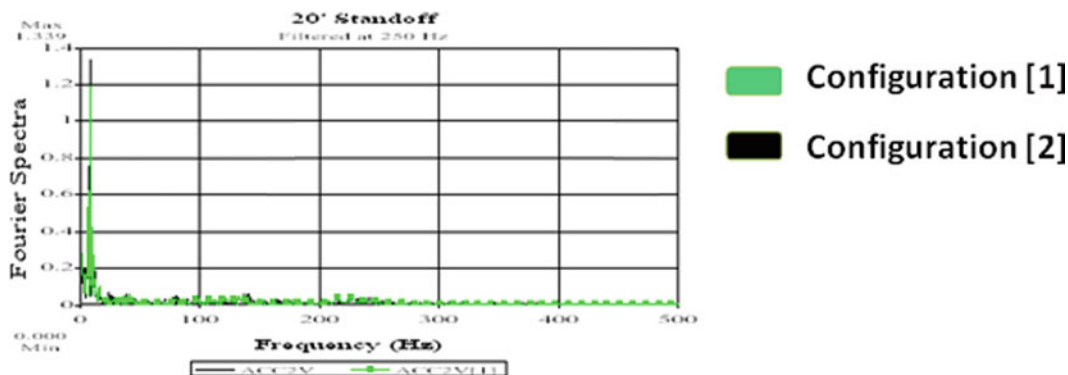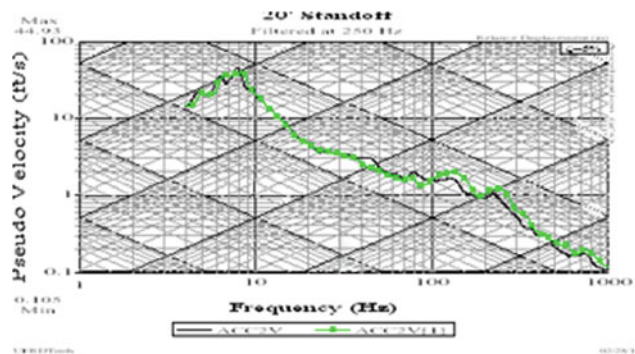Fig. 11.13  Accel



Fig. 11.14  SRS





Fig. 11.15  FFT

both configurations except at the 70–120 Hz region. The deck (1 V) also shows a similar PV rise in the 70–120 Hz region in the vertical direction (Figs. 11.16, 11.17, and 11.18).

**Response (4FB)—front/back**—The acceleration history, SRS and FFT spectrum are very similar to side (3SS) response except less high frequency content. The stiffer isolation system, configuration (2) shows 25.2 G' s versus 13.8 G's for configuration (1). The two-rise SRS plots closely match with high PV in the 70–120 Hz region. Similarly, the Fourier spectrum corresponds to the SRS with a spread of acceleration peaks in the high frequency region. Frequencies are widely distributed out to 220 Hz. As with 3SS, the 4FB peak 'G' is a very sharp spike in the acceleration-time history—first 20 ms (Figs. 11.19, 11.20, and 11.21).

## 11.6.2   Correlation of the Fourier Spectrum and SRS

Comparison of response measurements shows a close correlation of the Fourier spectrum and SRS with respect to the presence of high frequencies and the levels at which they are exhibited. As the higher frequencies become more prominent in the Fourier spectrum (for example at 70–120 Hz) they show-up as increased PV levels in the same frequency region
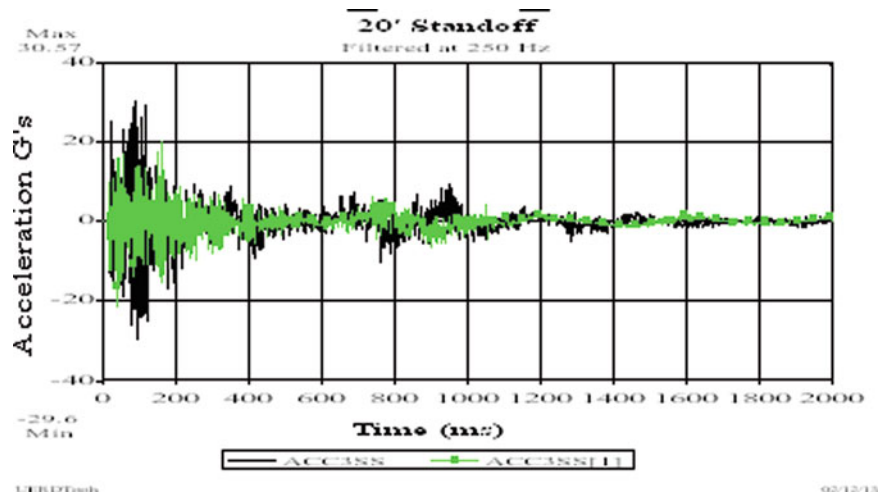
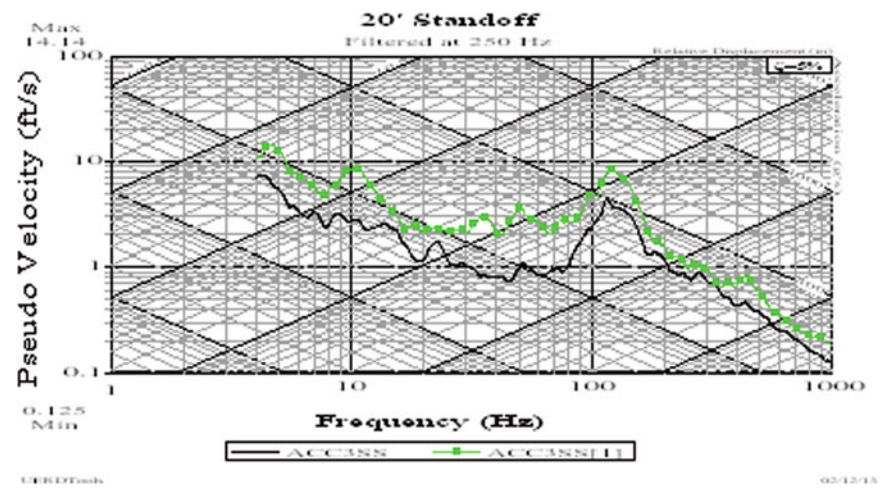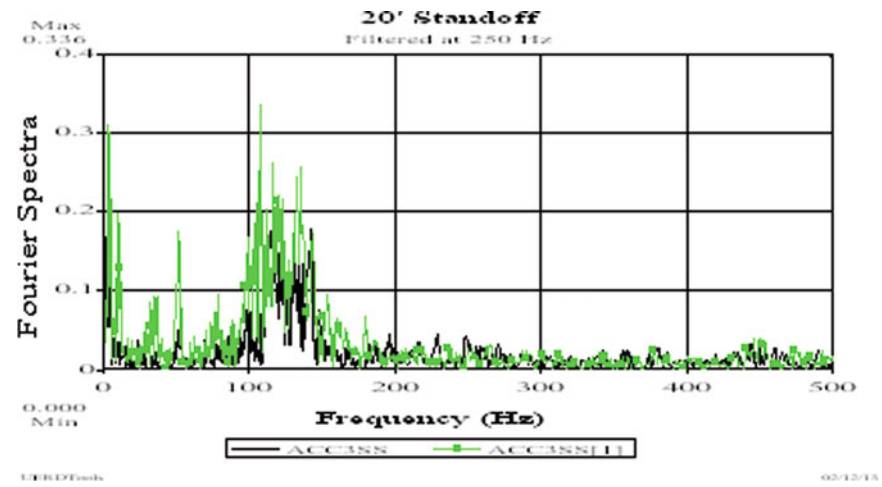**Fig. 11.16** Accel



**Fig. 11.17** SRS



**Fig. 11.18** FFT

**Fig. 11.19** Accel
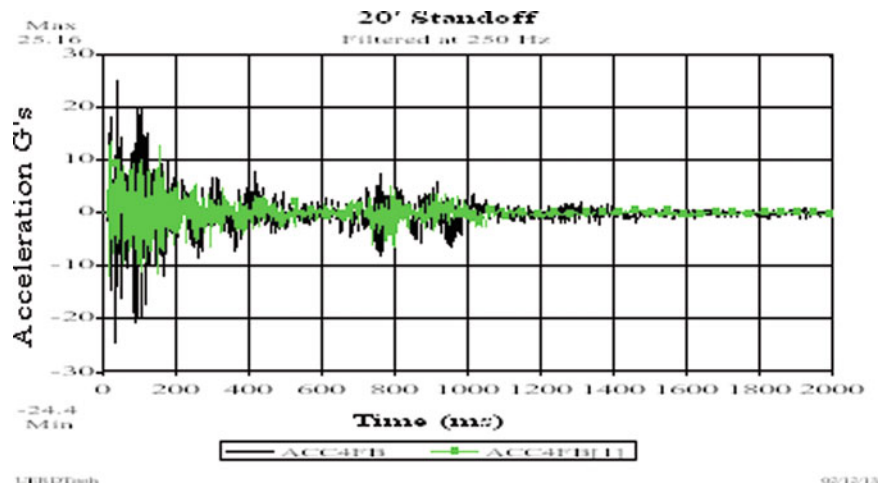


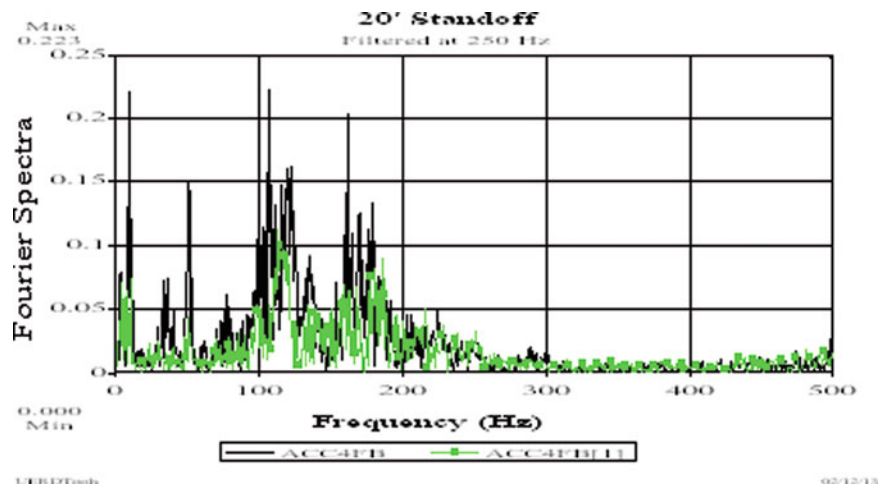**Fig. 11.20** SRS
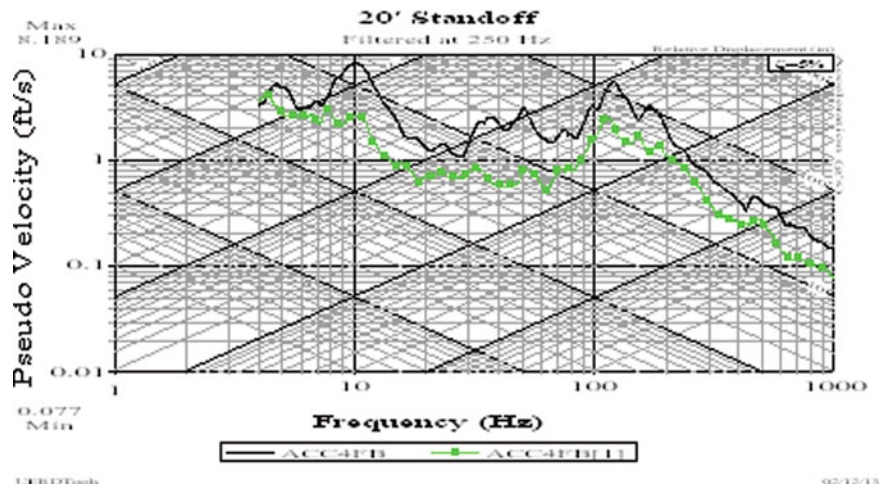


**Fig. 11.21** FFT
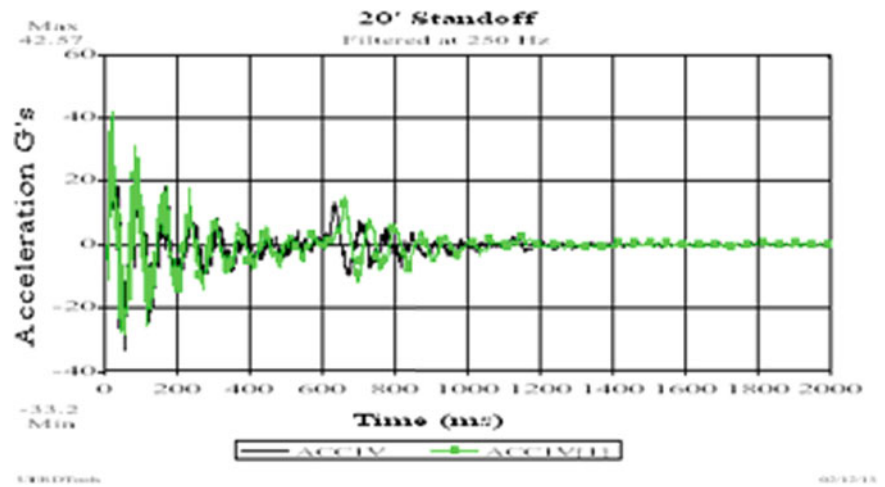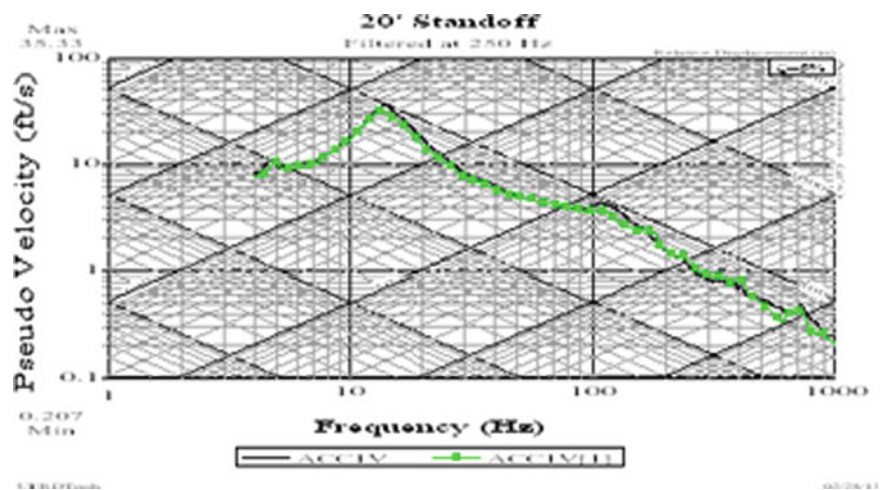
**Fig. 11.22** Accel



**Fig. 11.23** SRS



in the SRS. Similarly, where the amplitude and distribution of the higher frequencies are pronounced in the FFT, the SRS frequencies are also prominent.

### 11.6.3   14 Hz Deck Measurements

Following the 8 Hz deck barge tests, configuration (2) stiffer stabilizer, same isolation base as configuration (1) was shock tested twice on the 14 Hz deck—20-foot standoff. Tests were done in the same orientation as in the 8 Hz tests (rack facing sideways and also rotated at 90°) to the explosive charge.

**Input (1 V)—vertical direction**. Measured acceleration was nearly the same in both orientations, ranging from 37.3 to 45.6 G's. The SRS of each exhibited a relatively simple rounded peak shape in terms of PV versus frequency with a single rise near the 14 Hz deck frequency. The Fourier spectrum clearly showed the predominant 14 Hz mode and minimal energy content at higher frequencies. There were no significant differences in the input shock measurements in the two shots (Figs. 11.22, 11.23, and 11.24). It is surprising that the two input shocks matched so closely. Often there is a variation perhaps by as much as 20–25 % of peak acceleration from one shot to another.

**Response (2 V)**—Side response was nearly the same in both 14 Hz deck tests. The different orientations of the rack showed no significant differences in measurements. Peak acceleration ranged from 19.5 to 24.1 G's with a spike accounting for the 24.1 peak. The SRS was comparable in both tests. The Fourier spectrum displays a predominant mode at the 14 Hz deck frequency. Spectrum amplitudes were minimal at the higher frequencies. Overall PV levels were considerably reduced from the input shock (1 V) SRS levels, and less than 36 ips in the 70–120 Hz region (Figs. 11.25, 11.26, and 11.27).

Fig. 11.24 FFT
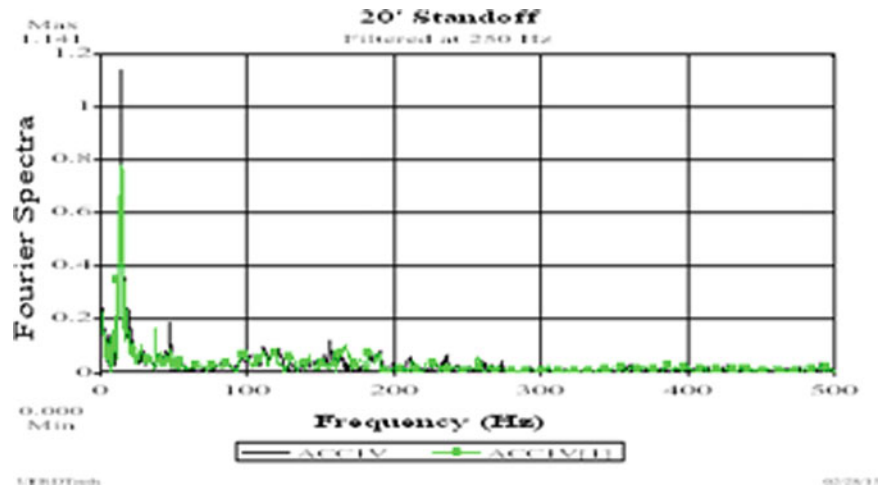


Fig. 11.25 Accel
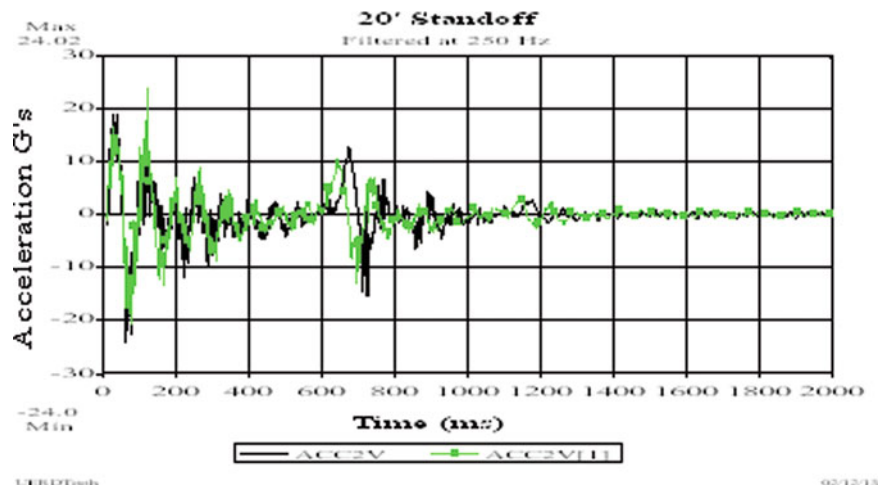


Fig. 11.26 SRS
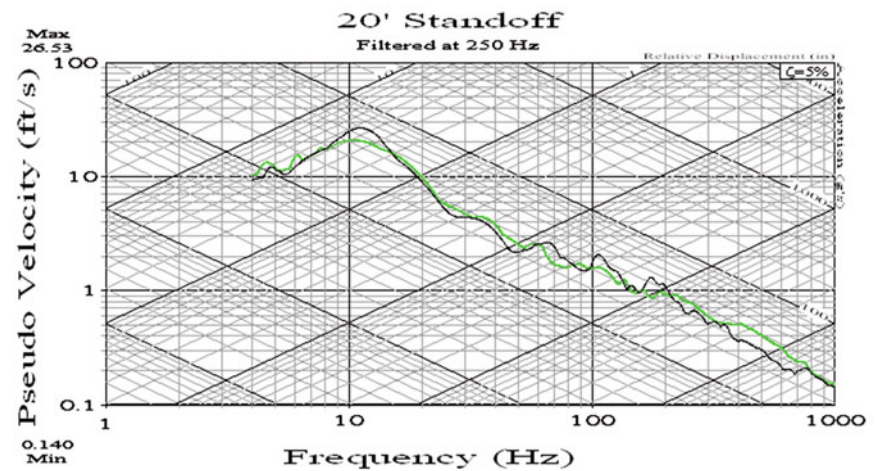


**Response (3SS)**—The response in the side direction exhibited similar characteristics in both tests. There was no significant effect from the re-orientation of the rack. Unlike the SRS and Fourier spectrum in the vertical direction, lateral acceleration responses show significant frequency content and higher PV in the 70–120 Hz region. The maximum acceleration is 26.3 G's. The mode at 5–6 Hz is an indicator of isolation system motion (Figs. 11.28, 11.29, and 11.30).

**Fig. 11.27** FFT
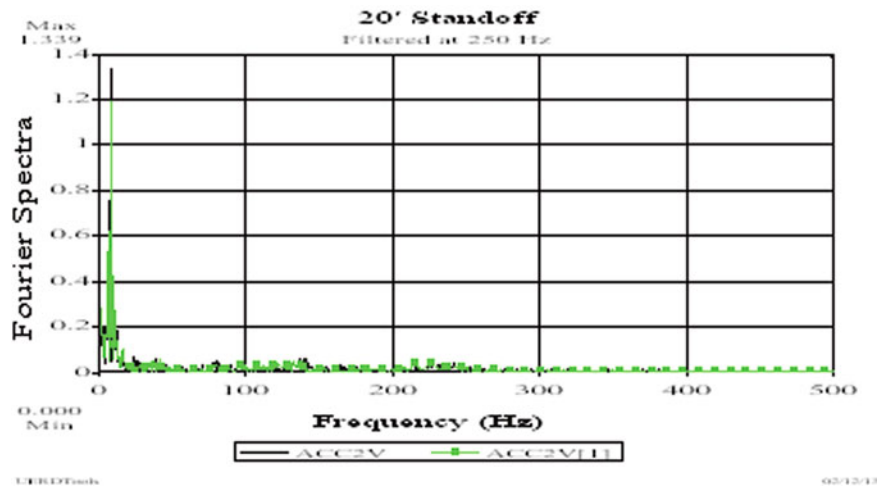


**Fig. 11.28** Accel
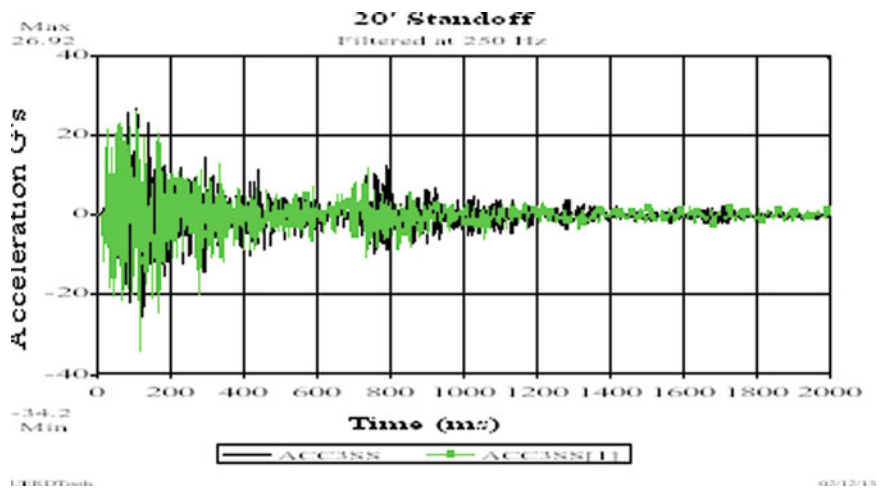


**Fig. 11.29** SRS
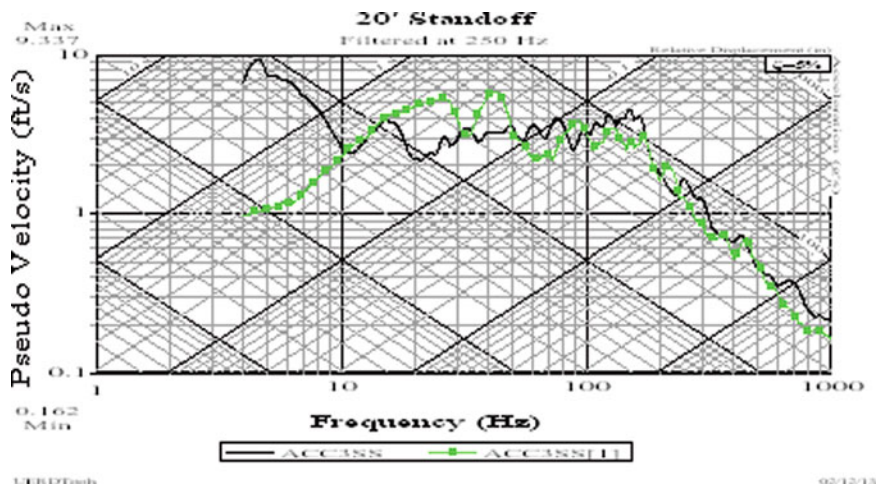


**Response (4FB)**—these acceleration-time measurements are very similar to (**3SS**) and show a similar distribution of PV in the 70–120 region. In general, peak PV's are less than 36 ips and mainly exhibit a declining slope of the spectrum at the higher frequencies above 14 Hz. The isolation system exhibits a 6–7 Hz principal mode in this direction (compression/tension of the stabilizer mounts) (Figs. 11.31, 11.32, and 11.33).

**Fig. 11.30** FFT
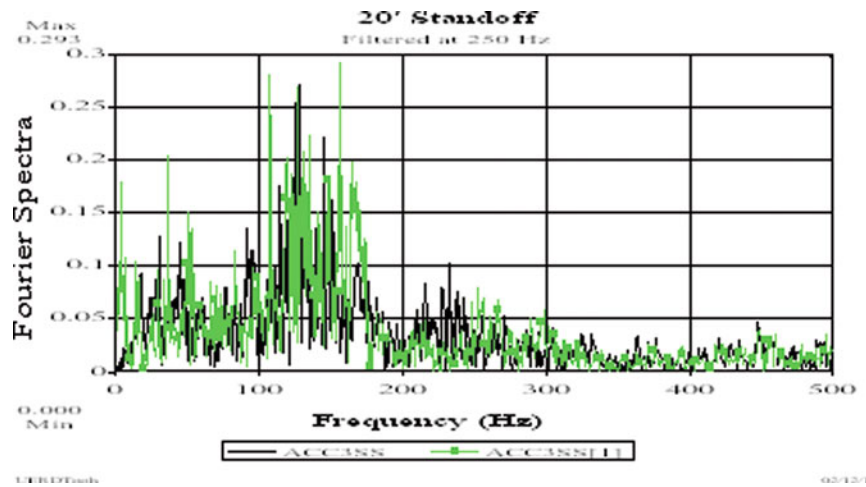


**Fig. 11.31** Accel
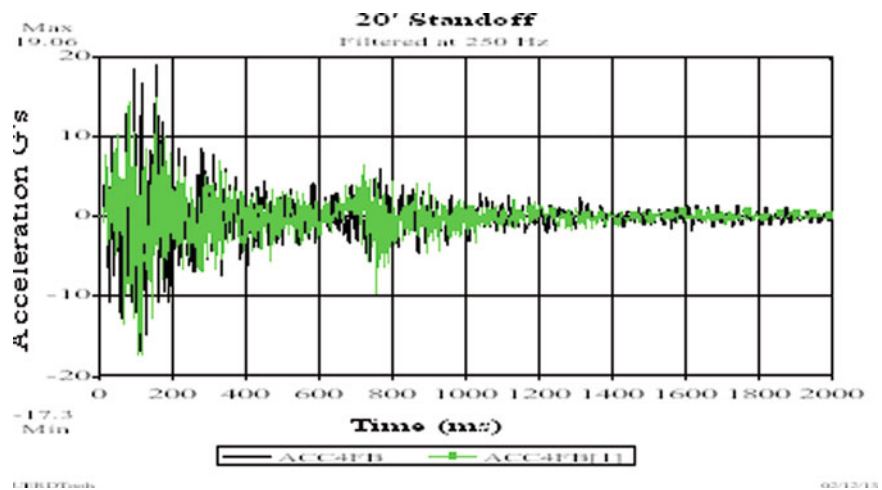


**Fig. 11.32** SRS
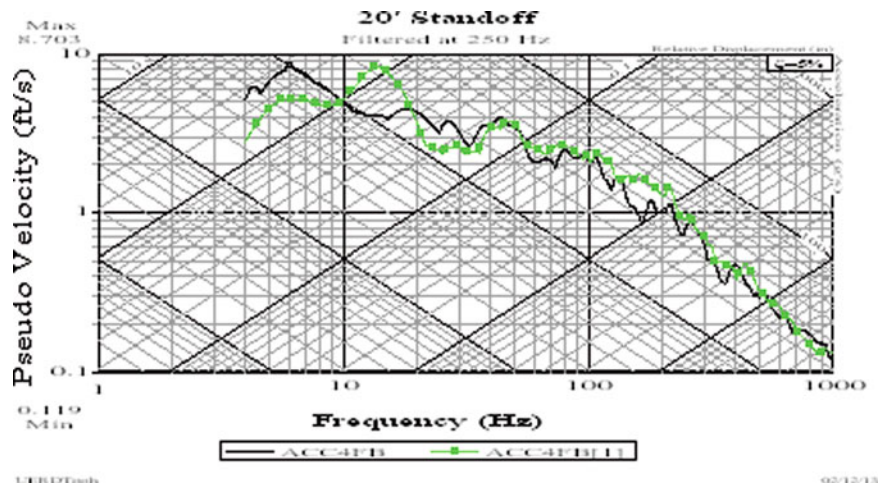


## 11.6.4 Barge Test of a Fully Populated Rack

To give one example of a recent test—the shock measured on the 14 Hz deck of the barge near to the mounting fixture was 69.5 g's at the 20-foot standoff. The acceleration is shown in Fig. 11.34. The response was slightly less than 20 g's. The relative vertical displacement of the rack in this test was 3.5–3.8 inches. Sway displacement (motion all around the rack at the

**Fig. 11.33** FFT
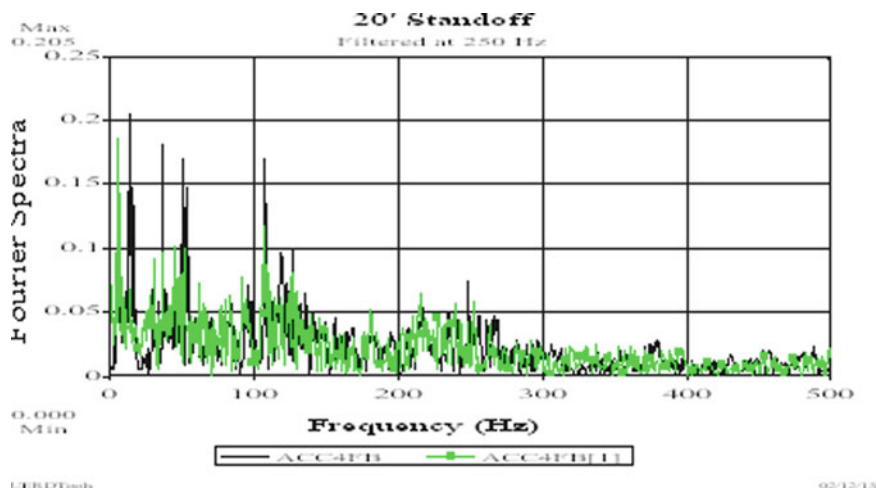


**Fig. 11.34** Accel
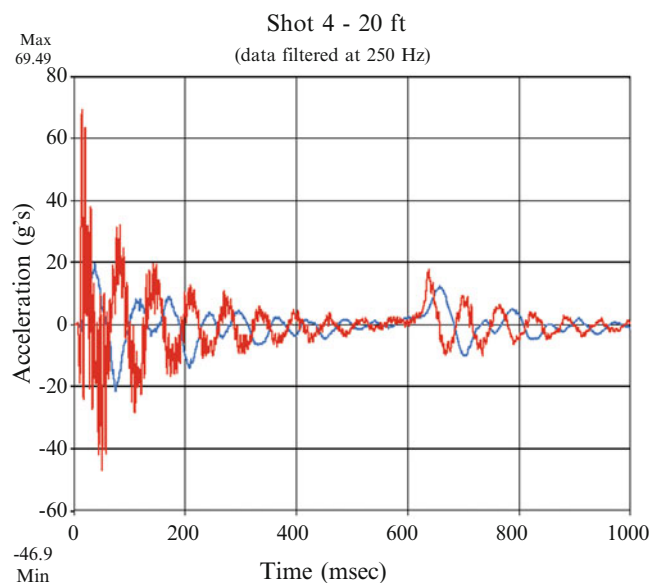


upper corners) was slightly less than 3 inches. The shock response, which had decayed to less than 5 G's at 0.6 s, increased to nearly 12 G's when the bubble pulse occurred at about 0.65 s.

The shock response spectra (SRS) data, Fig. 11.35; the isolated response was substantially less than the input at frequencies above 10 Hz. There is an especially large difference between the input and response pseudo velocities in the 50–150 Hz region and above. The predominant frequency of the isolation system is 5–6 Hz. The peak of the green curve shows the barge test deck frequency of 14 Hz. Pseudo velocities (PV) of the response were less than 50 ips versus 70–80 ips of the input at the same frequencies.

## 11.7   Summary and Conclusions

In the 8 Hz deck tests, the soft stabilizer system (configuration 1) exhibited large displacement particularly in the side direction however the measured shock response was well under allowable acceleration limits in all directions. Stabilizers were changed to a stiffer design (configuration 2) for greater restraint of the dummy loaded rack and reduction of sway at the front upper corners. Configuration 2 was also designed for improved balance and redistribution of load on the base mounts. Barge testing verified the expectation of reduced motion and sway to within acceptable limits. Response acceleration was nearly 25 G in the vertical axis. The maximum was 31 G's in the side direction. PV levels remained within design guidelines. Testing on the 14 Hz deck validated the selection of the stiffer stabilizer isolation system for use with the populated rack.

**Fig. 11.35** SRS
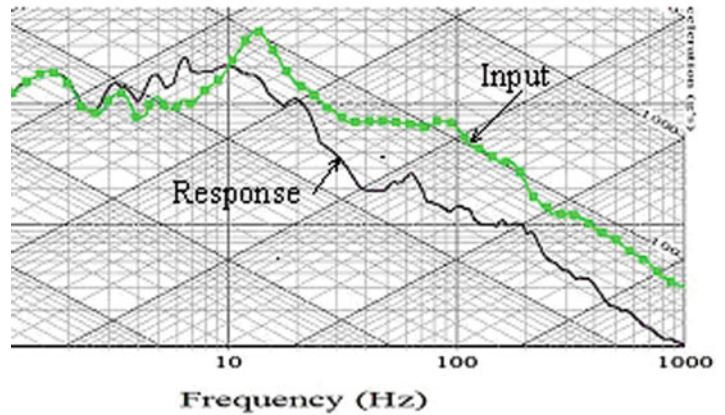


The combined method of comparing peak acceleration values and a survey of SRS results to determine whether or not there has been a noticeable reduction in PV levels is considered a useful tool for the design and evaluation of isolation systems.

Comparing results of 8 Hz and 14 Hz barge tests, it was shown that the same isolation system satisfactorily reduced shock levels at the rack to acceptable levels. This was further verification that an isolation system proven for the 8 Hz deck could also meet 14 Hz shock requirements. SRS and FFT analyses were helpful and confirmed the predicted use of the Seamount isolation design. The two slightly different isolator configurations effectively bracketed the expected response. Having the same base mounts, only the stabilizers were different. The preferred isolation system was then used for populated rack tests with excellent results.

# References

1. LeKuch H, Donovan N (2012) Describing the shock response of a dummy loaded isolated rack and internal components. In: 83rd Shock and Vibration conference. New Orleans, La
2. LeKuch H, Kayayan K (2012) Development of the seamount isolator. In: 83rd Shock and Vibration conference. New Orleans, La
3. Piersol AG, Paez TL (2010) Harris shock and vibration handbook, 6th edn. McGraw Hill Book Co, Inc., Newyork, Chapter 39
4. Powell P (1983) Engineering with polymers. Chapman and Hall, London
5. Gaberson HA, Pal D, Chapler RS (2000) Shock spectrum classification of violent environments that cause machinery failure. In: SEM-IMAC XVIII, San Antonio, TX
6. Gaberson HA (2012) Shock severity estimation. Sound and vibration magazine
7. Mantz P, Costenza FA (2009) An overview of UERDTools capabilities: a multi-purpose analysis package. In: IMAC—XXVII

# Chapter 12
# Nonlinear High Fidelity Modeling of Impact Load Response in a Rod

**Yu Liu, Andrew J. Dick, Jacob Dodson, and Jason Foley**

**Abstract**  In this paper, wave propagation through a polyurethane rod is studied by using an experimental system and through performing high fidelity numerical simulations. The rod model for the polyurethane rod is prepared accounting for the possibility of a material nonlinearity. Due to a significant impedance mismatch between the titanium transmission bar and the polyurethane rod along with the high damping level of the polyurethane, only a small amplitude, linear response was observed and predicted in the polyurethane rod. Ongoing work will focus on impedance matching in order to transfer greater amounts of energy into the polyurethane rod so that the nonlinear stress-strain relationship can be studied for larger magnitude response conditions.

**Keywords**  High fidelity • Impact • Rod • Wavelet • Wave propagation

## 12.1  Introduction

Nonlinear elastic wave propagation has been studied in recent years for a number of applications including the analysis of seismic motion, non-destructive methods for the evaluation of structures, and analysis for biomedical materials [1–3]. Nonlinear wave propagation can also be come significant when structures are exposed to extreme impact conditions. Large magnitude impulsive loading can result in significant nonlinear behavior. Short duration loading results in high frequency content which can also serves to increase the influence of the nonlinear properties on wave propagation. The finite element method has been identified as a useful tool for studying wave propagation in structures.

The finite element method (FEM) uses elements of various sizes and styles to create a discretized model of a structure. This model is then used to predict the structural response to impulsive loads. However, the flexibility provided by FEM results from the use of approximate shape functions which can limit performance under certain conditions. These issues can significantly affect accuracy when considering high frequency content. When predicting wave propagation, this can result in the introduction of spurious oscillations in the response resulting in a decreased level of performance. Efforts are underway to address this shortcoming through the use of more sophisticated shape functions and post-processing of the predicted response signal [4]. An alternative approach to address issues associated with accurately representing high frequency content is to use the spectral finite element method.

The spectral finite element method (SFEM) was developed by implementing the finite element method is a spectral-domain (i.e. the frequency-domain) [5]. By first transforming the linear equation of motion into the frequency-domain, it is possible to derive exact shape functions describing the behavior of the propagating waves. SFEM makes uses these exact shape functions to represent the spatial response behavior with perfect accuracy. However, this improved frequency performance comes at the cost of reduced flexibility from that provided by FEM and, as a result, the use of SFEM is limited to structures with relatively simple geometry. While SFEM is an intrinsically linear method, research efforts have developed new approaches to facilitate high fidelity studies of nonlinear wave propagation [6,7]. The frequency-domain implementation

Y. Liu • A.J. Dick (✉)
Nonlinear Phenomena Laboratory, Department of Mechanical Engineering, Rice University, Houston, TX 77005, USA
e-mail: andrew.j.dick@rice.edu

J. Dodson • J. Foley
Fuzes Branch, Munitions Directorate, Air Force Research Laboratory, Eglin AFB, FL, USA

of this approach can also provide additional limitations due to the wrap-around issues resulting from the periodic nature of the Fourier transform. By implementing SFEM in a wavelet-domain and then incorporating it in the alternating spectral-domain/time-domain framework, the Alternative Wavelet-Time Finite Element Method has been developed.

The Alternative Wavelet-Time Finite Element Method (AWT-FEM) was developed to provide high fidelity performance for studying wave propagation in nonlinear structures and avoid wrap-around issues [8]. AWT-FEM uses a spectrally-uncoupled wavelet-domain implementation of SFEM (WSFEM) [9]. Similar to the frequency-domain approach, this method functions by alternating between the wavelet-domain and time-domain in order to calculate the response with WSFEM in the wavelet-domain and to calculate the nonlinear terms in the time-domain avoiding computationally prohibitive convolution calculations. AWT-FEM can be applied to rod, beam, and thin plate structures and used to study models derived with nonlinear properties resulting from material nonlinearities and geometric nonlinearities.

In this research, AWT-FEM is applied to study wave propagation in a polyurethane rod. The polyurethane rod is modeled with a material nonlinearity in anticipation of significant influence from a nonlinear stress-strain relationship. An experimental setup is used to observe wave propagation through the polyurethane rod. Numerical simulations are performed to characterize the response.

In the next section, the nonlinear rod model is presented along with a brief description of AWT-FEM The experimental system and observed wave propagation are presented in the third section along with the results of numerical simulations. Concluding remarks are collected in the final section.

## 12.2 Modeling

In this section, the nonlinear rod model used in this study is derived. The Alternative Wavelet-Time Finite Element Method is also briefly introduced.

### 12.2.1 Nonlinear Rod Model

A rod model is derived for a material nonlinearity. A nonlinear constitutive model with a quadratic strain term is used [10–12]. This relationship is defined in Eq. (12.1).

$$\sigma = E \left( \epsilon + \alpha \epsilon^2 \right), \tag{12.1}$$

where $\sigma$ represents stress, $E$ is the Young's modulus, $\epsilon$ represents strain, and $\alpha$ is the nonlinear coefficient. When $\alpha > 0$, this represents a hardening nonlinear material. The model is derived by using a linear strain-displacement relationship. By using the extended Hamilton's principle, the nonlinear rod model presented in Eq. (12.2) is derived.

$$EA\frac{\partial^2 u}{\partial x^2} - \rho A\frac{\partial^2 u}{\partial t^2} + F\left(x, t\right) = 0, \tag{12.2}$$

where $A$ represents the cross sectional area, $\rho$ represents the density, $u$ is the axial displacement, and $F\left(x, t\right)$ is the nonlinear term. The nonlinear term for a material nonlinearity with a quadratic strain term is defined by Eq. (12.3).

$$F\left(x, t\right) = 2\alpha EA\frac{\partial u\left(x, t\right)}{\partial x}\frac{\partial^2 u\left(x, t\right)}{\partial x^2}. \tag{12.3}$$

In order to implement the nonlinear rod model in AWT-FEM, the nonlinear rod model is first transferred into the wavelet-domain. This is performed by using a spectrally-uncoupled single-scale wavelet transform [13]. The resulting wavelet-domain equation is presented in Eq. (12.4).

$$EA\frac{\partial^2 \hat{u}_j}{\partial x^2} - \lambda^2 \rho A\hat{u}_j + \hat{F}_j = 0, \quad j = 0, 1, \ldots, n-1, \tag{12.4}$$

where the hat symbol (ˆ) represents wavelet-domain variables.

By neglecting the nonlinear term, the linear equation is used to derive exact shape functions in order to prepare the dynamic stiffness matrix. The resulting matrix equation is defined by Eq. (12.5). In the wavelet-domain implementation, the angular frequency from the frequency-domain implementation is replace by $\omega = -i\lambda_j$, resulting from the wavelet transform.

$$\mathbf{K}\left(\lambda_j\right)\mathbf{q}_j = \mathbf{Q_N} + \mathbf{Q_E}, \tag{12.5}$$

where $\mathbf{K}$ is the dynamic stiffness matrix, $\mathbf{Q_N}$ is the nonlinear force vector, and $\mathbf{Q_E}$ is the external force vector and they are defined by Eqs. (12.6), (12.7), and (12.8), respectively.

$$\mathbf{K} = \int EA\mathbf{N_R'}^T\mathbf{N_R'}dx + \lambda_j^2 \int \rho A\mathbf{N_R}^T\mathbf{N_R}dx, \tag{12.6}$$

$$\mathbf{Q_N} = \int \mathbf{N_R}^T\mathbf{P}_j\,dx, \tag{12.7}$$

$$\mathbf{Q_E} = \int \mathbf{N_R}^T\hat{F}_j\,dx, \tag{12.8}$$

### 12.2.2   Alternating Wavelet-Time Finite Element Method

The Alternating Wavelet-Time Finite Element Method provides the means to apply the linear wavelet-domain spectral finite element method to study nonlinear systems. Since nonlinear terms appear as computationally expensive convolution operations in spectral domains, the alternating framework is employed to avoid these calculations. With the nonlinear term represented as an additional force, the linear model is used in the wavelet-domain and the resulting response is transferred into the time-domain by using an inverse wavelet transform. The process is initiated by first neglecting the nonlinear term and calculating the response of the linear system. In the time domain, the response is used to efficiently calculate the nonlinear term. Once calculated, the nonlinear term is transferred to the wavelet-domain by using a wavelet transform. An iterative process is applied to perform this operation in order to ensure successful convergence for the nonlinear term and accurate calculation of the nonlinear response. Full details of the AWT-FEM approach can be found in [8].

## 12.3   Experiments and Numerical Simulations

The experimental setup is introduced in the first subsection. Numerical simulations and the comparisons with experimental data are presented at the second subsection.

### 12.3.1   Experimental Setup

The experiment test apparatus was set up at the AFRL Shock Dynamics Laboratory. Analog signal conditioning for the strain gages is accomplished via a Precision Filter 28000 chassis with 28144A Quad-Channel Wideband Transducer Conditioner with Voltage and Current Excitation cards. A high rate instrumentation system using a National Instruments chassis paired with PXI-6133 multifunction input/output cards is used to digitize the analog data. The PXI-6133 samples at 2.5 MSa/s with 16 bits of vertical resolution.

   The experimental setup is shown in Fig. 12.1. A 72 inch titanium bar is the incident bar. A 21 inch polyurethane bar with embedded accelerometers is the transmission bar. Uniaxial strain gages are mounted on the incident bar. The gages are oriented axially on the bar in diametrically opposed pairs to allow bending and extensional cancellation. This is feasible since the data acquisition system has sufficient number of phases matched channels to independently capture the output from individual gages. Semiconductor strain gages are used on the incident bar. These have resistances of 120 or 350 $\Omega$ with a fast response time (10 ns) and correspondingly higher bandwidth (10 MHz) than foil gages (typically 300 kHz). The gage length is typically 1 mm and the gage factor is about 150, providing orders-of-magnitude improvement in sensitivity. The traditional disadvantage of semiconductor gages, a strong temperature dependence, is not a concern for these dynamic tests since the circuits can be balanced immediately prior to a test or run in an AC-coupled mode with minimal temperature excursions between data acquisition arming and trigger. The strain gages were wired with a floating shield/ground to avoid ground loops.

**Fig. 12.1** Experimental setup
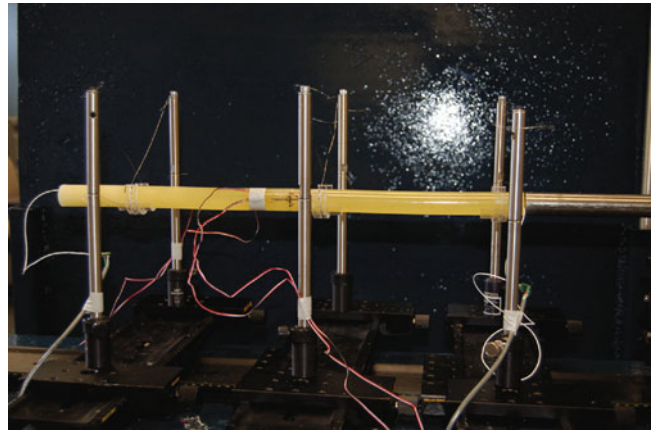


**Fig. 12.2** Complete time history of the axial strain at the midpoint of the incident bar
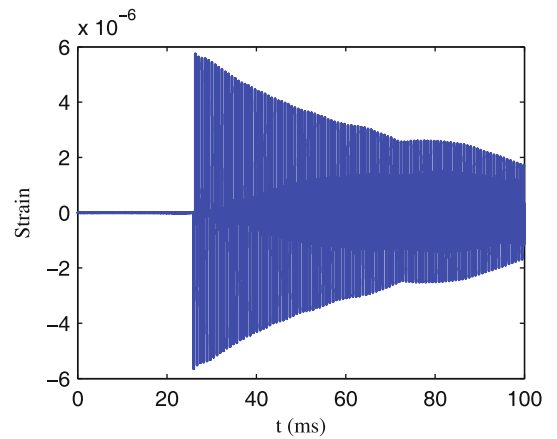


**Fig. 12.3** Complete time history of the acceleration at the midpoint of the transmission bar
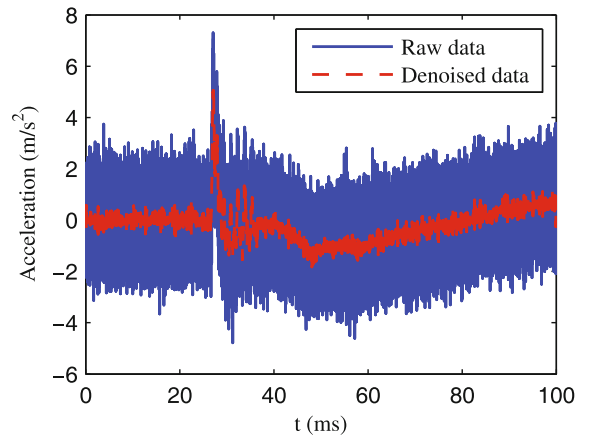


The two bars are pressed against each other via the placement of the wire supports. A steel striker impacts the incident bar to generate propagating waves into the transmission bar. The two bars stay in contact for most of (if not all) the data acquisition time. Wave responses at two positions are of interest: the midpoint of the incident bar and the midpoint of the transmission bar. The response of the axial strain at the midpoint of the incident bar is detected by the strain gages, as shown in Fig. 12.2. The response of acceleration wave at the midpoint of the transmission bar is measured by the accelerometer, as shown in Fig. 12.3. An interval-dependent denoising down to level 11 using the Daubechies wavelet with an order of 8 is performed and the result is plotted as the red dashed-line in Fig. 12.3.

**Fig. 12.4** Comparison between
the simulation and experimental
results of the strain waves at the
midpoint of the incident bar
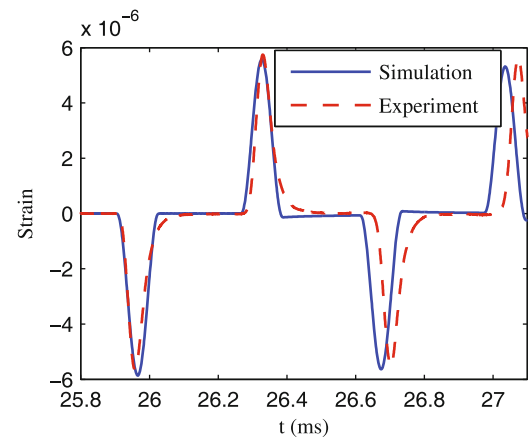


**Fig. 12.5** Comparison between
the simulation and experimental
results of the acceleration waves
at the midpoint of the
transmission bar
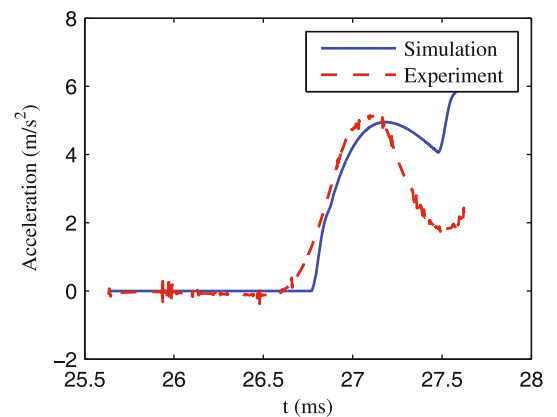


### 12.3.2 Numerical Simulations

In this preliminary study, numerical simulations using the AWT-FEM are performed to reproduce the wave response in the incident bar and the transmission bar. The two bar are assumed to be rigidly connected in the simulation. An extreme damping factor is tuned for the polyurethane bar to match the amplitude level of the experimental result.

The wave speed in the titanium bar is 5,160 m/s. A small part of the response with a window of 2 ms after the impact is chosen to be analyzed. The comparison between the simulation and experimental results of the strain waves at the midpoint of the incident bar is shown in Fig. 12.4. In the simulation, the propagating wave first arrives at the midpoint at 25.9 ms. The first reflected wave comes back at 26.3 ms. After that, another two reflections with both boundaries of the incident bar occur and pass through the midpoint at 26.7 ms and 27 ms. The first two pulses match with the experimental data very well. The later two pulses travel faster than the corresponding ones in the experimental result. This may be attributed to the complex dynamic behavior at the interface between the two bars and the influence of the wire support on the incident bar in the experiments.

The comparison between the simulation and experimental results of the acceleration waves at the midpoint of the incident bar is shown in Fig. 12.5. The two pulses match well with each other. The difference of the later part of the responses may be attributed to the influence of the interface and wire supports to the experimental data. Due to the presence of extreme damping in the transmission rod, it appears that the dynamic compressive wave does not make it to the far end of the bar. Therefore there is no tensile wave (reflected from the end of the polyurethane bar) to pull apart the interfaces. This can be illustrated by the velocity wave propagation along the two bars in Fig. 12.6. Multiple reflections can be observed in the incident bar but no complete wave profile reaches the end of the transmission bar.

**Fig. 12.6** Velocity wave
propagation along the connected
two bars
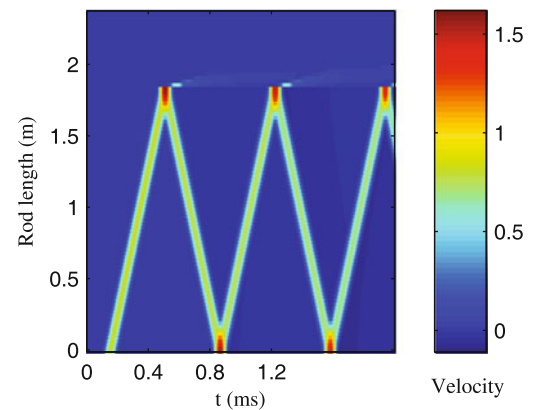


## 12.4  Concluding Remarks

In this paper, the alternating wavelet-time finite element method is applied to study the impact wave response in a two rods system. The high fidelity simulation responses accurately capture the dynamic behaviors in both the incident bar and the transmission bar. The validity of the proposed method is verified through comparison with experimental data. Due to the extremely high level of energy dissipation in the polyurethane rod and the large impedance mismatch between the titanium bar and the polyurethane bar, the magnitude of the wave propagating through the polyurethane rod was very small and no significant nonlinear properties were observed.

In the future, modifications to the experimental setup will be made in order to minimize the influence of the interface and wire support. A transmission rod with an impedance much closer to that of the polyurethane rod will also be used in order to transfer a greater amount of energy into the polyurethane rod. This is expected to provide better conditions for investigating the potential for a nonlinear constitutive relation.

## References

 1. Johnson PA, Jia X (2005) Nonlinear dynamics, granular media and dynamic earthquake triggering. Nature 437(7060):871–874
 2. Meo M, Zumpano G (2005)  Nonlinear elastic wave spectroscopy identification of impact damage on a sandwich plate.  Compos Struct 71(3–4):469–474
 3. Taylor P, Ford C (2009)  Simulation of blast-induced early-time intracranial wave physics leading to traumatic brain injury.  J Biomech Eng 131(6):61007–61018
 4. Idesman A (2007) A new high-order accurate continuous galerkin method for linear elastodynamics problems. Comput Mech 40(2):261–279
 5. Doyle J (1997) Wave propagation in structures. Springer, Berlin
 6. Lee U, Jang I (2011)  Nonlinear spectral element model for the blood flow in human arteries.  In: Proceedings of the 2011 international symposium of computational models for life sciences, pp 136–145. Toyama City, Japan,
 7. Liu Y, Ghaderi P, Dick A (2012)  High fidelity methods for modeling nonlinear wave propagation in one-dimensional waveguides.  In: Proceedings of the ASME 2012 international mechanical engineering congress and exposition. Houston, TX
 8. Liu Y, Dick A (2013)  Alternating wavelet-time finite element method: Modeling and analysis of nonlinear wave propagation in one and two-dimensional waveguides (submitted). J Sound Vib
 9. Williams JR, Amaratunga K (1997)  A discrete wavelet transform without edge effects using wavelet extrapolation.  J Fourier Anal Appl 3(4):435–449
10. Nayfeh A, Mook D (1995) Nonlinear oscillations. Wiley, New York
11. Ramabathiran A, Gopalakrishnan S (2012)  Time and frequency domain finite element models for axial wave analysis in hyperelastic rods. Mech Adv Mater Struct 19(1–3):79–99
12. Li J, Zhang Y (2008) Exact travelling wave solutions in a nonlinear elastic rod equation. Appl Math Comput 202(2):504–510
13. Mitra M, Gopalakrishnan S (2005)  Spectrally formulated wavelet finite element for wave propagation and impact force identification in connected 1-d waveguides. Int J Solid Struct 42(16):4695–4721

# Chapter 13
# On the Role of Boundary Conditions in the Nonlinear Dynamic Response of Simple Structures

Yu Liu and Andrew J. Dick

**Abstract** Nonlinear responses of structures under extreme impact loading with various boundary conditions are studied. A variety of structures including rods and beams are modeled with material and geometric nonlinearities. High fidelity responses are obtained by using the alternating wavelet-time finite element method (AWT-FEM). Nonlinear distortion and dispersion are identified in the response and the influence of the boundary conditions on the nonlinearity is explored.

**Keywords** Nonlinear • Boundary conditions • Wavelet • Spectral finite element • Wave propagation

## 13.1 Introduction

Research on nonlinear elastic waves has advanced significantly in both industrial and academic areas, like non-destructive evaluation [1], seismic motion analysis [2], and biomedical analysis [3]. When a structure is subject to an impact shock with short duration, the high frequency content will significantly magnify the influence of the nonlinear property in the response. A high fidelity analysis of the nonlinear response can enable a better understanding of both the structure and the impact load.

The finite element method (FEM) has been widely adopted to study wave propagation. However, for high fidelity analysis of impact waves, FEM may introduce spurious oscillations which result from erroneously introduced numerical dispersion [4, 5]. The spectral finite element method (SFEM) is a new powerful numerical technique for high fidelity wave analysis. Calculations are performed in a spectral-domain such as the frequency-domain by using fast-Fourier transform (FFT) and exact wave solution are used as spatial interpolation functions. For linear problems, only one element is needed to obtain a highly accurate response for a given position in a structural component like a rod or a beam. For nonlinear problems, an alternating frequency-time frame is constructed to avoid convolution operation of nonlinear terms in the spectral-domain [6, 7]. However, the FFT-based methods have a major drawback. Wrap-around errors may occur resulting from the periodic nature of the Fourier transform. Signals that do not decay within the given time-window will become wrapped around in the time-sequence and corrupt the real signal. Semi-infinite elements or non-reflecting boundary conditions are often added at ends of structures to leak energy out of the system [8]. For problems with physically realistic boundary conditions, a long time-window is needed to dissipate the energy and may cause convergence issue in the alternating frequency-time approach for nonlinear problems. This greatly limits the capability of nonlinear SFEM to study the interaction between propagating waves and different physical boundaries.

Mitra and Gopalakrishnan developed a wavelet-based spectral finite element method to avoid the wrap-around issue for linear wave propagation. The Fourier transform was replaced by a spectrally-uncouple single-scale wavelet transform. A wavelet extrapolation technique was employed to represent non-periodic boundary conditions [9]. Based on their work, the authors of this paper developed a new method named the alternating wavelet-time finite element method (AWT-FEM) to study nonlinear wave propagation problems [10]. It adapted the spectral-uncoupled wavelet transform into an iterative alternating wavelet-time approach. It can produce highly accurate responses for nonlinear problems with physical boundary conditions.

Yu Liu • A.J. Dick (✉)

Nonlinear Phenomena Laboratory, Department of Mechanical Engineering, Rice University, Houston, TX 77005, USA
e-mail: andrew.j.dick@rice.edu

In this paper, the AWT-FEM is applied to study nonlinear wave propagation in rod and beam structures with different boundary conditions. The focus of the study is on the influence of different boundary constraints on the nonlinear behavior in the response. The remainder of this paper is organized in the following manner. The AWT-FEM for a materially nonlinear rod and a geometrically nonlinear beam models are developed in the second section. In the third section, the results of numerical simulations are presented. Free-free and clamped-free boundaries for the rod model are first compared. Hinged-hinged (free to rotate and slide) and pinned-pinned boundaries for the beam model are then analyzed. Concluding remarks and the direction of future work are provided in the last section.

## 13.2  Modeling

The AWT-FEM formulation for a materially nonlinear rod and a geometrically nonlinear beam are briefly derived in the first and second subsections. The iterative alternating wavelet-time framework is then introduced in the last subsection.

### 13.2.1  Rod Model

A nonlinear stress-strain relationship with a quadratic nonlinear term for one-dimensional (1D) rod is reported in [11–13]. The formula is

$$\sigma = E\left(\epsilon + \alpha\epsilon^2\right), \tag{13.1}$$

where $\sigma$ is the stress, $\epsilon$ is the strain, $E$ is the elastic modulus, and $\alpha$ is the nonlinear coefficient. When $\alpha > 0$, the quadratic term exhibits a hardening effect on the constitutive curve. When $\alpha < 0$, a softening effect can be observed.

A linear strain-displacement relationship is assumed. By using Hamilton's principle, the governing materially nonlinear homogeneous wave equation for a rod is obtained as

$$EAu'' - \rho A\ddot{u} + F(x,t) = 0, \tag{13.2}$$

where

$$F(x,t) = 2\alpha EAu'u'', \tag{13.3}$$

the cross section area is represented by $A$, $\rho$ is the density, $u$ is the axial displacement, the prime represents a derivative with respect to the spatial coordinate $x$, and $F(x,t)$ is the nonlinear term.

By transforming Eq. (13.2) into the wavelet-domain by using the spectrally-uncoupled single-scale wavelet transform [14], the spectral governing equation of motion is obtained as

$$EA\hat{u}_j'' - \rho A\lambda_j^2\hat{u}_j + \hat{F}_j = 0, \quad j = 0, 1, \ldots, n-1, \tag{13.4}$$

where the (ˆ) symbol indicates that the corresponding variables are in the wavelet-domain.

By neglecting the nonlinear term $\hat{F}_j$, Eq. (13.4) can be reduced to a linear wave equation. Exact solutions to this linear equation are reported in [8] and they are adopted as spectrally-dependent shape functions $\mathbf{N}$. The angular frequency $\omega$ in the reference is replaced by $\omega = -i\lambda_j$. By following a standard finite element approach, the following matrix form can be obtained as

$$\mathbf{K}\left(\lambda_j\right)\mathbf{q}_j = \mathbf{Q_E} + \mathbf{Q_N}, \tag{13.5}$$

where

$$\mathbf{K} = \int EA\mathbf{N_R'}^T\mathbf{N_R'}dx + \int \rho A\mathbf{N_R}^T\mathbf{N_R}dx,$$

$$\mathbf{Q_N} = \int \mathbf{N_R}^T\hat{F}_j\,dx,$$

$$\mathbf{Q_E} = \int \mathbf{N_R}^T\hat{P}_j\,dx, \tag{13.6}$$

where $\mathbf{K}$ is the spectrally formulated stiffness matrix, $\mathbf{Q_N}$ is the equivalent nodal force term for the nonlinear term, and $\mathbf{Q_E}$ is the equivalent nodal force term for the distributive external load.

### 13.2.2   Beam Model

The *von Kármán* strain [15] is adopted to define the nonlinear strain-displacement relationship. The constitutive relationship is assumed to be linear. By using Hamilton's principle, the governing geometrically nonlinear homogeneous wave equations for a beam are obtained as

$$EAu'' - \rho A\ddot{u} + F_R(x,t) = 0, \tag{13.7}$$

$$EIw^{iv} + \rho A\ddot{w} + F_B(x,t) = 0, \tag{13.8}$$

where

$$F_R(x,t) = EAw'w'', \tag{13.9}$$

$$F_B(x,t) = EAw''\left[u' + \frac{1}{2}\left(w'\right)^2\right], \tag{13.10}$$

the transverse displacement is represented by $w$, $I$ is the second moment of inertia, $F_R(x,t)$ is the axial nonlinear force term, and $F_B(x,t)$ is the transverse nonlinear force term. By transforming Eqs. (13.7) and (13.8) into the wavelet-domain by using the spectrally-uncoupled single-scale wavelet transform [14], the spectral governing equations of motion are obtained as

$$EA\hat{u}_j'' - \rho A\lambda_j^2\hat{u}_j + \hat{F}_{Rj}(x) = 0, \tag{13.11}$$

$$EI\hat{w}_j^{iv} + \rho A\lambda_j^2\hat{w}_j - \hat{F}_{Bj}(x), \quad j = 0, 1, \dots, n-1. \tag{13.12}$$

By neglecting the nonlinear term $\hat{F}_{Rj}$ and $\hat{F}_{Bj}$, Eqs. (13.11) and (13.12) can be reduced to a set of linear wave equations. The spectrally-dependent shape functions $\mathbf{N_R}$ and $\mathbf{N_B}$ can be found in [8]. The angular frequency $\omega$ in the reference is replaced by $\omega = -i\lambda$. By following a standard finite element approach, the same matrix form as defined in Eq. (13.5) can be obtained. The dynamics stiffness matrix $\mathbf{K}$ becomes

$$\mathbf{K} = \begin{bmatrix} K_{R11} & 0 & 0 & K_{R12} & 0 & 0 \\ 0 & K_{B11} & K_{B12} & 0 & K_{B13} & K_{B14} \\ 0 & K_{B21} & K_{B22} & 0 & K_{B23} & K_{B24} \\ K_{R21} & 0 & 0 & K_{R22} & 0 & 0 \\ 0 & K_{B31} & K_{B32} & 0 & K_{B33} & K_{B34} \\ 0 & K_{B41} & K_{B42} & 0 & K_{B43} & K_{B44} \end{bmatrix}, \tag{13.13}$$

where $K_{Rij}$ and $K_{Bij}$ are components of $\mathbf{K_R}$ and $\mathbf{K_B}$, respectively.

$$\mathbf{K_R} = \int EA\mathbf{N_R'}^T\mathbf{N_R'}dx + \lambda_j^2\int \rho A\mathbf{N_R}^T\mathbf{N_R}dx, \tag{13.14}$$

$$\mathbf{K_B} = \int EI\mathbf{N_R''}^T\mathbf{N_B''}dx + \lambda_j^2\int \rho A\mathbf{N_R}^T\mathbf{N_B}dx. \tag{13.15}$$

The equivalent nodal nonlinear force term $\mathbf{Q_N}$ becomes

$$\mathbf{Q_N} = \begin{Bmatrix} \int N_{R1}\hat{F}_{Rj}dx \\ \int N_{B1}\hat{F}_{Bj}dx \\ \int N_{B2}\hat{F}_{Bj}dx \\ \int N_{R2}\hat{F}_{Rj}dx \\ \int N_{B3}\hat{F}_{Bj}dx \\ \int N_{B4}\hat{F}_{Bj}dx \end{Bmatrix} \tag{13.16}$$

where the terms $N_{Ri}$ and $N_{Bi}$ are elements of $\mathbf{N_R}$ and $\mathbf{N_B}$, respectively. The general spectral nodal displacement vector is defined as $\mathbf{q}_j = \begin{bmatrix} \hat{u}_1 & \hat{w}_1 & \hat{\theta}_1 & \hat{u}_2 & \hat{w}_2 & \hat{\theta}_2 \end{bmatrix}^T$, where $\hat{\theta}$ is the rotation angle in the wavelet-domain.

### 13.2.3 Alternating Wavelet-Time Finite Element Method

In the wavelet-domain, all the nonlinear terms are in the form of convolutions. Explicit evaluations of convolution operations in iterative procedures are computationally inefficient. Based on Eq. (13.5) for the rod and beam model, an alternating iterative procedure between the wavelet-domain and the time-domain is constructed to solve the nonlinear equations. The initial state is obtained from linear equations by setting the nonlinear terms as zero. For each iteration, new nodal values of the nonlinear terms are calculated in the time-domain from the current states. The results are transformed into the wavelet-domain and a spectral finite element approach is employed to obtain new nodal values of the unknowns. All nodal information is then transformed back to the time-domain to calculate the new values of the residual nonlinear forces terms for use in the next iteration. This process is continued until a predefined error measure is less than a given tolerance. For more details of AWT-FEM, refer to [10].

## 13.3 Numerical Simulations

In this section, results are presented for numerical simulations performed with a nonlinear rod model and a nonlinear beam model.

### 13.3.1 Rod

The parameters and the values used in the simulations for a materially nonlinear rod are listed in Table 13.1. In practical situations, the axial load is often applied onto the free end of a rod. Two different boundary conditions are considered. Free-free boundaries approximating the conditions for a suspended rod are shown in Fig. 13.1a. Clamped-free boundaries constrain the axial motion of one end, as shown in Fig. 13.1b. The Daubechies wavelet with an order of $N = 14$ is used for the spectrally-uncoupled wavelet transform and can yield sufficient smoothness in the responses. Fifty elements are used for the AWT-FEM meshing.

An impulse in the velocity is created by the impact load at 0.1 ms. The wave is reflected by the free end and travels back to the impacted position at 0.9 ms. The response at the impacted position is shown in Fig. 13.2. Detailed comparison between the linear and nonlinear responses are shown in the insert of Fig. 13.2. The differences between them are small. Response component $V_d$ is defined as the difference between the nonlinear response $V_n$ and the linear response $V_l$ by the formula $V_d = V_n - V_l$. The propagation of the nonlinear wave and the nonlinear component $V_d$ are shown in Figs. 13.3 and 13.4, respectively. In this free-free rod, the absolute value of the nonlinear component $V_d$ has a maximum velocity value of about 21%. At the impacted position, the nonlinear component $V_d$ is small enough to be neglected.

For the clamped-free rod, the wave shape is reversed by the clamped boundary and travels back to the impacted position. Strong nonlinear behavior is observed at the impacted position, as shown in Fig. 13.5. A distortion of the wave shape resulting

**Table 13.1** System parameters of a rod

| Parameter | Value |
|---|---|
| Elastic modulus, $E$ | 70 GPa |
| Cross section, $A$ | $\pi \times 25$ mm $\times 25$ mm |
| Mass density, $\rho$ | 2,800 kg/m$^3$ |
| Rod length, $L$ | 2 m |
| Time window, $T$ | 1 ms |
| Impact duration, $T_p$ | 50 $\mu$s |
| Impact amplitude, $T_a$ | 100 kN |
| Sampling frequency, $f$ | 1,000 kHz |
| Nonlinear coefficient, $\alpha$ | 20 |
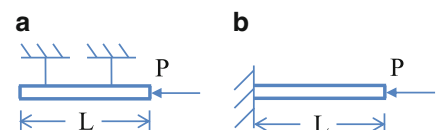


**Fig. 13.1** (**a**) Free-free rod; (**b**) Clamped-free rod

**Fig. 13.2** Comparison between the nonlinear and linear velocity response of the free-free rod at the impacted position
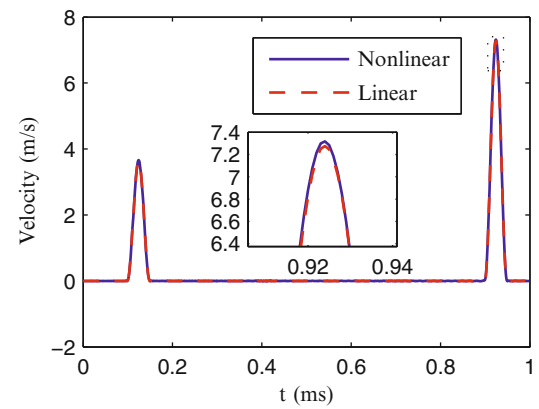


**Fig. 13.3** Velocity wave propagation in the free-free rod
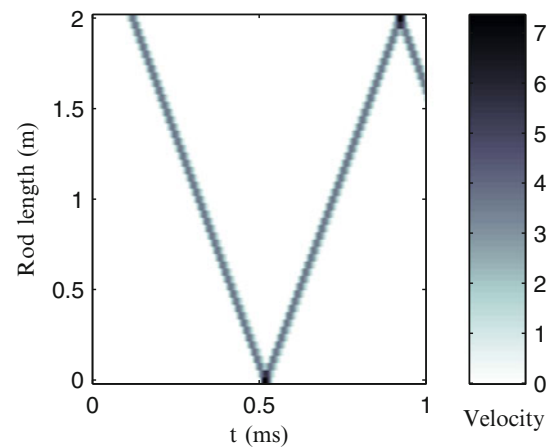


**Fig. 13.4** Velocity wave propagation of the nonlinear portion $V_d$ in the free-free rod
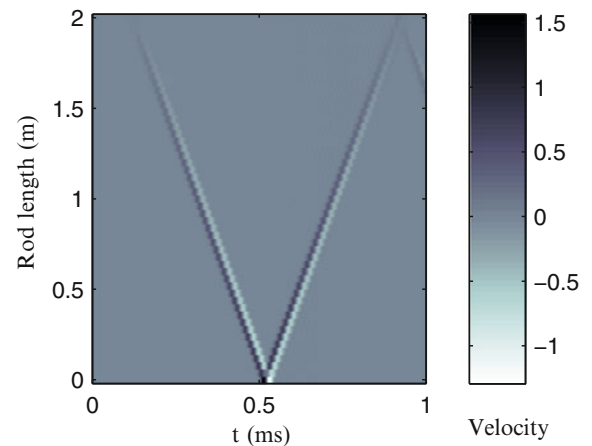


from nonlinear dispersion is captured in the insert of Fig. 13.5. The propagation of the nonlinear wave and the nonlinear component $V_d$ are shown in Fig. 13.6 and 13.7, respectively. In this clamped-free rod, the absolute value of the nonlinear component $V_d$ has a maximum velocity value of about 47%. This indicates that the fixed constraint at the left-end increases the influence of the nonlinear dispersion in the response.

## 13.3.2 Beam

The parameters and the values used in the simulations for a geometrically nonlinear beam are listed in Table 13.2. The impact load is applied at the middle of the beam. Two different boundary conditions are considered. Hinged-hinged boundaries enable the beam to slide and have no constraint on the axial motion, as shown in Fig. 13.8a. Pinned-pinned boundaries

**Fig. 13.5** Comparison between
the nonlinear and linear velocity
response of the clamped-free rod
at the impacted position



**Fig. 13.6** Velocity wave
propagation in the clamped-free
rod
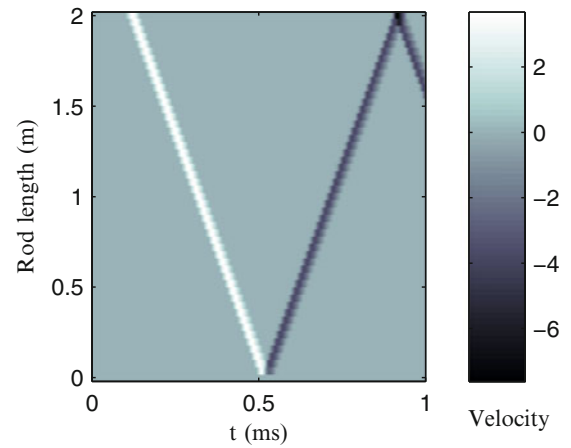


**Fig. 13.7** Velocity wave
propagation of the nonlinear
portion $V_d$ in the clamped-free
rod
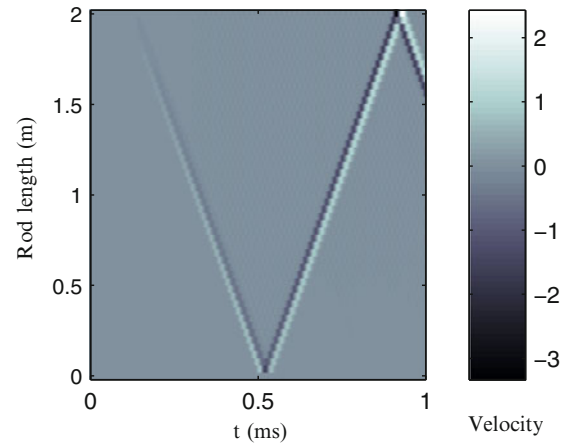


**Table 13.2** System parameters
of a beam

| Parameter | Value |
| --- | --- |
| Elastic modulus, $E$ | 70 GPA |
| Cross section, $A$ | 25×25 mm |
| Mass density, $\rho$ | 2,800 kg/m$^2$ |
| Beam length, $L$ | 1 m |
| Time window, $T$ | 1 ms |
| Impact duration, $T_p$ | 50 $\mu$s |
| Sampling frequency, $f$ | 1,000 kHz |

**Fig. 13.8** (**a**) Hinged-hinged
beam; (**b**) Pinned-pinned beam
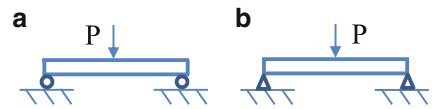


**Fig. 13.9** Comparison between
the nonlinear and linear velocity
response of the hinged-hinged
beam at the impacted position
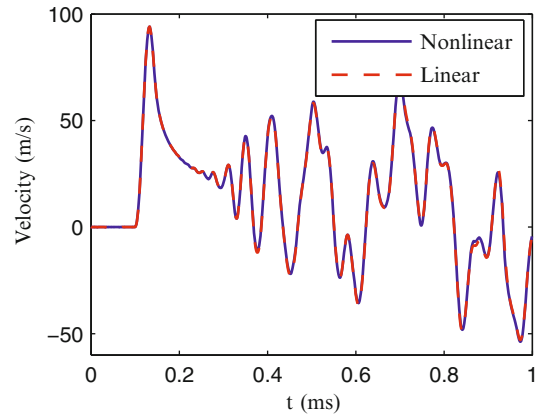


**Fig. 13.10** Velocity wave
propagation in the hinged-hinged
beam
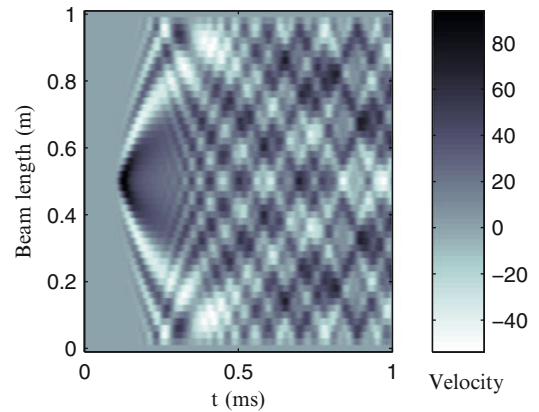


**Fig. 13.11** Velocity wave
propagation of the nonlinear
portion $V_d$ in the hinged-hinged
beam
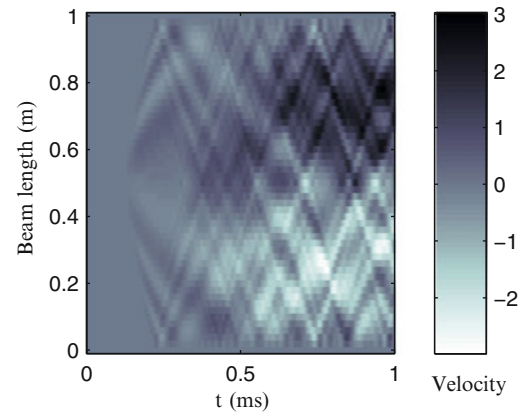


constrain the axial motions and only enable rotations at both ends, as shown in Fig. 13.8b. The Daubechies wavelet with an order of $N = 14$ is used for the spectrally-uncoupled wavelet transform and can yield sufficient smoothness in the responses. Fifty elements are used for the AWT-FEM meshing.

Lateral waves in beam are highly dispersive. For the hinged-hinged beam, the comparison between the nonlinear and linear responses is shown in Fig. 13.9 and the results are very close to each other. The propagation of the nonlinear wave and the nonlinear component $V_d$ are shown in Figs. 13.10 and 13.11, respectively. The absolute value of the nonlinear component $V_d$ has a maximum velocity value of about 3.5%.

For the pinned-pinned beam, the comparison between the nonlinear and linear responses is shown in Fig. 13.12. A nonlinear behavior is identified in the insert of Fig. 13.12. The wave shape is being shifted to the left resulting from

**Fig. 13.12** Comparison between the nonlinear and linear velocity response of the pinned-pinned beam at the impacted position
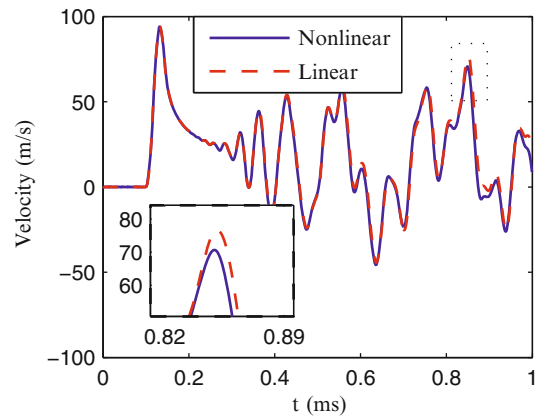


**Fig. 13.13** Velocity wave propagation in the pinned-pinned beam



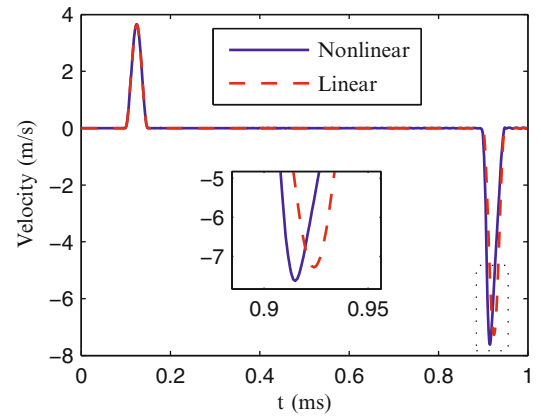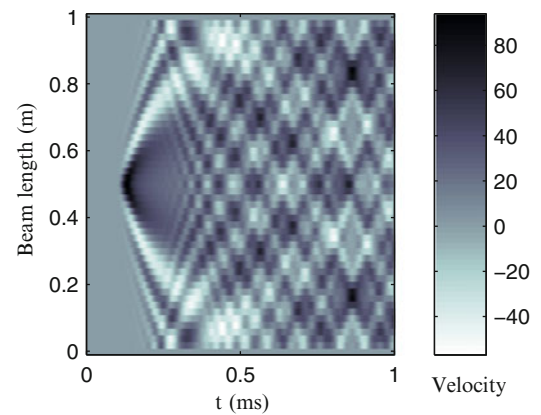**Fig. 13.14** Velocity wave propagation of the nonlinear portion $V_d$ in the pinned-pinned beam
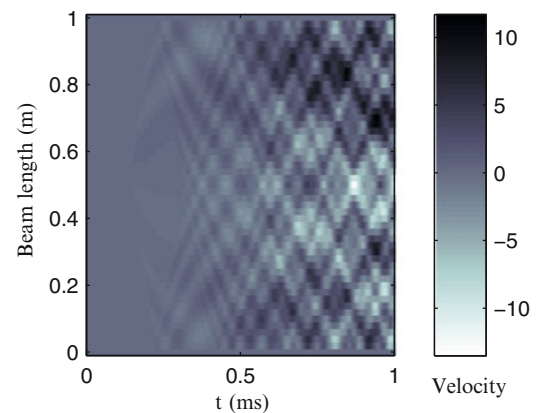


the introduced nonlinear dispersion. As shown in Figs. 13.13 and 13.14, The absolute value of the nonlinear component $V_d$ has a maximum velocity value of about 17.6%. This indicates that the axial constraints significantly strengthen the nonlinear behavior introduced by the geometric nonlinearity in the beam.

## 13.4 Concluding Remarks

In this paper, the alternating wavelet-time finite element method is applied to study the influence of boundary constraints on the nonlinear behavior in the wave propagation through simple structures. The results of numerical simulations demonstrate that axial constraints can further strengthen the nonlinear dispersion introduced by both material and geometric nonlinearities in rod and beam structures. Experimental works will be conducted in the future to verify this numerical study.

# References

1. Meo M, Zumpano G (2005)  Nonlinear elastic wave spectroscopy identification of impact damage on a sandwich plate.  Compos Struct 71(3–4):469–474
2. Johnson PA, Jia X (2005) Nonlinear dynamics, granular media and dynamic earthquake triggering. Nature 437(7060):871–874
3. Taylor P, Ford C (2009)  Simulation of blast-induced early-time intracranial wave physics leading to traumatic brain injury.  J Biomech Eng 131(6):61007–61018
4. Ham S, Bathe K (2012) A finite element method enriched for wave propagation problems. Comput Struct 94–95:1–12
5. Idesman A (2007) A new high-order accurate continuous galerkin method for linear elastodynamics problems. Comput Mech 40(2):261–279
6. Lee U, Jang I (2011)  Nonlinear spectral element model for the blood flow in human arteries.  In: Proceedings of the 2011 international symposium of computational models for life sciences, pp 136–145. Toyama City, Japan
7. Liu Y, Ghaderi P, Dick A (2012)  High fidelity methods for modeling nonlinear wave propagation in one-dimensional waveguides.  In: Proceedings of the ASME 2012 international mechanical engineering congress and exposition. Houston, TX
8. Doyle J (1997) Wave propagation in structures. Springer, Berlin
9. Williams JR, Amaratunga K (1997)  A discrete wavelet transform without edge effects using wavelet extrapolation.  J Fourier Anal Appl 3(4):435–449
10. Liu Y, Dick A (2013)  Alternating wavelet-time finite element method: Modeling and analysis of nonlinear wave propagation in one and two-dimensional waveguides (submitted). J Sound Vib
11. Nayfeh A, Mook D (1995) Nonlinear oscillations. Wiley, New York
12. Ramabathiran A, Gopalakrishnan S (2012)  Time and frequency domain finite element models for axial wave analysis in hyperelastic rods. Mech Adv Mater Struct 19(1–3):79–99
13. Li J, Zhang Y (2008) Exact travelling wave solutions in a nonlinear elastic rod equation. Appl Math Comput 202(2):504–510
14. Mitra M, Gopalakrishnan S (2005)  Spectrally formulated wavelet finite element for wave propagation and impact force identification in connected 1-d waveguides. Int J Solids Struct 42(16):4695–4721
15. Reddy J (2004) An introduction to nonlinear finite element analysis. Oxford University Press, Oxford

# Chapter 14
# Evaluation of On-Line Algebraic Modal Parameter Identification Methods

**F. Beltrán-Carbajal, G. Silva-Navarro, and L.G. Trujillo-Franco**

**Abstract**  This paper describes the application of a novel time domain and on-line algebraic modal parameter identification methodology based on differential algebra, module theory and Mikusiński operational calculus for mechanical structures with multiple degrees-of-freedom. The natural frequencies and damping ratios associated to a mechanical system are estimated in an on-line fashion from transient state real-time measurements (e.g., displacements or accelerations). The proposed identification methodology can be also extended for modal parameter identification using experimental frequency response functions. A comparison with usual modal identification techniques is performed in order to evaluate and establish the main contributions of the proposed approach. Some numerical and experimental results are included to show the efficient and robust performance and fast parametric estimation of the proposed algebraic identification approach.

**Keywords**  Modal parameter identification • On-line algebraic identification • Multi-degrees-of-freedom mechanical structures • Mikusiński operational calculus

## 14.1  Introduction

Modal parameter identification is a quite challenging and active area for analysis, modeling, design, control and monitoring of mechanical systems. Certainly, numerous identification algorithms in time or frequency domain have been reported in the literature, mainly in case of off-line estimation of modal parameters for mechanical system with multiple degrees-of-freedom (see, e.g., [1–8] and references therein). Most of these techniques, however, are essentially asymptotic, recursive, complex and slow for on-line parameter estimation implementations, using some minimum sensor number and persisting excitation, which could be required for efficient adaptive active noise and vibration control and other practical applications on dynamic mechanical structures [9–11].

On the other hand, a theoretical framework for algebraic parameter identification for continuous-time and invariant linear systems has recently been introduced by Fliess and Sira-Ramírez [12]. This identification approach is based on well-known powerful mathematical tools as module theory, differential algebra and operational calculus. It is important to remark that the operational calculus is a quite general approach based on different integral transformations of functions and generalized functions (e.g., Fourier, Laplace, Stieltjes, Hilbert, Bessel) [13, 14]. The application of operational calculus in mechanics is quite common in the transformation of functions from time to frequency domain and to solve differential equations.

In addition, an algebraic identification methodology has been proposed by Beltran-Carbajal and Silva-Navarro [15] to sequentially and quickly estimate system parameters, such as mass, stiffness and viscous damping, to adaptively control multiple degrees-of-freedom mass-spring-damper mechanical systems using on-line measurements of input-output data.

F. Beltrán-Carbajal

Departamento de Energía, Universidad Autónoma Metropolitana, Unidad Azcapotzalco, Av. San Pablo No. 180,
Col. Reynosa Tamaulipas, C.P. 02200 México, D.F., Mexico
e-mail: fbeltran@correo.azc.uam.mx

G. Silva-Navarro (✉) • L.G. Trujillo-Franco

Departamento de Ingeniería Eléctrica, Sección de Mecatrónica, Centro de Investigación y de Estudios Avanzados del I.P.N.,
Av. IPN No. 2508, Col. S.P. Zacatenco, C.P. 07360 México, D.F., Mexico
e-mail: gsilva@cinvestav.mx; forest_6@hotmail.com

On-line algebraic reconstruction of disturbance harmonic forces has also been introduced for adaptive-like vibration absorption by Beltran-Carbajal and Silva-Navarro [16]. Furthermore, algebraic identification methods for the simultaneous parameter estimation of mass, damping, stiffness and rotor eccentricity as well as on-line reconstruction of unknown centrifugal forces induced by rotor unbalance has been presented for active unbalance control on rotor-bearing systems by Beltran-Carbajal, Silva-Navarro and Arias-Montiel [17].

This paper proposes an on-line and time domain algebraic identification approach for the estimation of modal parameters on multiple degrees-of-freedom mechanical structures under free vibration condition. The values of the coefficients of the characteristic polynomial of the mechanical system are firstly estimated in a real-time manner, and then the natural frequencies and damping ratios are computed. During the design process, we have considered that only measurements of some position output variable is available for identification scheme implementations. However, the presented results can be extended to consider acceleration measurements or experimental records from Frequency Response Functions. For illustrative purposes, the algebraic modal parameter identification methodology is verified on a two degrees-of-freedom mechanical system excited by a change in its position initial condition. Some computer simulation results have been included to show the satisfactory performance of the proposed identification approach for the fast and effective estimation of the coefficients of the characteristic polynomial, natural frequencies and damping ratios.

## 14.2  Vibrating Mechanical System

Consider the $n$ Degrees-Of-Freedom (DOF) vibrating mechanical system shown in Fig. 14.1, where $x_i$, $i = 1, 2, \ldots, n$, are the displacements of $n$ mass carriages moving on rectilinear guides over a rigid platform, and $m_i$, $k_i$ and $c_i$ denote mass, stiffness and viscous damping associated to the $i$-th degree-of-freedom.

The mathematical model of this flexible mechanical system of $n$ DOF under free vibration condition is given by the ordinary differential equation

$$\mathbf{M}\ddot{\mathbf{x}} + \mathbf{C}\dot{\mathbf{x}} + \mathbf{K}\mathbf{x} = \mathbf{0}, \quad \mathbf{x} \in \mathbf{R}^n \tag{14.1}$$

where $\mathbf{x}$ is the vector of generalized coordinates (displacements), and $\mathbf{M}$, $\mathbf{C}$ and $\mathbf{K}$ are symmetric inertia, damping and stiffness $n \times n$ matrices, respectively, given by

$$\mathbf{M} = \begin{bmatrix} m_1 & 0 & 0 \ldots 0 & 0 \\ 0 & m_2 & 0 \ldots 0 & 0 \\ 0 & 0 & m_3 \ldots 0 & 0 \\ \vdots & & & \\ 0 & 0 & 0 \ldots 0 & m_n \end{bmatrix}, \quad \mathbf{C} = \begin{bmatrix} c_1 & 0 & 0 \ldots 0 & 0 \\ 0 & c_2 & 0 \ldots 0 & 0 \\ 0 & 0 & c_3 \ldots 0 & 0 \\ \vdots & & & \\ 0 & 0 & 0 \ldots 0 & c_n \end{bmatrix}, \quad \mathbf{K} = \begin{bmatrix} k_1 + k_2 & -k_2 & 0 \ldots & 0 & 0 \\ -k_2 & k_2 + k_3 & -k_3 \ldots & 0 & 0 \\ 0 & -k_3 & k_3 + k_4 \ldots & 0 & 0 \\ \vdots & & & & \\ 0 & 0 & 0 \ldots -k_n & k_n + k_{n+1} \end{bmatrix}$$

It is easy to verify that the system (14.1) is completely controllable and observable, stable when $\mathbf{K}$ is positive definite and $\mathbf{C} \equiv \mathbf{0}$, and asymptotically stable when $\mathbf{C}$ is positive definite (see, e.g., Inman [18]).

It is well-known that, the mathematical model (14.1) can be transformed to modal (principal) coordinates $q_i$, $i = 1, 2, \ldots, n$, as follows (see, e.g., [1])

$$\ddot{q}_i + 2\zeta_i \omega_i \dot{q}_i + \omega_i^2 q_i = 0 \tag{14.2}$$

with

$$\mathbf{x}(t) = \mathbf{\Psi}\mathbf{q}(t) \tag{14.3}$$
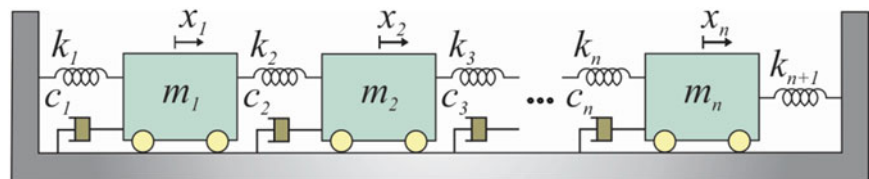


Fig. 14.1  Schematic diagram of a $n$ DOF mass-spring-damper system

where $\omega_i$ and $\zeta_i$ are the natural frequencies and damping ratios associated to the $i$-th vibration mode, respectively, and $\mathbf{\Psi}$ is the so-called $n \times n$ modal matrix given by

$$\mathbf{\Psi} = \begin{bmatrix} \psi_{11} & \psi_{12} & \ldots & \psi_{1n-1} & \psi_{1n} \\ \psi_{21} & \psi_{22} & \ldots & \psi_{2n-1} & \psi_{2n} \\ & \vdots & & & \\ \psi_{n-11} & \psi_{n-12} & \ldots & \psi_{n-1n-1} & \psi_{n-1n} \\ \psi_{n1} & \psi_{n2} & \ldots & \psi_{nn-1} & \psi_{nn} \end{bmatrix} \tag{14.4}$$

In notation of Mikusiński operational calculus [11, 12], the modal analysis representation or modal model (14.2) is described as

$$\left(s^2 + 2\zeta_i \omega_i s + \omega_i^2\right) q_i(s) = p_{0,i} + p_{1,i} s \tag{14.5}$$

where $p_{0,i}$ are constants depending on the system initial conditions at the time $t_0 \geq 0$.

From Eqs. 14.3 and 14.5, one then obtains that

$$x_i(s) = \sum_{j=1}^{n} \frac{\psi_{ij}\left(p_{0,j} + p_{1,j} s\right)}{s^2 + 2\zeta_j \omega_j s + \omega_j^2} \tag{14.6}$$

Therefore, the physical displacements $x_i$ are given by

$$p_c(s)\, x_i(s) = r_{0,i} + r_{1,i} s + \cdots + r_{2n-2,i} s^{2n-2} + r_{2n-1,i} s^{2n-1} \tag{14.7}$$

with

$$p_c(s) = s^{2n} + a_{2n-1} s^{2n-1} + \cdots + a_1 s + a_0 \tag{14.8}$$

where $p_c(s)$ is the characteristic polynomial of the mechanical system and $r_{i,j}$ are constants which can be easily calculated by using the values of the system initial conditions as well as the modal matrix components $\psi_{ij}$.

It is widely known that the roots of the characteristic polynomial (14.8) provide the damping factors and damped natural frequencies, and hence the natural frequencies and damping ratios of the flexible structure. Here, we propose an on-line algebraic identification approach to estimate the modal parameters of the mechanical system through the real-time estimation of the positive coefficients $a_k$ of the system's characteristic polynomial using only position measurements of some output variable.

**Remark** Note that, the mathematical model (14.1) can describe any general $n$ DOF mechanical system, including exogenous forces. Direct parameter identification of the system parameters as mass, stiffness and damping can be realized using algebraic parameter identification methods described in [15–17], where some comparisons with ARX and ARMAX methods are discussed. However, in typical experimental modal analysis techniques one starts from a modal model (14.2) associated to a Frequency Response Function, from output only data (e.g., simple excitation via initial conditions) or input-output data (e.g., impact hammer testing, sine sweep testing using shakers), whose modal parameters are estimated using modal parameter estimation techniques like *Peak Peaking*, *Curve Fitting*, etc. in order to get estimations of the modal parameters [1]. Here we propose a reliable extension of the algebraic parameter identification methods in [16] for general $n$ DOF modal models, which are fast and effective.

## 14.3 On-Line Algebraic Parameter Identification of Modal Parameters

Consider the mathematical model (14.7), where only measurements of some position variable $x_i$ is available to be used in the synthesis of an on-line algebraic identification scheme for the fast and effective estimation of the coefficients $a_k$ of the system's characteristic polynomial in time domain. Moreover, we assume that the mechanical system is solely excited by an initial condition change. Therefore, the parameter identification should be performed using the system transient response alone, avoiding the use of additional force actuators and, consequently, achieving a significant reduction in the implementation costs.

In order to eliminate the influence of the unknown constants $r_{i,j}$, Eq. 14.7 are differentiated four times with respect to the complex variable $s$:

$$
\sum_{k=0}^{2n} \frac{(2n)!\,(2n)!}{k!\,(2n-k)!\,(2n-k)!} s^{2n-k} \frac{d^{2n-k}}{ds^{2n-k}} x_i(s) + a_{2n-1} \sum_{k=0}^{2n-1} \frac{(2n)!(2n-1)!}{k!(2n-k)!(2n-1-k)!} s^{2n-1-k} \frac{d^{2n-k}}{ds^{2n-k}} x_i(s)
$$
$$
+ a_{2n-2} \sum_{k=0}^{2n-2} \frac{(2n)!\,(2n-2)!}{k!\,(2n-k)!\,(2n-2-k)!} s^{2n-2-k} \frac{d^{2n-k}}{ds^{2n-k}} x_i(s) + \cdots
$$
$$
+ a_1 \sum_{k=0}^{1} \frac{(2n)!(1)!}{k!\,(2n-k)!\,(1-k)!} s^{1-k} \frac{d^{2n-k}}{ds^{2n-k}} x_i(s) + a_0 \frac{d^{2n}}{ds^{2n}} x_i(s) = 0 \tag{14.9}
$$

where $\frac{d^0}{ds^0} x_i(s) = x_i(s)$.

Next, to avoid differentiation with respect to time, Eq. 14.9 are multiplied by $s^{-4}$ and transformed back to the time domain:

$$
\sum_{k=0}^{2n} (-1)^{2n-k} \frac{(2n)!\,(2n)!}{k!\,(2n-k)!\,(2n-k)!} \int_{t_0}^{(k)} (\Delta t)^{2n-k} x_i(t) + a_{2n-1} \sum_{k=0}^{2n-1} (-1)^{2n-k} \frac{(2n)!\,(2n-1)!}{k!\,(2n-k)!\,(2n-1-k)!} \int_{t_0}^{(1+k)} (\Delta t)^{2n-k} x_i(t)
$$
$$
+ a_{2n-2} \sum_{k=0}^{2n-2} (-1)^{2n-k} \frac{(2n)!\,(2n-2)!}{k!\,(2n-k)!\,(2n-2-k)!} \int_{t_0}^{(2+k)} (\Delta t)^{2n-k} x_i(t)
$$
$$
+ \cdots + a_1 \sum_{k=0}^{1} (-1)^{2n-k} \frac{(2n)!(1)!}{k!\,(2n-k)!\,(1-k)!} \int_{t_0}^{(2n-1+k)} (\Delta t)^{2n-k} x_i(t) + a_0 (-1)^{2n} \int_{t_0}^{(2n)} (\Delta t)^{2n} x_i(t) = 0
$$
$$
\tag{14.10}
$$

where $\Delta t = t - t_0$, and $\int_{t_0}^{(N)} \phi(t)$ are iterated integrals of the form $\int_{t_0}^{t} \int_{t_0}^{\sigma_1} \cdots \int_{t_0}^{\sigma_{N-1}} \phi(\sigma_N)\, d\sigma_N \ldots d\sigma_1$ with $\int_{t_0}^{(1)} \phi(t) = \int_{t_0}^{t} \phi(\sigma)\, d\sigma$, $\int_{t_0}^{(0)} \phi(t) = \phi(t)$ and $N$ a positive integer.

The integral-type equations (14.10), after some more integrations, leads to the following linear system of equations:

$$
\mathbf{A}(t)\boldsymbol{\theta} = \mathbf{B}(t) \tag{14.11}
$$

where $\boldsymbol{\theta} = \begin{bmatrix} a_0 & a_1 & \cdots & a_{n-1} & a_n \end{bmatrix}^T$ denotes the parameter vector to be identified, $\mathbf{A}(t)$ and $\mathbf{B}(t)$ are $n \times n$ and $n \times 1$ matrices, respectively, described by

$$
\mathbf{A} = \begin{bmatrix}
a_{11} & a_{1,2} & \ldots & a_{1n-1} & a_{1n} \\
a_{21} & a_{22} & \ldots & a_{2n-1} & a_{2n} \\
\vdots & & & & \\
a_{n-11} & a_{n-12} & \ldots & a_{n-1n-1} & a_{n-1n} \\
a_{n1} & a_{n2} & \ldots & a_{nn-1} & a_{nn}
\end{bmatrix}, \quad
\mathbf{B} = \begin{bmatrix}
b_1 \\
b_2 \\
\vdots \\
b_{n-1} \\
b_n
\end{bmatrix}
$$

with

$$a_{11} = (-1)^{2n} \int_{t_0}^{(2n)} (\Delta t)^{2n} x_i(t)$$

$$a_{12} = \sum_{k=0}^{1} (-1)^{2n-k} \frac{(2n)!(1)!}{k!(2n-k)!(1-k)!} \int_{t_0}^{(2n-1+k)} (\Delta t)^{2n-k} x_i(t)$$

$$\vdots$$

$$a_{1n-1} = \sum_{k=0}^{2n-2} (-1)^{2n-k} \frac{(2n)!(2n-2)!}{k!(2n-k)!(2n-2-k)!} \int_{t_0}^{(2+k)} (\Delta t)^{2n-k} x_i(t)$$

$$a_{1n} = \sum_{k=0}^{2n-1} \frac{(2n)!(2n-1)!}{k!(2n-k)!(2n-1-k)!} s^{-1-k} \frac{d^{2n-k}}{ds^{2n-k}} x_i(s)$$

$$b_1 = -\sum_{k=0}^{2n} (-1)^{2n-k} \frac{(2n)!(2n)!}{k!(2n-k)!(2n-k)!} \int_{t_0}^{(k)} (\Delta t)^{2n-k} x_i(t)$$

By solving Eq. 14.11 one obtains the parameter vector $\theta$ as

$$\boldsymbol{\theta} = \mathbf{A}^{-1}\mathbf{B} = \frac{1}{\Delta} \begin{bmatrix} \Delta_1 \\ \Delta_2 \\ \vdots \\ \Delta_{n-1} \\ \Delta_n \end{bmatrix} \tag{14.12}$$

Then, we propose the following algebraic identifiers to estimate the coefficients $a_k$ of the characteristic polynomial without problems of singularities when the determinant $\Delta = \det(\mathbf{A}(t))$ crosses by zero:

$$\widehat{a}_k = \frac{\int |\Delta_{k-1}|}{\int |\Delta|}, \quad k = 1, 2, \ldots, 2n-1 \tag{14.13}$$

In the above expression we can apply more integrations on the numerator and denominator to get smoother estimations but introducing slower responses.

Thus, one could implement the algebraic identifiers (14.13) using only those available position measurements $x_i$ of any specific mass carriage. From the estimated coefficients $\widehat{a}_k$, one can obtain the roots of the characteristic polynomial as follows

$$\widehat{\lambda}_i = \widehat{\sigma}_i + j\widehat{\omega}_{di}, \quad \widehat{\lambda}_i^* = \widehat{\sigma}_i - j\widehat{\omega}_{di}, \quad i = 1, 2, \ldots, n \tag{14.14}$$

where $\widehat{\sigma}_i$ and $\widehat{\omega}_{di}$ are estimates of the damping factors and damped natural frequencies of the mechanical system, respectively. Hence, the estimates of the natural frequencies and damping ratios are given by

$$\widehat{\omega}_{ni} = \sqrt{\widehat{\sigma}_i^2 + \widehat{\omega}_{di}^2}, \quad \widehat{\zeta}_i = -\frac{\widehat{\sigma}_i}{\sqrt{\widehat{\sigma}_i^2 + \widehat{\omega}_{di}^2}} \tag{14.15}$$

Note that, this identification approach can also be extended to the case of acceleration sensors, instead of displacement measurements. Specifically, one could simply multiply Eq. 14.6 by $s^2$ and describe an acceleration output as

$$y_i(s) = \sum_{j=1}^{n} \frac{\psi_{ij}\left(p_{0,j}s^2 + p_{1,j}s^3\right)}{s^2 + 2\zeta_j\omega_j s + \omega_j^2} \tag{14.16}$$

where $y_i(s) = s^2 x_i(s)$ is some acceleration output variable described in complex $s$ domain, and then follow the proposed algebraic identification methodology.

**Table 14.1** Mechanical system parameters for two DOF

| $m_1 = 1.2678$ kg | $m_2 = 1.3317$ kg | $k_3 = 360$ N/m |
|---|---|---|
| $c_1 = 2.9$ Ns/m | $c_2 = 1.7$ Ns/m | – |
| $k_1 = 178$ N/m | $k_2 = 360$ N/m | – |

**Fig. 14.2** Free vibration response of the first mass carriage $x_1$ and experimental FRF computed from a sine sweep from 0.1 to 10 Hz and constant force of 1.0 N
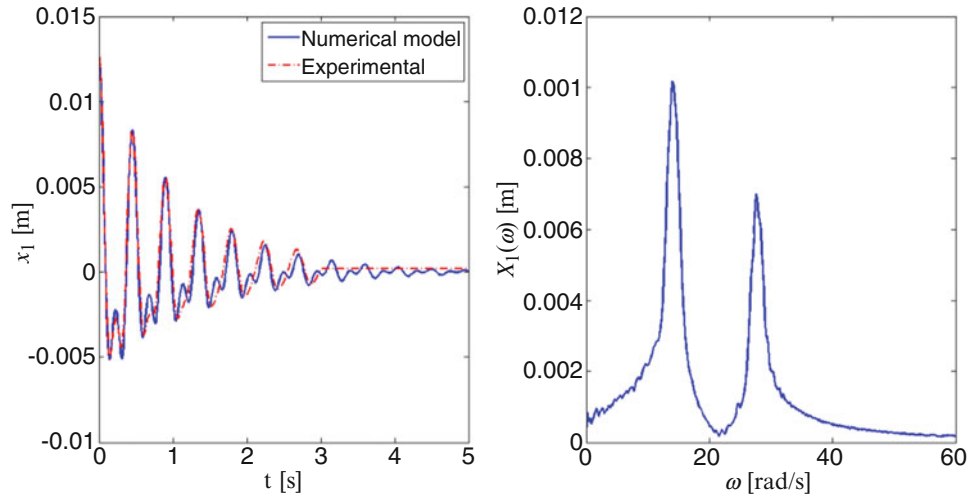


Moreover, one could replace $x_i(s)$ into Eq. 14.6 by some Frequency Response Function $H_i(\omega)$:

$$H_i(\omega) = \sum_{i=1}^{n} \rho_i(j\omega) \left( \frac{A_i}{j\omega - \lambda_i} + \frac{A_i^*}{j\omega - \lambda_i} \right) \tag{14.17}$$

where $\lambda_i$ are the system poles, $A_i$ are the residues and $\rho_i$ are polynomial functions representing the influence of the system initial conditions, and thus synthesize from Eq. 14.6 an algebraic identification scheme for on-line estimation of the modal parameters using some experimental Frequency Response Function.

## 14.4 An Illustrative Case: Simulation and Experimental Results

The experimental setup is a rectilinear mechanical plant (Model 210a) provided by *Educational Control Products®*. The mechanical system consists of two mass carriages, interconnected by bidirectional cylindrical helical springs. Each mass carriage suspension has anti-friction ball bearing systems and, therefore, the linear dashpots are included only to describe small viscous dampings. Each mass carriage has a (rotary) high resolution optical encoder to measure its actual positions via cable-pulley systems (with effective resolutions of 2,266 pulses/cm or $4.413 \times 10^{-3}$ mm/pulse). The signal and algebraic identification are obtained through a high-speed DSP board into a standard PC running under *Windows XP®* and *Matlab®/Simulink®*.

The performance of the proposed on-line algebraic modal parameter identification approach was numerically and experimentally verified on a two-DOF mechanical system with the set of physical system parameters given in Table 14.1.

Therefore, the actual values of the characteristic polynomial coefficients can be easily computed as: $a_0 = 1.5267 \times 10^5$, $a_1 = 1,778.44$, $a_2 = 967.94$, $a_3 = 3.564$, with corresponding modal parameters $\omega_{n1} = 14.1244$ rad/s, $\zeta_1 = 0.06679$, $\omega_{n2} = 27.6636$ rad/s and $\zeta_2 = 0.03032$. Here we only employ measurements of the position of the first mass carriage $x_1$.

The application of the algebraic identification scheme in Eqs. 14.13, 14.14 and 14.15 was performed in the numerical case using Runge-Kutta 4/5 methods with fixed step time of 9 ms and for the real-time (experimental) algebraic estimation case using cumulative trapezoidal numerical integration with fixed sampling time of 9 ms. In both cases the initial conditions were $x_1(0) = 0.01275$ m, $\dot{x}_1(0) = 0$ m/s, $x_2(0) = 0$ m and $\dot{x}_0(0) = 0$ m/s. The numerical and experimental transient response for the displacement $x_1$ and FRF computed only for the experimental data are shown in Fig. 14.2.

The algebraic estimation of the coefficients of the fourth order characteristic polynomial of the two DOF system is described in Fig. 14.3. Note the satisfactory performance of the algebraic identifiers (14.13), (14.14) and (14.15), using only measurements of the position output variable $x_1$. The effective and fast estimation of the coefficients of the characteristic
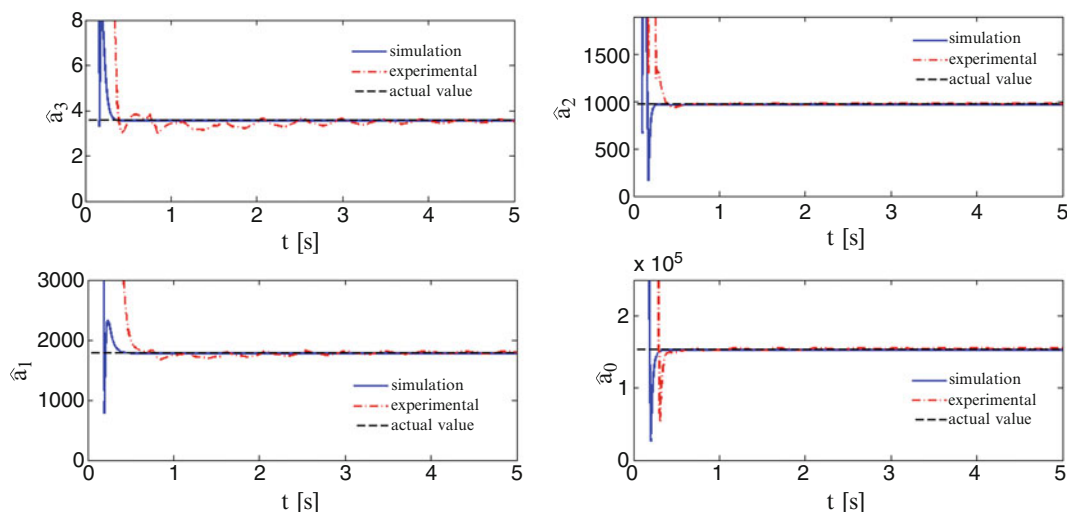
**Fig. 14.3** On-line algebraic identification of the characteristic polynomial coefficients of a two-DOF system

**Table 14.2** Algebraic estimation of coefficients of the fourth characteristic polynomial

| Procedure | $\widehat{a}_0$ | $\widehat{a}_1$ | $\widehat{a}_2$ | $\widehat{a}_3$ |
|---|---|---|---|---|
| Actual coefficients | $1.5267 \times 10^5$ | 1,778.44 | 967.94 | 3.564 |
| Algebraic estimation (numerical) | $1.527 \times 10^5$ | 1,778.0 | 968.1 | 3.564 |
| Algebraic estimation (experimental) | $1.543 \times 10^5$ | 1,793.0 | 980.4 | 3.534 |
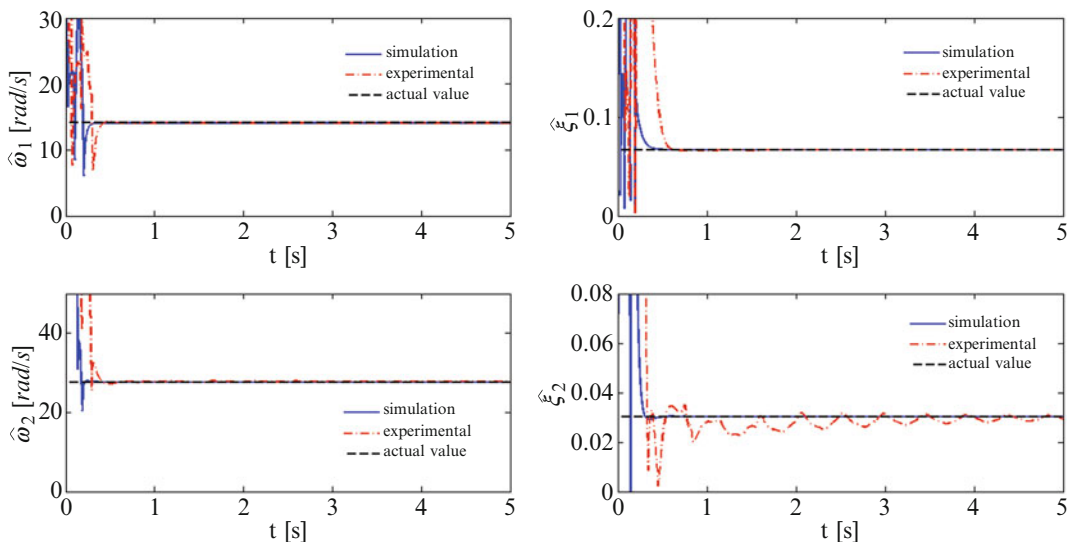


**Fig. 14.4** On-line algebraic identification of the modal parameters for the two-DOF system

polynomial, $a_0$, $a_1$, $a_2$ and $a_3$, for the two DOF mass-spring-damper mechanical system is quite evident, which makes possible the indirect estimation of the modal parameters in a short time about 0.44 s using the transient system response. A summary of the actual, numerical and experimental estimation of polynomial coefficients is presented in Table 14.2. The on-line algebraic estimation of the modal parameters is depicted in Fig. 14.4. In fact, the estimated numerical modal parameters after $t = 0.44$ s are $\widehat{\omega}_{n1} = 14.12$ rad/s, $\widehat{\zeta}_1 = 0.06679$, $\widehat{\omega}_{n2} = 27.67$ rad/s, $\widehat{\zeta}_2 = 0.03029$, which are practically similar to the actual values. The average values of the real-time estimated modal parameters are $\widehat{\omega}_{n1} \approx 14.13$ rad/s, $\widehat{\zeta}_1 \approx 0.06684$, $\widehat{\omega}_{n2} \approx 27.83$ rad/s, $\widehat{\zeta}_2 \approx 0.02932$, which are also good approximations to the actual values in spite of inherent unmodelled dynamics and noisy measurements.

## 14.5  Conclusions

It is proposed an algebraic identification approach for the on-line estimation of the natural frequencies and damping ratios for linear multiple degrees-of-freedom mechanical systems. The values of the coefficients of the characteristic polynomial of the mechanical system are firstly estimated in real-time, and then the modal parameters are obtained. In the design process, we have considered that only measurements of some position output variable is available for the identification scheme implementation. Nevertheless, one could easily extend the results for situations where acceleration measurements are preferred. The algebraic modal parameter identification was tested for a two-DOF mechanical system excited by a change of its position initial condition. In general, the simulation and experimental results show a satisfactory performance of the proposed identification approach with fast and effective estimations.

## References

 1. Heylen W, Lammens S, Sas P (2003) Modal analysis, theory and testing. Katholieke Universiteit Leuven, Belgium
 2. Vu VH, Thomas M, Lafleur F, Marcouiller L (2013) Towards an automatic spectral and modal identification from operational modal analysis. J Sound Vib 332:213–227
 3. Yang Y, Nagarajaiah S (2013) Output-only modal identification with limited sensors using sparse component analysis. J Sound Vib 332:4741–4765
 4. Liao Y, Wells V (2011) Modal parameter identification using the log decrement method and band-pass filters. J Sound Vib 330:5014–5023
 5. Chakraborty A, Basu B, Mitra M (2006) Identification of modal parameters of a mdof system by modified L-P wavelet packets. J Sound Vib 295:827–837
 6. Chen-Far H, Wen-Jiunn K, Yen-Tun P (2004) Identification of modal parameters from measured input and output data using a vector backward auto-regressive with exogenous model. J Sound Vib 276:1043–1063
 7. Cauberghe B, Guillaume P, Verboven P, Parloo E (2003) Identification of modal parameters including unmeasured forces and transient effects. J Sound Vib 265:609–625
 8. Fladung WA, Phillips AW, Allemang RJ (2003) Application of a generalized residual model to frequency domain modal parameter estimation. J Sound Vib 262:677–705
 9. Isermann R, Munchhof M (2011) Identification of dynamic systems. Springer, Berlin
10. Ljung L (1987) Systems identification: theory for the user. Prentice-Hall, Upper Saddle River, NJ
11. Soderstrom T, Stoica P (1989) System identification. Prentice-Hall, New York, NY
12. Fliess M, Sira-Ramírez H (2003) An algebraic framework for linear identification. ESAIM Control Optimiz Calculus Variations 9:151–168
13. Mikusiński J (1983) Operational calculus, vol 1, 2nd edn. PWN & Pergamon, Warsaw, Poland
14. Glaetske HJ, Prudnikov AP, Skrnik KA (2006) Operational calculus and related topics. Chapman and Hall/CRC, Boca Raton, FL
15. Beltran-Carbajal F, Silva-Navarro G (2013) Algebraic parameter identification of multi-degree-of-freedom vibrating mechanical systems. In: Proceedings of the 20th international congress on sound and vibration (ICSV20), Bangkok, Thailand, pp 1–8
16. Beltran-Carbajal F, Silva-Navarro G (2013) Adaptive-like vibration control in mechanical systems with unknown parameters and signals. Asian J Control 15(6):1613–1626
17. Beltran-Carbajal F, Silva-Navarro G, Arias-Montiel M (2013) Active unbalance control of rotor systems using on-line algebraic identification methods. Asian Journal of Control 15(6):1627–1637
18. Inman DJ (2006) Vibration with control. Wiley, NY

# Chapter 15
# Ambient Vibration Test of Granville Street Bridge Before Bearing Replacement

**Yavuz Kaya, Carlos Ventura, and Martin Turek**

**Abstract** The Granville Bridge, which carries eight-lanes of Highway 99 over False Creek in Vancouver, British Columbia, Canada, consists of several concrete approaches and seven steel truss spans. To improve the seismic performance of the bridge, the bearings under the steel truss spans are replaced. As part of this rehabilitation project, a permanent seismic monitoring system will be installed both to monitor the vibration characteristics over a long period of time and analyze the data, and to keep track of the structural health state of the bridge right after extreme events such as earthquake, strong wind, and ship collision. In support of this project, the University of British Columbia is carrying out a two-phase ambient vibration test (AVT). This includes measurements at the deck and at each pier of the steel spans to determine both the modal and vibration characteristics of the bridge before and after the replacement of bearings, and to find optimal locations for the permanent seismic instrumentation. This paper presents the results of the first phase of AVT.

**Keywords** Ambient vibration • Fourier amplitude • Modal identification • Natural frequency • Bridge dynamics

## 15.1 Introduction

The Granville bridge is one of the important bridges that connects downtown Vancouver area with the south Vancouver. It carries eight-lane of Highway 99 over False Creek in Vancouver, and it consists of several concrete approaches and steel truss spans. The City of Vancouver is carrying out a rehabilitation project to improve the seismic performance of the bridge. The project includes the replacement of bearings under the steel trusses with seismic isolation bearings. As part of this rehabilitation project, a permanent seismic monitoring system will be installed both to monitor the vibration characteristics over a long period of time and analyze the data, and to keep track of the structural health state of the bridge right after extreme events such as earthquake, strong wind, and ship collision.

In support of this project, the University of British Columbia (UBC) is carrying out a two-phase ambient vibration test (AVT). The first phase of the AVT was carried out on June 12th, 2013 before the bearing replacement started, and the second phase will be carried out when the bearing replacement project is over, which is expected to happen sometime in December, 2013. The first AVT included measurements at the deck and at each pier of the steel spans to determine both the modal and vibration characteristics of the bridge before the replacement of bearings. After second AVT, the change in dynamic characteristics of bridge will be better understood, and optimal locations for the permanent seismic instrumentation can be determined. This paper presents only the results of the first phase of AVT, which is carried out before bearing replacements.

Y. Kaya (✉) • C. Ventura • M. Turek
Earthquake Engineering Research Facility, Department of Civil Engineering, University of British Columbia,
6250 Applied Science Lane, Vancouver, Canada
e-mail: kayaya@mail.ubc.ca

## 15.2 Description of the Bridge

As seen in Fig. 15.1, the Granville Street Bridge is located in N49.2718 and -E123.1339 of geographical coordinates in Vancouver, British Columbia, Canada, and the longitudinal direction of the bridge is 45° oriented to east from the true magnetic north. The bridge, owned by the City of Vancouver, connects downtown Vancouver to south of Vancouver through Granville Island. Truck traffic and heavier types of tour buses are prohibited to use the bridge even though transit buses are allowed to transit the bridge, and it is posted for 27 tonne load limit.

Figure 15.2 shows the dimensions of the steel spans, the locations of the pin connections and the expansion joints on the bridge. The total length of the steel spans is 544 m, and length of each span varies from 28.6 to 121.16 m. Eight piers support the superstructure of the bridge, and the support conditions between superstructure and each pier is given in Fig. 15.3.
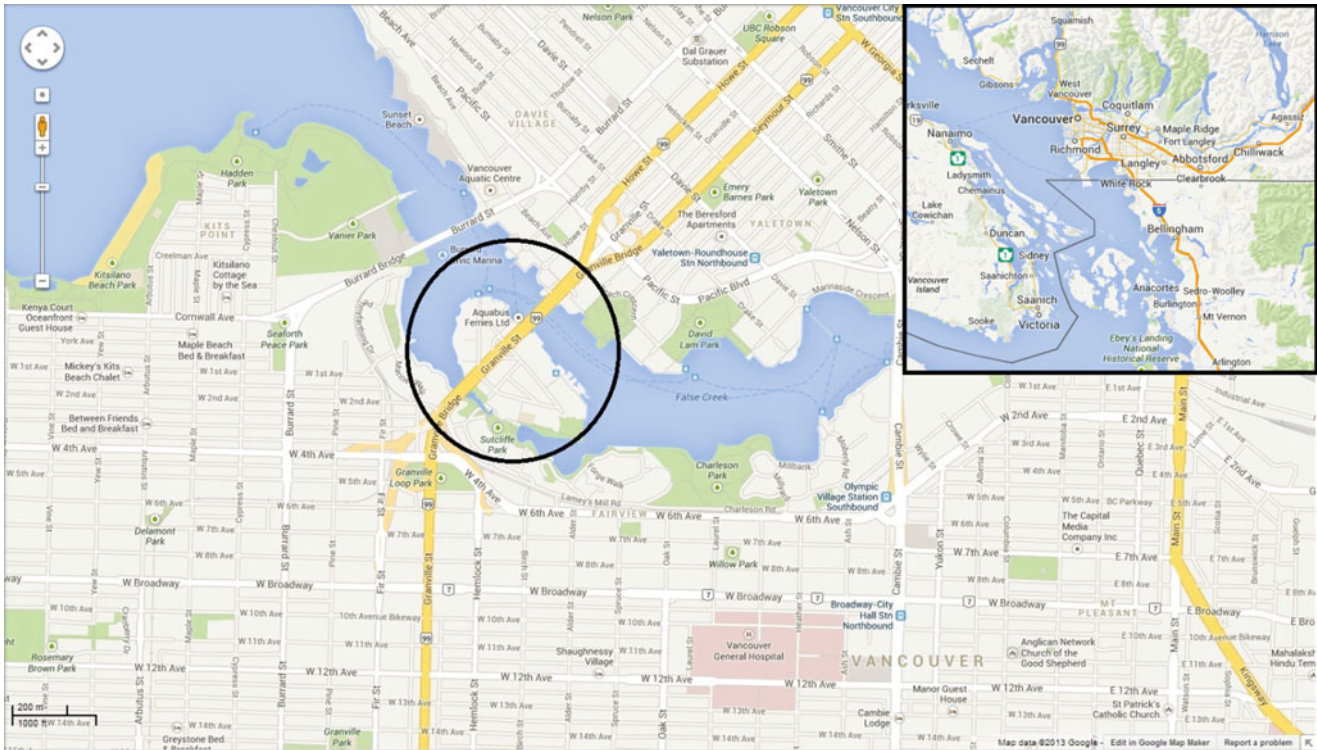


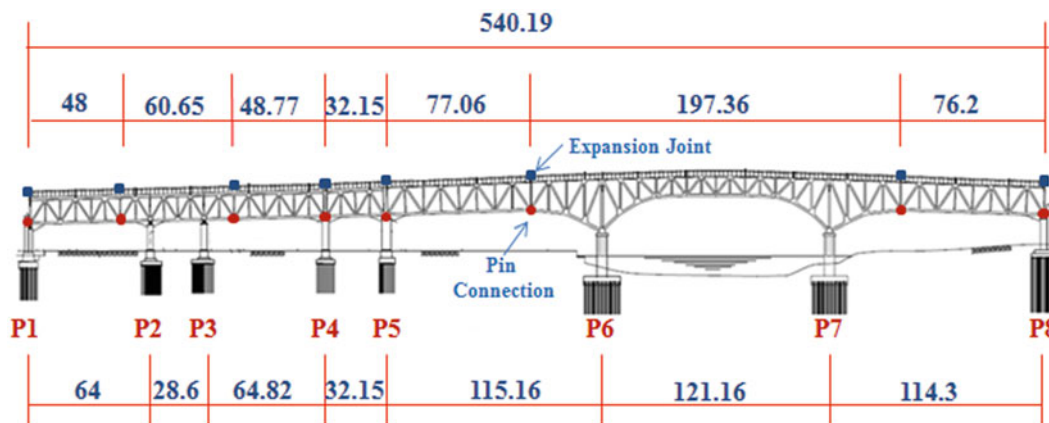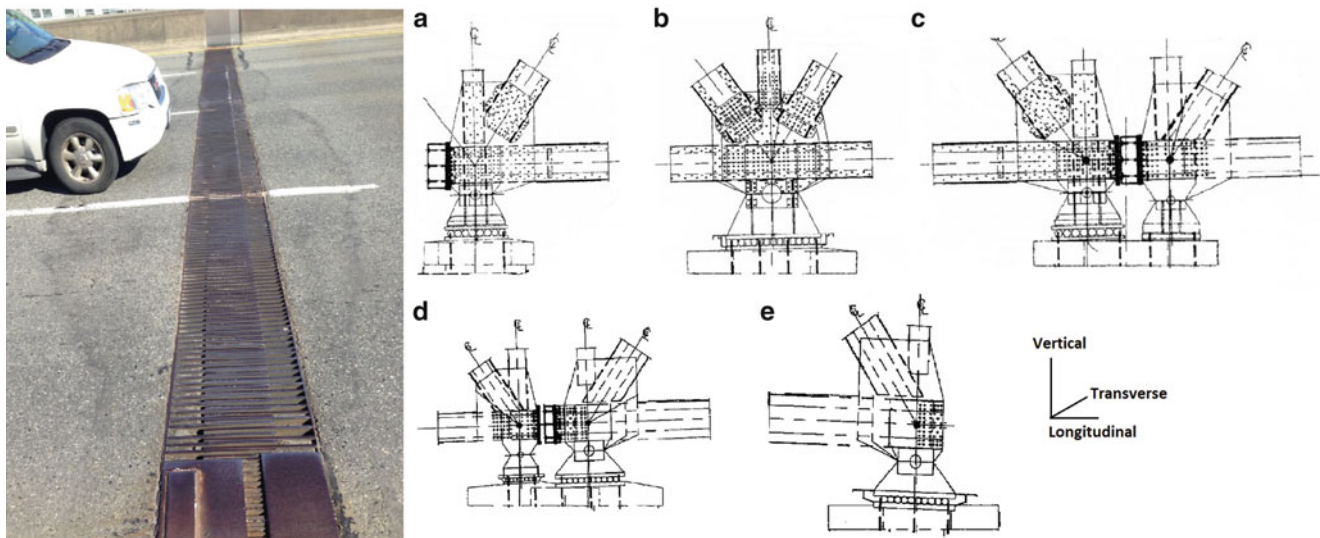**Fig. 15.1** Location of Granville Street Bridge



**Fig. 15.2** Dimensions of the steel truss spans of the Granville Street Bridge, and the locations of the pin connections (*red circle dots*) and expansion joints (*blue square dots*). All dimensions are in meter

**Fig. 15.3** Expansion joint at the Pier 7 free to display only in longitudinal direction. Support conditions between the superstructure of the bridge and each pier: (**a**) Pier 1: free to move in longitudinal direction and rotation about vertical direction, (**b**) Piers 2, 3 and 6: fixed in all directions, (**c**) Pier 4: left support is free to move in longitudinal direction and rotation about vertical, and the right support is fixed in all directions, (**d**) Pier 5: both left and right supports are fixed in all directions, (**e**) Pier 8: free to move in longitudinal direction and rotation about vertical direction

## 15.3 Description of the Ambient Vibration Test

The first phase of the AVT of the Granville Street Bridge carried out on Thursday June 12th, 2013. The test started 10:10 in the morning and lasted at 6:18 in the afternoon of the same day. The site temperature during the AVT was recorded between 13 to 18 °C: 13 °C at 10:00 am, reached to 18 °C at 03:00 pm, and down to16 °C at 06:00 pm.

Two concrete approaching viaducts, one at each end of the bridge, are included in the AVT. The length of south approach is 64 m and the north approach is 44.6 m. One of the nine sensors is used as a reference sensor located in the main span of the bridge. The remaining eight sensors are divided into two groups of four. Each of the groups is used exclusively on one side of the bridge: one group on the west side and the other on the east side. Two groups of sensors and the reference sensor located in the main span forms one setup of the AVT. Starting from the south end of the bridge, setups progress to the north end of the bridge. Using 13 setups of this kind, the entire bridge is monitored by 106 measurement points. The measurement points within each expansion joint are placed in equal distance. In each setup the north direction of each sensor is oriented to the longitudinal direction of the bridge (Fig. 15.4).

The test duration for each setup is 30 min, and the sampling rate of the recordings is 128 Hz. Low gain velocity measurement components of the sensor are used for both data analysis and modal identification. An external GPS attached to each sensor allowed the synchronization of sensor recordings both within each setup and between the setups.

The reference sensor is set up to run in continuous recording mode during the entire AVT, but it malfunctioned, and as a result of this some of the recorded data on the reference sensor had been overwritten. Only the last 3 h of data were able to be retrieved from the reference sensor: from 16:04 to 18:18 pm. Such a short duration of data made it impossible to calculate the mode shapes of the entire bridge. In addition to that, due to the technical difficulties beyond our control at site, no measurement had been conducted at measurement point 103, which is located at the concrete viaduct at the north end of the bridge.

## 15.4 Data Analysis

The noise components of the ambient vibration data, by its nature, usually appear as a random phenomenon in the data, whereas the response of the bridge is not random, but consistent at certain frequencies due to the resonance effect of the bridge. One, therefore, can minimize the effect of noise components by using statistical tools such as segmentation (or windowing), averaging and smoothing. To do this, the data is divided into equal lengths of segments (running windows) as indicated in Fig. 15.5, and each running window is shifted from the beginning of the data to the end by a predefined overlap
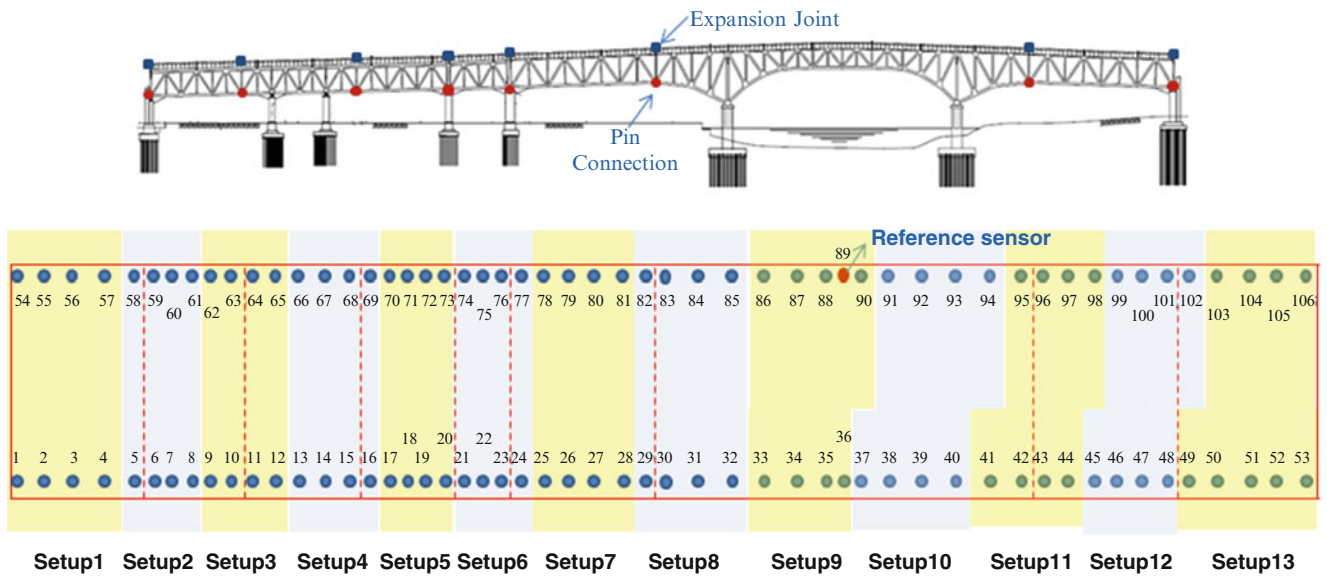
**Fig. 15.4** The measurement locations on the bridge deck
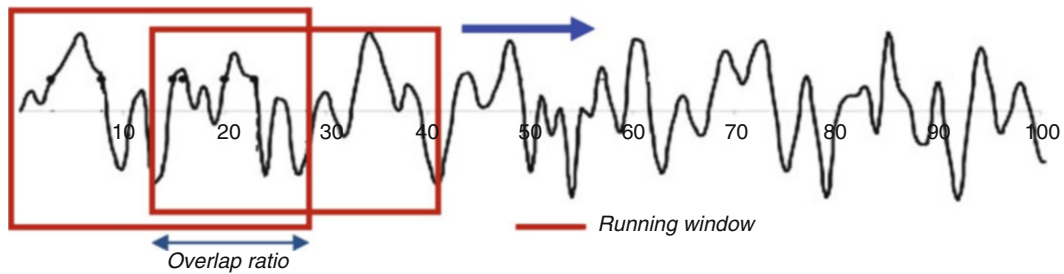


**Fig. 15.5** Running window moves within the length of the data by a predefined overlap ratio. The data in each running window is analysed separately, and sequential analysis results are averaged to form the overall output for the entire data

ratio. Each running window is analyzed separately where the analysis of each running window involves removing of mean value, de-trending, calculation of Fourier Amplitude Spectrum (FAS), and smoothing of FAS. Sequential analysis results are averaged to form the overall output for the entire data. More detailed information about how to process ambient vibration data can be found in [1].

## 15.5 Analysis Results

The maximum RMS velocity in both longitudinal and transverse directions is recorded between pier 1 & 2 of the bridge, whereas the maximum RMS velocity in vertical direction is between pier 3 & 4 of the bridge. The maximum RMS velocities measured on the bridge deck are 1.97, 0.98, and 0.44 mm/s, in vertical, transverse, and longitudinal directions, respectively. Table 15.1 lists the RMS values of the low gain velocities of different time windows of the day at 104 different locations on the bridge deck.

Figure 15.6 shows the velocities time histories recorded at measurement location 88 on the bridge deck and its FAS calculated for the three principal directions of the bridge: longitudinal, transverse, and vertical. Due to the recording failure in reference sensor, mode shapes of the bridge could not be calculated. Table 15.2 lists the modal frequencies of the bride that is identified from the FAS.

**Table 15.1** RMS values of the low gain velocity recordings, where X, Y, and Z represents the longitudinal, transverse and vertical direction of the bridge, respectively

| Location | RMS values (mm/s) | | | Location | RMS values (mm/s) | | | Location | RMS values (mm/s) | | |
|---|---|---|---|---|---|---|---|---|---|---|---|
| | Z | Y | X | | Z | Y | X | | Z | Y | X |
| 1 | 0.185 | 0.223 | 0.116 | 36 | 0.613 | 0.220 | 0.104 | 71 | 0.777 | 0.240 | 0.144 |
| 2 | 0.531 | 0.619 | 0.276 | 37 | 0.593 | 0.216 | 0.102 | 72 | 0.750 | 0.232 | 0.139 |
| 3 | 0.309 | 0.330 | 0.144 | 38 | 0.512 | 0.171 | 0.089 | 73 | 0.991 | 0.291 | 0.149 |
| 4 | 0.396 | 0.414 | 0.188 | 39 | 0.505 | 0.165 | 0.086 | 74 | 1.185 | 0.344 | 0.178 |
| 5 | 0.126 | 0.128 | 0.081 | 40 | 0.500 | 0.162 | 0.089 | 75 | 0.990 | 0.285 | 0.183 |
| 6 | 0.406 | 0.481 | 0.214 | 41 | 0.597 | 0.203 | 0.108 | 76 | 1.853 | 0.424 | 0.228 |
| 7 | 0.734 | 0.813 | 0.351 | 42 | 0.738 | 0.259 | 0.125 | 77 | 1.158 | 0.350 | 0.169 |
| 8 | 0.872 | 0.970 | 0.440 | 43 | 0.762 | 0.277 | 0.122 | 78 | 0.776 | 0.245 | 0.135 |
| 9 | 0.850 | 0.863 | 0.382 | 44 | 0.701 | 0.223 | 0.108 | 79 | 0.868 | 0.246 | 0.130 |
| 10 | 0.779 | 0.722 | 0.331 | 45 | 0.578 | 0.159 | 0.088 | 80 | 0.851 | 0.243 | 0.123 |
| 11 | 0.747 | 0.722 | 0.320 | 46 | 0.597 | 0.154 | 0.092 | 81 | 0.828 | 0.248 | 0.127 |
| 12 | 0.753 | 0.980 | 0.427 | 47 | 0.572 | 0.170 | 0.089 | 82 | 0.796 | 0.240 | 0.121 |
| 13 | 0.619 | 0.224 | 0.117 | 48 | 0.311 | 0.142 | 0.083 | 83 | 0.793 | 0.241 | 0.122 |
| 14 | 0.602 | 0.208 | 0.114 | 49 | 0.146 | 0.113 | 0.070 | 84 | 0.688 | 0.215 | 0.111 |
| 15 | 0.994 | 0.337 | 0.151 | 50 | 0.430 | 0.172 | 0.087 | 85 | 0.581 | 0.195 | 0.101 |
| 16 | 1.013 | 0.384 | 0.221 | 51 | 0.112 | 0.076 | 0.061 | 86 | 0.537 | 0.180 | 0.093 |
| 17 | 0.855 | 0.280 | 0.162 | 52 | 0.433 | 0.168 | 0.083 | 87 | 0.580 | 0.205 | 0.106 |
| 18 | 0.822 | 0.250 | 0.147 | 53 | 0.172 | 0.077 | 0.063 | 88 | 0.603 | 0.199 | 0.102 |
| 19 | 0.848 | 0.335 | 0.390 | 54 | 0.129 | 0.098 | 0.065 | 90 | 0.587 | 0.202 | 0.104 |
| 20 | 1.117 | 0.377 | 0.189 | 55 | 0.427 | 0.469 | 0.221 | 91 | 0.524 | 0.168 | 0.092 |
| 21 | 1.971 | 0.464 | 0.243 | 56 | 0.096 | 0.056 | 0.065 | 92 | 0.525 | 0.172 | 0.099 |
| 22 | 1.131 | 0.306 | 0.186 | 57 | 0.520 | 0.609 | 0.286 | 93 | 0.520 | 0.179 | 0.101 |
| 23 | 1.734 | 0.437 | 0.198 | 58 | 0.123 | 0.101 | 0.069 | 94 | 0.579 | 0.210 | 0.115 |
| 24 | 1.115 | 0.347 | 0.157 | 59 | 0.314 | 0.331 | 0.173 | 95 | 0.646 | 0.234 | 0.127 |
| 25 | 0.892 | 0.264 | 0.134 | 60 | 0.743 | 0.831 | 0.388 | 96 | 0.677 | 0.249 | 0.146 |
| 26 | 0.891 | 0.241 | 0.123 | 61 | 0.789 | 0.834 | 0.393 | 97 | 0.639 | 0.209 | 0.110 |
| 27 | 0.873 | 0.248 | 0.114 | 62 | 0.873 | 0.825 | 0.394 | 98 | 0.602 | 0.158 | 0.094 |
| 28 | 0.848 | 0.260 | 0.123 | 63 | 0.868 | 0.913 | 0.434 | 99 | 0.554 | 0.146 | 0.088 |
| 29 | 0.895 | 0.280 | 0.127 | 64 | 0.871 | 0.936 | 0.438 | 100 | 0.541 | 0.160 | 0.094 |
| 30 | 0.873 | 0.266 | 0.123 | 65 | 0.641 | 0.686 | 0.324 | 101 | 0.369 | 0.139 | 0.080 |
| 31 | 0.674 | 0.208 | 0.099 | 66 | 0.529 | 0.189 | 0.108 | 102 | 0.143 | 0.097 | 0.084 |
| 32 | 0.580 | 0.192 | 0.096 | 67 | 0.562 | 0.186 | 0.109 | 104 | 0.128 | 0.070 | 0.054 |
| 33 | 0.595 | 0.206 | 0.098 | 68 | 0.845 | 0.278 | 0.148 | 105 | 0.465 | 0.179 | 0.090 |
| 34 | 0.587 | 0.202 | 0.100 | 69 | 0.877 | 0.314 | 0.163 | 106 | 0.119 | 0.058 | 0.051 |
| 35 | 0.628 | 0.216 | 0.099 | 70 | 0.793 | 0.259 | 0.146 | | | | |

## 15.6 Conclusion

The City of Vancouver decided to install a permanent seismic monitoring system on Granville Street Bridge as part of the seismic rehabilitation project, which includes the replacement of existing bearings with new isolation bearings. The UBC is collaborating the City to conduct two phase of AVT on the bridge deck in order to better understand the dynamic behaviour of the bridge before and after the bearing replacement. The present paper summarizes the first phase of the AVT that is carried out before the bearing replacement.

The first phase of the AVT of the Granville Street Bridge carried out on Thursday June 12th, 2013, and it took 8 h to complete the test. The entire bridge is tested by 106 measurement locations using 13 test setups. Due to the malfunctioning of reference sensor located at measurement point 89, no mode shapes were able to be calculated.

The maximum RMS velocities recorded on the bridge are 1.97, 0.98, and 0.44 mm/s, in vertical, transverse, and longitudinal directions, respectively. The ambient vibration of the bridge at measurement location 88 indicated that the modal frequencies of the bridge as 0.79, 1.34, and 1.85 Hz in transverse, longitudinal, and vertical directions, respectively. Such values change from one measurement location to other due to many factors such as pier height, soil condition at both ends of the bridge and underneath each pier, boundary conditions between piers and superstructure, etc.

**a**



**b**
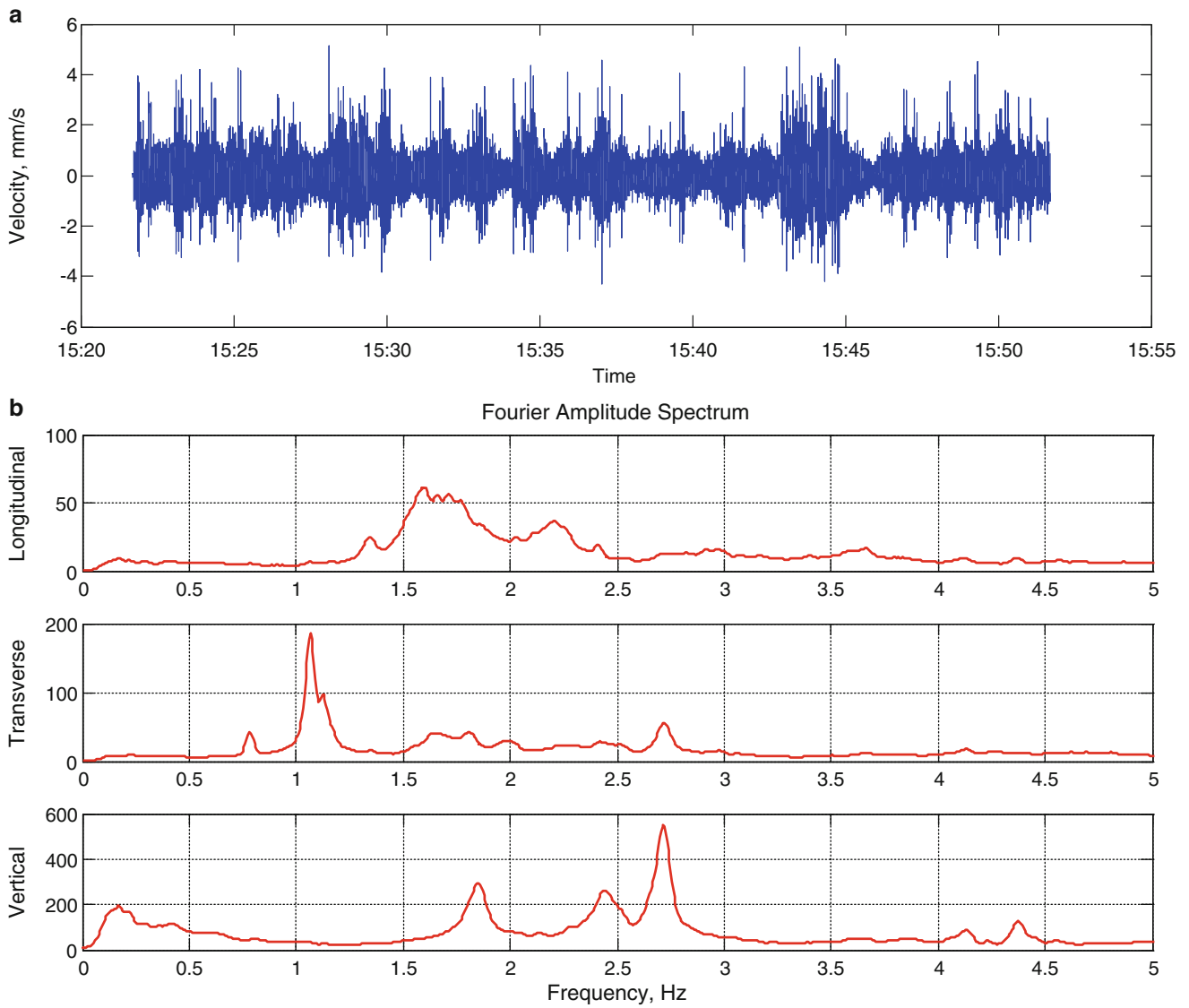


**Fig. 15.6** (**a**) Time history of the velocity data recorded at measurement location 88, (**b**) Fourier amplitude spectrum of the data at the same location

**Table 15.2** Model frequencies identified at measurement location 88

| Mode | Frequency (Hz) | Direction | Mode | Frequency (Hz) | Direction |
|---|---|---|---|---|---|
| 1 | 0.79 | T | 7 | 2.21 | L |
| 2 | 1.07 | T | 8 | 2.44 | V |
| 3 | 1.13 | T | 9 | 2.72 | V |
| 4 | 1.34 | L | 10 | 4.13 | V |
| 5 | 1.60 | L | 11 | 4.38 | V |
| 6 | 1.85 | V | | | |

L, T, and V are longitudinal, transverse, and vertical directions of the bridge, respectively

The bridge is currently undergoing the seismic rehabilitation project, and the second phase of the AVT will be conducted after the bearing replacement, which is expected to be finished later 2013. Comparing the results of two AVTs will allow the UBC to make recommendations about the permanent seismic monitoring to the City of Vancouver.

## Reference

1. Kaya Y, Safak E (2013) Real-time analysis and interpretation of continuous data from structural health monitoring (SHM) systems. Earthquake Spectra, in review

# Chapter 16
# Vibration Testing and Analysis of A Monumental Stair

**Mehdi Setareh and Xiaoyao Wang**

**Abstract** Excessive and annoying vibrations in buildings, stadiums, and footbridges have become more common in the past two decades due to several reasons including the tendency to optimize the use of building materials, use of higher strength and lighter structural properties, etc. Stair vibrations have also become an important design issue mainly due to the architects' desire to create more innovative, slender, light, and flexible monumental structures. Large vibrations and movements of stairs can become serious safety and serviceability problems, as they have the potential to disrupt the evacuation during an emergency and also people may feel unsafe during the normal use. Even though over the past two decades a large number of research studies on the floor vibrations have been conducted, very little information is available for stairs. This paper presents experimental and analytical studies of a large monumental stair. Using an electrodynamic shaker and a series of seismic accelerometers, a set of modal tests was performed on the structure. This was done to estimate the dynamic properties of the stair. A computer model of the structure was created using the common practices used in structural engineering design offices. Comparison of the measured stair responses and the results of computer analysis showed reasonable agreement. A Cumulative Modal Assurance Criterion (CMAC) was introduced, and was used to identify the degrees of freedom with low quality measured responses. It was found that CMAC performs better than Enhanced Coordinate Modal Assurance Criterion (ECOMAC) and Coordinate Modal Assurance Criterion (COMAC) when the response is due to the excitation of a single mode. Several walking and running tests were conducted on the structure, which showed the structure may not be susceptible to large levels of vibrations for everyday use.

**Keywords** Staircase • Vibration serviceability • Human vibrations • Cumulative modal assurance criterion (CMAC) • Coordinate modal assurance criterion (COMAC) • Enhanced coordinate modal assurance criterion (ECOMAC)

## 16.1   Introduction

In recent years, a trend in the architecture community to design long-span monumental stairs has started. These structures are generally slender, light, and flexible, which result in low natural frequencies. They are often susceptible to excessive vibrations that can become annoying to people. Serviceability problems as related to excessive vibrations of stairs have been studied by researchers since the 1970s.

Nilsson [1] measured the magnitude of the footfall force of fifteen people descending a stair at 2 steps/s (Hz) and found that it was up to four times the individuals' body weights. Alcock and Lander [2] measured the average forcing function for a single footfall on a stair and concluded that descending at a normal rate generates forces up to two times the body weight.

Bishop et al. [3, 4] measured the forcing functions on stairs, and studied the effects of group loading, in addition to the acceptable vibration levels for stairs. They found that the presence of people could increase the damping ratio with negligible effects on the natural frequency. Kerr and Bishop [5, 6] studied the difference between the floor and stair loadings due to people movements. With the help of twenty-five human subjects, an instrumented platform, and a staircase, they conducted various tests. They concluded that the most comfortable paces for ascent were near 2 Hz, and below 2.3 Hz for descents. When running, step frequencies of about 3.3 Hz for ascents and above 3.3 Hz for descents were the most comfortable speeds.

M. Setareh (✉) • X. Wang
Virginia Tech, Blacksburg, VA 24061, USA
e-mail: setareh@vt.edu

Bishop et al. [3, 4] studied stair vibration levels that can be acceptable to humans by introducing a non-dimensional factor, R, to be applied to the acceptable r.m.s. of acceleration based on the limits recommended by BS6472 [7]. They recommended R = 32 for the light-use stairs (for example in office buildings), R = 24 for heavy-use stairs (for example in public buildings), and R = 64 for very lightly-used stairs and for cases where group effects are expected. These recommended limits are based on the vibrations resulting from one person ascending or descending a staircase. However, the authors have not provided much detail on the basis and origin of these recommendations.

Kerr [8] used two stair mock-ups in the laboratory and conducted a number of tests with the help of twenty-five human subjects. He concluded that ascending at 2 Hz was most comfortable for walking and 3.3 Hz for running up the stair. When ascending the stair, the subjects' maximum speed was about 4.5 Hz. The subjects commented that they could easily descend at any speed below 4 Hz. The maximum step frequency for descents was about 5.5 Hz.

Kim et al. [9] used six steel and cast-in-place concrete stair mock-ups with relatively high natural frequencies, and found that, in general, the cast-in-place concrete stairs had better vibration serviceability performance than their steel structure counterparts. They also reported that the normal walking speed on the stairs was about 1.8 Hz. Davis and Murray [10] studied the vibration performance of a monumental stair using measurements and computer modeling. They measured the first mode natural frequency and damping ratio to be 7.3 Hz and 1.1 % respectively. They recommended an acceptable peak acceleration of 1.7 % g for walking by an individual, and 4.6 % g for when a person runs or for a group walk. These recommendations were based on Bishop et al. [3, 4], and the authors did not independently verify them.

Arbitrio [11] presented a study of the vibration analysis of a stair using the SAP2000 structural analysis software. He didn't conduct any vibration measurements on the structure. Huntington and Mooney [12] also conducted a Finite Element Analysis of a 39 ft long monumental stair made of steel. Without providing many details, they suggested the application of tuned mass dampers (TMD) to reduce the vibrations. Similar studies were conducted by Howes and Gordon [13] on two sets of stairs at the Art Gallery of Ontario, Toronto, Canada, which were designed by the renowned architect, Frank Gehry. They also installed a TMD in the landing area to reduce the vibrations; however, they did not provide any information on the level of stair vibration or the effectiveness of the TMD.

Howes et al. [14] studied the structural performance of a stair connecting three levels of a store in Las Vegas, Nevada. Their study was also limited to an analytical investigation using the SAP2000 structural analysis software. Eid et al. [15] conducted a simplified vibration analysis of a stair located at a Canadian University. Even though, they measured a damping ratio of 4 % based on the results of heel drop tests on a similar stair, they adopted a value of 1 % for their computer analysis.

Belver et al. [16] conducted a vibration analysis and testing of a steel staircase located at a British University, which had excessive vibrations when people ascended or descended. In addition to the structural vibration analysis using the ABAQUS computer software, they conducted an Operational Modal Analysis (OMA) of the ambient response of the stair. The measured first mode natural frequency was at 6.3 Hz with damping ratios between 0.4 and 0.6 %.

Kasperski and Czwikla [17] studied the effects of stair geometry on step frequency and dynamic load factor. They found that the slowest step frequency range was about 0.8–1.9 Hz when skipping a step during ascents. From the results of their tests they concluded that the normal walks occur at 1.2–1.5 Hz when ascending and 1.6–3.6 Hz for descents. However, the reported range by the authors for ascents seems to be low and the upper limit for descents to be high.

Cappellini et al. [18] conducted an Experimental Modal Analysis (EMA) of a stair using a shaker and a series of accelerometers to measure the dynamic properties of the structure. They also conducted an OMA of the same staircase. From these measurements, they estimated the first two mode natural frequencies and damping ratios to be: $f_1 = 4.7$ Hz, $\xi_1 = 0.4$ %; and $f_2 = 8.8$ Hz, $\xi_2 = 0.3$ %. The computed natural frequencies from their Finite Element Model were greatly overestimated ($f_1 = 7.7$ Hz and $f_2 = 13.7$ Hz).

From the presented brief summary of the literature available on the vibration serviceability of stairs, it is clear that there are still many issues related to stair vibrations that require further studies. Almost all structural designs of monumental stairs are carried out by structural engineers using various Finite Element software without conducting any field testing to verify their designs. Structural engineers generally use simple models considering frame element for linear elements (beams, stringers, etc.) and shell elements for surface elements (decking, in-fill steel plates, etc.). As indicated above, there are very few studies available on the comparison of such analytical models with measured data and appropriateness of these models for predicting stair vibrations. Therefore, this paper presents the results of the modal testing conducted on a monumental stair after installation and before the addition of non-structural elements, and an analytical study of the structure using a structural analysis software. The measured and computed dynamic properties of the structure are compared to each other. A Cumulative Modal Assurance Criterion (CMAC) is introduced and used to identify the degrees of freedom with low quality measured response of the structure. A brief evaluation of the measured vibration when an individual or group of people ascended or descended the stair at different speeds is presented.

## 16.2    Description of the Staircase

The staircase, which has a steel structure, is located at the Broad Art Museum in Lansing, Michigan. It connects the first and second levels of the building. Details of the initial static design of the structure and subsequent modifications to meet the dynamic requirements have been discussed by Setareh [19].

Since this paper presents the results of the dynamic analysis and testing of the structure after its installation and before the addition of the non-structural components such as cladding, plywood, cover, etc., only the structural elements of the stair will be described here. The staircase consists of stringers forming a truss with HSS12X3X5/16 for the top and bottom chords and HSS3X3X5/16 verticals at 1.22 m (4 ft) on center. The total depth (end to end) of the chords in the landing area is 1.10 m (43.5 in). Treads and risers are made of 6.4 mm (0.25 in) thick steel plates. Steel plates, 6.4 mm (0.25 in) thick, placed between the top and bottom chords of the stringers in the first two web panels from each end of the staircase. The plates are welded to the chords and verticals of the truss. In addition, HSS5X3X5/16 are used as diagonal members in the remaining truss panels. The bottom chords of the stair stringers are supported at their ends by the concrete beams through rigid connections. Figure 16.1 is a photo showing a partial view of the stair during the vibration tests, which occurred about two weeks after its installation.

## 16.3    Description of the Dynamic Tests

A modal test using an electrodynamic shaker (APS 113) and a number of accelerometers (PCB393C and PCB393B04) were conducted to estimate the dynamic properties of the structure. In addition, a number of walking tests were performed to evaluate the vibration acceptability of the staircase. The shaker was placed on a force plate, which was located at the corner of the stair landing (see Fig. 16.2).

Uniaxial accelerometers were oriented along three perpendicular directions. For vertical direction measurements, 393C accelerometers were placed on their bases, however, for lateral directions they were clamped to angle pieces as shown in Fig. 16.2. The accelerometers were placed along the exterior and interior stringers and at the middle of the steps (all along the truss verticals). Using a roving accelerometer approach, they were relocated from one position to another during the modal testing. A burst-chirp excitation of 6–19.5 Hz with 30 s on and 15 s off was selected. A measurement frequency resolution of 0.025 Hz (40 s duration) was used.

In addition to the modal tests, a number of controlled vibration tests with the help of three human subjects were conducted. An individual and the entire group ascended and descended the stair at various step frequencies. Using a metronome, the movements of the subjects on the stair were synchronized. Two different step frequencies based on the apparent first mode resonance frequency were selected: 146 spm (steps per minute) and 195 spm, representing the fourth and third sub-harmonics of the first mode resonance frequency of 9.8 Hz, respectively. In addition, an average walking step frequency of 120 spm, representing the most common walking speed was used. The subjects were also asked to move the fastest possible in addition to random walks (three persons only), and ascending while skipping a step (one person only). For each test, the subject(s) ascended and descended the stair. At the end of each ascent/descent, the individual(s) stopped motionless while the measurement was completed.

**Fig. 16.2** Placement of the
shaker and accelerometers during
the modal tests
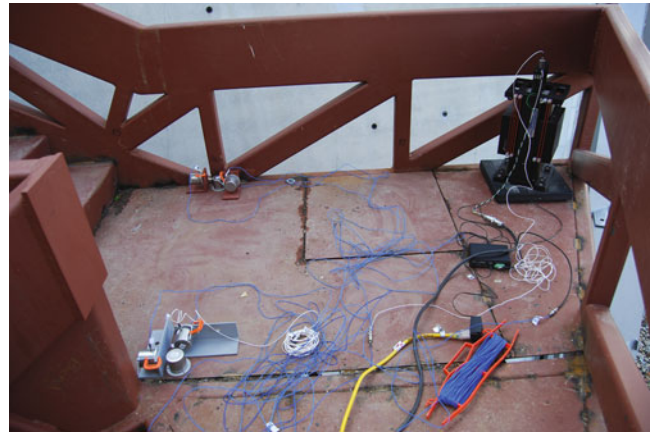


**Fig. 16.3** Analytical model of
the stair using SAP2000
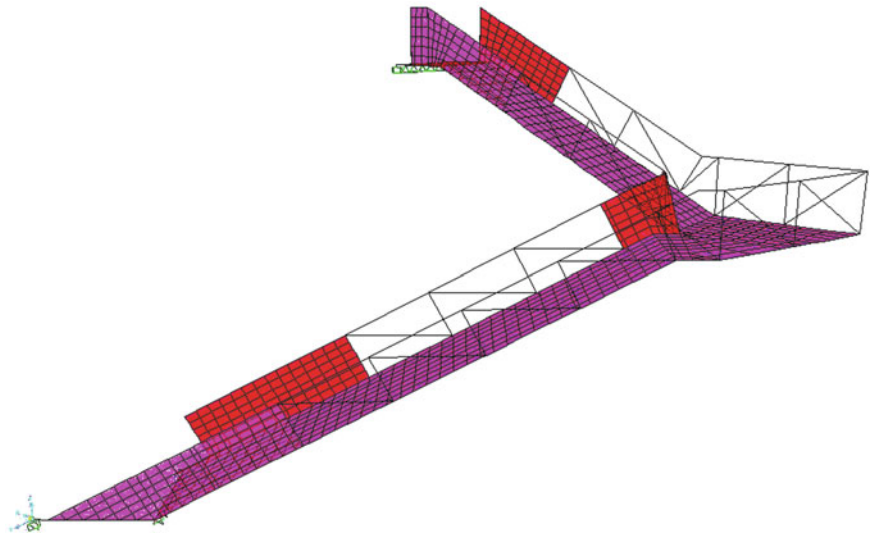


## 16.4 Analytical Modeling of the Staircase

SAP2000 [20] structural analysis program was used to create a computer model for dynamic analysis. To develop a computer model, which is consistent with the standard structural engineering design office practice, two noded frame elements were used to model the linear elements such as the stringers' top and bottom chords, diagonals, and verticals. The stair steps (treads and risers) were approximated by orthotropic shell elements. In addition, the landing area and steel infill plates within the stringers were modeled using isotropic shell elements. Figure 16.3 shows the analytical model.

## 16.5 Comparison of the Estimated Analytical and Measured Dynamic Properties

Using the ME' scope modal analysis software [21], the modal properties of the structure were estimated. Since the building was not completely enclosed during the tests and measurements, there were small variations in the resonance frequencies of the frequency response functions (FRF) due to temperature variations. For this reason, a local polynomial curve-fitting technique was adopted to estimate the natural frequencies and damping ratios. The estimated natural frequencies for the first two modes of vibration were 9.8 Hz and 18.3 Hz, respectively. It is clear that the second mode natural frequency cannot get excited by people walking or running on the stair [19]. Therefore, this study focuses on the evaluation of the first mode dynamic parameters and response of the structure. The estimated first mode damping ratio, $\xi_1$, from the results of the modal analysis was 0.42 %.

The structural analysis using the computer software resulted in the first two modes' natural frequencies of 11.55 Hz, and 21.05 Hz, respectively. They are about 15 % more than their corresponding measured values. Even though this discrepancy can be considered acceptable, in particular, since a simplified model of the structure was used, parametric studies were conducted to estimate the effects of some of the modeling assumptions.

As indicated before, the treads and risers were modeled using the flat shell elements with orthotropic properties. It is clear that the bending stiffness of the step in the transverse (along the width of the stair) is much larger than the bending stiffness of a flat steel plate, due to the folded shape of the deck. Setareh and Jin [22] conducted a parametric study to check the effects of changing the stiffness of steps in two orthogonal (longitudinal and transverse) directions through the use of bending stiffness property modifiers in the SAP2000 structural analysis software. From this study, it was found that, within a practical range, first mode natural frequency of the structure is not sensitive to variations of step stiffness. Therefore, it was concluded that the orthotropic properties of the shell elements do not contribute to the discrepancies between the measured and computed natural frequencies. Thus, the shell bending stiffness in the longitudinal direction was assumed to be equivalent to the stiffness of the 6.4 mm (0.25 in.) steel plate. The bending stiffness of the shell was increased in the transverse direction to incorporate the increase in the moment of inertia due to the folded shape of the steps.

Further studies showed that the folded geometry of the stair can have a greater effect on the natural frequencies of the structure [22]. However, this requires a much more elaborate modeling scheme and incorporation of solid structural elements, which are not usually considered by practicing engineers, as they are more costly.

## 16.6   Comparison of the Measured and Analytical Mode Shapes

The computed and measured mode shapes were compared by using the Modal Assurance Criterion (MAC). The MAC matrix for the first two modes is $\begin{bmatrix} 0.62 & 0.07 \\ 0.006 & 0.092 \end{bmatrix}$. It is clear that the MAC value for the second mode is not acceptable and the first mode is also low as the ideal value for MAC is 1.0.

Since there was a concern about the quality and accuracy of the measured modal amplitudes for the lateral degrees of freedom, three methods were used to identify the degrees of freedom that may have resulted in the low MAC value (Note that only the first mode response is of interest in this study since higher modes cannot get excited by people walking or even running on the stair). The first method was to use cumulative (or running) MAC (CMAC) value of various measured degrees of freedom in the structure, defined as:

$$CMAC\,(i,j) = \frac{\left| \sum_{i=1}^{n} {}_i\Psi_{mj}\,{}_i\Psi_{aj} \right|^2}{\sum_{i=1}^{n} {}_i\Psi_{mj}\,{}_i\Psi_{mj}^* \sum_{i=1}^{n} \left( {}_i\Psi_{aj} \right)^2} \tag{16.1}$$

The second and third methods used the ECOMAC and COMAC for each degree of freedom as defined by [23]:

$$ECOMAC(i) = \frac{\sum_{j=1}^{L} \left| {}_i\Psi_{mj} - {}_i\Psi_{aj} \right|}{2L} \tag{16.2}$$

$$COMAC(i) = 1 - \frac{\left\{ \sum_{j=1}^{L} \left| {}_i\Psi_{mj}\,{}_i\Psi_{aj} \right| \right\}^2}{\sum_{j=1}^{L} {}_i\Psi_{mj}\,{}_i\Psi_{mj}^* \sum_{j=1}^{L} \left( {}_i\Psi_{aj} \right)^2} \tag{16.3}$$

where ${}_i\Psi_{mj}$ and ${}_i\Psi_{aj}$ are the measured and analytical modal amplitudes for mode j of the ith degree of freedom, respectively, n is the total measured degrees of freedom, * represents complex-conjugate, and L is the total number of modes considered.
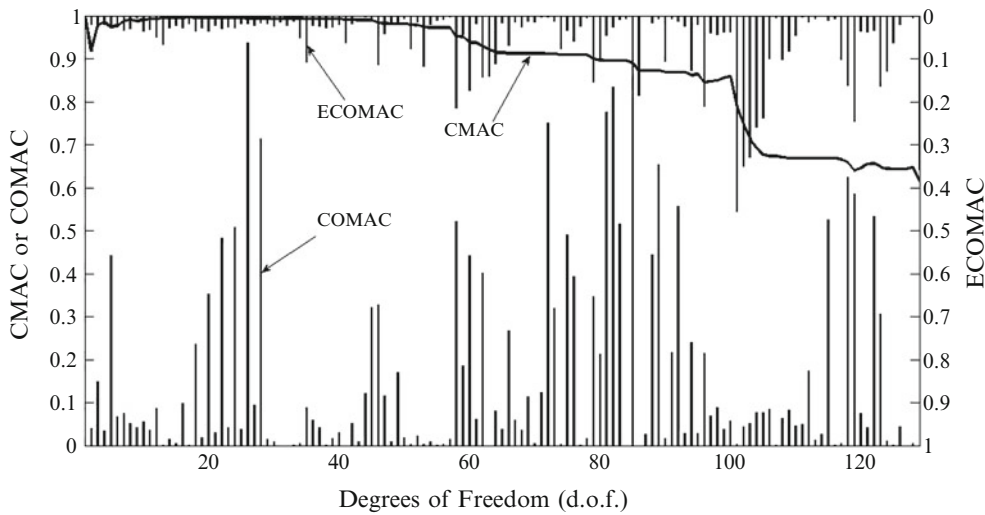
**Fig. 16.4** Comparison of CMAC, ECOMAC and COMAC for the first mode of the structure

**Fig. 16.5** Computed first mode CMAC value of the structure after the removal of the low quality measurements
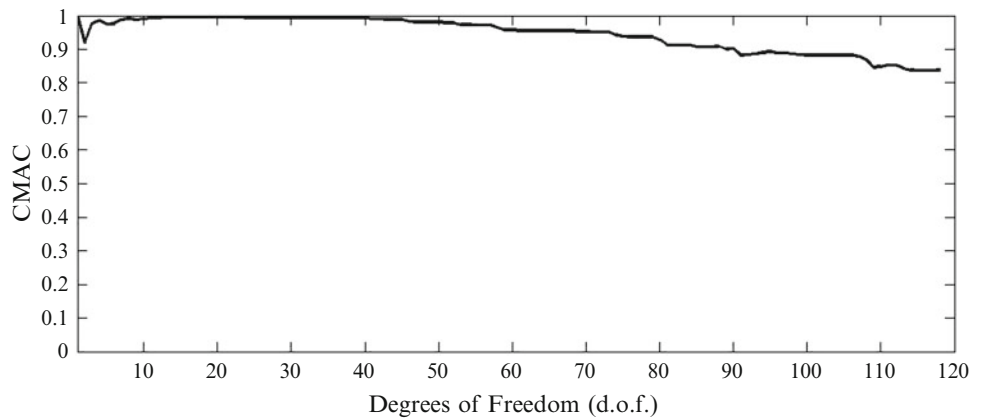


Since the considered modes at 9.8 Hz and 18.3 Hz are well separated and only the first mode is of interest, the CMAC, ECOMAC, and COMAC for the first mode are computed here. Figure 16.4 shows the CMAC, ECOMAC and COMAC for all 129 measured degrees of freedom (d.o.f.) during the modal tests. To better understand the effects of inaccuracies in the lateral measurements, the d.o.f.s are sorted such that the first group (43 d.o.f.s) represents the z-measurements (vertical) followed by x and y measured d.o.f.s (lateral), respectively. From the results shown, it is apparent that the CMAC can best identify the d.o.f.s that may result in large decreases in the MAC value. Even though for the most part, the ECOMAC and CMAC show a similar pattern, for a few d.o.f.s, the ECOMAC indicate reductions in the MAC value, which are not substantiated by the CMAC value. Figure 16.4 also shows that the COMAC cannot accurately predict the d.o.f.s that may have low correlations between the analysis and measurement and result in a drop in the MAC value. This is consistent with the conclusion reached by [23, 24].

Figure 16.5 shows the CMAC variations after the identified d.o.f.s that resulted in large drops in the MAC value have been removed from the measurements. The resulting MAC matrix is $\begin{bmatrix} 0.84 & 0.04 \\ 0.002 & 0.32 \end{bmatrix}$. The MAC value for the first mode seems to be acceptable for civil structures. As indicated before, the second mode of vibration is not of interest to this study.

It is interesting to note that the second mode MAC value improves greatly if all the measured lateral d.o.f.s are removed. The resulting MAC is $\begin{bmatrix} 0.99 & 0.33 \\ 0.10 & 0.78 \end{bmatrix}$. However, this result in spatial-aliasing as the off-diagonal elements are large, which is substantiated by the analytical Auto-MAC of $\begin{bmatrix} 1.00 & 0.33 \\ 0.33 & 1.00 \end{bmatrix}$. Figure 16.6 shows the measured and analytical first mode shapes of the structure.
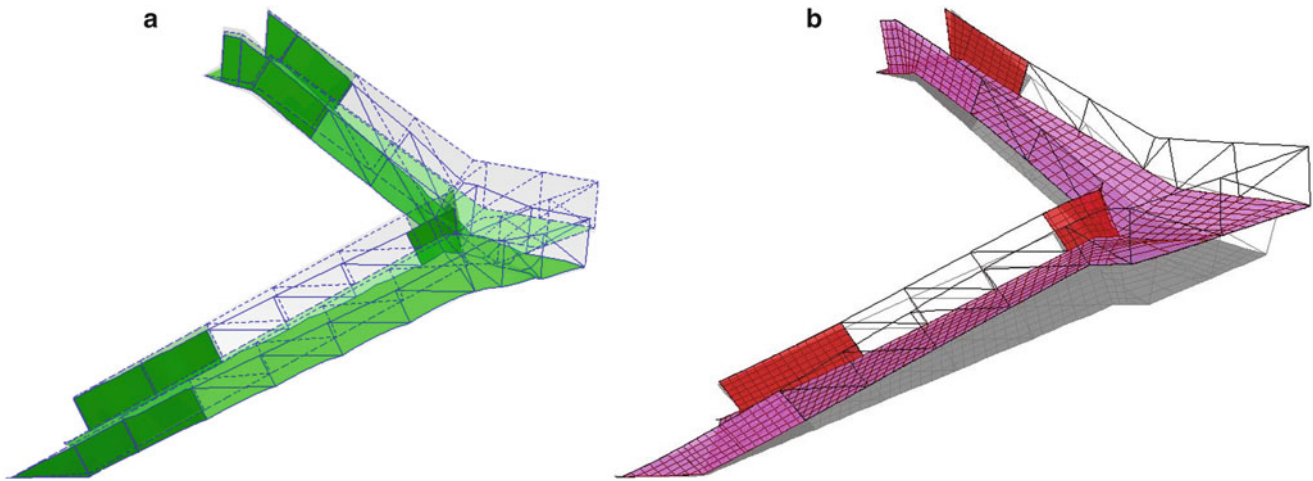
**Fig. 16.6** Measured and analytical first mode shapes of the structure. (**a**) Measured, (**b**) analytical

**Fig. 16.7** Comparison of the measured and analytical FRFs
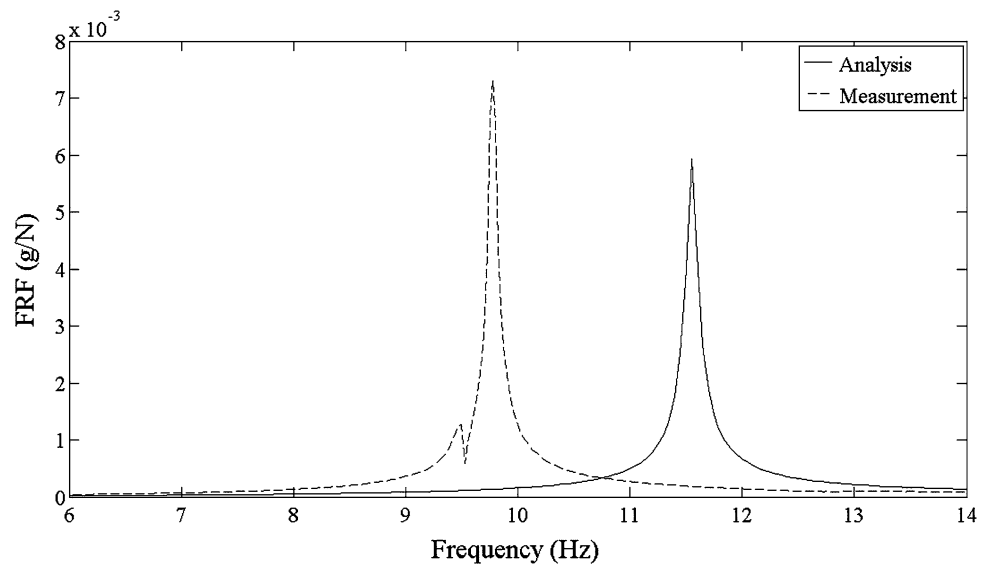


## 16.7 Comparison of the Analytical and Measured Responses

To check the level of accuracy of the analytical model to predict the structural response of the stair, the SAP2000 model was subjected to the same dynamic excitation during the modal testing and the responses were compared. To achieve this, a steady-state analysis of the structure was conducted by applying a harmonic excitation with a unit amplitude at the corner of the landing. The excitation frequency was varied in order to compute the frequency response functions (FRF) of any desired point on the stair structure. The measured first mode damping ratio was used to compute the responses of the analytical model. Figure 16.7 compares the largest measured and computed FRFs in the landing area. As can be noted, the responses are different by about 23 %, which can be considered within the acceptable range. It has to be noted that further refinement of the analytical model, in particular inclusion of the folded geometry of the stair, may result in improvements in the estimation of the dynamic properties of the structure and accuracy in prediction of its response subjected to dynamic loads (such as people's footfalls).

## 16.8 Evaluating the Stair Vibrations

The measured vibrations with human subjects ascending or descending the stair were used to evaluate the design of the stair for everyday use. The vibration limits as recommended by [4] were adopted. It has to be noted that the construction of the stair was not complete at the time of the tests as the non-structural elements were not yet installed.

From the results of the measurements, it was found that when one person ascended or descended the stair rapidly at 146 spm, or 195 spm, the maximum stair vibration could exceed the limit. However, when one or three people ascended or descended the stair at the normal walking speed of 120 spm, only one location on the stair reached a level more than the limit. The vibrations due to random walks were all within the acceptable range. The largest vibrations were found when three people descended the stairs at 195 spm or the fastest they could. Vibrations up to three times the acceptable limits were recorded. However, such speeds of motion represent running down a stair, which has a low probability of occurrence especially involving a group of people at a museum (except in the case of an emergency). From the analysis of the vibrations measured in the field, it was concluded that at its condition during the tests, when a person ascended or descended the stair at a slow to normal range-of-speed, the movements were within the acceptable range.

## 16.9 Conclusions

This paper presented a study of vibrations of a monumental stair due to human movements. It considered various field testing and computer modeling of the structure. Using the standard structural engineering practice for modeling such structures, a computer model of the structure was created. Comparison of the results of the dynamic tests and computer analysis showed that the computer model could reasonably predict the dynamic behavior of the structure.

A parametric study of the variations in the modeling assumptions showed that improvements in the structural response can be achieved by refining the computer model. To identify the degrees of freedom with low quality of collected data, a CMAC value was defined and computed. Comparing the value of CMAC with ECOMAC and COMAC for the first mode showed its superiority in identifying the problem degrees of freedom over the ECOMAC and COMAC. The measured and analytical FRFs for the location with the largest stair response were compared and found to be close within a practically acceptable range.

From the analysis of the collected responses from a number of tests when human subjects ascended and descended the stair, it was concluded that the stair vibrations (at the time of the tests) were within the acceptable range as long as people walked at or below the normal range of speed.

## References

1. Nilsson L (1976) Impact produced by human motion. Swedish Council for Building Research, Report No. D13: Part 1
2. Alcock NJ, Lander LE (1987) Vibration of staircases. Undergraduate project thesis, University of Bristol, UK
3. Bishop NWM, Willford M, Pumphrey R (1993) Multi-person excitation of modern slender staircases. In: Engineering for crowd safety, Elsevier Science Publishers, Amsterdam, pp 399–408
4. Bishop NWM, Willford M, Pumphrey R (1995) Human induced loading of flexible staircases. Safety Sci 18:261–276
5. Kerr SC, Bishop NWM (1997) Human induced loading of flexible staircases. In: Topping BHV, Leeming MB (eds) Innovation in civil and structural engineering. Civil-Comp Press, Edinburgh, pp 311–317
6. Kerr SC, Bishop NWM (2001) Human induced loading on flexible staircases. Eng Struct 23:37–45
7. BS 6472 (1984) Evaluation of human exposure to vibration in buildings (1 Hz to 80 Hz). In: International organization for standardization, Geneva, Switzerland
8. Kerr SC (1998) Human induced loading on staircases. Ph.D. thesis, Mechanical engineering department, University of London, London
9. Kim SB, Lee YH, Scanlon A, Kim H, Hong K (2008) Experimental assessment of vibration serviceability of stair systems. J Constr Steel Res 64:253–259
10. Davis B, Murray TM (2009) Slender monumental stair vibration serviceability. J Archit Eng, ASCE 15(4):111–121
11. Arbitrio V (2009) Longchamp stair optimization and vibration study. Structure 10–13
12. Huntington DJ, Mooney JW (2011) How to keep monumental stairs from vibrating. In: Structures congress 2011, ASCE, pp 2572–2584

13. Howes C, Gordon E (2011) The spiral stairs at the art gallery of Ontario. In: Structures congress 2011, ASCE, pp. 2594–2604
14. Howes C, Krynski M, Kordt S (2011) The feature stair at Louis Vuitton in crystals at city center. In: Structures Congress 2011, ASCE, pp. 2585–2593
15. Eid R, Seica M, Stevenson D, Howe B (2011) Staircase vibrations due to human activity. In: Structures Congress 2011, ASCE, pp. 2562–2571
16. Belver AV, Zivanovic S, Dang HV, Istrate M, Iban AL (2012) Modal testing and FE model updating of a lively staircase structure. In: Topics in modal analysis I, vol 5, Proceedings of the society for experimental mechanics conference, Series 30, pp. 547–557
17. Kasperski M, Czwikla B (2012) A refined model for human induced loads on stairs. In: Topics on the dynamics of civil structures, vol 1, Proceedings of the society for experimental mechanics conference, Series 26, pp. 27–39
18. Cappellini A, Manzoni S, Vanali M (2012) Experimental and numerical studies of the people effects on a structure modal parameters. In: Topics on the dynamics of civil structures, vol 1, Proceedings of the society for experimental mechanics conference, Series 26, pp. 17–25
19. Setareh M (2013) Vibration analysis and design of a monumental stair. In: Proceedings of the 2013 annual conference and exposition on experimental and applied mechanics, Lombard, IL, pp. 1–8
20. SAP2000 (2013) SAP2000-static and dynamic finite element analysis of structures. Version 15.1.0, Computers and Structures, Inc., Berkeley, CA
21. ME'scope VES (2013) ME'scope VES 6.0. Vibrant Technology, Inc., Scotts Valley, CA
22. Setareh M, Jin EJ (2013) Modal analysis and FE model updating of a monumental stair. Research report, School of architecture and design, Virginia Tech, Blacksburg, VA
23. Hunt DL (1992) Application of an enhanced coordinate modal assurance criterion. In: Proceedings of the international modal analysis conference, vol 10, pp. 66–71
24. Ewins DJ (2000) Modal testing-theory, practice, and application, 2nd edn. Research Studies Press, Baldock, England

# Chapter 17
# Evaluation of Stop Bands in Periodic and Semi-Periodic Structures by Experimental and Numerical Approaches

**P.G. Domadiya, E. Manconi, M. Vanali, L.V. Andersen, and A. Ricci**

**Abstract** Adding periodicity in structures leads to wavemode interaction, which generates pass- and stop-bands. Stop-bands are related to the periodic nature of the structure. Thus structural periodicity can be shaped in order to design vibro-acoustic filters to reduce vibration and noise transmission. The aim of this paper is to investigate numerically and experimentally stop-bands in periodic one-dimensional structures. Two methods for predicting stop-bands are described: the first applies to infinite structures using a wave approach; the second deals with the evaluation of a structural transmission loss coefficient. Numerical examples concerning periodic beams are presented. Results are discussed and validated experimentally. Very good agreement between the numerical and experimental models in terms of stop-bands is showed.

**Keywords** Guided waves • Vibro-acoustic filters • Periodic structures • Dispersion curves • Stop-bands

## 17.1 Introduction

Periodic structures, also called band-gap structures, ideally consist of an infinite assembly of identical elements joined in an identical manner. These structures exhibit stop-bands, where wave motion cannot propagate and thus no energy flow occurs, and pass-bands, where propagation occurs involving energy flow [1]. The idea to exploit these properties and use periodic structures as passive filters is dated long time ago. Wave filtering properties of periodic structures have been studied extensively and widely used in the fields of electromagnetism and optics, e.g. Bragg filters, and they are currently the subject of numerous studies for innovative applications related to metamaterials [2].

Due to their properties, periodic structures have also found applications in the passive control of noise and vibrations. Many works on free harmonic motion of periodic structures have been published—examples include periodical rods and beams, e.g. [3–6], multi-supported beams, e.g. [7, 8], periodical curved beams [9], two-dimensional structures, e.g. [10], stiffened plates, e.g. [11], etc. A review of some of the relevant and recent works done in the area of structural periodic structures can be found in [12]. However, band-gap structures have not yet been exploited in noise and vibration reduction as much as it has been done in electromagnetism and optics.

The main aim of this paper is to introduce and validate experimentally two methodologies for designing structural vibro-acoustic filters which can attenuate disturbance transmission in practical applications. Two methods for predicting stop-bands are described: the first applies to infinite structures using a wave approach; the second deals with the evaluation of a vibration transmission loss coefficient in semi-periodic one dimensional structures. The transmission loss coefficient is here defined to predict the performance in terms of noise and vibration insulation of a finite number of identical cells

_____

P.G. Domadiya • L.V. Andersen
Department of Civil Engineering, Aalborg University, Denmark

E. Manconi • M. Vanali (✉)
Department of Industrial Engineering, University of Parma, Parma, Italy
e-mail: marcello.vanali@gmail.com

A. Ricci
Institute of Sound and Vibration, University of Southampton, Southampton, UK

embedded semi-periodically into an otherwise uniform structure. The analysis presented can be generally applied to periodic structures that behave as one-dimensional waveguides, and therefore to a wide range of practical cases, e.g. acoustic tubes, stiffened cylinders, plate strips, wires etc. The paper focuses on one type of wave motion.

Numerical examples are given and results are discussed and validated experimentally. These concern transverse vibration of infinite and semi-infinite beams with periodic change in the cross-section and with periodically added masses. Very good agreement between the numerical and experimental models in terms of stop-bands is showed.

## 17.2 Stop-Bands in Periodic One-Dimensional Waveguides

In this section two methods for evaluating stop-bands in periodic one-dimensional waveguides are presented and discussed. The structures considered are linear under harmonic motion. No damping is assumed. For ease of reference, in what follows a period of the structure is termed "cell". The first method deals with infinite periodic one-dimensional structures; a schematic representation is given in Fig. 17.1a. The second method applies to a finite periodic structure, containing $N$ cells, embedded in a uniform structure as illustrated in Fig. 17.1b. Although the latter appears as a more realistic representation of a "physical" situation, numerical and experimental results showed that stop-bands are almost the same in the finite and the infinite structure when enough cells are considered. This is showed in Sect. 17.3 which deals with numerical and experimental results.

### *17.2.1 Periodic One-Dimensional Waveguides*

The fundamental behaviour of an infinite periodic structure can be summarised in its dispersion curves which give the relation between the propagation constant $\mu$ and the frequency $\omega$. As depicted in Fig. 17.2, at any frequency $\omega$ the motion of a cell is equal to $e^{-i\mu}$ times those of its neighbour [1], where $\mu$ is also known as *propagation constant*. According to Floquet's theorem, displacements at each side of the cell are related by

$$\mathbf{q}_R = \lambda \mathbf{q}_L, \tag{17.1}$$

where $\lambda = \exp(-i\mu)$. The cell displacement vector $\mathbf{q} = [\mathbf{q}_L^T, \mathbf{q}_R^T]^T$ is re-arranged to give

$$\mathbf{q} = \Lambda_R \mathbf{q}_L, \tag{17.2}$$

where $\Lambda_R = [\mathbf{I} \quad \lambda \mathbf{I}]^T$ and $\mathbf{I}$ is the identity matrix having the same size as $\mathbf{q}_L$. Internal forces at each side of the cell are sorted in a similar way, viz. $\mathbf{f} = [\mathbf{f}_L^T, \mathbf{f}_R^T]^T$. In the absence of external excitation, equilibrium at the left side of the cell implies that

$$\Lambda_L \mathbf{f} = \mathbf{0}, \tag{17.3}$$
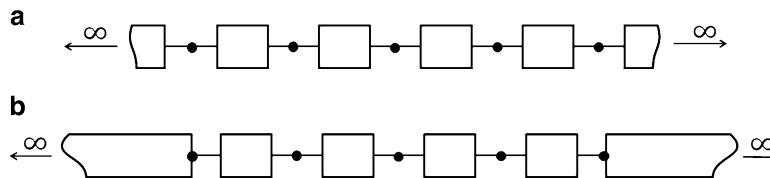


**Fig. 17.1** (**a**) Schematic representation of the infinite periodic waveguide; (**b**) schematic representation of the finite periodic waveguide embedded in a homogeneous waveguide
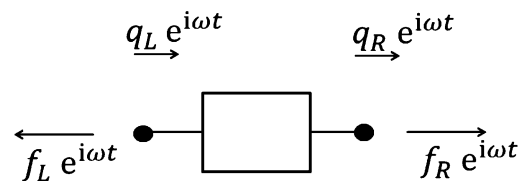


**Fig. 17.2** Displacements and forces of a unit cell

**Fig. 17.3** Transmission loss coefficient in a semi-periodic waveguide



where $\Lambda_L = [\mathbf{I} \quad \lambda^{-1}\mathbf{I}]$. Cell displacements and forces are also related by

$$\mathbf{D}(\omega)\mathbf{q} = \mathbf{f};$$
(17.4)

where $\mathbf{D}$ is the frequency dependent *dynamic stiffness matrix* of the cell. For a simple structure it is possible to obtain this dynamic stiffness matrix from the differential equation of motion [13]. For more complicated structures, or at higher frequencies, the equations of motion become very complicated at best and numerical approximations are often necessary. In the Wave Finite Element method [14, 15], the cell in Fig. 17.2 is modelled using a standard finite-element formulation.

In particular the mass $\mathbf{M}$ and the stiffness $\mathbf{K}$ matrices of the finite-element model are typically obtained using commercial finite-element packages, greatly simplifying the analysis. At each frequency $\omega$, the matrix $\mathbf{D} = [-\omega^2\mathbf{M}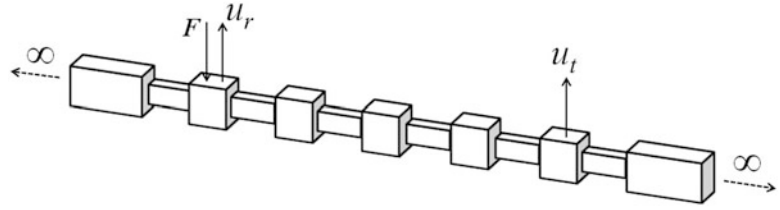 + \mathbf{K}]$ is the finite-element dynamic stiffness matrix of the cell. It is worth pointing out that internal nodal degrees of freedom in the finite-element model of the cell must be removed by a dynamic condensation, while mid-side nodes can be accommodated as shown in [14].

In order to obtain the dispersion curves using an efficient and robust formulation, the cell dynamic stiffness matrix is partitioned into

$$\mathbf{D} = \begin{bmatrix} \mathbf{D}_{LL} & \mathbf{D}_{LR} \\ \mathbf{D}_{RL} & \mathbf{D}_{RR} \end{bmatrix}.$$
(17.5)

Substituting Eqs. (17.2) and (17.5) into Eq. (17.4) and premultiplying both side of Eq. (17.4) by $\Lambda_L$, a quadratic polynomial eigenvalue problem in $\lambda$ is obtained:

$$\overline{\mathbf{D}}(\omega, \lambda)\mathbf{q}_L = [\mathbf{D}_{LR}(\omega)\lambda^2 + (\mathbf{D}_{LL}(\omega) + \mathbf{D}_{RR}(\omega))\lambda + \mathbf{D}_{RL}(\omega)]\mathbf{q}_L = \mathbf{0}.$$
(17.6)

This provides the dispersion curves/dispersion relation, that is the relation between $\lambda$ and $\omega$, or, similarly, the dispersion relation between the propagation constant $\mu = \mathrm{i}\ln(\lambda)$ and $\omega$. Equation (17.6) can be also easily recast as a standard linear eigenvalue problem and thus solved using well established and robust numerical routines.

Solutions of Eq. (17.6) come in pairs $(\lambda, 1/\lambda)$, where $\lambda$ can be written in general as $\lambda = \exp(-\mathrm{i}\tilde{\mu} + \tilde{\xi})$, $\tilde{\mu}$ representing the phase change from one cell to the next one, $\tilde{\xi}$ representing the attenuation. When the attenuation $\tilde{\xi}$ is zero, or similarly $|\lambda| = 1$, dispersion curves show a pass-band: propagating wave motion occurs involving energy flow to the right and to the left of the structure. If $\tilde{\xi}$ is different from zero, or $|\lambda| \neq 1$, no energy flow occurs and dispersion curves show a stop-band. Here stop-bands are thus predicted when $|\lambda| \neq 1$.

### 17.2.2 Semi-Periodic One-Dimensional Waveguide

Floquet's theorem applies to infinite structures; hence, in principle, it does not predict the behaviour of finite structures, which are more realistic models of a physical situation. For finite structures a more meaningful approach is to evaluate the transmission loss coefficient. In this section, a method to evaluate the transmission loss coefficient of a finite periodic structure embedded into a similar uniform structure of infinite extent is illustrated. A schematic representation of the model is showed in Fig. 17.1b. This well represents the case in which a finite periodic structure, separating two structural elements, is used to filter vibration or noise.

Consider a point force acting at the left side of the periodic structure as depicted in Fig. 17.3.

Forward and backward flexural waves are sent out into the beam. As an example, transmission to the right region of the structure is considered. The transmission loss coefficient is here defined as

$$\tau = 10\log\left(\frac{|u_r|^2}{|u_t|^2}\right),$$
(17.7)

where $u_r$ is a reference displacement, e.g. close to the forcing point, and $u_t$ is the displacement measured at a receiver point on the other side after a certain number of cells, cf. Fig. 17.3. In order to evaluate the transmission loss coefficient the finite-element matrices of the periodic structure are calculated and finite-element *transmitting boundary conditions* are used to mimic the behaviour of an attached infinite homogeneous structure as described in [16].

With reference to Eq. (17.7), the structure shows a perfect transmission at the frequencies for which $\tau = 0$. When $\tau \neq 0$ transmission is reduced. In particular the maximum values of $\tau$ estimate the minimum transmission of wave motion. Therefore the frequency bands that clearly show maximum values of $\tau$ estimate the stop-bands.

## 17.3 Numerical Examples and Experimental Results

Some numerical and experimental results are presented in this section. A beam with periodical change in the cross-section and a beam with periodically attached masses are considered. A schematic representation of the periodic beams is given in Fig. 17.4.

The first beam is made of steel and the geometric characteristics are: $L_1 = 0.1$ m, $L_2 = 0.17$ m, $h_1 = 0.01$ m, $h_2 = 0.025$ m, cf. Fig. 17.4a. The second beam is made of aluminum, it has a square-cross section of height $h = 0.015$ m; the periodic length is $L = 0.1$ m and the attached masses are weigh 45 g each, cf. Fig. 17.4b. Bending wave motion is evaluated, although longitudinal, shear and higher order motion can be investigated using the theory described in the previous sections.

Experimental results were obtained suspending the beams in the laboratory to simulate simply supported boundary conditions. The beams were instrumented using miniature piezo-accelerometers able to guarantee a flat frequency response between 0.5 and 10,000 Hz. A scheme of the experimental set-up, together with the accelerometer positions, is showed in Fig. 17.5. The natural frequencies extracted from the experimental frequency-response-function verified the simply supported boundary conditions. The beams were excited using a suspended mini-shaker and instrumented hammers. A stinger was used to connect the shaker device to the beam and a slow linear sweep varying from 100 to 6,000 Hz was given as input. Various tests where repeated to optimize the sweep duration and achieve the best possible results. The forcing signal power spectrum (or its power-spectral-density) were checked to ensure that a correct amount of energy was given at each frequency of interest. The accelerometers and excitation were acquired using a 24 bit analog to digital converter with built-in anti-aliasing filters. The sampling frequency was chosen from test-to-test according to the specific needs. The results were compared with those obtained exciting the beam using instrumented hammers. In the latter case a series of single impacts were given, and the resulting responses were triggered on the hammer signal and averaged to reduce measurement noise and uncertainties. In some cases it became too difficult to excite by a single impact due to multiple hammer hits, hence a series of random hammer impacts for at least 5 min were given and the excitation was treated as a casual input [17]. The results were in very good agreement with those obtained from the sweep tests.

Figures 17.6, 17.7, and 17.8 show the numerical results obtained applying the theory in Sects. 17.2.1 and 17.2.2. The first two stop-bands generated using Eq. (17.6) are shown in Fig. 17.6 for the first beam, cf. Fig. 17.4a. The frequency ranges where $|\lambda| \neq 1$ are those corresponding to the stop-bands. These are 240–440 Hz and 1,220–3,200 Hz. Figure 17.7 shows the transmission loss coefficient calculated as showed in Sect. 17.2.2. The reference displacement $u_r$ was evaluated at the left end of the periodic structure, where a nodal force of unit magnitude was applied. In Fig. 17.7a the displacement $u_t$ was calculated after 3, 6, 9 cells, showing that few periodicities are sufficient to drastically reduce disturbance transmission
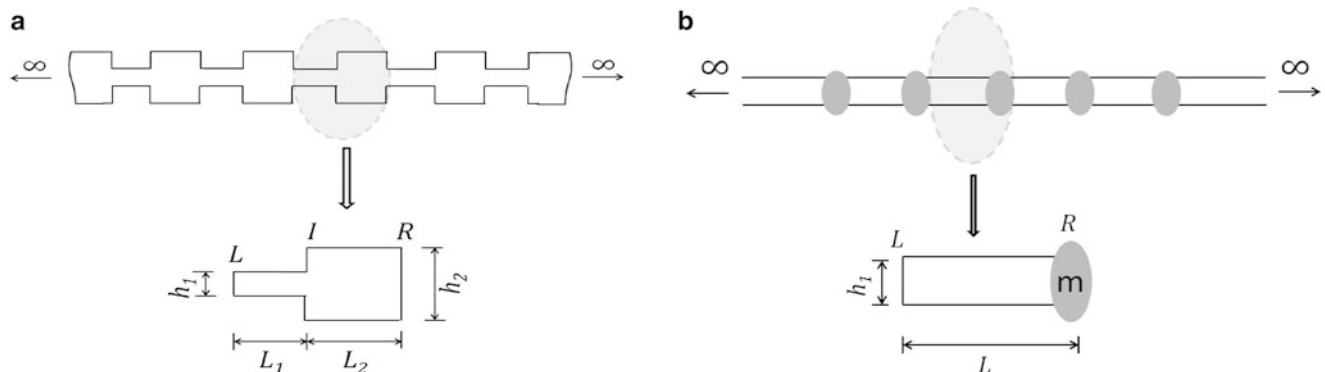


**Fig. 17.4** Schematic representation of the periodic beams
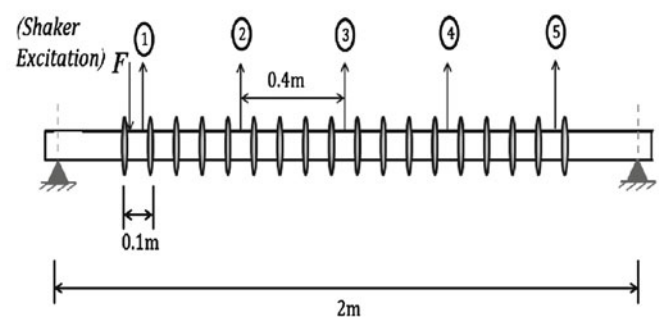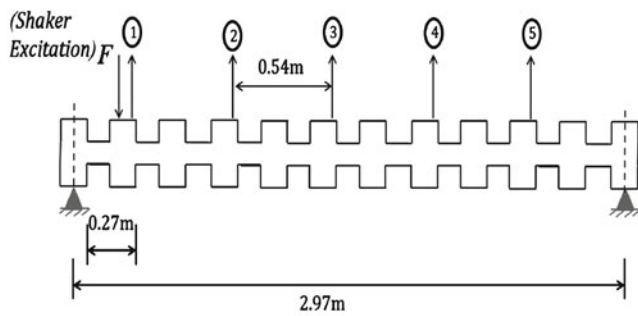
**Fig. 17.5** Instrumented beams suspended in the laboratory and schemes of the experimental set-up

**Fig. 17.6** Periodic beam with change in the cross-section. Dispersion curves
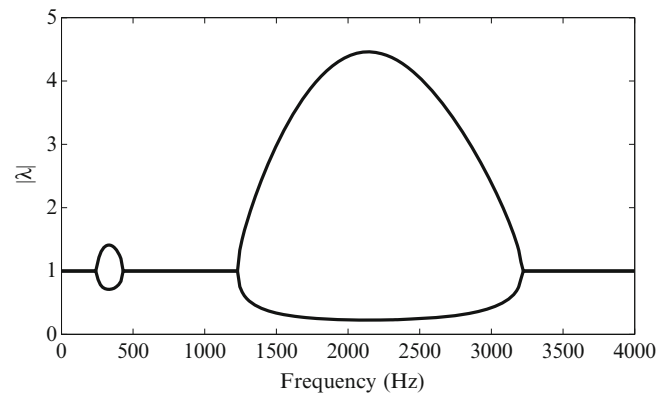


whose dominant frequencies fall within the stop-bands. Figure 17.7b shows the transmission loss coefficient obtained using the Euler-Bernoulli and the Timoshenko theories when 9 cells were considered. Figure 17.7b shows that the Euler-Bernoulli theory predicts the beam behaviour quite accurately in the frequency range considered. It can be noticed that both the theories predict approximately the same position and length of the stop-bands but, as expected, the frequency occurrence of the stop-bands for the Timoshenko model is lower then the Euler-Bernoulli one.

Figure 17.8 shows a comparison between the results predicted using the two methods. It can be seen that both the methods predict almost the same stop-bands, although stop-bands can be identified more clearly looking at the dispersion curves obtained for the infinite periodic beam.

Experimental results are showed in Figs. 17.9 and 17.10. Figure 17.9 shows the amplitude of the frequency-response-function for the non periodic beam and the periodic beam respectively, when the beams were excited by a series of single impacts using a miniature impact hammer. Figure 17.9c shows the acceleration-power-spectra of the periodic beam when a
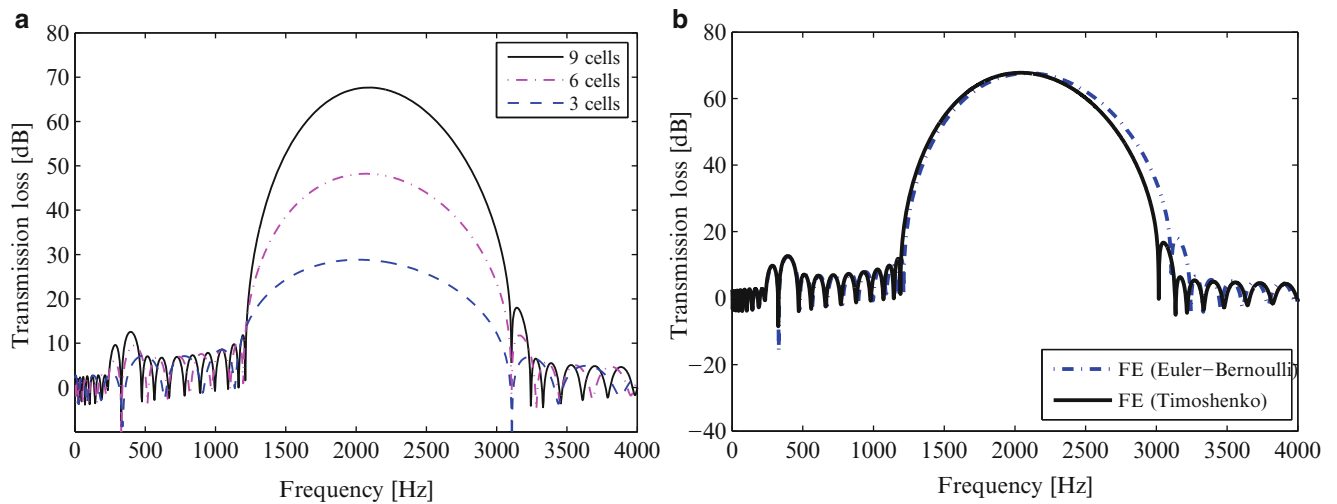
**Fig. 17.7** Beam with periodical change in the cross-section embedded in an uniform infinite beam. Transmission loss coefficient
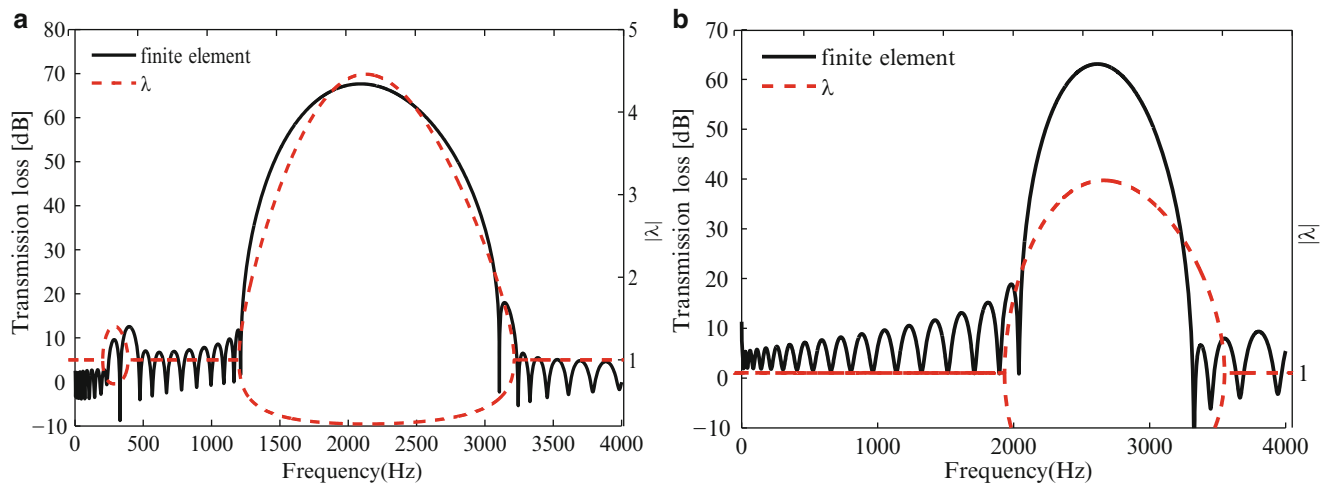


**Fig. 17.8** Comparison between dispersion curves and the transmission loss coefficient evaluated considering 9 cells. (**a**) Beam with periodical change in the cross-section; (**b**) beam with periodically added masses. Note: Different scales on the left and right ordinate axes

slow linear sweep varying from 100 to 6,000 Hz was applied using a suspended mini-shaker. The effect of the periodicity in terms of stop-bands can be clearly seen by a comparison between Fig. 17.9a and Fig. 17.9b,c. Comparison between the transmission loss coefficient obtained experimentally and numerically is given in Fig. 17.10.

The experimental transmission loss coefficient for the periodic beams was evaluated taking the accelerometer 1 as the reference channel, see Fig. 17.3. Differences between the results is explained considering that experimental results are affected by the boundary conditions and thus resonances at the natural frequencies of the finite beam are evaluated, while the numerical results are obtained for a finite-element model of a finite periodic beam to which transmitting boundary conditions are added. The negative peaks in transmission loss recorded in the experiment within the stop-bands for flexural wave propagation are assumed to be related to other wave modes, e.g. torsional waves, that are not accounted for within the applied theoretical models. Considering the simple model used to obtain the numerical results, it can be claimed that the numerical results are very well validated by the experimental results.
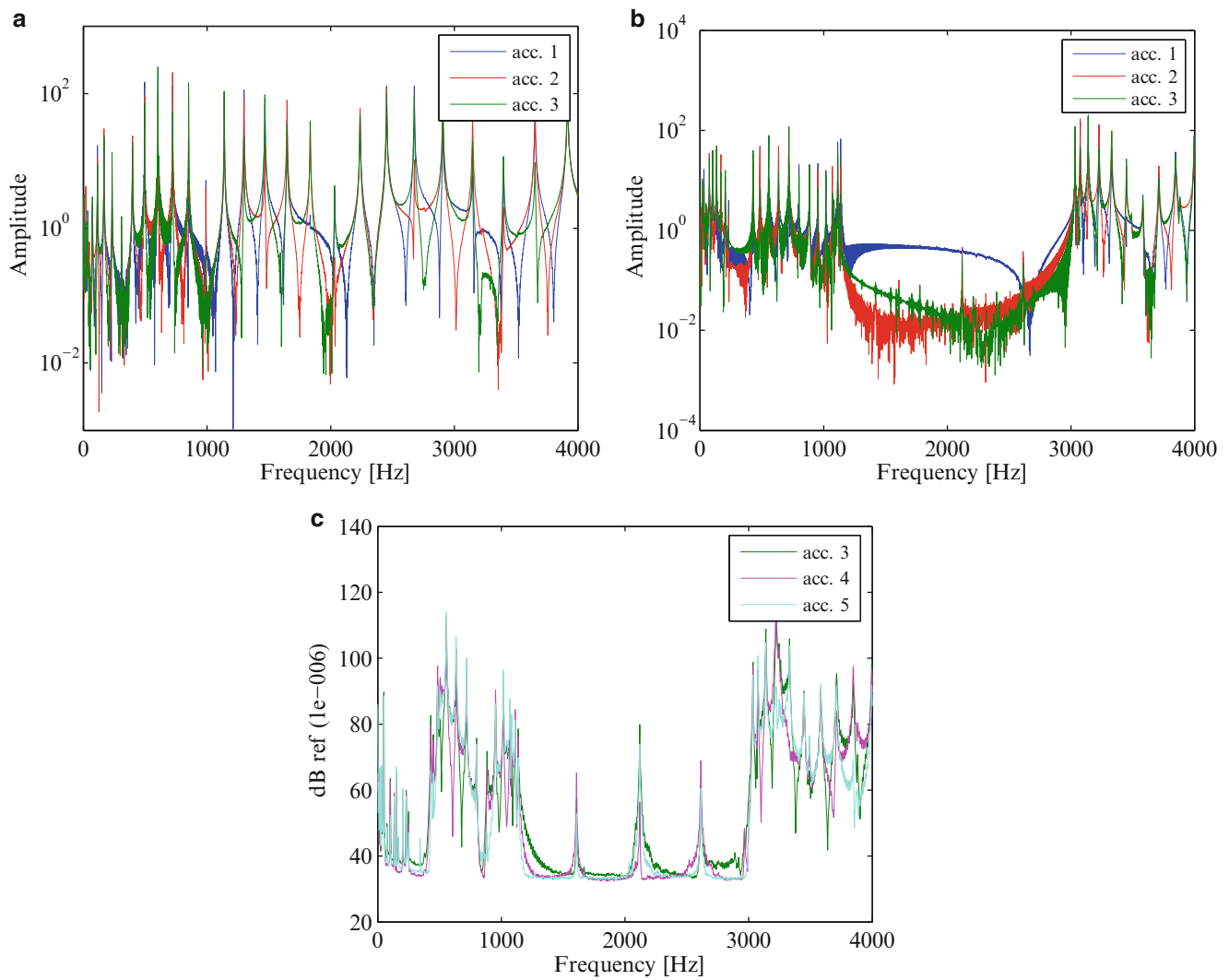
**Fig. 17.9** Experimental results: (**a**) frequency-response-function—homogenous beam; (**b**) frequency-response-function—beam with periodical change in the cross-section; (**c**) acceleration-power-spectra—beam with periodical change in the cross-section

## 17.4  Conclusions

Two approaches for predicting vibro-acoustic stop-bands were described: the first applies to infinite periodic structures using a wave approach; the second deals with the evaluation of a structural transmission loss coefficient, which is defined to predict the performance in terms of noise and vibration insulation provided by a certain number of periodic cells embedded semi-periodically into an otherwise uniform structure. Numerical examples concerning a beam with periodical change in the cross-section and a beam with periodically attached masses were presented. Results were discussed and validated experimentally. Stop-bands obtained using a simple wave approach (applied to the infinite periodic structure) predicted those obtained evaluating the transmission loss coefficient for the corresponding finite periodic structure when few cells are considered. Very good agreement between the numerical and experimental models in terms of stop-bands was found. Results showed that few repetitions of a cell are sufficient to drastically reduce disturbance transmission whose dominant frequencies fall within the stop-bands.
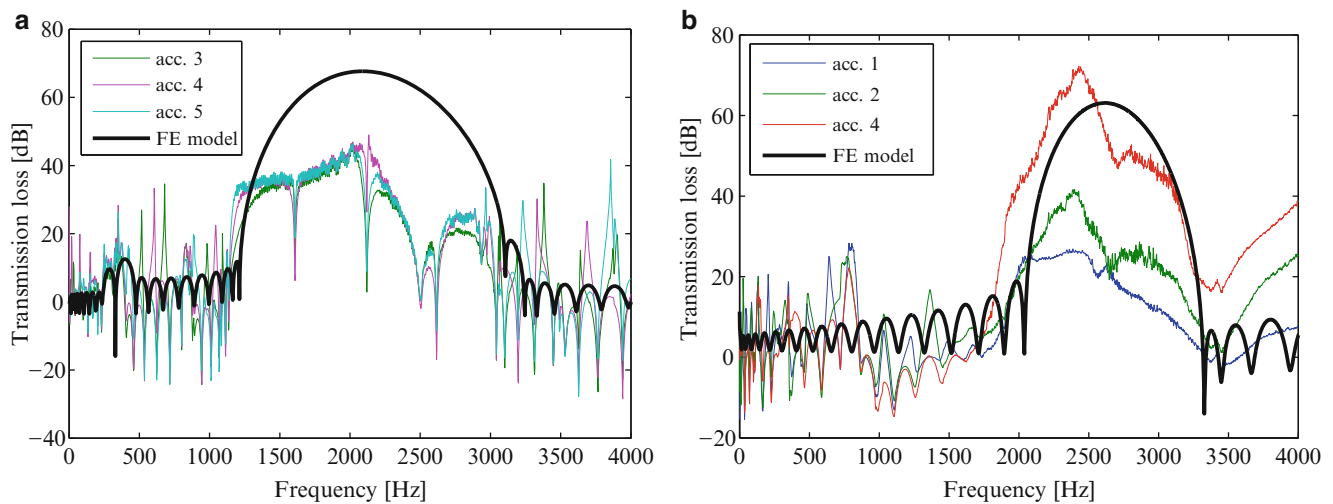
**Fig. 17.10** Transmission loss coefficient. Comparison between experimental and numerical results: (**a**) beam with periodic change in the cross section; (**b**) beam with periodically attached masses

# References

1. Brillouin L (1953) Wave propagation in periodic structures. Dover Publications, New York
2. Billings L (2013) Engineered structures with bizarre optical properties are set to migrate out of the laboratory and into the marketplace. Nature 500:138–140
3. Mead D (1975) Wave propagation and natural modes in periodic systems: I. mono-coupled systems. J Sound Vib 40:1–18
4. Mead D (1975) Wave propagation and natural modes in periodic systems: II. multi-coupled systems, with and without damping. J Sound Vib 40:19–39
5. Mead D (1986) A new method of analyzing wave propagation in periodic structures; applications to periodic timoshenko beams and stiffened plates. J Sound Vib 104:9–27
6. Ruzzene M, Baz A (2000) Control of wave propagation in periodic composite rods using shape memory inserts. J Vib Acoust 122:151–159
7. Romeo F, Luongo A (2003) Vibration reduction in piece wise bi-coupled periodic structures. J Sound Vib 268:601–615
8. Langley RS (1995) Wave transmission through one-dimensional near periodic structures: optimum and random disorder. J Sound Vib 188:717–743
9. Søe-Knudsen A, Darula R, Sorokin S (2012) Theoretical and experimental analysis of the stop-band behavior of elastic springs with periodically discontinuous of curvature. J Acoust Soc Am 132:1378–1383
10. Langley RS (1996) The response of two-dimensional periodicstructures to point harmonic forcing. J Sound Vib 197:447–469
11. Mace BR (1980) Periodically stiffened fluid-loaded plates, i: Response to convected harmonic pressure and free wave propagation. J Sound Vib 73:473–486
12. Mead D (1996) Wave propagation in continuous periodic structures: Research contributions from southampton, 1964–1995. J Sound Vib 190:495–524
13. Banerjee J (1997) Dynamic stiffness formulation for structural elements: A general approach. Comput Struct 63:101–103
14. Mace BR, Manconi E (2008) Modelling wave propagation in two-dimensional structures using finite element analysis. J Sound Vib 318:884–902
15. Manconi E, Mace BR (2009) Wave characterization of cylindrical and curved panels using a finite element method. J Acoust Soc Am 125:154–163
16. Andersen L, Nielsen S, Kirkegaard P (2001) Finite element modelling of infinite euler beams on kelvin foundations exposed to moving loads in convected co-ordinates. J Sound Vib 241:587–604
17. Ewins DJ (1984) Modal testing: theory and practice. Research Studies Press, Letchworth, Hertfordshire

# Chapter 18
# Operating Mode Shapes of Electronic Assemblies Under Shock Input

**Ryan D. Lowe, Jason R. Foley, David W. Geissler, and Jennifer A. Cordes**

**Abstract** Modeling the dynamic response of electronic assemblies is critical to predicting both the reliability and survivability of systems in harsh environments. However, a large number of unknowns are typically faced when simulating electronic response in any given scenario, including new/unknown materials, non-ideal interfaces, and uncertainty in input forces. In order to support the verification and validation of these models, the dynamic response of electronic assemblies to input shock loads are experimentally measured using a variety of instrumentation: accelerometers, strain gages, and laser vibrometers. The experimental operating mode shapes are compared with both implicit (i.e., computational modal analysis) and explicit (i.e., transient response) predictions. Finally, the models are then shown to more accurately predict the dynamic response and partitioning of vibrational energy under a variety shock loads.

**Keywords** Electronics • Printed circuit board (PCB) • Model validation • Shock • Modal analysis

## 18.1 Introduction

Modeling and simulation of electronic assemblies provides a powerful tool for predicting both the reliability and survivability of systems in harsh environments. Previous work [1] focused on examining the underlying constitutive response of electronics. This work focuses on the resulting operating mode shapes. A large number of variables beyond the control of an experimentalist/modeler necessitate experimental validation of simulations to develop confidence in reported results. New/unknown materials, non-ideal interfaces, and uncertainty in input forces are major challenges in the development of truly predictive models. This paper discusses a new method for exciting small, stiff printed circuit boards (PCB) for the purpose of experimentally validating numerically predicted mode shapes. The motivation for the development of the new method is motivated by the inherent challenges of using traditional methods, such as force hammers to excite small stiff structures.

R.D. Lowe
Air Force Research Laboratory, Eglin AFB Eglin, FL 32542-5430, USA

J.R. Foley (✉)
Air Force Research Laboratory, Eglin AFB, Eglin, FL 32542-5430, USA

AFRL/RWMF, 306 W. Eglin Boulevard, Building 432, Eglin AFB, Eglin, FL 32542-5430, USA
e-mail: jason.foley@eglin.af.mil

D.W. Geissler • J.A. Cordes
U.S. Army Armament Research, Development, and Engineering Command, U.S. Army ARDEC,
RDAR-MEF-E, Picatinny Arsenal, NJ 07806-5000, USA

**Fig. 18.1** Schematic of the trampoline experiment with electronics fixture and the circuit board under test
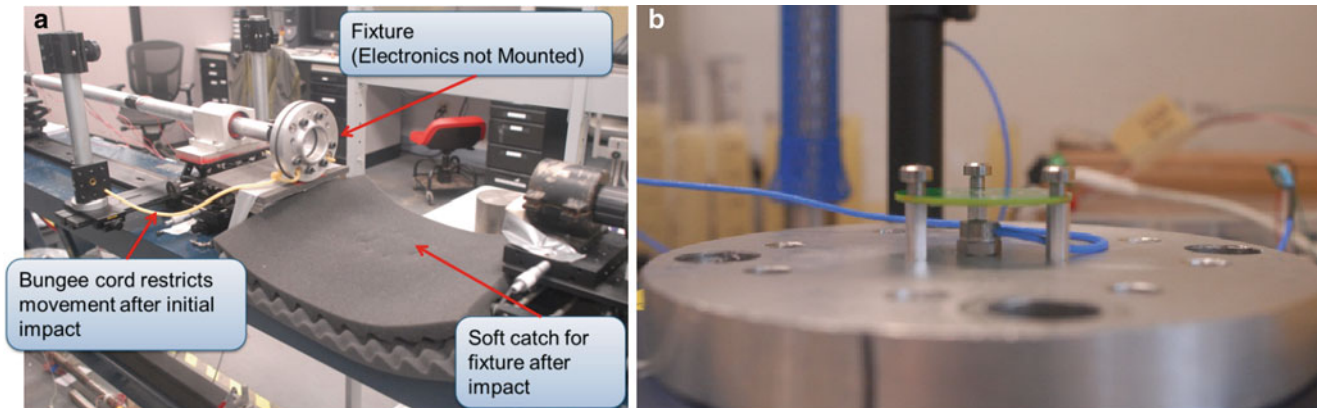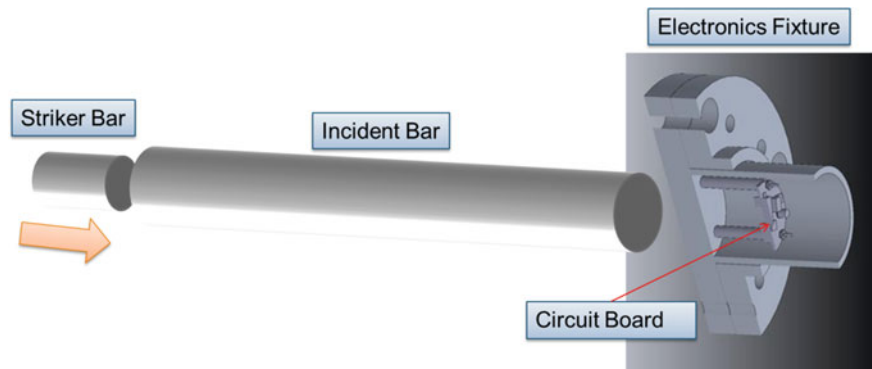




**Fig. 18.2** Photographs showing (**a**) initial experiment apparatus and a close-up (**b**) of the lower fixture with a mounted test board and reference accelerometer

## 18.2 Test Setup

The experimental test setup was designed specifically to excite small, stiff PCB samples for model validation. The so-called "trampoline" dynamic test, is a reverse Hopkinson bar experiment [2]. The trampoline uses an electronics housing fixture that is compatible with other shock tests. A striker impacts a long incident bar which transmits a dynamic compressive stress wave into the fixture supporting a circuit board assembly. This is shown schematically in Fig. 18.1.

Standoffs attach the circuit board to a cast aluminum fixture, providing a direct load path into the test articles, which are 41 mm diameter circular printed circuit boards. Photographs of the experimental setup are shown in Fig. 18.2. The incident bar has been instrumented with semiconductor strain gages and calibrated using a dispersion-correction technique [3]. A reference accelerometer (shown in Fig. 18.2b) is used to verify the local acceleration due to the applied force.

An OFV-332 Polytec laser vibrometer head [4] is used with the OFV-3020 high speed (20 m/s) controller/demodulator to provide a non-contact measurement of the surface velocity of the board. Figure 18.3a shows the surface velocity time history and equivalent acceleration of the center of the printed circuit board. The instantaneous acceleration (unfiltered, shown in Fig. 18.3b) exceeds 30,000$g$'s, indicating a far more severe local acceleration than anticipated.

## 18.3 Finite Element Simulation

Finite element models included the striker, incident bar, fixture, and electronics were simulated with ABAQUS 6.12.1. No symmetry was assumed in the modeling. The analysis was run as a dynamic explicit simulation with non-linear materials and non-linear geometry. Eight node brick elements with reduced integration and hourglass control were used to model all components. All sections have at least four elements through the thickness to approximate bending. Material property models included linear elastic, linear orthotropic and elastic/plastic material models as appropriate. Friction coefficients between interfaces were varied as part of the study and are described in later sections. Damping was applied to the FR4-06
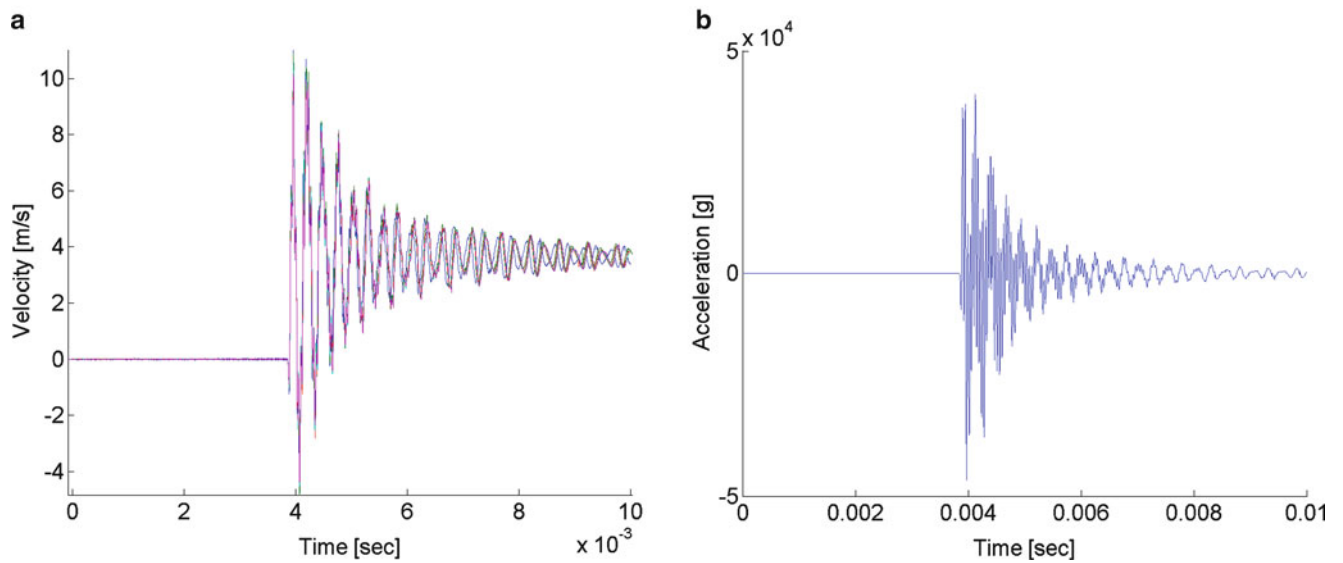
**Fig. 18.3** (**a**) Printed circuit board surface velocity of five unique tests and (**b**) equivalent instantaneous acceleration (in *g*'s) of the center of the printed circuit board in the trampoline experiment for a single test
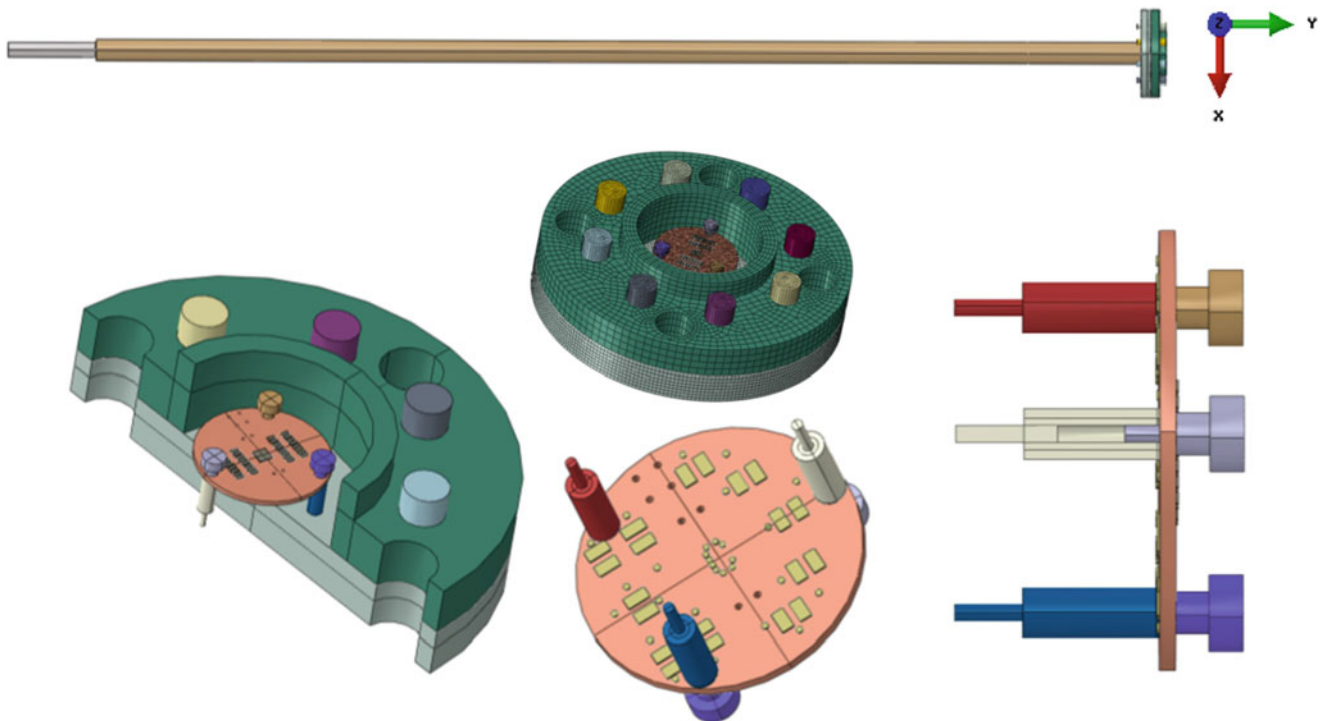


**Fig. 18.4** Representative mesh for high fidelity simulation of PCB response

material based on the first ten natural frequencies. All initial conditions were zero except for the initial velocity of the striker. The actual and modeled mass of the systems agreed to within 2.5 %. Please see [5] for full details of the model development including specific material properties. Illustrative images from the model are shown in Fig. 18.4. In addition to the explicit finite element model a linear modal analysis was performed to identify mode shapes.

A few mode shapes predicted by the finite element simulation are represented in Fig. 18.5. Not all modes are assumed to contribute to failure in the PCB. Specifically modes that represent significant deflection in the standoffs, but little deformation
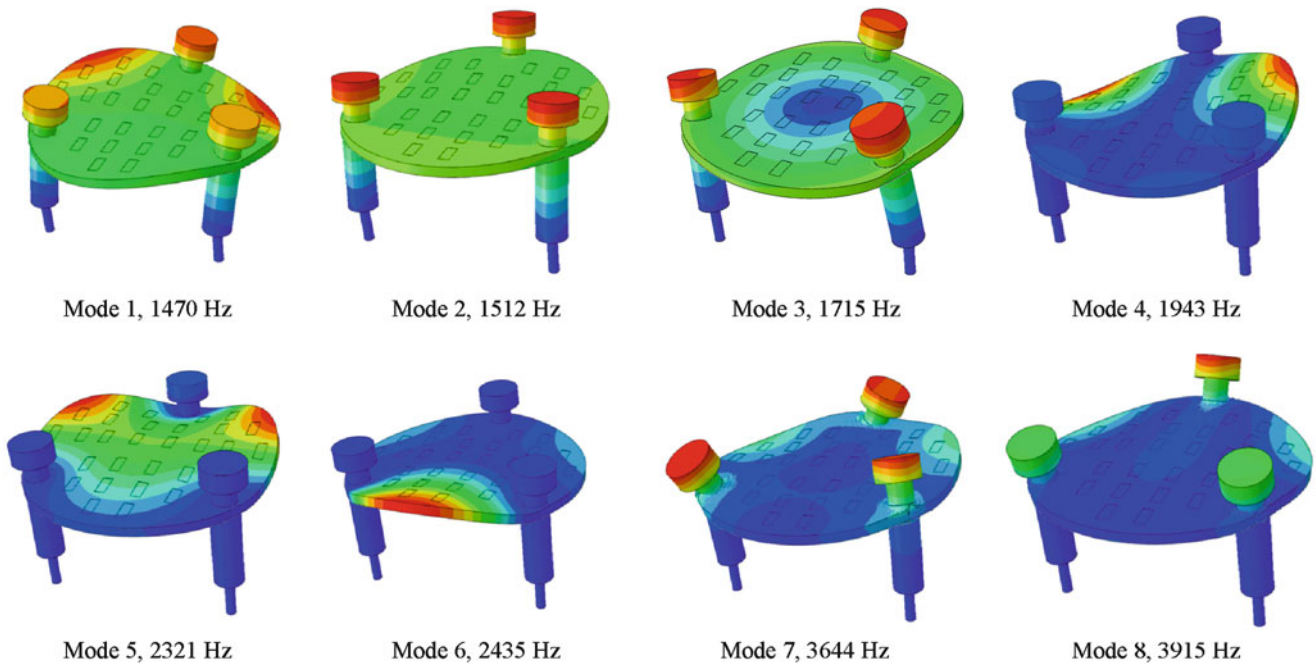
Fig. 18.5 Mode shapes of the PCB predicted with implicit simulation

Fig. 18.6 Effective modal mass
in the out of plane direction
(normal to the PCB)
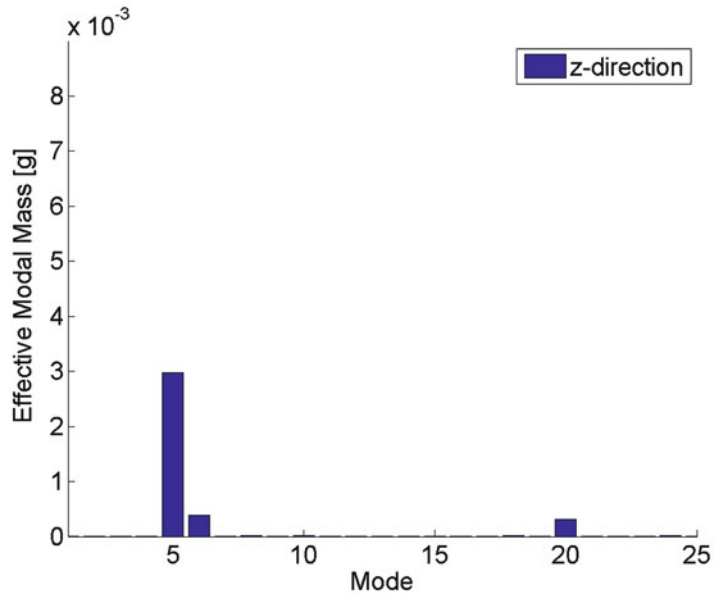


or bending in the PCB are assumed to have little effect on the survivability of the PCB and its components such as resistors, capacitors, and integrated circuits. The relative contribution of each mode to the response of the PCB was evaluated using the effective modal mass. Figure 18.6 shows that only a few modes contribute significantly to the response of the board. Alarmingly the sum of the effective modal mass for the first 25 modes only represented about half of the actual mass of the system. In a follow along study that is beyond the scope of this paper variations in material properties and their effect on natural frequencies were investigated for the same PCB geometry. Figure 18.7 shows the results of six similar simulations and the effective modal mass for the first 100 modes. By including a large quantity of modes the total effective modal mass was simulated to within 98 % of the actual mass. Surprisingly modes 60–70 (around 25–30 kHz) contribute significantly to the total modal mass.
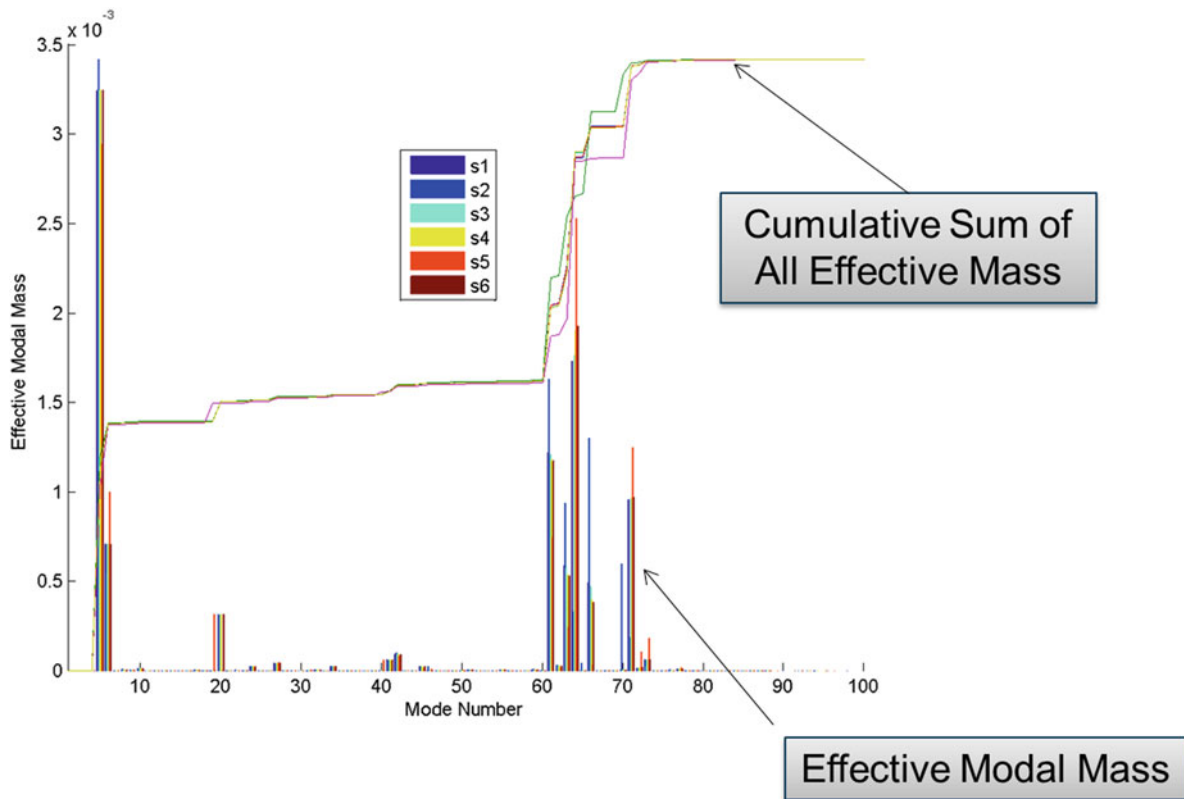
**Fig. 18.7** Sum of effective modal mass in the out of plane direction (w.r.t. the PCB) for an extended number of mode shapes. This chart is a summary of six cases each with a geometry identical the PCB studied in this paper, but using slightly different material properties
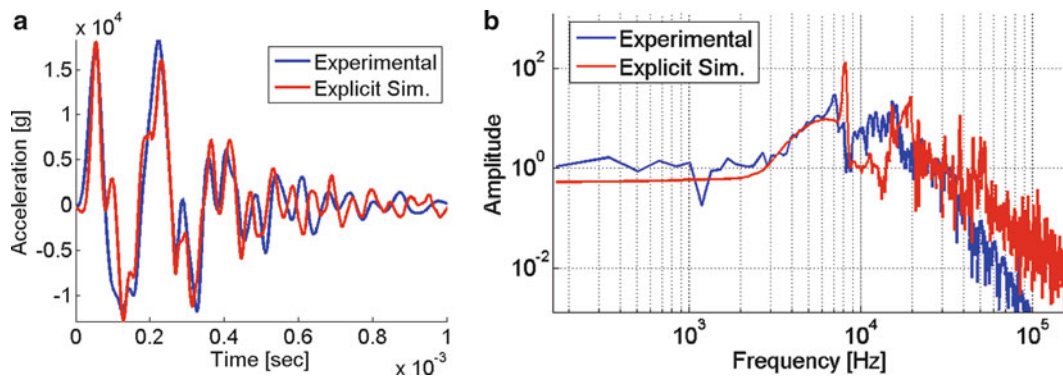


**Fig. 18.8** (**a**) Comparison of base excitation measured underneath PCB on fixture. (**b**) Frequency domain representation of time history shown in (**a**)

## 18.3.1  Experimental Validation of Model

Model validation using explicit dynamic simulations and implicit modal analysis was performed. First the acceleration measured underneath the PCB on the aluminum fixture was studied. A thorough understanding of the friction between the plates of the fixture was required to accurately model the acceleration of the fixture. Figure 18.8 illustrates the similarity between experiment and simulation in both the time and frequency domain. For the purposes of model validation the results are deemed acceptable for the intended use of the model.

Quantitative mode shape correlation proved difficult due to the limited sensing ability of the single point velocity measurement. The frequency content of the time history shown in Fig. 18.3a has dominant peaks that match with predicted mode shapes, but the predicted modes seem unlikely to physically be observable using our current measurement

**Fig. 18.9** Frequency domain
representation of PCB velocity
time history shown in Fig. 18.3a.
Dominant peaks are located at
3,815 and 22,200 Hz
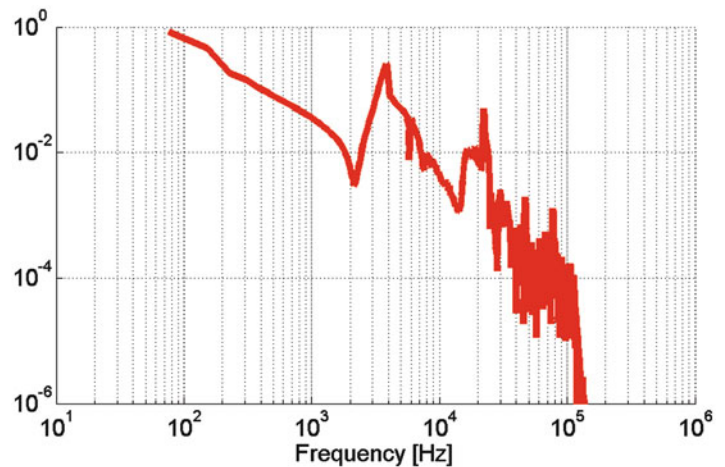


methods (Fig. 18.9). Furthermore none of the modes with significant modal mass are visible in Fig. 18.3. Unfortunately we
do not believe the results to be sufficient for the purposes of our model validation. Future work in both experimental and
numerical domains is being planned to increase correlation of observed and predicted mode shapes. Experience has shown
that simulation results are highly sensitive to small changes in the location of the mounting screws. The sensitivity of results
to material properties are believed to be much less severe, but the orthotropic constants used for the circuit board are also
candidates for improving experimental/simulation validation.

## 18.4 Summary

This work investigates the operational mode shapes of small stiff printed circuit board structures using a reverse Hopkinson
test method. The use of these methods was motivated by challenges in using a traditional force hammer to excite high
frequency modes. Details of the test method were provided along with a demonstration of the highly repeatable nature of
the method. Experimental validation was used to judge the results from both explicit and implicit finite element simulations.
The response of the fixture holding the electronics was validated to closely match with experimental results. Unfortunately
the observed mode shapes were not quantitatively validated with numerical predictions. A number of possible error sources
leading to the unsatisfactory result were discussed.

## References

1. Lowe RD, Dodson JC, Foley JR, Mougeotte CS, Geissler DW, Cordes JA (2014) Constitutive response of electronics materials. In: Challenges
   in mechanics of time-dependent materials and processes in conventional and multifunctional materials, vol 2. Springer, New York, pp 57–74
2. Bell W, Davie N (1987) Reverse Hopkinson bar testing. Sandia National Labs, Albuquerque, NM
3. Dodson JC, Lowe RD, Foley JR (2013) Dispersive wave propagation analysis and correction in Hopkinson bar experiments. J Shock Vib
   (in preparation)
4. OFV-552 Laser Vibrometer: Polytec Commercial product (2010)
5. Geissler D, Mougeotte C, Cordes J (2013) Numerical assessment of modeling and simulation of electronic components. Shock Vib Exchange

# Chapter 19
# Comparison of Modal Parameters Extracted Using MIMO, SIMO, and Impact Hammer Tests on a Three-Bladed Wind Turbine

**Javad Baqersad, Peyman Poozesh, Christopher Niezrecki, and Peter Avitabile**

**Abstract** As part of a project to predict full-field dynamic strain of rotating structures (e.g. wind turbines or helicopter rotors), a validated numerical model of a structure is required. In this case, a small wind turbine was used. To understand the dynamic characteristics and validate a finite element model of a three-bladed wind turbine, several experimental modal analysis tests were conducted on the turbine attached to a 500-lb steel block. The test structure consisted three 2.3-m blades mounted to a hub that was attached to the block using a shaft and a lathe chuck. In three separate tests, the structure was excited using a single shaker, multiple shakers, and an impact hammer; the responses of the structure to the excitations were measured using 12 triaxial accelerometers. The results reveal several very closely spaced modes present within the turbine in the test configuration. The natural frequencies and mode shapes obtained by using three different methods were compared to demonstrate the differences (e.g. strengths and weaknesses) between each excitation technique. The paper reports the results obtained and lessons learned during the experimental modal tests of the wind turbine.

**Keywords** Experimental modal analysis • Mode shape • Wind turbine • Multiple shakers

## 19.1 Introduction

Experimental modal analysis is extensively used to describe the dynamic characteristics of structures and to validate numerical models. Furthermore, these extracted modal parameters from the modal analyses are essential parts of many health-monitoring algorithms. Several experimental techniques are used to excite structures and to extract their modal parameters. Multiple-input multiple-output (MIMO) measurement, single-input multiple-output (SIMO) measurement, and impact hammer modal testing are three conventional approaches for experimental modal analysis. These three techniques may not always produce similar results if they are used for large complicated structures. Therefore, comparing the extracted parameters from these three techniques is desirable.

Modal impact hammer has been commonly used to extract the dynamic characteristics of wind turbine blades or wind turbine assemblies [1–7]. However, MIMO technique has been usually used for large structures such as a satellite [8] and inflatable torus [9]. A comparison between the MIMO and SISO (single-input single-output) results for a measurement on a membrane mirror satellite has been performed by Ruggiero et al. [10]. On the other hand, the number of studies found in the literature that compares the modal parameters estimated by using the three methods for a wind turbine that includes several subcomponents and has closely spaced modes is limited.

In the current paper, modal parameters extracted using MIMO, SIMO, and impact hammer modal techniques are compared to identify the differences between each excitation technique. The test structure, an assembled wind turbine, consisted of several substructures and has very closely spaced modes (less than 0.1 Hz difference). Therefore, the potential of each experimental modal approach in extracting the modal parameters of the structure can be examined. The current paper also summarized the results obtained and lesson learned during the experimental modal test of the wind turbine attached to a steel block.

J. Baqersad (✉) • P. Poozesh • C. Niezrecki • P. Avitabile
Structural Dynamics and Acoustic Systems Laboratory, University of Massachusetts Lowell,
One University Avenue, Lowell, MA 01854, USA
e-mail: javad_baqersad@student.uml.edu

## 19.2 Theoretical Background

### 19.2.1 Shaker Test with the Input Oblique to the Global Coordinate System

Often for convenience, shakers are installed in a direction parallel to one of the axes of the global coordinate system (X, Y, or Z) for SIMO or MIMO tests. The measured acceleration and force at the impedance head (as a reference) are required to properly obtain the frequency response functions of the structure at all the measurement points including the reference point to extract the mode shapes. However, installing a shaker parallel to an axis of the coordinate system does not excite the modes of the structure that have no component along that axis. For the current work, shakers were installed normal to the contact surface of the blade (at attached points) and oblique to the global coordinate system. For this setup, the direction of the input force and measured acceleration at an impedance head mounted to the shaker stinger cannot be defined using a single component of the global coordinate system (X, Y, or Z direction). Furthermore, finding the accurate orientation of the input force can be a challenge. Therefore, identifying an approach to easily orient the shakers in arbitrary configurations to conduct a modal test would be of particular interest [11]. The approach to extract the mode shapes when a shaker is installed in an oblique orientation is now described.

Experimental modal tests are performed to measure the frequency response functions of structures. The frequency response function (FRF) for a structure (i.e. the system transfer function evaluated in the frequency domain) can be defined as:

$$h_{ij}(j\omega) = \sum_{k=1}^{m} \frac{a_{ijk}}{(j\omega - p_k)} + \frac{a_{ijk}^*}{(j\omega - p_k^*)} \tag{19.1}$$

where, $p_k$ is the $k$-th mode of the system. Residues ($a_{ijk}$) can be calculated using the following equation:

$$a_{ijk} = q_k u_{ik} u_{jk} \tag{19.2}$$

where $u_{ik}$ and $u_{jk}$ are the $k$-th mode of the structure at point $i$ and $j$ respectively. As can be seen, the residues are directly related to the system mode shapes and are scaled by $q_k$, the scaling constant for $k$-th mode. The residue matrix for the whole set of measurement can be written as:

$$\begin{bmatrix} a_{11k} & a_{12k} & a_{13k} & \cdots \\ a_{21k} & a_{22k} & a_{23k} & \cdots \\ a_{31k} & a_{32k} & a_{33k} & \cdots \\ \vdots & \vdots & \vdots & \ddots \end{bmatrix} = q_k \begin{bmatrix} u_{11k} & u_{12k} & u_{13k} & \cdots \\ u_{21k} & u_{22k} & u_{23k} & \cdots \\ u_{31k} & u_{32k} & u_{33k} & \cdots \\ \vdots & \vdots & \vdots & \ddots \end{bmatrix} \tag{19.3}$$

If a particular reference such as *10y* (where the shaker is installed) is picked for the measurement, the set of data for a single reference can be written as:

$$\begin{Bmatrix} a_{1x10y} \\ a_{1y10y} \\ a_{1z10y} \\ a_{2x10y} \\ a_{2y10y} \\ \vdots \\ a_{10y10y} \\ \vdots \\ a_{40y10y} \\ a_{40z10y} \end{Bmatrix} == qu_{10y} \begin{Bmatrix} u_{1x} \\ u_{1y} \\ u_{1z} \\ u_{2x} \\ u_{2y} \\ \vdots \\ u_{10y} \\ \vdots \\ u_{40y} \\ u_{40z} \end{Bmatrix} \tag{19.4}$$

where, points 1–40 are measurement points. The drive point measurement (point *10y*) is used to scale the residues to get the scaled mode shapes for all the measurement points including the drive point.

$$a_{10y10y} = qu_{10y} u_{10y} \tag{19.5}$$

However, the structure can be excited using an oblique shaker to excite more modes of the system that might not be excited by a single shaker in $y$-direction. If the input force excites the system at point *41* and is orientated in an unknown direction called s, the set of data for a particular mode can be written as:

$$\left\{\begin{array}{c} a_{1x41s} \\ a_{1y41s} \\ a_{1z41s} \\ a_{2x41s} \\ a_{2y41s} \\ \vdots \\ a_{10y41s} \\ \vdots \\ a_{40y41s} \\ a_{40z41s} \\ a_{41s41s} \end{array}\right\} = qu_{41s} \left\{\begin{array}{c} u_{1x} \\ u_{1y} \\ u_{1z} \\ u_{2x} \\ u_{2y} \\ \vdots \\ u_{10y} \\ \vdots \\ u_{48y} \\ u_{48z} \\ u_{41s} \end{array}\right\} \tag{19.6}$$

and the drive point measurement is:

$$a_{41s41s} = qu_{41s}u_{41s} \tag{19.7}$$

Equation (19.7) can be used to scale the mode shape for points *1* to *40* in Eq. 19.6. However, once the mode shapes are scaled using the drive point measurement, point *41* can be excluded from the mode shape description. Thus, the mode shape of the structure can be extracted without identifying the orientation of the input force. The same procedure can be repeated for a MIMO measurement. This means that for the mode shape description, no geometric point exists at drive points (impedance heads).

## 19.3 Structure Description and Test Setup

As part of a project to predict full-field dynamic strain for a rotating structure and in order to validate a finite element model, an experimental modal measurement on a wind turbine in a fixed condition needed to be performed. In order to prepare a test set up for the wind turbine, three blades of a Southwest Windpower Skystream 4.7 were mounted to a central hub while connected to a 500-lb block using a lathe chuck and a shaft. The 2.3-m blades were made of a composite/plastic material. The hub included an aluminum component and a steel plate that were connected using 12 steel bolts. In order to isolate the vibration of the block from the ground and to prevent rattling along the contact surface, some layers of elastic foam were used. A photograph of the test set-up is shown in Fig. 19.1. Although different excitation techniques (three-shaker, single-shaker, and an impact hammer) were used for Cases 2–4, the test configuration and measurement steps were similar for all three cases and are now described.

The location of the sensors was selected using a finite element (FE) model of the wind turbine. By performing an eigensolution on the numerical model in a fixed boundary condition, FE mode shapes were extracted. Using the FE model, an appropriate set of sensor locations was selected so that all the modes of interest could be identified (see Fig. 19.2). The origin of the coordinate system for the turbine is located at the center of the hub where X-axis and Z-axis are in the rotating plane and Z points toward the tip of Blade 1 (see Fig. 19.2). The Y-axis refers to the transverse displacement of the blade (i.e. the out-of-plane or flapwise direction).

A 60-channel LMS data acquisition system was used to record the response of the structure and the input force. Because extracting both flapwise and edgewise modes were desirable, triaxial accelerometers were selected for the testing. Twelve accelerometers were mounted per blade distributed at locations over all three blades of the turbine. The frequency bandwidth of the acquisition system for all the measurements (Cases 1–4) was 128 Hz; however, due to spatial resolution, only the results below 80 Hz are shown in the current paper (mode shapes with natural frequencies higher than 80 Hz have curvatures that are difficult to show with the limited number of measurement points).

The limitations in the number of available accelerometers and the available channels of the data acquisition system did not allow all the measurements to be carried out in a single set-up of accelerometers. Therefore, the test was performed on four

**Fig. 19.1** A photograph of the test set-up showing the wind turbine attached to the steel-block (the accelerometers are mounted to Blade 3)
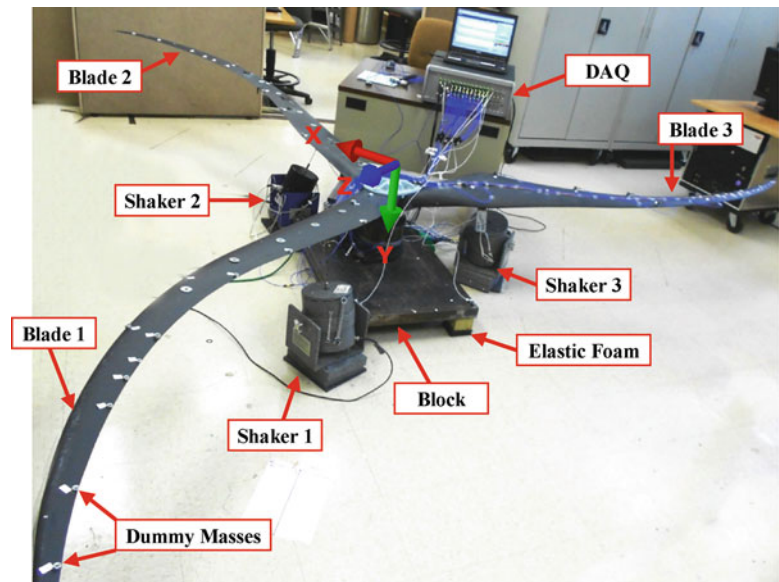


**Fig. 19.2** A drawing of the test set-up showing the sensor locations
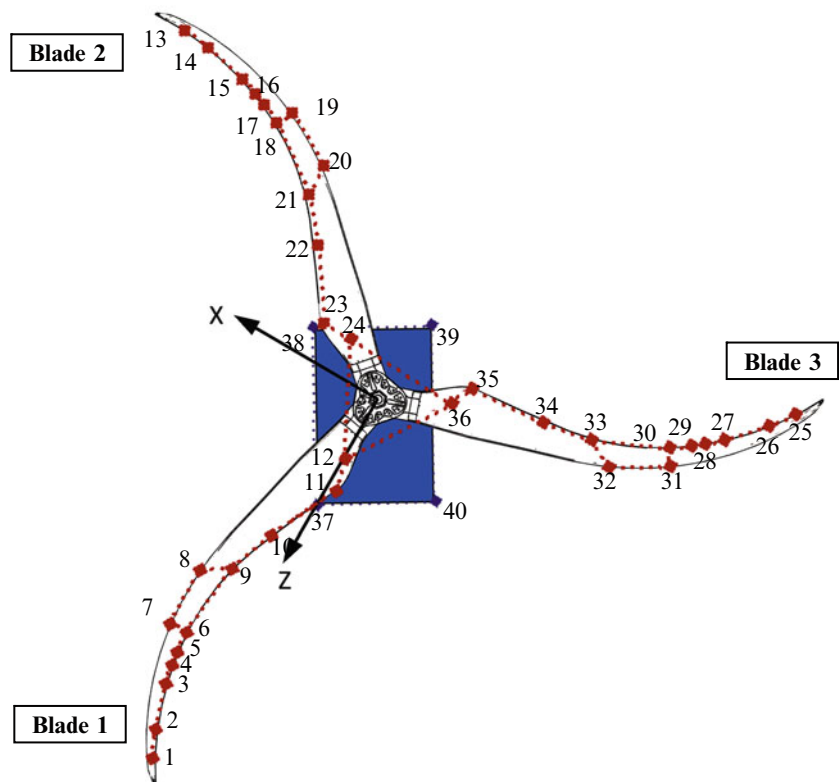


separate set-ups; however, this requires extra consideration to mass loading which is discussed further. For the first set-up, all the accelerometers were installed on Blade 1. The response of the turbine to the excitations was measured by using 12 triaxial accelerometers mounted to Blade 1 (36 channels). Then, the accelerometers were moved to Blade 2 and the response of the structure was measured. Next, the accelerometers were moved to Blade 3 and same measurements were repeated. The final set of measurement was performed when four of the triaxial accelerometers were attached to the support block and the turbine was exited by using impact hammers or shakers.

To compensate for the mass of the accelerometers, dummy masses were installed to emulate the weight of the accelerometers and connected wires. When the accelerometers are mounted to one blade, a set of dummy masses were used

on the accelerometer locations of the other two blades. In order to lower the mass loading effects, lighter accelerometers were used at the points near the tip of the blades. (The use of dummy masses on this type of lightweight blade structure is critical to the success of measuring and extracting useful mode shapes. If these compensation masses are not used then there would be a significant mass loading effect and the frequency response functions used for the modal extraction process would not be of sufficient quality to extract accurate mode shapes).

## 19.4   Test Cases Studied

### 19.4.1   Case 1: Impact Hammer Modal Test on the Fixture

The primarily objective of the work was to find the mode shapes of the wind turbine in a fixed configuration. However, providing a test condition for the turbine that replicates the built-in condition is very difficult. Considering the available equipment, the turbine was attached to a fixture that included a lathe chuck and a steel block placed on layers of elastic foam. However, some modes of the fixture might occur in the bandwidth of interest (the bandwidth that was used to extract the modes of the turbine in fixed condition). Therefore, due to interactions between the modes of the fixture and the wind turbine, the modes of the fixture needed to be determined before the fixture was attached to the turbine.

In order to identify the modes that were associated with the test rig, a modal impact hammer test was performed on the fixture alone (see Fig. 19.3). The purpose of this test was to understand the contribution of the test fixture to the overall dynamics of the complete turbine blade attached to the test fixture. On the other hand, the set up needed to consider the inertial effects of the turbine but not their mode shapes. In order to emulate the inertia effects of the blades, some masses were mounted to the shaft. Due to limitation in mountings, the added mass could partially replicate the masses of the blades (the added mass is only 11 kg while the mass of the turbine was 23 kg). Likewise, the rotational inertia effect of the turbine blades (that is due to off-center distribution of the mass of the blades) was not considered in this set up. These effects might cause some discrepancies between the modes extracted in this case and fixture modes extracted when the blades are also attached to the fixture; this will be addressed in Case 2 when the fixture modes are described.

Using four triaxial accelerometers, a modal impact hammer test was performed on the structure. Because, the flexible modes of the plate were in higher frequencies than the frequency bandwidth of interest, accelerometers were only mounted to the corners of the block. Figure 19.4 shows sample FRF and coherence plots of the measurement. The six modes of the structure extracted using a LMS PolyMAX [12] stability diagram are shown in Fig. 19.5.
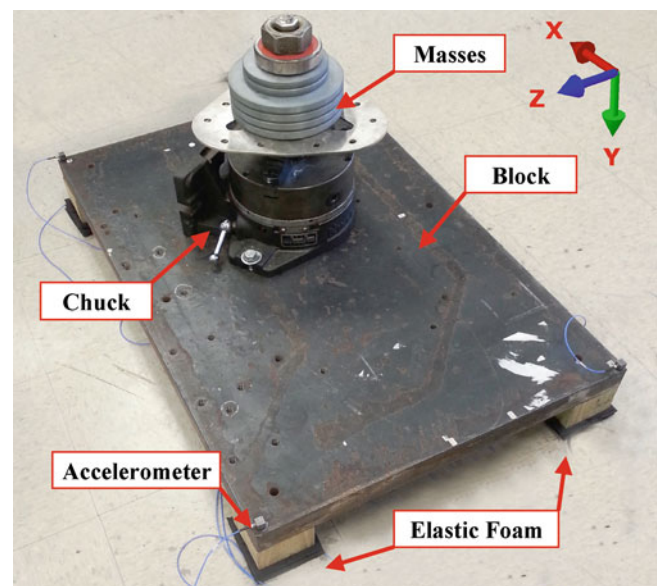


**Fig. 19.3** A photograph of the fixture showing the chuck, masses, and 500-lb block placed on layers of elastic foam
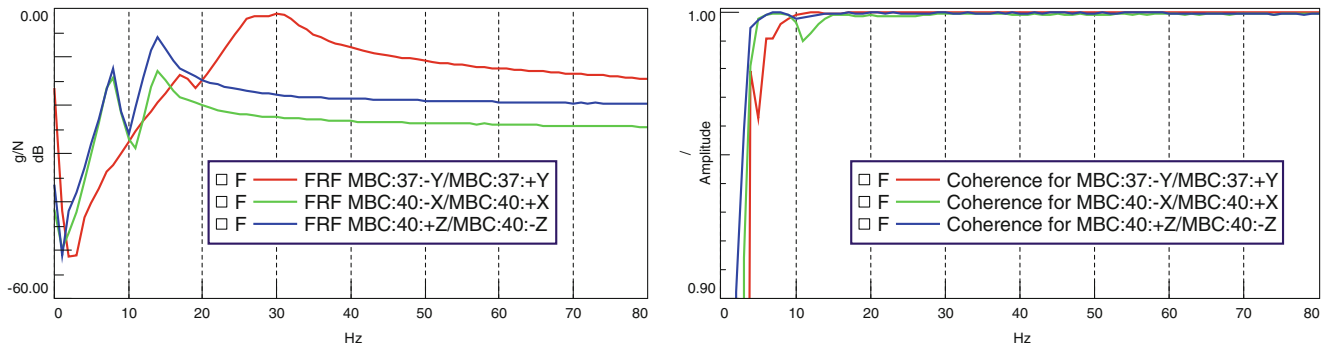
**Fig. 19.4** Sample FRF and coherence plots for the impact test measurement on the fixture
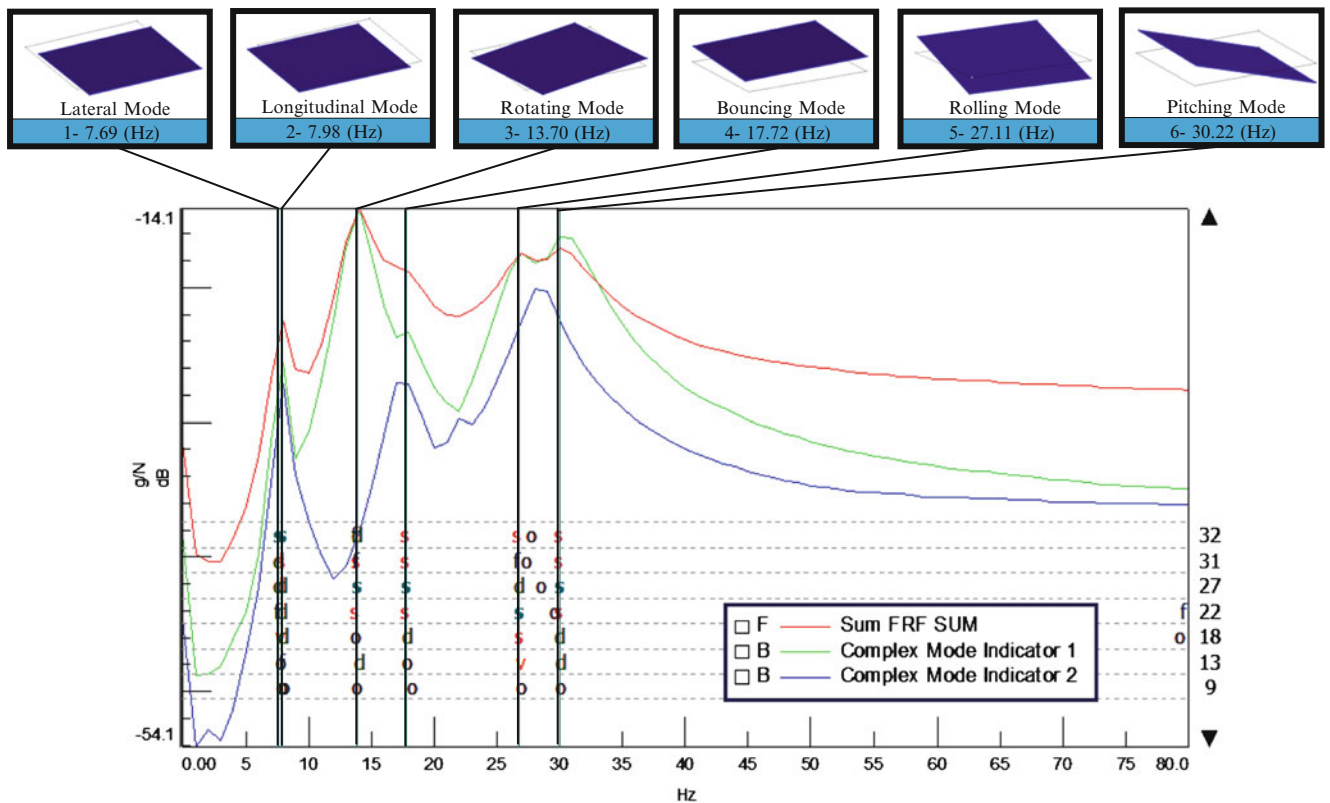


**Fig. 19.5** Stability diagram, natural frequencies, and mode shapes of the fixture (500-lb block and accessories) on layers of elastic foam

### 19.4.2 Case 2: MIMO Test on the Wind Turbine Assembly

A MIMO test was performed on the structure using three shakers (see Fig. 19.1). Each shaker was connected to a single blade and was exciting the turbine using a burst random input. Because there were very closely spaced modes in the structure, a high resolution was used for the data acquisition (1,024 spectral lines that needed 8 s of data recording). Before performing the measurement, a principle component analysis was performed to assure that all three shakers were uncorrelated and independent.

In order to identify the resonant frequencies of the assembly, a LMS PolyMAX [12] stability diagram was used. Figure 19.6 shows the natural frequencies and mode shapes of the wind turbine attached to the steel block. The color code shows the grouping of the modes.
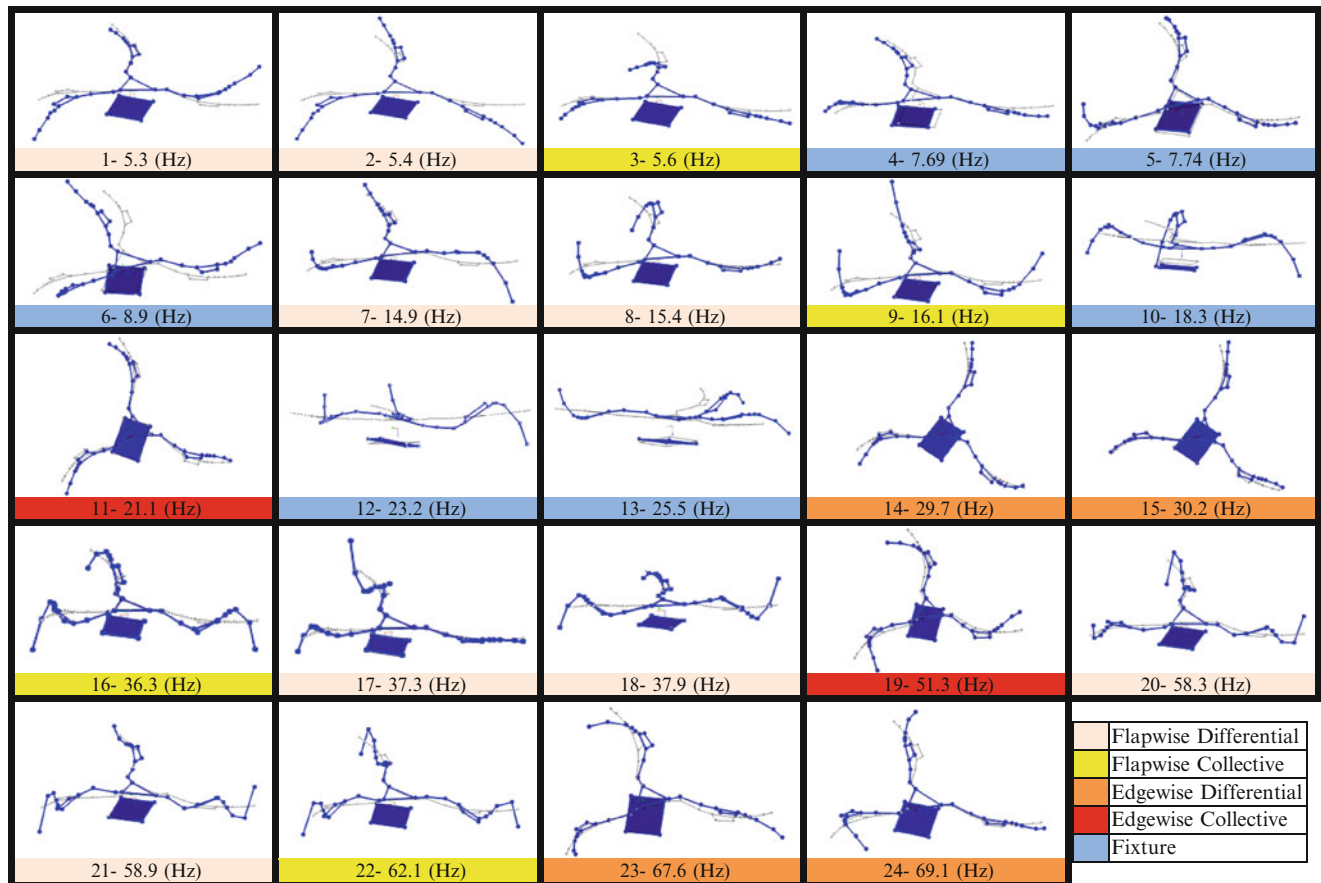
**Fig. 19.6** Natural frequencies and mode shapes of the wind turbine attached to the 500-lb block

The modes of the assembled structure that come from the modes of the test setup are called fixture modes in Fig. 19.6. These modes were identified by comparing their shapes and frequencies to the modes shown in Fig. 19.5. Comparing the results in Figs. 19.5 and 19.6, the natural frequencies for the modes of the test rig that were related only to the mass of the structure (modes 4, 5, and 10 in Fig. 19.6 that are respectively equivalent to lateral, longitudinal, and bouncing modes shown in Fig. 19.5) have slightly changed. However, the modes of the structure that were related to the rotational inertia of the assembly (modes 6, 12, and 13 in Fig. 19.6 that are respectively equivalent to rotating, rolling, and pitching modes shown in Fig. 19.5) show a significant change. This can be attributed to the fact that in the model shown in Fig. 19.2, the effect of the distributed mass of the turbine that would influence the rotational inertia of the structure was not considered.

The modes of a turbine can be categorized as either collective or differential modes. The collective modes are the modes with the same phase on three blades; the differential modes are the modes that the blades do not have the same phase or deflection.

### 19.4.3 Case 3: SIMO Test on the Wind Turbine Assembly

In the SIMO test, the test set up shown in Fig. 19.1 was used; however, only Shaker 1 was exciting the structure. The data acquisition system used the same set-up as previous measurement in Case 2. Most of the modes of the assembled structure that were shown in Fig. 19.6 could be extracted by the SIMO measurement. A comparison between the modal parameters extracted using MIMO, and SIMO measurement techniques is performed in the Sect. 19.5 of the paper.

**Fig. 19.7** A drawing of the turbine showing the impact locations/orientations for the modal impact hammer test (Y-axis shows out of plane; X-axis and Z-axis show in-plane impacts)
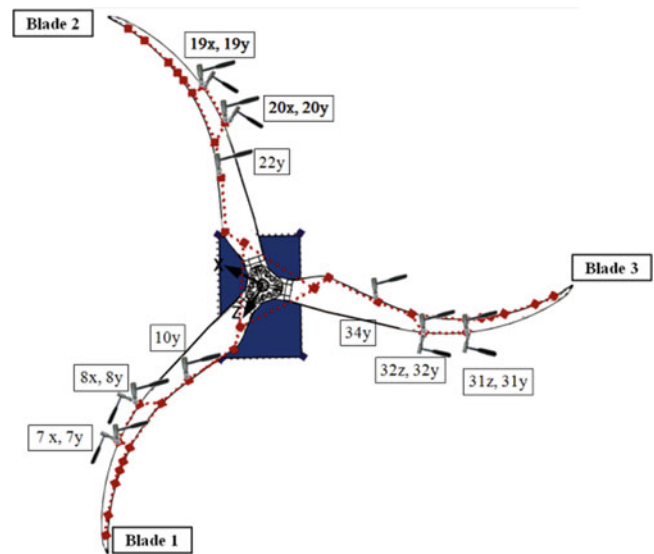


### 19.4.4   Case 4: Modal Impact Hammer Test on the Wind Turbine Assembly

Modal impact hammer test was also performed on the structure. For this measurement, the blades were excited in 15 locations/orientations as shown in Fig. 19.7 using a modal impact hammer with a rubber tip. The force impacts were made both in flap and edge directions. The data acquisition system was used with the same set up as the previous cases (frequency bandwidth of 128 and 1,024 Hz spectral lines). The extracted modal parameters are presented in the Sect. 19.5.

## 19.5   Discussion

### 19.5.1   Discussion 1: MIMO–SIMO Comparison

As previously described, the modes of the structure were extracted using MIMO and SIMO techniques in two separate tests. In this section, a comparison between the FRFs extracted with these methods is performed.

   To study the differences of the results when the structure is excited with multiple shakers and a single shaker, the measured FRFs at a measurement point located at the tip of the Blade 1 for MIMO and SIMO tests are shown in Fig. 19.8. As can be seen, the measured FRF for the MIMO test due to Shaker 1 and the measured FRF for the SIMO test overlap very well. That occurs because for the SIMO test, only Shaker 1 (attached to Blade 1 where the measured point is located) was exciting the structure. The FRF measured for the MIMO test due to excitation by Shakers 2 and 3 are also shown in Fig. 19.8. These FRFs reveal that some modes of the system have better been excited by using Shakers 2 and 3 rather than Shaker 1. For instance, the two modes of the system that were located near 8 Hz can be more clearly found in the excitation by Shakers 2 and 3 than Shaker 1 (see Fig. 19.8). Therefore, modes of the system were more effectively excited for a MIMO test rather than a SIMO test; that would lead to extracting more accurate FRFs for the MIMO test.

   For a comprehensive comparison between the measured FRFs using two techniques, three measured FRFs from the MIMO test due to Shaker 1 and SIMO test (that is also due to Shaker 1) and their corresponding coherences are overlaid in Fig. 19.9. The FRFs related to the measurement points at the tip of the three blades for x and y directions. As can be seen, the FRFs for point *1y* (i.e. the tip of the Blade 1 at the flap direction) compare very well for two techniques. It should be noted that for the SIMO test, the only shaker that was exciting the system (Shaker 1) was connected to Blade 1; this might describe why the measured FRFs at tip of that Blade 1 for MIMO and SIMO tests are very similar. However, the FRFs for the tip of the Blade 2 (Fig. 19.9 middle curve) do not compare as well as the tip of the Blade 1. This might be attributed to the fact that an energy loss occurred when the energy was transmitted through the hub and connections. In addition, this might be also attributed the shaker stingers; in the MIMO test the effect of the stingers is symmetrical while in SIMO test is not. As can be
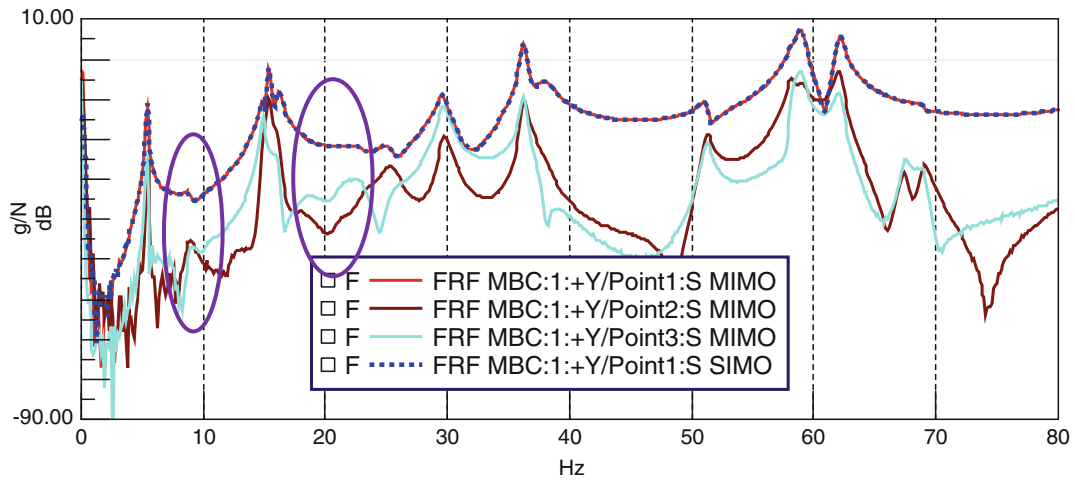
**Fig. 19.8** A comparison between the FRF for the tip point of Blade 1 due to different shakers for the MIMO test and due to the single shaker for the SIMO test (MBC: 1 is the tip of the Blade 1 and Points 1, 2, and 3 are the points that shakers are connected to Blades 1, 2, and 3 respectively); the *ovals* show the modes that have better been excited with shakers on Blades 2 and 3 rather than shaker installed on Blade 1
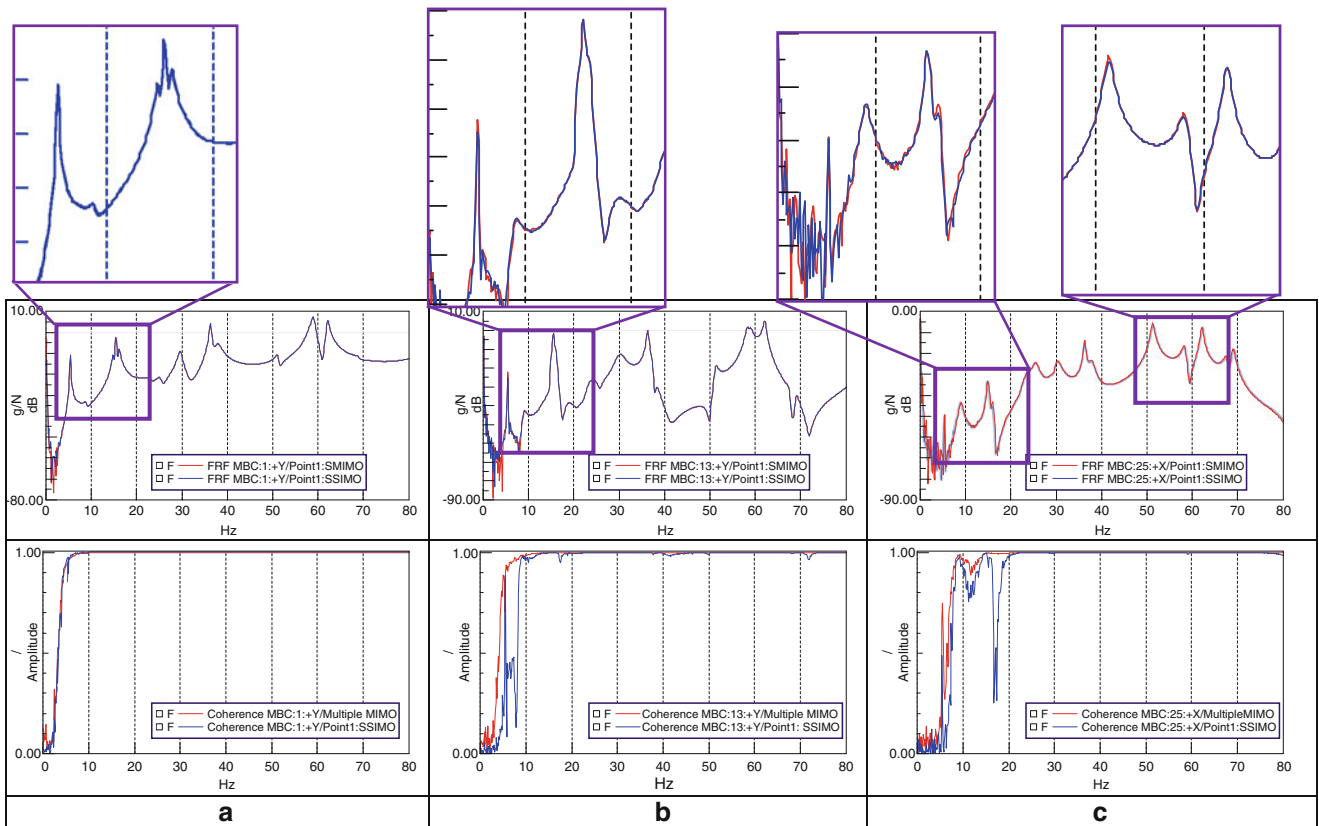


**Fig. 19.9** Comparisons between the FRF and coherence for the MIMO and SIMO tests for different locations/orientations, (**a**) measured FRF and coherence at the tip of the Blade 1 in the y direction due to shaker excitation attached to Blade 1, (**b**) measured FRF and coherence at the tip of the Blade 2 in the y direction due to shaker excitation attached to Blade 1, (**c**) measured FRF and coherence at the tip of the Blade 3 in the x direction due to shaker excitation attached to Blade 1

seen, the coherence of this measurement for the SIMO test is not at the same quality as that for the MIMO test. If the FRFs are measured for the points that do not have large deflections in the modes, the measured FRFs show a higher difference. As can be seen in Fig. 19.9 right plot, the measured FRFs for x direction show higher deviations between the two methods and the coherence for the SIMO test is not as good as the MIMO test.
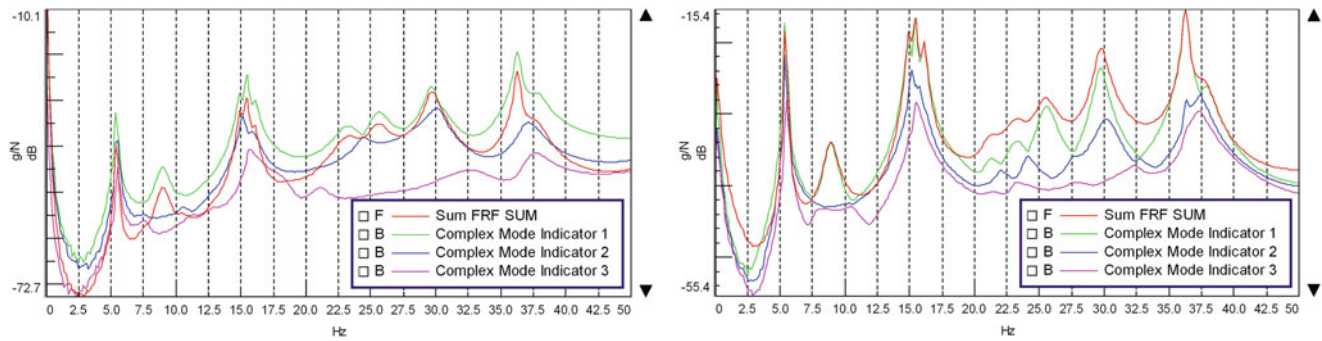
**Fig. 19.10** Summation and complex mode indicator functions of the measure FRFs for the MIMO test (*left*) and the impact hammer modal test (*right*); the *ovals* indicate modes that can be seen more distinctly using impact test rather than MIMO test

### 19.5.2 Discussion 2: Location of the Shakers

Selecting the location and orientation of the shaker is an important part of SIMO and MIMO measurements. A poor selection of the reference points may lead to weak representation of the mode shapes. A proper selection of the reference points, however, excites the desirable modes of the structure. Preferably, a shaker should be attached to a point that the mode shapes show a high value at (far from nodes of the modes). On the other hand, although the tips of the blades show high deflections for most of the modes, the shakers cannot be attached to those points because the shaker may not be able to generate the necessary displacement at these points during excitation. Therefore, the shakers were attached to the structure at points near the root of the blade. In fact, the drive points were located approximately 60 cm far from the center of the turbine so they can excite the first three flapwise modes of the turbine (the node of the first flapwise and edgewise modes of the single blades are near the root of the blades). Furthermore, by using an oblique installation of the shakers, both flapwise and edgewise modes of the structure could be excited.

In order to demonstrate the effects of the location and orientation of the shakers on exciting the modes of the structure, the stability diagram of the structure for the measured FRFs during MIMO test (Fig. 19.10, left) is compared to impact hammer test (Fig. 19.10, right). The modes of the structure can be identified by the peaks in the plot. As can be seen, there are some modes of the structure that have not been effectively excited for the MIMO test while for the impact test (Fig. 19.10, right) those peaks can be seen more distinctly. This occurs because of the location and orientation of the shakers. The shakers could excite the first three flapwise modes of the blades at approximately 5.5 Hz. However, the first edgewise modes of the blades could not be effectively excited (at approximately 21.1 Hz) because the stiffness of the blades in edge direction was much higher than the flapwise direction. Moreover, the shakers are more inclined toward the flap direction than edge direction because extracting flapwise modes were considered more important. Therefore, if a better representation of the edgewise modes were needed, the shakers would have to be installed far from the roots and more oblique toward the edge direction (it should be noted that installing the shakers close to tip of the blade is also a challenge because of the high flexibility of the blade near the tip). The impact hammer modal test, however, shows a clear peak at the frequency of the first edgewise mode of the turbine. This occurs because for the impact test, the force edgewise impacts could be made at points that were far from the hub. When the force is applied to the turbine at points far from the hub, the edgewise modes of the structure can be efficiently excited.

### 19.5.3 Discussion 3: Comparing the Modal Parameters Extracted using SIMO, MIMO, and Impact Tests

In this section, a comparison between the MIMO and SIMO tests along with a comparison between MIMO and impact tests are performed. The correlation shows the percentage of change in natural frequency and damping extracted using different techniques. The mode shapes are correlated using modal assurance criterion (MAC).

Table 19.1 shows a comparison between the MIMO and SIMO tests. The results show that for most of the modes, both of the techniques show similar results. A strong correlation between the results for the first mode extracted using the two methods can be seen. However, modes 2 and 3 do not show strong correlations. This can be attributed to the fact that usually MIMO test can have better distribution of energy over the structure. On the other hand, the location and orientation of the

**Table 19.1** Correlation between extracted modal parameters for MIMO and SIMO tests

| Mode # | MIMO test | | SIMO test | | Correlation | | |
|---|---|---|---|---|---|---|---|
| | Freq. (Hz) | Damp. (%) | Freq. (Hz) | Damp. (%) | Freq. diff. (%) | MAC (%) | |
| 1 | 5.3 | 0.9 | 5.3 | 0.7 | 0.6 | 97.0 | |
| 2 | 5.4 | 0.7 | 5.4 | 0.9 | 0.2 | 81.9 | |
| 3 | 5.6 | 0.5 | 5.6 | 0.3 | 0.3 | 78.0 | |
| 4 | 7.7 | 5.4 | – | – | N/A | N/A | Fixture mode |
| 5 | 7.7 | 3.6 | – | – | N/A | N/A | Fixture mode |
| 6 | 8.9 | 4.8 | 8.9 | 4.5 | 0.3 | 98.4 | Fixture mode |
| 7 | 14.9 | 1.3 | 14.9 | 1.2 | 0.0 | 99.3 | |
| 8 | 15.4 | 0.7 | 15.4 | 0.8 | 0.0 | 99.9 | |
| 9 | 16.1 | 1.3 | 16.1 | 1.4 | 0.0 | 99.8 | |
| 10 | 18.3 | 5.8 | 18.5 | 2.9 | 1.2 | 28.8 | Fixture mode |
| 11 | 21.1 | 3.3 | 21.0 | 2.2 | 0.8 | 47.7 | |
| 12 | 23.2 | 4.5 | 23.2 | 4.1 | 0.0 | 97.9 | Fixture mode |
| 13 | 25.5 | 2.8 | 25.5 | 2.7 | 0.1 | 99.0 | Fixture mode |
| 14 | 29.7 | 1.5 | 29.7 | 1.5 | 0.0 | 99.3 | |
| 15 | 30.2 | 3.1 | 30.2 | 3.1 | 0.1 | 98.0 | |
| 16 | 36.3 | 0.6 | 36.3 | 0.6 | 0.0 | 99.9 | |
| 17 | 37.3 | 2.4 | 37.4 | 2.3 | 0.3 | 92.6 | |
| 18 | 37.9 | 1.8 | 37.9 | 1.8 | 0.2 | 95.0 | |
| 19 | 51.3 | 0.7 | 51.2 | 0.7 | 0.1 | 99.7 | |
| 20 | 58.3 | 0.7 | 58.3 | 0.7 | 0.0 | 99.4 | |
| 21 | 58.9 | 0.7 | 58.9 | 0.7 | 0.0 | 99.7 | |
| 22 | 62.1 | 0.5 | 62.1 | 0.5 | 0.0 | 99.9 | |
| 23 | 67.6 | 0.6 | 67.5 | 0.6 | 0.0 | 91.2 | |
| 24 | 69.1 | 0.6 | 69.1 | 0.6 | 0.0 | 99.4 | |

shaker or the amount of energy imparted to the structure for SIMO test could not effectively excite the longitudinal, lateral, and bounce modes of the fixture (modes 4, 5, and 10); that is why these modes could not be identified for the SIMO test or they show a weak correlation. The weak correlation between the results for mode 11 also can be attributed to the improper excitation of that mode by a single shaker as could be predicted using the FRF in Fig. 19.8 (mode 11 is the first edgewise mode with a node located near the root of the blade).

A correlation between the modal parameters extracted using MIMO test and modal parameters extracted using impact test are shown in Table 19.2. The results of Table 19.2 show high correlations between the modes of the structure using these two methods. The first edgewise mode of the turbine also shows a high correlation. However, the lateral and longitudinal modes of the fixture (modes 4 and 5) could not be extracted using modal impact hammer method. This should be noted that although making impacts at the points of the blades far from the hub could efficiently excite the edgewise modes of the turbine (for those modes the turbine deforms along the hub axis and the hub is the nodes of these modes), these impacts did improve excitation of the transverse and lateral modes of the fixture. Moreover, the bouncing mode of the structure (mode 10) shows a weak correlation between two methods. These can be attributed to the fact that the small impact force applied by using the rubber head of the hammer could not excite the global modes of the structure. However, if a better representation of these modes were needed, some force impacts could have been made on the fixture with a bigger modal hammer.

Comparing the results of Tables 19.1 and 19.2, it is evident that the MIMO test results show a higher correlation to the impact hammer modal test rather than SIMO test. This can be attributed to the fact that for both MIMO and impact test measurements, a more uniform distribution of the input energy could be applied to all three blades. However, for the SIMO test, the input force was applied to the system through a single blade. Therefore, the energy might not be uniformly distributed for the entire structure.

## 19.6 Observation

In this section, several important lessons from the paper are pointed out that can be used in future measurements.

For Case 1, extracting modes of the fixture with considering the inertia of the blades was desirable. Therefore, to replicate the inertia of the blades, a lumped mass was added to the hub. However, the lumped mass could not mimic the rotational

**Table 19.2** Correlation between extracted modal parameters for MIMO and impact hammer tests

| Mode # | MIMO test | | Impact hammer test | | Correlation | | |
|---|---|---|---|---|---|---|---|
| | Freq. (Hz) | Damp. (%) | Freq. (Hz) | Damp. (%) | Freq. diff. (%) | MAC (%) | |
| 1 | 5.3 | 0.9 | 5.3 | 0.7 | 0.2 | 98.7 | |
| 2 | 5.4 | 0.7 | 5.4 | 0.6 | 0.0 | 99.5 | |
| 3 | 5.6 | 0.5 | 5.6 | 0.5 | 0.0 | 97.9 | |
| 4 | 7.7 | 5.4 | – | – | N/A | N/A | Fixture mode |
| 5 | 7.7 | 3.6 | – | – | N/A | N/A | Fixture mode |
| 6 | 8.9 | 4.8 | 8.9 | 4.9 | 0.8 | 98.6 | Fixture mode |
| 7 | 14.9 | 1.3 | 14.9 | 1.5 | 0.0 | 99.9 | |
| 8 | 15.4 | 0.7 | 15.4 | 0.7 | 0.0 | 99.9 | |
| 9 | 16.1 | 1.3 | 16.1 | 1.3 | 0.0 | 99.9 | |
| 10 | 18.3 | 5.8 | 18.9 | 2.8 | 3.2 | 22.0 | Fixture mode |
| 11 | 21.1 | 3.3 | 21.1 | 2.9 | 0.0 | 94.6 | |
| 12 | 23.2 | 4.5 | 23.3 | 4.1 | 0.2 | 98.4 | Fixture mode |
| 13 | 25.5 | 2.8 | 25.5 | 2.6 | 0.1 | 99.1 | Fixture mode |
| 14 | 29.7 | 1.5 | 29.7 | 1.5 | 0.1 | 99.5 | |
| 15 | 30.2 | 3.1 | 30.2 | 3.1 | 0.0 | 97.2 | |
| 16 | 36.3 | 0.6 | 36.2 | 0.6 | 0.1 | 99.9 | |
| 17 | 37.3 | 2.4 | 37.3 | 2.4 | 0.0 | 97.9 | |
| 18 | 37.9 | 1.8 | 37.9 | 1.8 | 0.2 | 98.9 | |
| 19 | 51.3 | 0.7 | 51.3 | 0.8 | 0.0 | 99.8 | |
| 20 | 58.3 | 0.7 | 58.3 | 0.7 | 0.0 | 99.5 | |
| 21 | 58.9 | 0.7 | 58.9 | 0.7 | 0.1 | 99.6 | |
| 22 | 62.1 | 0.5 | 62.1 | 0.5 | 0.1 | 99.9 | |
| 23 | 67.6 | 0.6 | 67.6 | 0.6 | 0.0 | 99.4 | |
| 24 | 69.1 | 0.6 | 69.1 | 0.3 | 0.1 | 99.9 | |

effects of the blades. After obtaining the modes of the assembly (Fig. 19.6), a considerable change in some modes of the fixture (Fig. 19.5) was seen. This change is more significant in the modes that are dependent to the rotational inertia of the blades. The results of this paper show the significant effects of rotational inertia on the structures where mass is distributed far from the rotation axis.

Another important lesson that can be learned from this measurement was the effects of impact locations on the extracted modes. For the impact test, if the measured FRFs for the case when impact forces are only made on a single blade were used, not all the modes could be extracted; this was observed in the results but was not presented in this paper due to space limitation. For instance, if the measured FRFs of the test when only Blade 1 was excited were used, mode 2 of the turbine could not be identified. Therefore, if the input force is distributed on all the components of a structure in a modal test, a better representation of the modes (or even more modes of the structure) can be extracted. This fact also clarifies why SIMO test results do not compare very well with the MIMO and impact tests. For SIMO test, the force was imparted to the turbine only through a single point and on a single blade; therefore, not all the modes might be effectively excited.

## 19.7   Conclusion

The results of the study revealed there are very closely space modes in the three-bladed turbine attached to the steel block. The modes of the assembled turbine were categorized into: (1) collective flapwise modes, (2) differential flapwise modes, (3) collective edgewise modes, (4) differential edgewise modes, and (5) fixture modes. In this paper, the technique for installing shakers in oblique orientations was implemented for a wind turbine blade; the modes of the structure could be found without the need for finding the installed angles of the shakers. Comparing the MIMO and SIMO results showed that a complicated structure such as a wind turbine that has several connections among the subcomponents needs to be excited by several shakers. Using multiple shakers leads to a uniform distribution of the energy over the entire structure and a better coherence in the measurement. On the other hand, a single shaker could not effectively excite all the modes of the structure. The results of the study also showed that impact hammer modal test is still one of the powerful techniques to excite structures for an experimental modal test. The results revealed that for a complicated structure with several substructures, impact hammer

modal test leads to better results rather than SIMO test. If only a few impact references are used and all of these references are located on one blade, then the results may not adequately represent the modes. However, if many impact reference locations are used on all three blades, then very good results can be obtained.

# References

1. Paquette J, Laird D, Griffith DT, Rip L (2006) Modeling and testing of 9m research blades. In: 44th AIAA aerospace sciences meeting, vol 19, pp 14569–14581
2. Ye Z, Ma H, Bao N, Chen Y, Ding K (2001) Structure dynamic analysis of a horizontal axis wind turbine system using a modal analysis method. Wind Eng 25(4):237–248
3. LoPiccolo J, Carr J, Niezrecki C, Avitabile P, Slattery M (2012) Validation of a finite element model used for dynamic stress-strain prediction. In: 30th IMAC, a conference on structural dynamics, vol 2, pp 205–214
4. Deines K, Marinone T, Schultz R, Farinholt K, Park G (2011) Modal analysis and SHM investigation of CX-100 wind turbine blade. In: 29th IMAC, a conference on structural dynamics, vol 5, pp 413–438
5. Marinone T, LeBlanc B, Harvie J, Niezrecki C, Avitabile P (2012) Modal testing of 9 m CX-100 turbine blades. In: 30th IMAC, a conference on structural dynamics, vol 2, pp 351–358
6. Harvie J, Avitabile P (2012) Comparison of some wind turbine blade tests in various configurations. In: 30th IMAC, a conference on structural dynamics, vol 2, pp 73–79
7. Baqersad J, Niezrecki C, Avitabile P, Slattery M (2013) Dynamic characterization of a free-free wind turbine blade assembly. In: 31th IMAC, a conference on structural dynamics, pp 215–220
8. Avitabile P, Singhal R, Peeters B, Leuridan J (2005) Modal parameter estimation approaches for large complicated multiple reference tests (then and now). In: 23th IMAC, a conference and exposition on structural dynamics
9. Ruggiero EJ, Park G, Inman DJ (2004) Multi-input multi-output vibration testing of an inflatable torus. Mech Syst Signal Process 18(5): 1187–1201
10. Ruggiero EJ, Inman DJ (2005) A comparison between SISO and MIMO modal analysis techniques on a membrane mirror satellite. J Intell Mater Syst Struct 16(3):273–282
11. Avitabile P (2009) MODAL SPACE: if I run a shaker test with the input oblique to the global coordinate system, how do I decompose the force into the specific components in each direction? Exp Tech 33(5):11–12
12. [LMS Test.Lab 10A] (2009) LMS International, Leuven, Belgium

# Chapter 20
# Modal Test Results of a Ship Under Operational Conditions

**Esben Orlowitz and Anders Brandt**

**Abstract** Sea vessels are exposed to a complex vibration environment, influenced by the sea as well as by operational conditions. Particularly, the hydrodynamic load effects are difficult to estimate analytically. Experimental results are therefore important to verify the analytical models. In the present paper preliminary results from a full-scale modal test of a Ro-Lo vessel carried out for three different operating conditions are presented. Since little full-scale modal testing seems to have been conducted on vessels in operation, the experimental setup together with preliminary modal parameters extracted from the measurements are presented. This preliminary study is focusing on investigating the data with respect to operational conditions and shows a significant variation of the modal damping of the vessel in operation, with approximately 400 %, 200 % and 400 % difference in the first three global vertical bending modes, respectively.

**Keywords** Operational Modal Test • Sea vessel • Full-scale measurement • Hydrodynamic loads • Damping

## 20.1 Introduction

The ship building industry faces the challenges to improve transportation capability, lower fuel consumption or increase speed, often in combination. Generally, this means lower weight and increased flexibility of the ship structures. Nevertheless the ships still have to fulfill the demands of classification societies concerning vibration levels and sustain a long service life.

   With the introduction of higher tensile steels in hull structures fatigue problems have been more imminent. Precise numerical models of the dynamics of the ship are therefore needed for fatigue prediction. These models are complicated by the hydrodynamic loading effects of the water surrounding the hull of the ship and the complex vibration environment ships face in operation. Hydrodynamic mass is commonly approximated by Lewis method that dates back to the twentieth century, which is added to the Finite element (FE) model of the ship. Recently this method is being substituted by boundary element methods combined with FE analysis [1]. It is known that in general the complete hydrodynamic load effect is not only depending on the additional mass from the water, but the full boundary conditions which are depending on the operational conditions (speed, sea state etc.), called hydroelastic effects. Especially the damping of the combined system (ship-sea) is difficult to estimate analytically. A solution is to estimate the damping from full-scale measurements to validate the numerical model. An investigation of the damping estimates was recommended by the committee of Dynamic Response at the recent Eighteenth ISSC[1] conference [2].

   One of the few studies utilizing operational modal analysis (OMA) on full-scale measurements that have been published [3] has shown that the technique can be successfully applied on a ship and in addition pointed out some of the challenges like harmonic contamination of the measurement data from the propulsion system of the ship. The measurements were performed on a roll-on roll-off vessel and the study presented global bending and torsional modes. The authors also mentioned that there seemed to be a dependency between increasing cruising speed and a decrease in the natural frequencies. Some more research

---

[1]International Ship and Offshore Structures Congress.

E. Orlowitz (✉) • A. Brandt
Department of Technology and Innovation, University of Southern Denmark, Odense, Denmark
e-mail: eo@iti.sdu.dk; abra@iti.sdu.dk

has been performed with OMA on scaled ship models. Predominantly to compare with analytical results, e.g. [4] where also dependency of the modal parameters on cruising speed was investigated, and has shown a significant increase (non-linear) of both natural frequencies and damping ratios with increasing speed, suggesting that damping must be evaluated at typical speeds. The increase of the natural frequencies with increasing cruising speed is in contradiction to what was indicated from the full scale test in [3].

For model experiments good conditions for OMA can be established, since random excitation can be provided, with the possibility of changing speed. For a full-scale measurement such a condition is difficult to establish because of harmonic contamination from the propulsion system. In addition a still open question remains on the consistency of the results and the dependency on the actual operational condition of the ship.

In the present paper the experimental setup and preliminary results from a 45 degree-of-freedom (DOF) three-direction full-scale measurement on a Roll-on Lift-off (Ro-Lo) vessel operating in the Baltic Sea is presented. OMA techniques are applied to obtain modal parameters for the first five global modes. This is conducted for three different operation conditions which is compared in order to study the influence on the global modes.

## 20.2   Experimental Setup

The measurement was performed under the test trial before delivery of the vessel. This gave many different operational conditions, but also applied hard constraints on the (measurement) time for each condition. In addition it should be noted that the ship was tested without any cargo.

Measurements of three operating conditions were conducted with the exact same equipment setup, see Sect. 20.3, and all measurement points and directions were measured simultaneously.

### 20.2.1   The Vessel

The Ro-Lo vessel, see Fig. 20.1, is a multipurpose/hybrid cargo ship capable of carrying trucks, cars and containers simultaneously. This makes the vessel's center of mass varying relatively much depending on the cargo combination, which has a large influence on the ship stability. Furthermore the ship is characterized by large mass concentrations fore and aft. The bridge house is located in the forward part and in the aft part a so-called flume tank[2] is located. The flume tank was empty during all measurements.



**Fig. 20.1**  The investigated roll-on lift-off

---

[2]The flume tank can be filled with water in order to change the stability of the structure, which could be needed because of the large deviations in cargo combination.
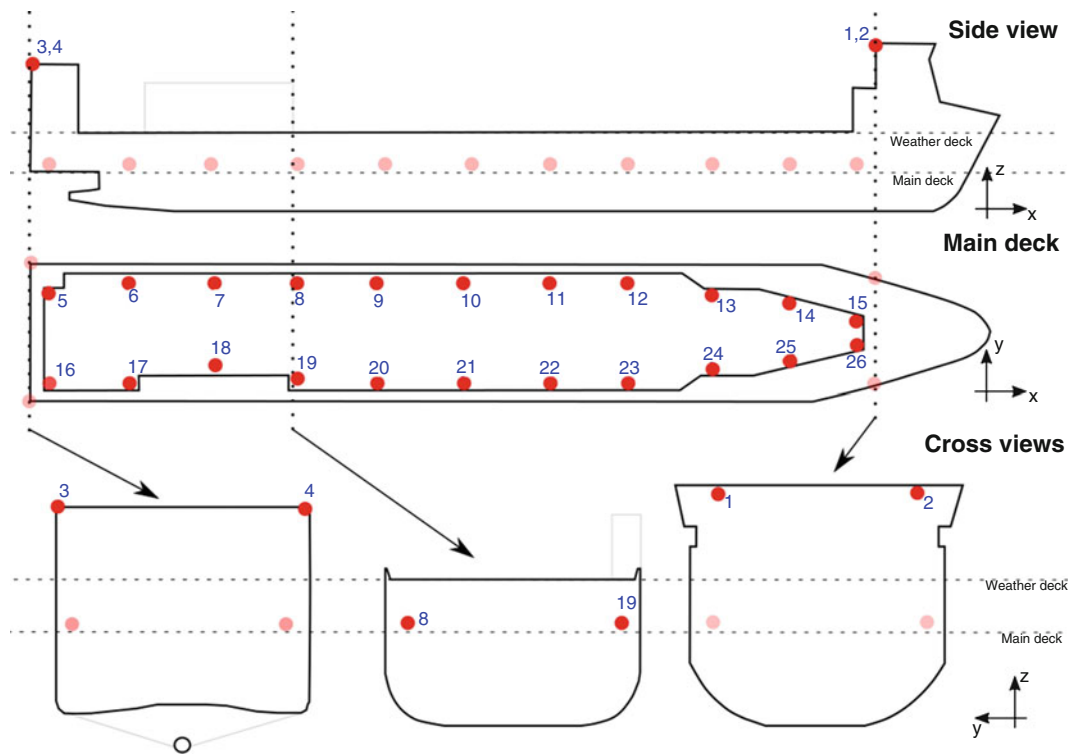
**Fig. 20.2** Overview drawing of the vessel, including the measurement grid used. All measurement DOF's are marked with *filled circles* and a *number*

The main data of the vessel is as follows:

– Shipyard: Flensburger Shiffbau-Gessellschaft.
– Total length: 210 m.
– Width (mid main deck): 29.60 m.
– Height to main deck: 10.90 m.
– Draught (design): 8.45 m.
– Deadweight: 19,200 tons.
– Design speed: 20 knots.

### 20.2.2  Measurement Equipment and Setup

The following Data Acquisition (DAQ) and sensor equipment was used:

– 3x National Instrument 4,497, 16 channel, 24 bit analog inputs cards.
– 45x Dytran 3097A3 accelerometers, 500 mV/g, IEPE.
– Up to 300 m coaxial cables, in total more than 5 km of coaxial cable.
– In-house software for DAQ control, based on MATLAB DAQ-toolbox.

The measurement points (26 in total) were spread out on the main deck of the vessel, two points on the deck house (fore), and two points on the flume tank (aft) as shown in Fig. 20.2.

The horizontal (x–y) plane was investigated for torsion modes and so all points were measured for vertical vibration (z-direction). The longitudinal vertical (x–z) plane is only investigated for bending modes, hence only points on one side of the deck (point 5–15) were measured for horizontal vibrations (y-direction). Longitudinal vibrations (x-direction) are not considered in the present work, but at the four points at the deck house and flume tank, where all three transversal directions were measured for further investigations of local phenomena, not included in the present work. At measurement point 5–15 where two directions were measured, small aluminum cubes were used for mounting the accelerometers, see Fig. 20.3.

**Fig. 20.3** Picture of mounting
cubes used for measuring in
multiple directions with single
accelerometers
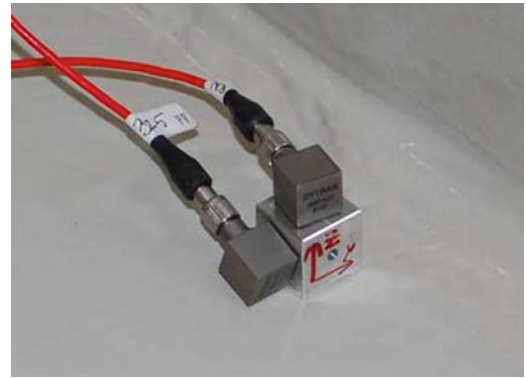


**Table 20.1** Operation conditions
for the three measurements

|          | Speed (knots) | Water depth (m) | Shaft speed (rpm) | Sea state |
|----------|---------------|-----------------|-------------------|-----------|
| ∼10 knots | $10 \pm 2$    | 20              | 65                | Calm      |
| ∼18 knots | $18 \pm 2$    | 20              | 98                | Calm      |
| Anchor    | 0             | 100             | 98                | Calm      |

The measurement time was limited to periods where nearly stationary conditions were established. In the present paper all three data sets consist of time histories of 30 min.

For hardware reasons the actual sampling frequency was 1 kHz, but for conveniences the time histories were down sampled to a sampling frequency of 8 Hz before further processing.

### 20.2.3 Measurement Conditions

As stated above three operating conditions are considered in this paper. Two conditions are identical except cruising speed at a water depth of approximating 30 m. The two cruising speeds were approximately 10 and 18 knots respectively, constant during the measurement (with variations less than 2 knots). These cruising conditions are from now on referred to as '∼10 knots' and '∼18 knots' respectively. The third condition is with the vessel anchored on deep water (∼100 m). For all three conditions the sea was very calm and the wind speed below 5 m/s.

The rotation speed of the propeller was 98 rpm for the ∼18 knots and anchor condition and 65 rpm for the ∼10 knots condition, giving blade pass excitation of 6.5 and 4.3 Hz, respectively, which is far from the modes presented in the present paper (<2.5 Hz). The measurement conditions are summarized in Table 20.1.

### 20.3 Results/Experimental Modal Analysis (Output-Only)

The variety of methods for OMA modal parameter estimation is large, many of them being modifications of some basic methods. In the present paper the Multiple-reference Ibrahim Time Domain (MITD) Method is used [5]. The original basis function for this method are impulse responses, which in the OMA case are replaced by correlation functions (CF's), which are estimated by the (indirect) Welch approach, see e.g. [6] or [7].

The MITD method constructs a block Hankel matrix. For determination of system order and to suppress noise the block Hankel matrix is decomposed by singular value decomposition is computed (SVD). From the SVD compressed block Hankel matrix an eigenvalue problem can be established for different system order (number of poles) the solutions of which are plotted in a stabilization diagram, from which the poles and mode shapes can be manually selected. An example of a stabilization diagram using the data of the present work is presented in Fig. 20.4.

In Fig. 20.4, around 1.6 Hz, the second mode is seen to be very close to a pole not obtaining the stability criteria. In this case this unstable pole is the propeller shaft fundamental rotation speed. In addition the damping is very low (0.04 %) which also indicates a harmonic rather than a mode.

**Fig. 20.4** Stabilization diagram. Here for the condition 18 knots. '+' indicates stable poles, 'o' unstable poles and the *solid curve* is a simple mode indicator function
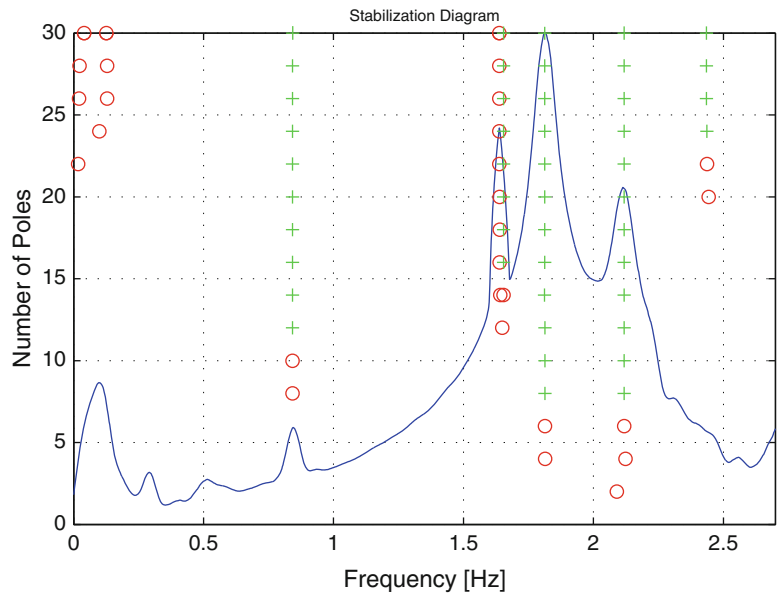


**Fig. 20.5** Auto MAC matrix, here for the condition ∼18 knots
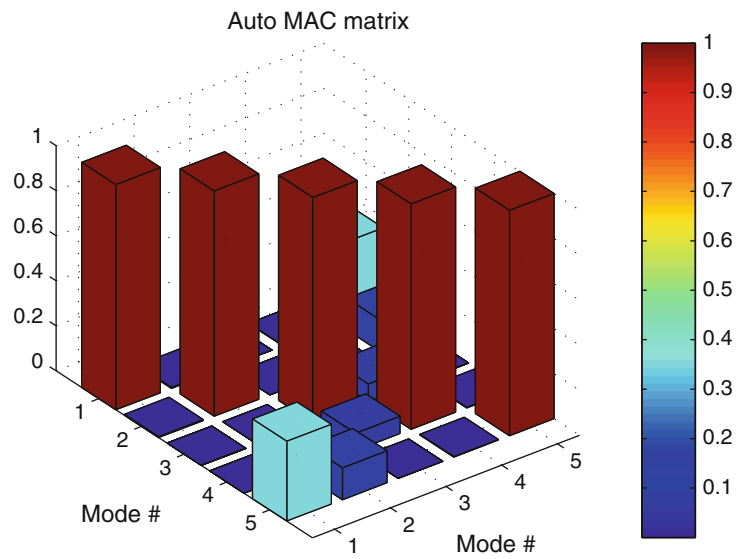


For the parameter estimation by the MITD method 150 lines from the CFs were used for the block Hankel matrix, which corresponds to 18.6 s of the CFs. The first five lines were discarded in order to avoid the influence of measurement noise, see e.g. [6]. The CFs are estimated with points 14 and 15 as references (two x- and y-directions).

With these references a relatively good decoupling of the first five modes is obtained, see the Modal Assurance Criterion (MAC) matrix in Fig. 20.5.

In the following two subsections a comparison between the results of the two cruising conditions and the results of the anchor condition are treated separately. The mode shapes for all three conditions are similar and are shown in Fig. 20.6, which can be justified by inspection of the cross MAC matrices in Figs. 20.7 and 20.8.

### 20.3.1 Cruising Condition

For the cruising condition the estimated natural frequencies and damping ratios for the first five modes are shown in Table 20.2, where also the differences are tabulated.

**Fig. 20.6** Mode shapes for the first five modes of the vessel. (**a**) 1. vertical bending mode, (**b**) 1. horizontal bending mode, (**c**) 2. vertical bending mode, (**d**) 1. torsional mode and (**e**) 3. vertical bending mode
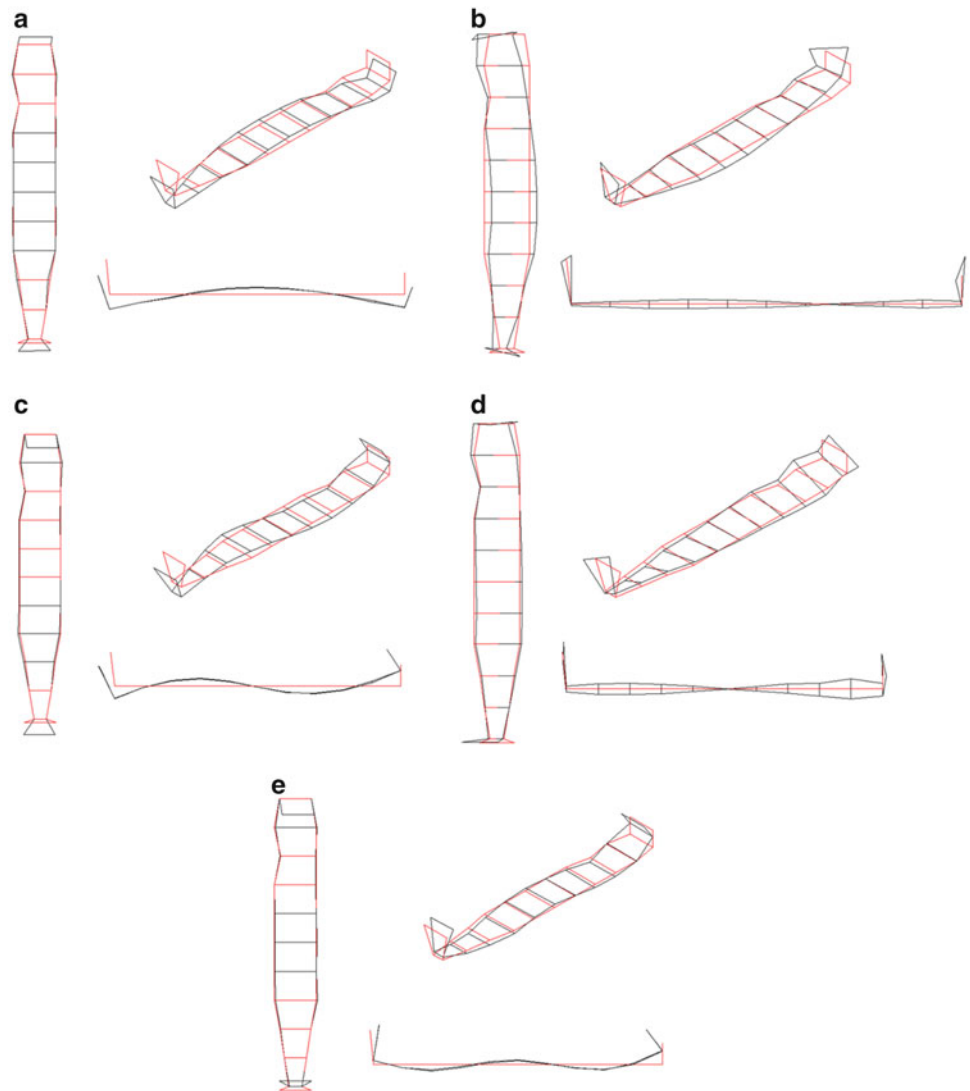


**Fig. 20.7** Cross MAC matrix between the two cruising conditions. NB. the order of second and third mode are exchanged for the ∼18 knots condition, to produce a diagonal MAC matrix
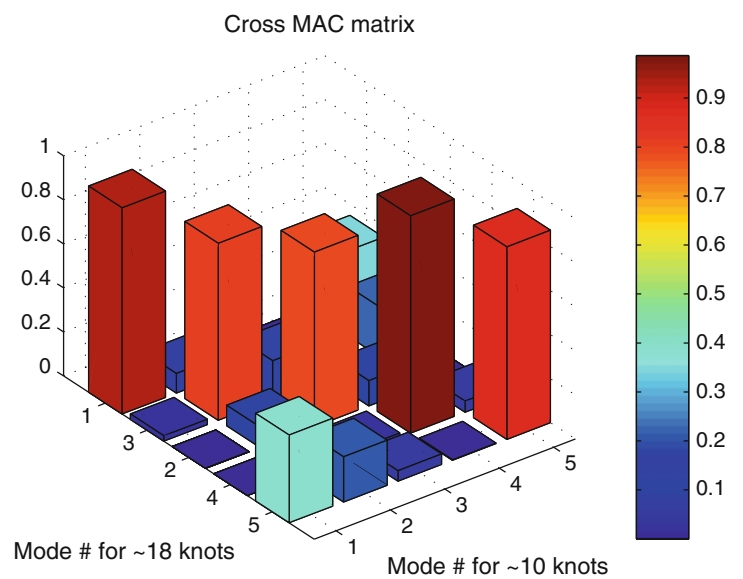
**Fig. 20.8** Cross MAC matrix
between the anchor and ∼10
knots conditions
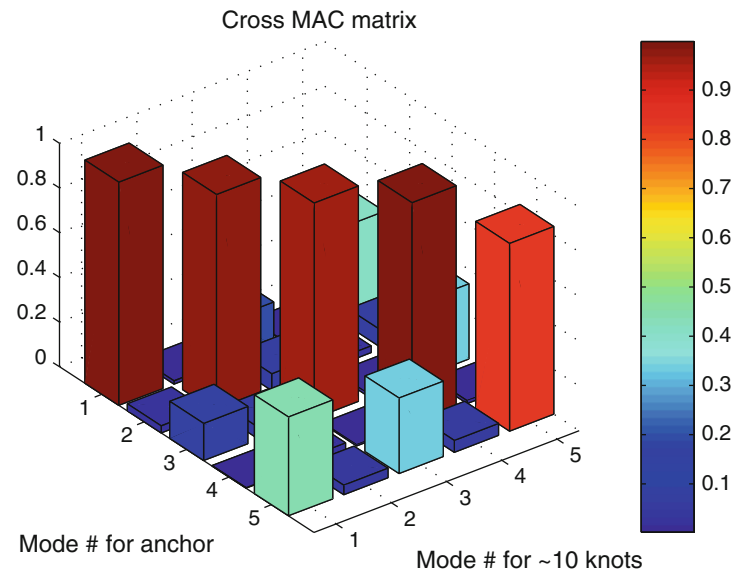


**Table 20.2** Estimated natural frequencies and damping ratios, for the two conditions (∼10 and ∼18 knots) and their differences for the separate modes

| Mode # | ∼10 knots | | ∼18 knots | | Difference | | Comment |
|---|---|---|---|---|---|---|---|
| | Frequency (Hz) | Damping (%) | Frequency (Hz) | Damping (%) | Frequency (%) | Damping (%) | |
| 1 | 1.004 | 0.394 | 0.843 | 2.073 | −16 | +426 | 1. Vertical bending mode |
| a2\|3 | 1.861 | 0.634 | 1.812 | 0.988 | −3 | +56 | 1. Horizontal bending mode |
| a3\|2 | 1.890 | 0.328 | 1.654 | 0.972 | −12 | +196 | 2. Vertical bending mode |
| 4 | 2.249 | 0.687 | 2.118 | 1.195 | −6 | +74 | 1. Torsional mode |
| 5 | 2.751 | 0.399 | 2.435 | 1.918 | −12 | +381 | 3. Vertical bending mode |

aThe order of the 1. horizontal and 2. vertical bending modes are exchanged for the two different conditions. The order from the ∼10 knots condition is kept

There are several interesting observations that can be drawn from these extracted modes. Generally the natural frequencies decrease and the damping ratios increase with increasing cruising speed. Specifically for the vertical bending modes there are some distinctive results due to increased cruising speed:

- Significant increase in damping for the vertical bending modes, by 200–400 %.
- Decrease in natural frequency (above 10 %) for the vertical bending modes.

From the cross MAC matrix, see Fig. 20.7, it can be seen that the extracted modes show strong similarities despite the changes in natural frequencies and damping ratios.

It should be noted again that the rotational speed of the propeller is very close to the 2. vertical bending mode for the ∼18 knots condition and that its influence on the extracted mode is not yet fully studied.

### 20.3.2  Anchor Condition

For the anchor condition the estimated natural frequencies and damping ratios are shown in Table 20.3. The MAC matrix between mode shapes from the anchor and the ∼10 knots condition are presented in Fig. 20.8, showing a relative strong similarity between the modes. No significant change in natural frequencies occurs compared to the ∼10 knots condition, but the damping ratio for the 1. torsional mode due changes significantly.

**Table 20.3** Estimated natural
frequencies and damping ratios,
for the anchor condition

| Mode # | Anchor | | Comment |
|---|---|---|---|
| | Frequency (Hz) | Damping (%) | |
| 1 | 1.033 | 0.259 | 1. Vertical bending mode |
| 2 | 1.869 | 0.855 | 1. Horizontal |
| 3 | 1.927 | 0.198 | 2. Vertical |
| 4 | 2.268 | 1.336 | 1. Torsional mode |
| 5 | 2.810 | 0.533 | 3. Vertical bending mode |

## 20.4 Conclusions and Future Work

An experimental setup, consisting of 45 accelerometers distributed over 26 measurement points—measured simultaneously, has been used on a Ro-Lo vessel during sea trial.

In the present paper a preliminary output-only modal analysis is presented for three different operating conditions of the vessel: one at anchor and two with cruising speeds of 10 and 18 knots respectively. The environmental condition was similar with very calm sea and the water depth was similar for the two cruising conditions (30 m).

The five first modes were successfully extracted for all three conditions and from the estimated modal parameters the following preliminary conclusions can be drawn

- The vertical bending modes show significant dependency on cruising speed.
- The natural frequencies decrease with increasing cruising speed.
- Modal damping increase with increasing cruising speed.
- From 10 to 18 knots cruising speed the modal damping of the vertical bending modes increases with 200–400 %.

The dependency of natural frequencies on cruising speed is in agreement with the full scale measurement presented in [3], but in contradiction with the results from the scaled model test in [4]. However the modal damping dependency is in accordance with the obtained results from the scaled model test.

The presented preliminary results are a part of ongoing research at University of Southern Denmark and the next step is to make a more thorough investigation of modal parameters and their statistic consistency, also including higher modes. This will also include the harmonic excitation from the propeller blades superimposed onto the responses of the vessel.

## References

1. Wilken M (2011) Efficient calculation of fluid structure interaction in ship vibration. In: Advances in marine structures: proceedings of the 3rd International Conference on Marine Structures, Hamburg, Germany
2. Dynamic response. In: 18th International Ship and Offshore Structures Congress (2012), Rostock, Germany
3. Rosenow SE, Uhlenbrock S, Schlottmann G (2007) In: Proceedings of second international operational modal analysis conference, Copenhagen, Denmark
4. Coppotelli G, Dessi D, Rimondi RMM (2008) Output-only analysis for modal parameter estimation of an elastically scaled ship. J Ship Res 52:45–56
5. Allemang R, Brown D (1987) Experimental modal analysis and dynamic component synthesis—vol 3: modal parameter estimation
6. Orlowitz E, Brandt A (2013) Influence of correlation estimation methods on damping estimates. In: Proceedings of fifth international operational modal analysis conference, Guimarães, Portugal
7. Brandt A (2011) Noise and vibration analysis—signal analysis and experimental procedures. Wiley, New York, NY

# Chapter 21
# Measuring Effective Mass of a Circuit Board

**Randall L. Mayes and Daniel W. Linehan**

**Abstract** Effective mass is a system property of a base mounted structural mode of vibration in a specific system axis. Effective mass is usually calculated with the finite element model. A method of deriving effective mass from dynamic measurements on the hardware was presented previously. The method is applied to a circuit board mounted on a fixture for the out of plane axis. The uncertainty of the method is evaluated using a nylon plate truth model of about the same dimensions and weight as the circuit board. The method measures frequency response functions on the fixture supporting the circuit board. Modes are extracted, and the mode shapes are processed to estimate the effective mass of each fixed base mode. These results will ultimately be used to support energy based failure analysis on the circuit board.

**Keywords** Effective mass • Modal participation factor • Experimental

## Nomenclature

| | |
|---|---|
| DoF | Degree of freedom |
| FRF | Frequency response function |
| SDoF | Single degree of freedom |
| $f$ | Force |
| $mm_k$ | Modal mass for mode k |
| $m_{TA}$ | Mass of the test article |
| $M_B$ | Mass of the fixture or base |
| $pmpf(k)$ | Pseudo-modal participation factor for mode $k$ |
| $P_k$ | Modal participation factor in one direction for mode $k$ |
| $\ddot{x}$ | Acceleration in one direction |
| $q$ | Generalized coordinate |
| $\mathbf{L}$ | Reduction matrix applying the constraint to equations of motion |
| $\Phi$ | Rigid body mode shape vector with ones in the direction of interest |
| $\Psi$ | Mass normalized real mode shape matrix |
| $\Gamma$ | Eigenvectors resulting from constraint Equations |
| $B$ | Subscript for the fixture or base |

R.L. Mayes (✉)
Experimental Mechanics, NDE and Model Validation Department, Sandia National Laboratories,
P.O. Box 5800-MS0557, Albuquerque, NM 87185, USA
e-mail: rlmayes@sandia.gov

D.W. Linehan
ATA Engineering, 11995 El Camino Real, Suite 200, San Diego, CA 92130, USA
e-mail: dan.linehan@ata-e.com

| $k$ | Subscript for mode number |
| $TA$ | Subscript for the test article |

## 21.1 Motivation and Application

Sandia National Laboratories has proposed a fatigue-damage metric based on the cumulative dissipated energy in a linear superposition of single-degree-of-freedom (SDoF) modal models as part of a framework for predicting failure of components subjected to random vibration loading. Edwards [1] showed how this method can predict the total energy absorbed by the test article in a random vibration environment. In order to utilize the proposed framework, the effective mass, fixed base natural frequency and damping is required for the SDoF modal models. Usually effective mass is obtained from finite element model (FEM) calculations, but in many cases, a FEM may not exist. In addition, the FEM may not be verified. It is desirable to have an experimental method to calculate the fixed base natural frequency, damping and the effective mass of each of the lower modes of the component. If the test article is available, it can be mounted on a fixture and a free modal test performed to extract parameters that can be utilized to calculate effective mass as shown by Mayes et al. [2]. In their work they showed that effective mass could be measured for the first ten modes in one direction within about 4 % of the test article mass. Their work addressed a test article with a mass of 72 kg for modes from about 35 to 1,350 Hz. Here we wish to extract the effective mass for a circuit board with a mass of 42.41 g and modal frequencies from 130 to 2,300 Hz.

In order to establish the uncertainty of the method for this class of test article, the effective mass experiment and calculation is applied to a "truth" structure which is a uniform nylon plate with the same length and width and almost the same weight as the circuit board. Both will be attached to an aluminum plate fixture with two posts to which the circuit board (or truth structure) is attached. One can see the circuit board as well as the truth structure attached to the fixture in Fig. 21.1. Since the truth test article is relatively simple, a FEM of the truth structure was generated to calculate effective mass. The "truth" effective mass in the out of plane direction is calculated, and the test effective mass will be compared to that to quantify uncertainty of the effective mass from the test approach. Finally, the test effective mass will be extracted for the real circuit board and the uncertainty is assumed to be the same as derived from the truth test.

## 21.2 Effective Mass Concept and History

The effective mass offers a physical interpretation of a physical system with multiple modes of vibration being excited dynamically from a base, similar to testing that occurs for many systems. The concept was proposed in the early 1970s by Bamford [3] with others. For a base excited system, it is represented as attached to a massless base, which will be excited in only direction with acceleration, $\ddot{x}$, with each mode represented by a single degree of freedom oscillator as shown in Fig. 21.2. The mass of each oscillator is valued so that it applies the same force to the base as the real system. The springs are scaled so that the mass vibrates at the appropriate modal frequency. In general, only the modes that have the significant



**Fig. 21.1** Circuit board and fixture (*left*), truth plate and fixture (*right*)
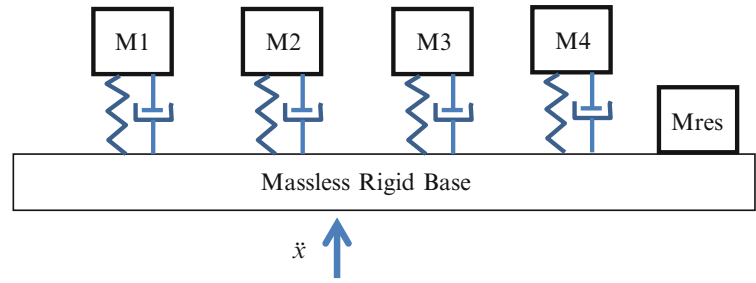
effective masses are required to represent the response up to some desired frequency. In the figure we show four such modes. The other modes are truncated. The effective mass of all the truncated modes is added directly to the base as a residual mass. When the base is accelerated with some vibration specification, the various effective mass oscillators will impose the correct reaction force on the base in the direction of excitation. As can be seen from this illustration, effective mass is based on a system that can be represented as having a base input. It depends also on the assumption that the base is rigid.

Effective mass is related to modal participation factor, $P_k$. The derivations of modal participation factor and effective mass can be found in the FEMA 451B Topic 4 Notes [10]. A major difference between effective mass and modal participation factor is that modal participation factor is different depending on the scaling of the modal mass, $mm_k$, whereas effective mass is a single defined value. In a fixed base eigenvalue problem of an analytical model of the system, the modal participation factor multiplied by $-\ddot{x}$ provides the modal force that will excite a particular mode for the rigid base acceleration, $\ddot{x}$. The effective mass, which provides the actual base reaction force associated with a particular mode, resolves any question about mode shape scaling and is calculated as

$$m_{eff,k} = P_k^2 mm_k \tag{21.1}$$

If $\Psi_{fixed}^k$ is the fixed base mode shape vector for mode $k$ and $\mathbf{M}$ is the mass matrix of the test article, the modal participation factor can be calculated from the rigid body mode shape vector, $\Phi$, of the system released and translating in the direction of acceleration of the base as

$$P_k = \overline{\Phi}^T \mathbf{M} \overline{\Psi}_{fixed}^k / mm_k \tag{21.2}$$

where the rigid body shape values of vector $\Phi$ in the direction of acceleration are equal to one and in orthogonal directions are equal to zero. The modal participation factor and effective mass are related to direction. If vector $\Phi$ represents the rigid body mode shape in the y direction, as opposed to the x direction as shown in the figure, a different modal participation factor (and effective mass) will be calculated for mode $k$.

As can be seen, this standard approach requires a finite element model. If the finite element model is in error, the modal participation factor and effective mass will be in error.

## 21.3   Effective Mass Measurement Approach

The method of Mayes [2] will be utilized for this application. The effective mass of each mode is desired for the out of plane (vertical) direction for the nylon plate and the circuit board shown in Fig. 21.1. The steps to obtain the effective mass are:

1. Perform a freely supported modal test on the fixture to determine its elastic shapes that might be in the frequency band of interest. The fixture must be instrumented so that all the rigid body shapes and any elastic shapes extracted are independent (so the test mode shape matrix may be inverted).
2. Perform a freely supported modal test on the test article mounted to the fixture. The fixture must be instrumented but it is not required that the test article be instrumented.
3. Constrain the test article and fixture so that all elastic modes of the fixture and rigid body rotation modes and rigid body lateral modes are constrained to zero. Only one rigid body mode in the vertical direction and elastic modes of the attached test article remain.
4. Calculate the pseudo modal participation factors from the partially constrained modal results of step 3, which requires the mode shape of the fixture, the mass of the fixture and the mass of the test article.

5. Constrain the final rigid body mode to zero displacement using data from step 3 and capture the **L** matrix and resulting **Γ** modal vectors.
6. Finally calculate the fixed base modal participation factor estimates using pseudo modal participation factors from step 4 and the **L** and **Γ** matrices from step 5. Then Eq. 21.1 can be utilized to calculate the effective mass for each mode.

This work is made possible by the recent theory [4–7] that can be applied to mode shapes gathered from an unconstrained modal test to constrain the modal degrees of freedom of the test fixture to which the test article is connected. The **L** matrix is the matrix that applies the constraints to an unconstrained system in the primal formulation of dynamic substructuring (see De Klerk, Rixen and Voormeeren's, framework for all substructuring methods [8]). The **Γ** matrix is the matrix of eigenvectors resulting from the eigenvalue problem solution on the constrained system.

## 21.4  Abbreviated Effective Mass Measurement Theory

The derivation of the theory for extracting experimental effective mass was published [2] and will not be repeated here. The pertinent final equations are given below. The required measurements are the modal mass of each mode, the mode shapes measured on the fixture, the mass of the fixture and the mass of the test article. The mode shapes must include the rigid body modes and any elastic modes of the fixture that may influence results in the frequency band of interest. No measurement of the mode shape on the test article is required, but it may provide valuable insight. The mode shapes are constrained so that:

1. elastic modes of the fixture have been constrained; and
2. all rigid body modes are constrained except the one in the direction for which effective mass is desired.

Then one must calculate the pseudo modal participation factors. The first pseudo modal participation factor is for the rigid body mode and is calculated as

$$pmpf(1) = m_{TA}\Psi_B^1 \tag{21.3}$$

where $m_{TA}$ is the mass of the test article and $\Psi_B^1$ is the mass normalized mode shape of the rigid body mode on the base (test fixture) in the direction of interest. The pseudo modal participation factor for each elastic mode is calculated as

$$pmpf(k) = -M_B\Psi_B^k \tag{21.4}$$

where $M_B$ is the mass of the base (test fixture) and is the mode shape of the particular elastic mode on the base (test fixture). The estimate of the modal participation factors are calculated from

$$P_k = \begin{bmatrix} pmpf(1) \ pmpf(2) \ \dots \ pmpf(n) \end{bmatrix} \bar{\mathbf{a}}_k \tag{21.5}$$

where $\bar{\mathbf{a}}_k$ is the $k$th column of **LΓ**.

## 21.5  Modal Test of Fixture with Truth Plate

To capture the elastic fixture modes, the bare fixture without test articles was suspended by a small bungee cord and impacted with a PCB Model 086C01 with white plastic tip. The sensitivity of the hammer was confirmed by impacting a suspended 4.5 kg mass with a calibrated accelerometer, and it reproduced the analytical mass line within 2 %. An elastic mode at about 5,464 Hz was extracted for the bare fixture which looked like a standard first plate twisting mode. Then the truth plate was attached by two screws to the fixture and the hardware shown in the right side of Fig. 21.1 was suspended with a small bungee cord. Two sets of FRFs were gathered for accelerometers mounted on the fixture. In one set the impact was at the center of the fixture, and in the other the impact was at one corner (not one of the corners with a mounting post). Accelerometers were attached to the fixture as shown in Fig. 21.3. Accelerometers measured in the Y and Z directions for node 101, the XYZ directions for node 102, the X and Y directions for node 103 and only the Y direction for nodes 104 and 105. Mode shapes for both FRF data sets were extracted using a Sandia in-house algorithm SMAC [9].

**Fig. 21.3** Accelerometer layout
on the aluminum fixture
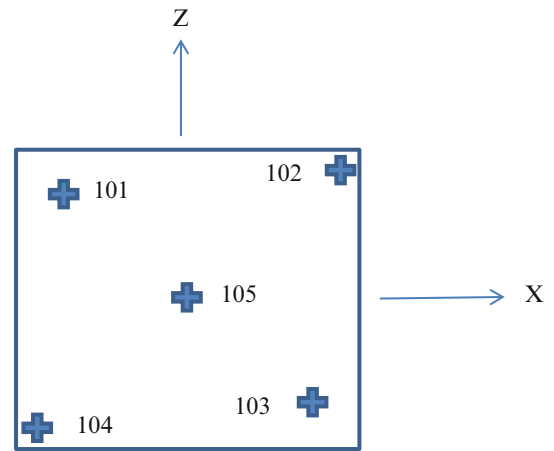


**Fig. 21.4** Drive point FRF and
synthesis for center of plate
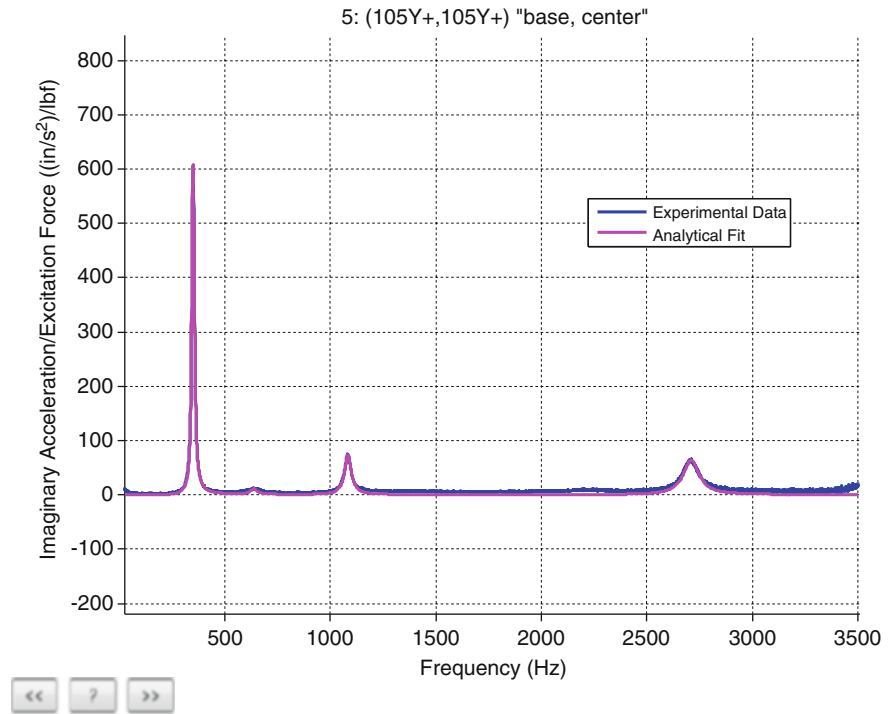


The imaginary portion of the driving point FRF for each data set is shown in Figs. 21.4 and 21.5. The actual data are in blue and the FRF synthesized from the modal parameters are in green. Three distinct modes and one weak one were extracted from the center of plate impacts and seven were extracted from the corner of the plate data.

The center plate impact tends to excite modes that have effective mass in the direction of impact while the corner plate impact excites those modes plus anti-symmetric modes that may not have much effective mass in the translation direction. In addition to the elastic modes extracted from test, the rigid body mode shapes were analytically calculated and added to these data sets for processing to extract effective mass in the Y direction.

## 21.6  Finite Element Model Truth Calculations

The truth calculations for the effective mass comparisons came from finite element model simulations utilizing NX NASTRAN and were performed by ATA Engineering. The fixture was modeled, and its first mode is shown in Fig. 21.6. The nylon plate was modeled as isotropic and its modulus was tuned to match the first free mode of the nylon plate by itself at 646 Hz. Its first mode is shown in Fig. 21.7. Then the nylon plate was mounted to the fixture by equivalencing the nodes at

**Fig. 21.5** Drive point FRF and synthesis for corner of plate
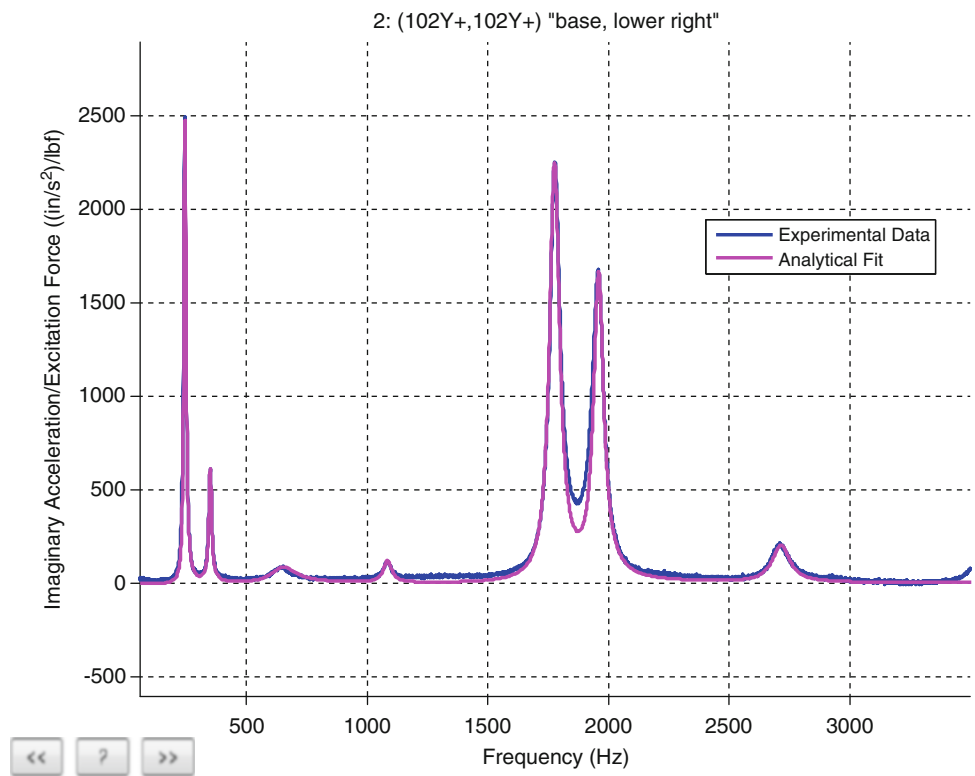


**Fig. 21.6** FE model of first fixture elastic mode
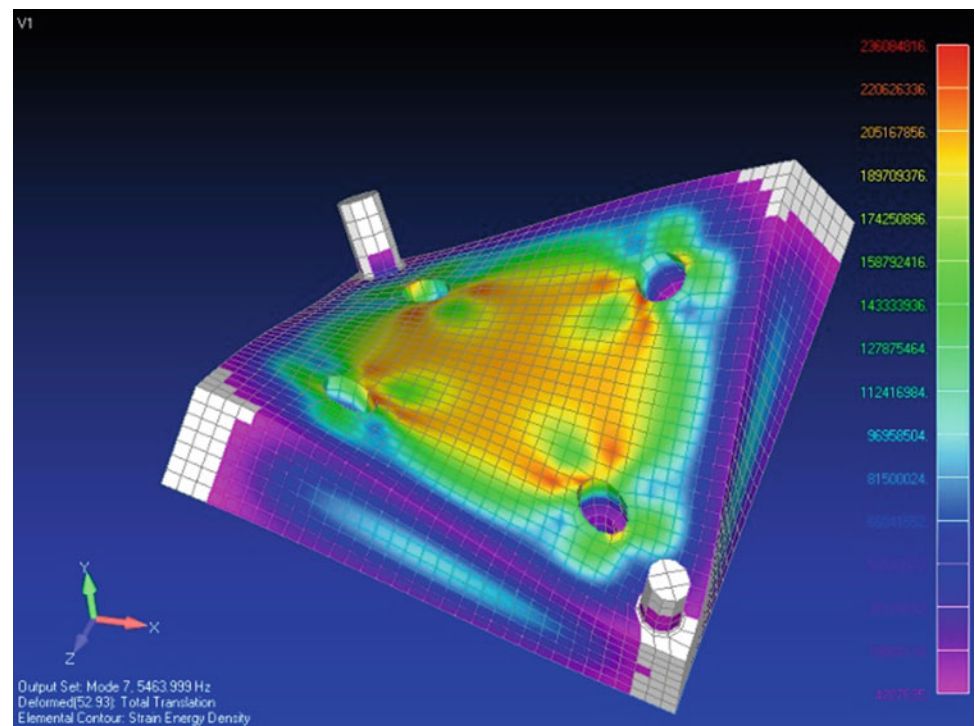


the post. This result produced a natural frequency that was slightly higher than what was seen in the modal test of the fixture and nylon plate. The boundary condition was adjusted to include some springs representing the joint compliance to better match the first test mode. Then the modes of the nylon plate were calculated with the fixed and the springs fixed to ground to give bounds on the effective mass of each mode of the plate. This is why there is a range of effective mass shown in the previous tables.

**Fig. 21.7** First free elastic mode of nylon plate
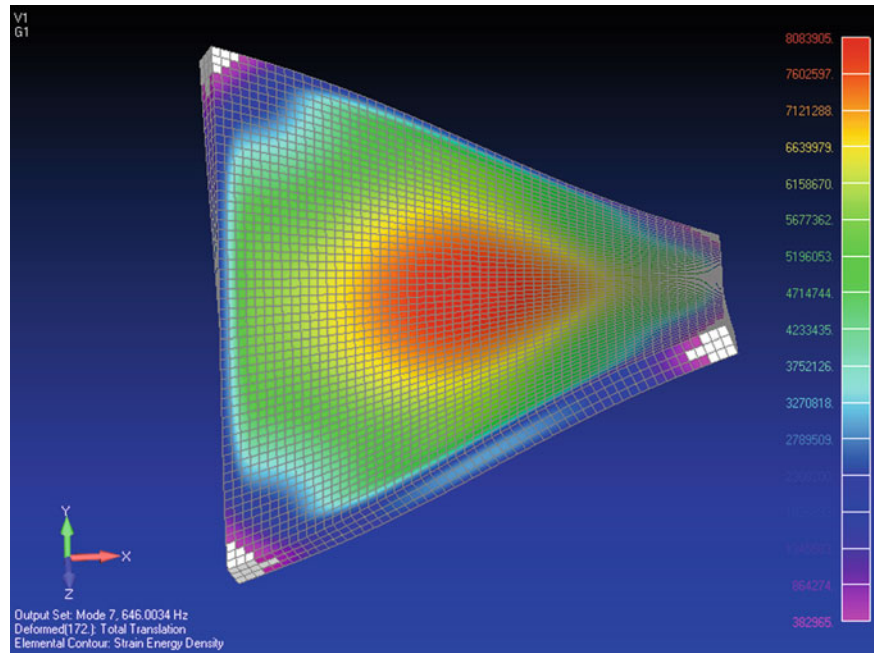


The mode shapes for the nylon plate fixed at the two posts are given in Fig. 21.8. The fixed frequencies for the equivalence and spring boundary conditions and the constrained test data are shown in Table 21.1. Note that modes 4, 5 and 9 would not be excited well by impacting at the center or the unsupported corner. They would be excited by impacting at a supported corner, which we did not impact. There is pretty good agreement for the first couple of fixed frequencies between the FE spring model and the test data. At higher frequencies there are greater discrepancies, and the test results should be more accurate for the higher modes, even with the constraining mathematics because the fixed base modes are only very slightly different than the free modes of the nylon plate attached to the fixture. So there may be a bit of error in the FE model estimates of effective mass which we are considering "truth."

## 21.7 Experimental Effective Mass Extractions

The effective mass extraction procedure was applied to both sets of data to obtain the Y direction effective mass. The best results for effective mass came from the center plate impact and are given in Table 21.2. These results are normalized to the total mass of the test article. The difference between the test result and the truth FE result is expressed as the percentage of the TOTAL mass of the test article.

The results for normalized effective mass from the corner plate impact are given in Table 21.3.

Table 21.3 results provide some additional interesting information. There are three modes that have zero normalized effective mass out to four decimal places. The fact that these zero effective mass modes are predicted with zero effective mass is encouraging. The highest effective mass has more error than from the center plate result. The results from impacts at the corner of the plate will be affected by errors in applied moments and errors in dimensions in moment arms. Impacts at the center of the plate do not even excite the pitching modes, so those errors are minimized. It should be noted that accurate dimensions, mass properties and accelerometer placements and hammer impact locations and directions are required to get accurate rigid body mode shapes and FRFs.

## 21.8 Test Anomaly

In Tables 21.1 and 21.2 one may notice a test mode with a small effective mass that does not correspond to any FE mode. This rogue mode was studied further to determine its cause. The modal damping was nearly 10 % for this mode around 640 Hz, and it was extracted from both data sets. Eventually the cause was discovered. This is a false mode. This can be explained
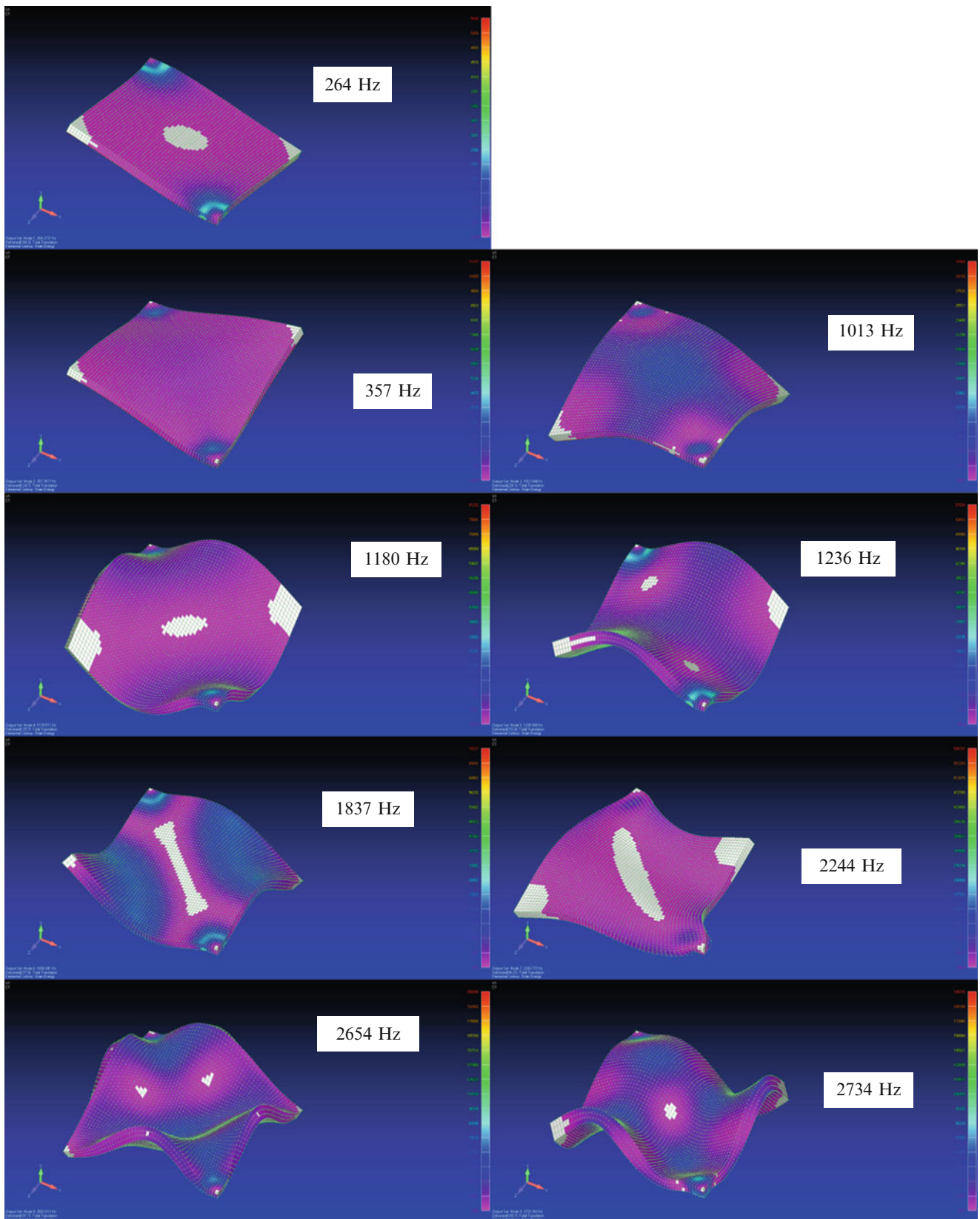
**Table 21.1** Fixed frequencies for modes of nylon plate

| Mode no. | Test frequency (Hz) | Equivalenced FE frequency | Spring FE frequency |
|---|---|---|---|
| 1 | 238 | 264 | 240 |
| 2 | 339 | 357 | 344 |
| 3 | 1,081 | 1,012 | 1,000 |
| 4 | – | 1,179 | 1,110 |
| 5 | – | 1,235 | 1,182 |
| 6 | 1,683 | 1,836 | 1,775 |
| 7 | 1,920 | 2,244 | 2,070 |
| 8 | 2,705 | 2,654 | 2,590 |
| 9 | – | 2,733 | 2,619 |

**Table 21.2** Normalized test effective mass from center plate impact compared to FE model

| Test frequency (Hz) | Effective mass from test | Effective mass from FE model | Difference as % of total mass of test article |
|---|---|---|---|
| 339.4 | 0.815 | 0.816–0.831 | −0.1 to −1.6 |
| 638.6 | 0.018 | – | – |
| 1,081.4 | 0.069 | 0.058–0.062 | −1.1 to −0.7 |
| 2,705 | 0.040 | 0.0041–0.0043 | −0.01 to −0.03 |

**Table 21.3** Normalized test effective mass from corner impact compared to FE model

| Test frequency (Hz) | Effective mass from test | Effective mass from FE model | Difference as % of total mass of test article |
|---|---|---|---|
| 238.2 | 0.0000 | 0.0000 | 0 |
| 340.1 | 0.788 | 0.816–0.831 | −2.8 to −4.3 |
| 650.2 | 0.016 | – | – |
| 1,082.6 | 0.057 | 0.058–0.062 | −0.1 to −0.5 |
| 1,683 | 0.0000 | 0.0000 | 0 |
| 1,920 | 0.0000 | 0.0000 | 0 |
| 2,712 | 0.028 | 0.0041–0.0043 | 2.4 |

by investigating the FRF, and the autospectra of the drive point accel and the force which are shown in Fig. 21.9. Notice that in the FRF there are four resonances, but in the accelerometer autospectrum only three resonances. In the hammer force autospectrum one can see an anomaly (circled in red) which is not uncommon in certain hammers. This is a pollution of the autospectrum due to the first bending mode of the hammer. After impact the hammer vibrates which causes this dynamic effect. This effect is not sensed by the accelerometer because the impact is over. This produces a false mode in the data.

## 21.9 Effective Mass of Circuit Board

The circuit board on the left side of Fig. 21.1 was tested in the same manner as the nylon plate with the center plate hammer impact. Normalized effective mass extractions are shown in Table 21.4. The uncertainty is assumed to be on the order of 0.02 from the previous work.

## 21.10 Conclusions

Effective mass was calculated from the center impact reference for three modes to within 2 % of the total mass of the test article, when compared with a FE truth model. A corner impact reference resulted in effective mass for three additional modes as zero out to four decimal places, which agreed with the truth model. The corner impact reference data produced effective mass within 5 % of the total mass of the test article when compared with the truth model. It was found that the corner impact had a small geometry error which could have impaired its results slightly, since that would affect the mode shape and modal mass extraction. Accurate rigid body mode shapes as well as extracted elastic mode shapes are required for the data processing to extract effective mass from experiment. A false mode was discovered in the truth test, which was due to the dynamics of the hammer, which appeared to have a normalized effective mass of nearly 0.02. The effective mass extraction process appears to be fairly robust for the truth test geometry and setup since the FRFs seem to exhibit linear behavior.

**Fig. 21.9** Cause of Rogue
Mode—FRF/Accel
Autospectrum/Hammer
Autospectrum
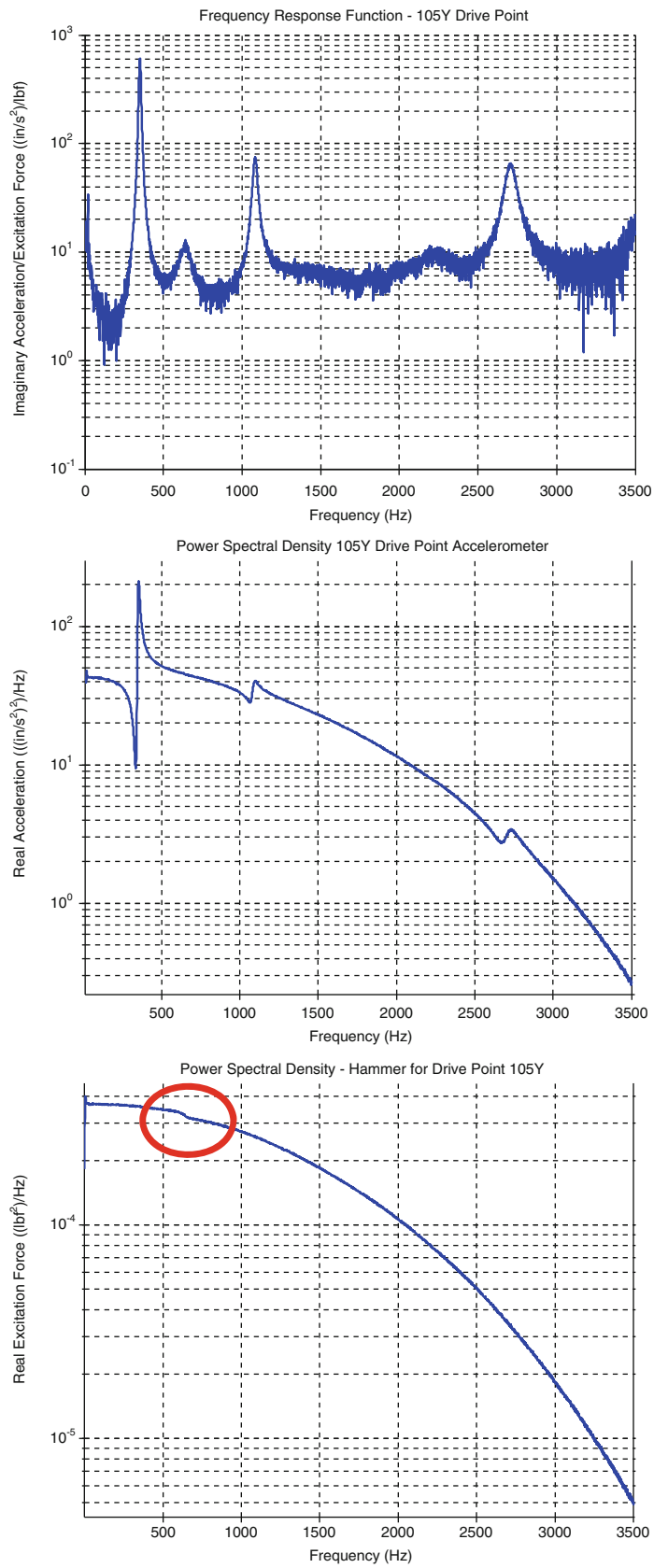
**Table 21.4** Normalized test effective mass for circuit board

| Test frequency (Hz) | Effective mass from test |
|---|---|
| 134 | 0.170 |
| 181 | 0.640 |
| 654 | 0.057 |
| 725 | 0.012 |
| 1,065 | 0.016 |
| 1,174 | 0.003 |
| 1,416 | 0.009 |
| 1,650 | 0.008 |
| 2,031 | 0.001 |
| 2,174 | 0.004 |
| 2,283 | 0.005 |

# References

1. Edwards TS (2009) Power delivered to mechanical systems by random vibrations. Shock Vib 16(3):261–271
2. Mayes RL, Schoenherr TF, Blecke J, Rohe, DP (2013) Efficient method of measuring effective mass of a system. In: Proceedings of the 31st international modal analysis conference, Garden Grove, CA, paper number 194
3. Wada BK, Bamford R, Garba JA (1972) Equivalent spring-mass system: a physical interpretation. The Shock and Vibration Bulletin, US Naval Station—Key West, FL, pp 215–224
4. Mayes RL, Bridgers LD (2009) Extracting fixed base modal models from vibration tests on flexible tables. In: Proceedings of the 27th international modal analysis conference, Orlando, FL, paper 67
5. Allen MS, Gindlin HM, Mayes RL (2011) Experimental modal substructuring to estimate fixed-base modes from tests on a flexible fixture. J Sound Vib 330:4413–4428
6. Mayes RL, Allen MS (2011) Converting a driven base vibration test to a fixed base modal analysis. In: Proceedings of the 29th international modal analysis conference, Jacksonville, FL, paper 36
7. Mayes RL (2012) Refinements on estimating fixed base modes on a slip table. In: Proceedings of the 30th international modal analysis conference, paper 162
8. De Klerk D, Rixen DJ, Voormeeren SN (2008) General framework for dynamic substructuring: history, review, and classification of techniques. AIAA J 46(5):1169–1181
9. Hensley DP, Mayes RL (2006) Extending SMAC to multiple references. In: Proceedings of the 24th international modal analysis conference, pp 220–230
10. http://www.ce.memphis.edu/7119/fema_notes.htm, Topic 4 Notes

# Chapter 22
# Acoustic Cavity Modal Analysis for NVH Development of Road Machinery Cabins

**Hongan Xu, Owen Dickinson, John Wang, and Hyunseok Kang**

**Abstract**  Noise and vibration comfort is a critical design criterion for road machinery. An acoustic modal analysis provides useful insights to understanding interior acoustic characteristics and to developing noise mitigation strategies, to improve operator comfort. In this study, an acoustic cavity modal analysis of a compactor cabin is done by utilizing analytical solution, FEA and experimental measurements. While the analytical method and FEA calculate the normal modes of a rigid-walled acoustic cavity, the physical test measures the acoustic modes *in-situ* that account for the vibro-acoustic coupling effect between the interior cavity and flexible panels. The discrepancies of resultant modal parameters extracted by testing and simulation are discussed. In addition, the impacts of the seat and steering column assembly on the acoustic cavity modes are also investigated. Last but not least, a local vibro-acoustic behavior of the cab and its relation to the interior booming noise is deeply investigated. From the NVH development standpoint for a practical cabin, the findings of this investigation not only help troubleshooting cabin noise issues but also lead to improvement in virtual acoustical modal predictions and guide the design to achieve a robust NVH performance.

**Keywords**  Road machinery cabins • Acoustic transfer function • Low frequency booming noise • Acoustic cavity modal analysis • Panel-cavity coupling • Panel resonance

## 22.1  Introduction

The cabin acoustic comfort is one of the most important factors that affect an operator's work environment. As the legal regulations become more and more stringent to limit the interior noise level of construction equipment, designing a quiet cabin appear more critical for both designers and analysis engineers. In order to improve the interior noise performance, a good understanding of cabin vibro-acoustic characteristics is of critical importance to provide insights into the acoustic design and noise mitigation strategies.

Typically, the operator cabin is considered as a structural-acoustical system composed of an acoustic enclosure surrounded by flexible panels that are bonded to the cab frames. Therefore, the interior sound field is significantly affected by the acoustic cavity resonances, panel vibration modes and the panel-cavity interaction. In this study, the cabin acoustical characteristics are investigated using analytical solution, FEA calculation, and *in-situ* experimental analysis, respectively. As the analytical solution is based on the assumption of a rigid-walled cavity, it does not account for the panel-cavity coupling effect, which could lead to a remarkable predicting discrepancy from the real acoustical characteristics. In comparison with the analytical solution, FEA employs the modal coupling theory to accommodate the structure-acoustic interaction in modeling the acoustic cabin cavity. However, the model coupling approach has two main limitations in that it is only suitable for weak coupling and it does not satisfy the basic requirement of velocity continuity on the panel-cavity coupling interface. In contrast to simulation, the experimental acoustic modal analysis provides more meaningful information in characterizing the realistic vibro-acoustic behavior of the cab cavity *in-situ*. Hence it continues to be used as a practical troubleshooting tool and

H. Xu (✉) • J. Wang • H. Kang
Virtual Product Development, Volvo Construction Equipment, Shippensburg, PA 17257, USA
e-mail: hongan.xu@volvo.com

O. Dickinson
Operator Platform and Environment, Volvo Construction Equipment, Shippensburg, PA 17257, USA

an informative benchmark for modal correlation. Especially, a local vibro-acoustic behavior that is induced by a panel resonance can be easily identified via an acoustic mapping of the interior sound field. This case scenario will be examined in the following discussion.

Good efforts have been made in recent studies to improve the prediction accuracy of acoustic cavity modal characteristics. Pan and Bies [1] conducted an excellent review on the coupled structural-acoustic system composed of an acoustic space and a flexible wall surface. Du, Li and Xu, etc. [1, 2] proposed a general Fourier series method predicting the acoustical behavior of a rectangular cavity with arbitrary impedance boundary conditions. This method not only accounts for the non-uniform boundary conditions, but also allows a truthful enforcement of the velocity continuity condition on or near the fluid–structure interface. Sanderson and Onsay [4] carried out an experimental acoustic modal analysis aiming to investigate the impact of the flexibility of cab panels and the addition of seats on changing acoustic frequencies and mode shapes. Kavarana and Schroeder [5] proposed a modified FEA method to improve the vibro-acoustic cavity modal correlation. They utilized an omni-directional sound source to duplicate the test scenario and scale the relative amplitudes of vibro-acoustic modes using acoustic transfer functions from the measured locations. Tsuji, Enomoto and Maruyama etc. [6] attempted to improve the simulation accuracy by utilizing the experimental acoustic mode shapes that determine the detailed sound pressure distribution at the coupled interfaces of the acoustic and structural system. Mamede, Varoto and Oliveira [7] investigated the vibro-acoustic coupling phenomena by using an experimental study of the interaction between acoustic and structural modes for a vehicle interior cavity for the low frequency range. Specifically, they focused on the extraction of cavity modal properties from measured acoustic-structural FRFs. Cherng, Bonhard and M. French [8] studied the influence of the seat orientation and trimmed material properties on the acoustic cavity modal behaviors using a mock-up passenger compartment.

One of the motivations for the investigation detailed in this report was the incidence of booming noise in a SD upgrade compactor [9]. The booming noise was perceived as a deep resonant sound with a significant increase in the sound pressure level (SPL) measured at the operator's ear position while the drum spins at 2,025 rpm. In order to identify the root cause(s) of the booming noise, an extensive experimental NVH investigation was carried out. As a key part of booming noise trouble shooting process, the acoustic cavity modal analysis not only helps the root cause identification, but also benefits the FEA prediction for the virtual Cab NVH development at early design phases. The objective of this work mainly focuses on but is not limited to:

1. Revisit the feasibility of using a rigid-walled acoustic cavity to approximate its *in-situ* counterpart in terms of modal characteristics.
2. Examine the impact of the seat and steering column on changing acoustic modal frequencies and mode shapes.
3. Investigate the local vibro-acoustic behavior and its relation to the low frequency compactor booming noise.

## 22.2   Analytical Acoustic Description of a Cavity

At early design stage, the cabin acoustic modes can be approximately determined using analytical solutions for a rigid-walled rectangular cavity. Figure 22.1 depicts a rectangular acoustical cavity of dimensions $L_x \times L_y \times L_z$ with an associated coordinate system.
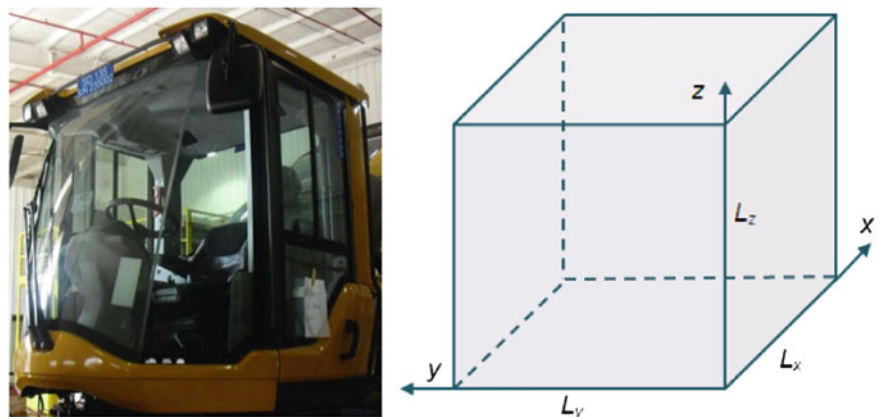


**Fig. 22.1** ISO view of the cabin and its equivalent box dimensions

**Fig. 22.2** FE cavity model:
(**a**) no seat and steering column;
(**b**) with seat and steering column
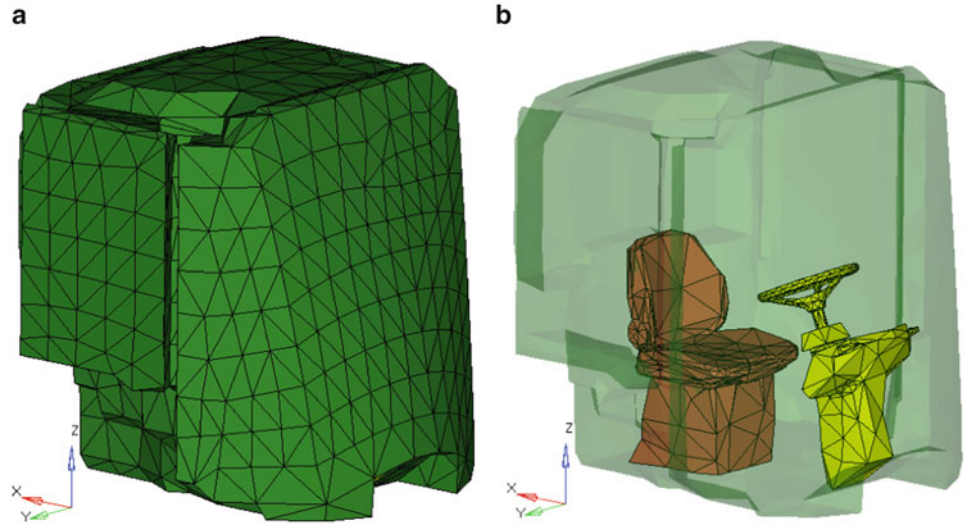


The exact values for the natural frequencies of a rigid-walled rectangular cavity are well known as:

$$f_n = \frac{c_0}{2} \sqrt{\left(\frac{n_x}{L_x}\right)^2 + \left(\frac{n_y}{L_y}\right)^2 + \left(\frac{n_z}{L_z}\right)^2} \qquad (22.1)$$

where $c_0$ is the speed of sound, $L_x$ is the depth, $L_y$ is the width, and $L_z$ is the height of the cavity. In addition, $n_x, n_y$ and $n_z$ denote the modal orders in $x$, $y$ and $z$ directions, respectively. The modal functions for rigid-walled rectangular cavity are simply the products of cosine functions in three dimensions:

$$\Psi_{n_x n_y n_z} = \cos \cos \lambda_{n_x} x \cos \cos \lambda_{n_y} y \cos \cos \lambda_{n_z} z \qquad (22.2)$$

where $\lambda_{n_s} = n_s \pi / L_s$ ($s = x, y,$ or $z$)

In this case, $L_x = 1.34m$ and is measured as the average distance between the front windshield to rear window, $L_y = 1.54m$ and is the distance between two side windows, and $L_z = 1.75m$ is the height of the cavity measured from floor to roof.

## 22.3 FEA Calculation

FEA is also commonly used at early design phase to predict the fundamental trends of the acoustical cavity. Fig. 22.2 shows the FE acoustic cavity being modeled with and without steering assembly and seat. The 2nd order solid tetra elements were used to mesh the cavity. The entire cavity mesh consists of 15,000 elements with an average size of 80 mm. By accommodating the real geometry layout, FEA is more accurate than analytical solution in predicting rigid-walled cavity acoustical behavior. Even though the rigid-walled assumption is not realistic due to the fact that the actual cabin consists of a number of flexible panels, the rigid-walled acoustic modes still provide a benchmarking for investigating the acoustic modal difference due to the structure-acoustic interaction. Therefore, the rigid-walled cavity model will be utilized in the following case study.

## 22.4 Physical Acoustic Cavity Characterization

Two testing cases were performed on the cab shell with and without the seat and steering column, respectively. The cab was settled on two airbags to simulate a free-free boundary condition, shown in Fig. 22.3a. A low frequency omni-directional volume velocity sound source was used to excite the cab cavity. The source was placed at the front left corner of the cavity and isolated with soft foam from the cab body as shown in Fig. 22.3b. A white noise signal from 20 to 500 Hz was used as the driving signal to excite the acoustic modes of interest. Figure 22.4 illustrates the acoustic instrumentation. An array consisting of 6 microphones spanned the interior and was moved along the depth (front to rear) and height (floor to roof) of
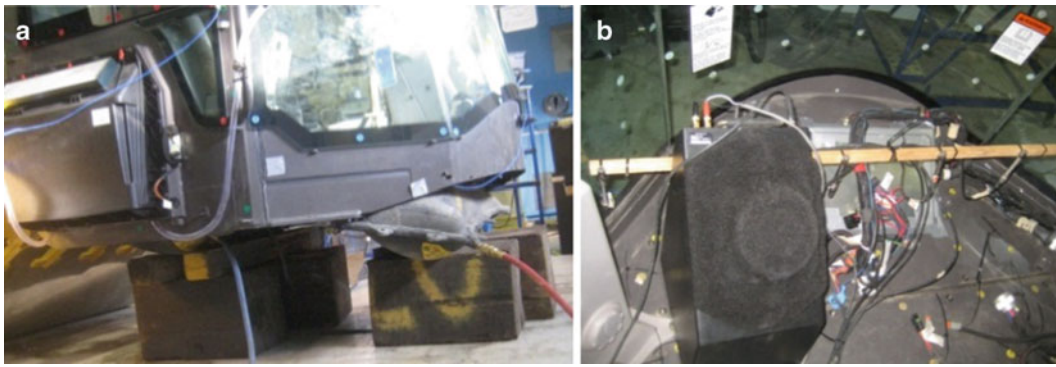
**Fig. 22.3** (**a**) Completely detached cab shell sitting on airbags; (**b**) omni-directional volume velocity sound source
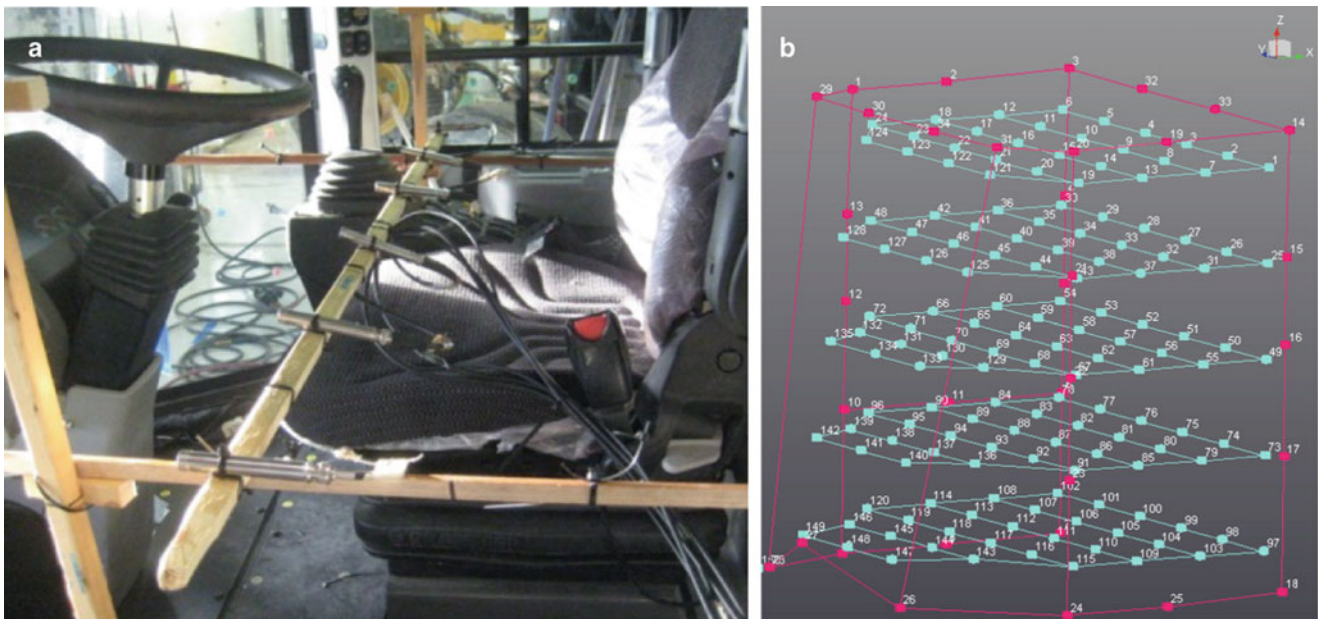


**Fig. 22.4** (**a**) Microphone array setup; (**b**) measurement grid

the cab which defined a measurement grid. Two wooden strips extending from the front to the rear of the cab support the roving microphone array. The vertical wooden frames were used to raise and lower the moveable array throughout the space. The acoustic transfer functions (*P/Q*) were measured between microphone responses at all grid points with respect to the volume velocity of the source. The acoustic modal parameters were extracted using PolyMAX method.

## 22.5  Results and Discussion

### 22.5.1  *Feasibility of Rigid-Walled Assumption in Predicting Acoustic Cavity Modal Characteristics of the Cab In-Situ*

The rigid-walled assumption is frequently used to estimate the cab cavity resonances by design engineers at early cab development stage. However, the level of accuracy for this approximated prediction is rarely examined due to the lack of a comprehensive experimental benchmark. This session is aiming at filling this void by quantitatively investigating the feasibility of rigid-walled acoustic cavity in approximating its *in-situ* counterpart in terms of modal characteristics.

Due to the fact that most challenging cab noise issues are in the low frequency range, for example, the booming noise, only *1D*, *2D* and the first *3D* modes are considered. Table 22.1 shows the comparisons of the first 7 modal frequencies obtained by

**Table 22.1** Comparison of acoustic modal frequencies

| $n_x$ | $n_y$ | $n_z$ | Analytical mode (Hz) | | FEA mode (Hz) | | Test mode (Hz) | | Analytical vs. test | FEA vs. test | Analytical vs. FEA (%) |
|---|---|---|---|---|---|---|---|---|---|---|---|
| 0 | 0 | 1 | 1 | 97.2 | 1 | 115.9 | 4 | 112.1 | −13.3 | 3.4 | 16.1 |
| 0 | 1 | 0 | 2 | 110.7 | 2 | 132.7 | 2 | 93.6 | 18.7 | 41.8 | 16.6 |
| 1 | 0 | 0 | 3 | 126.9 | 3 | 149.9 | 6 | 137.4 | −7.6 | 9.1 | 15.3 |
| 0 | 1 | 1 | 4 | 147.3 | 4 | 185.3 | 7 | 171.7 | −14.2 | 7.9 | 20.5 |
| 1 | 0 | 1 | 5 | 159.8 | 5 | 194.8 | – | | – | – | 18.1 |
| 1 | 1 | 0 | 6 | 168.4 | 6 | 215.7 | – | | – | – | 21.9 |
| 1 | 1 | 1 | 7 | 194.4 | 8 | 228.7 | 9 | 230.5 | −15.6 | −0.8 | 15.0 |

analytical solution, FEA and test. Note that the modal sequence achieved from test is quite different from the one predicted by analytical solution and FEA. For instance, the vertical mode (0, 0, 1) is the first mode in analytical solution and FEA but the fourth mode in test. Also, in test the vertical mode (0, 0, 1) comes after the lateral mode (0, 1, 0) whereas in analytical solution and FEA the sequence of these two modes is switched. In addition, the natural modes given by test are slightly lower compared to the FEA prediction. This is because the flexibility of panels surrounding the cavity results in an "elastic" acoustical boundary condition hence making the cavity acoustically longer than the physical dimensions [4]. For the cab *in-situ*, the side panels are made of glass whereas the roof and floor are steel, therefore the cavity wall is softer laterally but stiffer vertically, which makes the cavity acoustically longer in lateral direction (*y*-axis) than the vertical direction (*z*-axis). It is also noticed that modes (1, 0, 1) and (1, 1, 0) are missing in test, which is due to the elastic cavity wall as well. The prediction accuracy of analytical solution and FEA can be measured by the percentage discrepancy against experimental results. The accuracy level of anlytical prediction is between 80 and 90 % and the one of FEA prediction is as high as 90 % except for the 2nd mode (0, 1, 0) which has a 40 % predicting deviation.

The mode shapes associated with Table 22.1 are plotted in Fig. 22.5. Note that FEA and test have a nearly perfect match for *1D* and *2D* modes and a reasonable agreement for the first *3D* mode (1, 1, 1). It should be emphasized once again that the experimental modal sequence needs to be adjusted to match the counterpart mode shapes given by analytical solution and FEA. Besides, a fairly reasonable agreement is found between analytical solution and FEA, especially in the case of *1D* and *2D* modes. This implies that the geometrical deviation between an FE model and its equivalent rectangular box is not so significant in predicting the lower order acoustic cavity mode shapes.

Figure 22.6 depicts the unique testing modes that are not listed in Table 22.1. Note that the first mode in test is a longitudinal mode (1, 0, 0) at 79.7 Hz in *x*-axis, shown in Fig. 22.6a. The third testing mode shown in Fig. 22.6b is a *quasi-*vertical mode in *z*-axis meaning a transition mode between the 2nd lateral mode and the 4th vertical mode. Figure 22.6c, d present the modes in such a way that they can be somewhat treated as a (0, 0.5, 0.5) mode and a (1, 0.5, 0.5) mode, respectively. Again, these unique modes can be attributed to the vibro-acoustic coupling effect between the air cavity and the flexible cab panels.

## 22.5.2 Impact of the Seat and Steering Column on Experimental Acoustic Modal Parameters

The addition of the seat and steering column introduces a mass coupling effect to the interior sound field which could generate a substantial impact on the cavity acoustic behaviors [8].

Table 22.2 shows the acoustical natural frequencies and modal damping that were extracted from measurements with and without the addition of the seat and steering column. The first observation is that the modal frequencies are uniformly shifted downwards by 1–5 % after adding the seat and steering column. Particularly, the vertical mode #4 shifts more to the lower value than the lateral mode #3 and the longitudinal mode (mode #5 for with seat and mode #6 for no seat). The addition of the seat and steering column causes a little frequency shift for the *3D* mode (1, 1, 1), which is a combination of longitudinal, lateral and vertical mode.

However, the results are counter intuitive because the interior volume of the cavity decreases with the addition of the seat and steering column, which should increase the modal frequencies. The same observation was found in previous publications [4, 8].

In order to further investigate the acoustic modal behavior, a sum block of measured acoustic transfer functions (*P/Q*) is plotted in Fig. 22.7 for the two cases. The sum block is essentially an averaged response of acoustic transfer functions measured at all microphone locations, which is useful to identify the modes as well as the relative strength of modes. The averaged acoustic transfer function shows that the two cases generally share a similar trend in terms of peaks and valleys in the frequency range of interest except for the mode at 121.2 Hz, which is absent with the addition of the seat and steering
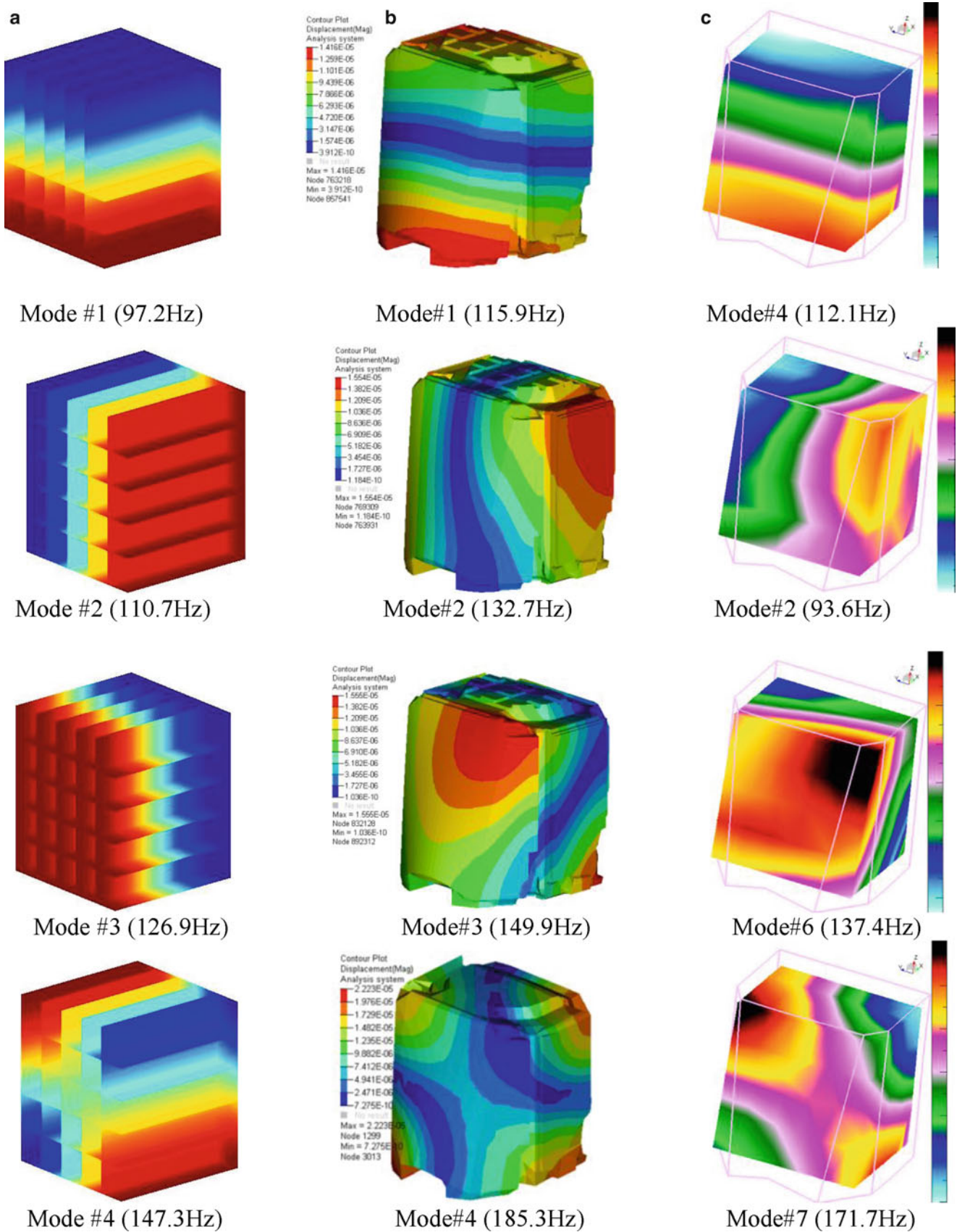
**Fig. 22.5** Comparison of cavity mode shapes: (**a**) analytical solution; (**b**) FEA; (**c**) test

Mode #5 (159.8Hz)          Mode#5 (194.8Hz)          N/A

Mode #6 (168.4Hz)          Mode#6 (215.7Hz)          N/A

Mode #7 (194.4Hz)          Mode#8 (228.7Hz)          Mode#9 (230.5Hz)
Analytical solution        FEA                        Test
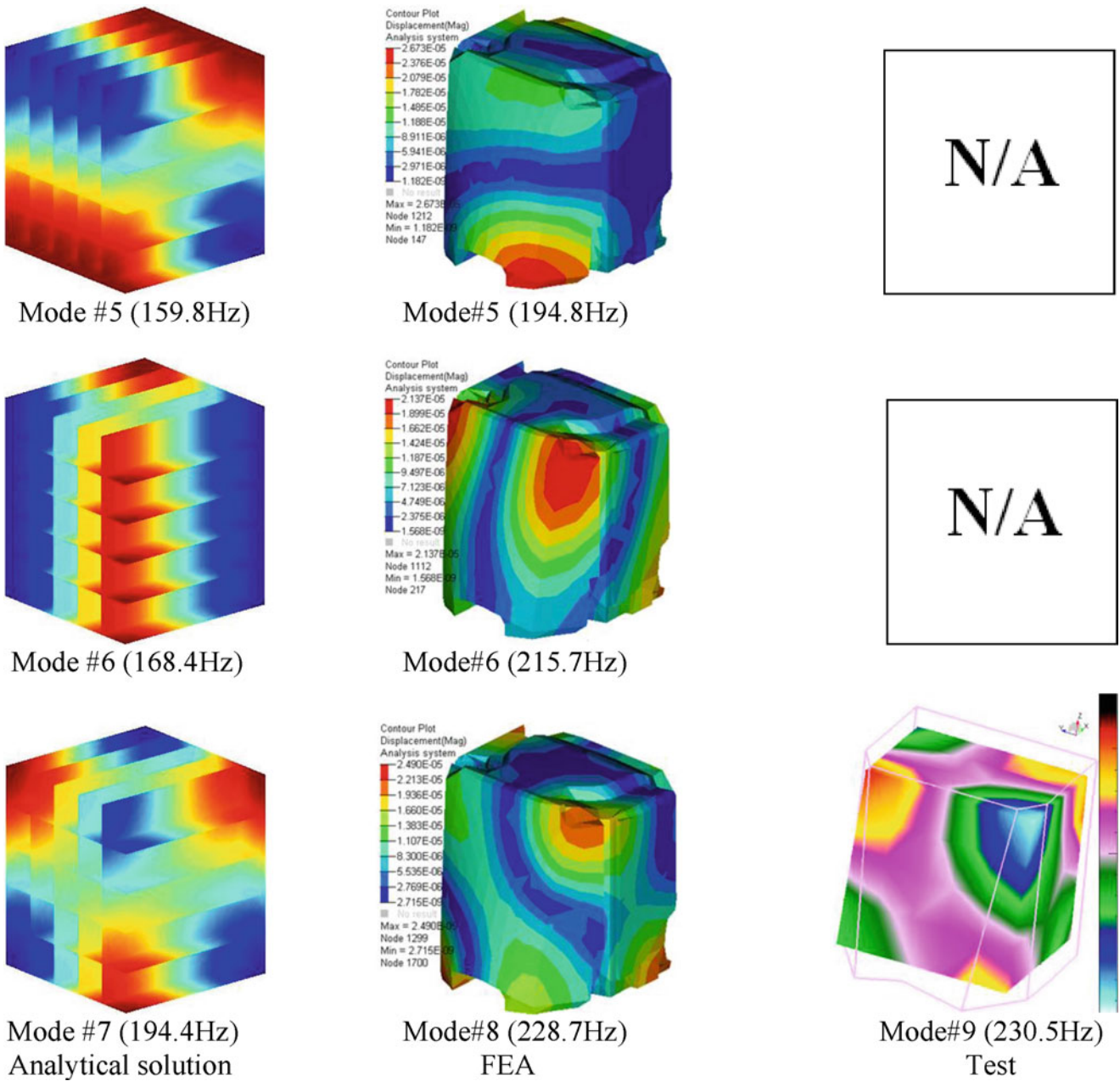
**Fig. 22.5** (continued)

column. It is also noted that the modal response increases with the addition of the seat and steering column. Regarding the relative strength of modes, the vertical mode #4 is the most dominant one for both cases. In practice, this vertical mode may induce high sound pressure levels if it is coincident with excitation frequencies such as the engine firing orders. Such a mode should be precisely identified from the FEA model prior to the physical prototype to facilitate the cab NVH development.

The corresponding mode shapes are compared in Fig. 22.8. Note that when the seat and steering column are added, the vertical mode #4 somehow tends to start coupling with a lateral mode in $y$-axis. For the longitudinal mode #6, the region where the maximum pressure response concentrates migrates from the front top left corner to the front bottom right corner.

Mode #1 (79.7Hz)    Mode#3 (100.9Hz)    Mode#5 (121.2Hz)    Mode#8 (191.7Hz)
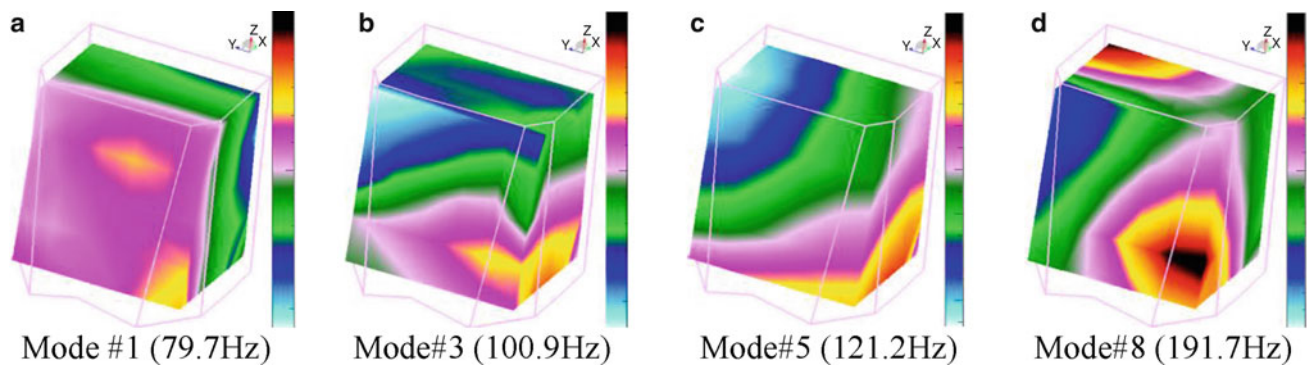
**Fig. 22.6** Experimental vibro-acoustic cavity modes missed in theoretical and FEA prediction

**Table 22.2** Comparison of acoustical natural frequencies and damping extracted from measurements with and without seat and steering column

| With seat and steering column | | | No seat and steering column | | | Frequency difference (%) |
|---|---|---|---|---|---|---|
| Mode | Frequency (Hz) | Damping (%) | Mode | Frequency (Hz) | Damping (%) | (No seat–with seat)/no seat |
| 1 | 79.1 | 0.4 | 1 | 79.7 | 1.7 | 0.8 |
| 2 | 92.8 | 1.1 | 2 | 93.6 | 1.8 | 0.9 |
| 3 | 99.3 | 1.1 | 3 | 100.9 | 0.9 | 1.6 |
| 4 | 108.1 | 3.5 | 4 | 112.1 | 2.6 | 3.6 |
| – | – | – | 5 | 121.2 | 2.5 | – |
| 5 | 135.1 | 3.9 | 6 | 137.4 | 3.2 | 1.7 |
| 6 | 164.1 | 1.8 | 7 | 171.7 | 2.3 | 4.2 |
| 7 | 190.7 | 1.52 | 8 | 191.7 | 2.2 | 0.5 |

**Fig. 22.7** Comparison of block ATF with and without seat and steering column



### 22.5.3 Local Vibro-Acoustic Behavior and Its Relation to the Low Frequency Booming Event

As previously mentioned, one of the motivations of this study is to help identify the root cause of a low frequency booming noise on a compactor. The booming noise was perceived as a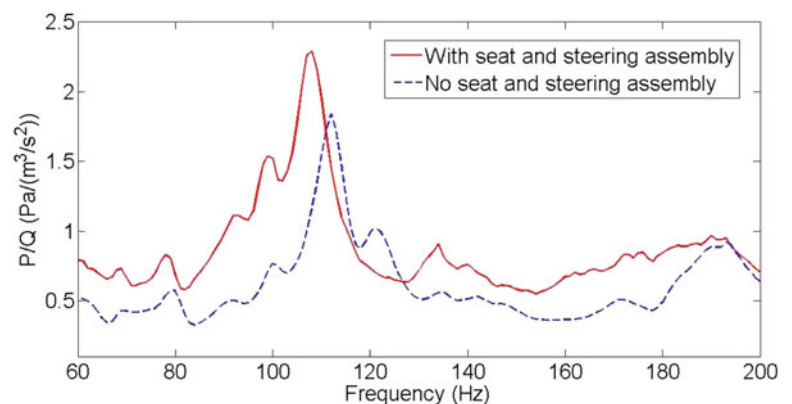 deep resonant sound at the operator's ear position at 34 Hz. The cab dimension of 1.34 m × 1.54 m × 1.75 m indicates that the lowest flexible acoustic mode would be around 100 Hz which is much higher than the booming frequency. Besides, the initial diagnostic test subjectively found that the noise level remains almost the same regardless of positions. It implies that the noise is neither related to a standing wave nor a cavity mode. Based on the aforementioned facts, the booming event is therefore suspected to be due to a local vibro-acoustic response that could be induced by a cab panel resonance.

Figure 22.9 plots the averaged acoustic transfer function for the case with no seat and steering column in a range of 30–200 Hz. Note that there is peak at approximately 35 Hz dictating the entire frequency range. This peak, however, is actually related to a local panel resonance instead of a cavity mode, which can be verified through plotting the imaginary part of all measured acoustic transfer functions, as illustrated in Fig. 22.10.
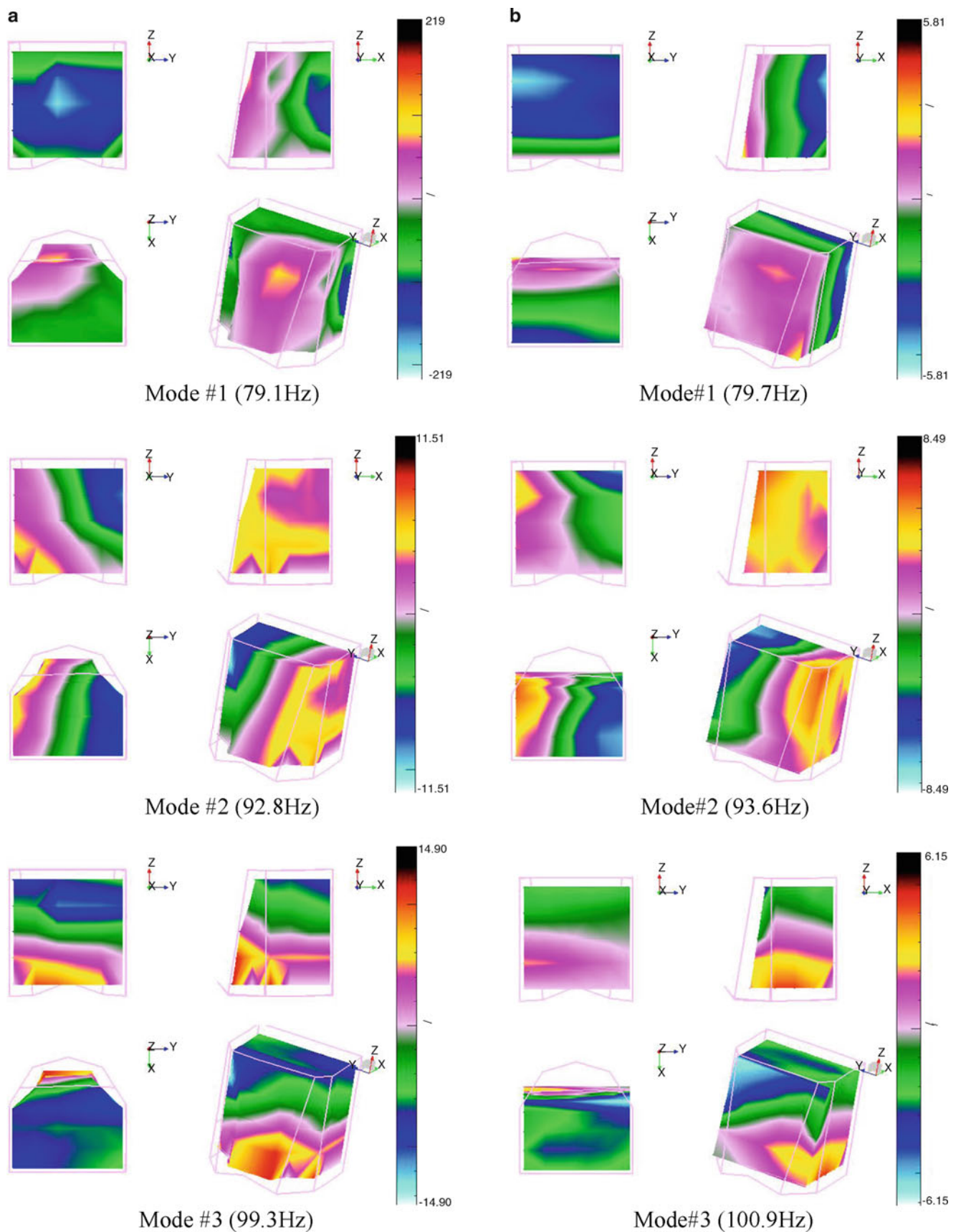
**Fig. 22.8** Comparison of experimental cavity modes with (**a**) and without (**b**) seat and steering column. (**a**) With seat and steering column (**b**) No seat and steering column

Mode #4 (108.1Hz)

Mode#4 (112.1Hz)

Mode #5 (135.1Hz)

Mode#6 (137.4Hz)

Mode #6 (163.1Hz)

Mode#7 (171.7Hz)

**Fig. 22.8** (continued)

Mode #7 (190.7Hz)
With seat & steering column

Mode#8 (191.7Hz)
No seat & steering column

**Fig. 22.8** (continued)

**Fig. 22.9** Averaged acostic transfer function with no seat and steering column



**Fig. 22.10** Imaginary part of the acoustic transfer functions measured at all microphone locations

**Fig. 22.11** Illustustration of a local vibro-acoustic behavior caused by a panel resonance 35 Hz. (**a**) Contour of pressure distribution at 35 Hz (**b**) Cab structural mode at 35 Hz
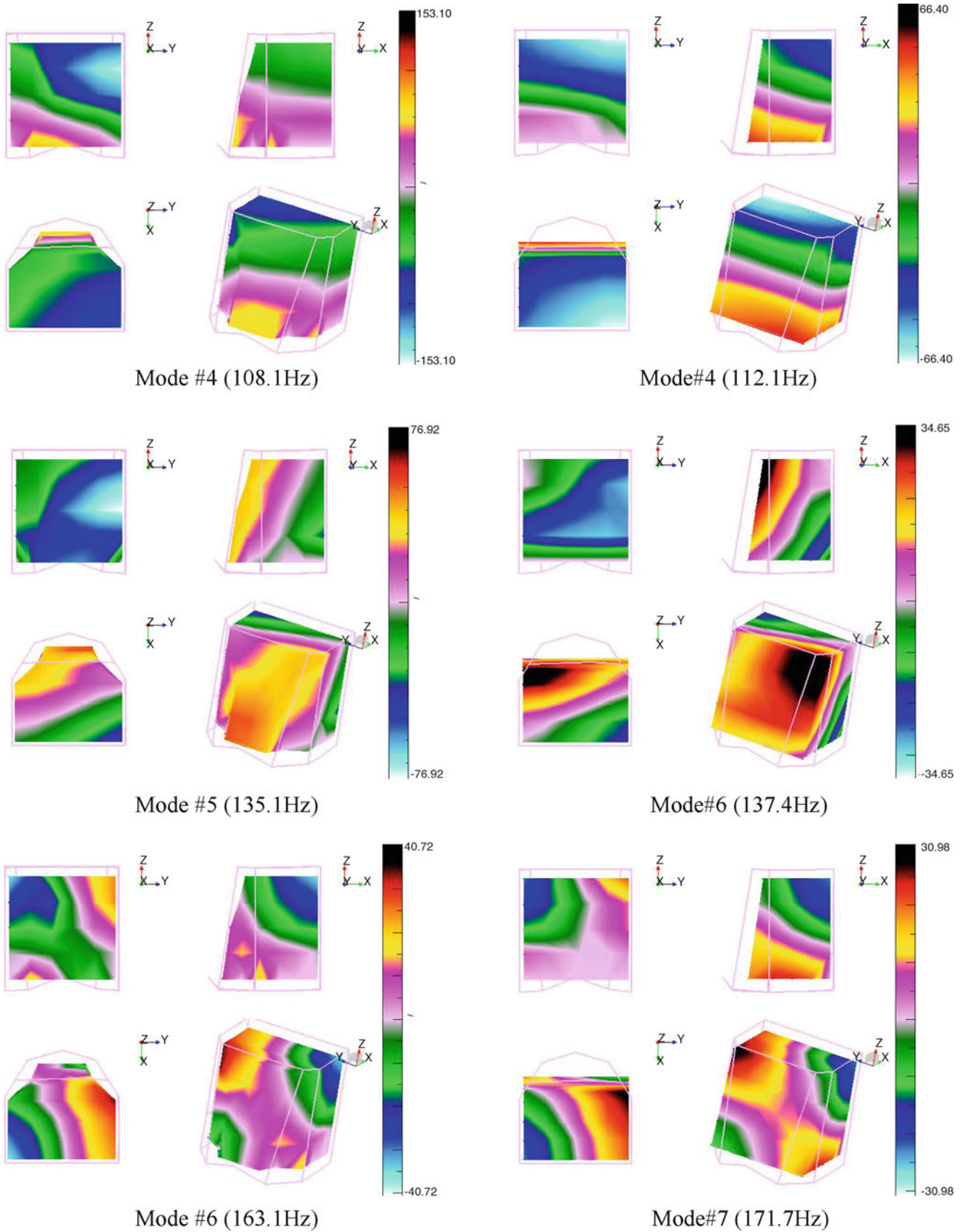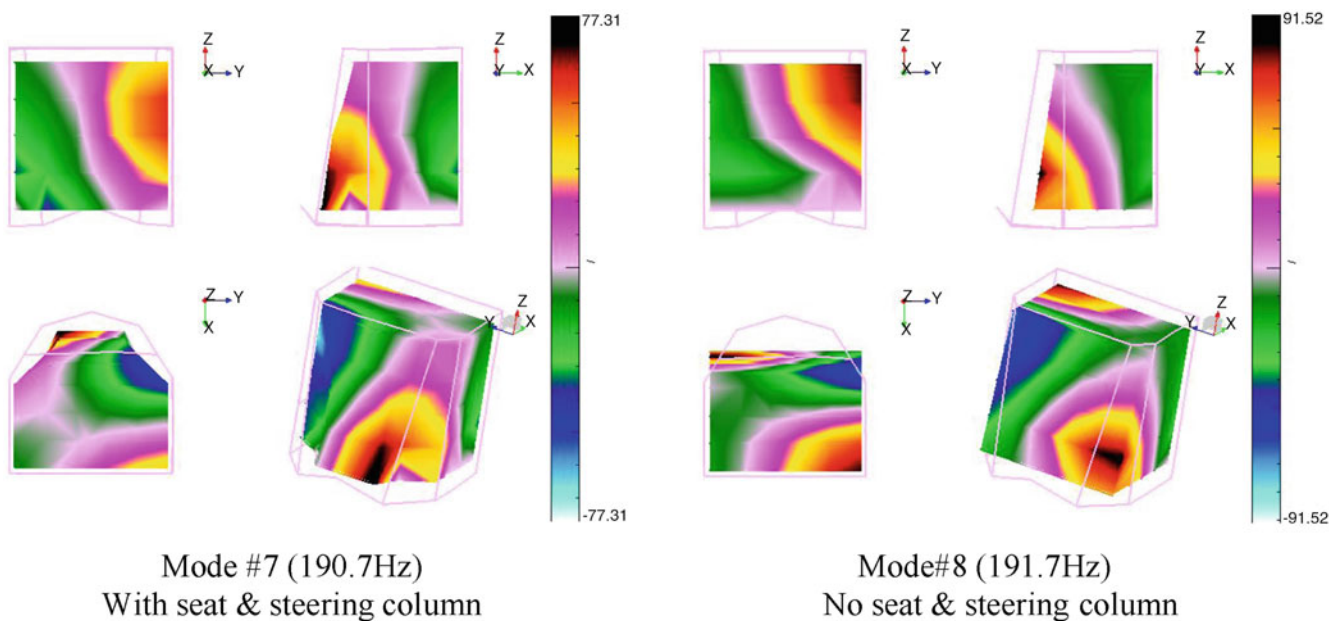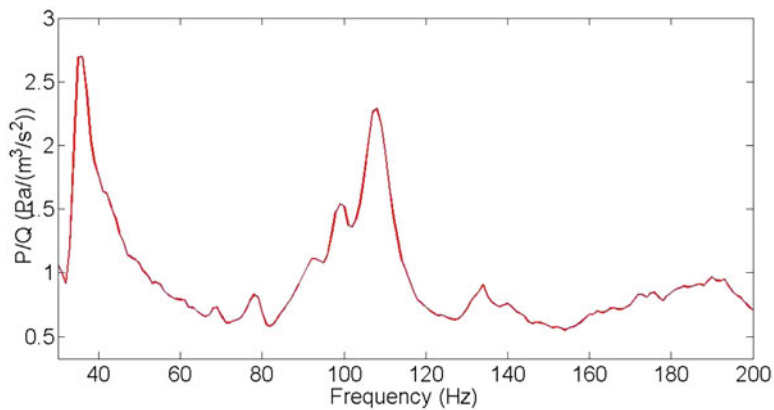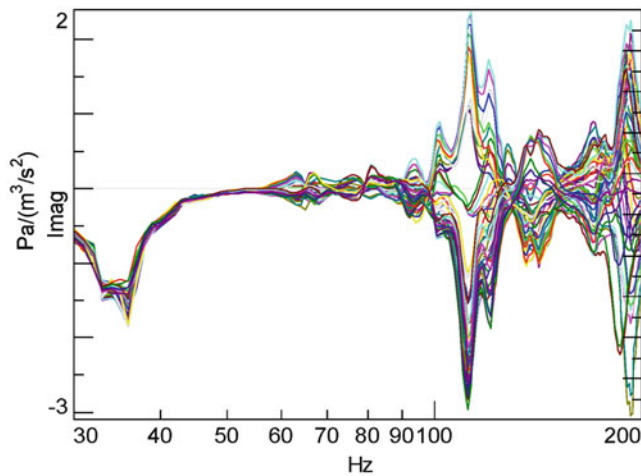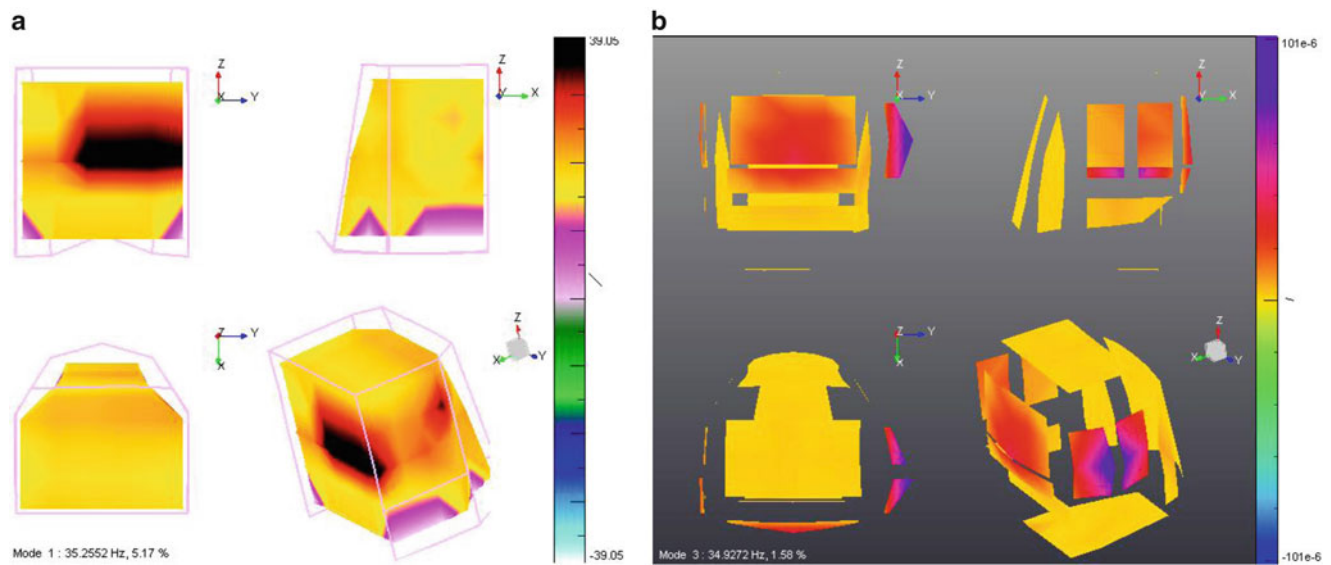
By definition, the imaginary parts of the frequency response functions for each modal frequency represent the associated mode shape. Particularly, to identify an acoustic mode, a sign change in the imaginary parts is essentially required. It is clearly showed in Fig. 22.10 that all the peaks of the imaginary parts point in the same direction. Thus we can conclude that the peak at 35 Hz is irrelevant to the acoustic cavity resonances.

To validate that the peak at 35 Hz is due to a local panel resonance, we conducted an experimental modal analysis on the cab structure. A structural mode was found at 35 Hz which is coincident with the booming frequency. For comparison, the structural mode shape is depicted together with an acoustic pressure mapping contour in Fig. 22.11. While the pressure distribution contour shows a high pressure concentration next to the rear and side windows, the structural mode shape indicates a local resonance of the rear and side panels accordingly. Apparently, the root cause of the booming noise is due to a local vibro-acoustic behavior that is initiated by the structural resonance of the rear and side panels. To suppress this local vibro-acoustic behavior, a practical countermeasure was implemented to shift the panel resonance away from the drum excitation frequency and the interior booming noise was tremendously attenuated.

## 22.6 Conclusion

The acoustic modal behaviors have been characterized qualitatively and quantitatively using analytical solution, FEA and experimental measurement. The primary findings and conclusions are summarized as below:

1. Based on the assumption of a rigid-walled cavity, the lower order modal frequencies predicted by the analytical solution and FEA differ 10–20 % and 10 %, respectively, from those obtained by tests. The experimental modal sequence is also quite different from the analytical and numerical ones. The prediction discrepancies are mainly attributed to the unrealistic rigid-walled assumption.
2. While the modal frequencies predicted by FEA and analytical solution have a deviation around 15–20 %, the predicted modal sequence is nearly the same. This could be due to the high irregularity of the cab geometry and the nearly identity 3D aspect ratio (*x/y/z*) of cab dimensions.
3. Regarding the mode shapes, FEA and test have a nearly perfect match for *1D* and *2D* modes and a reasonable match for the first *3D* mode (1, 1, 1). Analytical solution and FEA have a reasonable agreement for the *1D* and *2D* modes. This implies that the geometrical deviation between an FE model and its equivalent rectangular box is not so significant in predicting lower order acoustic cavity mode shapes.
4. The addition of the seat and steering column shifts the modal frequencies down to lower values by 1–5 % but makes a little difference to the mode shapes.

5. The averaged acoustic transfer function (*P/Q*) plays an important role in determining the relative strength of acoustical modes.
6. The local vibro-acoustic behavior is of critical importance in affecting the interior sound field. The root cause of the local vibro-acoustic behavior is attributed to the panel resonances.

## References

1. Pan J, Bies DA (1990) The effect of fluid-structural coupling on sound waves in an enclosure—theoretical part. J Acoust Soc Am 87(2):691–707
2. Du JT, Li WL, Liu ZG, Xu HA, Ji ZL (2011) Acoustic analysis of a rectangular cavity with general impedance boundary conditions. J Acoust Soc Am 130(2):807–817
3. Du JT, Li WL, Xu HA, Liu ZG (2002) Vibro-acoustic analysis of a rectangular cavity bounded by a flexible panel with elastically restrained edges. J Acoust Soc Am 131(4):2799–2810
4. Sanderson MA, Onsay T (2007) FEA interior cavity model validation using acoustic modal analysis. SAE Technical Paper 2007-01-2167
5. Kavarana F, Schroeder A (2012) A practical FEA approach to determine acoustic cavity modes for vehicle NVH development. SAE Technical Paper 2012-01-1184
6. Tsuji H, Enomoto T, Maruyama S, Yoshimura T (2012) A study of experimental acoustic modal analysis of automotive interior acoustic field coupled with the body structure. SAE Technical Paper 2012-01-1187
7. Mamede WF, Varoto PS, de Oliveira LRP (2002) Vibro-acoustic modal testing of a vehicle cabin, Proceedings of the 27th International Seminar on Modal Analysis (ISMA 27), 2002
8. Cherng J, Bonhard RB, French M (2002) Characterization and validation of acoustic cavities of automotive vehicles. Soc Photo Opt Instrum Eng 1:290–294
9. Xu H, Wang J, Owen D, Kang H (2013) Experimental vibro-acoustic analysis for troubleshooting compactor cab booming noise. In: Proceedings of Noise-Con 2013, August 26–28, Denver, CO

# Chapter 23
# Strain-Based Dynamic Measurements and Modal Testing

**Fábio Luis Marques dos Santos, Bart Peeters, Marco Menchicchi, Jenny Lau, Ludo Gielen, Wim Desmet, and Luiz Carlos Sandoval Góes**

**Abstract** The most common and established way of performing experimental modal analysis is to use acceleration or velocity based transducers that lead to the calculation of the displacement mode shapes. However, there are applications where the use of strain measurements makes for a more attractive and interesting option. For instance, since strain measurements are more directly related to stress, fatigue and failure, strain-based measurement methods can be a good option for structural health monitoring methods and monitoring systems. Moreover, applications where sensor size and placement might be critical are also good candidates for strain-based methods. Helicopters, wind turbines and gas turbines are a good example where strain gauges are more suited for vibration measurements. Additionally, any sort of system that uses strain gauges for static testing can also use the same sensors for dynamic testing without incurring additional sensor costs, which can be very useful in some situations. Some application cases of dynamic strain measurements and dynamic strain modal analysis are shown in this work, with test subjects such as a composite helicopter blade, a small wind turbine blade and a composite beam. Different types of sensors and excitation methods were also used as well as correlation with a computational model.

**Keywords** Strain modal analysis • Dynamic strain • Strain field • Modal analysis • Mode shape

## 23.1 Introduction

Modal testing has been, for a long time, associated with the use of displacement responses (or their derivatives with respect to time). The use of strain sensors for modal testing [1, 2], on the other hand, has been less accentuated, with the difficulties of using strain gauges slowing down the advent of strain modal analysis. But the increased interest from both industry and academia on assessing and evaluating structural integrity on design prototype stages and also monitoring in real-time (with structural health monitoring systems (SHM)), has led to an increase in the number of dynamic strain applications, to the development of improved identification and measurement techniques, as well as to improved sensor technology [3, 4].

F.L.M. dos Santos (✉)
LMS, A Siemens Business, Interleuvenlaan 68, 3001 Leuven, Belgium

Katholieke Universiteit Leuven (KUL), Division PMA, Celestijnenlaan 300B, 3001 Heverlee, Belgium

Instituto Tecnológico de Aeronáutica (ITA), Praça Marechal Eduardo Gomes, 50 - Vila das Acácias CEP 12.228-900,
São José dos Campos - SP, Brazil
e-mail: fabio.santos@lmsintl.com

B. Peeters • M. Menchicchi • J. Lau • L. Gielen
LMS, A Siemens Business, Interleuvenlaan 68, 3001 Leuven, Belgium

W. Desmet
Katholieke Universiteit Leuven (KUL), Division PMA, Celestijnenlaan 300B, 3001 Heverlee, Belgium

L.C.S. Góes
Instituto Tecnológico de Aeronáutica (ITA), Praça Marechal Eduardo Gomes, 50 - Vila das Acácias CEP 12.228-900,
São José dos Campos - SP, Brazil

Strain gauges have been commonly used for static load testing of mechanical products in the aeronautic, automotive and mechanical industry. Moreover, fatigue testing [5], durability analysis and lifetime prediction [6] has also been a common application where strain gauges are used. This sort of testing is a common part of the product development process, and additional information on product durability and dynamic performance can be assessed by obtaining the modal parameters of the system, while still using the same instrumentation.

A very important contribution on the field of strain measurement are the fiber optic sensors, or Fiber Bragg Grating (FBG) sensors [7, 8]. Their robustness to magnetic interference, added to the easiness of creating sensor arrays with multiple sensors, plus the possibility of embedding these sensors in composite structures, makes for an attractive solution for use in SHM systems. The availability of such an array of sensors, ready to be used and adequate for modal testing, is another incentive to carrying out a strain modal analysis, saving up on time and instrumentation.

Another application of dynamic strain measurements is related to the strain displacement relations [9]. In many systems, strain gauges are used as the standard vibration sensor, especially when size or sensor location is an issue. Such is the case in aerospace applications, like gas turbines, wind turbines and helicopters [10], where size and weight are very restricted, and any sensor place on a blade should affect its aerodynamic properties as little as possible. One particular use of the strain measurements and strain to displacement relations is the strain pattern analysis (SPA), where strain measurements are used to predict blade displacements.

## 23.2   Theoretical Background

To obtain the strain modal formulation, one can start with the fundamental theory of modal analysis. Modal theory states that the displacement on a given coordinate can be approximated by the summation of a $n$ number of modes:

$$u(t) = \sum_{i=1}^{n} \phi_i q_i(t)$$
(23.1)

where $u$ is the displacement response in $x$ direction, $\phi_i$ is the $i$th (displacement) vibration mode, and $q_i$ is the generalized modal coordinate and $t$ is time. For small displacements, given the theory of elasticity, the strain/displacement relation is:

$$\varepsilon_x = \frac{\partial}{\partial x} u$$
(23.2)

And similarly, the same relationship exists between the strain vibration modes and the displacement modes:

$$\psi_i = \frac{\partial}{\partial x} \phi_i$$
(23.3)

This way, by the relations on Eqs. (23.2) and (23.3), the expression on (23.1) can be rewritten as:

$$\varepsilon(t) = \sum_{i=1}^{n} \psi_i q_i(t)$$
(23.4)

Moreover, the relationship between the generalized modal coordinate $q$ and an input force $F$ is:

$$q_i = \Lambda_i^{-1} \phi_i F, \text{with} \Lambda_i = (-\omega^2 m_i + j\omega c_i + k_i)$$
(23.5)

where $m_i$, $c_i$ and $k_i$ are the $i$th modal mass, modal damping and modal stiffness, and $\omega$ is the excitation frequency.

Substituting (23.5) into (23.4), the relation between a force input and a strain output, in terms of displacement and strain modes is represented as:

$$\varepsilon_i = \sum_{i=1}^{n} \psi_i \Lambda_i^{-1} \phi_i F$$
(23.6)

And finally, the strain frequency response function (SFRF) can be obtained, in matrix form:

$$[H^\varepsilon] = \sum_{i=1}^{n} \Lambda_i^{-1} \{\psi_i\} \{\phi_i\} = [\psi] [\Lambda]^{-1} [\phi]^T$$
(23.7)

The expansion of (23.7) is:

$$
\begin{bmatrix}
H_{11}^{\varepsilon} & H_{12}^{\varepsilon} & \cdots & H_{1N_i}^{\varepsilon} \\
H_{21}^{\varepsilon} & H_{22}^{\varepsilon} & \cdots & H_{2N_i}^{\varepsilon} \\
\vdots & \vdots & \vdots & \vdots \\
H_{N_o1}^{\varepsilon} & H_{N_o2}^{\varepsilon} & \cdots & H_{N_oN_i}^{\varepsilon}
\end{bmatrix}
= \sum_{i=1}^{n} \Lambda_i^{-1} \cdot
\begin{bmatrix}
\psi_{1i}\phi_{1i} & \psi_{1i}\phi_{2i} & \cdots & \psi_{1i}\phi_{N_ii} \\
\psi_{2i}\phi_{1i} & \psi_{2i}\phi_{2i} & \cdots & \psi_{2i}\phi_{N_ii} \\
\vdots & \vdots & \vdots & \vdots \\
\psi_{N_oi}\phi_{1i} & \psi_{N_oi}\phi_{2i} & \cdots & \psi_{N_oi}\phi_{N_ii}
\end{bmatrix}
\tag{23.8}
$$

where $N_o$ represents the number of strain gauge measurement stations (or the number of output measurements) and $N_i$ represents the number of excitation points (or the number of inputs).

The columns of the matrix correspond to the strain responses due to the excitation points along the rows of the matrix. Some important characteristics can be inferred from Eq. (23.8). First of all, differently from displacement FRFs, the SFRF matrix is not symmetric, that is, for instance, $H_{12}^{\varepsilon} \neq H_{21}^{\varepsilon}$. This means that reciprocity is not guaranteed for strain modal analysis—exciting point $a$ and measuring point $b$ will not yield the same FRF as if exciting point $b$ and measuring point $a$. Moreover, any column of the SFRF matrix contains all the information regarding the strain modes ($\psi$), while any row of the SFRF matrix contains information about the displacement modes ($\phi$). This particular property leads to practical applications—to obtain the strain mode shapes, one must use a fixed excitation point and measure the strain responses. On the other hand, by using a strain gauge as a fixed reference sensor and moving the excitation point (as with impact testing), the displacement mode shapes can be obtained.

Due to the similarity of the strain modal formulation and the displacement modal formulation, the same modal identification methods can be used in both cases, as long as the appropriate caution is taken. In this article, the PolyMAX identification method [11] was used without any modifications.

Moreover, there is the possibility of obtaining reciprocal FRFs in strain modal testing, if the excitation input is not a force that acts on displacement, but is actually a direct strain input. This case is achievable if, for instance, a piezo patch actuator is used, but it will not be covered in this study, as the most common methods of carrying out modal analysis still use displacement based excitation sources.

The following section on the experimental analysis will show some experimental examples of the characteristics mentioned above.

## 23.3   Experimental Analysis

Three analysis cases were chosen to illustrate some of the characteristics of strain modal analysis seen in the previous section. The first test subject, a small composite wind turbine blade, was tested with strain gauges and an impact hammer, and the experimental results were compared with a finite element (FEM) simulation model. Then, a composite T-shaped beam was tested using piezo-based strain sensors, accelerometers and shaker excitation. Finally, a large composite helicopter main rotor blade was tested with shaker and hammer tests.

### 23.3.1   Wind Turbine Blade

A small composite wind turbine blade was used on the first strain modal test [12]. For this purpose, 20 strain gauges were glued to the surface of the blade and an impact hammer with an impedance head was used to excite the structure at several locations. The blade was fixed at its root, to impose a cantilevered condition. Of the 20 strain gauges, one of them consisted of a strain gauge rosette to measure purely shear strain, while the other 19 strain gauges were aligned with the radius of the blade and were measuring normal strain. Figure 23.1 shows the wind turbine blade, its sensor locations represented in the acquisition software and a finite element model of the blade.

The first step of the experimental procedure is to measure the strain frequency response functions (SFRFs), that are used later on the modal analysis procedure. Figure 23.2a shows the SFRF of an arbitrary strain gauge, where the resonance peaks are clearly visible. Moreover, the phase shift due to the resonances is the same for the SFRF, where the phase shifts in 180 degrees whenever there is a resonance peak.

Additionally for this experiment, a reciprocity check was carried out to verify if the theory for strain modal analysis was correct—for this purpose, two measurement points were picked and the impact hammer was used to excite those
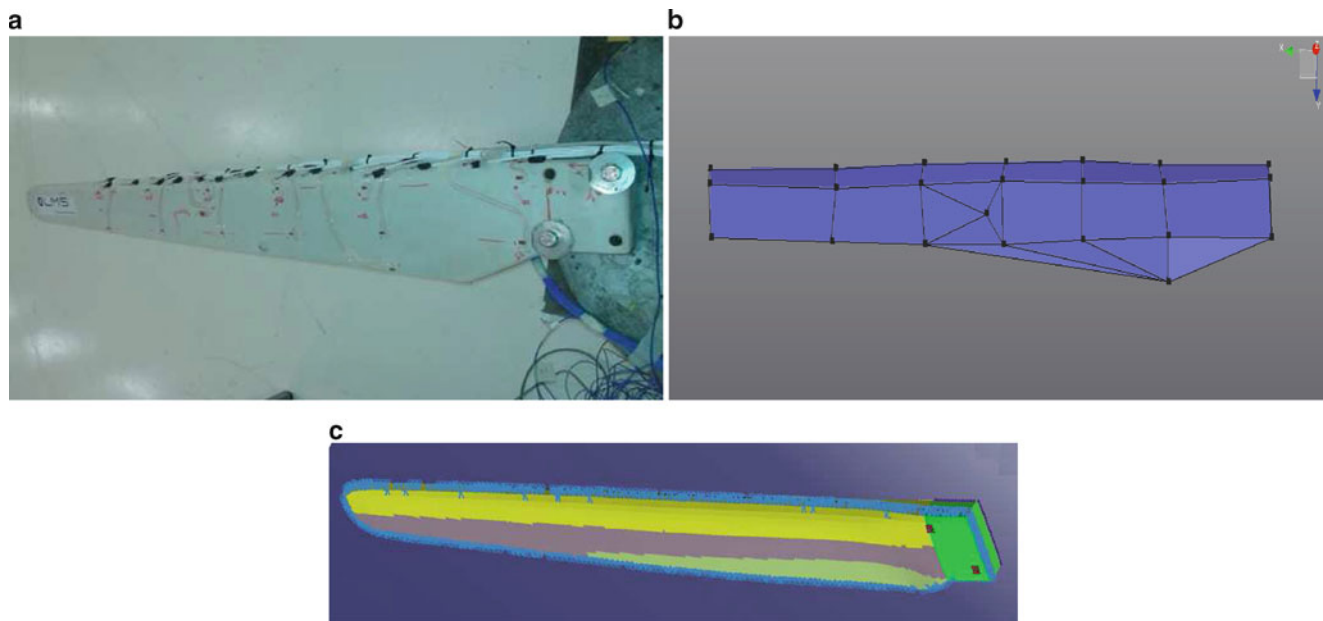
**Fig. 23.1** Small wind turbine blade, sensor locations and FEM model. (**a**) Composite small wind turbine blade. (**b**) Sensor locations on wind turbine blade. (**c**) Wind turbine blade FEM model
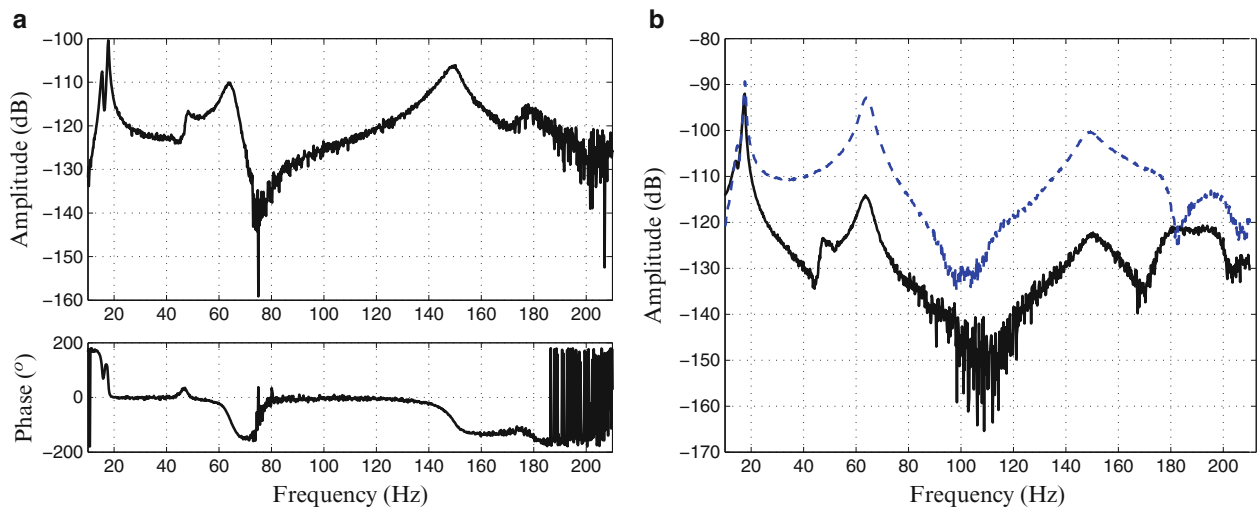


Wind turbine blade - Strain FRF from an arbitrary measurement point    Wind turbine blade-reciprocity check using strain measurements

**Fig. 23.2** Wind turbine blade: (**a**) strain FRF; (**b**) reciprocity check using a strain gauge—reciprocity is not guaranteed

points. A successful reciprocity check should yield identical or almost identical FRFs for a classical displacement modal analysis. In the case of the strain modal analysis, as it can be seen on Fig. 23.2b, reciprocity is not guaranteed for the strain measurements, since the SFRFs do not match each other.

After the reciprocity check, the modal analysis and strain modes identification was carried out. For this purpose, the PolyMAX identification method was used. A bandwidth from 10 to 210 Hz was taken into account as 6 clear modes were identified in that frequency range—these modes consist of bending, in-plane and torsional modes. Table 23.1 shows the natural frequencies and mode types of the identified modes. Finally, the strain modes obtained with the modal analysis procedure were compared with the strain modes obtained from a FEM analysis of the blade, from the model shown on Fig. 23.1c. The strain modes of the FEM model are extracted via the strain tensor matrix, where the appropriate strain directions are taken according to the orientation of the strain gauges on the blade, and the strain gauge location and size are approximated to one element of the finite element model.

**Table 23.1** Composite wind turbine blade: natural frequencies and vibration mode types

| Mode number | Frequency (Hz) | Mode type |
|---|---|---|
| 1 | 17.25 | Bending |
| 2 | 46.29 | In-plane |
| 3 | 63.99 | Bending |
| 4 | 148.97 | Bending |
| 5 | 178.38 | Torsional |
| 6 | 199.79 | In-plane |

**Table 23.2** Strain modes comparison—experiment and simulation

| Mode number | Natural frequency strain gauges (Hz) | Natural frequency accelerometers | Natural frequency simulation (Hz) | Difference % | MAC |
|---|---|---|---|---|---|
| 1 | 17.25 | 17.22 | 15.6 | 9.56 | 0.834 |
| 2 | 46.29 | 46.30 | 38.6 | 16.61 | 0.8 |
| 3 | 63.99 | 63.95 | 65.5 | 2.35 | 0.75 |
| 4 | 148.97 | 147.52 | 148.4 | 0.38 | 0.833 |
| 5 | 178.38 | 178.33 | 158.6 | 11.08 | 0.33 |
| 6 | 199.79 | 200.0 | 183.9 | 7.95 | 0.863 |

**Fig. 23.3** Modal assurance criterion—comparison of computational strain modes and experimental strain modes for the wind turbine blade



An initial analysis of the data from Table 23.2 shows that there is good agreement between the simulation model and the experiment. Regarding the natural frequencies, most of them are within 10 % of difference, except for modes 2 and 5. Moreover, the MAC values show very good correlation, except for mode 5. The lack of correlation for this mode is understandable—it is a torsional mode, which means that most of its energy comes from shear strain, while only one of the strain gauges (the strain rosette) is measuring shear strain, and the others are measuring normal strain.

Two methods of comparison were used to compare the simulation and experimental analysis, the percentage difference in natural frequency between experiment and simulation, and the modal assurance criterion (MAC). Table 23.2 shows the natural frequencies comparison and percentage difference, as well as the diagonal MAC value. Additionally, the natural frequency values obtained using a traditional accelerometer based impact test are also show, for the purpose of comparison. Moreover, Fig. 23.3 shows the full MAC matrix for all the considered modes.

### 23.3.2  Composite T-Beam

The composite T-beam used for the experiments is better described in [13]. It is a very simple structure by design, being composed of carbon fiber reinforced plastics (CFRP) with 8 plies in total, and it has a T-shaped cross section. This sort of cross section leads to a high bending stiffness, while the torsional stiffness is not affected as much. This means that for a

**Fig. 23.4** Composite T-beam test set-up and strain sensor. (**a**) Composite T-beam test set-up used for experiments. (**b**) Piezo strain sensor. (**c**) Shaker set-up
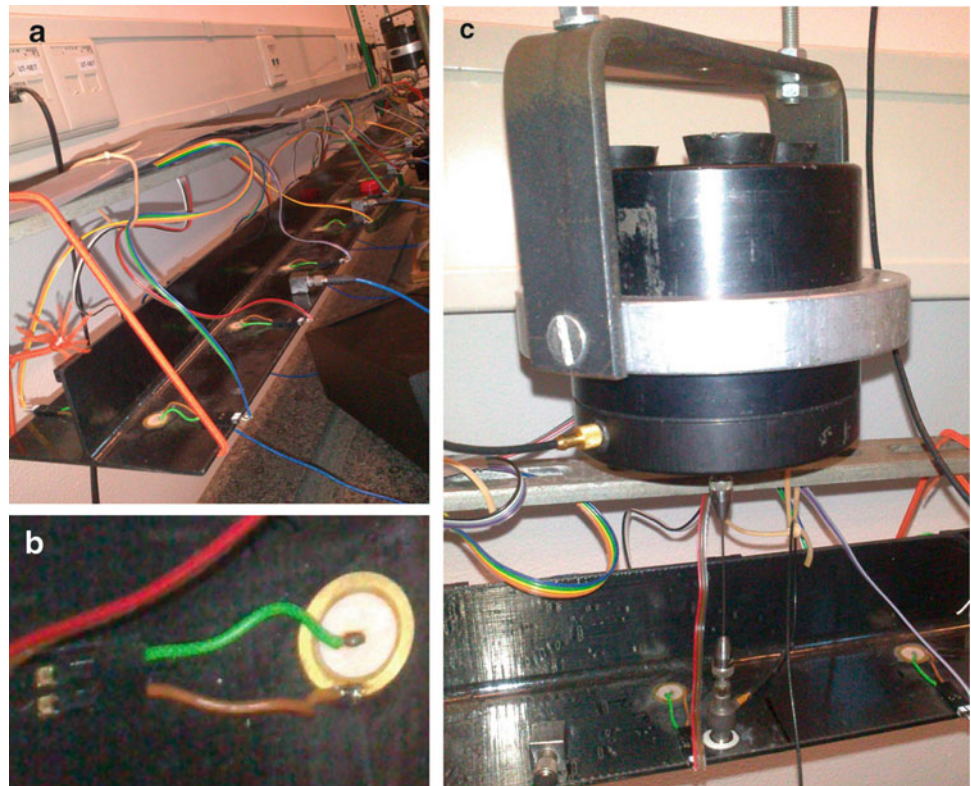


**Table 23.3** Composite T-beam: natural frequencies and vibration mode types

| Mode number | Frequency (Hz) | Mode type |
|---|---|---|
| 1 | 34.12 | Torsional |
| 2 | 59.91 | Torsional |
| 3 | 94.76 | Torsional |
| 4 | 144.26 | Torsional |
| 5 | 203.75 | Bending |
| 6 | 309.32 | Torsional |
| 7 | 386.54 | Torsional |
| 8 | 452.70 | Bending |

given frequency range, the system has high amount of torsional modes and very few bending modes. Such a characteristic makes it for a interesting test subject for strain modal analysis, as torsional modes (that lead to a lot of shear strain) are hard to measure with conventional strain gauges. In this case, circular-shaped piezo strain sensors were used instead of the regular resistance based strain gauges.

The test set-up for the experiment consisted of 24 piezo strain sensors placed along two lines on each side of the beam, and 10 accelerometers, used mainly to be able to verify the validity of the strain measurements. The beam was suspended by two elastic cords and was excited with a burst random signal with a small electrodynamic shaker and the acquisition unit was an LMS Scadas Mobile with 8 VB8 modules. Figure 23.4 shows the test set-up with some details—Fig. 23.4a shows the suspended t-beam with the sensors, Fig. 23.4b shows a close up of the round piezo sensors and Fig. 23.4c shows the electrodynamic shaker used to excite the structure.

The SFRF for the T-beam was acquired and a total 8 modes were clearly identified within the bandwidth of 20–500 Hz. Of these, 6 of them are torsional modes and 2 are bending modes. Table 23.3 shows the natural frequencies and mode types— the distinction between bending and torsional modes was made using the accelerometers and displacement mode shapes. Moreover, as it can be seen from the SFRF (Fig. 23.5a), the bending and torsional modes are also present in the strain measurements, meaning that the circular piezo sensors were effective in identifying the torsional modes as well as the bending modes. Figure 23.5b shows the first torsional mode (both the displacement mode shape and the strain mode shapes are shown), and Fig. 23.5c shows the first bending mode, with strain field and displacement as well.

First torsional mode at 34.12 Hz

First bending mode at 203.75 Hz
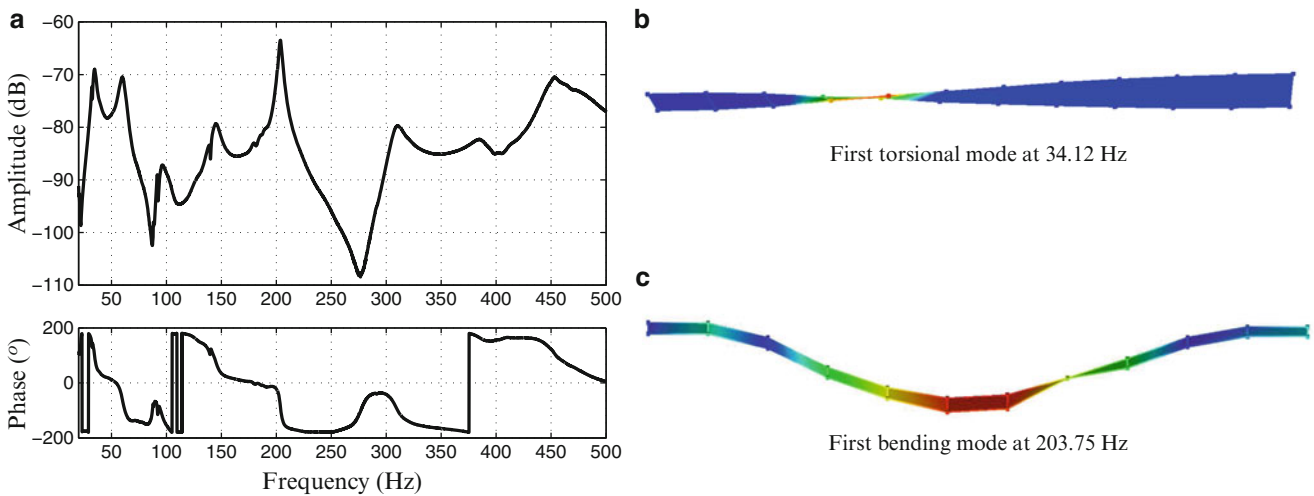
Composite T-beam - Strain FRF from an arbitrary measurement point

**Fig. 23.5** Composite T-beam: (**a**) SFRF from an arbitrary strain sensor; (**b**) First torsional mode (coloring indicates strain field); (**c**) First bending mode (coloring indicates strain field)



Helicopter main rotor blade used for tests

FBG sensor on helicopter blade

FBG sensor locations on blade
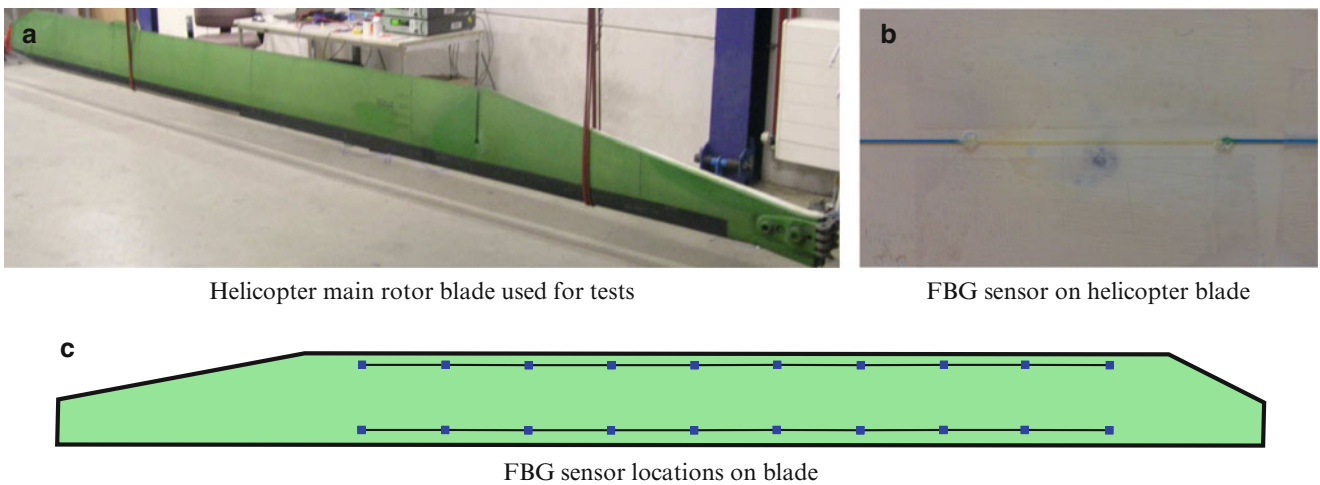
**Fig. 23.6** Helicopter main rotor blade: (**a**) Blade used for the tests; (**b**) Fiber Bragg Grating sensor; (**c**) Location of sensors on blade, corresponding to 2 fiber lines

### 23.3.3 Helicopter Main Rotor Blade

The main rotor blade of a PZL SW-3 helicopter was used for the last strain modal analysis verifications. For this experiment, the blade was suspended with elastic cords to obtain a free-free boundary condition, as shown in Fig. 23.6a and fiber bragg grating sensors were used to measure the dynamic strain on the surface of the blade. A close-up of one of these sensors can be seen on Fig. 23.6. In total, 20 FBG sensors were instrumented on the surface of the blade, following two straight fiber lines of 10 sensors each. Figure 23.6c shows the position of the sensors on the two fiber lines on the surface of the blade.

The blade was excited using an electrodynamic shaker, and the driving point was chosen close to the tip of the blade, near the trailing edge, with a sine sweep excitation. Two acquisition units were used—an LMS Scadas Mobile with VB8 modules and a FiberSensing BraggMETER. A frequency range from 8 to 80 Hz was chosen for the experiment—this range excludes the first vibration mode of the blade (at around 4 Hz), which was hard to excite with the shaker. From the experiment, 10 vibration modes were identified—5 bending modes, 3 in-plane modes and 2 torsional modes. The natural frequencies and the mode types for these modes are shown on Table 23.4. The displacement modes of the blade (and their types) were already known from previous experiments [14].

Figure 23.7a shows a typical SFRF obtained from the experiment. From the figure, it can be seen that most modes are clearly visible, except for the second torsional mode at 61.14 Hz. This behavior is understandable, since the sensors were

**Table 23.4** Natural frequencies
and mode types for the helicopter
main rotor blade

| Mode number | Natural frequency (Hz) | Mode type |
| --- | --- | --- |
| 1 | 10.27 | Bending |
| 2 | 13.9 | In-plane |
| 3 | 20.28 | Bending |
| 4 | 30.44 | Torsional |
| 5 | 33.78 | Bending |
| 6 | 37.61 | In-plane |
| 7 | 49.55 | Bending |
| 8 | 61.14 | Torsional |
| 9 | 67.17 | Bending |
| 10 | 75.82 | In-plane |

Helicopter main rotor blade-Strain FRF from
an arbitrary measurement point

Blade bending mode at 10.27 Hz

Blade in-plane mode at 13.9 Hz

Blade torsional mode at 30.44 Hz
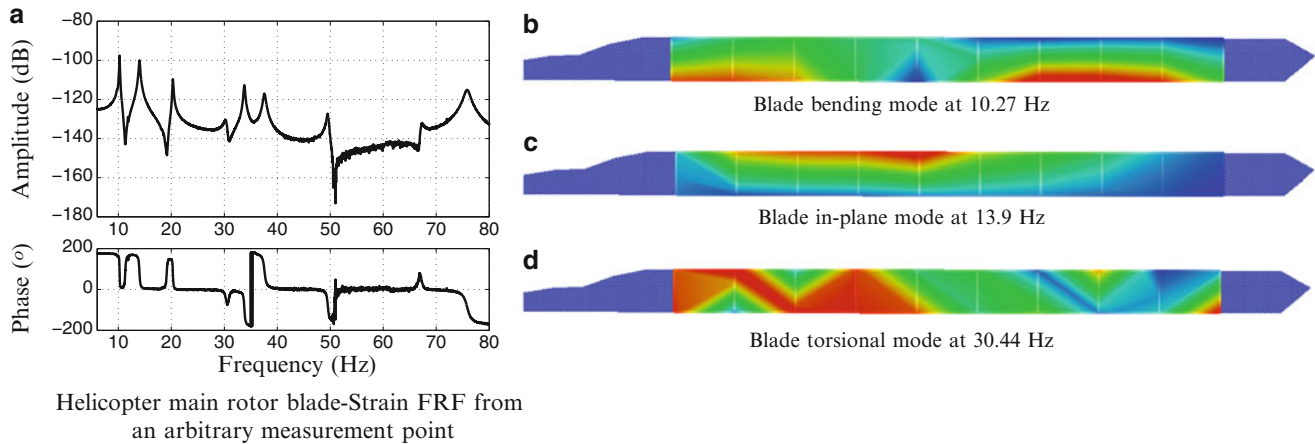
**Fig. 23.7** Helicopter blade—(**a**) SFRF and vibration modes; (**b**) bending mode; (**c**) in-plane mode; (**d**) torsional mode

instrumented to capture normal strain, while the torsional modes should induce shear strain. Nonetheless, both torsional modes are still identified by the identification procedure. The first identified strain modes are also shown on Fig. 23.7—the first bending mode is shown on Fig. 23.7b, the first in-plane mode is shown on Fig. 23.7c and the first torsional mode is shown on Fig. 23.7d.

Moreover, additional tests were carried out with the blade. The main objective of the second experiment was to assess if strain gauges could also be used as the reference sensor for a roving hammer impact testing. For this purpose, an accelerometer measuring the bending direction and a strain gauge aligned with the span of the blade, were collocated on a chosen reference point. Then, the impact testing was carried out in 55 different points and the identified modes using the accelerometer as reference were compared with the modes using the strain gauge as reference.

The natural frequencies obtained with the impact test using an accelerometer as reference were almost identical as the ones obtained from the impact test using the strain gauge as reference, and the MAC between the two sets of modes also yielded very good results. Figure 23.8 shows the natural frequencies and the MAC color values for the comparison between the two systems. As it can be seen, the MAC values are very well matched, except for the second torsional mode, which is not identified when using the strain gauge reference, and also the last mode, which is an in-plane mode, while the impacts normal to the surface of the blade, so this type of mode is very hard to correlate in these circumstances.

## 23.4 Results Analysis and Conclusion

In this paper, the concepts of strain modal analysis were introduced and verified experimentally. For this purpose, three experimental cases were shown—a small composite wind turbine blade, a composite T-beam and a composite helicopter main rotor blade.

The first experiment was carried out using impact testing and multiple resistive strain gauges. Some basic characteristics and utilities of the strain modal analysis were shown in this experiment. The first concept is the lack of reciprocity, as described in the theory section of this work. Moreover, it was shown how the strain mode shapes obtained from test can be

**Fig. 23.8** Modal assurance criterion—comparison between impact testing using an accelerometer (natural frequencies shown on the side) and a strain gauge (natural frequencies shown on top) as reference
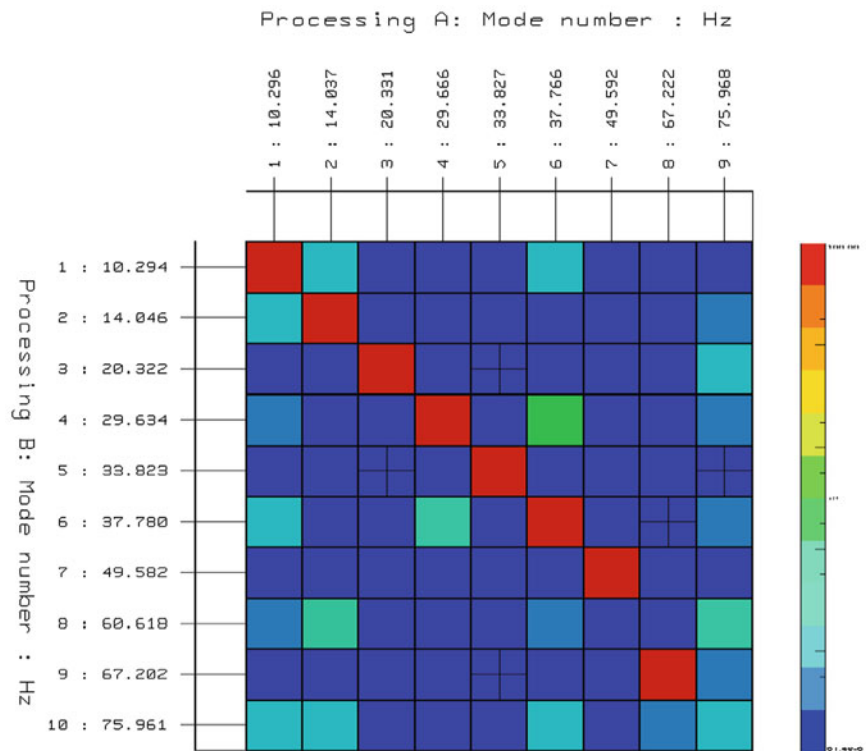
correlated with a finite element model, and how torsional modes, that induce shear strain, are harder to be correlated when most of the sensors are measuring normal strain.

Secondly, the composite T-beam was tested with an electrodynamic shaker. In this case, round piezo sensors and accelerometers were used, with the purpose of being able to capture both normal and shear strain, and verify the mode types by checking the displacement mode shapes. Overall, the sensors were successful in measuring both normal and shear strain, as seen on the SFRF and the mode shapes.

Finally, some other concepts were verified with the helicopter main rotor blade. Initially, Fiber Bragg Grating sensors were used to carry out a strain modal analysis of the blade using shaker excitation. The sensors were able to capture all mode types (bending, in-plane and torsional) but the strain mode shapes were only useful in the visualization of the bending and in-plane modes. Moreover, a second type of test was carried out—this time, impact testing was done to compare mode shapes obtained with the test using an accelerometer or a strain gauge as reference. Like suggested by the theory, both practices yielded displacement mode shapes and the strain gauge was effective in obtaining almost all of the mode shapes, with the exception of a higher frequency torsional mode.

Future studies include the investigation of sensor placement for better strain field interpretation, hotspot (high stress and strain) locations, the time and modal relations between strain and displacement and methods of scaling the strain modes.

# References

1. Bernasconi O, Ewins DJ (1989) Application of strain modal testing to real structures. In: Proceedings of the 7th international modal analysis conference, vol 2, pp 1453–1464
2. Vári LM, Heyns PS (1994) Using strain modal testing. In: Proceedings of the 12th international conference on modal analysis, vol 2251, pp 1264
3. Li S, Wu Z (2005) Structural identification using static macro-strain measurements from long-gage fiber optic sensors. J Appl Mech 8:943–948
4. Reich GW, Park KC (2001) A theory for strain-based structural system identification. J Appl Mech 68(4):521–527

5. Wentzel H (2013) Fatigue test load identification using weighted modal filtering based on stress. Mech Syst Signal Process 40:618–627
6. Vandepitte D, Sas P (1990) Case study of fracture of a mechanical component due to resonance fatigue. Mech Syst Signal Process 4(2):131–143
7. Kang L-H, Kim D-K, Han J-H (2007) Estimation of dynamic structural displacements using fiber bragg grating strain sensors. J Sound Vib 305(3):534–542
8. Ling H-Y, Lau K-T, Cheng L (2004) Determination of dynamic strain profile and delamination detection of composite structures using embedded multiplexed fibre-optic sensors. Compos Struct 66(1):317–326
9. Pisoni AC, Santolini C, Hauf DE, Dubowsky S (1995) Displacements in a vibrating body by strain gage measurements. In: Proceedings of the 13th international conference on modal analysis
10. Tourjansky N, Szechenyi E (1992) The measurement of blade deflections-a new implementation of the strain pattern analysis. ONERA TP 1
11. Peeters B, Van der Auweraer H, Guillaume P, Leuridan J (2004) The polymax frequency-domain method: a new standard for modal parameter estimation? Shock Vib 11:395–409
12. Menchicchi M (2013) Theoretical and experimental study of strain modal analysis. Master's thesis, Department of Civil and Industrial Engineering, Universita di Pisa
13. Loendersloot R, Ooijevaar TH, Warnet L, Boer A, Akkerman R (2011) Vibration based structural health monitoring and the modal strain energy damage index algorithm applied to a composite t-beam. Vib Struct Acoust Anal 121–150
14. Marques dos Santos FL, Peeters B, Van der Auweraer H, Carlos Sandoval Góes L (2013) Modal-based damage detection of a composite helicopter main rotor blade. In: 54th AIAA/ASME/ASCE/AHS/ASC structures, structural dynamics, and materials conference

# Chapter 24
# AIRBUS A350 XWB GVT: State-of-the-Art Techniques to Perform a Faster and Better GVT Campaign

**P. Lubrina, S. Giclais, C. Stephan, M. Boeswald, Y. Govers, and N. Botargues**

**Abstract** In April and May 2013, the ONERA-DLR specialized team has performed the GVT (Ground Vibration Testing) campaigns of the new composite design AIRBUS A350 XWB. The first GVT was performed on the first aircraft prototype with duration of nine measurement days. Another GVT was performed within two measurement days on the third prototype with focus on the nose landing gear dynamics.

The very short time devoted to those test campaigns, imposed by a strict and busy planning from AIRBUS A350 XWB FAL (Final Assembly Line), required to adapt test techniques and methods and an optimized workflow to meet the challenging test requirements.

A strong synergy between AIRBUS, ONERA and DLR teams allowed performing the shortest GVT campaign on a long range aircraft never before realized. The test program involved mixing PSM (Phase Separation Methods) and PRM (Phase Resonance Methods), addressing nonlinear behaviours. Due to novel database systems, the most complete modal model database ever delivered was obtained.

This paper is devoted to describe the processes followed and the methods used in this particularly hard context and how those contributed to the successful achievement of this demanding test campaign.

**Keywords** Ground vibration testing • Structural nonlinearities • Modal identification • Phase separation method • Phase resonance method

## 24.1 Introduction

In April and May 2013, the ONERA-DLR specialized team has performed the GVT (Ground Vibration Testing) campaigns of the new composite design AIRBUS A350 XWB. The first GVT was performed on the first aircraft prototype with duration of nine measurement days. Another GVT was performed within two measurement days on the third prototype with focus on the nose landing gear dynamics.

The very short time devoted to those test campaigns, imposed by a strict and busy planning from AIRBUS A350 XWB FAL (Final Assembly Line), required to adapt test techniques and methods (ref. [1–3] notably) and an optimized workflow to meet the challenging test requirements. If the PSM (Phase Separation Method) was the main method used, some modes were measured thanks to the PRM (Phase Resonance Method) (Fig. 24.1).

P. Lubrina (✉) • S. Giclais
Office National d'Etudes et de Recherches Aérospatiales (ONERA) DADS-ADSE, Châtillon, France
e-mail: pascal.lubrina@onera.fr

C. Stephan • M. Boeswald • Y. Govers
DLR Institute of Aeroelasticity, Goettingen, Germany

N. Botargues
Department of EGLAV, AIRBUS, Toulouse, France

**Fig. 24.1** Artist view of the
A350-XWB-900



**Table 24.1** A350-XWB-900 characteristics

| Dimensions | | Capacity | | Performance | |
| --- | --- | --- | --- | --- | --- |
| Overall length | 66.89 m | Pax typical seating | 314(3 classes) | Range | 15 000 km8 000 nm |
| Fuselage width | 5.96 m | Freight: | | Mmo | Mach 0.89 |
| Max cabin width | 5.61 m | LD3 capacity underfloor | 36 | Max take off weight | 268.0 t |
| Wing span (geometric) | 64.91 m | Max pallet number underfloor | 11 | Max landing weight | 205.0 t |
| Height | 17.05 m | Bulk hold volume | 11.3 m$^3$ | Max zero fuel weight | 192.0 t |
| Track | 10.60 m | Total volume | 172.3 m$^3$(LD3 + bulk) | Max fuel capacity | 138 000 l |

**Fig. 24.2** A350 XWB Material
breakdown
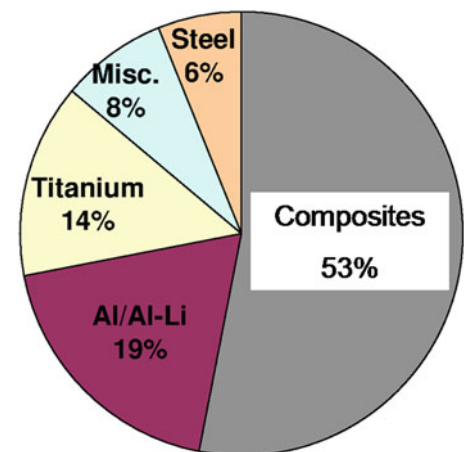


## 24.2   Airbus A350-XWB-900 Description

The A350 XWB is an all new family of mid-sized wide-body twin-engine airliners to shape the efficiency of medium-to-long haul airline operations, overcoming the challenges of volatile fuel prices, matching rising passenger expectations and addressing increasing environmental concerns.

The A350 XWB Family consists of three passenger versions with true long-range capability of flying up to 8,500 nm/15,580 km. The current paper deals the first Ground Vibration Test of the family done on the intermediate version (-900: 314 seats in a typical three-class configuration).

The A350-XWB-900 is powered with two Engines RR Trent XWB (374 kN each one, 84,000 lbs each one) (Fig. 24.2).

The A350 XWB brings together the very latest in aerodynamics, design and advanced technologies. Over 70 % of the A350 XWB weight efficient airframe is made from advanced materials combining composites (53 %), titanium and advanced aluminium alloys. The aircraft innovative all new Carbon Fibre Reinforced Plastic (CFRP) fuselage results in lower fuel burn as well as easier maintenance.

From structural dynamics point of view, the vast number of innovations raised a big challenge by moving away from known structures.

The A350 XWB final assembly has been thought out with efficiency in mind, in order to reduce the assembly time compared to current programmes and to enable a more effective test programme. Elements of the aircraft arrive at the A350 XWB assembly facility—located in Toulouse, France—already equipped and tested. Like a well-planned, high-technology puzzle, the jetliner then comes together through an optimised workflow that moves in steps through several stations within the integration building.

As a full part of this streamlined process, GVT coming just before painting, it had to guarantee an optimised workflow fully integrated to the assembly line.

## 24.3   GVT General Specifications

GVTs have been performed on first A350 XWB prototypes. Tests were on the critical path of the programme. Impact on planning has been reduced to the very minimum thanks to an optimised workflow and to enhanced integration with Final Assembly Line (FAL). At the end:

- First aircraft MSN was exclusively dedicated to main vibration testing during 9 days from 7 am to12 pm 7/7.
- Nose Landing Gear testing has been performed over a week-end.
- FAL working parties were resumed during remaining night shifts.

During this reduced and fixed timeframe, the GVTs had to address two fuel mass configurations, several hydraulic configurations for control surfaces and several Nose Landing Gear configurations (steering system, shock absorber lengths).

For each configuration, key dynamic structural properties had to be identified:

- eigen-frequencies,
- mode shapes,
- generalized mass and damping,
- transfer function,
- structural non-linear behaviour.

Measurement and excitation strategies had both:

- to be optimised to fit with the strong time constraint,
- to be adjusted live taking into account encountered structural specificities:

    – to remain in acceptable levels versus structural/hardware limitations,
    – to provide the best measurement quality.

Modal data were directly post-processed and were analysed on site to allow live trouble shooting and early model calibration.

## 24.4   GVT Equipments

For conducting such a GVT, it is mandatory to have enough equipment for vibration excitation and for measurement of vibration response. Due to the size and weight of an aircraft, the frequency range considered is typically low. Except for special purpose measurements, the upper frequency limit of excitation has been in this case not higher than 50 Hz. The lower limit of the frequency range depends on the suspension characteristics. Except for dedicated measurements for the identification of eigenfrequencies of rigid body motion, the lower frequency limit of the measurements was around 1 Hz. Consequently, the shakers used have a long coil stroke to excite at such low eigenfrequencies with sufficient excitation force (Fig. 24.3).

For FRF measurements, swept-sine excitation with multiple shakers has been used. The excitation forces are typically selected for symmetric or anti-symmetric excitation (Fig. 24.4).

For this purpose, the power amplifiers driving the shakers should have "Zero-Phase" characteristic, i.e. no phase shift between drive signal input to the amplifier and the excitation force output generated by the shaker. Without zero-phase characteristic, it would be difficult to realize symmetric or anti-symmetric excitation, especially in excitation configurations where shakers/amplifiers of different type are mixed.

Tripods are required to locate shakers at specific positions on the aircraft. These tripods must be stable enough to carry the shakers and to compensate the excitation force. In addition, they must be capable of fine tuning the relative position of shakers with respect to the aircraft. On the other hand, the tripods must include an elastic degree of freedom propitious to avoid the parasite motion of the shaker due to the possible flexibilities of the tripods, platforms and scaffoldings on which they are installed.

For risk mitigation purposes, the excitation forces are measured twice with different measurement principles. Primarily, the excitation forces are measured using piezo-electric force sensors installed at the excitation points of the structure. In addition, the excitation forces are measured using the coil current provided by the shaker power amplifiers. Displacement sensors are used to measure the relative displacement of the shaker armature in the shaker housing, e.g. for optimization of

**Fig. 24.3** View of the aileron exciter (1st GVT)



**Fig. 24.4** View of the nose landing gear exciters (second GVT)



excitation force signals in the very low frequency range, where the limitation is not the peak force of the shaker, but the driving point displacement response.

The vibration response is mainly measured in terms of acceleration response using acceleration sensors qualified for the very low frequency range. More than 500 acceleration sensors have been installed for the GVT on A350 and have been measured simultaneously.

The whole data acquisition system was based on ONERA's and DLR's combined LMS Scadas III frontends controlled by the Test.Lab software. Distributed data acquisition has been realized by placing 8 LMS Scadas III frontends around the aircraft. These frontends were connected by fibre-optical cables to allow for data flow in a ring-shaped data bus. The V12-L acquisition modules inside the LMS Scadas III frontends have been used due to their very low cut-off frequency of 0.05 Hz of the analogue high-pass filters. As these modules provide 24-bits accuracy of data acquisition, the time consuming process of acquisition channels range setting is useless.

**Fig. 24.5** Inside the GVT command room container

## 24.5 GVT Teams

The aircraft access was organized in three shifts. While two shifts were dedicated to vibration testing, the third shift was for the aircraft manufacturer. Therefore the ONERA-DLR GVT team was split into two teams, one for each shift.

A single team consists of several positions.

1. team manager,
2. technicians for shaker handling,
3. electronics specialists,
4. engineers for data acquisition and data checks,
5. engineers for modal identification,
6. engineers for model correlation.

This kind of team setup guarantees a highly efficient GVT performance which is especially relevant since the time slot offered by aircraft manufacturers to conduct such a GVT (Fig. 24.5).

In addition to the excitation equipment necessary to perform the PRM in a good way (number of exciters to be controlled simultaneously) compared to the PSM, it may be noticed another difference between these methods. While the PRM does not require extensive post-treatment and then human resources, the PSM involves a lot of investigations by several specialists in modal analysis to assemble a final modal model in "real time" (see Sect. 7.3).

## 24.6 GVT Methods Applied

Two complementary kinds of excitation methods were applied during the tests:

- Phase Separation Method (PSM).
- Phase Resonance Method (PRM).

The PSM was used most of the time since it has the best compromise between time-consuming and modes providing (ref. [4]). It is basically a curve-fitting of Frequency Response Functions (FRFs) with a linear modal model. FRFs are obtained from applying random or swept-sine excitations, with two shakers in general. Preliminary swept sine excitations at low force or random excitations give a first series of FRFs. Then the Force Notching process, introduced for the Airbus A380-800 GVT in 2005, is applied by knowing these FRFs. Frequency dependent excitation forces are automatically designed by maximizing the force levels over the frequency band, without exceeding maximum levels of acceleration required by Airbus.

For very few excitation force patterns, during the second GVT dedicated to the modal identification of the nose landing gear modes, the multisine simultaneous sweep technique introduced successfully by ONERA and DLR on previous GVT (ref. [5]) has been applied.

PRM, the standard method used by ONERA and DLR for aircraft GVTs before 2000, is sometimes considered as an outdated method. Nevertheless PRM is up to now the most accurate and robust method for modal analysis, especially when nonlinear structural behaviours are encountered. Contrary to PSM, PRM aims to make a structure vibrate as a purely real mode by finding the best excitation force pattern; then it gives a snapshot of a mode and does not need any complex mathematical algorithms for post-processing. Accompanied methods such as Force in quadrature and/or Complex Power are applied to evaluate both structural damping coefficients and generalized mass values.
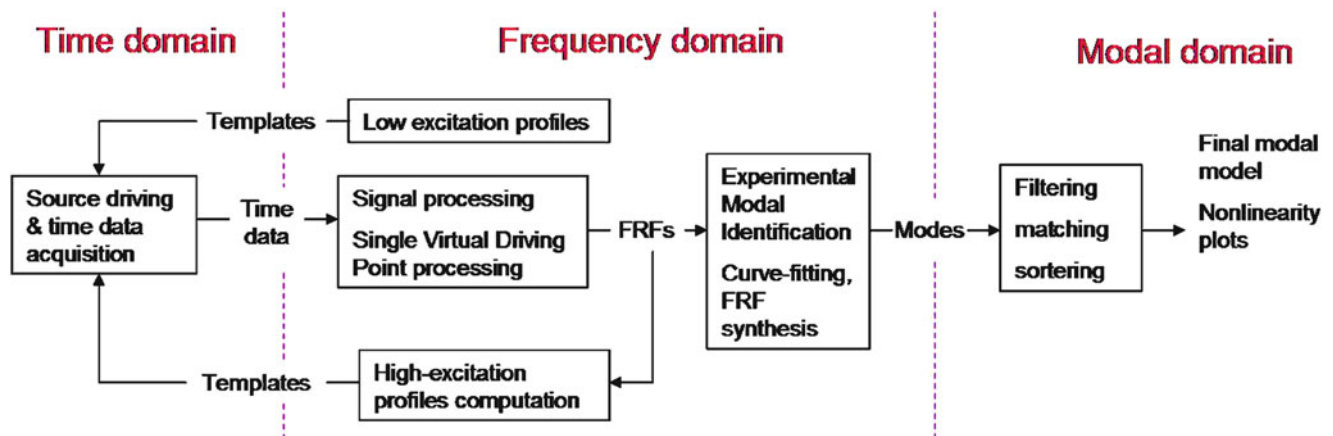
**Fig. 24.6** Data workflow for PSM

A second asset of PRM is its applicability on highly nonlinear structure. In the case of landing gear dynamics, PSM could not provide any useful results, as FRFs based curve-fitting rely on linear behaviour and cannot take into account strong nonlinear phenomena like multi-harmonic responses or jumps. Even if a kind of linearization could be obtained by applying random excitation, this solution has not been selected during this test as it does not allow significant level of response. Only PRM can be applied because it guarantees that, even if responses show a nonlinear structural behaviour (such as multi-harmonic), identified modes are the best linearizations for a constant level of excitation. Applying PRM for different levels of forces makes an access to the dependencies of eigenfrequency, structural damping and generalized mass with those forces and the amplitudes of structural responses.

Even if PRM could be very time-consuming, it was mandatory to keep the ability to apply it during a test since its precision is worth the effort. During the primary test on full aircraft, three modes were identified by PRM since they involve engines-wings joints which are particularly important for aircraft design. Furthermore, all the nose landing gear modes delivered during the second GVT were obtained by this modal tuning method.

### 24.6.1 Data Work Flow

As a rule; the data workflow is organized according to the nature of data used as inputs. For the PRM, the workflow is simple since only two works stations are involved : the first one for the excitation control and measurement, the second one for the post-treatment when necessary (Fig. 24.6).

For the PSM (see following figure), three successive kinds of data are handled: time data such as accelerometers and force cells signals, frequency data (FRFs, auto and cross spectral powers) and finally modes.

After signals have been acquired, Frequency Response Functions (FRFs) are computed thanks to the Single Virtual Driving Point algorithm. Then a linear modal is obtained by curve-fitting FRFs for each run. All modes coming from these different runs are finally stored into a database and used for forming the final modal model.

In order to be sure that the maximum level of force is applied to the structure, a feedback step in frequency domain aims to compute the best excitation profiles according to FRFs at low excitation.

### 24.6.2 Modal Identification

Since PSM became the dominant method in GVT, modal identification appeared to be the bottleneck of post-processing. Here modal identification only refers to the curve-fitting process of FRFs by a linear modal model. Even with using mature commercial tools, it is still a challenge to find a satisfying model on experimental data. In fact, there are two effects that explain this situation.

Contrary to PRM, PSM method enables analysts to identify several modes for the same run. As curve-fitting algorithms have become more robust, it is now possible to find "high-frequency" modes, i.e. modes above main structural modes. Hence

**Fig. 24.7** Maximizing level of force excitation over frequency range
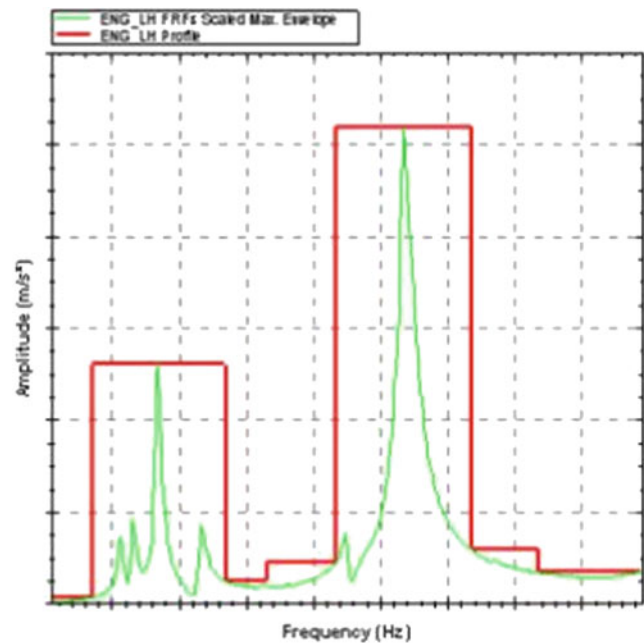


a balance is achieved between the time saved during curve-fitting, and the time devoted to these modes which were not analysed in previous GVTs.

As a consequence, there was the counterintuitive need to increase human resources significantly for curve-fitting process, as more and more modes were identified during GVT.

## 24.7  ONERA DLR Specific Tools

### 24.7.1  *Force Notching*

The force notching is used for maximizing the level of force excitation provided over frequency band (ref. [5]). It relies on previous knowledge of structure dynamics, such as FRFs obtained at a low level of force excitation. By using the relation between input and outputs given by FRFs, it is possible to compute a maximum level of force for each frequency. In practice, the frequency band is automatically split into several sub-bands (see Fig. 24.7), according to amplitude evolution of FRFs. With this force pattern computation, an excitation template is generated for the sweep-sine which maximizes the force level, with respect to limitations (maximum acceleration levels, maximum exciter strokes, maximum voltage of amplifiers). The resulting excitation signal is a swept-sine whose amplitude is modulated over time (see Fig. 24.8).

The new version of the LMS Test.Lab software makes easy the use of computed excitation stimuli files.

### 24.7.2  *SVDP: Single Virtual Driving Point*

In general, for an aircraft, swept-sine excitationsare either symmetric or antisymmetric forces applied with two shakers. As forces are in this case by definition correlated, it is not possible to use the H1 estimator on data directly

$$H_1 (\omega) = P_{XX} (\omega) \, P_{XF}^{-1} (\omega)$$

where $P_{XX}(\omega)$ and $P_{XF}(\omega)$ are respectively the output and input–output densities of spectral powers.

One solution consists to build augmented matrices from the combination of all runs, for instance two runs in the case of symmetric and anti-symmetric excitations. Although it is mathematically correct, here the Single Virtual Driving Point (SVDP) process is preferred since it allows the use of existing Single Input Multiple Outputs (SIMO) processing on each

**Fig. 24.8** Example of
amplitude-modulated excitation
signal
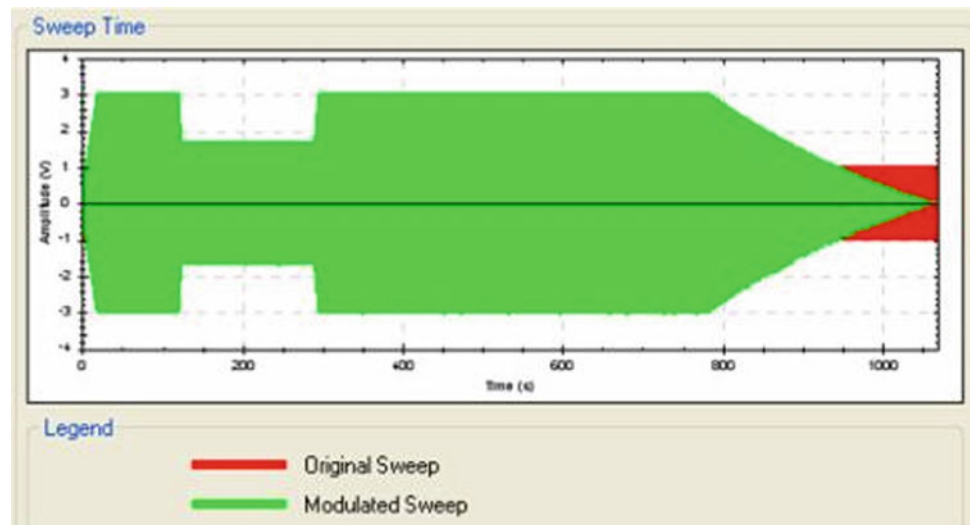


run (ref. [5–7]). The SVDP defines a mathematical construction of a virtual driving point, which would have given rise to vibratory responses strictly similar to those obtained with correlated forces. SVDP relies on the equivalent complex power

$$P\left(\omega\right) = \sum_{sha\,\ker s} F_s\left(\omega\right) \dot{X}_s\left(\omega\right)$$
$$P\left(\omega\right) = F_V\left(\omega\right) \dot{X}_V\left(\omega\right)$$

where $F_s(\omega)$ is a excitation force acting on a driving point $s$, $\dot{X}_s\left(\omega\right)$ the velocity at driving point $s$, $F_v(\omega)$ the virtual force and $\dot{X}_v\left(\omega\right)$ the velocity response of the virtual driving point. Once the SVDP process has been applied, SIMO FRFs are obtained and classical curve-fitting can be directly used on them (Figs. 24.9 and 24.10).

### 24.7.3 Modal Model Assembly

Considering a linear structural behaviour, it would be sufficient to use only very few excitation points to excite all modes of an aircraft. However the practical application shows that several excitation configurations are needed during GVT: vertical and lateral engine excitations, vertical and axial wing excitations, HTP excitation, VTP excitation . . . The general goal is to put as much energy as possible per mode, i.e. to increase the level of generalized force until maximum per mode. These numerous tests are mandatory for optimising the reliability of experimental modal model and taking into account nonlinear structural behaviour. In practice, for each excitation configuration, several runs are performed at different levels of excitations. From all these runs, each structural mode can be identified a significant number of times. During the modes sorting and filtering process, the whole set of modes identified by curve-fitting is carefully analysed by structural engineers and sorted by nature.

All identified modes are stored into a database system with multi user access. Each mode is stored not only with its modal properties but also with numerous fields containing meta information. A specially designed software tool called "Correlation Tool" was developed to review the modes in the database. The Correlation Tool can be installed on different computers, even on the customer computer to give online access (read only) to the current modal data.

One feature of this database software is that modes which have been identified from different FRF datasets with almost identical properties can be grouped in a mode family based on MAC correlation. For each family, the most representative mode is selected as a member of the final modal model delivered to Airbus. To support the process of correlation of modal datasets and finally the generation of the final modal model different quality indicators and other criteria are applied, for example, level of excitation, generalized force and value of Mode Indicator Function (MIF) are used here. The concept of mode families can also be applied to evaluate scatter on test results or even to analyse the results in terms of non-linear behaviour. If the members of a mode family are considered to be reliable enough (i.e. confidence in the results assessed by quality indicators), they can become affiliated to a "master mode" and their damping ratios and eigenfrequencies can be plotted as a function of force level or other parameter of the database. In this GVT, the work of modal correlation was a specific challenge. Finally, the huge amount of data was condensed down from about 2,600 poles identified from all FRF

**Fig. 24.9** Example of FRFs for all accelerometers (imaginary and real parts)
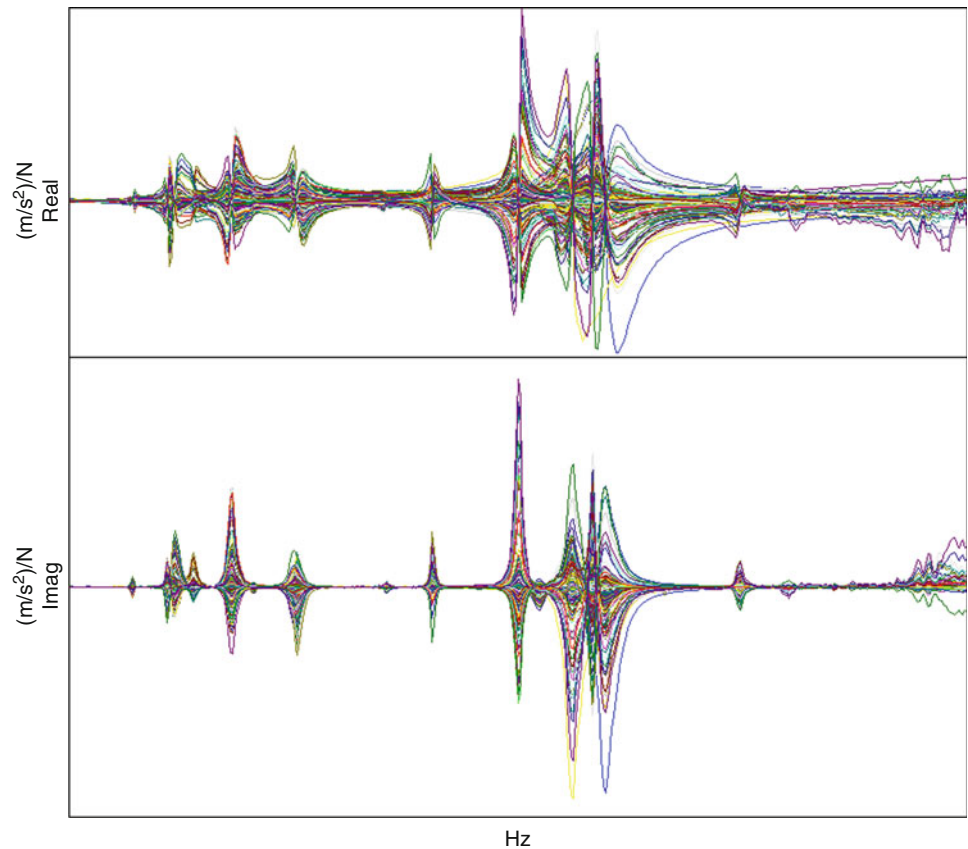


datasets to only 180 master modes in the final modal model for the main configuration. For sure, this correlation work had to be performed in a short period of time leading to specific requirements of the graphical user interface ergonomics (Figs. 24.11, 24.12, 24.13, 24.14, and 24.15).

### 24.7.4   PRM Environment

Even if this method is test time consuming and needs many exciters to be installed and controlled simultaneously, the faculty of this traditional modal tuning method to deliver reliable "local" modal parameters in case of significant non linear structural behaviour (here "local" means for a certain excitation force level introduced in the structure) has motivated its use for only three engines modes during the first GVT but for all the nose landing gear modes identified during the second GVT.

In addition to the know—how transferred by ONERA and DLR to LMS for a better performance of the Test.Lab NMT (Normal Mode Testing) workbook, other developments, such as multi-Lissajous ellipses preparation, complex power and force in quadrature corrections, were carried out to make the pre-test and post-test works easier in using the PRM technique.

## 24.8   Results

For the main configuration tested (empty fuel) performed in seven working days, we consider as modal identification inputs the 143 excitations runs performed from 23 excitation force patterns. These ones are mainly symmetrical and anti-symmetrical forces. The frequency band [1:50 Hz] was divided in two sub-bands, and for each sub-band at least two force levels were applied. Furthermore, very low frequency excitations were dedicated to rigid body modes and higher frequency bands up to 80 Hz were applied on engines for sustained engine imbalance purpose.

For the main mass configuration, those modal identifications provided approximately 2,600 poles. From this set of poles, 975 modes were reliable enough to be kept and to contribute to linearity plots. Finally 180 of them, including rigid body

**Fig. 24.10** Example of FRFs :
the real driving points (blue and
green curves) and the SVDP (red
curve)
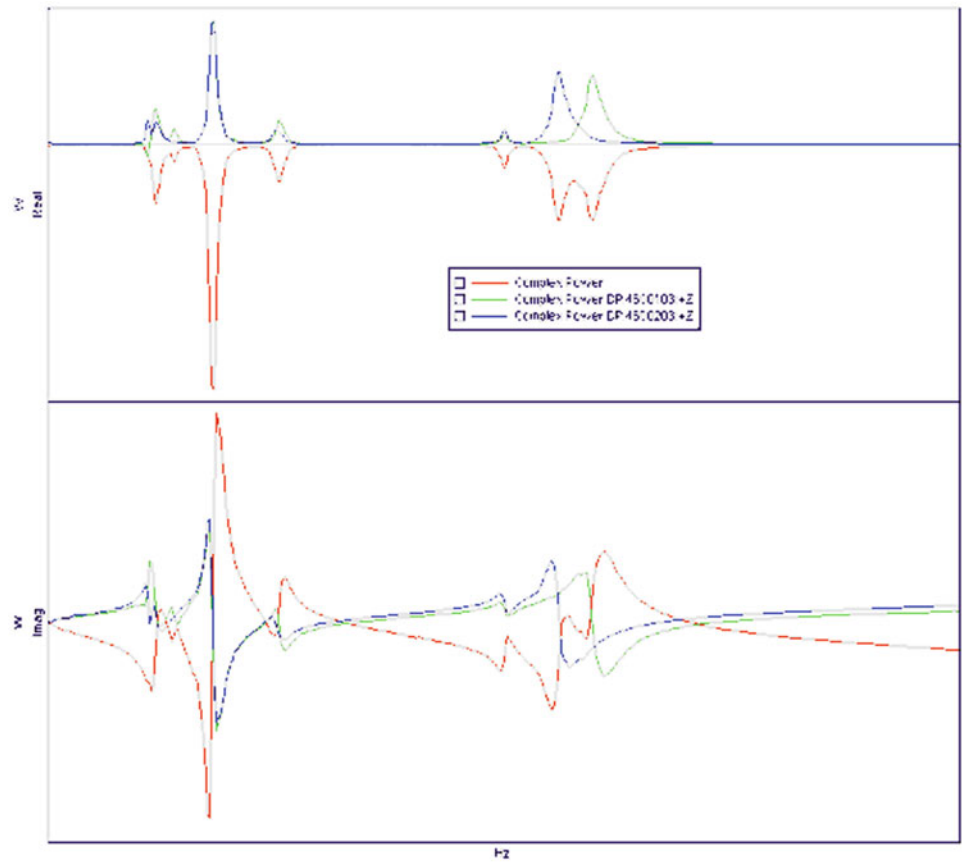


**Fig. 24.11** Auto-MAC matrix
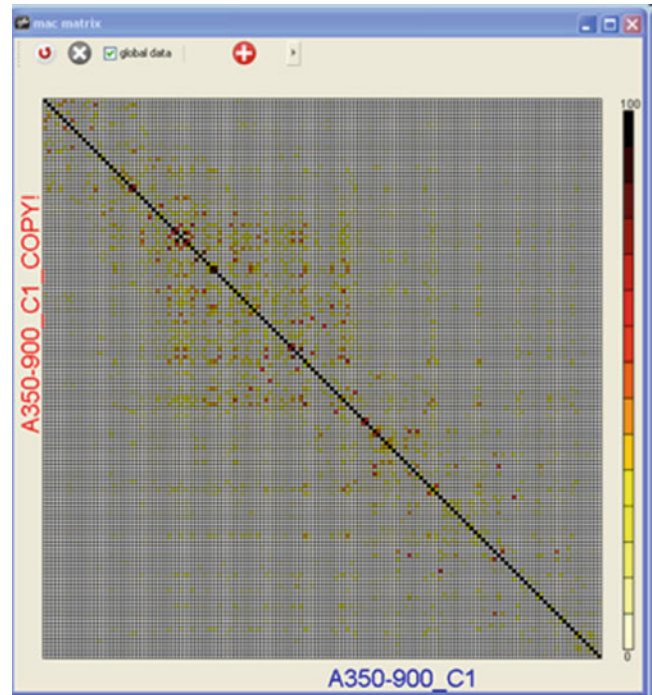


modes, were considered as master modes and constitute the modal model propitious to be used for the FEM updating and
flutter computation. It may be noticed that excitation runs performed from engines Y and Z and wings X and Z provided the
majority of modes.

**Fig. 24.12** MIF and SVDP FRFs of the run analysed

**Fig. 24.13** Polar diagram of one selected mode shape



For the second mass configuration, wing tanks were partially filled. Although only one working day was dedicated to it, there were enough runs to identify 50 master modes in the modal model of this mass configuration (Figs. 24.16, 24.17, 24.18, 24.19, 24.20, and 24.21).

## 24.9 Conclusions

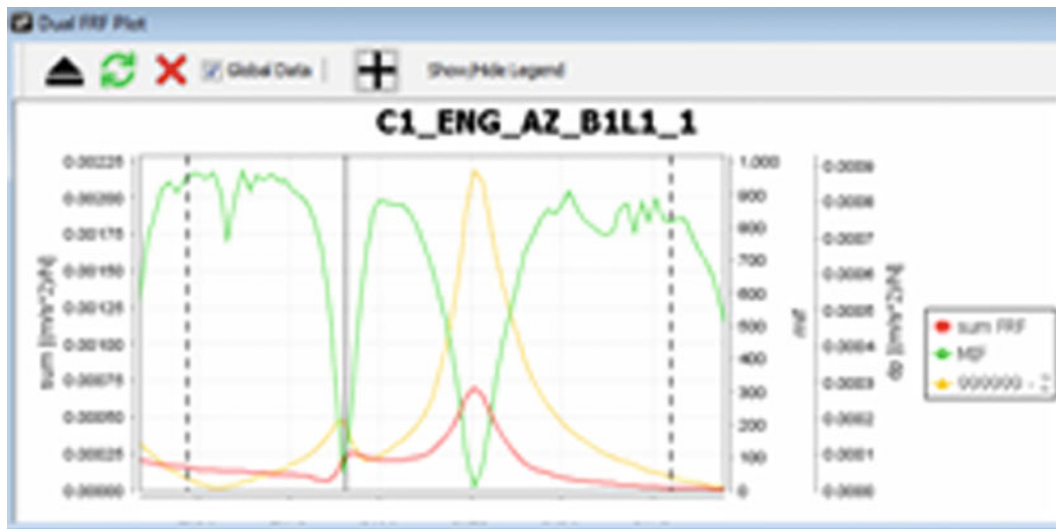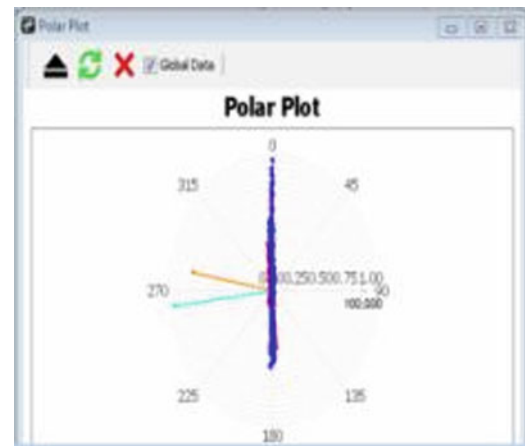Ground Vibration Test is a major milestone on the critical path of aircraft development process. It is performed for several goals. First of all, it delivers the modal model which can be used for flutter predictions and model updating. The results of computation are then a support for first flight safety and allow a fast flight domain opening. And finally, they serve as means of compliance in front of Airworthiness Authorities.

The success of such a test relies on several complementary aspects. High-end test hardware and best in class customized software were developed, implemented and used for productivity and quality. Innovative methods and optimized data-flow inspired from production line enables a time reduction without decreasing the amount of data. And, of course, the human factor is also a strong feature during a test. A highly skilled, integrated and flexible team was particularly involved during this test, and their work is directly linked to the quality of delivered results. Thanks to all these elements, the A350 XWB GVT has been fulfilled in a record time, with respect to very challenging specifications and with all expected results delivered in required quality.
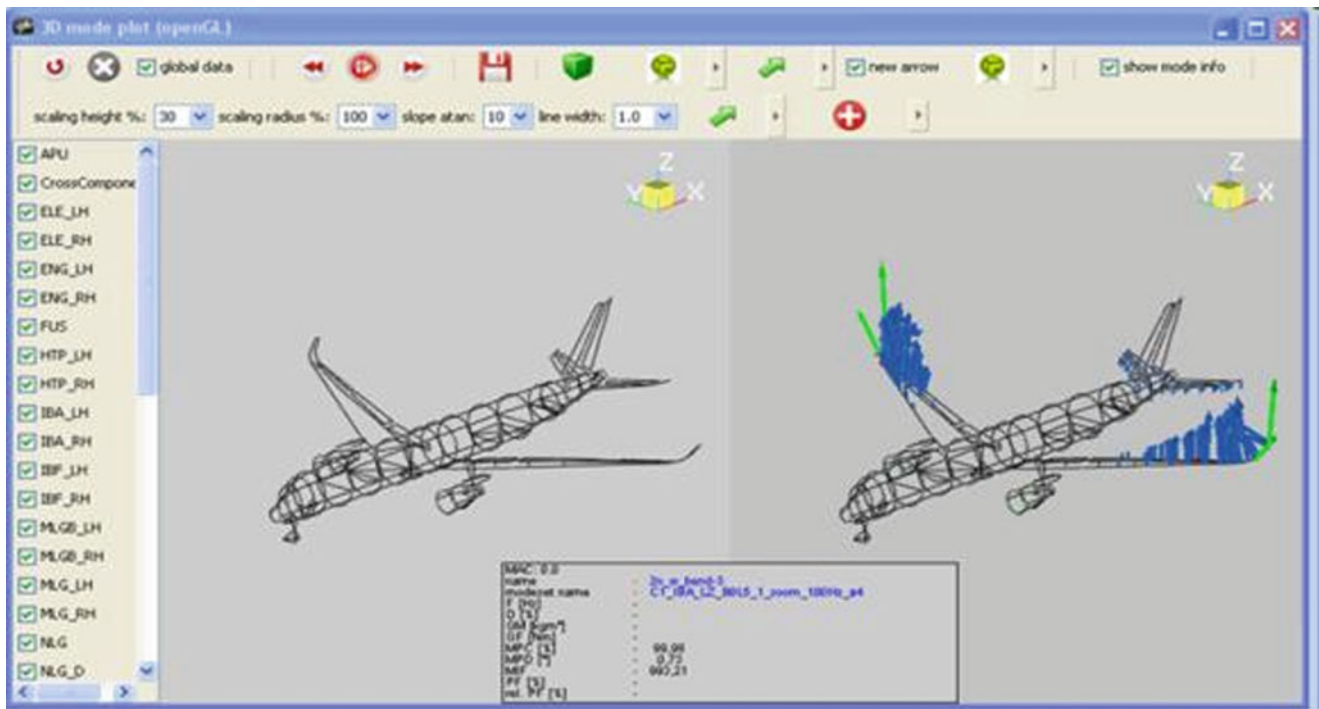
**Fig. 24.14** Dual mode shapes plot



**Fig. 24.15** Linearity plot (resonance frequency and structural damping ratio/Generalized excitation Force)

**Fig. 24.16** Diagram of the modes numbers from the different methods for the last major Airbus GVTs
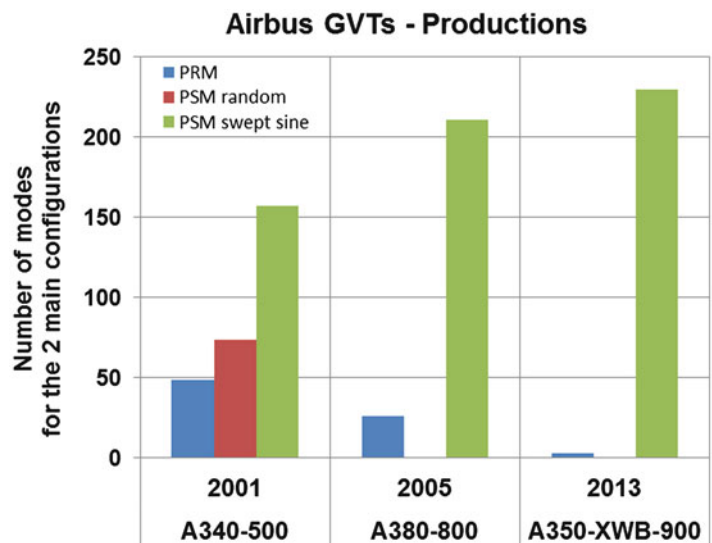
**Fig. 24.17** Diagram of the GVT duration and productivities for the last major Airbus GVTs
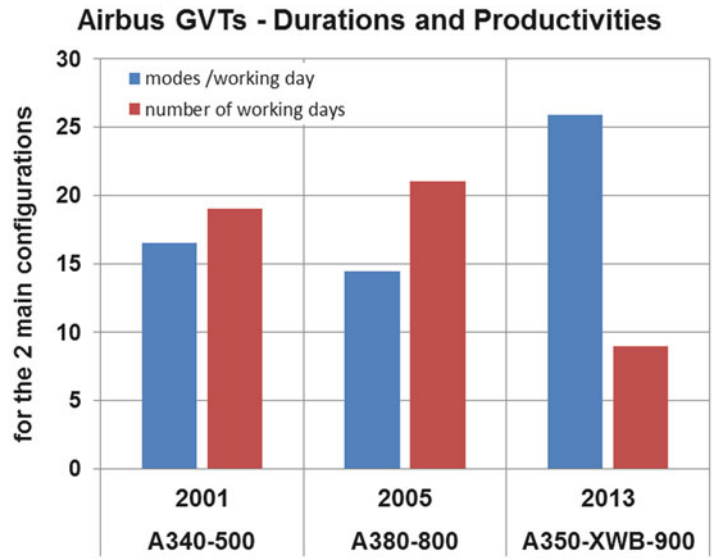


**Fig. 24.18** Diagram of the mode productivities of the different driving points
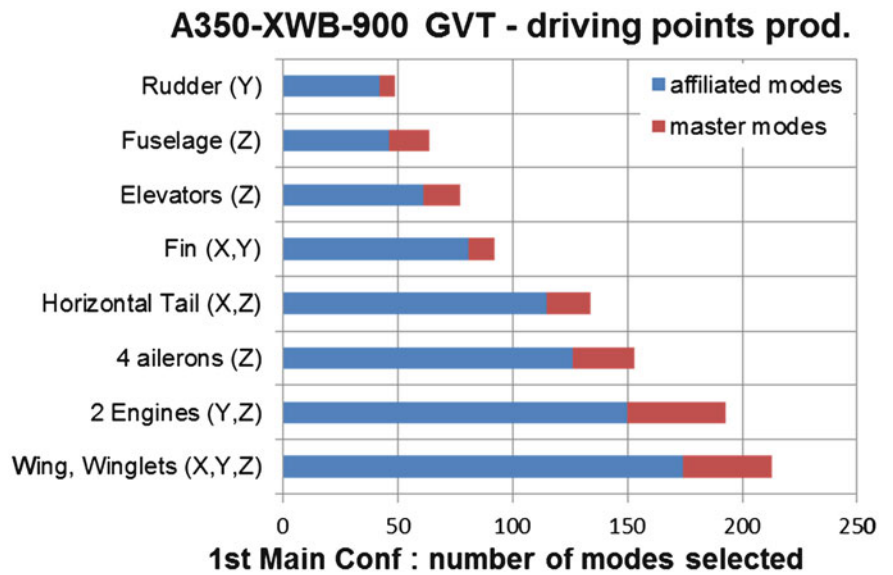


**Fig. 24.19** MIF values of the 180 modes delivered
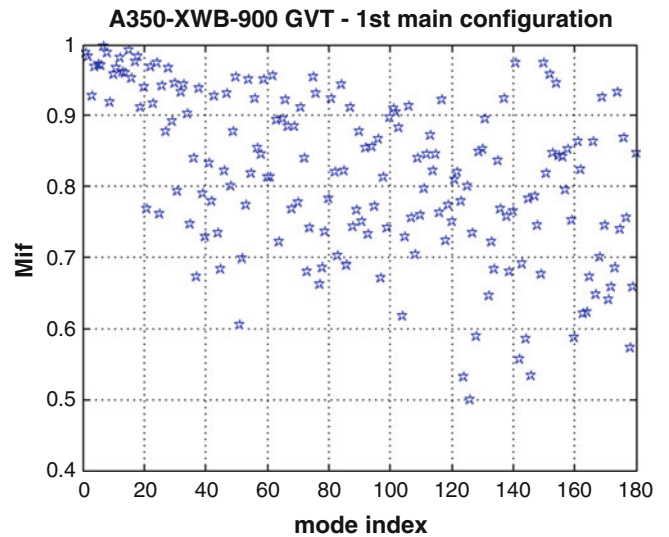
**Fig. 24.20** Example of linearity plot



A350-900XWB MSN1 - Conf.1 - 2n_w_x-S
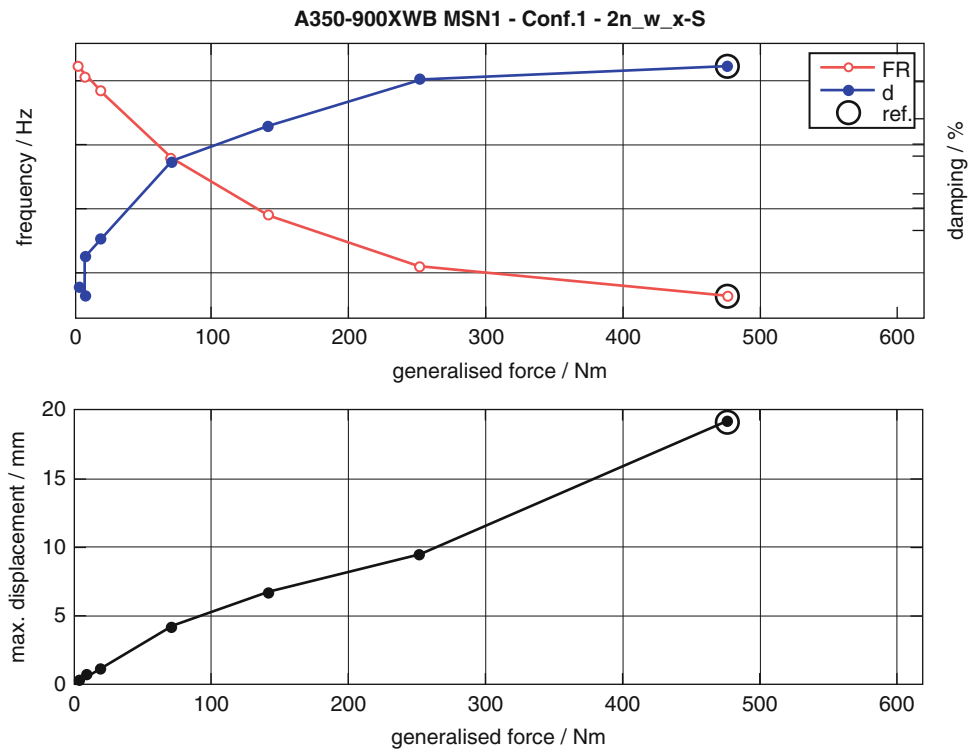
**Fig. 24.21** Example of mode shape plot
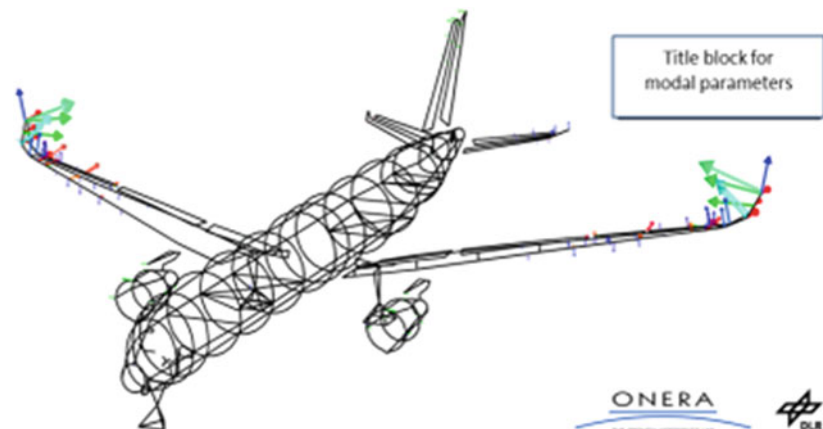
# References

1. Göge D, Böswald M, Füllekrug U, Lubrina P (2007) Ground vibration testing of large aircraft—State-of-the-art and future perspectives. In: IMAC 25, Orlando, FL
2. Peeters B, Climent H, de Diego R, de Alba J, Rodriguez Ahlquist J, Carreño José M, Hendricx W, Rega A, García G, Deweer J, Debille J (2008) Modern solutions for ground vibration testing of large aircraft. In: Proceedings of IMAC 26, Orlando, FL
3. Boeswald M, Goege D, Fuellekrug U, Govers Y (2006) A review of experimental modal analysis methods with respect to their applicability to test data of large aircraft structures. In: International conference on noise and vibration engineering, Leuven, Belgium
4. Gloth G, Sinapius M (2004) Analysis of swept-sine runs during modal identification. Mech Syst Signal Pr 18:1421–1441
5. Giclais S, Lubrina P, Stéphan C, Boeswald M, Govers Y, Ufers J, Botarguès N (2011) New excitation signals for aircraft ground vibration testing. In: IFASD-2011, Paris, France
6. Gloth G, Lubrina P (2005) Ground vibration testing of the AirbusA380–800. In: IFASD-2005, Munich, Germany
7. Fuellekrug U, Boeswald M, Goege D, Govers Y (2008) Measurement of FRFs and modal identification in case of correlated multi-point excitation. Shock Vib 15(3):435–445

# Chapter 25
# Bayesian System Identification of MDOF Nonlinear Systems Using Highly Informative Training Data

**P.L. Green**

**Abstract** The aim of this paper is to utilise the concept of "highly informative training data" such that, using Markov chain Monte Carlo (MCMC) methods, one can apply Bayesian system identification to multi-degree-of-freedom nonlinear systems with relatively little computational cost. Specifically, the Shannon entropy is used as a measure of information content such that, by analysing the information content of the posterior parameter distribution, one is able to select and utilise a relatively small but highly informative set of training data (thus reducing the cost of running MCMC).

**Keywords** System identification • Bayesian inference • Markov chain Monte Carlo • Shannon entropy • Nonlinear dynamics

## 25.1 Introduction

This paper is concerned with the system identification of nonlinear dynamical systems using physics-based models. In this context the overall aim of system identification is to infer, using experimental data, a reliable and robust physical-law based model of a real system. This requires the selection of an appropriate model structure as well as estimation of the parameters within that model. This is a procedure which, as a result of measurement noise and modelling uncertainties, is best approached using probability logic. Adopting a Bayesian framework allows one to take a probabilistic approach to both parameter estimation and model selection.

Using Bayes' Theorem, one can express the parameter estimation and model selection levels of inference as

$$P(\boldsymbol{\theta}|\mathcal{D}, \mathcal{M}) = \frac{P(\mathcal{D}|\boldsymbol{\theta}, \mathcal{M}) P(\boldsymbol{\theta}|\mathcal{M})}{P(\mathcal{D}|\mathcal{M})} \tag{25.1}$$

and

$$P(\mathcal{M}|\mathcal{D}) = \frac{P(\mathcal{D}|\mathcal{M}) P(\mathcal{M})}{P(\mathcal{D})} \tag{25.2}$$

respectively. With regards to Eq. (25.1), $P(\boldsymbol{\theta}|\mathcal{D}, \mathcal{M})$ is termed the "posterior distribution". The posterior is a probability density function (PDF) which represents the probability that the parameter vector $\boldsymbol{\theta} \in \mathbb{R}^{N_\theta}$ is "true" given some experimentally obtained training data $\mathcal{D}$ and a chosen model structure $\mathcal{M}$. It is proportional to the product of the "likelihood" $P(\mathcal{D}|\boldsymbol{\theta}, \mathcal{M})$, and the "prior" $P(\boldsymbol{\theta}|\mathcal{M})$. The prior is a PDF which represents one's prior knowledge of the parameters before the experimental data was realised. The likelihood is a PDF which, given a model structure $\mathcal{M}$ with parameters $\boldsymbol{\theta}$, represents the probability that the data $\mathcal{D}$ was realised. Consequently then, defining the likelihood involves the selection of a noise model

P.L. Green (✉)

Department of Mechanical Engineering, University of Sheffield, Sir Frederick Mappin Building, Mappin Street, Sheffield S1 3JD, UK
e-mail: p.l.green@sheffield.ac.uk

which represents the errors due to the measurement and modelling processes. The denominator of Eq. (25.1) is termed the "evidence"—this is a constant given by

$$P(\mathcal{D}|\mathcal{M}) = \int \dots \int P(\boldsymbol{\theta}|\mathcal{D}, \mathcal{M}) d\theta_1 \dots d\theta_{N_\theta} \tag{25.3}$$

thus ensuring that the posterior will integrate to unity. The evidence term also appears in the numerator of Eq. (25.2) such that, having successfully evaluated Eq. (25.1) for model structure $\mathcal{M}$, the probability that model is a good replication of the physics of the real system (relative to other competing model structures) can then be evaluated.

Unfortunately, it is often the case that the high-dimensionality and complex geometry of the posterior distribution makes evaluation of Eq. (25.3) difficult. With regards to parameter estimation, this problem can be overcome through the use of Markov chain Monte Carlo (MCMC) methods (such as the well-known Metropolis [1] and Hamiltonian Monte Carlo [2] algorithms) which allow one to generate samples from the posterior PDF in Eq. (25.1) without having to evaluate the evidence term. Indeed, there are also MCMC methods which allow one to tackle the issue of model selection—the Transitional MCMC algorithm proposed in [3] can be used to estimate the evidence term in Eq. (25.1) while the Reversible Jump MCMC algorithm [4] is capable of generating samples from a PDF of varying dimension (thus allowing one to simultaneously evaluate a set of competing model structures of varying levels of complexity).

While undoubtedly useful, the number of model runs required tend to make MCMC algorithms computationally expensive (thus restricting their use to relatively small models). The aim of this paper is to investigate whether this cost can be reduced through the use of small but highly informative sets of training data. To that end, the Shannon entropy is used to quantify the information content of a set of training data. It is shown that, in the Bayesian parameter estimation of a MDOF nonlinear dynamical system, this can reduce the cost of running MCMC algorithms.

## 25.2  Bayesian Framework

In this section the Bayesian framework for the parameter estimation of a $N_D$ DOF dynamical system is described. While this is not new, it will help to establish the notation used throughout this work.

This paper is concerned with systems whose state-space equations of motion are of the form:

$$\dot{x} = y \tag{25.4}$$

and

$$\dot{y} = M^{-1}(Cy + Kx + \eta + f) \tag{25.5}$$

where $x \in \mathbb{R}^{N_D}$ and $y \in \mathbb{R}^{N_D}$ represent the displacements and velocities of each DOF, $M$ is the mass matrix, $C$ is the linear damping matrix, $K$ is the linear stiffness matrix, $\eta$ is a vector which contains the nonlinear terms and $f$ is a vector which describes the excitation force being delivered to each mass. The training data $\mathcal{D}$ consists of $N$ points of recorded time history from the force vector $f$ as well as the resulting displacement measurements ($N$ from each DOF). For the $i$th degree of freedom, the measured and simulated displacement time histories will be written as

$$x_{1:N}^{(i)} = \{x_1^{(i)}, x_2^{(i)}, \dots, x_N^{(i)}\} \tag{25.6}$$

and

$$\hat{x}_{1:N}^{(i)} = \{\hat{x}_1^{(i)}, \hat{x}_2^{(i)}, \dots, \hat{x}_N^{(i)}\} \tag{25.7}$$

respectively. Drawing on the central limit theorem, it is assumed that each measured data point is corrupted by Gaussian noise of variance $\sigma^2$ such that, after some manipulation, the likelihood can be written as:

$$P(\mathcal{D}|\boldsymbol{\theta}, \mathcal{M}) = (2\pi\sigma^2)^{-NN_D/2} \exp\left(-\frac{1}{2\sigma^2} \sum_{i=1}^{N_D} J_i(\boldsymbol{\theta})\right) \tag{25.8}$$

where

$$J_i(\boldsymbol{\theta}) = [x_{1:N}^{(i)} - \hat{x}_{1:N}^{(i)}][x_{1:N}^{(i)} - \hat{x}_{1:N}^{(i)}]^T. \tag{25.9}$$

Throughout the following analysis $\sigma$ is treated as an additional unknown parameter for which probabilistic estimates can also be realised.

From now on, for the sake of simplicity, the likelihood will be written as:

$$P(\mathcal{D}|\boldsymbol{\theta}, \mathcal{M}) = \frac{1}{Z_L} \exp(\boldsymbol{J}(\boldsymbol{\theta})) \tag{25.10}$$

where

$$\boldsymbol{J}(\boldsymbol{\theta}) = -\frac{1}{2\sigma^2} \sum_{i=1}^{N_D} J_i(\boldsymbol{\theta}). \tag{25.11}$$

and $Z_L$ is the likelihood normalisation constant.

## 25.3 Informative Training Data

With aim of being able to identify training data which is "highly informative" with regards to one's parameter estimates, the Shannon entropy is used as measure of information content throughout this paper. A similar idea was also developed by MacKay in [5] (although this was within the context of machine learning).

The Shannon entropy of the posterior distribution is defined as

$$S = -\int P(\boldsymbol{\theta}|\mathcal{D}, \mathcal{M}) \ln(P(\boldsymbol{\theta}|\mathcal{D}, \mathcal{M})) d\boldsymbol{\theta} \tag{25.12}$$

which cannot be evaluated as the geometry of the posterior is unknown. To proceed, a Taylor series expansion about the most probable parameter estimates ($\boldsymbol{\theta}_0$) is used to approximate the posterior as being Gaussian. Before this can be accomplished one must first define the prior distribution—throughout this paper Gaussian priors of the form

$$P(\boldsymbol{\theta}|\mathcal{M}) = \frac{1}{Z_P} \exp\left(-\frac{1}{2}[\boldsymbol{\theta} - \boldsymbol{\theta}_0^-]\boldsymbol{B}[\boldsymbol{\theta} - \boldsymbol{\theta}_0^-]^T\right) \tag{25.13}$$

are used. $Z_P$ is a normalising constant, $\boldsymbol{\theta}_0^-$ represent the mean of one's prior parameter estimates and $\boldsymbol{B}$ is a diagonal, user-defined covariance matrix. Recalling the definition of the likelihood (Eq. (25.10)), the posterior distribution can now be written as

$$P(\boldsymbol{\theta}|\mathcal{D}, \mathcal{M}) = \frac{1}{Z_L Z_P P(\mathcal{D}|\mathcal{M})} \exp(G(\boldsymbol{\theta})) \tag{25.14}$$

where

$$G(\boldsymbol{\theta}) = \boldsymbol{J}(\boldsymbol{\theta}) - \frac{1}{2}[\boldsymbol{\theta} - \boldsymbol{\theta}_0^-]\boldsymbol{B}[\boldsymbol{\theta} - \boldsymbol{\theta}_0^-]^T \tag{25.15}$$

($\boldsymbol{J}(\boldsymbol{\theta})$) was defined in Eq. (25.11)). Expanding $G(\boldsymbol{\theta})$ about $\boldsymbol{\theta}_0$ using the Taylor series (as one does when using Laplace's method) then, after some manipulation, one can approximate the posterior as being Gaussian:

$$P(\boldsymbol{\theta}|\mathcal{D}, \mathcal{M})^* = \frac{1}{Z^*} \exp\left(-\frac{1}{2}[\boldsymbol{\theta} - \boldsymbol{\theta}_0]\boldsymbol{A}[\boldsymbol{\theta} - \boldsymbol{\theta}_0]^T\right) \tag{25.16}$$

where the asterisk is used to represent the approximation and $Z^*$ is the posterior normalising constant. The elements of the matrix $\boldsymbol{A}$ are given by

$$\boldsymbol{A}_{i,j} = \left.\frac{\partial^2 G(\boldsymbol{\theta})}{\partial(\theta_i)^2}\right|_{\boldsymbol{\theta}_0}. \tag{25.17}$$

which can be approximated using finite difference methods. It is then relatively simple to shown that the Shannon entropy of $P(\boldsymbol{\theta}|\mathcal{D}, \mathcal{M})^*$ is given by

$$S = \ln(Z^*) + \frac{N_\theta}{2}. \tag{25.18}$$

Assuming that the matrix $A$ is diagonal (which is equivalent to ignoring parameter correlations) and ignoring terms which do not change as a function of the training data one can write Eq. (25.18) in a simpler form:

$$S = \sum_{i=1}^{N_\theta} \ln \left( \frac{1}{A_{i,i}} \right). \tag{25.19}$$

It is important to note that the Shannon entropy also acts as a measure of uncertainty—a highly informative data point will cause a *decrease* in the entropy. It is also interesting to note that the inverse of $A$ is the covariance matrix of $P(\theta|\mathcal{D}, \mathcal{M})^*$. Consequently then, by monitoring the Shannon entorpy, one is actually monitoring the diagonal elements of the covariance matrix of $P(\theta|\mathcal{D}, \mathcal{M})^*$ as a function of the training data. This is equivalent to monitoring the width of the approximately Gaussian posterior—an informative data point is one which causes are large reduction in the width of the posterior.

## 25.4 Potential Issues

### 25.4.1 Most Probable Parameter Estimates

The method presented in Sect. 25.3 relies on one having a reasonable estimate of $\theta_0$. Consequently, the accuracy of the information estimates will depend on the accuracy of one's prior knowledge—Throughout this work, with the aim of improving one's prior estimates of $\theta_0$ the Data Annealing (DA) algorithm [6] has been utilised. Essentially, the DA algorithm is similar to the well-known Simulated Annealing algorithm except that, to save computational cost, the annealing procedure is achieved through the gradual introduction of training data into the likelihood. Additionally, in a similar fashion to "Fast Simulated Annealing" [7], the DA algorithm also utilises a proposal distribution with relatively heavy tails to reduce the changes of becoming stuck in "local traps" (regions of high probability mass which are not globally optimum). As a result, DA can be used to improve one's information estimates with relatively little computational cost.

The assumption that there is a single set of optimum parameters is one of the potential issues with the method outlined in this paper. In reality there may be several sets of, or in fact a continuous set of, optimum parameters (this are referred to as being "locally identifiable" and "unidentifiable" cases in [8]). The danger with using small sets of training data is that one may inadvertently provoke a situation where no one single optimum parameter vector exists. As a first step to addressing this issue, the DA algorithm can be run multiple times so that multiple estimates of the optimum parameter vector are established—it should be ensured that these estimates are reasonably repeatable. Secondly, once a highly informative subset of the training data has been selected, one should utilise an MCMC algorithm which, while being more expensive than "traditional" MCMC, is capable of sampling from PDFs with complex geometries (in fact, one could argue that these algorithms should *always* be employed over more traditional methods). Such algorithms include Adaptive Metropolis Hastings (AMH) [9], Transitional Markov chain Monte Carlo (TMCMC) [3] and Asymptotically Independent Markov Sampling (AIMS) [10]. TMCMC is utilised throughout the following analysis as it is both well-established and works well when higher-dimensional problems are considered.

## 25.5 Nonlinear System

To demonstrate the concept of highly informative training data, the parameter estimation of a nonlinear 3DOF system will be analysed (Fig. 25.1). From left-to-right, the masses are connected by springs with linear stiffness coefficients $k_1, k_2, k_3$, and dampers with linear damping coefficients $c_1, c_2, c_3$. The second spring also has a cubic stiffening component with nonlinear stiffness coefficient $k^*$. The first mass is excited with a Gaussian white noise signal ($w$ in Fig. 25.1). Consequently, the relevant system matrices are:

$$\boldsymbol{K} = \begin{bmatrix} -k_1 - k_2 & k_2 & 0 \\ k_2 & -k_2 - k_3 & k_3 \\ 0 & k_3 & -k_3 \end{bmatrix} \tag{25.20}$$

**Fig. 25.1** 3 DOF nonlinear system
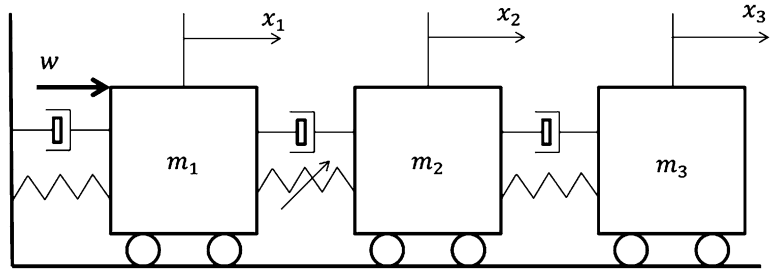


**Table 25.1** Mean and standard deviation of Gaussian priors

| Parameter | Prior mean | Prior standard deviation |
|---|---|---|
| $k_1$ | 50 | 10 |
| $k_2$ | 50 | 10 |
| $k_3$ | 50 | 10 |
| $c_1$ | 0.05 | 0.01 |
| $c_2$ | 0.05 | 0.01 |
| $c_3$ | 0.05 | 0.01 |
| $k^*$ | 1,000 | 100 |
| $\sigma$ | 0.05 | 0.02 |

$$C = \begin{bmatrix} -c_1 - c_2 & c_2 & 0 \\ c_2 & -c_2 - c_3 & c_3 \\ 0 & c_3 & -c_3 \end{bmatrix} \tag{25.21}$$

$$\eta = \left\{ \begin{array}{c} -k^*(x_1 - x_2)^3 \\ -k^*(x_2 - x_1)^3 \\ 0 \end{array} \right\} \tag{25.22}$$

$$f = \left\{ \begin{array}{c} w \\ 0 \\ 0 \end{array} \right\}. \tag{25.23}$$

The parameter values were generated from Gaussian distributions (the moments of which are shown in Table 25.1). These distributions were then used as priors throughout the following analysis. Care was taken to ensure that the author did not know the true parameter values—only the size of the prior was known. The "full" set of output data consisted of 1,000 displacement measurements (from each DOF). The next section details the selection of a highly informative subset of this data.

## 25.6  Results

Five Data Annealing runs were carried out—this took around 6 min to compute. The estimates of the most probable parameter estimates were found to be reasonably consistent. The Shannon entropy of the training data was then calculated (every 50 points were analysed). This process also took roughly 6 min.

The Shannon entropy is plotted as a function of the number of points in the training data in Fig. 25.2. According to the figure, the majority of the learning is achieved using the first 300 data points—thus leaving the remaining 700 points relatively uninformative.

To test this hypothesis, the TMCMC algorithm was used to generate samples from the posterior for varying amounts of training data. The resulting prior and posterior samples (TMCMC is initiated with samples from the prior) are shown respectively in Figs. 25.3, 25.4, 25.5 and 25.6 for the cases where 100, 200, 300 and 1,000 points of training data were used.

**Fig. 25.2** Shannon entropy as a function of the number of points in the training data
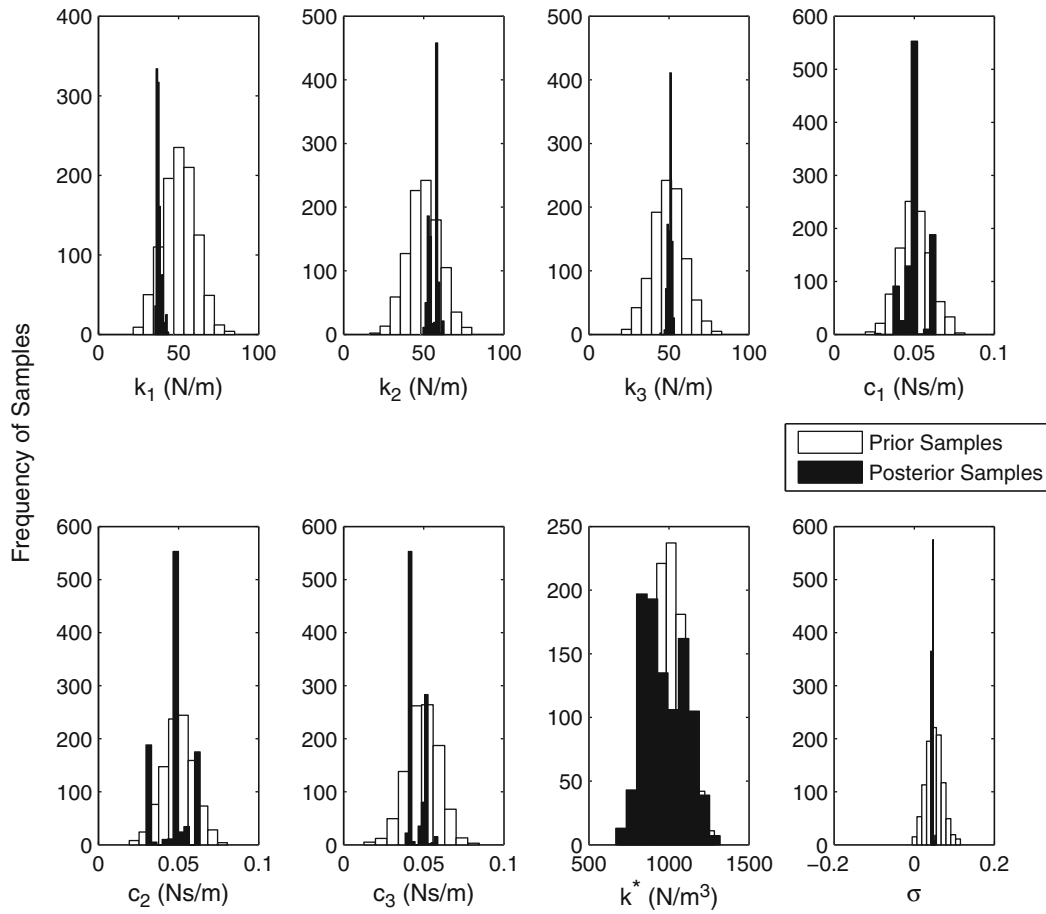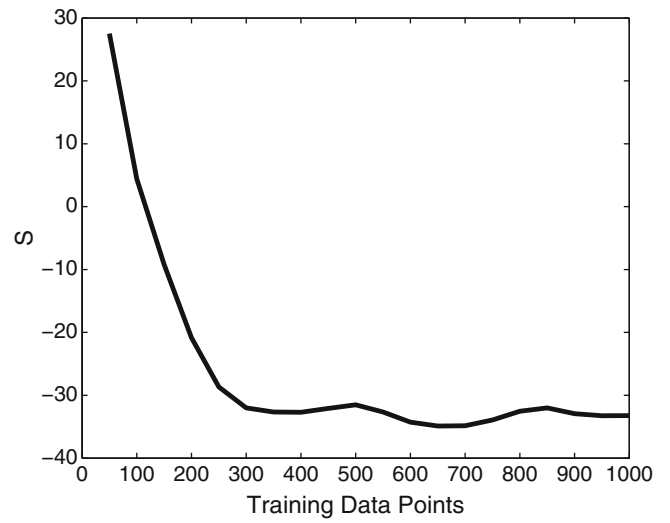




**Fig. 25.3** TMCMC results using 100 points of training data
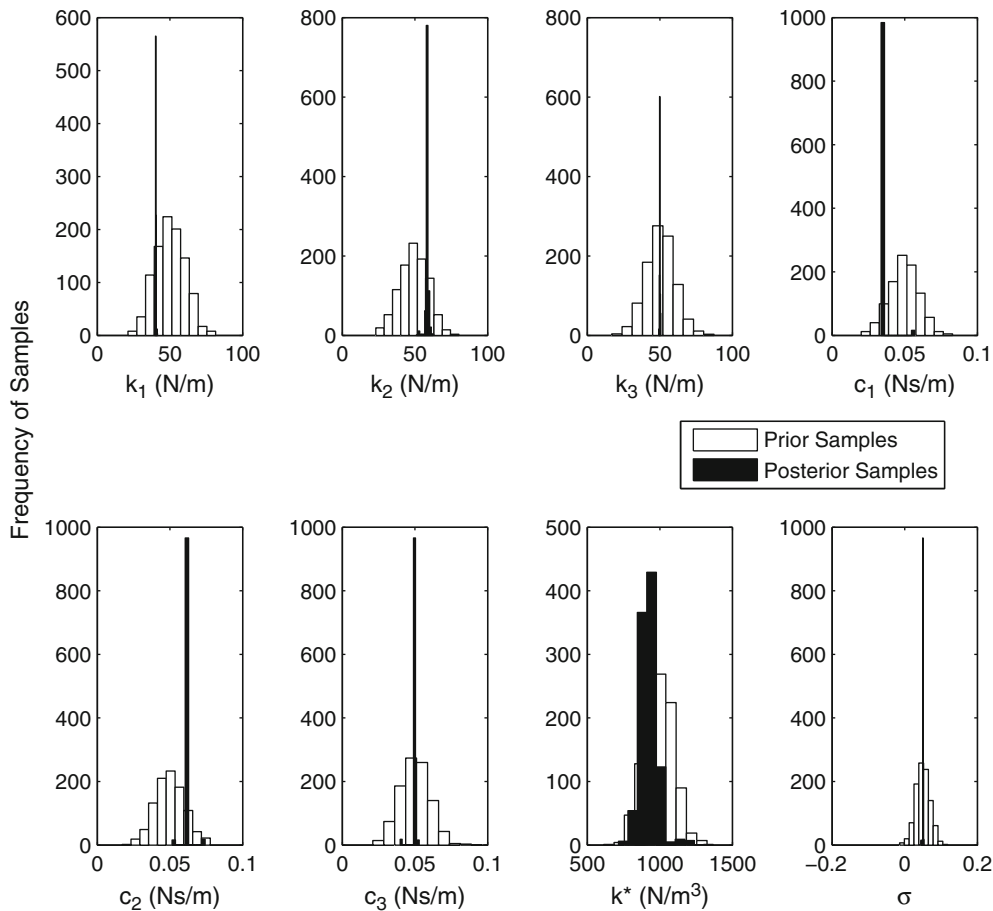
**Fig. 25.4** TMCMC results using 200 points of training data

It is clear that, through using 300 data points instead of 100, a significant amount of information has been gained. However, by comparing Fig. 25.5 with Fig. 25.6, it is clear that little benefit can be gained through using the additional points 700. This is as predicted in Fig. 25.2. It is also interesting to note that the posterior has multiple modes for the 100 point case but that, through the use of more training data, it appears to be uni-modal for all the other cases (The true parameter values are shown in Table 25.2).

## 25.7   Conclusions

This paper was concerned with the Bayesian parameter estimation of nonlinear dynamical systems through the use of Markov chain Monte Carlo (MCMC) methods. Using the Shannon entropy as an information measure it was shown that, by electing to use small amounts of "highly informative" training data, the computational cost of running MCMC algorithms can be greatly reduced. This was then demonstrated with regards to the probabilistic parameter estimation of a MDOF nonlinear system. It was also shown that, through the use of small amounts of training data, one may induce multi-modal posterior distributions. This was addressed though the use of Transitional MCMC which is able to sample from posterior distributions with complex geometries.
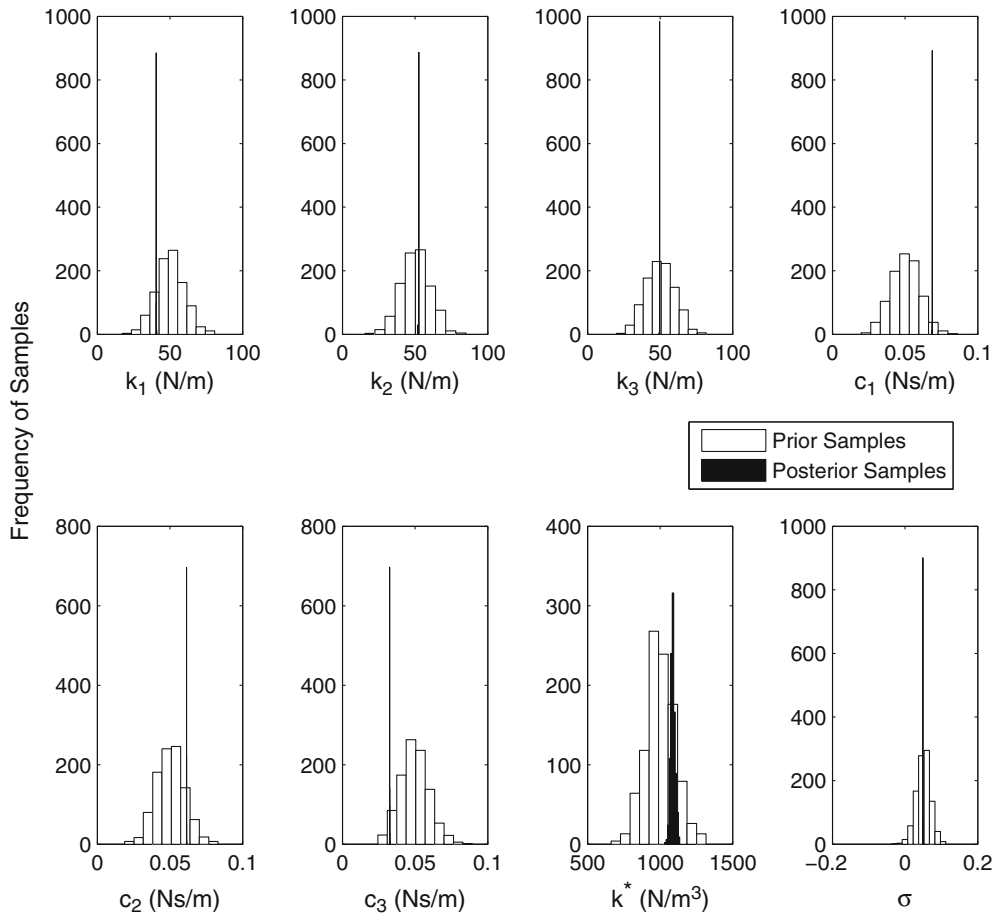
**Fig. 25.5** TMCMC results using 300 points of training data

**Fig. 25.6** TMCMC results using 1,000 points of training data

**Table 25.2** True parameter estimates
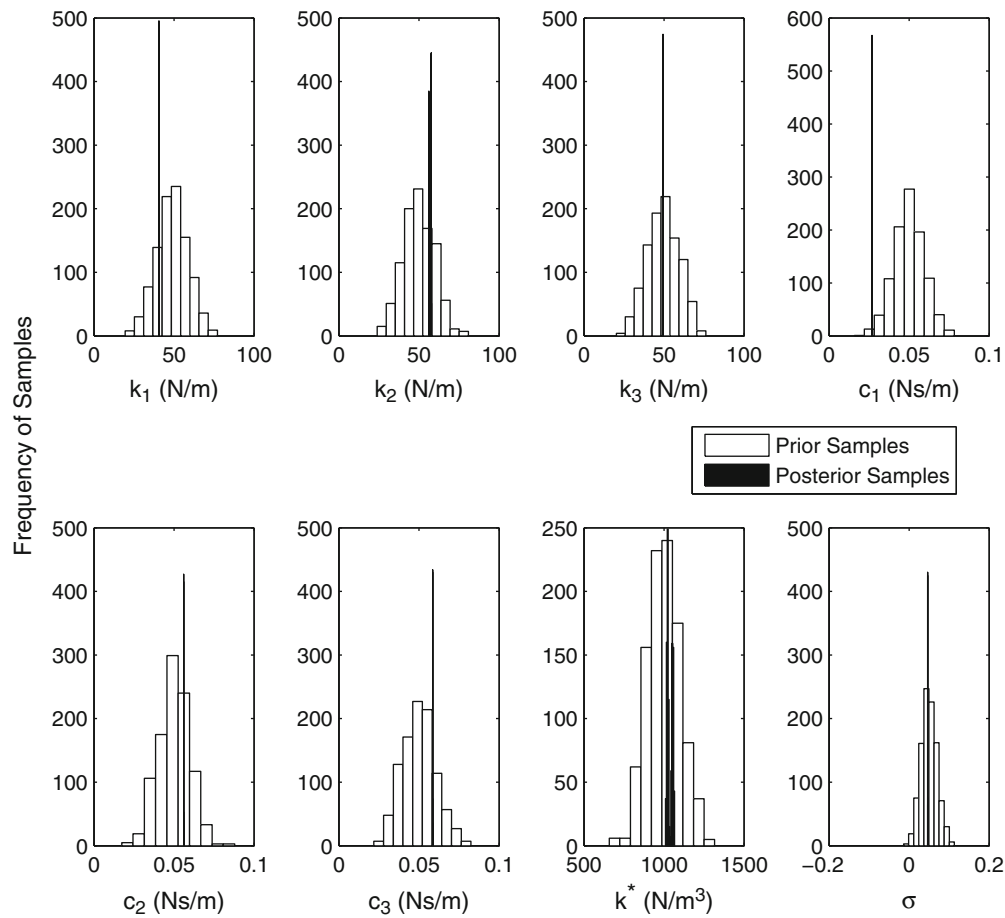
| Parameter | True value |
|-----------|------------|
| $k_1$ | 40.58 |
| $k_2$ | 54.30 |
| $k_3$ | 49.70 |
| $c_1$ | 0.054 |
| $c_2$ | 0.068 |
| $c_3$ | 0.040 |
| $k^*$ | $1.1 \times 10^3$ |
| $\sigma$ | 0.05 |

# References

1. Metropolis N, Rosenbluth AW, Rosenbluth MN, Teller AH, Teller E (1953) Equation of state calculations by fast computing machines. J Chem Phys 21:1087
2. Duane S, Kennedy AD, Pendleton BJ, Roweth D (1987) Hybrid Monte Carlo. Phys Lett B 195(2):216–222
3. Ching J, Chen YC (2007) Transitional Markov Chain Monte Carlo Method for Bayesian Model Updating, model class selection, and model averaging. J Eng Mech 133(7):816–832
4. Green PJ (1995) Reversible Jump Markov Chain Monte Carlo Computation and Bayesian Model Determination. Biometrika 82(4):711–732
5. MacKay DJC (1992) Information-based objective functions for active data selection. Neural Comput 4(4):590–604
6. Green PL (2013) Bayesian system identification of a nonlinear dynamical system using a novel variant of simulated annealing (under review). Mech Syst Signal Process
7. Szu H, Hartley R (1987) Fast simulated annealing. Phys Lett A 122(3):157–162
8. Beck JL, Katafygiotis LS (1998) Updating models and their uncertainties. I: Bayesian statistical framework. J Eng Mech 124(4):455–461
9. Beck JL, Au SK (2002) Bayesian updating of structural models and reliability using Markov Chain Monte Carlo simulation. J Eng Mech 128(4):380–391
10. Beck JL, Zuev KM (2013) Asymptotically independent Markov sampling: a New Markov Chain Monte Carlo scheme for Bayesian inference. Int J Uncertainty Quantification 3(5):445–474

# Chapter 26
# Finite Element Model Updating Using the Separable Shadow Hybrid Monte Carlo Technique

**I. Boulkaibet, L. Mthembu, T. Marwala, M.I. Friswell, and S. Adhikari**

**Abstract** The use of Bayesian techniques in Finite Element Model (FEM) updating has recently increased. These techniques have the ability to quantify and characterize the uncertainties of dynamic structures. In order to update a FEM, the Bayesian formulation requires the evaluation of the posterior distribution function. For large systems, this functions is either difficult (or not available) to solve in an analytical way. In such cases using sampling techniques can provide good approximations of the Bayesian posterior distribution function. The Hybrid Monte Carlo (HMC) method is a powerful sampling method for solving higher-dimensional complex problems. The HMC uses the molecular dynamics (MD) as a global Monte Carlo (MC) move to reach areas of high probability. However, the acceptance rate of HMC is sensitive to the system size as well as the time step used to evaluate MD trajectory. To overcome this, we propose the use of the Separable Shadow Hybrid Monte Carlo (S2HMC) method. This method generates samples from a separable shadow Hamiltonian. The accuracy and the efficiency of this sampling method is tested on the updating of a GARTEUR SM-AG19 structure.

**Keywords** Bayesian • Sampling • Finite element model updating • Markov Chain Monte Carlo • Hybrid Monte Carlo method • Shadow Hybrid Monte Carlo

## 26.1 Introduction

Finite element model (FEM) is a numerical method used to model complex engineering problems [1, 2]. FEM is often used to compute displacements, stresses and strains in complex structures under a given set of loads. Due to the uncertainties (among other approximations) associated with the process of constructing a finite element model of a structure the analytical results are different from those obtained from experimental measurements [3, 4]. Thus for practical purposes the FE model needs to be updated. In recent years the use of the Bayesian framework to build model updating techniques has shown promising results in this system identification problem [4, 6–8]. This approach allows system modelling uncertainties to be expressed in terms of probability.

This can be done by representing the parameters that need to be updated as random vectors with a joint probability distribution function (pdf). This distribution function is known as the posterior distribution function. For sufficiently complex problems this pdf is not available in analytical form. This is the case for the FEM updating problem where the parameter search space is non linear and of high dimension. When an analytical solution is not available sampling methods, such as the Markov Chain Monte Carlo (MCMC), offer the only practical solution to estimating the desired posterior distribution function [4, 7, 8]. One improvement on the classic MCMC is the Hybrid Monte Carlo (HMC) sampling technique. This algorithm is able to deal with an updating vector of a large size.

In the HMC the derivative of the target log-density probability is used to guide the Monte Carlo trajectory and leads towards areas of high probability [5, 7, 11, 18]. An auxiliary variable, called the momentum vector is introduced and the

I. Boulkaibet (✉) • L. Mthembu • T. Marwala

Electrical and Electronic Engineering Department, The Centre For Intelligent System Modelling (CISM),
University of Johannesburg, PO Box 524, Auckland Park 2006, South Africa
e-mail: iboulkaibet@student.uj.ac.za

M.I. Friswell • S. Adhikari
College of Engineering, Swansea University, Singleton Park, Swansea SA2 8PP, UK

updated vector is treated as a system displacement. The total system energy—called the Hamiltonian function- is evaluated using the Störmer-Verlet (also called leapfrog) algorithm. The leapfrog algorithm requires the log-density derivative, which can be seen as a guide used to deliver global moves with a higher acceptance probability. The Hamiltonian function is numerically evaluated using the popular Störmer-Verlet integrator [18]. This integrator does not conserve the energy especially when the time step used by the leapfrog algorithm or/and the system size is considered large. To overcome this limitation an algorithm called the Shadow Hybrid Monte Carlo (SHMC) has been proposed [9, 16]. The SHMC uses a modified Hamiltonian function for sampling and a reweighting to improve the acceptance rate of HMC [9, 16]. However the SHMC uses a non-separable Hamiltonian which generates the momenta in a computationally expensive way. Furthermore this method requires an extra tuning parameter to balance the cost of rejection of momenta and positions [9, 16, 17]. In this paper the Separable Shadow Hybrid Monte Carlo (S2HMC) [17] is implemented. The S2HMC is able to sample the posterior distribution function of FEM updating parameters by using a separable shadow Hamiltonian function and without involving any extra parameters.

This method is tested on updating a GARTEUR SM-AG19 aeroplane structure. The efficiency, reliability and limitations of the S2HMC technique are investigated when a Bayesian approach is implemented on an FEM updating problem.

In the next section, the finite element model background is presented. In Sect. 26.3, an introduction to the Bayesian framework is introduced where the posterior distribution of the uncertain parameters of the FEM is presented. Section 26.4 introduces the HMC techniques. Section 26.5 introduces the Shadow Hamiltonian function. Section 26.6 introduces the S2HMC technique which is used to predict the posterior distribution. Section 26.6 presents an implementation on a GARTEUR SM-AG19 aeroplane structure. Finally, the Sect. 26.7 concludes the paper.

## 26.2   Finite Element Model Background

In finite element modelling, an $N$ degree of freedom dynamic structure can be described by the second order equation of motion [8, 12, 16]:

$$\mathbf{M}\ddot{\mathbf{x}}(t) + \mathbf{C}\dot{\mathbf{x}}(t) + \mathbf{K}\mathbf{x}(t) = \mathbf{f}(t), \qquad (26.1)$$

where $\mathbf{M}$, $\mathbf{C}$ and $\mathbf{K}$ are the mass, damping and stiffness matrices of size $N \times N$, $\mathbf{x}(t)$ is the vector of $N$ degrees of freedom and $\mathbf{f}(t)$ is the vector of loads applied to the structure. In the case that no external forces are applied to the structure and if the damping terms are neglected ($\mathbf{C} \ 0$), the dynamic equation may be written in the modal domain (natural frequencies and mode shapes):

$$\left[ -\left(\omega_i^m\right)^2 \mathbf{M} + \mathbf{K} \right] \phi_i^m = \boldsymbol{\varepsilon}_i \qquad (26.2)$$

$\omega_i^m$ is the $i$th measured natural frequency, $\phi_i^m$ is the $i$th measured mode shape vector and $\varepsilon_i$ is the $i$th error vector. In Eq. 26.2, the error vector $\boldsymbol{\varepsilon}_i$ is equal to $\mathbf{0}$ if the system matrices $\mathbf{M}$ and $\mathbf{K}$ correspond to the modal properties ($\omega_i^m$ and $\phi_i^m$). However, $\boldsymbol{\varepsilon}_i$ is a non-zero vector if the system matrices obtained analytically from the finite element model do not match the measured modal properties $\omega_i^m$ and $\phi_i^m$.

## 26.3   Bayesian Inferences

In this work the Bayesian method is used to solve the FEM updating problem in the modal domain. Bayesian approaches are governed by Bayes rule [4, 5, 8, 16]:

$$P\left(\mathbf{E}|\, D\right) \propto P\left(D|\mathbf{E}\right) P\left(E\right) \qquad (26.3)$$

where $\mathbf{E}$ represent the vector of updating parameters and the mass $\mathbf{M}$ and stiffness $\mathbf{K}$ matrices are functions of the updating parameters $\mathbf{E}$. The quantity $P(\mathbf{E})$, known as the prior probability distribution, is a function of the updating parameters in the absence of the data. $D$ is the measured modal properties; the natural frequencies $\omega_i$ and mode shapes $\phi_i$. The quantity $P(\mathbf{E}|D)$ is the posterior probability distribution function of the parameters in the presence of the data $D$. $P(D|\mathbf{E})$ is the likelihood probability distribution function [4, 5, 13].

The likelihood distribution can be seen as the probability of the modal measurements in the presence of uncertain parameters [8]. This function can be defined as the normalized exponent of the error function that represents the differences between the measured and the analytic frequencies.

It can be written as:

$$P\left(D\middle|\mathbf{E}\right) = \frac{1}{\left(\frac{2\pi}{\beta}\right)^{N_m/2}\prod_{i=1}^{N_m}\omega_i^m}\exp\left(-\beta\sum_i^{N_m}\left(\frac{\omega_i^m - \omega_i}{\omega_i^m}\right)^2\right) \tag{26.4}$$

where $\beta$ is a constant, $N_m$ is the number of measured modes and $\omega_i$ is the $i$th analytical frequency.

The prior density function represents the prior knowledge about the updating parameters $\mathbf{E}$ and quantifies the uncertainty of the parameters $\mathbf{E}$ [8]. This knowledge can be facts like some parameters need to be updated more intensely than others. For example in structural systems parameters next to joints should be updated more intensely than for those corresponding to smooth surface areas far from joints. Here the prior probability distribution function for parameters $\mathbf{E}$ is assumed to be Gaussian and is given by [13, 14, 16]:

$$P\left(\mathbf{E}\right) = \frac{1}{(2\pi)^{Q/2}\prod_{i=1}^{Q}\frac{1}{\sqrt{\alpha_i}}}\exp\left(-\sum_i^Q\frac{\alpha_i}{2}||\,\mathbf{E} - \mathbf{E0}\,||^2\right) \tag{26.5}$$

where $Q$ is the number of groups of parameters to be updated, E0 represents the mean value (initial value) of the updated vector, and $\alpha_i$ is the coefficient of the prior density function for the $i$th group of updating parameters. The notation $||*||$ denotes the Euclidean norm of *. In Eq. 26.5, if $\alpha_i$ is constant for all of the updating parameters then the updated parameters will be of the same order of magnitude. Equation 26.5 is chosen to be Gaussian because many natural processes tend to have a Gaussian distribution.

The posterior distribution function of the parameters $\mathbf{E}$ given the observed data $D$ is denoted as $P(\mathbf{E}|D)$ and is obtained by applying Bayes' theorem as represented in Eq. 26.3. The distribution $P(\mathbf{E}|D)$ is calculated by substituting Eqs. 26.4 and 26.5 into Eq. 26.3 to give

$$P\left(\mathbf{E}\middle|D\right) = \frac{1}{Z_s\left(\alpha,\beta\right)}\exp\left(-\beta\sum_i^{N_m}\left(\frac{\omega_i^m - \omega_i}{\omega_i^m}\right)^2 - \sum_i^Q\frac{\alpha_i}{2}||\,\mathbf{E} - \mathbf{E0}\,||^2\right) \tag{26.6}$$

where

$$Z_s\left(\alpha,\beta\right) = \left(\frac{2\pi}{\beta}\right)^{N_m/2}\prod_{i=1}^{N_m}\omega_i^m(2\pi)^{Q/2}\prod_{i=1}^Q\frac{1}{\sqrt{\alpha_i}} \tag{26.7}$$

In FEM updating the analytical form of the posterior distribution function solution is not available. As discussed sampling techniques simplify the Bayesian inference by providing a set of random samples from posterior distribution [5, 7, 8, 13, 15]. In the case that $Y$ is the observation of certain parameters at different discrete time instants the total Probability theorem provides probabilistic information for the prediction of the future responses $Y$ at different time instants. Consider the following integral:

$$P\left(Y\middle|D\right) = \int P\left(Y\middle|\mathbf{E}\right)P\left(\mathbf{E}\middle|D\right)d\,[\mathbf{E}] \tag{26.8}$$

Equation 26.8 depends on the posterior distribution function. The dimension of the updating parameters makes it very difficult to obtain an analytical solution. Therefore, sampling techniques, such as Markov Chain Monte Carlo (MCMC) methods are employed to predict the updating parameter distribution and subsequently to predict the modal properties. Given a set of $N_s$ random parameter vector drawn from $P(\mathbf{E}|D)$, the expectation value of any observed function $Y$ can be easily estimated.

The integral in Eq. 26.8 can be solved using sampling algorithms [5, 7, 10, 11]. These algorithms are used to generate a sequence of vectors $\{\mathbf{E}_1, \mathbf{E}_2, \ldots, \mathbf{E}_{N_s}\}$ where $N_s$ is the number of samples and these vectors can be used to form a Markov chain. This generated vector is then used to predict the form of the posterior distribution function $P(\mathbf{E}|D)$. The integral in Eq. 26.8 can be approximated as

$$\tilde{Y} \cong \frac{1}{N_s} \sum_{i=1}^{N_s} G\left(\mathbf{E}_i\right) \tag{26.9}$$

where $G$ is a function that depends on the updated parameters $\mathbf{E}_i$. As an example, if $\mathbf{G} = \mathbf{E}$ then $\tilde{Y}$ becomes the expected value of $\mathbf{E}$. Generally, $\tilde{Y}$ is the vector that contains the modal properties and $N_s$ is the number of retained states. In this paper, the SHMC method is used to sample from the posterior distribution function.

## 26.4   The Hybrid Monte Carlo Method

The Hybrid Monte Carlo method, also known as the Hamiltonian Markov Chain method, is a sampling method for solving higher-dimensional complex problems [5, 7, 11, 16, 18]. The HMC combines a Molecular Dynamic (MD) trajectory with a Monte Carlo (MC) rejection step [8, 13]. In HMC, a dynamical system is considered in which auxiliary variables, called momentum $\mathbf{p} \in R^N$ are introduced. The updated parameters in the posterior distribution are treated as displacements. The total energy (Hamiltonian function) of the new dynamical system is defined by $H(\mathbf{E}, \mathbf{p}) = V(\mathbf{E}) + W(\mathbf{p})$, where the potential energy is $V(\mathbf{E}) = -\ln(P(\mathbf{E}|D))$ and the kinetic energy is $W(\mathbf{p}) = \mathbf{p}^T \mathbf{M}^{-1} \mathbf{p}/2$. The kinetic energy depends only on $\mathbf{p}$ and some chosen positive definite matrix $\mathbf{M} \in R^{N \times N}$.

The joint distribution derived from the Hamiltonian function can be written in the following form: $f(\mathbf{E}, \mathbf{p}) = K . \exp (-H(\mathbf{E}, \mathbf{p}))$ where $K$ is normalization constant. It is easy to see that $f(\mathbf{E}, \mathbf{p})$ can be written as $f(\mathbf{E}, \mathbf{p}) = K . \exp (-V(\mathbf{E}) . \exp(-W(p))$ or $f(\mathbf{E}, \mathbf{p}) = K . P(\mathbf{E}|D) . \exp(-\mathbf{p}^T \mathbf{M}^{-1} \mathbf{p}/2)$. Sampling $\mathbf{E}$ from the posterior distribution can be obtained by sampling $(\mathbf{E}, \mathbf{p})$ from the joint distribution $f(\mathbf{E}, \mathbf{p})$. Also, the vectors $E$ and $p$ are independent according to $f(\mathbf{E}, \mathbf{p})$. The evolution of $(\mathbf{E}, \mathbf{p})$ through time $t$ and time step $\delta t$ is given by the following Störmer-Verlet algorithm [7, 8]

$$\mathbf{p}\left(t + \frac{\delta t}{2}\right) = \mathbf{p}(t) - \frac{\delta t}{2} \nabla V\left[\mathbf{E}(t)\right] \tag{26.10}$$

$$\mathbf{E}\left(t + \delta t\right) = \mathbf{E}(t) + \delta t \mathbf{M}^{-1} \mathbf{p}\left(t + \frac{\delta t}{2}\right) \tag{26.11}$$

$$\mathbf{p}\left(t + \delta t\right) = \mathbf{p}\left(t + \frac{\delta t}{2}\right) - \frac{\delta t}{2} \nabla V\left[\mathbf{E}\left(t + \delta t\right)\right] \tag{26.12}$$

where $\nabla V$ is obtained numerically by finite difference as

$$\frac{\partial V}{\partial E_i} = \frac{V\left(\mathbf{E} + \Delta h\right) - V\left(\mathbf{E} - \Delta h\right)}{2h\Delta_i} \tag{26.13}$$

$\Delta = [\Delta_1, \Delta_2, \ldots, \Delta_N]$ is the perturbation vector and $h$ is a scalar which dictates the size of the perturbation of $\mathbf{E}$. After each iteration of Eqs. 26.10–26.12, the resulting candidate state is accepted or rejected according to the Metropolis criterion based on the value of the Hamiltonian $H(\mathbf{E}, \mathbf{p})$. Thus if $(\mathbf{E}, \mathbf{p})$ is the initial state and $(\mathbf{E}^*, \mathbf{p}^*)$ is the state after the above equations have been updated then this candidate state is accepted with probability $\min(1, \exp\{H(\mathbf{E}, \mathbf{p}) - H(\mathbf{E}^*, \mathbf{p}^*)\})$. The obtained vector $\mathbf{E}$ will be used for the next iteration and the algorithm stopping criterion is defined by the number of $\mathbf{E}$ samples ($N_s$).

Theoretically, these moves preserve the total energy $H(\mathbf{E}, \mathbf{p})$ where the value of the total energy is constant. This can make the acceptance rate 100 % since the term $\exp\{H(\mathbf{E}, \mathbf{p}) - H(\mathbf{E}^*, \mathbf{p}^*)\} = 1$. However, the Hamiltonian dynamics is a discretised problem where the Störmer-Verlet is used to evaluate the pair $(\mathbf{E}, \mathbf{p})$ through time. This integrator does not achieve the exact energy conservation. In this case, the time step needs to be small enough to reduce the error caused by the Störmer-Verlet integrator.

The HMC algorithm can be summarized as follows:

1. An initial value $\mathbf{E}_0$ is used to initiate the algorithm.
2. Initiate $\mathbf{p}_0$ such that $\mathbf{p}_0 \ N(0, \boldsymbol{M})$.
3. Initiate the leapfrog algorithm with $(\mathbf{E}, \mathbf{p})$ and run the algorithm for $L$ time steps to obtain $(\mathbf{E}^*, \mathbf{p}^*)$.
4. Update the FEM to obtain the new analytic frequencies and then compute $H(\mathbf{E}^*, \mathbf{p}^*)$.
5. Accept $(\mathbf{E}^*, \mathbf{p}^*)$ with probability $\min(1, exp\{H(\mathbf{E}, \mathbf{p}) - H(\mathbf{E}^*, \mathbf{p}^*)\})$.
6. Repeat steps (3–5) to get $N_s$ samples.

## 26.5   The Separable Shadow Hamiltonian Function

The S2HMC improves the sampling by changing the configuration spaces. This accelerates the convergence of averages computed with the method [17]. As a result the S2HMC improves the acceptance rate of HMC at a comparatively negligible computational cost. The S2HMC uses a processed velocity Verlet (VV) integrator instead of Verlet. The goal of a processing integrator is to increase the effective order of accuracy by using *pre-processing* and *post-processing* steps [17].

The rationale for increasing the effective order of accuracy is that a more accurate integrator has better acceptance rate in HMC. The S2HMC also uses a modified potential energy function, which is conserved to $O(\delta t^4)$ by the processed method instead of just $O(\delta t^2)$ by the unprocessed method. Moreover the S2HMC requires a reweighting step to compensate for modification of the potential energy. The shadow Hamiltonian function used in S2HMC is separable and fourth order [17]:

$$\tilde{H}\left(\mathbf{E}, \mathbf{p}\right) = \frac{1}{2}\mathbf{p}^{\mathbf{T}}\mathbf{M}^{-1}\mathbf{p} + V\left(\mathbf{E}\right) + \frac{\delta t^2}{24}V_{\mathbf{E}}^{T}\mathbf{M}^{-1}V_{\mathbf{E}} + O\left(\delta t^4\right) \qquad (26.14)$$

$V_E$ is the derivative of the potential energy $V$ with respect to $\mathbf{E}$. The modified or shadow Hamiltonian is a result of applying backward error analysis to numerical integrators [17]. In the analysis of numerical integrators for Hamiltonian systems, the shadow Hamiltonian has quantities that are better conserved than the true Hamiltonian. In particular, a fourth order shadow Hamiltonian is conserved within $O(\delta t^4)$, where $\delta t$ is the discretization time step. For symplectic integrators one can construct shadow Hamiltonians of arbitrarily high order.

The pre-processing step is given by:

$$\widehat{\mathbf{p}} = \mathbf{p} - \frac{\delta t}{24}\left(V_{\mathbf{E}}\left(\mathbf{E} + \delta t\mathbf{M}^{-1}\widehat{\mathbf{p}}\right) - V_{\mathbf{E}}\left(\mathbf{E} - \delta t\mathbf{M}^{-1}\widehat{\mathbf{p}}\right)\right) \qquad (26.15)$$

$$\widehat{\mathbf{E}} = \mathbf{E} + \frac{\delta t^2}{24}\mathbf{M}^{-1}\left(V_{\mathbf{E}}\left(\mathbf{E} + \delta t\mathbf{M}^{-1}\widehat{\mathbf{p}}\right) + V_{\mathbf{E}}\left(\mathbf{E} - \delta t\mathbf{M}^{-1}\widehat{\mathbf{p}}\right)\right) \qquad (26.16)$$

Equations 26.15 and 26.16 require an iterative solution for $\widehat{\mathbf{p}}$ and a direct computation for $\widehat{\mathbf{E}}$.
The post-processing step is given by:

$$\mathbf{E} = \widehat{\mathbf{E}} - \frac{\delta t^2}{24}\mathbf{M}^{-1}\left(V_E\left(\mathbf{E} + \delta t\mathbf{M}^{-1}\widehat{\mathbf{p}}\right) + V_E\left(\mathbf{E} - \delta t\mathbf{M}^{-1}\widehat{\mathbf{p}}\right)\right) \qquad (26.17)$$

$$\mathbf{p} = \widehat{\mathbf{p}} + \frac{\delta t}{24}\left(V_{\mathbf{E}}\left(\mathbf{E} + \delta t\mathbf{M}^{-1}\widehat{\mathbf{p}}\right) - V_{\mathbf{E}}\left(\mathbf{E} - \delta t\mathbf{M}^{-1}\widehat{\mathbf{p}}\right)\right) \qquad (26.18)$$

Equations 26.17 and 26.18 require an iterative solution for $\mathbf{E}$ and a direct computation for $\mathbf{p}$. Finally, in order to calculate balanced values of the mean, the results must be reweighted. The average of an observable $A$ is giving by [17]:

$$\langle A \rangle = \frac{\sum_{i=1}^{Ns} B.a_i}{\sum_{i=1}^{Ns} a_i}, \text{ where } a_i = \frac{\exp\left(-H\left(\mathbf{E}, \mathbf{p}\right)\right)}{\exp\left(-\tilde{H}\left(\mathbf{E}, \mathbf{p}\right)\right)} \qquad (26.19)$$

The S2HMC algorithm can be summarized as follows [17]:

1. An initial value $\mathbf{E}_0$ is used to initiate the algorithm.
2. Initiate $\mathbf{p}_0$ such that $\mathbf{p}_0 \  N(0, \mathbf{M})$.
3. Compute the initial shadow energy $\tilde{H}\left(\mathbf{E}, \mathbf{p}\right)$ using Eq. 26.14.
4. Pre-processing: Starting from $(\mathbf{E}, \mathbf{p})$, solve iteratively for $\widehat{\mathbf{p}}$ and a directly compute $\widehat{\mathbf{E}}$ using Eqs. 26.15 and 26.16.
5. Initiate the leapfrog algorithm with $\left(\widehat{\mathbf{E}}, \widehat{\mathbf{p}}\right)$ and run the algorithm for $L$ time steps to obtain $\left(\widehat{\mathbf{E}}^*, \widehat{\mathbf{p}}^*\right)$.
6. Post-processing: Starting from $\left(\widehat{\mathbf{E}}^*, \widehat{\mathbf{p}}^*\right)$, solve iteratively for $\widehat{\mathbf{E}}$ and a directly compute $\widehat{\mathbf{p}}$ using Eqs. 26.17 and 26.18.
7. Update the FEM to obtain the new analytic frequencies and then compute $H(\mathbf{E}^*, \mathbf{p}^*)$.
8. Accept $(\mathbf{E}^*, \mathbf{p}^*)$ with probability $\min\left(1, exp\left\{\tilde{H}\left(\mathbf{E}, \mathbf{p}\right) - \tilde{H}\left(\mathbf{E}^*, \mathbf{p}^*\right)\right\}\right)$.
9. Repeat steps (3–5) to get $N_s$ samples.
10. Compute weight: To compute the averages of a quantity $A(\mathbf{E})$ using the S2HMC, reweighting of the sequence of A is needed (26.19).

## 26.6   The Modelled Structure and FE Model

All the finite element modeling was simulated using version 6.2 of the Structural Dynamics Toolbox (SDT®) under the MATLAB® environment. In this paper, a GARTEUR SM-AG19 aeroplane structure is used to investigate the optimization capability of the four algorithms. The GARTEUR SM-AG19 structure was used as a benchmark study by 12 members of the GARTEUR Structures and Materials Action Group 19 [19–23]. One of the aims of the study was to compare the S2HMC and HMC methods with different time steps [16]. The benchmark study also allowed participants to test a single representative structure using their own test equipment. The experimental test data used in our analysis is data obtained from DLR Data, Göttingen, Germany.

The above aeroplane has a length of 1.5 m and a width of 3 m. The depth of the fuselage is 15 cm with a thickness of 5 cm. Figure 26.1 shows the FE model of the aeroplane. In our models all element materials are considered standard isotropic. The model elements are Euler–Bernoulli beam elements. The measured natural frequency (Hz) data is: 6.38, 16.10, 33.13, 33.53, 35.65, 48.38, 49.43, 55.08, 63.04, 66.52 Hz.

The parameters to be updated are the right wing stiffnesses ($I_{min}, I_{max}, I_{tors}$), the left wing stiffnesses ($I_{min}, I_{max}, I_{tors}$), vertical tail stiffnesses ($I_{min}$) and the overall structure's density ($\rho$). The constant $\beta$ of the posterior distribution is set equal 100, and all coefficients $\alpha_i$ are set equal to $\frac{1}{\sigma_i^2}$, where $\sigma_i^2$ is the variance of the parameter $E_i$. The vector of $\sigma_i$ is defined as $\boldsymbol{\sigma} = [5 \times 10^5, 50 \times 10^{-10}, 50 \times 10^{-10}, 5 \times 10^{-9}, 50 \times 10^{-10}, 5 \times 10^{-9}, 5 \times 10^{-10}, 5 \times 10^{-10}]$. The initial position vector $\boldsymbol{E} = [\rho, VTP - I_{min}, L - I_{min}, L - I_{max}, L - I_{tors}, R - I_{min}, R - I_{max}, R - I_{tors}]$ and its bounds are given in Tables 26.1 and 26.2 where *VTP*- Vertical Tail Plane, *R* -Right and *L*- Left. The time step is $\delta t = 3$ *ms* and the number of samples is $N_s = 1,000$.

Table 26.3 presents the initial value (the mean material or geometric value) of the update vector **E**, as well as the updated values obtained by HMC and S2HMC methods for two different time step scenarios ($\delta t = 0.003$ *s* and $\delta t = 0.0048$ *s*).

In the first scenario ($\delta t = 0.003$ *s*), the updated parameters obtained by the S2HMC algorithm are closer to the mean values i.e. they are physically realistic. There is a noticeable difference between the final updated values obtained by the HMC and S2HMC. The time step used for simulations in both methods, $\delta t = 0.003$ *s*, provides a very good acceptance sampling rate—99.9 %—for both methods. In the second scenario ($\delta t = 0.0048$ *s*) the updated parameters using the S2HMC method are much closer to the mean value.
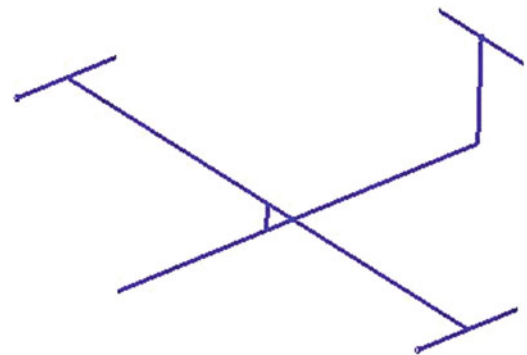


**Fig. 26.1**  FEM GARTEUR structure

**Table 26.1**  The parameter vector and the mean values

| Parameter | $\rho$ (kg/m$^3$) | $VTP - I_{min}$ ($10^{-9}$ m$^4$) | $L - I_{min}$ ($10^{-9}$ m$^4$) | $L - I_{max}$ ($10^{-7}$ m$^4$) |
|---|---|---|---|---|
| | 2,700 | 8.3 | 8.3 | 8.3 |
| Parameter | $L - I_{tors}$ ($10^{-8}$ m$^4$) | $R - I_{min}$ ($10^{-9}$ m$^4$) | $R - I_{max}$ ($10^{-7}$ m$^4$) | $R - I_{tors}$ ($10^{-8}$ m$^4$) |
| | 4.0 | 8.3 | 8.3 | 4.0 |

**Table 26.2**  The Max/Min bounds of the updated vector

| | $Max_{position}$ | $Min_{position}$ |
|---|---|---|
| $\rho$ | 3,000 | 2,500 |
| $VTP - I_{min}$ | $10 \times 10^{-9}$ | $7.3 \times 10^{-9}$ |
| $L - I_{min}$ | $10 \times 10^{-9}$ | $7.3 \times 10^{-9}$ |
| $L - I_{max}$ | $10 \times 10^{-7}$ | $7.3 \times 10^{-7}$ |
| $R - I_{min}$ | $10 \times 10^{-9}$ | $7.3 \times 10^{-9}$ |
| $L - I_{max}$ | $10 \times 10^{-7}$ | $7.3 \times 10^{-7}$ |
| $L - I_{tors}$ | $6 \times 10^{-8}$ | $3 \times 10^{-8}$ |
| $L - I_{tors}$ | $6 \times 10^{-8}$ | $3 \times 10^{-8}$ |

**Table 26.3** Initial and updated parameter values

| | Initial **E0** | HMC method ($\delta t = 3$ ms) | S2HMC method ($\delta t = 3$ ms) | S2HMC method ($\delta t = 4.8$ ms) |
|---|---|---|---|---|
| $\rho$ | 2,700 | 2,967.2 | 2,930.9 | 2,869.9 |
| $VTP - I_{min}$ | $8.3 \times 10^{-9}$ | $9.893 \times 10^{-9}$ | $9.844 \times 10^{-9}$ | $9.483 \times 10^{-9}$ |
| $L - I_{min}$ | $8.3 \times 10^{-9}$ | $9.991 \times 10^{-9}$ | $9.959 \times 10^{-9}$ | $9.910 \times 10^{-9}$ |
| $L - I_{max}$ | $8.3 \times 10^{-7}$ | $8.593 \times 10^{-7}$ | $8.585 \times 10^{-7}$ | $8.512 \times 10^{-7}$ |
| $R - I_{min}$ | $8.3 \times 10^{-9}$ | $9.9777 \times 10^{-9}$ | $9.9517 \times 10^{-9}$ | $9.909 \times 10^{-9}$ |
| $L - I_{max}$ | $8.3 \times 10^{-7}$ | $7.335 \times 10^{-7}$ | $7.310 \times 10^{-7}$ | $7.269 \times 10^{-7}$ |
| $L - I_{tors}$ | $4 \times 10^{-8}$ | $3.639 \times 10^{-8}$ | $3.622 \times 10^{-8}$ | $3.633 \times 10^{-8}$ |
| $R - I_{tors}$ | $4 \times 10^{-8}$ | $3.744 \times 10^{-8}$ | $3.681 \times 10^{-8}$ | $3.669 \times 10^{-8}$ |

The reason is that the time step is large enough to allow significant jumps of the algorithm during the searching process. This also will lead to better results (see Table 26.4). In this setting the HMC method gives poor updating parameters (the same initial values) not shown in Table 26.3. This can be explained because the time step $\delta t = 0.0048$ $s$ does not conserve the Hamiltonian function. This time step causes significant numerical errors of the integrator used (VV). In this case, the Hamiltonian function decreases with time which causes a sudden decrease of the acceptance rate (the acceptance rate decreases to less than 1 % when the time step is ($\delta t = 0.0048$ $s$)). The acceptance rate for the S2HMC is 71 %, which is an acceptable rate compared to that for the HMC method.

Table 26.4 shows the modal results and output errors for the different sampling algorithms. The results show that the updated FEM natural frequencies are better than the initial FEM for all methods. The S2HMC provides a smaller final sum error compared to the HMC for both time steps.

In the $\delta t = 0.003$ $s$ case, the error between the first measured natural frequency and that of the initial model is 10.47 %. With the HMC method this error is reduced to 3.84 % and by implementing the S2HMC it was further reduced to 3.73 %. A similar observation can be made for the fourth, fifth, sixth, eighth and ninth natural frequencies. The total initial error was 45.9875 % but after using the HMC and S2HMC methods it reduce to 16.2145 % and 15.00 % respectively. Both methods converge fast and they almost have the same convergence rate (the algorithms start converging in the first 350–400 iterations).

Changing the time step for both methods gives different results. In the case where the time step is increased ($\delta t = 0.0048$ $s$), the S2HMC method improves the most. This can be seen in Table 26.4 where the total error is reduced to 14.2353 % with an acceptance rate of 71 %. However, this is not the case for HMC where the acceptance rate decreases to less than 1 %. Using this time step, the updated vector obtained from the HMC does not improve the FEM results.

The time step, $\delta t = 0.003$ $s$, provides a good acceptance sampling rate for both methods: HMC and S2HMC (99.9 %). Choosing a different time step may reduce the acceptance sampling rate for the HMC method which can significantly affect the results obtained as well as the convergence rate. At the same time, it may provide a good convergence rate for the S2HMC method since the S2HMC provides samples when the time step is large.
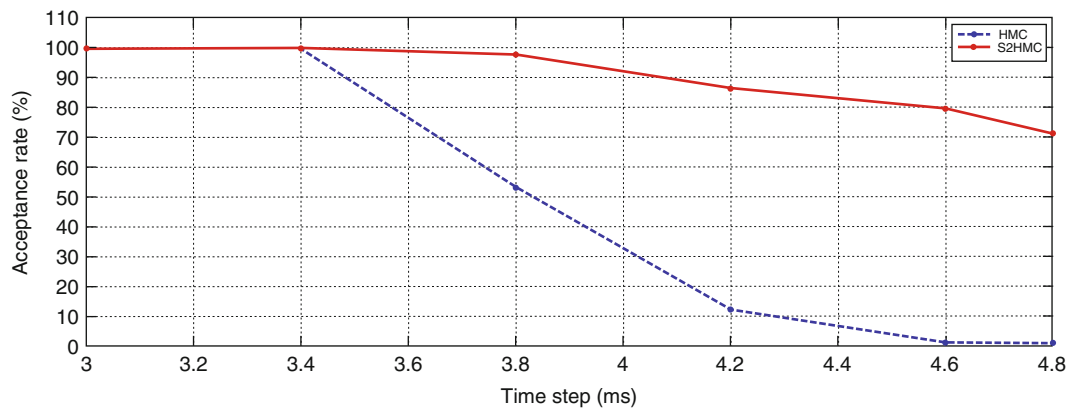
Figure 26.2 shows the acceptance rate when the time step varies between 3 and 4.8 ms. The acceptance rate for both methods is 99.9 % when the time step is 3 ms. The acceptance rate starts decreasing when the time step increases for both methods but this decrease is faster and more significant in the case of the HMC method. When the time step $\delta t = 3.4$ ms, the acceptance rate for the HMC method decreases slightly to 98.7 % and stays the same for the S2HMC methods (99.9 %). When the time step used is 3.8 ms, the S2HMC acceptance rate reduces slightly to 97.8 %. However, it reduces significantly to 53.2 % in the case of the HMC method. Finally, when the time step reaches 4.8 ms, the S2HMC acceptance rate reduces to 71.3 % which is an acceptable rate comparing to that obtained by the HMC method (less than 1 %).

## 26.7 Conclusion

In this paper Bayesian FEM methods are used to update a GARTEUR SM-AG19 aeroplane structure. To evaluate the posterior distribution function, two Markov Chain Monte Carlo (MCMC) sampling techniques have been implemented; the Separable Shadow Hybrid Monte Carlo method (S2HMC) and the Hybrid Monte Carlo (HMC) technique. In the simulation the S2HMC method gave better results than HMC for both implementations when the time step is equal to 3 and 4.8 ms. Moreover, the S2HMC method is more efficient than the HMC method where it provides samples with a large step time which is not the case with the HMC method. The sampling rate for the HMC method significantly decreases when the time step increases. Also, a large time step provides better results when the S2HMC method is used to update an FEM.

**Table 26.4** Modal results and errors for S2HMC and HMC at two different time steps

| Mode | Measured frequency (Hz) | Initial FEM frequencies (Hz) | Error (%) | Frequencies HMC method (Hz) (δt = 3 ms) | Error (%) | Frequencies S2HMC method (Hz) (δt = 3 ms) | Error (%) | Frequencies S2HMC method (Hz) (δt = 4.8 ms) | Error (%) |
|---|---|---|---|---|---|---|---|---|---|
| 1 | 6.38 | 5.71 | 10.47 | 06.135 | 3.84 | 06.142 | 3.74 | 06.1534 | 3.55 |
| 2 | 16.10 | 15.29 | 5.01 | 16.482 | 2.37 | 16.482 | 2.37 | 16.4222 | 2.00 |
| 3 | 33.13 | 32.53 | 1.82 | 32.955 | 0.53 | 33.306 | 0.73 | 32.8793 | 0.76 |
| 4 | 33.53 | 34.95 | 4.23 | 33.716 | 0.55 | 33.530 | 0.000 | 33.535 | 0.015 |
| 5 | 35.65 | 35.65 | 0.0117 | 35.702 | 0.15 | 35.693 | 0.12 | 35.5769 | 0.21 |
| 6 | 48.38 | 45.14 | 6.69 | 47.351 | 2.13 | 47.519 | 1.78 | 47.8262 | 1.15 |
| 7 | 49.43 | 54.69 | 10.65 | 51.638 | 4.47 | 51.710 | 4.61 | 51.8290 | 4.85 |
| 8 | 55.08 | 55.60 | 0.94 | 54.841 | 0.43 | 54.974 | 0.19 | 55.0520 | 0.05 |
| 9 | 63.04 | 60.15 | 4.59 | 62.823 | 0.35 | 63.015 | 0.04 | 63.1771 | 0.22 |
| 10 | 66.52 | 67.56 | 1.57 | 67.458 | 1.41 | 67.467 | 1.42 | 67.4765 | 1.44 |
| Total errors | | | 45.99 | | 16.21 | | 15.00 | | 14.2353 |

**Fig. 26.2** The acceptance rate obtained for different time steps using HMC and S2HMC methods

# References

1. Oñate E (2009) Structural analysis with the finite element method. Linear statics. Volume 1: basis and solids. Springer, Dordrecht
2. Rao SS (2004) The finite element method in engineering, 4th edn. Elsevier Butterworth Heinemann, Burlington
3. Friswell MI, Mottershead JE (1995) Finite element model updating in structural dynamics. Kluwer Academic Publishers, Dordrecht
4. Marwala T (2010) Finite element model updating using computational intelligence techniques. Springer, London, UK
5. Bishop CM (2006) Pattern recognition and machine learning. Springer, New York
6. Yuen KV (2010) Bayesian methods for structural dynamics and civil engineering. Wiley, New York
7. Cheung SH, Beck JL (2009) Bayesian model updating using Hybrid Monte Carlo simulation with application to structural dynamic models with many uncertain parameters. J Eng Mech 135(4):243–255
8. Boulkaibet I, Marwala T, Mthembu L, Friswell MI, Adhikari S (2012) Sampling techniques in Bayesian finite element model updating. Proc Soc Exp Mech 29:75–83
9. Izaguirre JA, Hampton SS, Comput J (2004) Shadow hybrid Monte Carlo: an efficient propagator in phase space of macromolecules. J Comput Phys 200:581–604
10. Neal RM (2000) Slice sampling. Technical report no. 2005. Department of Statistics, University of Toronto
11. Hanson KM (2001) Markov Chain Monte Carlo posterior sampling with the Hamiltonian method. Proc SPIE 4322:456–467
12. Ewins DJ (1984) Modal testing: theory and practice. Research Studies Press, Letchworth
13. Marwala T, Sibisi S (2005) Finite element model updating using Bayesian approach. In Proceedings of the international modal analysis conference, Orlando, FL, USA, 2005. ISBN: 0-912053-89-5
14. Bishop CM (1995) Neural networks for pattern recognition. Oxford University Press, Oxford
15. Ching J, Leu SS (2009) Bayesian updating of reliability of civil infrastructure facilities based on condition-state data and fault-tree model. Reliab Eng Syst Saf 94(12):1962–1974
16. Boulkaibet I, Mthembu L, Marwala T, Friswell MI, Adhikari S (2013) Finite element model updating using the shadow hybrid Monte Carlo technique. Proc Soc Exp Mech 6:489–498
17. Sweet CR, Hampton SS, Skeel RD, Izaguirre JA (2009) A separable shadow Hamiltonian hybrid Monte Carlo method. J Chem Phys 131(17):174106
18. Beskos A, Pillai NS, Roberts GO, Sanz-Serna JM, Stuart AM (2013) Optimal tuning of the hybrid Monte-Carlo algorithm. Bernoulli 19: 1501–1534
19. Carvallo J, Datta BN, Gupta A, Lagadapati M (2007) A direct method for model updating with incomplete measured data and without spurious modes. Mech Syst Signal Process 21(7):2715–2731
20. Datta BN (2002) Finite element model updating, eigenstructure assignment and eigenvalue embedding techniques for vibrating systems. Mech Syst Signal Process 16:83–96
21. Guyon I, Elisseeff A (2003) An introduction to variable and feature selection. J Mach Learn Res 3:1157–1182
22. Link M, Friswell MI (2003) Generation of validated structural dynamic models—results of a benchmark study utilizing the GARTEUR SM-AG19 Testbed. Mech Syst Signal Process 17(1):9–20, COST Action Special Issue
23. Mthembu L (2012) Finite element model updating. Ph.D. thesis, Faculty of Engineering and the Built Environment, University of the Witwatersrand

# Chapter 27
# Bayesian System Identification of Dynamical Systems Using Reversible Jump Markov Chain Monte Carlo

**D. Tiboaca, P.L. Green, R.J. Barthorpe, and K. Worden**

**Abstract** The purpose of this contribution is to illustrate the potential of Reversible Jump Markov Chain Monte Carlo (RJMCMC) methods for nonlinear system identification. Markov Chain Monte Carlo (MCMC) sampling methods have come to be viewed as a standard tool for tackling the issue of parameter estimation using Bayesian inference. A limitation of standard MCMC approaches is that they are not suited to tackling the issue of model selection. RJMCMC offers a powerful extension to standard MCMC approaches in that it allows parameter estimation and model selection to be addressed simultaneously. This is made possible by the fact that the RJMCMC algorithm is able to "jump" between parameter spaces of varying dimension. In this paper the background theory to the RJMCMC algorithm is introduced. Comparison is made to a standard MCMC approach.

**Keywords** Nonlinear dynamics • System identification • Bayesian inference • MCMC • RJMCMC

## 27.1 Introduction

Since their invention in 1953, Markov Chain Monte Carlo (MCMC) sampling methods have been used in many research areas where they have proved their capacity of sampling from probability density functions (PDFs) with complex geometries. In the domain of system identification (SID), MCMC has been extensively used as a tool for parameter estimation. MCMC sampling methods are part of a group of algorithms that, through the use of generated samples from geometrically complicated PDFs, can be implemented to estimate the parameters on which a system depends. Because they make use of PDFs, MCMC algorithms have proven to work extremely well within a Bayesian framework. By joining these two concepts, one can conduct SID for either linear or nonlinear models efficiently. This is of great interest in structural dynamics, at a time when nonlinear models still remain difficult to identify and understand.

The aim of this contribution is to give a better understanding of the RJMCMC algorithm and its application in system identification. A comparison is made between the Metropolis-Hastings (one of the MCMC samplers) algorithm and the RJMCMC algorithm in order to demonstrate the advantages of the later in model selection. The detailed balance principle is explained and it is proven that it is respected by both Metropolis-Hastings and RJMCMC algorithms. The power of RJMCMC is demonstrated through its ability of dealing efficiently with model selection and parameter estimation (simultaneously) for both linear and nonlinear models.

Work of particular relevance in SID, with the use of Bayesian inference and MCMC algorithms, was conducted by Beck and Au [1]. The authors proposed a MCMC approach to sample from PDFs with multiple modes. A Metropolis-Hasting algorithm with a version of the Simulated Annealing algorithm were used together to obtain the "regions of concentration" of the posterior PDF. In [1] there are two different models used to demonstrate the validity of their proposed method, one locally identifiable and one unidentifiable (the locally identifiable model had multiple optimum parameter vectors while the unidentifiable model had a continuum of optimum parameter vectors). Paper [1] tackles the problems of uncertainty and reliability as well. Rather than selecting the model considering the data as was done in previous work with SID, the paper proposes a predictive approach which puts together all possible models according to their probability of being the

---

D. Tiboaca (✉) • P.L. Green • R.J. Barthorpe • K. Worden

Department of Mechanical Engineering, University of Sheffield, Sir Frederick Mappin Building, Mappin Street, Sheffield S1 3JD, UK

e-mail: daniela.tiboaca@sheffield.ac.uk

right choice, given the data. Other work worth mentioning in the fields of Bayesian Inference and MCMC was conducted by Worden and Hensman [2] and Green and Worden [3]. The work discussed in [2] is concerned with offering a Bayesian framework to nonlinear system identification (i.e. parameter estimation and model selection). The importance of the work presented was particularly related to the use of Bayesian inference and MCMC sampling methods on nonlinear systems. Two different systems were simulated to demonstrate the validity of the approach: the Duffing Oscillator and the "Bouc-Wen" hysteresis model. The Metropolis-Hastings MCMC method was used to generate samples, demonstrate parameter correlations and help in model selection. Green and Worden [3] tackles the problems of parameter estimation and also model selection for an existing nonlinear system (i.e. the data used was from a real system rather than a simulated one) using a Bayesian approach through MCMC methods. The nonlinearities introduced were of a Duffing kind (i.e. cubic stiffness) and friction type (using viscous, Coulomb, hyperbolic tangent and LuGre friction models). Other work on MCMC can be found by the interested reader in [4].

Even though MCMC is an impressive approach when it comes to parameter estimation, when system identification is conducted, there is also the need to tackle the model selection issue. As most MCMC methods do not cover model selection, Green [5] introduced Reversible Jump Markov chain Monte Carlo (RJMCMC), a tool that covers both problems of system identification, i.e parameter estimation and model selection. In the past few years there has been a lot of research conducted in model selection using Green's [5] RJMCMC algorithm. Some mentionable work with RJMCMC was done by Dellaportas et al. [6], where they employed RJMCMC on the problems of logistic regression and simulated regression, using a Gibbs sampler, which is an alternative MCMC sampling method used for parameter estimation. In order to demonstrate the computational efficiency of the algorithm on Nonlinear Autoregressive Moving Average with eXogenous (NARMAX) input models, Baldacchino et al. [7] presented a comparison between the forward regression method and the RJMCMC method. A thorough explanation of the RJMCMC method can be found in [8] where Green, the developer of the algorithm, provides further explanations of the method. There is also some work done in signal processing using RJMCMC and it can be found in [9] and [10].

The current paper aims to introduce the RJMCMC algorithm in the context of structural dynamics, explaining how the algorithm works and how it can be related to one particular sampler of MCMC, the Metropolis-Hastings algorithm. The paper is structured as follows. Section 27.2 will be an introduction to Bayesian inference and its relevance in system identification. Section 27.3 introduces the background of MCMC sampling methods, in particular the Metropolis-Hastings sampler, together with its importance in SID. Section 27.4 is concerned with describing background on RJMCMC and linking RJMCMC with the Metropolis-Hastings algorithm (in the context of structural dynamics). The last section, Sect. 27.5, gives insight on future work and concludes the present contribution.

## 27.2    Bayesian Inference

When it comes to structural dynamics, one of the classes of interest is system identification (SID). The main concerns of SID are parameter estimation (every system will depend on a set of parameters) and model selection. Unfortunately, when it comes to identifying systems, uncertainties will inevitably arise. This allows one to know a system only to a probabilistic extent. Probability helps to extract order from randomness and one cannot talk about probability without making use of the concept of a probability distribution. One of the conditions of probability theory is that the probability distribution must always integrate to 1.

In this case, the "random variables" one is interested in are the parameters of the system of interest. There has been defined at this point a set of parameters, $\boldsymbol{\theta} = \{ \theta_1, \theta_2, \ldots, \theta_R \}$ which needed to be estimated.

This paper makes use of probability theory through a Bayesian framework. The Bayesian approach is based on degrees of belief. It is assumed for the moment that one knows the model, denoted by $M$, so that model selection is not a problem for the time being. Bayesian inference is being used to address the issue of parameter estimation. Bayes' theorem states that the posterior will equal the product of the likelihood and prior, divided by the evidence:

$$P(\boldsymbol{\theta}|D, M) = \frac{P(D|\boldsymbol{\theta}, M) P(\boldsymbol{\theta}|M)}{P(D|M)} \tag{27.1}$$

The posterior, $P(\boldsymbol{\theta}|D, M)$, is the probability of the parameters $\boldsymbol{\theta}$ after one has seen some measured data, $D$, the data being whatever response was measured. The evidence, $P(D|M)$, acts as a normalising constant and it ensures the area under the posterior is unity, as required by probability theory. The prior, $P(\boldsymbol{\theta}|M)$, is the probability assigned to the parameters

before one has seen the data. It represents one's knowledge about the system from previous experience. For further reading about priors, relevant information can be found in [11].

The likelihood, $P(D|\theta, M)$, is the probability of seeing the data given the selected model and the parameters that one wishes to estimate. It is typically viewed as the most important function (in spite of its form, the likelihood is not a probability distribution when the data is constant and $\theta$ is varied) to evaluate in Bayes' theorem. Analytical evaluation of the likelihood term is often hard to achieve when one has a set of parameters.

Numerical evaluation of the evidence is not feasible once the number of parameters is bigger than 3, as it gets computationally expensive. MCMC algorithms typically allow one to generate samples without having to evaluate the evidence term.

## 27.3  MCMC Sampling Methods

Markov Chain Monte Carlo methods are sampling algorithms that employ the use of random variables. Their purpose is to solve the issues of generating samples from a probability distribution with complex geometry. MCMC algorithms work by creating a Markov chain of parameter samples, $\theta_i$, whose stationary distribution is equal to the desired, target distribution. The desired distribution is the posterior.

There are many MCMC methods, each with their own advantages and disadvantages, but for the time being and for the purpose of this paper only, the Metropolis-Hastings (MH) method will be explained as it has been the most employed for parameter estimation. One begins by choosing a target density, $\pi(\theta)$, (which in this case will be the posterior parameter distribution). Then, one chooses a proposal density, $Q(\theta'|\theta)$, which is often a multivariate Gaussian (multivariate because one must not forget that $\theta$ is a set of parameters). The next step is to generate a sample $\theta'$ from the proposal density, $Q(\theta'|\theta)$ and a quantity $\alpha$ is built (as shown below). This is known as the Metropolis acceptance rule and it is used to decide if the proposed sample will be accepted or if the chain remains at the current state.

**To generate N parameter samples using the MH algorithm [12]:**

*Initialize*
**for** $n = 1 : N$ **do**
    *Generate $\theta'$ from $Q(\theta'|\theta)$* ;
    *Calculate $\alpha = \frac{\pi(\theta') \, Q(\theta^{(n)}|\theta')}{\pi(\theta^{(n)}) \, Q(\theta'|\theta^{(n)})}$* ;
    **if** $\alpha \geq 1$ **then**
        *−new state accepted;*
        $\theta^{(n+1)} = \theta'$ ;
    **else**
        *−new state accepted with probability $\alpha$* ;
        $\theta^{(n+1)} = \theta^{(n)}$ ;
    **end if**
**end for**

For further insights into the Metropolis-Hastings algorithm, the interested reader is directed to [13].

So far the work presented in this contribution has been about parameter estimation when the model is known. However, it is possible that there are multiple models, $M = \{M^{(1)}, M^{(2)}, \ldots, M^{(l)}, \ldots, M^{(L)}\}$ that may explain the physical behaviour of the experimental system. Even if the models are of the same dimension, they could be differently parameterized. If one takes into consideration that the models might be of different dimensions as well, the issue is amplified. RJMCMC can handle model selection.

## 27.4  RJMCMC

With Reversible Jump MCMC one can address parameter estimation and model selection simultaneously. The way the algorithm works is that it can move/"jump" between parameter spaces of different dimension. The vector set of parameters is not fixed to each model; it can vary in both length and values. Reversible Jump MCMC is capable of "jumping" from one model to the other and select the most likely model while generating parameter samples for that particular type of system.

In the set of models, $M$, the models will be arranged in the order of their complexity; in this particular case a more complex model is defined as one with more parameters.

There are three main moves in the RJMCMC method:

- Birth move—which implies that if the birth move condition is satisfied, the algorithm moves to a model with an additional parameter;
- Death move—which implies that if the death move condition is satisfied, the algorithm "jumps" to a model with one less parameter;
- Update move—which implies that if neither the birth move condition nor death move condition were satisfied, the algorithm remains within the same model and the use of the normal MH algorithm is employed, as presented before, for parameter estimation.

The birth move will be randomly attempted with probability $b_l$, where:

$$b_l = p\min\left\{1, \frac{P(l+1)}{P(l)}\right\} \tag{27.2}$$

The death move will be randomly attempted with probability $d_l$, where:

$$d_{l+1} = p\min\left\{1, \frac{P(l)}{P(l+1)}\right\} \tag{27.3}$$

Lastly, the update move will be randomly attempted with probability $u_l$, so that

$$b_l + d_l + u_l = 1 \tag{27.4}$$

The variable $l$ is an indicator of the current model, the variable $p$ adjusts the proportion of the update move in relation with the birth and death moves, and the probabilities, $P(l)$ and $P(l+1)$, are prior probabilities of the models at iteration $l$ and $l+1$ respectively.

By using Eqs. (27.2) and (27.3) one can see that:

$$\frac{b_l P(l)}{d_{l+1} P(l+1)} = 1 \tag{27.5}$$

It is assumed at this point that one has a set of two potential models of a SDOF system, $M = \{M^{(1)}, M^{(2)}\}$, where model $M^{(1)}$ has one unknown, $\theta$, while model $M^{(2)}$ has two unknown parameters, $\{\theta, \theta_2^{(2)}\}$.

The first model is described by the following equation:

$$m\ddot{y} + c\dot{y} + ky = F \tag{27.6}$$

The second model is described by the following equation:

$$m\ddot{y} + c\dot{y} + ky + k_3^{(2)}y^3 = F \tag{27.7}$$

where $y \in D$ is the data available for the two models and $F \in D$ is the excitation applied to each system. Figure 27.1 is a possible representation of the two models. In the context of the two equations of motion and the models presented above, the mass $m$ is assumed known as well as the damping coefficient, $c$, while $k = \theta$ and $k = \theta$, $k_3^{(2)} = \theta_2^{(2)}$ are the unknown parameters.

**The RJMCMC algorithm is implemented as follows [7, 9]:**

**for** $n = 1 : N$ **do**
    *Get u from $U[0, 1]$ —generates a random number from an uniform distribution*;
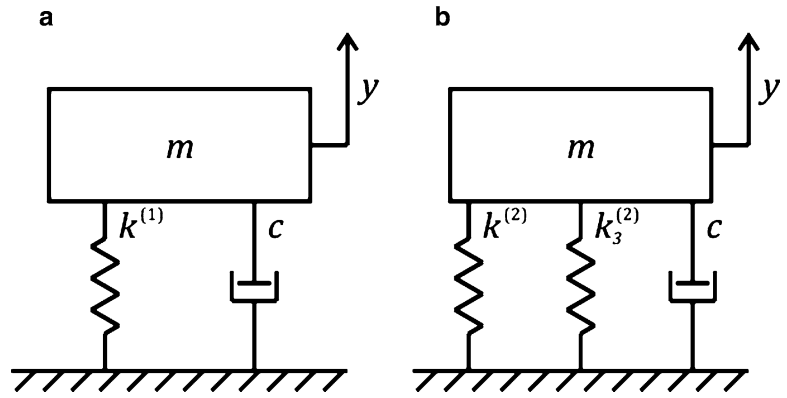    **if** $u \leq b_l^{(n)}$ —birth move condition; **then**
        *—do birth move*
        *Get $u_b$ from $U[0, 1]$ —generates a random number from an uniform distribution*;
        *Evaluate $\alpha_m$ (detailed below)*
        **if** $u_b \leq \alpha_m$ **then**

**Fig. 27.1** (**a**) Linear system, (**b**) Nonlinear system of Duffing type



$-update\ to\ model\ l + 1\ and\ update\ model\ parameters$;
   **else**
    $-stay\ in\ model\ l$;
   **end if**
  **else**
   **if** $u \le (b_l^{(n)} + d_l^{(n)})$ $-death\ move\ condition$; **then**
    $-do\ death\ move$
    $Get\ u_d\ from\ U[0,1]$ $-generates\ a\ random\ number\ from\ an\ uniform\ distribution$;
    $Evaluate\ \alpha'_m$ $(detailed\ below)$
    **if** $u_d \le \alpha'_m$ **then**
     $-go\ to\ model\ l - 1\ and\ update\ model\ parameters$;
    **else**
     $-stay\ in\ model\ l$;
    **end if**
   **else**
    $normal\ MH\ algorithm,\ model\ remains\ at\ l\ state,\ update\ parameters\ only$;
   **end if**
  **end if**
 **end for**

The acceptance probabilities of the birth and death moves, respectively $\alpha_m$, $\alpha'_m$, will be evaluated in Sect. 27.4.2. The generated $u$ dictates what the proposal will be. An important point to remember is that for $l = 1$, there is no death move and for $l = L$, there is no birth move.

With the models introduced at the beginning of this section one notices a difference in dimensions: the first model has only one unknown parameter while the second model has two unknown parameters. This makes it a good point to introduce the concept of detailed balance, a principle that must be respected in order for MCMC or RJMCMC methods to generate samples from the target PDF. This is simpler to demonstrate for MH as the dimension space remains the same. With RJMCMC it becomes harder to maintain because the dimension space varies.

### 27.4.1   Detailed Balance and MH Sampler

The most important aspect of MCMC methods is that detailed balance is respected. In general terms, detailed balance states that at equilibrium every process should be balanced out by its reverse process. In the context of MH sampling, detailed balance ensures that ergodicity and a limiting distribution are respected [5]. Further details on ergodicity and limiting distributions can be found in [12].

The following analysis will make use of the concept of mappings, which are functionals that can relate one state to another [14]. In the current work, the mapping $h : \boldsymbol{\theta} \to \boldsymbol{\theta}'$ is defined as the path from $\boldsymbol{\theta}$ to $\boldsymbol{\theta}'$ with its inverse, $h^{-1}$ being defined as the path from $\boldsymbol{\theta}'$ to $\boldsymbol{\theta}$. Detailed balance states that, for the standard Metropolis-Hastings algorithm, for a model $M$ that depends on two parameters, i.e. $\boldsymbol{\theta} = \{\theta_1, \theta_2\}$

$$\pi(\theta)T(\boldsymbol{\theta} \to \boldsymbol{\theta}') = \pi(\boldsymbol{\theta}')T(\boldsymbol{\theta}' \to \boldsymbol{\theta}) \tag{27.8}$$

The above equation is true no matter what path one chooses to take from $\boldsymbol{\theta}$ to $\boldsymbol{\theta}'$, which in mathematical terms translates into:

$$\int \pi(\boldsymbol{\theta})T(\boldsymbol{\theta} \to \boldsymbol{\theta}') \, d\boldsymbol{\theta} = \int \pi(\boldsymbol{\theta}')T(\boldsymbol{\theta}' \to \boldsymbol{\theta}) \, d\boldsymbol{\theta} \tag{27.9}$$

Putting the above equation in the extended form, results in the following equation:

$$\iint \pi(\boldsymbol{\theta})q(\boldsymbol{\theta}'|\boldsymbol{\theta}')\alpha(\boldsymbol{\theta} \to \boldsymbol{\theta}') \, d\theta_1 d\theta_2 = \iint \pi(\boldsymbol{\theta}')q(\boldsymbol{\theta}|\boldsymbol{\theta}'\alpha)(\boldsymbol{\theta}' \to \boldsymbol{\theta}) \, d\theta_1' d\theta_2' \tag{27.10}$$

Assuming that one had a mapping $h$, $h : \boldsymbol{\theta} \to \boldsymbol{\theta}'$, then a relationship can be expressed using the Jacobian matrix, once the substitution rule was applied:

$$d\theta_1' d\theta_2' = \left| \frac{\partial (\theta_1', \theta_2')}{\partial (\theta_1, \theta_2)} \right| d\theta_1 d\theta_2 \tag{27.11}$$

where

$$\left| \frac{\partial (\theta_1', \theta_2')}{\partial (\theta_1, \theta_2)} \right| = \det \begin{bmatrix} \frac{\partial \theta_1'}{\partial \theta_1} & \frac{\partial \theta_1'}{\partial \theta_2} \\ \frac{\partial \theta_2'}{\partial \theta_1} & \frac{\partial \theta_2'}{\partial \theta_2} \end{bmatrix} \tag{27.12}$$

So, replacing into the previous equation gives the new expression for detailed balance:

$$\pi(\boldsymbol{\theta})q(\boldsymbol{\theta}'|\boldsymbol{\theta})\alpha(\boldsymbol{\theta} \to \boldsymbol{\theta}') = \pi(\boldsymbol{\theta}')q(\boldsymbol{\theta}|\boldsymbol{\theta}')\alpha(\boldsymbol{\theta}' \to \boldsymbol{\theta}) \left| \frac{\partial (\theta_1', \theta_2')}{\partial (\theta_1, \theta_2)} \right| \tag{27.13}$$

Assuming that the mapping $h$ exists, one can look into its form. One could choose to propose new parameters $\theta_1'$ and $\theta_2'$ using Gaussian distributions centred around the current parameters:

$$\theta_1' = \theta_1 + a \tag{27.14}$$

and

$$\theta_2' = \theta_2 + b \tag{27.15}$$

where $a$ and $b$ are generated from a Gaussian. The above is defining the mapping $h$ which can be written now in matrix form as:

$$\begin{Bmatrix} \theta_1' \\ \theta_2' \end{Bmatrix} = \begin{bmatrix} a \\ b \end{bmatrix} + \begin{Bmatrix} \theta_1 \\ \theta_2 \end{Bmatrix} \tag{27.16}$$

Calculating the Jacobian using Eqs. (27.14) and (27.15) one finds that:

$$\frac{\partial \theta_1'}{\partial \theta_1} = 1, \frac{\partial \theta_1'}{\partial \theta_2} = 0, \frac{\partial \theta_2'}{\partial \theta_1} = 0, \frac{\partial \theta_2'}{\partial \theta_2} = 1 \tag{27.17}$$

This means that the determinant becomes equal to 1, no matter what the generated values of $a$ and $b$ might be. The above explanations will hold and prove detailed balance when using the MH algorithm because the dimension matching requirement is met.

### 27.4.2 Detailed Balance and RJMCMC

Detailed balance, when it comes to RJMCMC, gets more complicated to evaluate because each variable is part of a space of different dimension. This implies that one cannot be sure that the space dimension of the right hand side is necessarily equal to the space dimension of the left hand side.

Going back to the two models presented at the beginning of the section, one assumes that the mass $m$ is known and that these will be damped, forced systems with known damping coefficients $c$. This implies that model $M^{(1)}$ is dependent only on the unknown stiffness $k = \theta$ and that the nonlinear model $M^{(2)}$ is dependent on the stiffness $k = \theta$ and the cubic

stiffness that introduces the nonlinear element, $k_3^{(2)} = \theta_2^{(2)}$. One can see that there is a mismatch in dimensions. Jumping from model $M^{(1)}$ to model $M^{(2)}$ is not possible at this point in time as the detailed balance principle is not respected (a space of dimension 1 does not equal a space of dimension 2). In order to match the dimensions one must make model $M^{(1)}$ depend on an additional parameter $\lambda$, such that both spaces are of the same dimension. The parameter $u_b$ influences the choice of $\theta_2'$. This was referred by Green [5] as "dimension matching". Writing the detailed balance for the two models for RJMCMC algorithm, one has:

$$\pi(\boldsymbol{\theta}^{(1)})q(\boldsymbol{\theta}^{(2)}|\boldsymbol{\theta}^{(1)})\alpha(\boldsymbol{\theta}^{(1)} \to \boldsymbol{\theta}^{(2)}) = \pi(\boldsymbol{\theta}^{(2)})q(\boldsymbol{\theta}^{(1)}|\boldsymbol{\theta}^{(2)})\alpha(\boldsymbol{\theta}^{(2)} \to \boldsymbol{\theta}^{(1)})\left|\frac{\partial\,(k^{(2)}, k_3^{(2)})}{\partial\,(k^{(1)}, u_b)}\right| \quad (27.18)$$

where, in this case, $\boldsymbol{\theta}^{(1)} = \{\,k, \lambda\,\}$ and $\boldsymbol{\theta}^{(2)} = \{\,k, k_3^{(2)}\,\}$.

Again, the mapping will be of the following form:

$$\left\{\begin{matrix}\theta \\ \theta_2'\end{matrix}\right\} = \begin{bmatrix}0 \\ \mu\end{bmatrix} + \begin{bmatrix}\theta \\ \lambda\end{bmatrix} \quad (27.19)$$

which assures that the Jacobian, as before, will be unity.

Matching the dimensions above proved that the chosen mapping $h$ is differentiable. Remember from before that the detailed balance only holds if the chosen mapping is differentiable and unique. The mapping was proven to be differentiable but one has to prove that it is $(1 - 1)$. This is very straightforward. There is a theorem, called the inverse function theorem, that confirms that as long as the Jacobian at a point $\theta$ is nonzero (which was proved to be true, the Jacobian is 1 all the time) then the mapping $h$ is unique [14].

The work presented until this point demonstrated detailed balance for the RJMCMC algorithm. This means that one can evaluate the acceptance probabilities of move, $\alpha_m()$ and $\alpha_m'()$, on which the conditions of birth and death depend on. The acceptance probability of the birth move can be evaluated as:

$$\alpha_m(\boldsymbol{\theta}_I^{(1)} \to \boldsymbol{\theta}_I^{(2)}) = \min\left\{\,1, \frac{\pi(\boldsymbol{\theta}_I^{(2)})}{\pi(\boldsymbol{\theta}_I^{(1)})g(\lambda)}\right\} \quad (27.20)$$

where all the values are known or can be estimated and one can notice that the Jacobian is not included as it is always equal to 1, no matter the conditions.

The acceptance probability of the birth move can be written also as:

$$\alpha_m(\boldsymbol{\theta}_I^{(1)} \to \boldsymbol{\theta}_I^{(2)}) = \min\{\,1, r_m\} \quad (27.21)$$

where $r_m$ is the ratio of move and is computed as:

$$r_m = \frac{\pi(\boldsymbol{\theta}_I^{(2)})}{\pi(\boldsymbol{\theta}_I^{(1)})g(\lambda)} \quad (27.22)$$

The acceptance probability of the death move can be evaluated as:

$$\alpha_m'(\boldsymbol{\theta}_I^{(2)} \to \boldsymbol{\theta}_I^{(1)}) = \min\{\,1, r_m^{-1}\} \quad (27.23)$$

At this point one gets a better grasp of the concepts needed to understand the RJMCMC algorithm and the mathematical tools for implementing it with either real or simulated data.

## 27.5   Conclusions

This current contribution introduced the RJMCMC algorithm and provided a comparison between the most widely used MCMC sampling method, the MH, and RJMCMC. While the first one only covers parameter estimation, the RJMCMC method is used to cover both issues of SID, parameter estimation and model selection.

As part of future work on the subject, the authors plan to introduce the RJMCMC in the context of nonlinear dynamical systems and its applicability will be demonstrated through application to an exemplar system for which alternative models exist.

# References

1. Beck LJ, Au S-K (2002) Bayesian updating of structural models and reliability using markov chain monte carlo simulation. J Eng Mech 391:128–380
2. Worden K, Hensman JJ (2012) Parameter estimation and model selection for a class of hysteretic systems using bayesian inference. Mech Syst Signal Process 32:153–169
3. Green PL, Worden K (2013) Modelling friction in a nonlinear dynamic system via bayesian inference. In: IMAC XXXI Proceedings
4. Carlin BP, Chib S (1995) Bayesian model choice via markov chain monte carlo methods. J Roy Stat Soc Ser B (Methodological) 57:473–484
5. Green PJ (1995) Reversible jump markov chain monte carlo computation and bayesian model determination. Biometrika 82:711–732
6. Dellaportas P, Ntzoufras I, Forster JJ (2002) On bayesian model and variable selection using mcmc. Stat Comput 36:12–27
7. Baldacchino T, Kadirkamanathan V, Anderson SR (2013) Computational system identification for bayesian narmax modelling. Automatica 49:2641–2651
8. Green PJ, Hastie DI (2012) Model choice using reversible jump markov chain monte carlo. Statistica Neerlandica 309–338
9. Andrieu C, Doucet A (1999) Joint bayesian model selection and estimation of noisy sinusoids via reversible jump mcmc. IEEE Trans Signal Process
10. Andrieu C, Doucet A, Djuric PM (2001) Model selection by mcmc computation. Signal Process 81:19–37
11. Geinitz S (2009) Prior covariance choices and the g prior.
12. MacKay DJC (2003) Information theory, inference, and learning algorithms. Cambridge University Press, Cambridge
13. Chib S, Greenberg E (1995) Understanding the metropolis-hastings algorithm. Am Stat
14. Schutz B (1980) Geometrical methods of mathematical physics. Cambridge University Press, Cambridge

# Chapter 28
# Assessment and Validation of Nonlinear Identification Techniques Using Simulated Numerical and Real Measured Data

**A. delli Carri and D.J. Ewins**

**Abstract** In the last ten years, particular effort has been spent dealing with the identification of multi degrees of freedom nonlinear systems. The ever increasing complexity of the structures has gone along with the increasing sophistication of mathematical techniques, so the structural dynamicist often finds himself with many methods to choose from, each of which is—however—capable of addressing just subsets of the whole problem.

In IMAC XXXI, a new (modal) parameters identification toolbox approach was introduced, capable of dealing with the different aspects of the nonlinear phenomenon, namely: detection, characterisation, localisation and quantification. A review of available methods was also presented.

This paper brings forward the previous idea, assembling a functional toolbox of techniques useful to estimate the dynamics of nonlinear structures using common test practices, without requiring exotic excitations or setups. These techniques are validated against a 4DOF numerical test case with multiple nonlinearities and, finally, applied to a real aeronautical test structure supplied by industry.

**Keywords** Review • Nonlinear modal testing • Reverse path • Subspace identification • Experimental data

## 28.1 Introduction

The analysis of nonlinear systems has evolved considerably over the last few years, driven by the ever increasing industry needs for accuracy and reliability in the understanding and description of their dynamical systems. In general, engineering structures may be regarded as largely linear in their dynamic behaviour, but they often include a discrete number of features or elements which are distinctly nonlinear, such as joints. The basic concept that applies is that for every system there is considered to be an Underlying Linear Model (ULM)—which is usually the model that applies at zero displacement response—to which there are non-linear elements added.

During IMAC XXXI a toolbox approach was presented [1] designed to extract different levels of information from a nonlinear system using different methodologies and algorithms. Each piece of information extracted represents a different aspect and answers a different question about the nonlinear phenomenon, namely:

- Detection: is there nonlinearity?
- Characterisation: which type of nonlinearity is it?
- Localisation: where is the nonlinearity?
- Quantification: what are the nonlinear parameters?

---

A. delli Carri (✉)
University of Bristol, Bristol BS8 1TH, UK
e-mail: a.dellicarri@bristol.ac.uk

D.J. Ewins
University of Bristol, Bristol BS8 1TH, UK

Imperial College London, London SW7 2AZ, UK
e-mail: d.ewins@imperial.ac.uk

| Method | Excitation | Response | D | C | L | Q | E | Notes |
|---|---|---|---|---|---|---|---|---|
| Hg | any (2) | any | ✓ | | | ✓ | | SDOF only |
| HT | any | any | ✓ | | | | | Indirect detection. May fail in experimental tests |
| RP | broadband | disp | ✓ | ✓ | ✓ | ✓ | [2] | Subject to numerical issues. Frequency domain |
| SVD | any | disp, vel, acc | ✓ | ✓ | ✓ | ✓ | | Massive request of input data |
| CFRF | stepped sine | disp (any) | ✓ | | | ✓ | ✓ | SDOF only. Many test runs required |
| NNM | harmonic(n) | disp (acc) | ✓ | ✓ | | ✓ | ✓ | SDOF only. Complex theory. Peculiar test |
| RFS | any | disp, vel, acc | ✓ | ✓ | | ✓ | ✓ | SDOF only. Massive request of input data |
| NOFRFs | broadband (2) | acc | | | ✓ | | ✓ | Complex theory. Only works for inline DOF |
| FNSI | broadband | any | | | | ✓ | [3] | Frequency domain |
| | | | | | | | | |
| • | • | • | • | • | • | • | • | • |

**Fig. 28.1** Considered methods and their categorisation: detection (D), characterisation (C), localisation (L), quantification (Q), and experimental evidence (E)

Figure 28.1 collects all the different methods that have been gathered since the start of this work. It represents a non-exhaustive database of all the different nonlinear analysis methods currently available in literature. The scope of this paper is to widen the number of considered methods and to select the best ones for inclusion in a future nonlinear modal testing toolbox for use in an industrial environment.

The criteria for the inclusion in this toolbox are generally linked to the requirements of the industrial framework, which demands reliable performance and low cost. This consideration leads to the exclusion of methods that use many test runs or require non-standard setups or measurements as well as ones that are too simple to be of any use for a complex MDOF dynamical system.

Based on these assumptions, two of the methods from Fig. 28.1 were chosen for inclusion in the toolbox: (a) the Reverse Path method (RP) has all the capabilities to identify the nonlinear phenomena but it performs poorly in the quantification step, and (b) the Frequency-domain Nonlinear Subspace Identification (FNSI) which is able to quantify the nonlinear coefficients but it needs knowledge about the location and functional form of the nonlinearities, so the two methods complement each other.

## 28.2 A Review of the Selected Methods

In this section, two of the methods presented in Fig. 28.1 will be reviewed in a little more detail: the Reverse Path method has already been covered in the previous iteration of this work [1] but it is now presented with more insight, while the Frequency-domain Nonlinear Subspace Identification is a recent addition.

These two methods together are able to cover many of the different aspects of the nonlinear phenomenon—from detection to quantification—using common test practices, without requiring exotic excitation or setups. More important, they both require time histories data but exploit the frequency domain which leads generally to faster estimation and lower computing burden.

### 28.2.1 Reverse Path Method (RP)

The Reverse Path method was initially proposed by Bendat in 1990 [4]. The method is known as Reverse Path since the input and output quantities are reversed (Fig. 28.3). The processing is performed in the frequency domain using conventional Multiple-Input-Single-Output (MISO) techniques and estimates of both the Underlying Linear Model and the nonlinearity locations and types are obtained from a single analysis.

**Fig. 28.2** A system with grounded nonlinearity described by a nonlinear operator g(.) and coefficient p
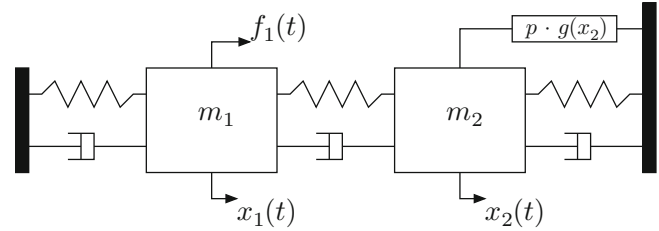


**Fig. 28.3** The 2DOF system is broken into two MISO analyses
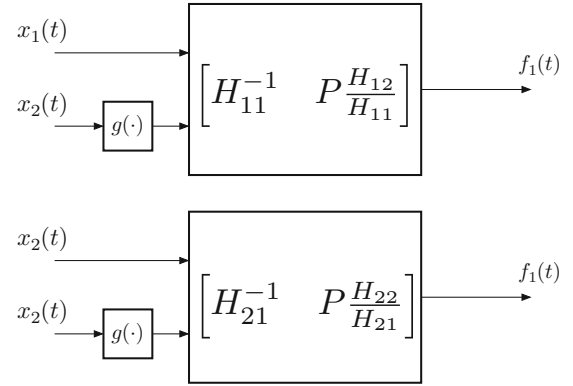


To explain the reverse path technique better, the simple 2DOF system presented in Fig. 28.2 is used. This system can be modeled in the frequency domain as:

$$\left\{ \begin{array}{c} X_1 \\ X_2 \end{array} \right\} = \left[ \begin{array}{cc} H_{11} & H_{12} \\ H_{21} & H_{22} \end{array} \right] \left\{ \begin{array}{c} F_1 \\ -P \cdot \mathscr{F}(g(x_2)) \end{array} \right\} \tag{28.1}$$

The matrix formulation can then be expanded in the equations:

$$\begin{array}{c} X_1 \cdot H_{11}^{-1} + \frac{H_{12}}{H_{11}} \cdot P \cdot \mathscr{F}(g(x_2)) = F_1 \\ X_2 \cdot H_{21}^{-1} + \frac{H_{22}}{H_{21}} \cdot P \cdot \mathscr{F}(g(x_2)) = F_1 \end{array} \tag{28.2}$$

Each of these equations can be rearranged in a reverse-path fashion with the forces at the output, actually forming a set of MISO analyses, one per DOF (Fig. 28.3).

The inputs of the MISO analyses consist of a single measured DOF and all the nonlinearities present in the system. If the location or the type of nonlinearity is unknown, one can feed guesses into the system and use the multiple coherence function (28.3) as an index for the goodness of estimation.

The multiple coherence function is a linear relationship that measures the causality between one output and all the input signals. As the standard coherence, it ranges between 0 (no correlation) and 1 (the output is completely caused by the input). The coherence function for a nonlinear system will always be less than unity because of the linear nature of the coherence operator.

$$\gamma^2 = \frac{G_{FX} G_{XX}^{-1} G_{FX}^H}{G_{FF}} \tag{28.3}$$

As long as the guesses are good, the multiple coherence function will continue to improve over the frequency range and eventually it will be maximised when all the nonlinearities have been characterised and localised (Fig. 28.11).

The guessing process could be totally blindfolded, iterating over previously defined locations and nonlinear characteristics, but it also permits the user to exploit any knowledge of where or what type of nonlinearity might be present. Once the best coherence has been achieved, the selected guesses can be used to quantify their coefficients.

The Reverse Path method needs time histories of forces, displacements and velocities acquired using a broadband excitation. Time histories are needed because they have to pass through the nonlinear operator before they get transformed into the frequency domain and fed to the system. Displacements are used to construct stiffness-based nonlinearities and

velocities are used to construct damping-based ones. To retrieve displacements and velocities one could generally integrate the accelerations with appropriate filtering; this reduces the accuracy of the quantification using the reverse path method, but does not affect the localisation and characterisation steps.

The Reverse Path method has been shown to work well in experimental environments [2] and has been applied to various mechanical systems with zero-memory nonlinearities, indicating that the method is robust and well suited for use in engineering applications.

### 28.2.2 Frequency-domain Nonlinear Subspace Identification Method (FNSI)

The FNSI method is a natural extension of the well-known Subspace Identification by Van Overschee and De Moor [5] to nonlinear systems. The main assumption is that the nonlinearities are characterised and localised and there exists an Underlying Linear Model of vibration in which these nonlinearities act. The method is capable of addressing the quantification step in a nonlinear identification, contextually retrieving the frequency response functions of the Underlying Linear Model.

A nonlinear system is governed by the differential equation of motion:

$$M\ddot{y}(t) + C\dot{y}(t) + Ky(t) + g\left(y(t), \dot{y}(t)\right) = f(t) \tag{28.4}$$

Where $M, C, K \in \mathbb{R}^{r \times r}$ are the mass, damping and stiffness matrices, respectively; $x(t)$ and $f(t) \in \mathbb{R}^r$ are the generalised displacement and external forces vectors; $g(t) \in \mathbb{R}^r$ is the nonlinear restoring force vector, and $r$ is the number of degrees of freedom of the structure obtained after spatial discretisation. The effect of the $m$ discrete nonlinearities are modelled using the summation:

$$g\left(y(t), \dot{y}(t)\right) = \sum_{i=1}^{m} \alpha_i \cdot W_i \cdot q_i\left(y(t), \dot{y}(t)\right) \tag{28.5}$$

Each term contains information about the unknown nonlinear coefficient $\alpha_i \in \mathbb{R}$, the (known) location of nonlinearity $W_j \in \mathbb{R}^r$ and the corresponding (known) functional form $q_i(\cdot)$.

Equation 28.4 is then cast in a first-order state-space form

$$\begin{cases} \dot{x}(t) = Ax(t) + B^{nl}q(t) + Bf(t) \\ y(t) = Cx(t) + Df(t) \end{cases} \tag{28.6}$$

with the state vector $x = \left(y^T \ \dot{y}^T\right)^T$ and the nonlinear coefficient matrix $B^{nl} \in \mathbb{R}^{r \times m}$ alongside the classical $A, B, C, D$ matrices of the state-space realisations.

Given $f(t)$ and $y(t)$, the FNSI method is able to determine the five matrices $A, B, C, D, B^{nl}$.

The estimation of the nonlinear coefficients $\alpha_i$ and Underlying Linear Model FRFs is subsequently carried out via the recasting of the equations from state space to physical space. The estimated nonlinear coefficients are frequency-dependent and complex, but a good estimation should deliver real-valued constant coefficients. More information on the algorithm can be found in [6].

## 28.3    Simulated Numerical Results

The algorithms were first tested with a simple numerical 4DOF system featuring two nonlinearities (Fig. 28.4). All the parameters are listed in Table 28.1.

The system is first excited at low level of vibration (0.1 N) exhibiting linear characteristics with a clearly-defined FRF. At higher vibration levels (10 N) the difference in the FRF become significant, indicating a nonlinear behaviour (Fig. 28.5).

For the purpose of identification, the 4DOF system in Fig. 28.4 was excited with a random signal at 10 N RMS and displacements computed for each mass. The Sampling Frequency was set to 300Hz. Figure 28.6 shows the measured FRF and coherence of the system: it is clear that the curves suffer from deterioration and this is almost certainly due to the nonlinear behaviour.
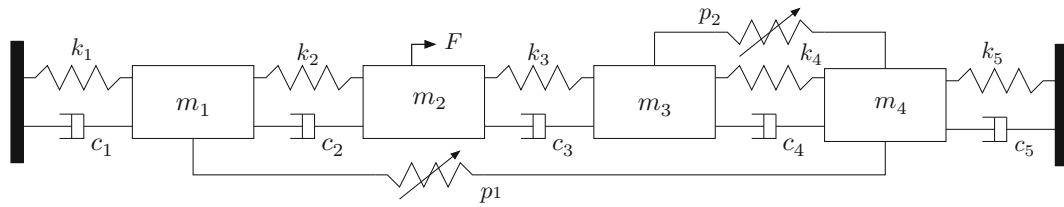
**Fig. 28.4** Simulated numerical case featuring non-grounded cubic and quadratic stiffness nonlinearities

**Table 28.1** Parameters for simulated numerical case

| Mass | | | Stiffness | | | Damping | | |
|---|---|---|---|---|---|---|---|---|
| $m_1$ | 1 | Kg | $k_1$ | 1e4 | N/m | $c_1$ | 10 | Ns/m |
| $m_2$ | 2 | Kg | $k_2$ | 1.5e4 | N/m | $c_2$ | 10 | Ns/m |
| $m_3$ | 2 | Kg | $k_3$ | 8e3 | N/m | $c_3$ | 5 | Ns/m |
| | | | $k_4$ | 2e5 | N/m | $c_4$ | 10 | Ns/m |
| | | | $k_5$ | 1e4 | N/m | $c_5$ | 10 | Ns/m |
| | | | p1 | 2e14 | N/m$^3$ | | | |
| | | | p2 | 1e9 | N/m$^5$ | | | |

**Fig. 28.5** Low and high level FRFs for the 4DOF numerical system (driving point)
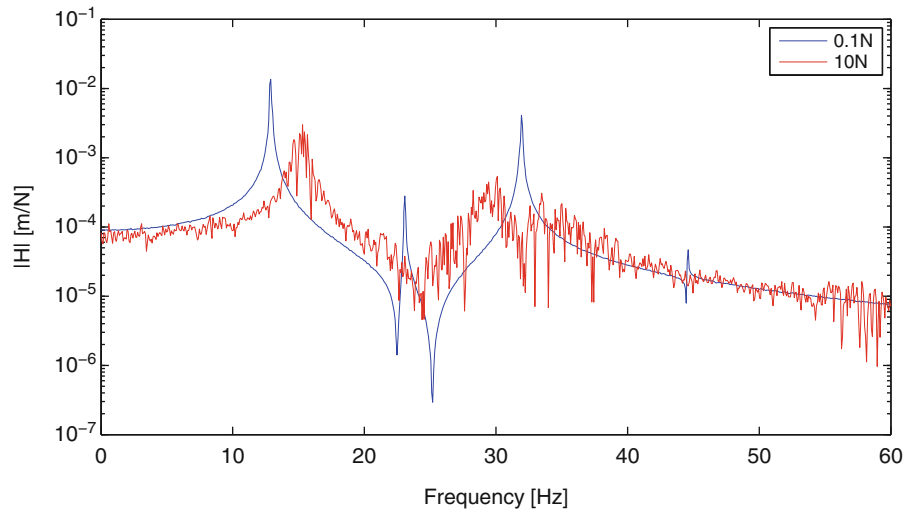


**Fig. 28.6** FRF (*blue*) and coherence (*green*) of the numerical 4DOF system excited at 10 N RMS (Colour figure online)
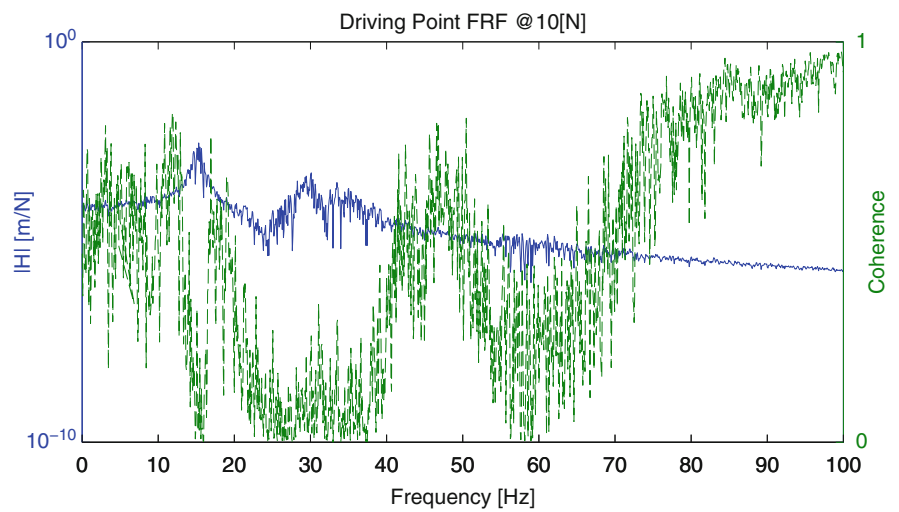
**Fig. 28.7** The worst coherent
point is DOF4, which features
two nonlinearity attached
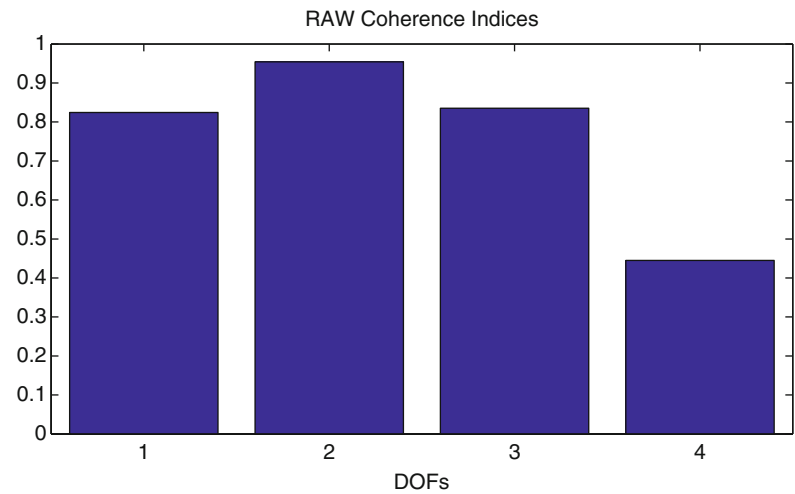


**Fig. 28.8** The MISO system is
fed with nonlinear terms
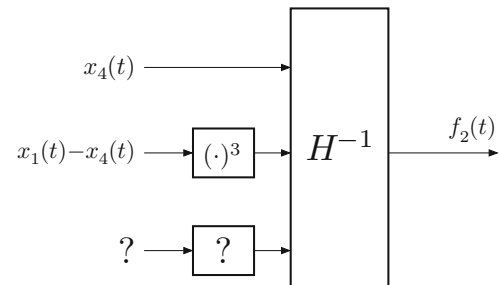


The Reverse Path method seeks to improve the coherence by breaking the MIMO system into several MISO equivalents, feeding in the right combination of nonlinearity location and characteristic for each. Each MISO system exhibits a different coherence level, but since for speed purposes it is preferable to analyse just one MISO system, one shall focus on the DOF that exhibits the worst overall coherence level. This can be seen in Fig. 28.7 where the worst coherent point is acknowledged to be DOF#4.

The next step is to try each nonlinear location and characteristic in a blindfolded fashion and look for the combinations that leads to the most improved coherence index. The left side of Fig. 28.10 depicts the first iteration of this step: as one can notice, the best improvement in the worst coherence is found with a cubic nonlinearity between DOF#1 and DOF#4. This is accurate, according to Fig. 28.4 and Table 28.1.

The second iteration is now carried out holding the first one as input to the MISO system (Fig. 28.8). The results are shown in the right side of Fig. 28.9, revealing another nonlinearity between DOF #3 and #4 with a fifth-order characteristic. Again, this result is accurate according to Fig. 28.4 and Table 28.1.

Once this step is concluded, the coherence indices are maximised. That means that the output of the MISO system can be totally explained by linear and nonlinear inputs, so the iterative process can stop (Fig. 28.10).

Once the nonlinearities are fully localised and characterised, it is possible to extract the Underlying Linear Model from each MISO analysis (Fig. 28.11) and to quantify the nonlinear coefficients (Fig. 28.12).

The nonlinear coefficients of the system considered hereare constant over the frequency range and real-valued, whereas the parameters extracted by the reverse path method are complex-valued and non-constant over the frequency range, even for noiseless data. This leads to a heavy underestimation of the parameters and the need for a proper quantification routine.

The quantification step is then addressed by the Frequency-domain Nonlinear Subspace Identification technique presented in Sect. 28.2.2 above. This algorithm needs to know in advance the locations and characteristics of nonlinearities, which have already been provided by the Reverse Path method. The FNSI method produces a stabilisation diagram (Fig. 28.13) from which the user can select the appropriate order to be modelled.

In this case, four columns of stable poles are easily recognisable and the FNSI algorithm can then reconstructs the underlying linear FRFs (Fig. 28.14).

The extracted nonlinear coefficients are complex-valued and generally non-constant. A good estimation should, however, lead to mostly real-valued coefficients which are fairly constant over the frequency range. Figure 28.15 shows that the real part of the extracted coefficients are constant over frequency, excluding some small regions around the resonances. Also, the
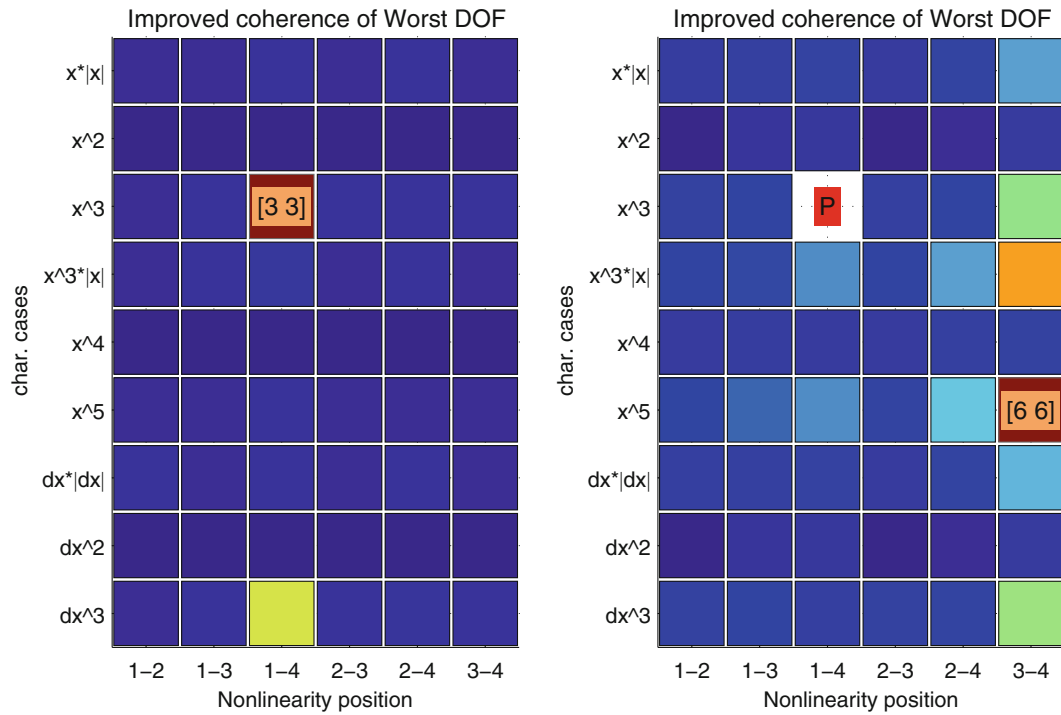
**Fig. 28.9** First (*left*) and second (*right*) iteration of the combined characterisation-localisation step of the reverse path method

**Fig. 28.10** Coherence indices for each DOF before and after the processing. Since the processed coherences approach unity, the iterative procedure can be stopped
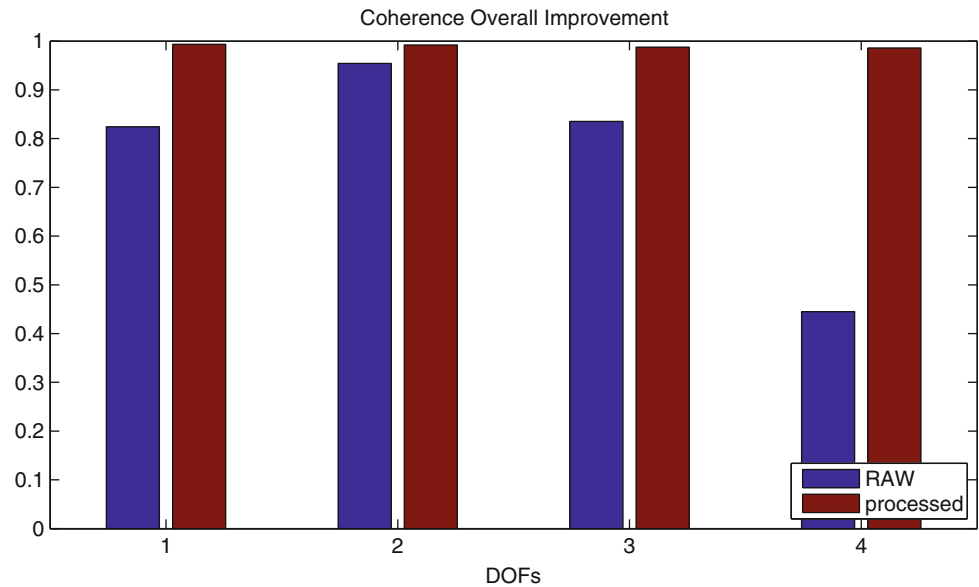


magnitudes of the imaginary parts are more than three order smaller than their real parts, so this can be regarded as a valid estimation. Since a single value for each coefficient is required, the mean value of the real part of each coefficient is extracted and compared with the actual value from Table 28.1, confirming the goodness of the estimation.

One of the other checks that can be performed to assess the quality of the identification is to compare the extracted Underlying Linear Model with the corresponding linear model obtained by stripping out the nonlinearities from the system. In Fig. 28.16 one can notice an almost perfect correspondence between the Underlying Linear Model and the real linear one.
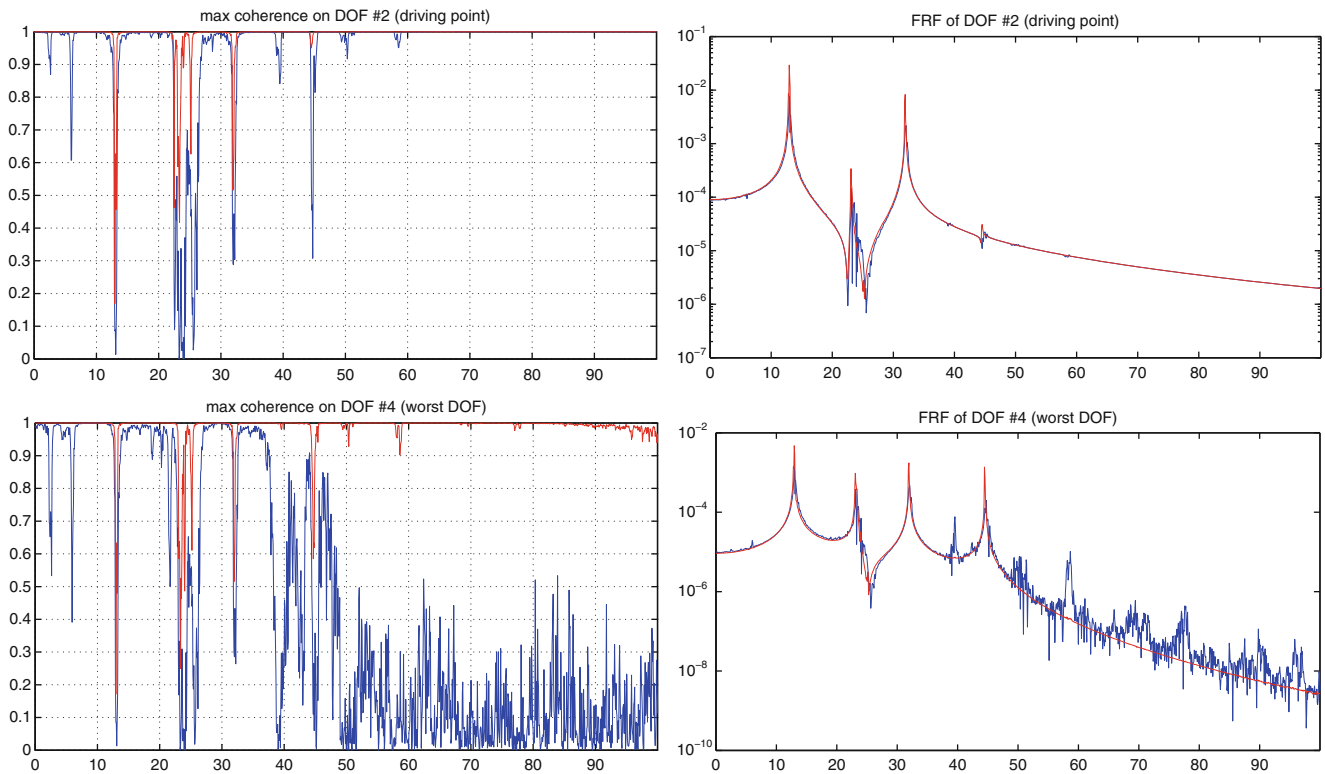
**Fig. 28.11** FRF of driving point and worst coherent DOF before (*blue*) and after processing (*red*) (Colour figure online)

**Fig. 28.12** Real parts of nonlinear coefficients extracted via reverse path
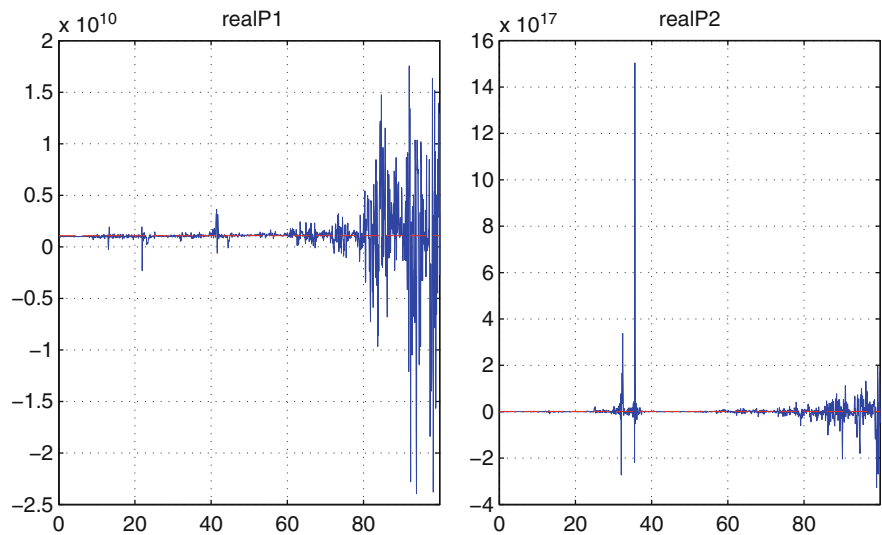


## 28.4 Real Measured Data Results

To ensure the algorithms could properly be used in an industrial environment, components from a tail rotor test rig provided by AgustaWestland were used to assess the congruency of the algorithms in localising, characterising and quantifying the nonlinear effects. Since the rig is essentially symmetric, only its left side was instrumented (Fig. 28.17) taking into account its main parts: the blade (5 accelerometers), the trunnion (4 accelerometers) and the spider plate on the hub (1 accelerometer). The force gauge is located on point #111 of the blade, in the direction out of the rig plane.

Figure 28.18 depicts the FRF of the tail rotor rig excited with random signals at low and high level. It can be easily noticed that there is a clear difference between the two curves, thus indicating a strong nonlinear behaviour.
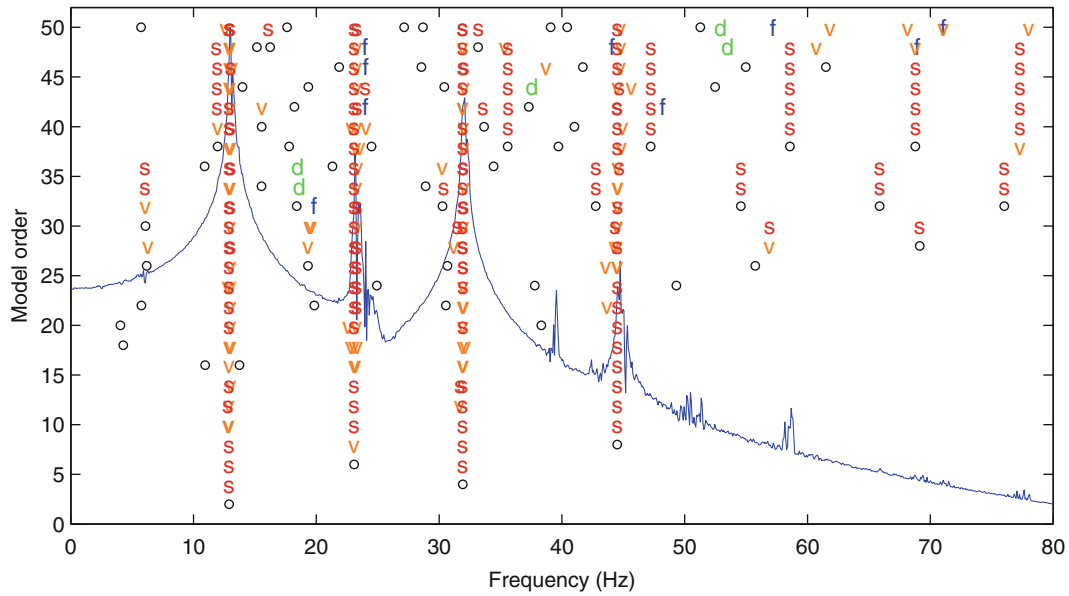
**Fig. 28.13** Stabilisation diagram for the 4DOF system
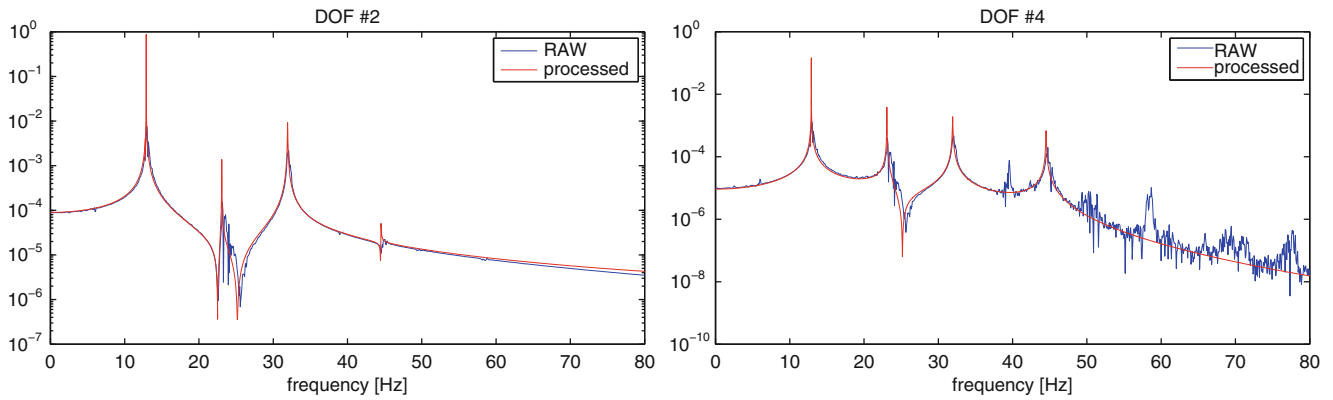


**Fig. 28.14** Reconstructed underlying linear FRFs (*red*) compared to the raw system FRFs (*blue*) for DOF#2 (*left*) and DOF#4 (*right*) (Colour figure online)
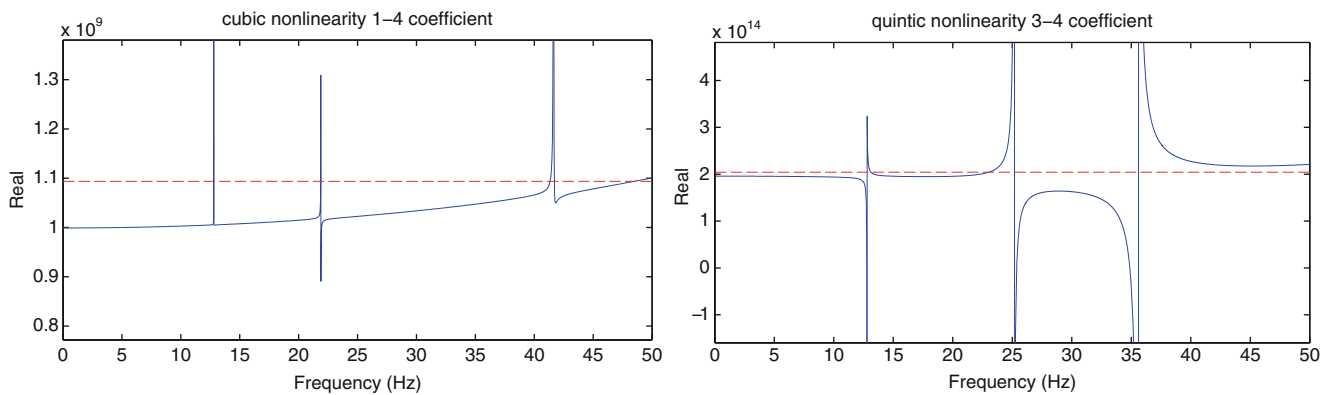


**Fig. 28.15** Estimated nonlinear coefficients (*solid*) and their mean values (*dashed*) extracted with FNSI

For the purpose of testing, the rig was forced with a Random high-level excitation. The processing was divided in two subset depending on the directions, in order to simplify the process and speed it up.

**Fig. 28.16** Comparison between raw FRF (*blue*, *dotted*) processed FRF (*red*) and Underlying Linear Model FRF (*black*, *dash-dot*) (Colour figure online)
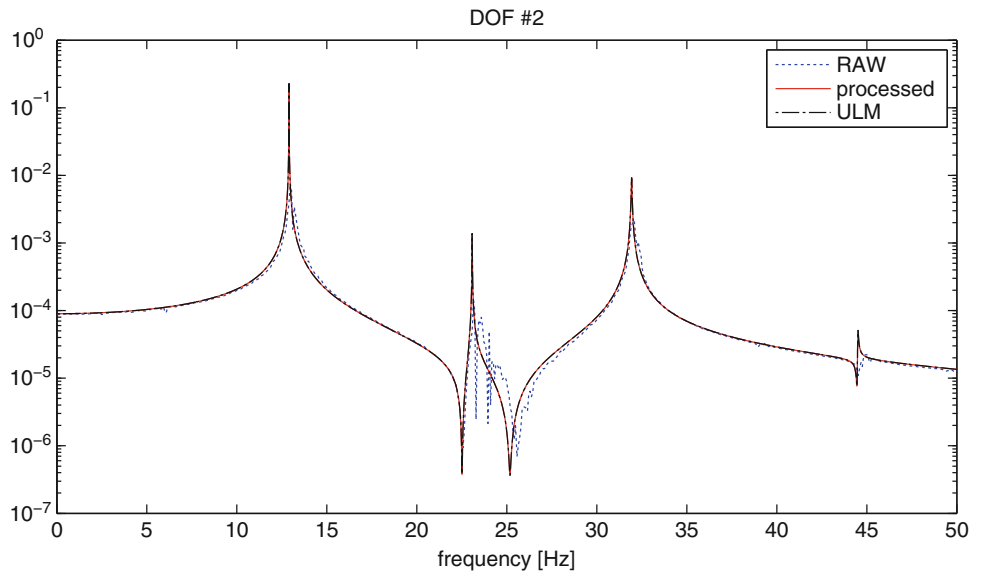


**Fig. 28.17** AW rig instrumentation: blade (*blue lines*), trunnion (*red lines*) and plate (*green line*) (Colour figure online)
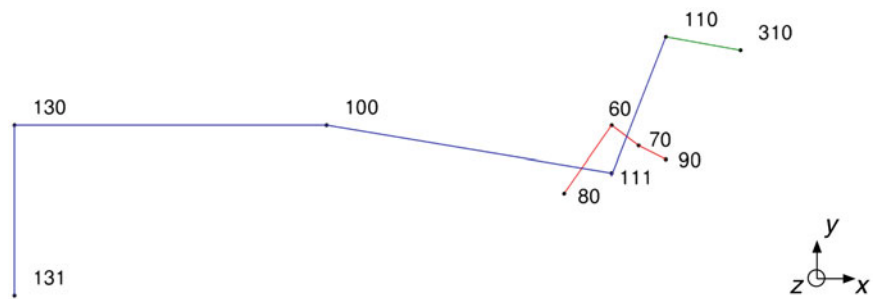


**Fig. 28.18** Low and high level FRFs for the tail rotor rig
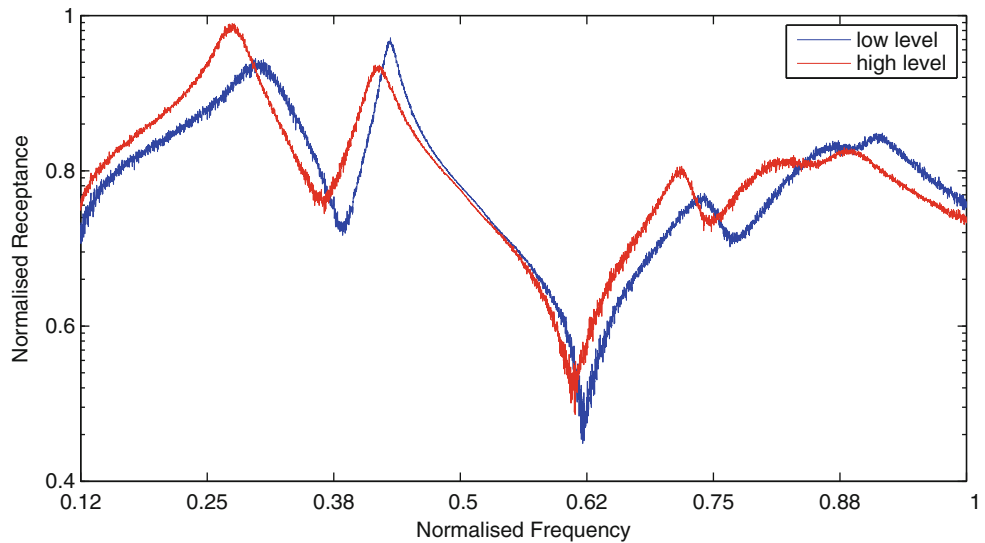


The first part of the process involved the y-directions. The first iteration shows that the quadratic stiffness and quadratic damping effects are dominating the structure, and the first located nonlinearity is the quadratic stiffness between point #60 and point #100. The second iteration locates also a cubic effect between point #60 and #100, thus suggesting a complex polynomial nonlinearity in that location. This is later confirmed by the third and fourth iterations which add a fourth and fifth order to the polynomial between the same points. Lastly, the fifth iteration finds the source of the quadratic damping between the driving point #111 and point #70. At this point the coherence threshold of 97 % is met (Fig. 28.19) and the code stops searching for nonlinearities (Fig. 28.20).

**Fig. 28.19** Coherence overall improvement for Y-analysis
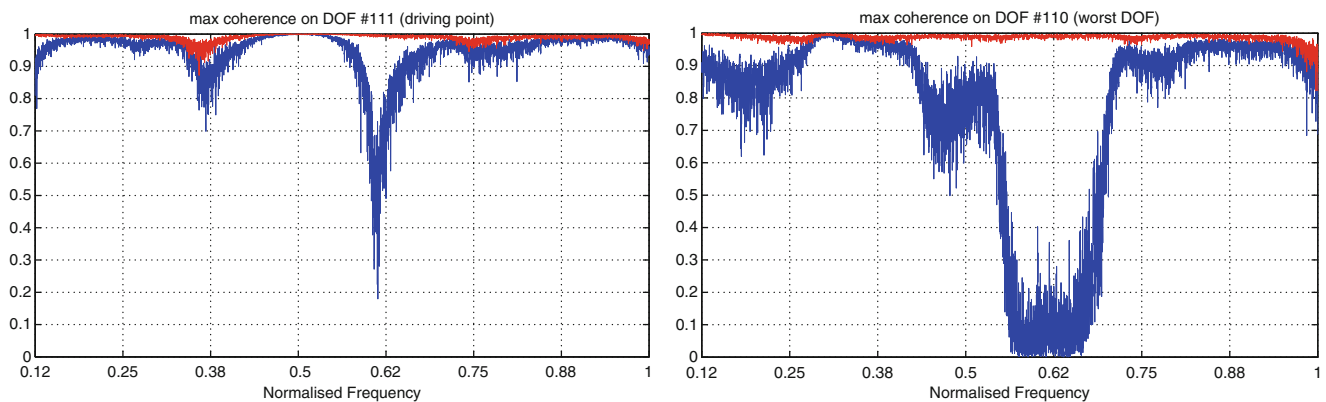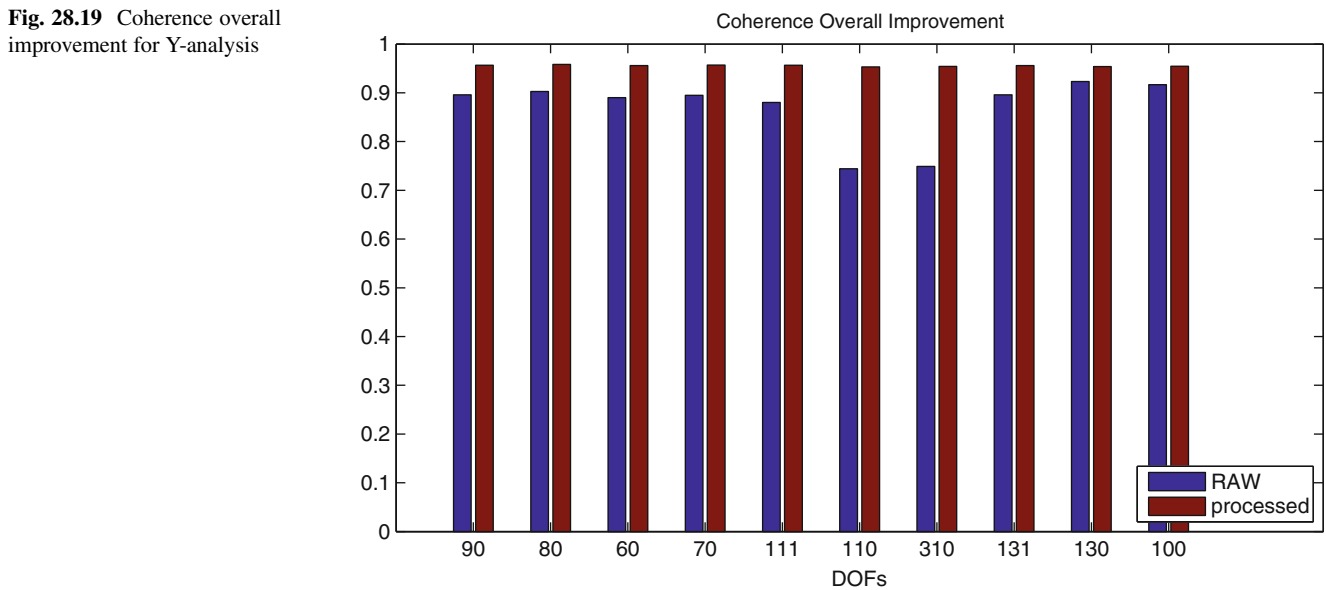


**Fig. 28.20** Coherence improvements for best (*left*) and worst (*right*) behaving DOF for Y-analysis

The second part of the processing involves the z-direction DOF: the first through third iterations find a high order polynomial nonlinear effect modelling the shearing effect of the joint connecting point #60 to point #310, while the fourth and fifth iterations find a third order polynomial damping effect that models the shear of the elastomeric bearing connecting point #70 and point #111. The coherence improved over all the DOF (Fig. 28.21) thus assessing the reliability of the localisation and characterisation steps (Fig. 28.22).

The quantification step is then performed using the FNSI method. The stabilisation diagram is very cluttered but it shows some generally stable columns of poles (Fig. 28.23).

It is hard to interpret the diagram, therefore the singular values are used to help the user to choose the right model order (Fig. 28.24). The 18th order is the one that models 95 % of the system, so this is chosen as the system order.

The Underlying Linear Model FRF of the driving point is compared to the respective low and high levels FRF of the real system in Fig. 28.25.

## 28.5  Conclusions and Future Work

This paper represents the second iteration of a work first introduced [1] with the presentation of a novel toolbox approach to the identification of nonlinear dynamic systems. Most of the methods presented in literature were previously assessed versus numerical simulated data. In this paper, the most promising methods have been assessed in an experimental environment in order to evaluate their stability and applicability to real problems.

**Fig. 28.21** Coherence overall improvement for Z-analysis
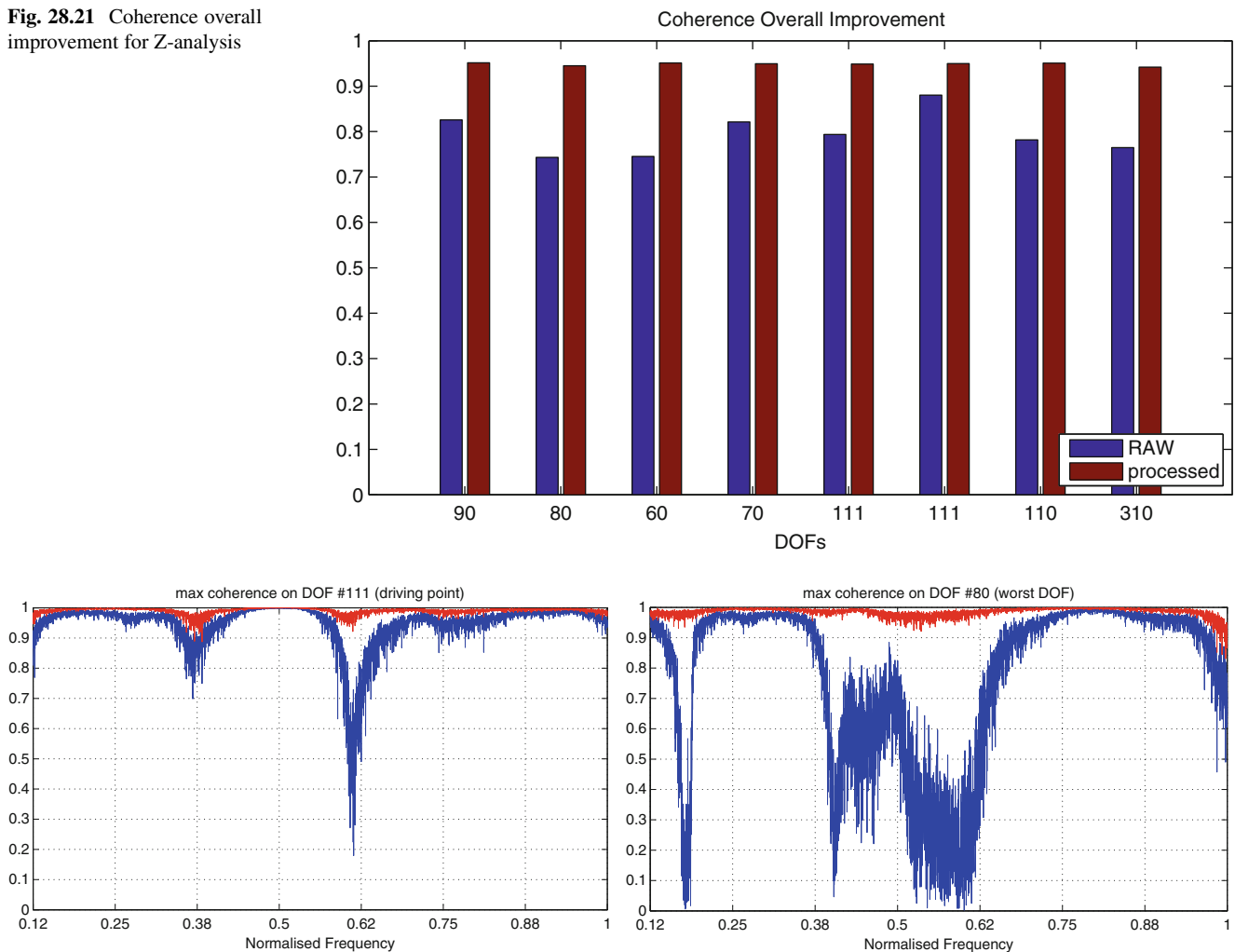


**Fig. 28.22** Coherence improvements for best (*left*) and worst (*right*) behaving DOF for Z-analysis

The *Reverse Path* is a powerful algorithm capable of both characterisation and localisation of nonlinear elements. Its weakest point seem to be the trial-and-error methodology of the guessing step which, combined with the fact there is no unique solution to the nonlinear problem, may lead to erroneous estimations. Another limitation is that this method is only capable to address zero-memory nonlinearities such polynomial ones, and it may fail to identify the effects that falls outside this condition. One way in which the Reverse Path method could be enhanced is by using the so-called Conditioned Reverse Path [7] which takes into account the linear relationship between nonlinearities and linear DOF, thus eliminating numerical illness of the matrices and leading to better estimations.

The *Frequency-domain Nonlinear Subspace Identification* is a method that extends the classical Subspace Identification to nonlinear systems and it is able to quantify the nonlinear coefficients once the locations and functional forms of nonlinearities are known. Its main limitation is the difficulty to properly interpret the crowded stabilisation diagram that comes from an experimental test, thus the need for a routine that streamlines this process for the final user.

Both algorithms can be used together in order to identify the nonlinear characteristics of a system fully, and this is shown very well with the simulated numerical data (Sect. 28.3). Dealing with an experimental case, much more attention must be given to the interpretation of the results, since the answers are not known a priori. There is still an open question about the proper validation of the methods against experimental data: the easiest check that can be performed is the comparison of the extracted Underlying Linear Model FRFs with low-level excitation FRFs, but this may not always be possible because of the very nature of some nonlinearities, such as clearance or friction.
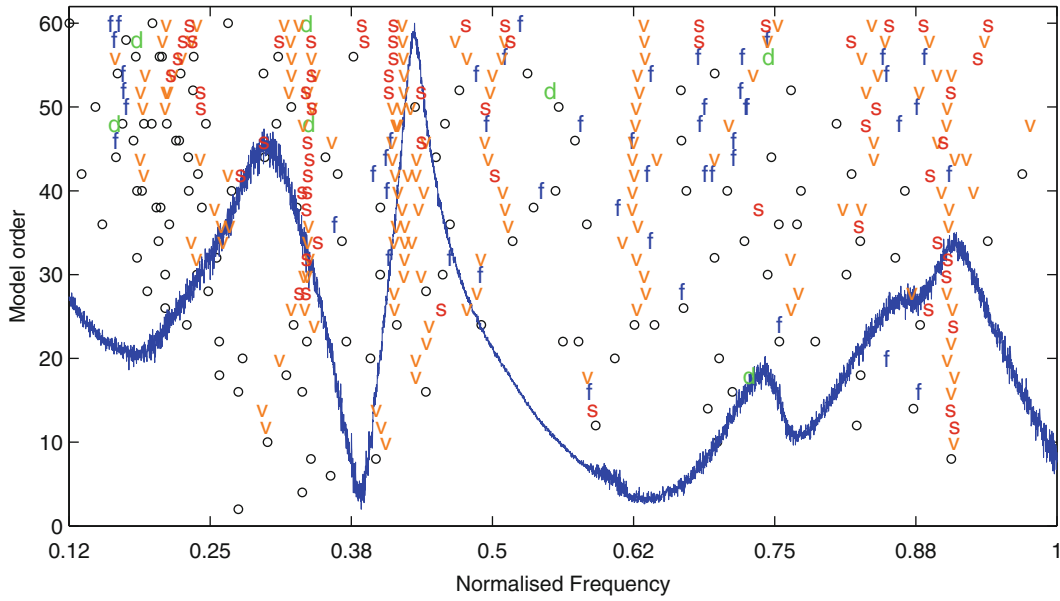
**Fig. 28.23** Stabilisation diagram for the AW tail rotor rig

**Fig. 28.24** Singular values plot for the AW rotor rig system
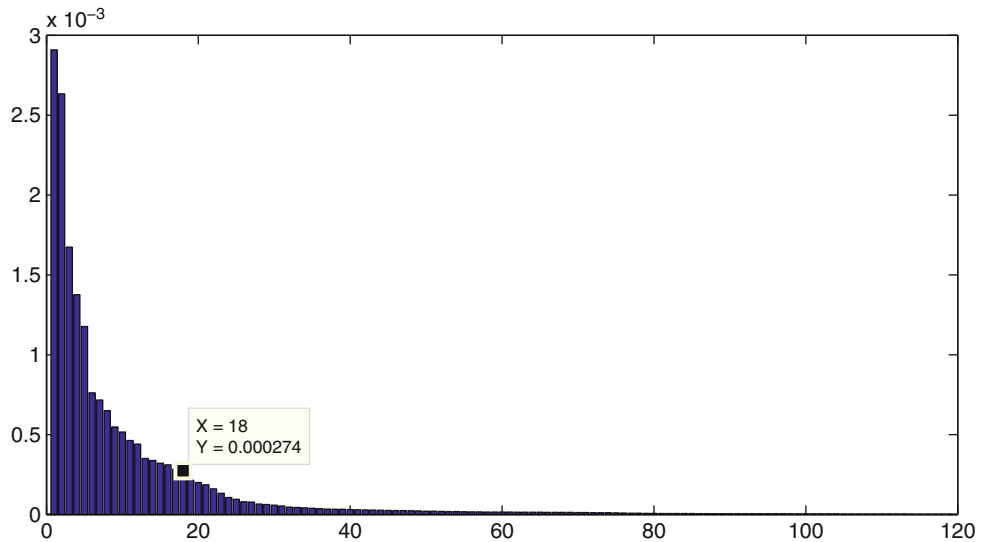


Finally, it is stressed that this is an ongoing work aimed at the creation of a toolbox for studying nonlinear systems. The more algorithms are added to Fig. 28.1 the easier will become for the experimentalist to have a thorough understanding of the nonlinear phenomena.

**Fig. 28.25** The Underlying
Linear Model FRF of the driving
point is compared to the
respective low and high level
FRFs
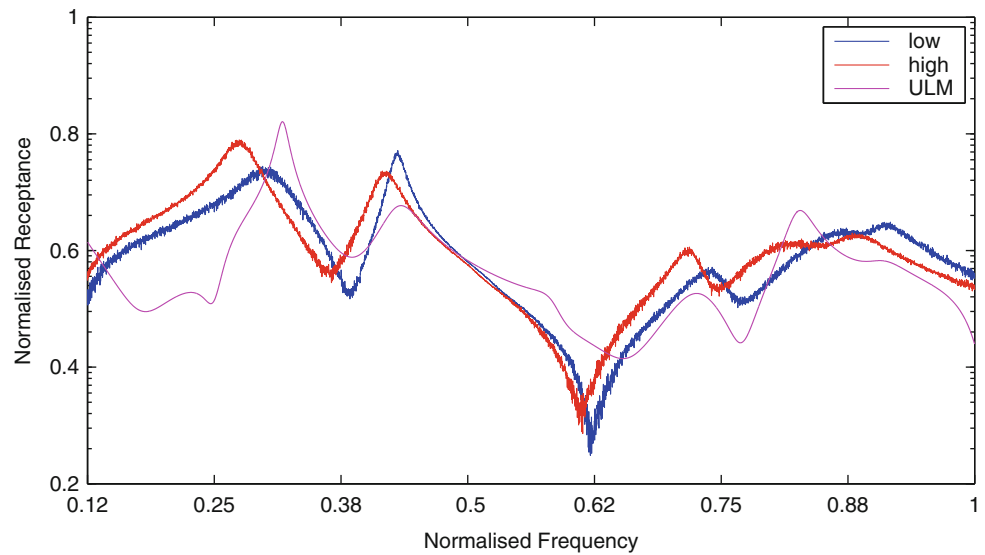


# References

1. delli Carri E, Ewins D (2013) A systematic approach to modal testing of nonlinear structures. Topics in Modal Analysis, Volume 7. Conference Proceedings of SEM Series 2014, pp 273–286
2. Magnevall M (2011) Simulation and experimental methods for characterization of nonlinear mechanical systems. Blekinge Institute of Technology, Sweden
3. Noël J, Kerschen G, Foltête E, Cogan S (2013) Frequency-domain subspace identification of nonlinear mechanical systems: application to a solar array structure. Nonlinear Dyn 1
4. Bendat JS (1993) Spectral techniques for nonlinear system analysis and identification. Shock Vib 1(1):21–31
5. Van Overschee P, De Moor B (1994) N4SID: subspace algorithms for the identification of combined deterministic-stochastic systems. Automatica, San Francisco, CA
6. Noël J, Kerschen G (2013) Frequency-domain subspace identification of nonlinear mechanical systems. Proceedings of the 5th International Operational Modal Analysis Conference
7. Richards CM, Singh R (1998) Identification of multi-degree-of-freedom non-linear systems under random excitations by the 'Reverse Path' spectral method. J Sound Vib 213(4):673–708

# Chapter 29
# Effects of Errors in Finite Element Models on Component Modal Tests

**Masayoshi Misawa and Hidenori Kawasoe**

**Abstract**  It has become increasingly difficult to perform modal tests for large structures because they are not strong enough to withstand the force of gravity. This study aimed to predict the dynamic characteristics of large structures with component modal tests. In this method, to simulate the dynamic behavior of structures, the effect of untested components is considered as additional mass and stiffness attached to a tested component. Additional mass and stiffness are calculated with mass and stiffness matrices of both structure and tested component. Because additional mass and stiffness vary with modeling errors in finite element models, it is difficult to obtain structure frequencies and modes by component modal tests. In this paper, the method is extended in order to deal with modeling errors. A formulation is given to show that modal tests for different tested components give an identical predicted frequency when there are no modeling errors. Variation in predicted frequency obtained for different tested components is the basis of frequency error estimation. Numerical examples are given to show that the proposed method has the potential to predict the dynamic characteristics of large structures.

**Keywords**  Component modal test • Additional mass • Additional stiffness • System identification • Large space structures

## Nomenclature

| | |
|---|---|
| $f$ | Structure frequency, Hz |
| $\boldsymbol{K}$ | Stiffness matrix |
| $\overline{K}$ | reduced stiffness |
| $\Delta K$ | Additional stiffness |
| $\boldsymbol{L}$ | Transformation vector used in coordinate reduction |
| $\boldsymbol{M}$ | Mass matrix |
| $\boldsymbol{M}_0$ | Rigid body mass matrix |
| $\overline{M}$ | Reduced mass |
| $\Delta M$ | Additional mass |
| $n_e$ | The number of finite elements |
| $n_g$ | The number of groups of mass and stiffness matrices |
| $n_T$ | The number of measured frequencies |
| $\boldsymbol{R}$ | Rigid body displacement matrix |
| $\boldsymbol{T}$ | Transformation matrix |
| $\boldsymbol{x}$ | Displacement vector |
| $\alpha, \beta, \gamma$ | Lagrange multipliers, $n_T$ is the total number of measured modes |
| $\boldsymbol{\phi}$ | Mode vector |
| $\eta, \nu$ | Modification coefficients |

M. Misawa (✉) • H. Kawasoe
Department of Mechanical Engineering, Shizuoka University, 3-5-1 Johoku, Hamamatsu, Shizuoka 432-8561, Japan
e-mail: tmmisaw@ipc.shizuoka.ac.jp

| $\sigma$ | Frequency used in finding additional mass and stiffness, Hz |
| $\omega$ | Angular frequency, rad/s |
| $\boldsymbol{\Omega}^2$ | Diagonal matrix with $\omega_i{}^2$ $(i = 1, 2, \ldots, n_T)$ |

## Subscripts

| $b$ | Boundary coordinates of component |
| $c$ | Quantity of component |
| $id$ | Quantity of identified model |
| $k$ | Internal coordinates of component |
| $o$ | Quantity of original model |
| $p$ | Translational coordinate with additional mass and stiffness |
| $q$ | Coordinates without additional mass and stiffness |
| $s$ | Quantity of structure |
| $t$ | Quantity of tested component |
| $test$ | Measured quantity |

## 29.1   Introduction

To confirm the dynamic characteristics of a structure, it is necessary to perform a modal test of the fabricated structure. However, there is a problem in performing modal tests when the structure increases in size. For large flexible structures, such as deployed antennas and solar paddles for satellite use, gravitational considerations may prevent a fully assembled ground modal test because these structures are not strong enough to withstand the force of gravity. Component modal tests can provide a means of predicting the dynamic characteristics of the structure without testing the whole structure.

There are a variety of approaches associated with experimental component modal synthesis (CMS). An experimental CMS procedure was presented to assemble a global model of the coupled structural dynamics through equivalent mass and stiffness representations of the components [1]. This procedure relies on accurate response and force measurements because mass normalized normal modes at boundary coordinates are the basis of the analytical synthesis. Doebling et al. [2] presented a method for estimating the residual flexibility from structural vibration data for experimental CMS. Morgan et al. [3] developed the forced response method with experimentally based CMS models and measured response data. An approach to CMS was presented for application in the testing of large flexible space structures [4]. This approach uses the test-based characteristics of individual components determined experimentally through modal and static tests. Chen and Cherng [5] proposed an experimental procedure to measure the generalized dynamic compliance with rotational effects. Rotational displacements at the boundary are used for the coupling of components. Komatsu et al. [6] improved the predicted dynamic characteristics of structures with rotational displacements found by introducing a polynomial approximation for the measured modes.

For verifying constrained modes when fixed-base testing proves impractical, a free-boundary modal test with the residual flexibility method has been investigated [7, 8]. Martinez et al. [9] presented a method to create a combined experimental/analytical model of a structure for improving the accuracy of the analytical model. This model is assembled using a component mode synthesis technique. Free-free modes and the residual flexibility at the boundary of a tested component are measured and used in the coupling. Admire et al. [10] also used the same approach to develop a constrained model for deriving constrained modes and frequencies. Tinker [11] described the application of the free-suspension residual flexibility test method to Space Station modules. After correlation of the Pathfinder finite element model to residual flexibility test data, constrained frequencies and modes obtained with the model are compared to fixed-base test results. A practical dynamic flexibility method based on a combination of test and analysis information was also proposed [12]. This method enables the computation of the approximate value of the dynamic flexibility using the power series expansion. Under two special situations, this method has a limitation and was improved [13]. Morgan et al. [14] presented an experimentally based nonbaseband CMS method with residual flexibility for the dynamic analysis of a proportionally damped system.

An alternate approach for verification of constrained models is the mass additive method. This method forces local deformation near boundaries by adding mass to the boundaries of a tested structure. By subtracting the mass from the equation of motion of the tested structure, constrained modes are estimated. Admire et al. [15] developed a mass additive

modal test method, which uses free-boundary mass-loaded modes along with analytical mass and stiffness matrices. The mass additive method has also been applied to component mode synthesis [16–21]. The basic method of CMS using mass loaded boundaries has previously been presented [17]. Fictitious masses are used to improve the accuracy of modal-based structural analyses [18, 19]. To add masses to boundaries causes low frequency modes to contain local displacements near the boundary which improves subsequent modal coupling. This method (the fictitious-mass modal coupling method) was applied to a space-type structure with measured component modes to demonstrate the effectiveness of the method [20]. A method was proposed for coupling substructures using mass additive mode including residual flexibility or constraint modes of components [21]. This paper showed that the mass additive mode synthesis technique, including constraint modes, worked well. In an application not related to CMS, Coleman et al. [22] described a mass-additive modal tests as applied to the Space Shuttle ASTRO-1 payload.

This study aimed to predict the dynamic characteristics of large structures with component modal tests [23–25]. In this method, to simulate the dynamic behavior of structures, the effect of untested components are considered as mass and spring attached to a tested component. The feature of this method is to predict natural frequencies and modes of large structures with component modal tests and needs no CMS. In general, finite element models of complex structures have modeling errors, but the previous studies assumed that there are no modeling errors because the main purpose is to confirm whether the method has the potential to predict natural frequencies and modes of structures. In this paper, the method will be extended to cover the case with modeling errors.

## 29.2   Development and Procedure of Dynamic Characteristics Prediction of Structures

### 29.2.1   Indication to Predict Target Frequency and Mode of Structures

In the finite element method, an analytical model of structures is expressed by mass and stiffness matrices, which sometimes include modeling errors. In the proposed testing method, natural frequencies and their modes of structures are predicted by component modal tests with additional masses and stiffnesses. Because additional mass and stiffness are calculated with mass matrix, stiffness matrix, and analytical frequency of structures, modeling errors cause an error in additional mass and stiffness. This error affects frequencies and modes of structures obtained by component modal tests. One cannot obtain information on accurate frequencies and modes of structures because this study deals with large structures that are difficult to perform modal test on the ground due to the force of gravity. For this reason, a procedure to predict target frequency and its mode with component modal tests is required in case the mass and stiffness matrices have modeling errors.

Denote a translational coordinate with the $i$-th additional mass and stiffness as $p_i$ and the rest as $q_i$. Additional mass is defined by the difference between reduced masses $\overline{M}_{s,p_i}$ and $\overline{M}_{t,p_i}$. These masses are determined by reducing the mass and stiffness matrices of both structure and tested component to a mass additive coordinate $p_i$, respectively. The following displacement relationship is used for coordinate reduction.

$$x_s = x_{s,p_i} L_{s,p_i} \tag{29.1}$$

where

$$x_s = \begin{Bmatrix} x_{s,q_i} \\ x_{s,p_i} \end{Bmatrix}, \quad L_{s,p_i} = \begin{Bmatrix} C_{s,p_i} \\ 1 \end{Bmatrix}, \quad C_{s,p_i} = -\left( K_{s,q_i q_i} - (2\pi\sigma)^2 M_{s,q_i q_i} \right)^{-1} \left( K_{s,q_i p_i} - (2\pi\sigma)^2 M_{s,q_i p_i} \right) \tag{29.2}$$

Note that $x_{s,p_i}$ is scalar. Displacement relationship of Eq. (29.1) is the basis of this method. To accurately predict the dynamic characteristics by component modal tests, it is indispensable that the displacement relationship of Eq. (29.1) holds when structures vibrate. Only when frequency $\sigma$ is equal to structure frequency, tested component behaves as the part of the structure vibrating at structure frequency and the displacement relationship holds. Namely, displacements $x_{s,qi}$ at coordinate $q_i$, which are calculated with a displacement $x_{s,pi}$ at mass additive coordinate $p_i$, are identical to those of structures. The dynamic equation of the structure is expressed as

$$\left( -\omega_s{}^2 M_s + K_s \right) x_s = 0 \tag{29.3}$$

Pre-multiplying Eq. (29.3) by $\boldsymbol{L}_{s,pi}{}^T$ and using the displacement relation, one obtains

$$\left(-\omega_s{}^2 \overline{M}_{s,p_i} + \overline{K}_{s,p_i}\right) x_{s,p_i} = 0 \tag{29.4}$$

where reduced mass $\overline{M}_{s,p_i}$ and reduced stiffness $\overline{K}_{s,p_i}$ are expressed by

$$\overline{M}_{s,p_i} = \boldsymbol{L}_{s,p_i}{}^T \boldsymbol{M}_s \boldsymbol{L}_{s,p_i}, \quad \overline{K}_{s,p_i} = \boldsymbol{L}_{s,p_i}{}^T \boldsymbol{K}_s \boldsymbol{L}_{s,p_i} \tag{29.5}$$

Adding $\left(-\omega_s{}^2 \overline{M}_{t,p_i} + \overline{K}_{t,p_i}\right) x_{t,p_i}$ to both sides of Eq. (29.4) gives

$$\left(-\omega_s{}^2 \Delta M_i + \Delta K_i\right) x_{t,p_i} + \left(-\omega_s{}^2 \overline{M}_{t,p_i} + \overline{K}_{t,p_i}\right) x_{t,p_i} = 0 \tag{29.6}$$

Note that $x_{s,pi} = x_{t,pi}$ because dynamic behavior of the tested component is identical with that of the part of the structure vibrating at structure frequency. Here the $i$-th additional mass $\Delta M_i$ and additional stiffness $\Delta K_i$ are expressed as

$$\Delta M_i = \overline{M}_{s,p_i} - \overline{M}_{t,p_i}, \quad \Delta K_i = \overline{K}_{s,p_i} - \overline{K}_{t,p_i} \tag{29.7}$$

Rewriting Eq. (29.6) into matrix form gives

$$
\left(-\omega_s{}^2 \boldsymbol{L}_{t,p_i}{}^T \begin{bmatrix} \boldsymbol{0} & \boldsymbol{0} \\ \boldsymbol{0} & \Delta M_i \end{bmatrix} \boldsymbol{L}_{t,p_i} + \boldsymbol{L}_{t,p_i}{}^T \begin{bmatrix} \boldsymbol{0} & \boldsymbol{0} \\ \boldsymbol{0} & \Delta K_i \end{bmatrix} \boldsymbol{L}_{t,p_i}\right) x_{t,p_i}
$$
$$
+ \left(-\omega_s{}^2 \boldsymbol{L}_{t,p_i}{}^T \begin{bmatrix} \boldsymbol{M}_{t,q_i q_i} & \boldsymbol{M}_{t,q_i p_i} \\ \boldsymbol{M}_{t,p_i q_i} & \boldsymbol{M}_{t,p_i p_i} \end{bmatrix} \boldsymbol{L}_{t,p_i} + \boldsymbol{L}_{t,p_i}{}^T \begin{bmatrix} \boldsymbol{K}_{t,q_i q_i} & \boldsymbol{K}_{t,q_i p_i} \\ \boldsymbol{K}_{t,p_i q_i} & \boldsymbol{K}_{t,p_i p_i} \end{bmatrix} \boldsymbol{L}_{t,p_i}\right) x_{t,p_i} = 0 \tag{29.8}
$$

Equation (29.8) is rewritten by using the displacement relationship of Eq. (29.1) as

$$
\left(-\omega_s{}^2 \begin{bmatrix} \boldsymbol{M}_{t,q_i q_i} & \boldsymbol{M}_{t,q_i p_i} \\ \boldsymbol{M}_{t,p_i q_i} & \boldsymbol{M}_{t,p_i p_i} + \Delta M_i \end{bmatrix} + \begin{bmatrix} \boldsymbol{K}_{t,q_i q_i} & \boldsymbol{K}_{t,q_i p_i} \\ \boldsymbol{K}_{t,p_i v} & \boldsymbol{K}_{t,p_i p_i} + \Delta K_i \end{bmatrix}\right) x_t = \boldsymbol{0} \tag{29.9}
$$

This equation shows that frequency and mode of structures can be obtained by component modal tests. Note that Eq. (29.9) holds for arbitrary tested components. Therefore, modal tests for different tested components with additional mass and stiffness provide an identical frequency when analytical model has no errors. The identical frequency is the target frequency of structures. When using several additional masses and stiffness, Eq. (29.9) is obtained from Eq. (29.3) in a similar way. On the other hand, if modeling errors exist, Eq. (29.1) is just an assumption that $x_{s,p_i} \boldsymbol{C}_{s,p_i}$ is replaced with $x_{s,q_i}$. Because $x_{s,p_i} \boldsymbol{C}_{s,p_i}$ never equals $x_{s,q_i}$, target mode cannot be obtained. In this case, it can be seen from Eqs. (29.5) and (29.7) that additional mass and stiffness have errors, and target frequency also cannot be obtained. Since the tested component used in the modal test has no errors, the mass and stiffness matrices of the tested component ($\boldsymbol{M}_t$ and $\boldsymbol{K}_t$) in Eq. (29.9) are exact. Therefore, measured frequency only depends on errors in both additional mass and stiffness which take different values for different tested components. As a result, there is not an identical frequency among test frequencies obtained by using different tested components. For this reason, the target frequencies of the structure are predicted by checking the correspondence between modes obtained for different tested components. This method uses a variation in the target frequencies as an indication to estimate predicted frequency error. In the following sections, to predict dynamic characteristics, descriptions of the procedure shown in Fig. 29.1 will be provided.

### 29.2.2  Modeling Error Reduction

The first step is to calculate structure frequencies $f_{s,o}$ and modes $\boldsymbol{\phi}_{s,o}$ by solving the following dynamic equation of the original model.

$$(2\pi f_{s,o})^2 \boldsymbol{M}_{s,o} \boldsymbol{x}_{s,o} = \boldsymbol{K}_{s,o} \boldsymbol{x}_{s,o} \tag{29.10}$$
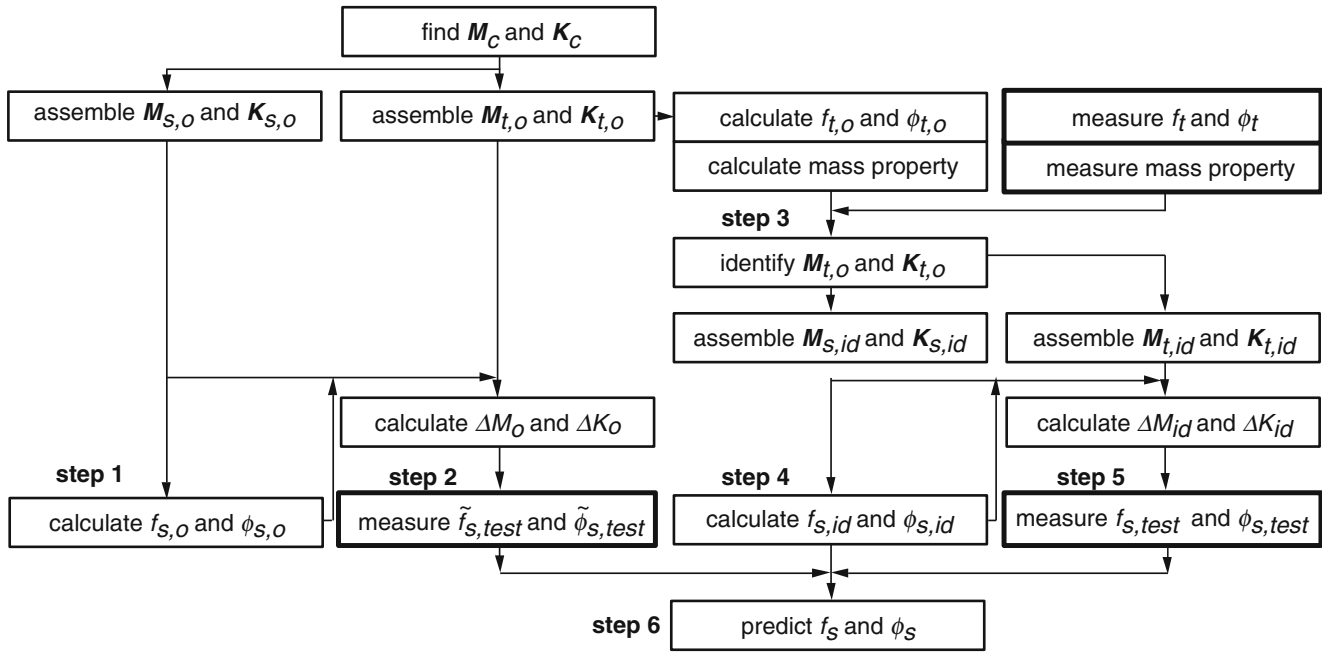
**Fig. 29.1** Procedure to predict frequency and mode of structure

Mass and stiffness matrices of structures ($M_{s,o}$ and $K_{s,o}$) are assembled with mass and stiffness matrices of each component ($M_c$ and $K_c$) according to the finite element method. Frequencies $f_{s,o}$, mass matrix $M_{s,o}$ and stiffness matrix $K_{s,o}$ are used to calculate additional mass and stiffness.

In the second step, structure frequencies $\tilde{f}_{s,test}$ and modes $\tilde{\varphi}_{s,test}$ are measured through component modal tests. Mass and stiffness matrices of the tested component ($M_{t,o}$ and $K_{t,o}$) are assembled to calculate additional mass $\Delta M_o$ and stiffness $\Delta K_o$. Note that there is no error in the tested component subjected to the modal test. Modeling errors are included only in the finite element model. Therefore, frequencies $\tilde{f}_{s,test}$ and modes $\tilde{\varphi}_{s,test}$ are frequencies and modes of structures if the modeling error is small. In this case, target frequencies obtained by using different tested components are almost the same. If the differences between the target frequencies obtained by different tested components are not minute, modeling errors should be reduced to predict accurate frequencies and modes of structures. In this case, test frequencies $\tilde{f}_{s,test}$ ought to be closer to structure frequencies than analytical frequencies $f_{s,o}$ because no error is included in tested component.

The next step is to reduce modeling errors. System identification is a powerful tool to reduce errors in mass and stiffness matrices. Efficient indications of modeling error reduction are physical quantities such as frequencies, modes, and mass properties (weight, center of gravity, etc.). For this reason, modal and mass property tests are performed for each tested component, and mass and stiffness matrices of tested components are identified to mate with the measured dynamic characteristics and mass properties. Then frequencies, modes, and mass properties are calculated using identified mass and stiffness matrices. If the difference between the calculated results and the measured data is very small, one proceeds to the next step. If this is not the case, one needs to confirm the effect of the number of modes used in system identification on the calculated results. When the increase in the number of modes is not effective for reducing the difference, the finite element model should be reconstructed and the identification process repeated.

System identification technique [26] proposed by the authors was used. The feature of this technique is to keep mass and stiffness distribution of each finite element. A brief description is provided here to help readers understand numerical examples. Because the dynamic characteristics of structures depend on mass and stiffness distributions, the identified mass and stiffness matrices must give mass and stiffness distributions that resemble those of real structures. It will be effective to consider these distributions for system identification. This method groups the mass and stiffness matrices of each finite element into several matrices called grouped ones. It is possible to group the mass and stiffness matrices by considering several physical quantities: mode shape, mass properties, and so on. The analytical (original) mass and stiffness matrices of element $i$ ($m_{Ai}$ and $k_{Ai}$) can be expressed as the sum of the grouped matrices ($m_{Ai,j}$ and $k_{Ai,j}$) including only the degrees of freedom of group $j$ as

$$m_{Ai} = \sum_{j=1}^{n_g} m_{Ai,j}, \quad k_{Ai} = \sum_{j=1}^{n_g} k_{Ai,j} \tag{29.11}$$

The element mass and stiffness matrices are transformed from local to global coordinates and assembled to obtain the mass and stiffness matrices of the structures as

$$M_{t,o} = \sum_{i=1}^{n_e} \sum_{j=1}^{n_g} M_{Ai,j}, \quad K_{t,o} = \sum_{i=1}^{n_e} \sum_{j=1}^{n_g} K_{Ai,j} \tag{29.12}$$

where

$$M_{Ai,j} = T^t m_{Ai,j} T, \quad K_{Ai,j} = T^t k_{Ai,j} T \tag{29.13}$$

Matrix $T$ is a coordinate transformation matrix. Using modification coefficients $\eta$ and $\nu$, the identified mass and stiffness matrices are given by

$$M_{t,id} = \sum_{i=1}^{n_e} \sum_{j=1}^{n_g} \eta_{ij} M_{Ai,j}, \quad K_{t,id} = \sum_{i=1}^{n_e} \sum_{j=1}^{n_g} \nu_{ij} K_{Ai,j} \tag{29.14}$$

The mass matrix is identified using the constrained minimization theory. The Lagrange function is given by

$$\Psi_M = \frac{1}{2} \sum_{i=1}^{n_e} \sum_{j=1}^{n_g} \left\| \eta_{ij} M_{Ai,j} - M_{Ai,j} \right\| + \sum_{a=1}^{6} \sum_{b=1}^{6} \alpha_{ab} \left( R^t M R - M_0 \right)_{ab} + \sum_{a=1}^{n_T} \sum_{b=1}^{n_T} \beta_{ab} \left( \varphi^t M \varphi - E_{n_T} \right)_{ab} \tag{29.15}$$

The constraints in Eq. (29.15) are specified from physical points of view. The first term on the right-hand side of Eq. (29.15) is the Euclidean norm, the second term is the mass property constraints, and the last term is the mode orthogonal constraints. Note that the modal mass constraints are not considered because these constraints give non-unique identified mass matrices [27, 28]. $(A)_{ab}$ shows the $(a, b)$ element of matrix $A$. The mass matrix is identified by finding a solution minimizing $\Psi_M$.

Stiffness matrix identification is also done in the same way as mass matrix identification. The Lagrange function to be minimized is given by

$$\Psi_K = \frac{1}{2} \sum_{i=1}^{n_e} \sum_{j=1}^{n_g} \left\| \nu_{ij} K_{Ai,j} - K_{Ai,j} \right\| + \sum_{a=1}^{n_T} \sum_{b=1}^{n_T} \gamma_{ab} \left( \varphi^t K \varphi - \varphi^t M \varphi \Omega^2 \right)_{ab} \tag{29.16}$$

The first term in the right-hand side of Eq. (29.16) is the Euclidean norm, and the last term is the modal stiffness and the mode orthogonality constraints. The stiffness matrix is identified by finding a solution minimizing $\Psi_K$.

The next step is to find frequencies and modes of structures analytically. Assembling identified mass and stiffness matrices of tested components ($M_{t,id}$ and $K_{t,id}$) gives the mass and stiffness matrices of structures ($M_{s,id}$ and $K_{s,id}$). When considering a structure consisting of two components, one obtains the dynamic equation of the structure as

$$\omega_s^2 \begin{bmatrix} M_{t_1,kk} & M_{t_1,kb} & 0 \\ M_{t_1,bk} & M_{t_1,bb} + M_{t_2,kk} & M_{t_2,kb} \\ 0 & M_{t_2,bk} & M_{t_2,bb} \end{bmatrix} \begin{Bmatrix} x_{1,k} \\ x_{1,b} \\ x_{2,k} \end{Bmatrix} = \begin{bmatrix} K_{t_1,kk} & K_{t_1,kb} & 0 \\ K_{t_1,bk} & K_{t_1,bb} + K_{t_2,kk} & K_{t_2,kb} \\ 0 & K_{t_2,bk} & K_{t_2,bb} \end{bmatrix} \begin{Bmatrix} x_{t_1,k} \\ x_{t_1,b} \\ x_{t_2,k} \end{Bmatrix} \tag{29.17}$$

If mass and stiffness matrices include modeling errors, exact frequencies of structures are unknown. For this reason, this method assumes that the solution (frequencies $f_{s,id}$ and modes $\phi_{s,id}$) of Eq. (29.17) is the reference for evaluating the accuracy of test frequency obtained by component modal tests. This will be a reasonable assumption because modeling errors of the tested component are reduced so as to agree with measured data (frequencies, modes, and mass properties).

### 29.2.3 Target Frequency Error Estimation

The next step is to measure structure frequencies $f_{s,test}$ and modes $\phi_{s,test}$. The measured data provide information to predict frequency and mode of structures. Mass and stiffness matrices of tested component ($M_{t,id}$ and $K_{t,id}$) are assembled with identified component mass and stiffness matrices. Additional mass $\Delta M_{id}$ and stiffness $\Delta K_{id}$ are calculated with matrices $M_{s,id}$, $M_{t,id}$, $K_{s,id}$, and $K_{t,id}$ from Eq. (29.7). Identified frequencies $f_{s,id}$ are also used in additional mass and stiffness

calculations. Comparing additional mass $\Delta M_{id}$ and stiffness $\Delta K_{id}$ with original additional mass $\Delta M_o$ and stiffness $\Delta K_o$, one can confirm how system identification reduces modeling errors. The measured frequencies and modes of structures are obtained by component modal tests with identified additional mass $\Delta M_{id}$ and stiffness $\Delta K_{id}$.

The final step is to predict frequencies and modes of structures. Note that modeling errors affect only additional mass and stiffness because the tested component subjected to the modal test has no errors in mass and stiffness distributions. If there is no modeling error in the analytical model, frequencies $f_{s,id}$ and $f_{s,test}$ are identical. Therefore, $\varepsilon_1$ defined by the following equation gives an indication showing the frequency error of structures.

$$\varepsilon_1 = \left| \frac{f_{s,id} - f_{s,test}}{f_{s,id}} \right| \times 100\,(\%) \tag{29.18}$$

If frequency error $\varepsilon_1$ is small, the test frequency may be structure frequency. The other indication is defined by the measured frequencies. As stated in Sect. 29.2.1, predicted frequencies obtained by using different tested components are identical if there is no modeling error. Therefore, it is reasonable to use an indication defined by Eq. (29.19) to predict structure frequencies.

$$\varepsilon_2 = \max \left| \frac{f_{s,test_i} - f_{s,test_j}}{f_{s,test_i}} \right| \times 100\,(\%) \quad (i = 1, 2, \ldots, n; j = i + 1, i + 2, \ldots, n) \tag{29.19}$$

Though the exact frequencies of structures are unknown, structure frequency can be predicted within some error. It is important to confirm how additional mass and stiffness vary with the different number of modes used in system identification. If identified frequencies $f_{s,id}$ vary with the increasing number of modes, those frequencies must approach structure frequencies.

## 29.3  Numerical Examples

Figure 29.2 shows an analytical model consisting of two components. Arabic numbers denote the location number. Location 9 is the boundary location of two components. Each element length is 100 mm. Figure 29.2 also shows the test configuration of the tested components with an additional mass $\Delta M$ and an additional stiffness $\Delta K$. The subscript of $\Delta M$ and $\Delta K$ shows
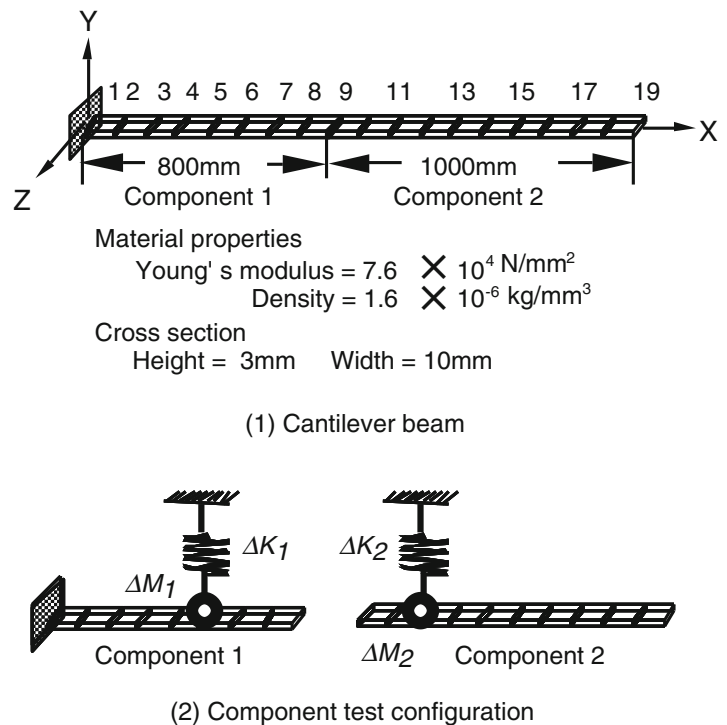


**Fig. 29.2** Analytical model and component test configuration

**Table 29.1** Selected coordinates with additional mass and stiffness

| | | Tested component | |
|---|---|---|---|
| Mode number | Boundary location | Component 1 | Component 2 |
| 1 | 9 | 9Y | 19Y |
| 2 | 9 | 9Y | 9Y |
| 3 | 12 | 7Y | 9Y |
| 4 | 10 | 5Y | 10Y |
| 5 | 12 | 8Y | 12Y |

**Table 29.2** Material properties

| | Young's modulus ($\times 10^4$ N/mm$^2$) | Density ($\times 10^{-6}$ kg/mm$^3$) |
|---|---|---|
| Exact | 7.55 | 1.63 |
| Analysis | 9.06 | 1.30 |

**Table 29.3** Beam frequencies of bending mode in the $Y$ direction

| Mode number | Exact (Hz) | Analysis (Hz) |
|---|---|---|
| 1 | 1.0 | 1.2 |
| 2 | 6.4 | 7.8 |
| 3 | 17.9 | 21.9 |
| 4 | 35.0 | 42.9 |
| 5 | 57.9 | 70.9 |

a tested component number. In the following, only bending modes in the X–Y plane are considered. Therefore, additional mass and stiffness are attached to the Y coordinate of a location on the tested component. In this case, a tested component is set so that the Y-axis may be parallel to the gravitational force when performing component modal tests.

Table 29.1 shows selected coordinates with additional mass and stiffness for each tested component. Because location 9 is close to the node of the third and fifth modes, it is difficult to obtain these modes by component modal tests. For this reason, boundary location is change for location 12 with large displacement when target mode is the third and fifth modes. For the fourth mode, boundary location 10 is selected to accurately obtain the target mode.

## 29.3.1 Frequencies

Because component modal tests were not performed, different input data for the system identification were taken into account to construct the simulated test and analytical models. Table 29.2 shows material properties of the beam. Material properties in "Exact" give simulated test frequencies and modes, and material properties in "Analysis" provide analytical frequencies and modes when the finite element model has modeling errors. Although one usually cannot understand what kinds of modeling errors exist in the finite element models in practice, modeling errors are assumed to be known in the numerical examples to show the effectiveness of the proposed method. However, the assumption never disturbs the purpose of this paper that predicts frequencies and modes of structures by using a variation in the target frequencies as an indication.

Table 29.3 shows analytical beam frequencies. Because Young's modulus is more than the exact value by 20 % and the density is 20 % less than the exact value, the analytical natural frequencies are about 22 % higher than the exact frequencies due to the modeling errors. There is no significant difference between the analytical and exact modes.

Table 29.4 shows the simulated test frequencies obtained with each tested component when additional mass and stiffness include modeling errors. Note that only additional mass and stiffness include modeling errors. One should use the finite element model of the tested component without the modeling errors because the tested component subjected to the modal test has no errors. When target frequency is the first frequency, frequencies of 1.2, 22.8, 73.5, 153.4 and 262.9 Hz are obtained when component 1 is the tested component. One has no information on which frequency corresponds to the first frequency of the beam. For this reason, different tested components are subjected to modal tests to predict the first frequency of the beam. When component 2 is tested component, one obtains frequencies of 0, 1.2, 17.7, 50.8, and 102.3 Hz. If there are no errors in additional mass and stiffness, component modal tests for different tested components provide an identical frequency. This frequency is considered as the target frequency. However, identical frequencies generally cannot be obtained because of modeling errors. Therefore, the target frequency of the beam is predicted by checking the correspondence between two modes obtained from tested components 1 and 2, respectively. Frequency of 1.2 Hz in tested component 1 and frequency of 1.2 Hz in tested component 2 are predicted as the first beam frequency. In the same way, one predicts beam frequencies for the second and higher frequencies, as shown by bold numbers. The predicted frequency slightly approaches the exact frequency listed in Table 29.3 due to using the mass and stiffness matrices of the tested component without modeling errors in the simulated tests. However, there are still differences between the two frequencies.

**Table 29.4** Simulated test frequencies with additional mass and stiffness found by the original finite element model

|  |  | Target frequency (Hz) | | | | |
|---|---|---|---|---|---|---|
| Tested component | Mode number | 1st | 2nd | 3rd | 4th | 5th |
| 1 | 1 | **1.2** | **7.5** | **20.2** | 12.5 | 28.8 |
|  | 2 | 22.8 | 24.5 | 32.3 | **39.3** | **68.2** |
|  | 3 | 73.5 | 75.3 | 80.1 | 90.5 | 90.5 |
|  | 4 | 153.4 | 155.1 | 159.5 | 149.0 | 172.1 |
|  | 5 | 262.9 | 264.7 | 289.7 | 294.7 | 263.5 |
| 2 | 1 | 0.0 | 0.0 | 0.0 | 0.0 | 0.0 |
|  | 2 | **1.2** | **7.1** | 13.6 | 14.0 | 14.2 |
|  | 3 | 17.7 | 19.5 | **19.0** | **42.5** | 42.5 |
|  | 4 | 50.8 | 52.3 | 47.6 | 64.0 | **64.0** |
|  | 5 | 102.3 | 104.1 | 98.5 | 104.5 | 104.5 |

**Table 29.5** Tested component frequencies (boundary location 9)

|  | Component 1 | | Component 2 | |
|---|---|---|---|---|
| Mode number | Test (Hz) | Analysis (Hz) | Test (Hz) | Analysis (Hz) |
| 1 | 5.2 | 6.3 | 0.0 | 0.0 |
| 2 | 32.3 | 39.6 | 0.0 | 0.0 |
| 3 | 90.5 | 110.9 | 21.0 | 25.7 |
| 4 | 177.7 | 217.6 | 57.9 | 70.9 |
| 5 | 294.7 | 360.9 | 113.6 | 139.1 |

**Table 29.6** Mass properties of each tested component (boundary location 9)

| Item |  | Component 1 | | Component 2 | |
|---|---|---|---|---|---|
|  |  | Test | Analysis | Test | Analysis |
| Weight (g) | $m$ | 39.1 | 31.3 | 48.9 | 39.1 |
| Center of gravity (mm) | $X_{cg}$ | 400.0 | 400.0 | 400.0 | 400.0 |
| Moment of inertia (kg mm$^2$) | $I_{xx}$ | 3.8 | 3.0 | 4.7 | 3.8 |
|  | $I_{yy}$ | $8.4 \times 10^3$ | $6.7 \times 10^3$ | $8.8 \times 10^4$ | $6.9 \times 10^3$ |
|  | $I_{zz}$ | $8.4 \times 10^3$ | $6.7 \times 10^3$ | $8.8 \times 10^4$ | $6.9 \times 10^3$ |

## 29.3.2   System Identification of Tested Components

Reducing modeling errors should be required to accurately predict frequencies and modes of structures. The measured frequencies and mass properties of the tested components are used for system identification. When boundary is location 9, natural frequencies of each tested component are shown in Table 29.5. Note that test frequencies do not include modeling errors. Therefore, frequency difference between "Test" and "Analysis" is only due to modeling errors.

Table 29.6 shows an example of the mass properties of components when boundary is location 9. Since all the finite elements include identical errors in density, the center of gravity of each tested component is the same in "Test" and "Analysis".

The mass and stiffness matrices are grouped by considering mode shape. The beam has four fundamental modes: an axial mode, two bending modes in different directions, and a torsional mode. Therefore, Groups 1 to 4 are defined as follows:

Group 1: degrees of freedom that influence the axial modes
Group 2: degrees of freedom that influence the bending modes in the Y direction
Group 3: degrees of freedom that influence the bending modes in the Z direction
Group 4: degrees of freedom that influence the torsional modes

Figure 29.3 shows the modification coefficients of the group for each finite element when using the lower three test frequencies and modes: one Y bending mode and two Z bending modes. For mass matrix identification, exact modification coefficients are 1.25 because the density is less than the exact value by 20 % in all the finite elements. The modification coefficients agree with the exact values for components 1 and 2. This shows that the identified mass matrix represents the true mass distribution of the beam. Although the axial and torsional modes are not used in the identification, the modification coefficients of groups 1 and 4 agree with the exact value. The reason why the mass matrix is identified is to satisfy the mass property constraints.

For stiffness matrix identification, exact modification coefficients are 0.83 because the Young's modulus is 20 % more than the exact value in all the finite elements. As shown in Fig. 29.4, modification coefficients of groups 1 and 4 remain one because the axial and torsional modes are not used in the identification. For component 1, modification coefficient of group 2
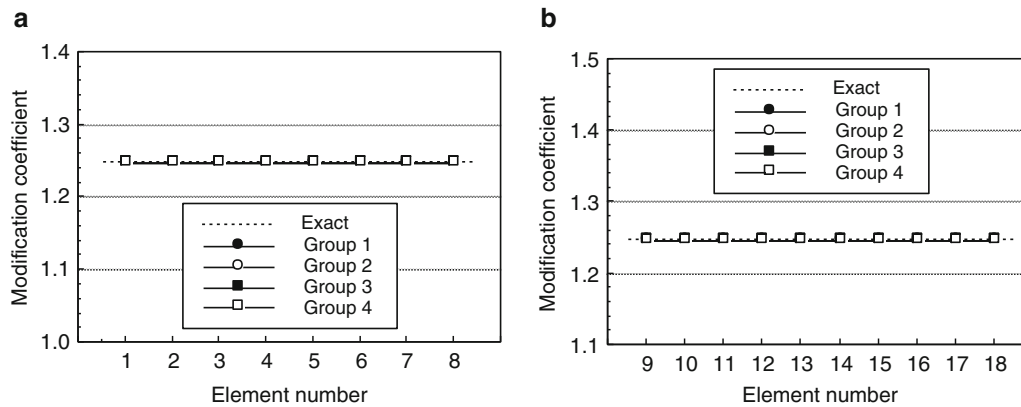
**Fig. 29.3** Modification coefficient for mass matrix identification. (**a**) Component 1. (**b**) Component 2
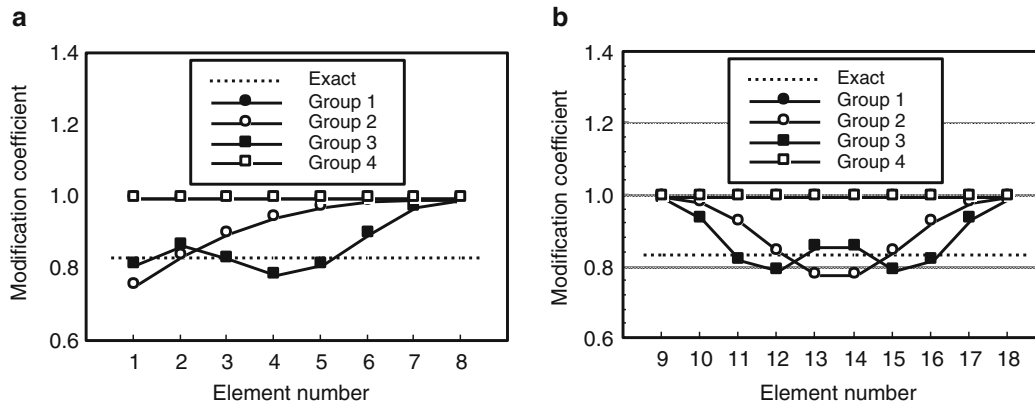


**Fig. 29.4** Modification coefficient for stiffness matrix identification. (**a**) Component 1. (**b**) Component 2

concerning the Y bending mode does not change as element gets close to the tip of the beam. Modification coefficient of group 3 concerning the Z bending mode approaches the exact values, but it does not change as the element approaches the tip of the beam. For component 2, modification coefficients of groups 2 and 3 change a little near the free edges. Modal stiffness can provide the reason [26]. For example, modal stiffness of the first mode is very small at elements near the tip of the beam because the modal stiffness constraints are satisfied by correcting the grouped matrices of elements near the root of the beam. Because the number of modes used for the identification is small, these modification coefficients do not approach the exact value. Therefore, it is expected that the modification coefficient will be improved by increasing the number of modes. The modification coefficients are found when using the lower seven test frequencies and modes: two Y bending modes and five Z bending modes. Modification coefficient of group 3 is almost identical with the exact value.

Substituting the modification coefficients $\eta$ and $\nu$ for Eq. (29.14) provides the identified mass and stiffness matrices. The residues of the mass property constraints and the mode orthogonal constraints were calculated to confirm modeling error reduction of mass matrix. The maximum residue of the constraints is almost zero. Also for stiffness matrix identification, the maximum residue of the modal stiffness and the mode orthogonality constraints is almost zero. Natural frequencies and modes computed with the identified mass and stiffness matrices agree well with exact ones of each tested component.

The mass and stiffness matrices of the beam are assembled with the identified mass and stiffness matrices of tested components. Namely, the dynamic equation of the beam can be obtained. Table 29.7 shows natural frequencies of the beam obtained by solving this equation. We call these frequencies "identified frequencies" hereafter. Arabic numbers in parenthesis show frequency error to exact frequency. As the number of test frequencies and modes used in system identification has an influence on identified mass and stiffness matrices, the lower three and seven modes are used in system identification to confirm the effect of the number of modes on natural frequencies of the beam. Table 29.7 shows that frequency error decreases with increasing the number of modes. Identified frequencies are almost identical with the exact frequencies.

Exact additional mass and stiffness are calculated with exact frequencies shown in Table 29.2. Analysis frequencies and identified frequencies are used to find original and identified additional mass and stiffness, respectively. Errors in additional mass and stiffness of component 1 are shown in Fig. 29.5 when they are attached to the selected coordinates listed in

**Table 29.7** Identified frequencies of the beam

| | | Identified frequency (Hz) | |
|---|---|---|---|
| Mode number | Exact frequency | 3 modes | 7 modes |
| 1 | 1.0 | 1.0 (1.0 %) | 1.0 (1.0 %) |
| 2 | 6.4 | 6.6 (2.7 %) | 6.4 (0.3 %) |
| 3 | 17.9 | 18.1 (1.0 %) | 17.9 (0.1 %) |
| 4 | 35.0 | 35.5 (1.5 %) | 34.9 (0.3 %) |
| 5 | 57.9 | 58.7 (1.3 %) | 57.8 (0.2 %) |
| 6 | 86.5 | 88.5 (2.3 %) | 86.4 (0.1 %) |
| 7 | 120.9 | 123.7 (2.3 %) | 120.7 (0.1 %) |
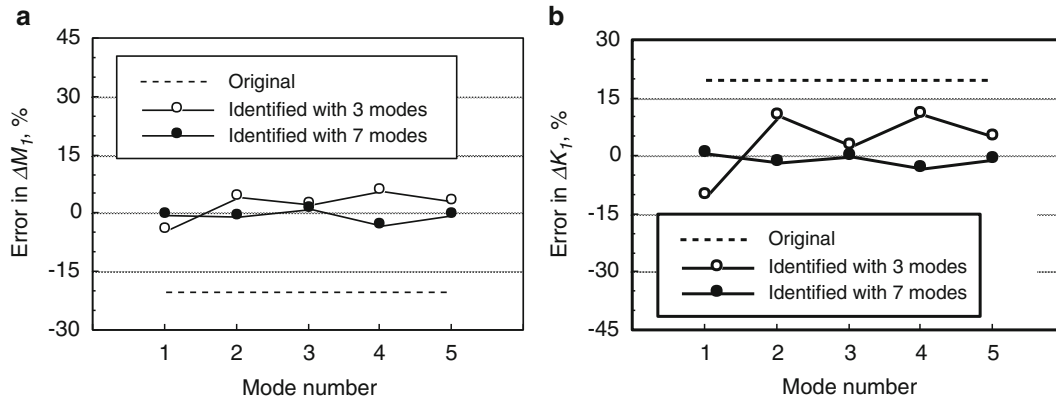


**Fig. 29.5** Error variations in additional mass and stiffness for component 1. (**a**) Additional mass $\Delta M_1$ (**b**) Additional stiffness $\Delta K_1$

**Table 29.8** Simulated test frequencies with additional mass and stiffness found by identified finite element model (three modes)

| | | Target frequency (Hz) | | | | |
|---|---|---|---|---|---|---|
| Tested component | Mode number | 1st | 2nd | 3rd | 4th | 5th |
| 1 | 1 | **1.0** | **6.6** | **18.0** | 12.3 | 28.8 |
| | 2 | 22.8 | 24.1 | 32.2 | **35.5** | **58.6** |
| | 3 | 73.5 | 74.8 | 78.1 | 90.5 | 90.4 |
| | 4 | 153.3 | 154.7 | 157.7 | 145.6 | 172.1 |
| | 5 | 262.9 | 264.3 | 289.3 | 294.7 | 260.8 |
| 2 | 1 | 0.0 | 0.0 | 0.0 | 0.0 | 0.0 |
| | 2 | **1.0** | **6.6** | 14.0 | 17.4 | 18.3 |
| | 3 | 17.3 | 16.2 | **18.1** | **35.5** | 31.8 |
| | 4 | 50.2 | 48.4 | 47.2 | 57.1 | **58.7** |
| | 5 | 101.6 | 99.4 | 98.1 | 113.4 | 109.2 |

Table 29.1 for each mode. The original errors in additional mass are decreased by mass matrix identification and is only 2 % when using the lower seven modes. Errors in additional stiffness also decrease by increasing the number of modes used for stiffness matrix identification. For component 2, errors in additional mass and stiffness show the same tendency.

### 29.3.3 Dynamic Characteristics After Reducing Modeling Errors

Table 29.8 shows the simulated test frequencies of tested components. Frequency shown by boldface is the predicted frequency of the beam. Because modeling errors are reduced by system identification, simulated tests with different tested components provide almost the same predicted frequencies. In addition, the predicted frequencies are almost the same as the identified ones of the beam shown in Table 29.7. When using seven modes in system identification, the predicted frequencies of tested component 1 are identical with those of component 2. Therefore, if frequency difference between predicted and identified frequencies is small, and also variation in frequency difference is small for different number of modes used in system identification, it is reasonable to consider test frequency as structure frequency.
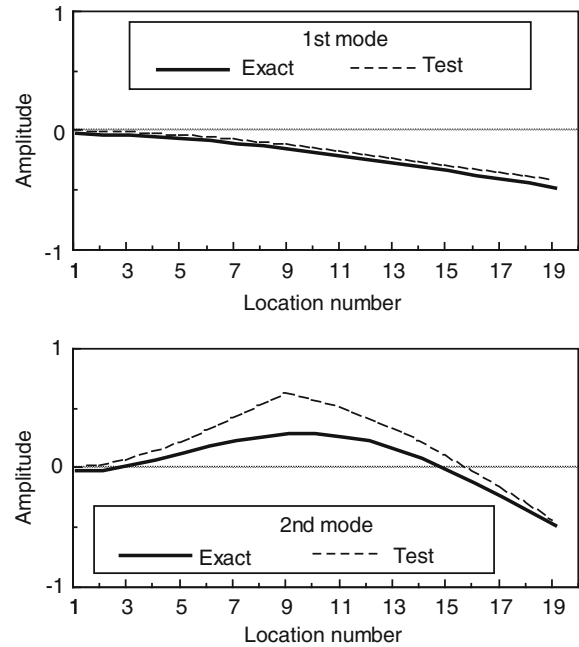
Frequency error is found to predict the natural frequency of structures. Figure 29.6 (1) shows frequency error $\varepsilon_1$. The simulated test frequencies listed in Table 29.4 are used to calculate original frequency error. Although the original frequency
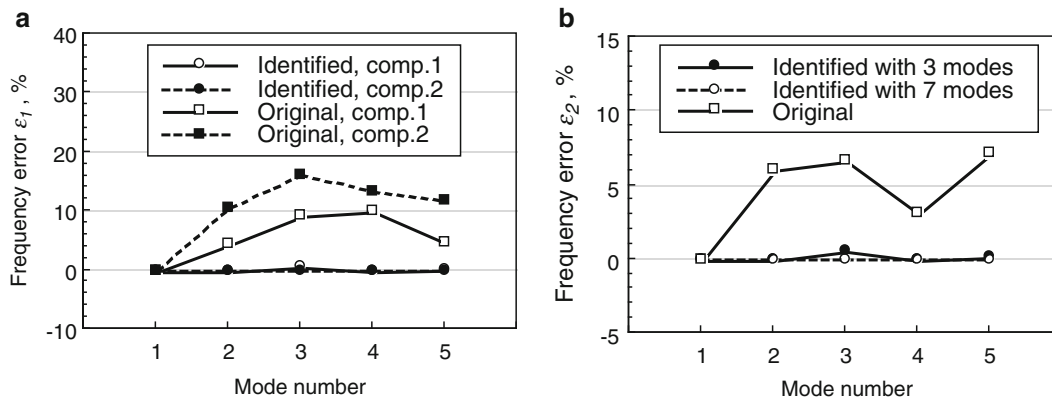
**Fig. 29.6** Frequency error. (**a**) $\varepsilon_1$. (**b**) $\varepsilon_2$

**Fig. 29.7** Mode shape of cantilever beam



error of the first mode is 0, this does not mean that the first frequency is accurate. The first simulated test frequency equals the first analysis frequency, but both frequencies include modeling errors. If modeling errors in original mass and stiffness matrices are small, the second and higher frequencies ought to be accurate. Because original frequency error is not small, it is difficult to consider the simulated test frequency as beam frequency. By identifying mass and stiffness matrices of tested components with the lower three modes, frequency error $\varepsilon_1$ is significantly reduced (maximum error 0.5 %) for both tested components. When using seven modes for system identification, the component modal tests provide the simulated test frequency identical with identified frequency. This suggests that one must check the influence of the number of modes used on identified frequencies because error of identified frequency affects frequency error $\varepsilon_1$. Figure 29.6 (2) shows frequency error $\varepsilon_2$. If mass and stiffness matrices have no modeling errors, predicted frequencies take the same value. Therefore, frequency error $\varepsilon_2$ is an indication to predict accurate target frequencies. The maximum frequency error of $\varepsilon_2$ is 0.5 %. Because frequency errors $\varepsilon_1$ and $\varepsilon_2$ are very small, we conclude that the predicted frequencies are beam frequencies.

Figure 29.7 shows examples of comparison between exact and simulated test modes of the beam. The solid line shows the exact mode, and the dotted line indicates the test mode obtained by simulated component modal tests. It can be seen from Fig. 29.7 that the simulated test modes are similar with the exact modes for both the first and third modes. Table 29.9 lists MAC representing the correspondence between the exact and test modes. MAC is higher than 0.9. For the second, fourth and fifth modes, MAC is also higher than 0.9. This means that the test modes are almost identical to the exact modes.

**Table 29.9** MAC of exact and simulated test modes

| Mode number | 3 modes | 7 modes |
| --- | --- | --- |
| 1 | 1.00 | 1.00 |
| 2 | 0.99 | 0.99 |
| 3 | 0.94 | 0.94 |
| 4 | 0.90 | 0.90 |
| 5 | 0.91 | 0.91 |

**Table 29.10** Material property errors

| Case | | Young's modulus Error (%) | Density Error (%) |
| --- | --- | --- | --- |
| 1 | Component 1 | 20 | −20 |
| | Component 2 | 10 | 5 |
| 2 | Element 1 | 20 | 10 |
| | Others | 10 | 5 |
| 3 | Element 1 | 30 | 10 |
| | Others | 20 | 10 |
| | Element 18 | 20 | 40 |

### 29.3.4 Effect of Different Modeling Errors on Identified Results

The component mass and stiffness matrices are identified for different modeling errors as listed in Table 29.10 to confirm the effect of modeling errors on frequencies and modes obtained by component modal tests. Modeling errors of component 1 are different from those of component 2 in Case 1. In Case 2, errors in element 1 (near the fixed edge) and other elements are different. In addition, different modeling errors are contained in element 18 (near free edge) in Case 3. Identifying component mass and stiffness matrices with seven modes provides the same results as those stated in Sect. II. A three in all cases. From the above results, one can conclude that the proposed method has potential to predict the frequencies and modes.

## 29.4 Conclusions

A component modal testing method was described to obtain the dynamic characteristics of large structures consisting of several components. In this method, to simulate the dynamic behavior of structures, the effect of untested components is considered as additional mass and stiffness attached to a tested component. Because additional mass and stiffness are calculated with mass and stiffness matrices of both structure and tested component, it is difficult to obtain the dynamic characteristics of large structures by component modal tests when finite element models have modeling errors. In this paper, the method was extended to cover the case with modeling errors. Modal tests for different tested components with additional mass and stiffness give an identical frequency, and this frequency is considered as the frequency of structures. It is shown analytically that the identical frequency cannot be obtained when there are modeling errors. Variation in predicted frequency obtained for different tested components is the basis of frequency error estimation. A numerical example shows that the proposed method has potential to be applicable to predicting the dynamic characteristics of large structures even though there are modeling errors in finite element models.

## References

1. Alvin KF, Peterson LD, Park KC (1995) Minimal-order experimental component mode synthesis: new results and challenges. AIAA J 33(8):1477–1485
2. Doebling SW, Peterson LD, Alvin KF (1996) Estimation of reciprocal residual flexibility from experimental modal data. AIAA J 34(8): 1678–1685
3. Morgan JA, Pierre C, Hulbert GM (1997) Forced response of coupled substructures using experimentally based component mode synthesis. AIAA J 35(2):334–339
4. Soucy Y, Humar JL (2003) Experimental verification of a test-based hybrid component mode synthesis approach. AIAA J 41(5):912–923
5. Chen WH, Cherng JS (1985) Modal synthesis via combined experimental consideration of rotational effects. J Sound Vib 103(1):1–11
6. Komatsu K, Sano M, Kai T, Tsujihata A, Mitsuma H (1991) Experimental modal analysis for dynamic models of spacecraft. J Guid Control 14(3):686–688

7. MacNeal RH (1971) A hybrid method of component mode synthesis. Comput Struct 1(4):581–601
8. Rubin S (1975) Improved component-mode representation for structural dynamic analysis. AIAA J 13(8):995–1006
9. Martinez DR, Carne TG, Gregory DL, Miller AK (1984) Combined experimental/analytical modeling using component mode synthesis. In: 25th AIAA/ASME/ASCE/AHS structures, structural dynamics & materials conference, AIAA 1984–0941
10. Admire JR, Tinker ML, Ivey EW (1994) Residual flexibility test method for verification of constrained structural modes. AIAA J 32(1): 170–183
11. Tinker ML (1998) Free-suspension residual flexibility testing of space station pathfinder: comparison to fixed-base results. In: 39th AIAA/ASME/ASCE/AHS/ASC structures, structural dynamics and materials conference and exhibit, AIAA-98-1791
12. Liu F, Zhang DW, Zhang L (2001) Dynamic flexibility method for extracting constrained structural modes from free test data. AIAA J 39(2):279–284
13. Zhang DW, Wei FS (2003) Improved dynamic flexibility method for extracting constrained structural modes from free test data. AIAA J 41(3):498–503
14. Morgan JA, Pierre C, Hulbert GM (1999) Nonbaseband residual flexibility method of component mode synthesis for proportionally damped system. AIAA J 37(10):1285–1291
15. Admire JR, Tinker ML, Ivey EW (1993) Mass-additive modal test method for verification of constrained structural models. AIAA J 31(11):2148–2153
16. Baker M (1986) Component mode synthesis methods for test-based, rigidly connected flexible components. J Spacecr Rockets 23(3):316–322
17. Gwinn KW, Lauffer JB, Miller AK (1988) Component mode synthesis using experimental mode enhanced by mass loading. In: 6th international modal analysis conference, pp 1988–1993
18. Karpel M, Raveh D (1996) Fictitious mass element in structural dynamics. AIAA J 34(3):607–613
19. Karpel M, Ricci S (1997) Experimental modal analysis of large structures by substructuring. Mech Syst Signal Process 11(2):245–256
20. Karpel M, Raveh D, Ricci S (1996) Ground modal tests of space-structure component using boundary masses. J Spacecr Rockets 33(2): 272–277
21. Chandler KO, Tinker ML (1997) A general mass-additive method for component mode synthesis. In: 38th AIAA/ASME/ASCE/AHS/ASC structures, structural dynamics, and materials conference, AIAA-1997-1381
22. Coleman AD, Anderson JP, Driskill TC, Brown DL (1988) A mass additive technique for modal testing as applied to the space shuttle ASTRO-1 payload. In: 6th international modal analysis conference, pp 154–159
23. Misawa M, Funamoto K (2005) Dynamic characteristic prediction of large satellite antennas by component tests. J Spacecr Rockets 42(5): 845–849
24. Misawa M (2010) Component modal tests with additional mass and stiffness. AIAA J 48(8):1840–1847
25. Misawa M, Nakajima J, Kawasoe H (2013) Dynamic characteristics prediction of large structures by component modal tests. AIAA J 51(8):2024–2027
26. Misawa M, Hori K (2007) System identification preserving the mass and stiffness distributions. In: Proceedings of 2007 SEM annual conference & exposition on experimental and applied mechanics, Springfield, paper no. 4
27. Baruch M (1997) Modal data are insufficient for identification of both mass and stiffness matrices. AIAA J 35(11):1797–1798
28. Hirano A, Misawa M (2002) A new method to obtain a unique solution in system identification. In: Proceedings of the 20th international modal analysis conference, Los Angeles, pp 1445–1451

# Chapter 30
# Estimating Frequency-Dependent Mechanical Properties of Materials

**Jason R. Foley and Jacob C. Dodson**

**Abstract** Predicting the dynamic response of structures to impulsive input loads is challenging for a variety of practical and theoretical reasons, but a lack of material properties is the most commonly cited. Material properties are often assumed to be frequency-independent in the analysis of transient data. However, this presents difficulties when dispersion, interface dynamics, and other phenomenology participate in the structural response. A frequency-dependent framework is proposed and implemented to explore the full spectral response of materials under impulsive loads. Experimental data from a modified split Hopkinson pressure bar is used in conjunction with this model to estimate the complex modulus of polyurethane. The estimates of the complex modulus are obtained for three different parameterizations of the complex modulus as a function of frequency, specifically constant, linear, and quadratic models. Results of the estimation are discussed and compared.

**Keywords** Constitutive modeling • High strain rate • Frequency-dependent properties • Viscoelasticity • Hopkinson bar • Experimental mechanics

## Nomenclature

| Note | For symbols where both scalar and vector constants are used in this paper, the bold symbol is the vector quantity and the italics symbol indicates the scalar quantity. |
|---|---|
| Symbol | Description (Units) |
| $\alpha$ | Attenuation coefficient (m$^{-1}$) |
| $\varepsilon$ | Strain (time domain)(m/m) |
| $\tilde{\varepsilon}$ | Strain (frequency domain) (s$^{-1}$) |
| $\gamma$ | Complex wavenumber (m$^{-1}$) |
| $\lambda, \mu$ | Lamé constants (–) |
| $\sigma$ | Stress (time domain)(Pa) |
| $\tilde{\sigma}$ | Stress (frequency domain) (Pa) |
| $\tau$ | Integration variable (s) |
| $\omega$ | Angular/radian frequency (rad/s) |
| $\mathbf{v}$ | Error vector (–) |
| $A$ | Estimation parameters (MPa) |
| $E^*(\omega)$ | Dynamic elastic modulus (Pa) |
| $f$ | Frequency (Hz) |
| $i$ | Imaginary number (–) |
| $j$ | Subdomain index (–) |

J.R. Foley (✉) • J.C. Dodson
Air Force Research Laboratory, AFRL/RWMF, 306 West Eglin Boulevard, Building 432, Eglin AFB, FL 32542-5430, USA
e-mail: jason.foley@eglin.af.mil

| $k$ | Wave propagation coefficient ($m^{-1}$) |
|-----|------------------------------------------|
| $t$ | Time (s) |
| $u$, $\mathbf{u}$ | Displacement (m) |
| $Y$ | Stress relaxation function (Pa·s) |

## 30.1  Introduction

Predicting the dynamic response of structures to impulsive input forces is relevant to many applications. However, transient analysis of a structure depends on the availability of material properties. These are commonly modeled as either frequency-independent (i.e., assumed constant over the analysis range) or as a parameterized rate-dependent constitutive model in a finite element code. However, other phenomenology can influence the apparent stiffness and/or damping of a structure, such as when dispersion, interface dynamics, viscoelastic damping, and/or nonlinear phenomenology participate in the structural response. Other analytic frameworks, especially spectral techniques such as spectral element modeling [1], also implicitly assume knowledge of frequency-dependent properties.

The complex modulus is one widely-used concept that accommodates a range of frequency-dependent responses in materials, particularly viscoelastic materials such as polymers. A representative rheological representation of a viscoelastic material is shown below in Fig. 30.1. Nunziato and Sutherland [2] introduced a stress relaxation function at very high frequencies (ultrasonic) or equivalently short time scales (sub-microsecond). The time-dependent relaxation leads to a complex modulus; see Lundberg and Ödeen [3] for a discussion and example using strain data to estimate the viscoelastic properties of materials. Ahonsi et al. [4] solves for the complex wavenumbers (including both attenuation and propagation) in a PMMA bar at frequencies up to 80 kHz; complex wavenumbers are readily converted into an effective complex modulus. Ödeen and Lundberg [5] reported using bar accelerations in lieu of strain data. Mousavi et al. have simultaneously estimated complex extensional and shear moduli and the Poisson's ratio for both PMMA and polypropylene bars [6, 7] up to frequencies of 40 kHz. Other material systems include compacted pharamaceutical materials (e.g., cellulose and starch binders) [8] and nylon [9].

The estimation of complex material properties is a challenging inverse problem, especially at higher frequencies. Welch and Strømme [10] implemented a form of truth modeling in an analytic study to estimate the valid frequency range for split Hopkinson pressure bar (SHPB) testing in the presence of practical experimental effects, such as noise and finite sample rates. Mahata et al. [11] has also contributed a significant amount of theoretical development of how to estimate the complex properties of viscoelastic materials. Willis et al. [12] performed dynamic characterization experiments using a piezoelectric exciter in a controlled pressure and temperature chamber, and the complex modulus was subsequently estimated from a finite element simulation of the system and solved using inverse problem techniques. Soderstrom [13], Rensfelt and Söderström [14], and Mahata and Söderström [15] have implemented and extended system identification techniques for estimating material functions, the latter introducing Bayesian methods. Finally, Liu and Subhash [16] has implemented a time-domain deconvolution technique to estimate the impulse response function of a polymer bar.

## 30.2  Theory

### 30.2.1  Complex (Frequency-Domain) Material Properties

The stress $\sigma(t)$ in a linearly viscoelastic (i.e., rate-dependent) material can be expressed as the convolution [17] of the stress relaxation function $Y(t)$ and the instantaneous strain rate $\dot{\varepsilon}(t)$,
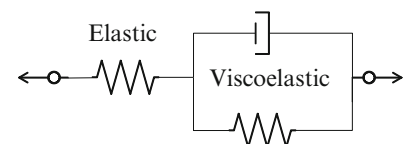
**Fig. 30.1** Simplified rheological model for viscoelastic media

$$\sigma(t) = Y(t) * \dot{\varepsilon}(t) = \int_0^t Y(t - \tau) \, \dot{\varepsilon}(\tau) \, d\omega, \tag{30.1}$$

where $\tau$ is an integration variable. Transformation into the frequency domain of Eq. (30.1) yields

$$\tilde{\sigma}(\omega) = i\omega \tilde{Y}(\omega) \tilde{\varepsilon}(\omega), \tag{30.2}$$

where the time derivative and convolution properties of the Fourier transform have been used [18]. Eq. (30.2) represents a complex, frequency-domain expression equivalent to Young's Law. Thus, the complex elastic modulus $\tilde{E}^*(\omega)$ is

$$\tilde{E}^*(\omega) = i\omega \tilde{Y}(\omega) = \tilde{E}'(\omega) + i \, \tilde{E}''(\omega), \tag{30.3}$$

where $\tilde{E}'(\omega)$ and $\tilde{E}''(\omega)$ are the real and imaginary components of $\tilde{E}^*$. The corresponding complex form of Young's equation is then

$$\tilde{\sigma}(\omega) = \tilde{E}^*(\omega) \tilde{\varepsilon}(\omega). \tag{30.4}$$

### 30.2.2  One-Dimensional Wave Propagation in a Bar

The One-dimensional equation of motion in a bar is

$$\frac{\partial \sigma}{\partial x} - \rho \frac{\partial^2 u}{\partial t^2} = 0 \tag{30.5}$$

Taking the Fourier transform of Eq. (30.5), the frequency-domain equation of motion is obtained:

$$\frac{\partial \tilde{\sigma}}{\partial x} + \rho \omega^2 \tilde{u} = 0, \tag{30.6}$$

where $\tilde{\sigma}$ and $\tilde{u}$ represent the frequency-domain stress and particle displacement, respectively. Next, the spatial derivative $(\partial/\partial x)$ is taken,

$$\frac{\partial^2 \tilde{\sigma}}{\partial x^2} + \rho \omega^2 \frac{\partial \tilde{u}}{\partial x} = 0. \tag{30.7}$$

Finally, it is trivial to transform the definition of strain,

$$\varepsilon(x, t) \equiv \frac{\partial}{\partial x} [u(x, t)], \tag{30.8}$$

into the frequency domain,

$$\tilde{\varepsilon}(x, \omega) = \frac{\partial}{\partial x} [\tilde{u}(x, \omega)]. \tag{30.9}$$

Substituting Eq. (30.9) into Eq. (30.7) leads to a convenient form of the equation of motion, i.e.,

$$\tilde{E}^* \frac{\partial^2 \tilde{\varepsilon}}{\partial x^2} + \rho \omega^2 \tilde{\varepsilon} = 0. \tag{30.10}$$

By defining the complex wavenumber $\gamma$ as

$$\gamma\left(\omega\right) \equiv i\omega \sqrt{\frac{\rho}{\tilde{E}^*}}, \tag{30.11}$$

the equation of motion is then

$$\frac{\partial^2 \tilde{\varepsilon}}{\partial x^2} - \gamma^2 \tilde{\varepsilon} = 0. \tag{30.12}$$

It should be emphasized that the complex wavenumber $\gamma$ contains both real and imaginary terms; these correspond to a real wave propagation constant $k$ (wavenumber) and an attenuation coefficient $\alpha$, i.e.,

$$\gamma = \alpha + ik. \tag{30.13}$$

The general solution to Eq. (30.12) is then

$$\tilde{\varepsilon}\left(x, \omega\right) = \tilde{P}\left(\omega\right) e^{-\gamma x} + \tilde{N}\left(\omega\right) e^{\gamma x}, \tag{30.14}$$

where $\tilde{N}\left(\omega\right)$ and $\tilde{P}\left(\omega\right)$ are the coefficients for the positive- and negative-going waves, respectively. The coefficients for each subdomain are found from the simultaneous solution of system of equations found through enforcing boundary conditions of a particular configuration. The coefficients will correspondingly be specific to the experiment configuration (the subscript $j$ denotes which subdomain) as well material. For example, a classic split Hopkinson pressure bar will have three subdomains: the incident bar, sample, and transmission bar.

### 30.2.3   Semi-Infinite Two-Bar System

The first configuration considered are two bars of identical diameter in intimate contact. In this case, we assume the transmission bar is made of highly attenuating material to has no reflection from the end (semi-infinite bar), which leads to the boundary condition

$$\tilde{N}_2 \to 0. \tag{30.15}$$

Two boundary conditions are then enforced at the interface $(x = L_i)$ and subsequently transformed to the frequency domain. First, we note that the frequency-domain displacement and force are

$$\tilde{u}_j\left(x, \omega\right) = \int \tilde{\varepsilon}_j\left(x, \omega\right) \, dx = -\frac{1}{\gamma_j\left(\omega\right)} \tilde{P}_j\left(\omega\right) e^{-\gamma_j(\omega)x} + \frac{1}{\gamma_j\left(\omega\right)} \tilde{N}_j\left(\omega\right) e^{\gamma_j(\omega)x} \tag{30.16}$$

and

$$\begin{aligned}
\tilde{F}_j\left(\omega\right) &= A_j \, \tilde{\sigma}_j\left(\omega\right) = A_j \tilde{E}_j^*\left(\omega\right) \tilde{\varepsilon}_j\left(\omega\right) \\
&= A_j \tilde{E}_j^*\left(\omega\right) \tilde{P}_j\left(\omega\right) e^{-\gamma_j(\omega)x} + A_j \tilde{E}_j^*\left(\omega\right) \tilde{N}_j\left(\omega\right) e^{\gamma_j(\omega)x},
\end{aligned} \tag{30.17}$$

respectively. An additional response, boundary, or initial condition is necessary to fully determine the system response. This can come from either a sensor (response) or by making assumptions based on the geometry or other features of the system response. The three boundary conditions are shown schematically in Fig. 30.2 and summarized below.

*BC1*: A strain time history $\varepsilon(t)$, observed at the sensor location $x = X_1$, applies a known strain to the system, i.e.,

$$e^{-\gamma_1 X_1} \tilde{P}_1\left(\omega\right) + e^{\gamma_1 X_1} \tilde{N}_1\left(\omega\right) = \tilde{\varepsilon}_1\left(\omega\right) \tag{30.18}$$

which is rewritten as
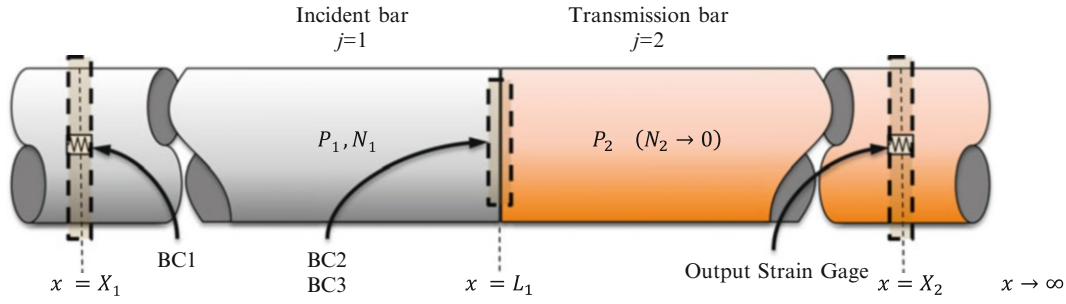
**Fig. 30.2** Location of sensors and boundary conditions for a split Hopkinson bar

$$\left[ e^{-2\gamma_1 X_1} \; 1 \; 0 \right] \left\{ \begin{array}{c} \tilde{P}_1 \\ \tilde{N}_1 \\ \tilde{P}_2 \end{array} \right\} = \tilde{\varepsilon}_1 e^{-\gamma_1 X_1}. \tag{30.19}$$

*BC2*: Continuity of velocity at the interface $(x = L_1)$ is

$$i\omega \tilde{u}_1 = i\omega \tilde{u}_2 \tag{30.20}$$

since $\mathscr{F}(\dot{u}) \to i\omega\tilde{u}$. Substituting Eq. (30.16) and solving for the coefficients leads to

$$-\frac{1}{\gamma_1} e^{-\gamma_1 L_1} \tilde{P}_1(\omega) + \frac{1}{\gamma_1} e^{\gamma_1 L_1} \tilde{N}_1(\omega) + \frac{1}{\gamma_2} e^{-\gamma_2 L_1} \tilde{P}_2(\omega) = 0 \tag{30.21}$$

which can be rewritten as a linear system of equations after dividing through by $\gamma_1^{-1} e^{\gamma_1 L_1}$, i.e.,

$$\left[ -e^{-2\gamma_1 L_1} \; 1 \; \frac{\gamma_1}{\gamma_2} e^{-(\gamma_1+\gamma_2)L_1} \right] \left\{ \begin{array}{c} \tilde{P}_1 \\ \tilde{N}_1 \\ \tilde{P}_2 \end{array} \right\} = 0 \tag{30.22}$$

*BC3*: Force equilibrium at the interface $(x = L_1)$ gives

$$\tilde{F}_1 - \tilde{F}_2 = 0. \tag{30.23}$$

Substituting Eq. (30.17) and solving for the coefficients leads to

$$A_1 \tilde{E}_1^* e^{-\gamma_1 L_1} \tilde{P}_1(\omega) + A_1 \tilde{E}_1^* e^{\gamma_1 L_1} \tilde{N}_1(\omega) + A_2 \tilde{E}_2^* e^{-\gamma_2 L_1} \tilde{P}_2(\omega) = 0. \tag{30.24}$$

By dividing through by $A_1 \tilde{E}_1^* e^{-\gamma_1 L_1}$, a second linear system of equations is obtained:

$$\left[ e^{-2\gamma_1 L_1} \; 1 \; \frac{A_2 \tilde{E}_2^*}{A_1 \tilde{E}_1^*} e^{-(\gamma_1+\gamma_2)L_1} \right] \left\{ \begin{array}{c} \tilde{P}_1 \\ \tilde{N}_1 \\ \tilde{P}_2 \end{array} \right\} = 0 \tag{30.25}$$

The resulting system of equations is

$$\begin{bmatrix} e^{-2\gamma_1 X_1} & 1 & 0 \\ -e^{-2\gamma_1 L_1} & 1 & \frac{\gamma_1}{\gamma_2} e^{-(\gamma_1+\gamma_2)L_1} \\ e^{-2\gamma_1 L_1} & 1 & \frac{A_2 \tilde{E}_2^*}{A_1 \tilde{E}_1^*} e^{-(\gamma_1+\gamma_2)L_1} \end{bmatrix} \left\{ \begin{array}{c} \tilde{P}_1 \\ \tilde{N}_1 \\ \tilde{P}_2 \end{array} \right\} = \left\{ \begin{array}{c} \tilde{\varepsilon}_1 e^{-\gamma_1 X_1} \\ 0 \\ 0 \end{array} \right\}. \tag{30.26}$$

th the coefficients now determined, this solution can be used to predict the results at other locations in the bar. For example, if we have observed an isolated strain time history $\varepsilon_2(t)$ at the location $x = X_2$ on the transmission bar, then the coefficients

can be used to predict the strain at that location, i.e.,

$$e^{-\gamma_2(\omega)X_2}\tilde{P}_2(\omega) = \tilde{\varepsilon}_2(\omega).\tag{30.27}$$

The predicted response can then be readily inverse Fourier transformed into the time domain. This is an inverse problem where minimizing the difference between observed and predicted data will yield the best estimate of the material properties. This is commonly solved via least squares minimization of the inner product of the error vector ($\boldsymbol{v}$), i.e., the difference between the model and data in the time domain,

$$\boldsymbol{v}^T\boldsymbol{v} = \sum_i \left[\varepsilon_2^{model}(t_i) - \varepsilon_2^{data}(t_i)\right]^2.\tag{30.28}$$

However, data in the transmission bar can also be considered analytically once the coefficients are determined. In this case, the complex wavenumber is found analytically by solving for $\gamma_2(\omega)$,

$$\gamma_2(\omega) = -\frac{1}{X_2}\ln\left[\frac{\tilde{\varepsilon}_2(\omega)}{\tilde{P}_2(\omega)}\right].\tag{30.29}$$

The moduli are then found via fitting to the complex wavenumber.

## 30.3 Experiment

The experiment consists of a modified Hopkinson pressure bar test apparatus at the AFRL Shock Dynamics Laboratory. The system consists of two bars: a hollow 72″ aluminum incident bar (major diameter 1″, minor diameter 0.9″) and a 21″ transmission bar cast from the material of interest, polyurethane. Both the incident and transmission bars are instrumented using strain gages.

A combination of direct mechanical (i.e., strain-based) and non-contact (laser vibrometer) measurements are performed on the bars. In the preliminary experimental effort discussed here, the primary measurements are the strain time history in the incident and the transmission bars on both sides of the interface. Uniaxial strain gages are mounted to the bar at a single point, the midpoint of each bar, on both the incident and transmission bars. The axial distribution allows tracking of the stress wave propagating through the system. The gages are oriented axially on the bar in diametrically opposed pairs to allow bending and/or extensional cancellation. This is feasible since the data acquisition system has sufficient number of phase-matched channels to independently capture the output from individual gages: the bending and extension are calculated from the axial strain in post-processing. Semiconductor strain gages are used on the incident bar; these have resistances of 120 or 350 Ω with a fast response time ( 10 ns) and correspondingly higher bandwidth ( 10 MHz) than foil gages (typically 300 kHz [19]). The gage length is typically  1 mm and the gage factor is about 150 [20], providing orders-of-magnitude improvement in sensitivity. The traditional disadvantage of semiconductor gages, a strong temperature dependence, is not a concern for these dynamic tests since the circuits can be balanced immediately prior to a test or run in an AC-coupled mode with minimal temperature excursions between data acquisition arming and trigger. The strain gages were wired with a floating shield/ground to avoid ground loops. Bi-axial foil gages were applied to the transmission bar due to the expected large strain. Additionally, an OFV-522 Polytec laser vibrometer was used (paired with an OFV-500 high speed (20 m/s) controller/demodulator) to perform a non-contact measurement of the surface velocity of the transmission bar with a bandwidth of up to 1.5 MHz [21] (Figs. 30.3 and 30.4).

Analog signal conditioning for the strain gages, (i.e., regulated constant-current excitation, analog filtering at 700 kHz, and amplification), is accomplished via a Precision Filter 28000 chassis with 28144A Quad-Channel Wideband Transducer Conditioner with Voltage and Current Excitation cards [22]. A high rate instrumentation system using a National Instruments chassis paired with PXI-6133 multifunction input/output cards is used to digitize the analog data. The PXI-6133 samples at 2.5 MSa/s with 16 bits of vertical resolution [23]. A typical strain time history is shown in Fig. 30.5.
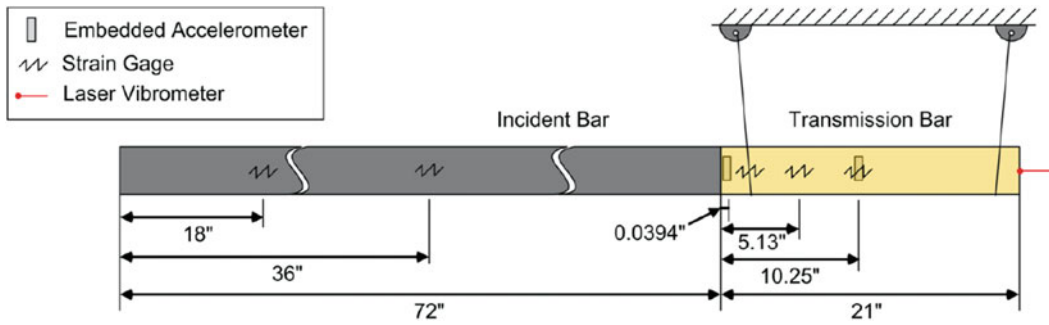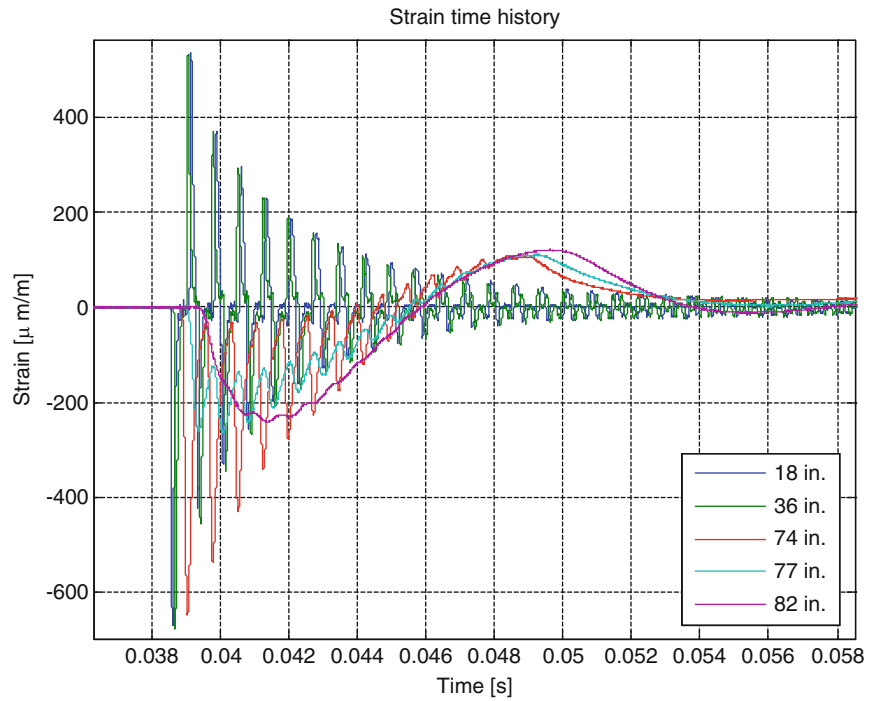
**Fig. 30.3** Schematic of two-bar experiment showing sensor locations and the polymer bar support mechanism
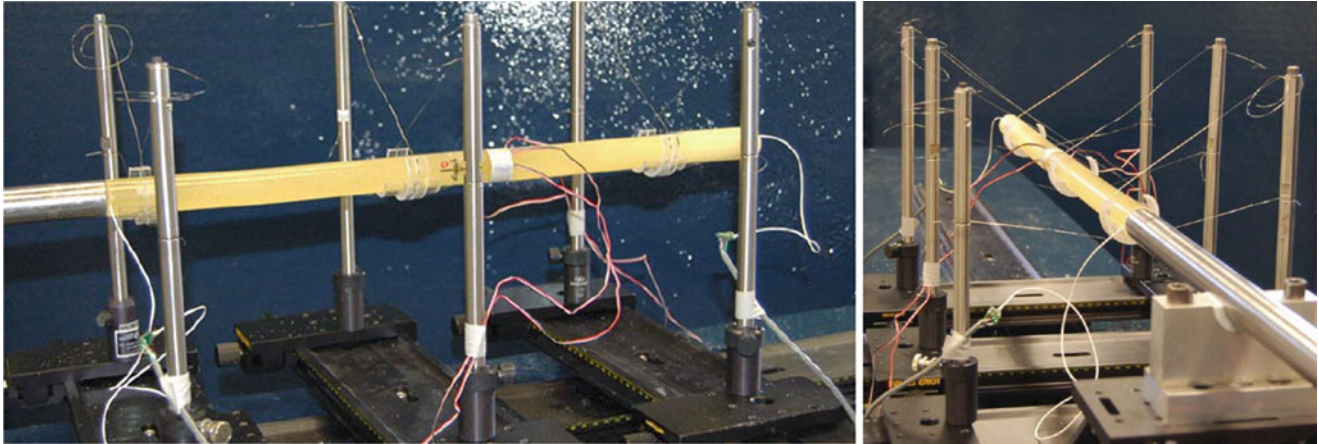


**Fig. 30.4** Photos of two-bar experiment highlighting the polymer bar support mechanism

**Fig. 30.5** Strain time history in
the hollow aluminum incident
($x_i = 18$ and 36 in.) and solid
polyurethane transmission
($x_i = 74$, 77, and 82 in.) bars

## 30.4 Analysis

We initially calculate the velocity at various frequencies from a simple One-dimensional wave propagation model using time-of-arrival of the waves. The results of this analysis for the aluminum and polyurethane bars are shown in Fig. 30.6 up to 50 kHz. Assuming the density of aluminum and polyurethane are known ($\rho \approx 2,700$ and 975 kg/m$^3$), the resulting wave speed can be used to provide a first-order estimate of the modulus using the well-known One-dimensional wave speed relationship,

$$E = c^2 \rho. \tag{30.30}$$

The corresponding modulus for aluminum is 72 GPa and polyurethane is 64 MPa.

This implicitly makes the assumption of constant properties; the variable wave speed evident in Fig. 30.6 imply that some frequency dependence exists in the modulus. The frequency dependence of the complex modulus is parameterized using simple functions and discussed in detail below.

### 30.4.1 Estimation of Parameterized Frequency Distribution

The simplest parameterization of the frequency dependence is a constant complex modulus, i.e., $E^* = E' + iE'' = A_1 + iA_2$ where $A_1$ and $A_2$ are estimation parameters. Similarly, a linear parameterization is

$$E'(\omega) = A_1 + A_2\omega, \tag{30.31}$$

$$E''(\omega) = A_3 + A_4\omega, \tag{30.32}$$

and a quadratic model is

$$E'(\omega) = A_1 + A_2\omega + A_3\omega^2, \tag{30.33}$$
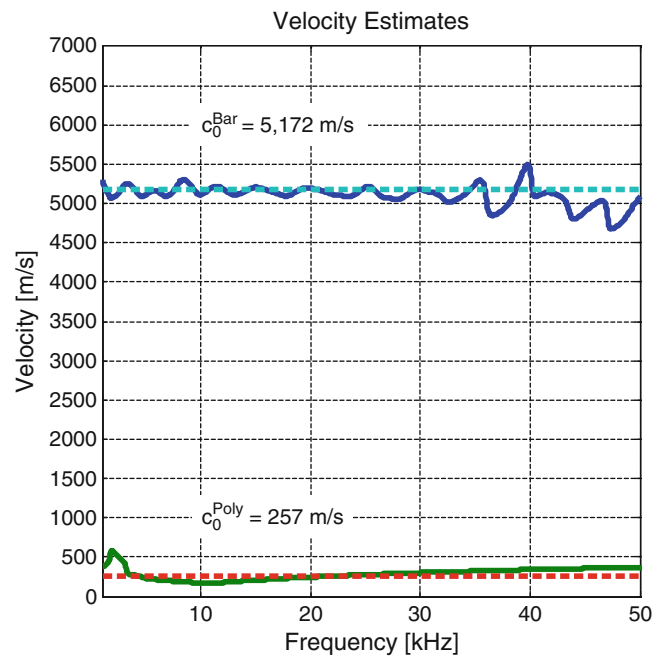


**Fig. 30.6** Frequency-dependent velocity

**Table 30.1** Estimation parameters, including initial and final iteration values, from analysis of the strain data using constant, linear, and quadratic parameterizations of the complex modulus

| Symbol | Min | Initial | Final | Max | Units | Parameter |
|---|---|---|---|---|---|---|
| *Constant* | | | | | | |
| $A_1$ | 0 | 64 | 66.87 | 1,000 | MPa | Modulus coefficient (real) |
| $A_2$ | 0 | 0.064 | 0.1397 | 100 | MPa | Modulus coefficient (imaginary) |
| *Linear* | | | | | | |
| $A_1$ | 0 | 50 | 15.54 | 1,000 | MPa | Modulus coefficient (real) |
| $A_2$ | −1 | 0.00025 | −0.004907 | 1 | MPa/rad/s | Modulus coefficient (real) |
| $A_3$ | 0 | 0.5 | 1.211 | 100 | MPa | Modulus coefficient (imaginary) |
| $A_4$ | −1 | 0.0001 | 0.003137 | 1 | MPa/rad/s | Modulus coefficient (imaginary) |
| *Quadratic* | | | | | | |
| $A_1$ | 0 | 50 | 21.38 | 1,000 | MPa | Modulus coefficient (real) |
| $A_2$ | −1 | 0.00025 | 0.7074 | 1 | MPa/rad/s | Modulus coefficient (real) |
| $A_3$ | −1 | 0.1 | 0.02585 | 1 | MPa/rad$^2$/s$^2$ | Modulus coefficient (real) |
| $A_4$ | 0 | 0.500 | 0.6268 | 100 | MPa | Modulus coefficient (imaginary) |
| $A_5$ | −1 | 0.0001 | 0.03490 | 1 | MPa/rad/s | Modulus coefficient (imaginary) |
| $A_6$ | −1 | 0.1 | −0.01973 | 1 | MPa/rad$^2$/s$^2$ | Modulus coefficient (imaginary) |

$$E''(\omega) = A_4 + A_5\omega + A_6\omega^2, \tag{30.34}$$

where $A_i$ are again estimation parameters. The complex modulus can then be written equivalently as

$$E_2^*(\omega) = E'(\omega) + iE''(\omega) = \left(A_1\omega^2 + A_2\omega + A_3\right) + \left(A_4\omega^2 + A_5\omega + A_6\right) i \tag{30.35}$$

for the quadratic case.

As noted in the theory, the estimation is performed by minimizing the error between the data and model in a least squares framework. The built-in optimization function *lsqnonlin* is used in Matlab to obtain the estimates; the gradient-based minimizer accommodates upper and lower bounds on the estimation parameter [24]. The results of the three cases (constant, linear, and quadratic) are shown below in Table 30.1.

The time domain results of the fitting, shown in Fig. 30.7, indicate that the linear parameterization generates the best agreement (as indicated by the lower value of the least squares error, $\mathbf{v}^T\mathbf{v}$). This counterintuitive result is currently being explored, but is likely due to the estimator finding a local, as opposed to global, minimum. The corresponding complex modulus, shown in Fig. 30.8 for frequencies from 0 to 10 kHz, also exhibits a wide range of values. The linear model is the same order of magnitude as the constant model; however, the imaginary component has a higher value than the real value. Additionally, the real value is negative for frequencies above about 700 Hz, which is aphysical. The quadratic model is clearly overpredicting the modulus, but again there is no assurance that the estimated values are at the global minimum. Additional analysis and global optimization methods will be required to increase the fidelity of these estimates.

## 30.5  Future Work

The initial work presented here will be extended in several ways. The first is to include data from complementary experiments, such as dynamic mechanical analysis (DMA), as prior information when estimating the complex modulus of the material. Other aspects of Bayesian analysis, such as using multiple data sets and describing material properties via probability distributions, have been introduced in related work using DMA [25] and are currently being applied for complex modulus estimation from dynamic strain data. Lastly, the one-dimensional analysis will be extended to axisymmetric three-dimensional cases to capture the effects of dispersive wave propagation.

**a**



Constant, $\mathbf{v}^T\mathbf{v} = 1.42\mathrm{e}7$

**b**



Linear, $\mathbf{v}^T\mathbf{v} = 6.66\mathrm{e}5$

**c**



Constant, $\mathbf{v}^T\mathbf{v} = 5.31\mathrm{e}6$
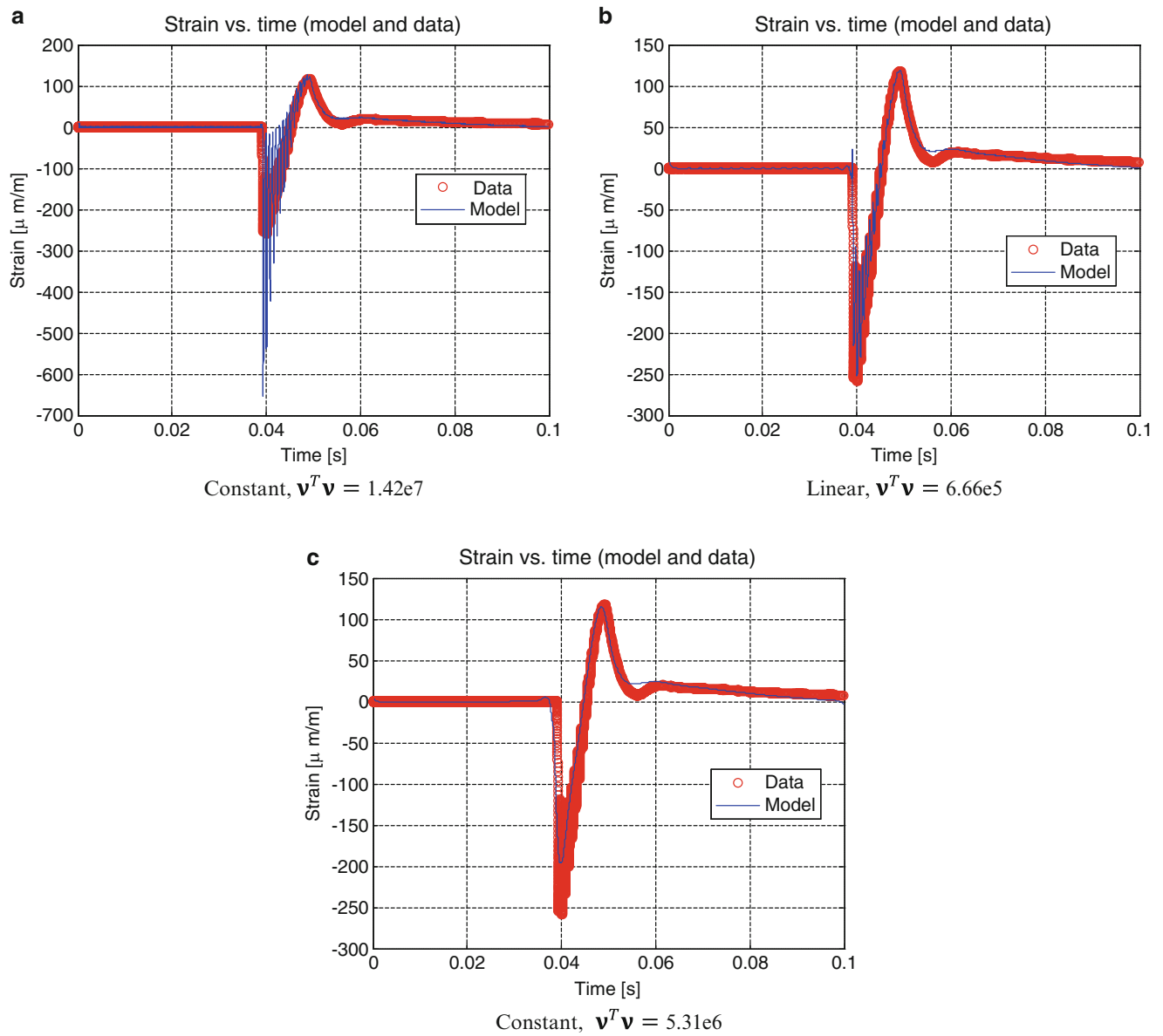
**Fig. 30.7** Data and model fitting results for (**a**) constant, (**b**) linear, and (**c**) quadratic parameterized complex modulus

**Fig. 30.8** Estimates of the complex modulus as a function of frequency for constant, linear, and quadratic parameterizations
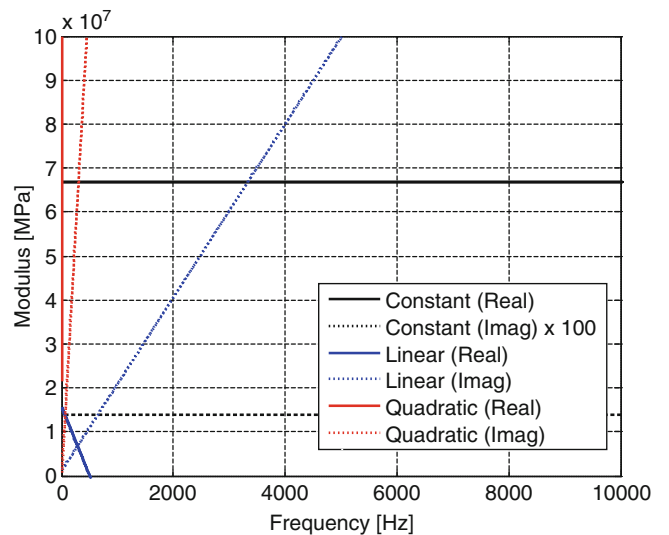
## 30.6   Summary

A frequency-dependent framework was developed and implemented to describe one-dimensional stress wave propagation through a modified split Hopkinson bar. Experimental data from a modified split Hopkinson pressure bar is used in conjunction with this model to estimate the complex modulus of polyurethane. The estimates of the complex modulus are obtained for three different parameterizations of the complex modulus as a function of frequency, specifically constant, linear, and quadratic models. Results of the estimation are discussed and compared.

# References

1. Doyle JF (1997) Wave propagation in structures: spectral analysis using fast discrete fourier transforms. Springer, New York
2. Nunziato JW, Sutherland HJ (1973) Acoustical determination of stress relaxation functions for polymers. J Appl Phys 44(1):184–187
3. Lundberg B, Ödeen S (1993) In situ determination of the complex modulus from strain measurements on an impacted structure. J Sound Vib 167(3):413–419
4. Ahonsi B, Harrigan JJ, Aleyaasin M (2012) On the propagation coefficient of longitudinal stress waves in viscoelastic bars. Int J Impact Eng 45:39–51
5. Ödeen S, Lundberg B (1993) Determination of complex modulus from measured end-point accelerations of an impacted rod specimen. J Sound Vib 165(1):1–8
6. Mousavi S, Nicolas DF, Lundberg B (2004) Identification of complex moduli and Poisson's ratio from measured strains on an impacted bar. J Sound Vib 277(4–5):971–986
7. Mousavi S, Welch K, Valdek U, Lundberg B (2005) Non-equilibrium split Hopkinson pressure bar procedure for non-parametric identification of complex modulus. Int J Impact Eng 31(9):1133–1151
8. Welch K, Mousavi S, Lundberg B, Strømme M (2005) Viscoelastic characterization of compacted pharmaceutical excipient materials by analysis of frequency-dependent mechanical relaxation processes. Eur Phys J E Soft Matter 18(1):105–112
9. Collet P, Gary G, Lundberg B, Mohr D (2012) Complex modulus estimation respecting causality: application to viscoelastic bars. EPJ Web of Conferences 26:01012
10. Welch K, Strømme M (2007) Low frequency limitations of the split Hopkinson pressure bar method for identification of complex modulus. Int J Impact Eng 34(6):1036–1046
11. Mahata K, Mousavi S, Söderström T (2006) On the estimation of complex modulus and Poisson's ratio using longitudinal wave experiments. Mech Syst Signal Process 20(8):2080–2094
12. Willis RL, Wu L, Berthelot YH (2001) Determination of the complex Young and shear dynamic moduli of viscoelastic materials. J Acoust Soc Am 109(2):611–621
13. Söderström T (2002) System identification techniques for estimating material functions from wave propagation experiments. Inverse Probl Eng 10(5):413–439
14. Rensfelt A, Söderström T (2011) Parametric identification of complex modulus. Automatica 47(4):813–818
15. Mahata K, Söderström T (2007) Bayesian approaches for identification of the complex modulus of viscoelastic materials. Automatica 43(8):1369–1376
16. Liu Q, Subhash G (2006) Characterization of viscoelastic properties of polymer bar using iterative deconvolution in the time domain. Mech Mater 38(12):1105–1117
17. Mousavi S (2007) Identification of viscoelastic materials by use of wave propagation methods. Digital Comprehensive Summaries of Uppsala Dissertations from the Faculty of Science and Technology 369:59
18. Bracewell RM (1965) The fourier transform and its applications. McGraw-Hill, New York, pp 6–7, 244–250
19. Ueda K, Umeda A (1998) Dynamic response of strain gages up to 300 khz. Exp Mech 38(2):93–98
20. 2001, Kulite Strain Gage Manual, Kulite Semiconductor Products
21. 2010, OFV-552 Laser Vibrometer, Polytec
22. 2009, Precision 28144 Quad-Channel Wideband Transducer Conditioner with Voltage and Current Excitation (Datasheet), Precision Filters, Ithaca
23. 2003, NI PXI-6133 Specifications, National Instruments, Austin
24. 2011, Matlab User's Manual (version 2011b), Mathworks
25. Foley JR, Jordan JL, Siviour CR (2012) Probabilistic estimation of the constitutive parameters of polymers. EPJ Web of Conferences 26:04041

# Chapter 31
# Flexible Dynamic Modeling of Turret Systems by Means of Craig-Bampton Method and Experimental Validation

**Fatih Altunel and Murat Aykan**

**Abstract**  Today's mechanical systems are designed and manufactured with increasing functionality due to the increase in the design requirements. This leads to use of higher numbers of degrees of freedom, causing system modeling process become more complicated, including structural and dynamic aspects. The sources of complexity arise mainly from the connection mechanisms like gears, bearings and gear boxes and dynamic behavior of the structural parts in motion. Usually, each of these subsystems is analyzed individually by analytical and/or numerical methods. However, the whole system performance should be modeled and analyzed in the assembly configuration in order to observe the interaction of subsystems. Furthermore, critical structural parts should be modeled flexible and connection mechanisms' dynamic properties need to be identified accurately. Modeling parts elastically also result in additional degrees of freedom which makes the model difficult to solve for kinematic analysis. Therefore, Craig-Bampton reduction method is used to reduce the size of elastically modeled parts. In this study, dynamic modeling process and analysis results of a turret will be presented. Furthermore, comparisons between the analysis results and the assembled prototype turret tests are presented.

**Keywords**  Craig-Bampton • Dynamical modeling • Turret system • Experimental validation • Flexible modeling

## 31.1 Introduction

Advancements in various fields of technology moves defense, automotive and aerospace industries forward for better products. Even though this makes systems more user-friendly and increases the functionality, it makes the mechanical designs complicated and difficult to simulate. The biggest reason for this is the increasing usage of fragile electronic equipments such as cameras, sensors and antennas in the designs.

Development of new technologies increases the performance expectations of users. This also forces the designers to pursue continuous research and development. Furthermore, the duration of a product's design cycle (conceptual design to the final prototype) is steadily declining. That's why; the design-analysis-prototype manufacturing process has to improve continuously. Today, computer aided design and analysis techniques are used to improve this process. Especially, computer aided engineering (CAE), (i.e. finite element method (FEM)), improves the design process drastically and makes it possible to design advanced products. After the introduction and application of FEM around 1960s and 1970s, mechanical system simulations accelerated the design cycle of the products [1]. Over the years, advanced methods have been developed to speed up the process. In this scope, even the first stage of prototype testing is now performed by computer simulation. Defense, automotive and aerospace industries have already added this step to their R&D processes. A sample product design cycle, shown in Fig. 31.1, is now mostly carried out in the simulated environment.

In the design process, mostly sub-products are analyzed by using computer simulation. Even if a sub-system has no problems when used on its own, it can pose problems if combined with other sub-systems. That's why, analyzing only the sub-systems separately is not sufficient. Thus, system level simulations have to be performed. The biggest advantage of
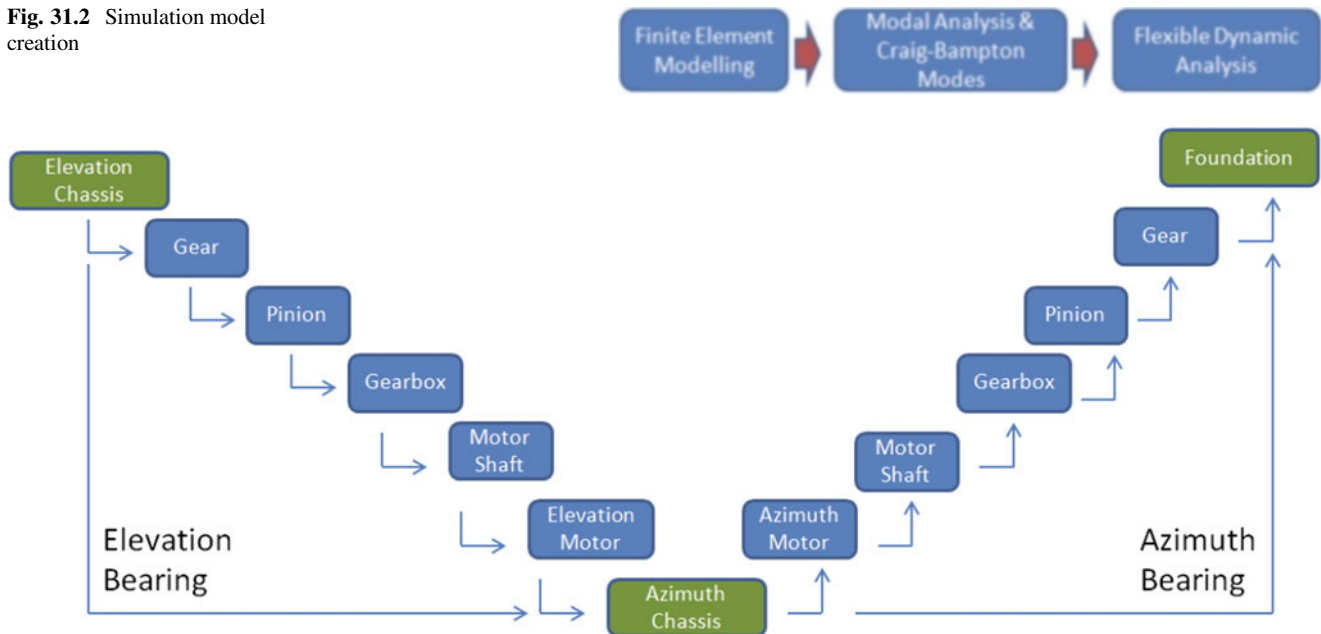
---

F. Altunel (✉) • M. Aykan

Division of Defense Systems Technologies, ASELSAN Inc., Ankara 06172, Turkey
e-mail: faltunel@aselsan.com.tr
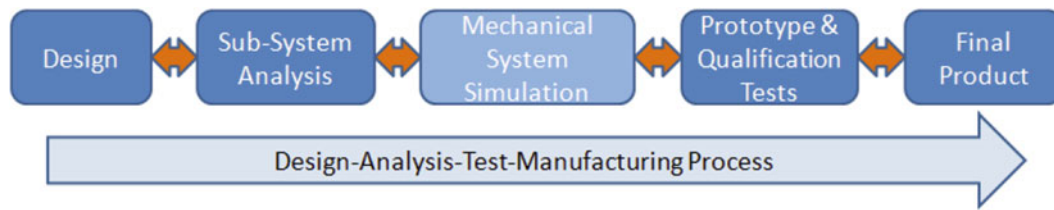
**Fig. 31.1** Product design cycle

**Fig. 31.2** Simulation model creation





**Fig. 31.3** Wiring diagram for the entire system

system level simulations is that problems can be identified before the physical prototype is manufactured and the number of prototypes and testing time may be reduced. As a result, reducing the number of prototype units, even one unit, is of great importance in terms of both cost and time.

The increasing complexity of designs is also forcing complex systems to be divided into sub-systems and designed by different teams. Therefore, in order to have a correct system model, the subsystems need to be brought together and analyzed as a whole. In this scope, different methods were developed to be used both for sub-system and system level simulations [2, 3].

In this study, self-propelled defense turret is investigated to determine the dynamic performance of the system by simulation environment. By developing a flexible dynamical model of the turret;

- Sine-sweep, modal analysis, etc. studies can be performed in simulation environment,
- The dynamic characteristics of the system can be accurately determined,
- Stability control strategy used in precision feedback can be provided,
- Sub-system modification effects can be analyzed without manufacturing new prototypes,
- Performance and working conditions of engine, gearbox, bearings, etc. can be evaluated correctly,
- Effects of foundation stiffness and system level natural frequency to the system performance can be analyzed.

LMS Virtual Lab (VL) was used for flexible dynamic analysis of the turret. In order to get Craig-Bampton modes of the flexible parts, MSC Nastran was used. This process is summarized in Fig. 31.2.

Mechanical connecting parts like bearings, gears, motor shafts, gearboxes and motors are modelled using springs and dampers (linear and nonlinear). All of the system components are connected to each other by using specific joints. Wiring diagram for the entire system is summarized in Fig. 31.3.

VL environment allows modeling details given below by adding spring-damper components:

- Backlash between gears
- Gap (clearance) inside bearings
- Friction in gears and bearings,
- The elasticities of motors, motor shafts, bearings, gearboxes and gears

These details, which are difficult to define in standard finite element modeling softwares, can be defined by various ways in VL environment.

## 31.2 Theory

Finite element analysis of motionless systems and sub-systems is a standardized analysis process. For the past 10 years, more and more complex systems with actuators are designed and need to be analyzed simulating real boundary conditions. Therefore, flexible multi body dynamic analysis is required. The main objective in flexible multi body dynamic analysis is to determine the dynamical flexibility of the system. Once this information is obtained, both the structural and dynamic performance of the systems during operation can be examined. One of the most important advances is addition of reduced finite element models of sub-systems and their modal parameters into the dynamical analysis of whole system. The reduction can be performed by using various algorithms. Some of the most popular ones are Guyan Reduction, Dynamic Reduction, System Equivalent Reduction Expansion Process and Craig-Bampton methods [4]. Craig-Bampton method is used widely inside many commercial flexible multibody dynamical analysis softwares. In this method, the motion of the whole structure is represented as a combination of boundary points (master degrees of freedom) and modes of the structure assuming that the master degrees of freedom are held fixed. Unlike Guyan reduction, which only accounts for the stiffness matrix, Craig-Bampton accounts for both the mass and stiffness [5].

VL software uses Craig-Bampton method for flexible multibody dynamic analysis. In this method, as in other methods, system matrices of a sub-system modeled with thousands of degrees of freedom (DOF) are reduced by defining master nodes. For example, a sample meshed beam structure shown in Fig. 31.4. The original structure has 5,500 DOF. It is reduced to 12 DOF where each point in circle has 6 DOF.

Equation of motion of an undamped sub-system can be written as:

$$[M]\{\ddot{u}\} + [K]\{u\} = \{F\} \tag{31.1}$$

where [M] is the mass matrix, [K] is stiffness matrix, {F} is force vector, {u} and {ü} are the displacement and acceleration vectors, respectively.

The most important step in reducing the degree of freedom is to group the system matrices into master and slave nodes. After grouping is performed, Eq. (31.1) is rewritten as follows [6]:

$$\begin{bmatrix} M_{mm} & M_{ms} \\ M_{sm} & M_{ss} \end{bmatrix} \begin{Bmatrix} \ddot{u}_m \\ \ddot{u}_s \end{Bmatrix} + \begin{bmatrix} K_{mm} & K_{ms} \\ K_{sm} & K_{ss} \end{bmatrix} \begin{Bmatrix} u_m \\ u_s \end{Bmatrix} = \begin{Bmatrix} F_m \\ 0 \end{Bmatrix} \tag{31.2}$$

where the subscripts "m" and "s" refer to master and slave nodes, respectively. At this point, the system equations are converted into modal coordinates via below transformation matrix:

$$\begin{Bmatrix} u_m \\ u_s \end{Bmatrix} = T \begin{Bmatrix} u_m \\ q \end{Bmatrix} \tag{31.3}$$
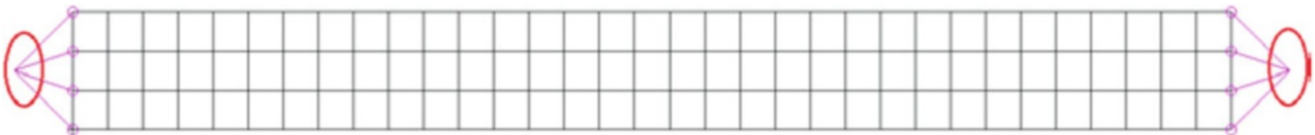


**Fig. 31.4** Reduction of a structure into two connecting master points (12 DOF)
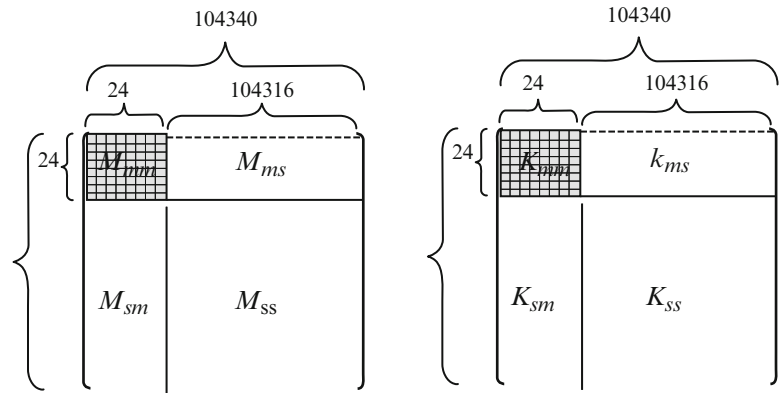
Then, reduction is performed at these modal coordinates. In this way, the reduced dynamic equation of motion is obtained as follows:

$$\underbrace{\begin{bmatrix} M_{bb} & M_{bq} \\ M_{qb} & M_{qq} \end{bmatrix}}_{F_{reduced}} \begin{Bmatrix} \ddot{u}_m \\ \ddot{q} \end{Bmatrix} + \underbrace{\begin{bmatrix} K_{bb} & 0 \\ 0 & K_{qq} \end{bmatrix}}_{K_{reduced}} \begin{Bmatrix} u_m \\ q \end{Bmatrix} = \underbrace{\begin{matrix} F_m \\ 0 \end{matrix}}_{F_{reduced}} \qquad (31.4)$$

where subscript "q" represents the modal coordinates, "b" stands for reduced boundary representation. If damping is added to the equation and reduction is performed by using Craig-Bampton method, reduced dynamic equation of motion is written as follows:

$$\begin{bmatrix} M_{bb} & M_{bq} \\ M_{qb} & I \end{bmatrix} \begin{Bmatrix} \ddot{u}_m \\ \ddot{q} \end{Bmatrix} + \begin{bmatrix} 0 & 0 \\ 0 & 2\xi\omega \end{bmatrix} \begin{Bmatrix} \dot{u}_m \\ \dot{q} \end{Bmatrix} + \begin{bmatrix} K_{bb} & 0 \\ 0 & \omega^2 \end{bmatrix} \begin{Bmatrix} u_m \\ q \end{Bmatrix} = \begin{Bmatrix} F_m \\ 0 \end{Bmatrix} \qquad (31.5)$$

where $\xi$ and $\omega$ stand for damping ratio and eigenfrequency, respectively. For example, if 104,340 DOF system is reduced into 24 DOF, then system matrices become as given in Fig. 31.5.

Using the reduction process, dynamic characteristics of elastic parts can be included in the multibody analysis of the entire system with ease. Pan et al. [7] carried out dynamic simulations of a power generator using this method, and compared with the test results. While the frequencies found are not exactly the same with the test results, values are considered acceptable by authors. Thus, he reported that the method is effective and accurate for practical cases. This method is being used as a standard method for many companies in recent years.

Inside many actuated systems, there are components like gearbox, motor, bearing, etc. that are not suitable to model as flexible elements by classical FEM tools in terms of time required and complexity level. On the other hand, their flexibilities must be added to the system analysis since they have an important contribution to the flexibility of the entire system. In this study, the most suitable approach is considered as including these flexibilities as spring and damper elements to the system.

## 31.3 Turret Case Study

### 31.3.1 Prototype Modal and Torque Frequency Sweep Tests

For this study, a prototype of the turret was manufactured. On this prototype, two different tests are performed with the aim of validating the VL simulation model. Firstly, accelerometers are placed at designated locations on the prototype and then impact testing is performed by a modal hammer. This process is performed for elevation chassis, azimuth chassis and the gun. Secondly, turret system is given motion in azimuth direction by applying torque on the azimuth motor, keeping the accelerometers at the same location as the modal test. Torque sweep is applied for the 1–100 Hz bandwidth and acceleration response is acquired.

**Fig. 31.6** Representative gun
turret
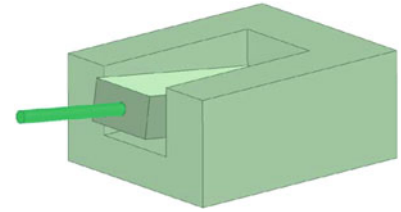


**Fig. 31.7** FRF graph for point
one for fixed-free boundary
condition, axes values are
normalized
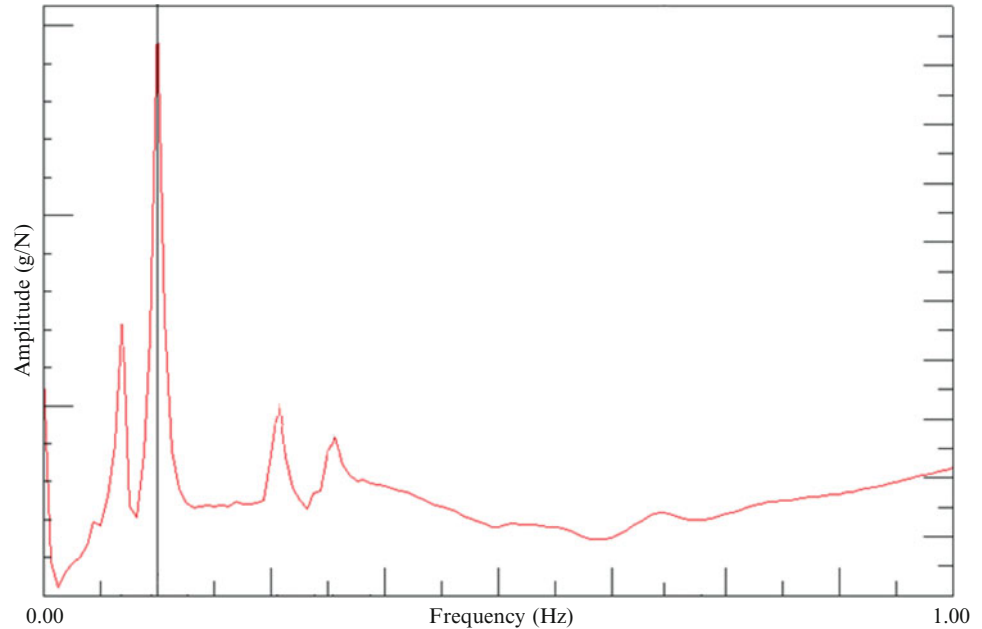


Due to some interface problems, turret could not be integrated on a rigid base. Instead, it was mounted on a six DOF motion platform. During torque sweep tests, accelerometers were also installed on motion platform in order to see if the resonances of the motion platform are excited or not. A representative drawing of the turret system on the motion platform is shown in Fig. 31.6.

### 31.3.1.1 Barrel, Elevation and Azimuth Chassis Modal Tests

The gun that is used in this turret is too large and complex to be modeled as flexible. On the other hand, the barrel is considered to have considerably high inertia and flexibility compared to the some other components of the turret. Therefore, barrel is modeled as flexible to include its dynamic characteristics. Within this scope, the barrel is tested as fixed-free in order to determine the natural frequencies. Here, fixed means that the barrel is attached to the gun. Test results were also needed to validate the finite element model of the barrel. Frequency response function graph obtained from the accelerometer at the gun tip is shown in Fig. 31.7.

Different frequency response function graphs are analyzed and the first bending mode of the barrel is identified. The corresponding mode shape is shown in Fig. 31.8.

In the scope of turret chassis modal tests, accelerometers are placed onto desired locations of the elevation chassis. Modal hammer is used to drive the chassis at various accelerometer locations. A sample FRF obtained from one of the sensors is shown in Fig. 31.9, with peak frequencies emphasized.

Similar studies were carried out on the azimuth chassis. A sample FRF functions from these tests and peak frequencies are shown in Fig. 31.10.
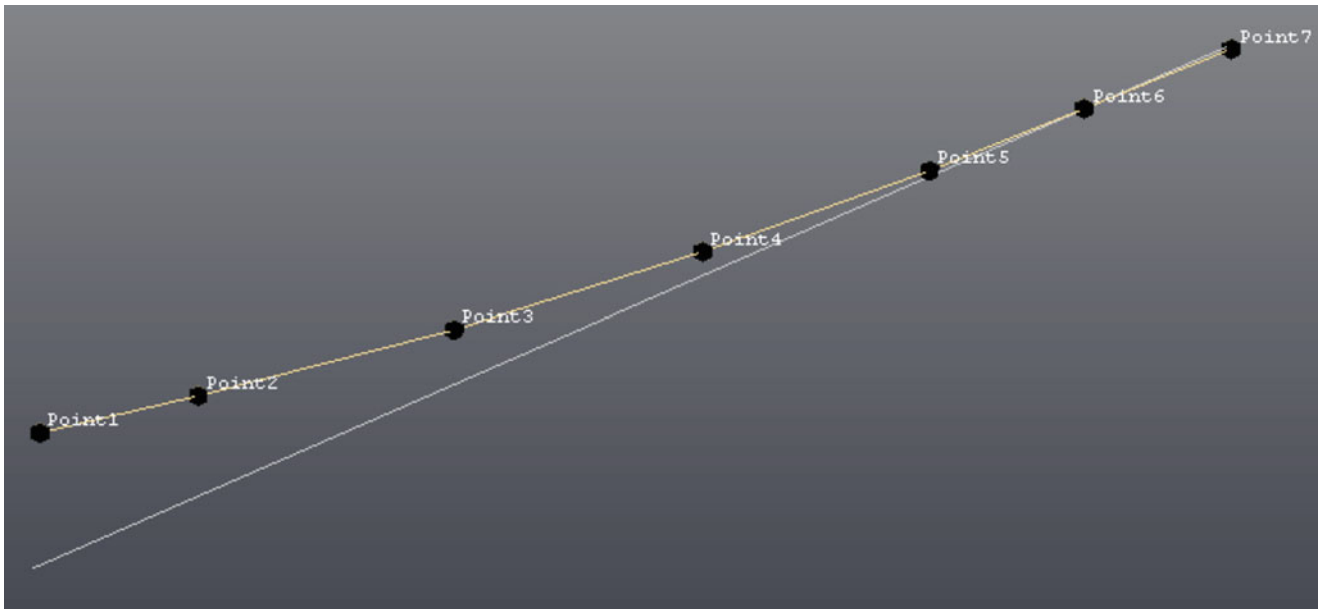
**Fig. 31.8** Barrel first mode shape
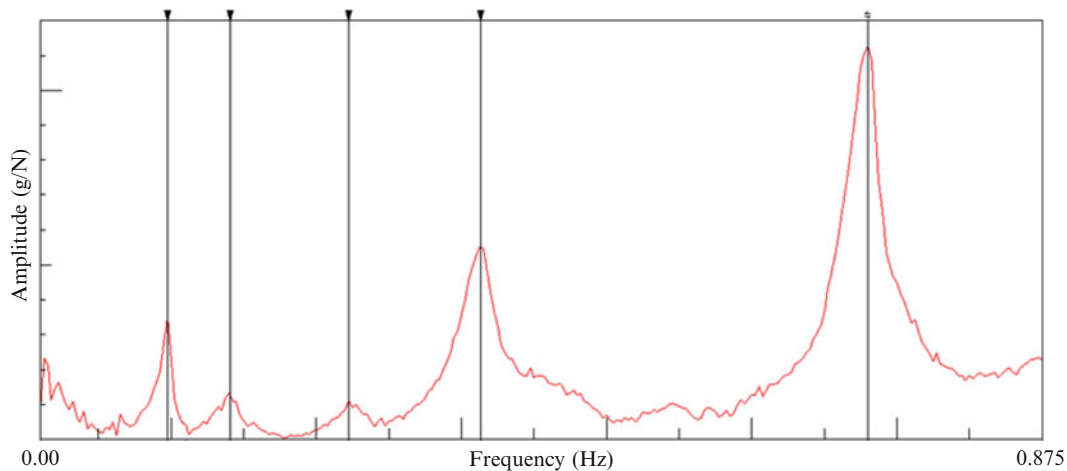


**Fig. 31.9** Elevation chassis FRF at accelerometer 5, axes values are normalized

#### 31.3.1.2 Torque Frequency Sweep Test

Torque frequency sweep tests were carried out on the turret in addition to the modal tests. These tests were performed only on the azimuth axis. Yet, accelerometers were located on both azimuth and elevation chassis. Sweep tests were performed between 1 and 100 Hz with a sweep rate of 0.5 Hz. At each frequency step, 16 cycles were covered (Fig. 31.11).

The FRF plot shown in Fig. 31.12 is obtained from the sensor at gyro location on the elevation chassis in azimuth direction. The barrel affects the elevation gyro response at barrel's first natural frequency because of its high inertia. Also, according to the FRF plot (Fig. 31.13) of azimuth gyro location, barrel is effective on azimuth as well.

### 31.3.2 Two-Mass System Model

The complex system is also simplified as a two-mass system with a torsional spring connection to evaluate the primary resonances. For the sake of clarity, a two DOF model of the elevation chassis will be derived as shown in Fig. 31.14. In order to find the fundamental natural frequencies, Valenzuela et al. [8] analyzed a simple two-mass model.
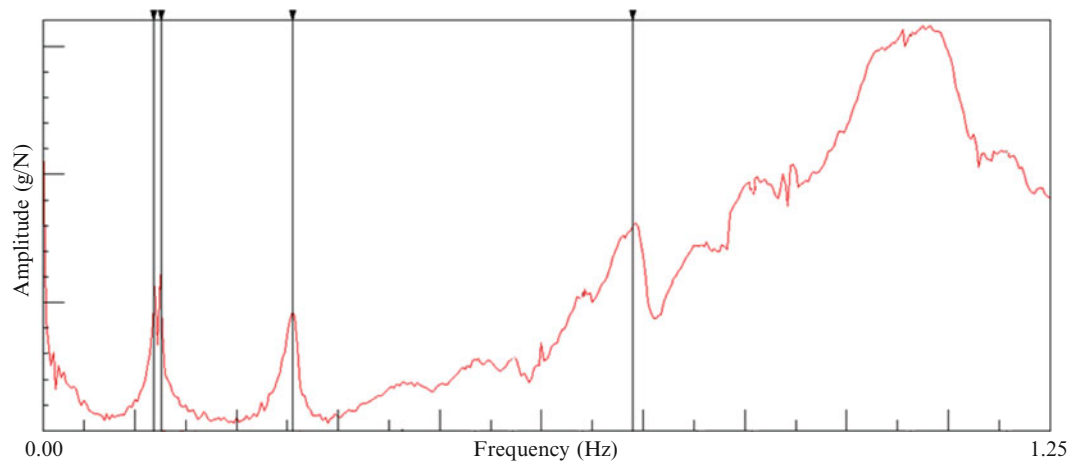
**Fig. 31.10** Azimuth chassis FRF at accelerometer 6, axes values are normalized
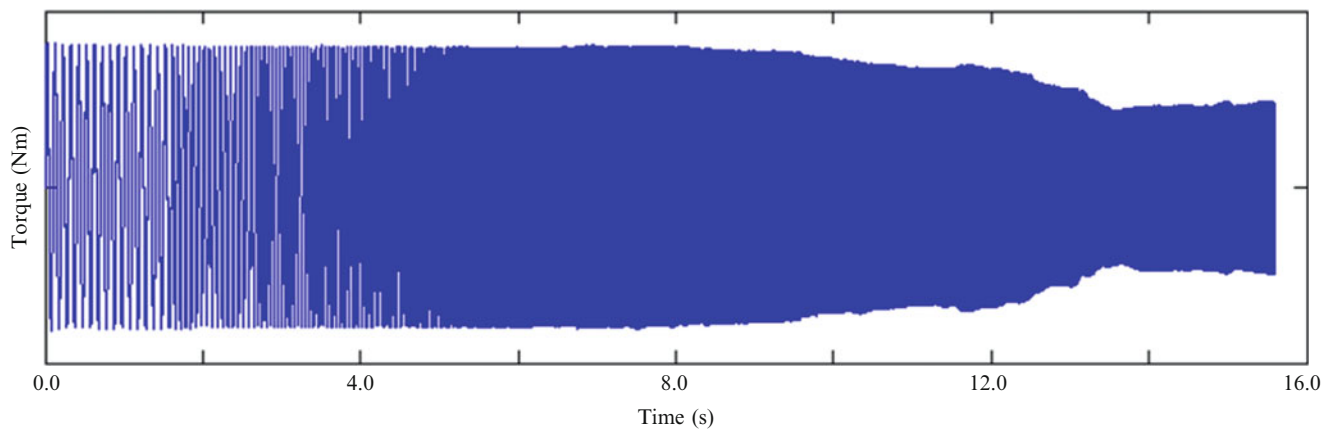


**Fig. 31.11** Azimuth frequency sweep test torque graph in terms of time, axes values are normalized
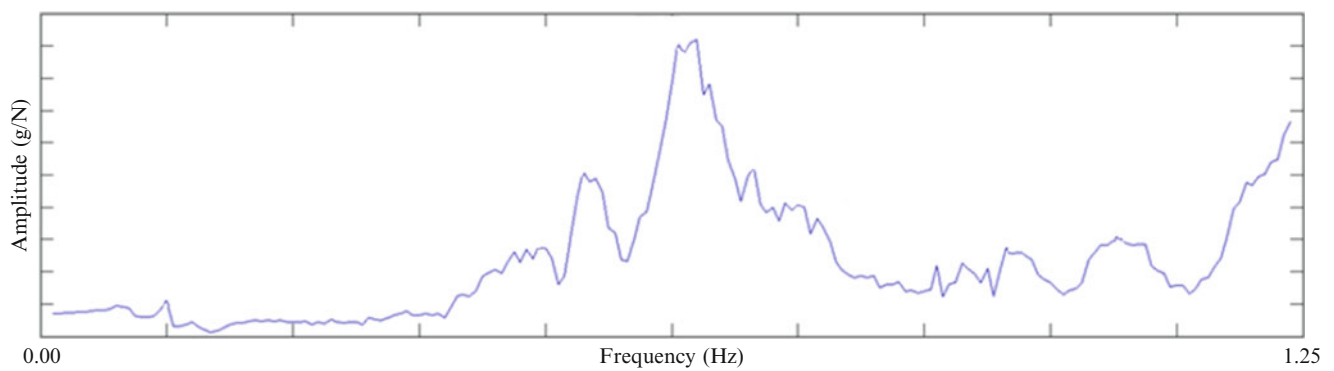


**Fig. 31.12** FRF graph on the elevation gyro after azimuth axis frequency sweep test, axes values are normalized

In this model, there are bearings at each end. The torsion spring (k) represents equivalent torsional stiffness of gearbox, chassis, engine shaft and gear-pinion assembly which are considered to be connected in series. $J_m$ Represents inertia of
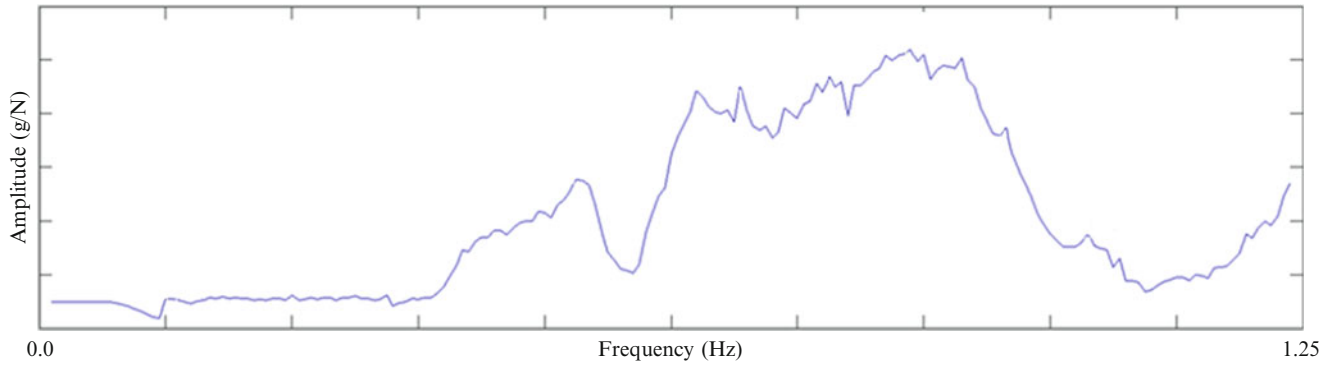
**Fig. 31.13** FRF graph on the azimuth gyro after azimuth axis frequency sweep test, axes values are normalized

**Fig. 31.14** Two-mass system with a torsional spring connection
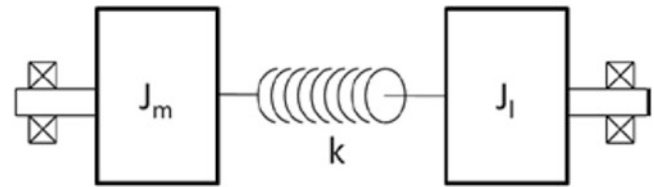


gearbox, motor, motor shaft and gear-pinion couple. On the other hand, $J_l$ represents inertia of the chassis. If system equation is written in terms of motor displacement, inertia and flexibility matrices are obtained as follows:

$$J_t = \begin{pmatrix} J_m & 0 \\ 0 & \frac{J_1}{N_1^2 . N_2^2} \end{pmatrix} \tag{31.6}$$

$$k_t = \begin{pmatrix} \dfrac{k_l . k_m . k_s}{k_m . k_s . N_1^2 . N_2^2 + k_l . k_m + k_l . k_s} & -\dfrac{k_l . k_m . k_s}{k_m . k_s . N_1^2 . N_2^2 + k_l . k_m + k_l . k_s} \\ -\dfrac{k_l . k_m . k_s}{k_m . k_s . N_1^2 . N_2^2 + k_l . k_m + k_l . k_s} & \dfrac{k_l . k_m . k_s}{k_m . k_s . N_1^2 . N_2^2 + k_l . k_m + k_l . k_s} \end{pmatrix} \tag{31.7}$$

where the transmission gear ratio and gear-pinion transmission are represented by $N_1$ and $N_2$, respectively. Also, motor shaft, gearbox and chassis torsional flexibilities are represented as $k_m$, $k_s$ and $k_l$, respectively.

Natural frequencies of this two DOF system are calculated and first anti-resonance and resonance are found. Frequency response function graph of this system is shown in Fig. 31.15.

When prototype modal test FRF peaks and two DOF model results are compared, a small difference is observed. If motor is fixed in torsional axis on the two DOF model, anti-resonance turns out to be seen as resonance.

### 31.3.3 Flexible Dynamic Analysis

#### 31.3.3.1 Model Preparation

At the beginning stage of the flexible multibody dynamics model creation, it is necessary to decide which parts are to be modeled as flexible or rigid. Modelling whole system as flexible makes the simulation very complex and increases the calculation time. On the other hand, if whole system is modelled as rigid, flexibilities of chassis parts are not included. In this respect, chassis parts are decided to be modelled as flexible. However, motor, motor shaft, gearbox and gears are modelled as rigid due to their compact structure where their stiffness and damping is included as springs and dampers Fig. 31.16.

Flexible dynamic model building process is carried out in two stages. First, each flexible part is subjected to modal analysis before creating the kinematic model. Modal analysis of the flexible parts are performed using MSC Nastran. Assemble connection points are introduced in these analyses in order to get the reduced model; in other words, the Craig-Bampton model.

**Fig. 31.15** Frequency response function at motor side, axes values are normalized
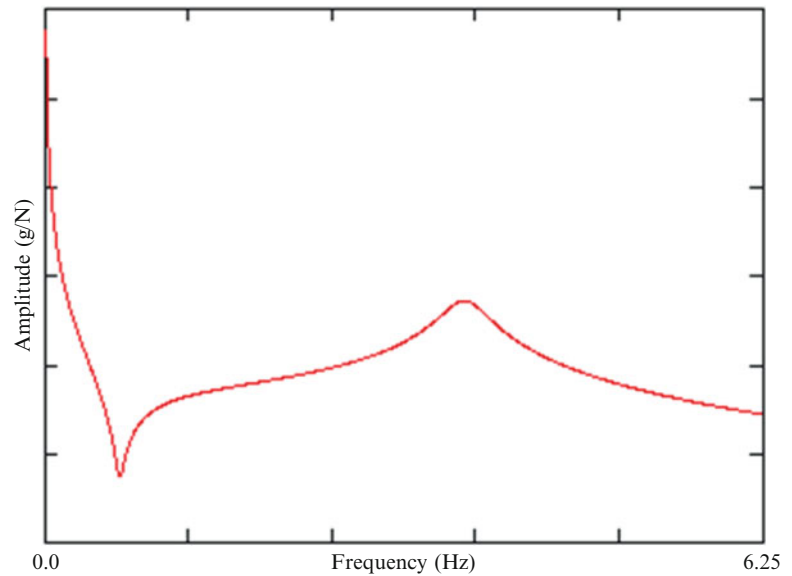


**Fig. 31.16** Parts and connector point identification
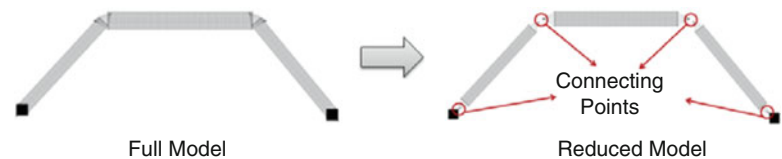


**Fig. 31.17** Revolute and translational joint representations



In the second stage, each reduced part is transferred into VL environment and Craig-Bampton model is obtained. Standard joints are defined between flexible and rigid bodies in VL environment. For example, revolute (hinge) joint is introduced at the center of elevation bearing in order to simulate the connection between elevation and azimuth chassis. Similarly, revolute joint is introduced between motor and motor shaft. Also, since barrels are free to move in the gun axis, translational joint is defined in that direction between gun and elevation chassis. These connectors restrict or permit the movement in specific degrees of freedom. Simplified revolute and translational joints are shown in Fig. 31.17.

#### 31.3.3.2   Machine Elements Flexibilities

Gear-pinion clearances, gearbox backlash, motor shaft, gearbox, gear-pinion flexibilities are modeled using torsional spring-damper and bush elements. Special attention has to be given to the flexibilities of the bearings, motors, shafts, gear-pinion and gearboxes. Also, backlash in gearbox and gear-pinion should be defined carefully.

Although the electric motors are modelled as solid, motor and motor shaft exhibits some flexibility. In this respect, shaft flexibility is included in the system with torsion spring.

Motor shaft torsional flexibility is calculated by analytical methods using the commercial software Kisssoft. Its angular torsion is calculated as shown in Fig. 31.18 with respect to length of the shaft.

Gear and pinion system is modelled by using Hertzian contact analysis. Detailed finite element models of gear and pinion are shown in Fig. 31.19.

Gearboxes are complex systems for finite element modelling. On this reason they are modelled as torsional spring-damper and flexibilities are found by testing. Gearbox stiffness function is introduced to the model as shown in Fig. 31.20. As seen from the graph, backlash is also included.

**Fig. 31.18** Torsion of elevation chassis motor shaft under torque
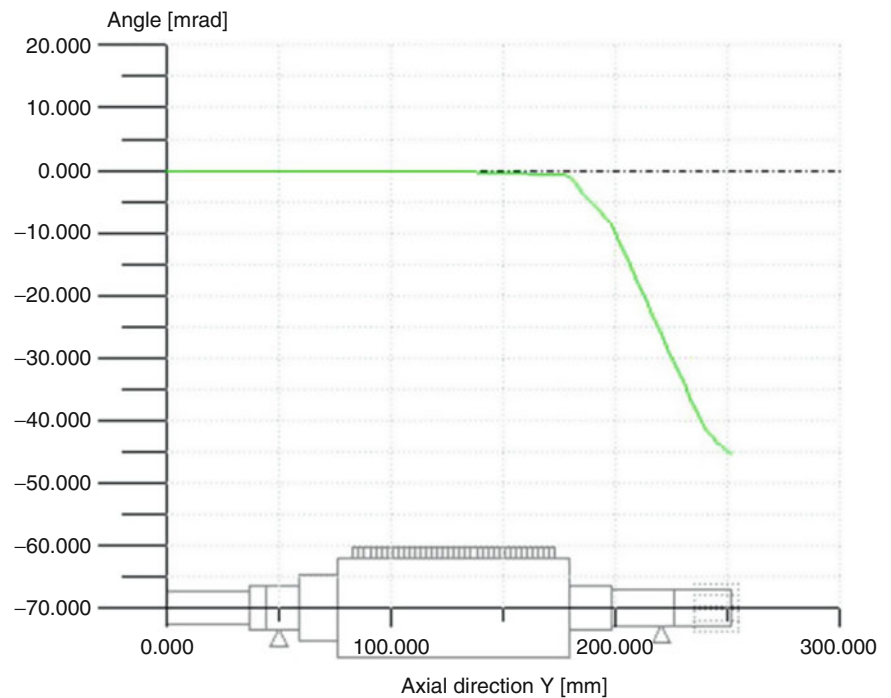


**Fig. 31.19** Finite element model of gear-pinion for Hertzian contact analysis
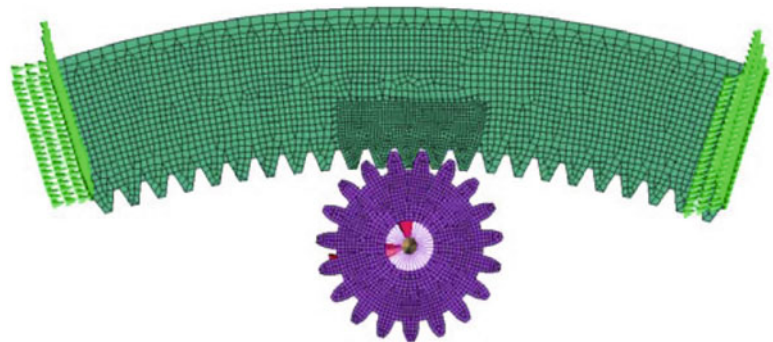


For the bearings, radial, axial, torsional and conical stiffness values are taken from manufacturer catalogues. Also, damping for a bearing is applied as shown in Fig. 31.21.

Gearbox and gear-pinion transmission ratio have multiplication affect on neighbour part flexibilities [9]. In this scope, torsional flexibility of the motor shaft was multiplied with $i^2$ and $j^2$, where appropriate. Here i and j represent gearbox and gear-pinion transmission ratio, respectively.

### 31.3.3.3 Simulation Results

Flexible dynamic analysis of the Craig-Bampton model yields acceleration, velocity, displacement, stress, force and torque transfer, etc. results at any point in the model. Essential information can be obtained for mechanical, electronical and control design of the turret.

System dynamic transfer function calculation is a critical step in order to have better stabilization control strategy in elevation and azimuth axes. Azimuth axis angular velocity transfer function which is calculated at the elevation gyro is shown in Fig. 31.22.

Besides the gyro location, it is possible to obtain the transfer function for other critical locations. For example, transfer function can be obtained for gun tip (Fig. 31.23) which is very difficult to obtain by prototype testing.

Low frequencies (1–50 Hz) are of great importance in the studies of the control algorithm. It may be necessary to increase or decrease natural frequencies by mechanical design changes. In this study, design of experiment (DOE) of flexibilities was carried out. By using VL, effect of tenfold increase or decrease in the torsional flexibility of the motor shaft on the natural
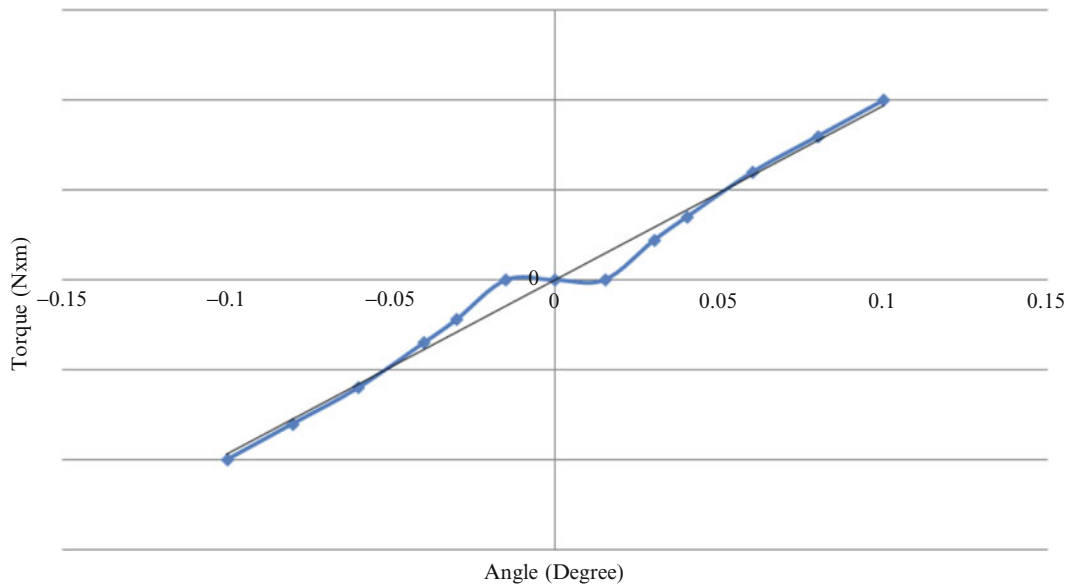
**Fig. 31.20** Azimuth gearbox backlash
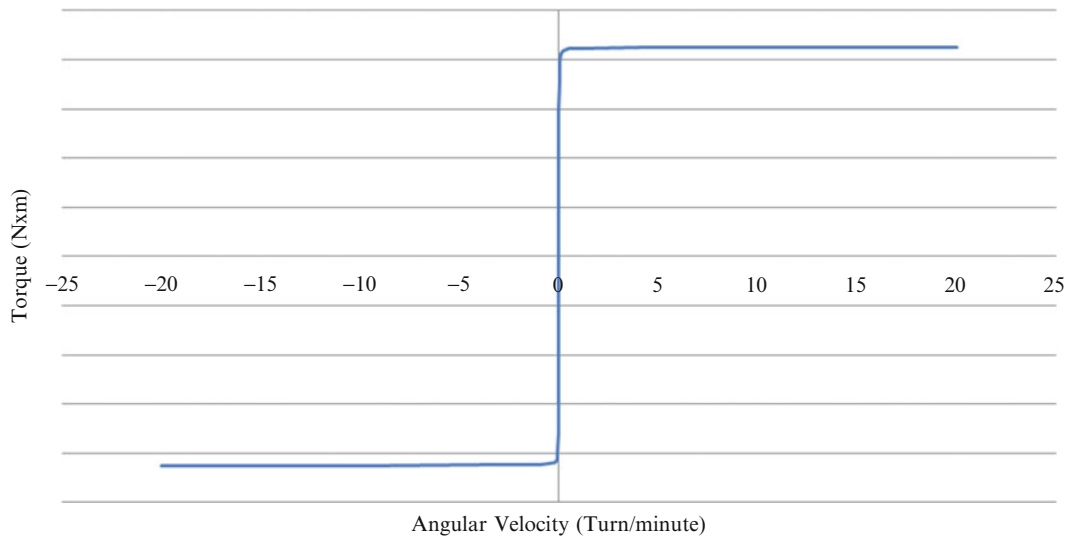


**Fig. 31.21** Azimuth bearing damping

frequencies can be analyzed. For example, effect of this change on angular velocity of the barrel tip is analyzed as shown in Fig. 31.24.

Turrets are integrated on specially designed foundations. Dynamic and static strength of the foundation is of critical importance for the performance of the turret. Backwards bending of the turret during gunfire occurs if foundation is not tough enough which affects the gunfire performance. Cost, weight, vibration, and harshness studies need to be done in order to find optimized foundation flexibility. Therefore, gunfire simulations are performed in order to find the optimum foundation stiffness by using the VL model. Two different foundation stiffnesses as soft and hard are analyzed and vertical motion of the barrel is obtained. As shown in Figs. 31.25 and 31.26, barrel up-down movement on hard foundation is lower than the soft foundation. This gives opportunity to tune the foundation flexibility.

Stress and strains on the flexible parts are also obtained for the gunfire simulations. This gives the opportunity to analyze and optimize the structural durability of the parts. Also, material selection is revised according to these results.

In addition to gunfire and torque sweep simulations, natural frequency analysis of the whole system at specific time segments can be calculated. Since, system has different flexibilities at different time points, system has different dynamic
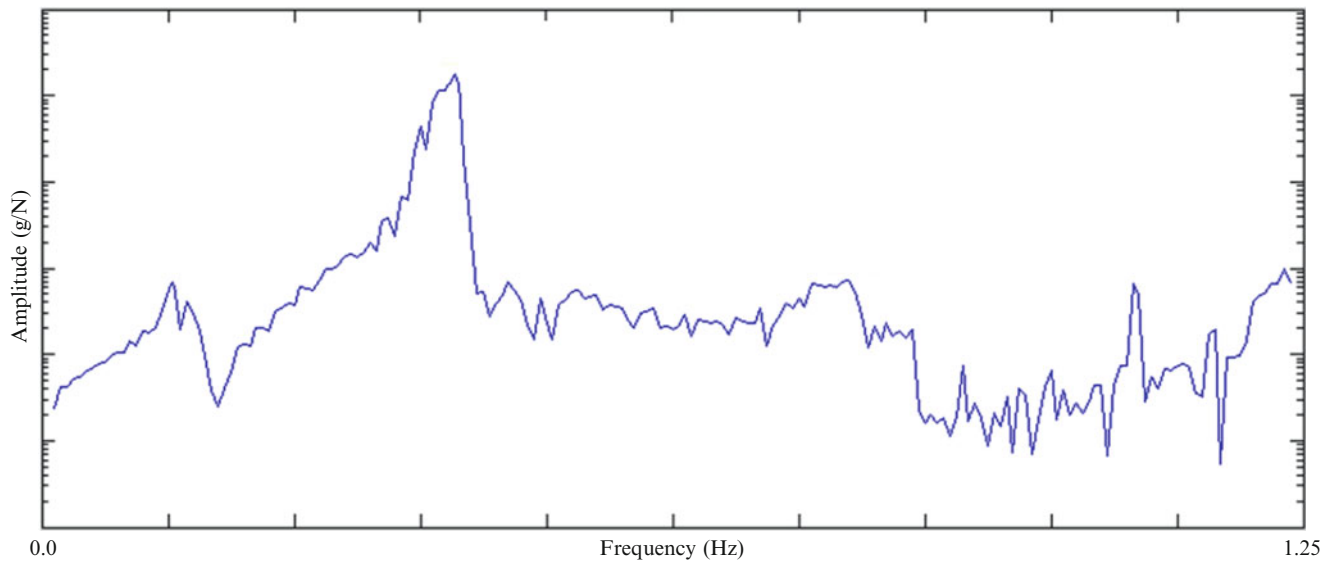
**Fig. 31.22** Elevation Gyro azimuth axis angular velocity transfer function, axes values are normalized
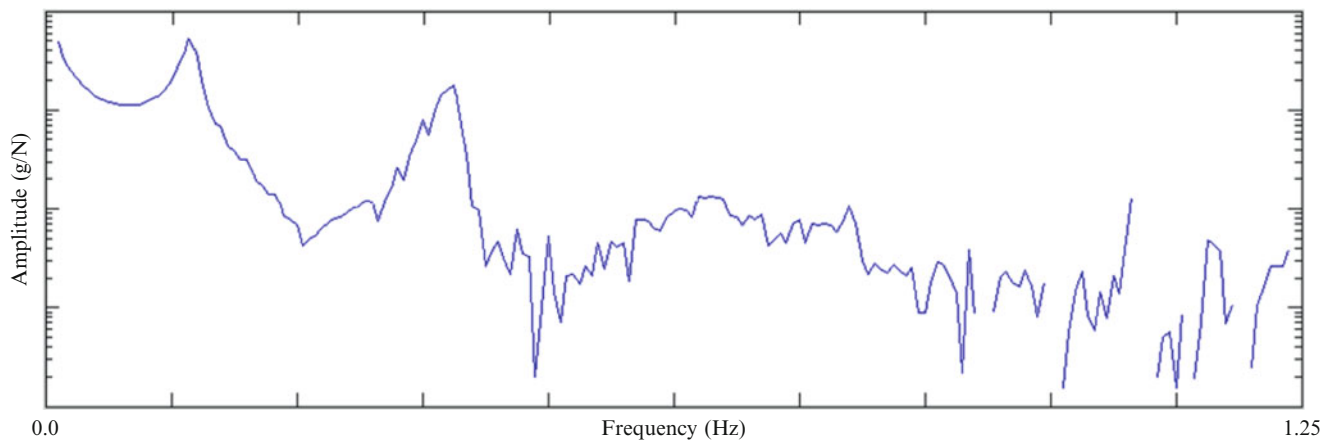


**Fig. 31.23** Barrel tip azimuth axis angular velocity transfer function, axes values are normalized

characteristics. In this context, the dynamic properties of the system at different times have to be analyzed for better understanding of the system behaviour.

## 31.4  Conclusion

Systems in defense, aerospace and automotive industries have increasing number of electronic and mechanic components. This brings out problems in vibration, control and integration. These difficulties led to the emergence of new technologies. Flexible dynamic analysis using Craig-Bampton method is one of these advancements used to solve vibration and control problems. This method is used to analyze a military turret system in order to determine dynamical properties. Also, simulation results are compared with the prototype tests.

Stabilization control studies of the turret-like motion systems concentrate mostly after prototype manufacturing. It is not easy to develop and finalize control algorithms for complex turrets which have flexibilities of structures, nonlinearities, clearances, contacts, backlashes, etc. Instead of sub-structure analysis, whole system has to be modelled and analyzed including every critical parameter. For this reason, most of the defense, aerospace and automotive industries are using flexible dynamic analysis methods to have better analysis models. Using this simulation model, transfer functions, natural frequencies and mode shapes of the system are calculated before prototype manufacturing. This simulation technique led to lower costs by decreasing time and number of prototypes.
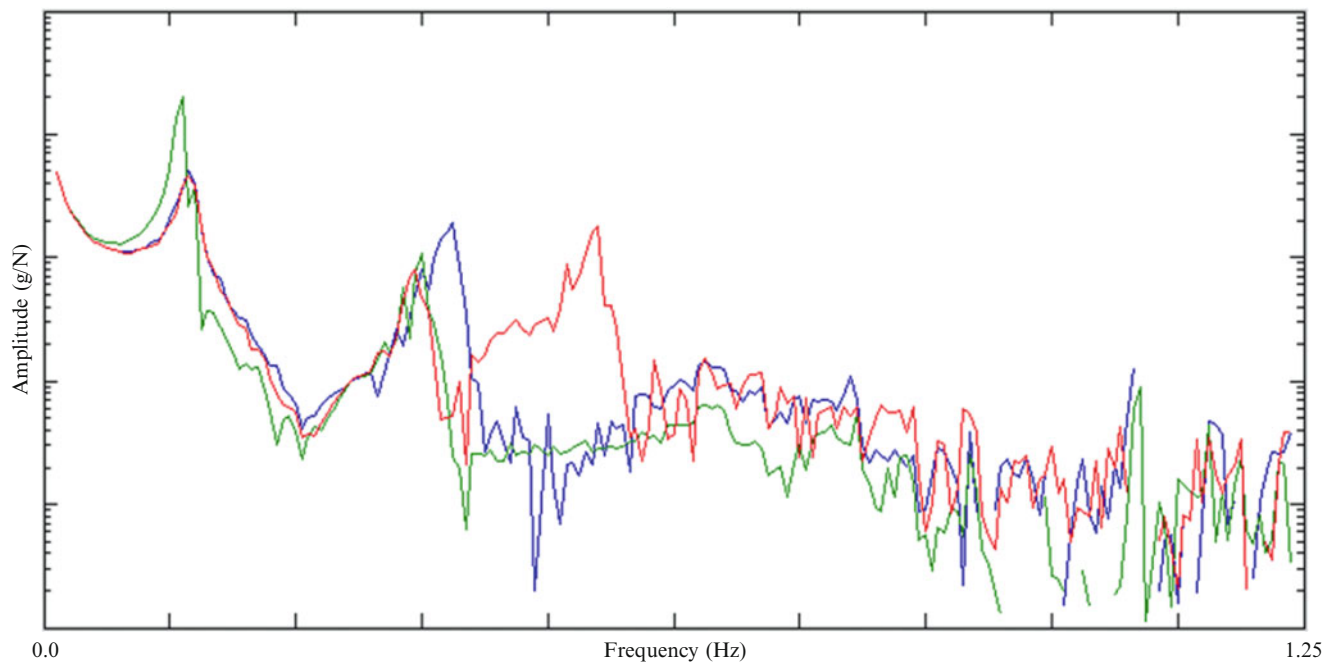
**Fig. 31.24** Effect of elevation motor shaft flexibility (k) change on barrel tip angular velocity transfer function (*Blue*: k; *Red*: k/10; *Green*: k*10), axes values are normalized (Colour figure online)
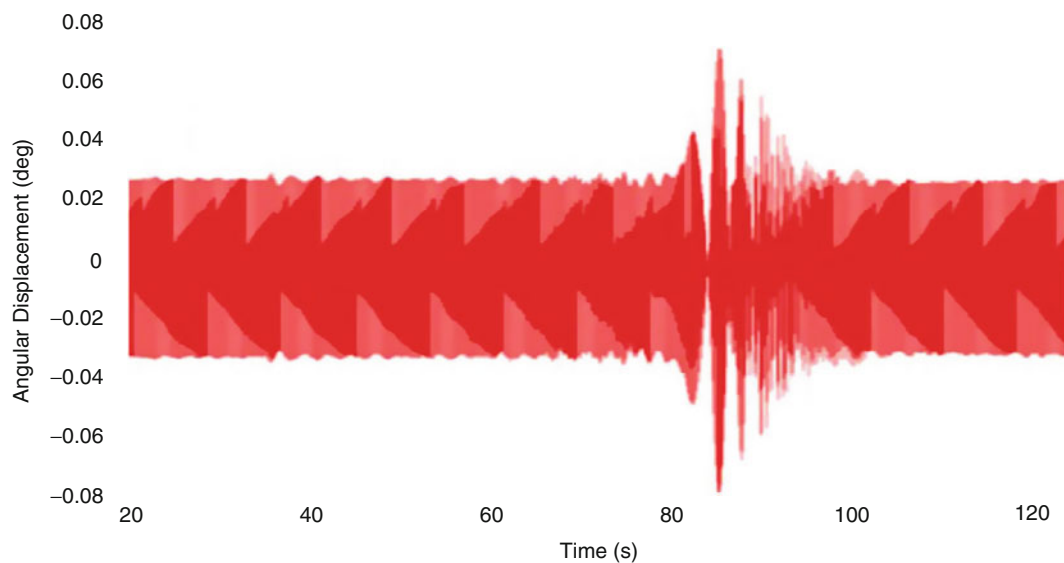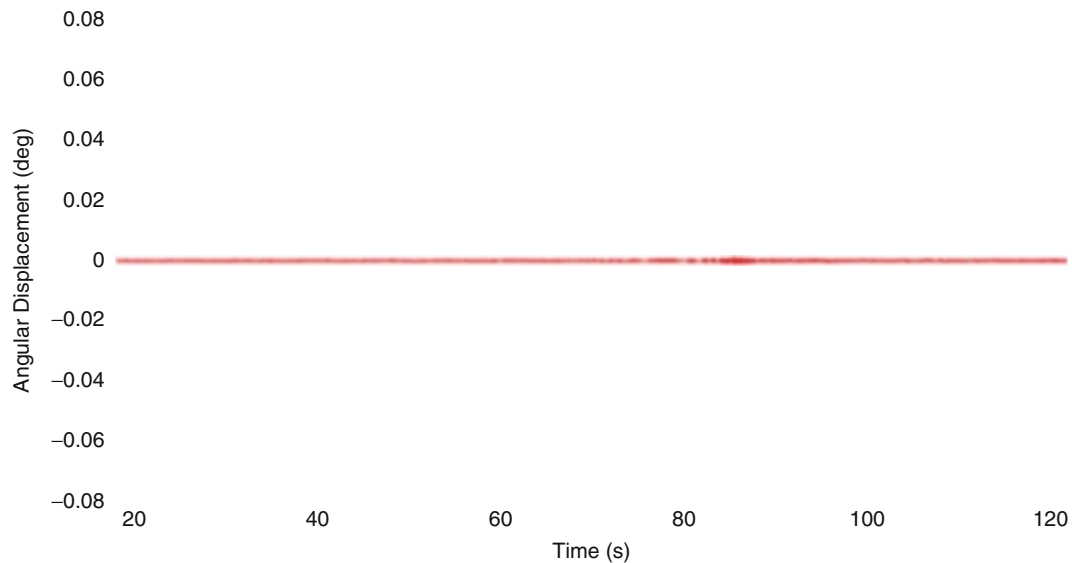


**Fig. 31.25** Barrel tip displacement at soft foundation, axes values are normalized

Toughness of the foundation on which turret is integrated is of great importance in terms of stability performance and it affects the system natural frequencies. By using flexible dynamic analysis, it is possible to analyze the effects of foundation stiffness on turret performance. This simulation environment is used within the scope of this paper and optimized foundation stiffness is found.

Flexible dynamic analysis can be applied to several loading conditions. In this study, barrel tip angular displacement is solved by gunfire analysis. In this way, total flexibility of the system is calculated and weak sections can be easily determined.

Flexible dynamic analysis in the design process allows understanding the effects of each gearbox, bearing, gear-pinion, etc. on the system performance. Thus, design optimization studies can be performed before manufacturing the prototype. In the scope of this study, this optimization is performed for each machine element and their effects on transfer functions are analyzed.

**Fig. 31.26** Barrel tip displacement at hard foundation, axes values are normalized

Flexible dynamic analysis methods make a significant contribution from conceptual design to prototype production as outlined throughout the study. However, like any other software, simulation results also vary according to the degree of detail modeled and accuracy of the input. The system may also include nonlinear elements which can require laboratory tests to be performed for each component characterization.

# References

1. http://en.wikipedia.org/wiki/ Finite_element_method
2. Klerk D de, Rixen DJ, Voormeeren SN (2008) General framework for dynamic substructuring: History, review, and classification of techniques. AIAA J 46(5). doi: http://10.2514/1.33274
3. Voormeeren SN (2012) Dynamic substructuring methodologies for integrated dynamic analysis of wind turbines, PhD Thesis, Delft University of Technology, Uitgeverij Boxpress
4. Koutsovasilis P, Beitelschmidt P (2008) Model reduction of large elastic systems. A comparison study on the elastic piston rod. Multibody Syst Dyn 20(2):111–128
5. Deshpande L, Sawalhi N, Randall RB (2011) Gearbox fault simulation using finite element model reduction technique. Proceedings of ACOUSTICS 2011, Paper Number 111, Gold Coast, Australia
6. Sawalhi N, Deshpande L, Randall RB (2011) Improved simulations of faults in gearboxes for diagnostic and prognostic purposes using a reduced finite element model of the casing, 7th DSTO International Conference on Health & Usage Monitoring (HUMS 2011), Melbourne, Australia
7. Pan C, Chen XL, Brackett ME, Dokun OD (2006) Electrical power generator package forced response simulation and validation, IMAC-XXIV Conference & Exposition on Structural Dynamics, Missouri, USA
8. Valenzuela MA, Bentley JM, Lorenz RD (2005) Evaluation of Torsional Oscillations in Paper Machine Sections, IEEE Transactions on Industry Applications 41(2)
9. Enwall A, Sjögren R (1999) Simulation of vehicle response to throttle Tip-in and Tip-out, Master Thesis, University of Karlskrona/Ronneby, Karlskrona, Sweden

# Chapter 32
# Material Characterization of Gyroscope Isolator Using Modal Test Data

**Özge Mencek and Murat Aykan**

**Abstract** Gyroscopes are widely used in stabilization of turret systems where high shocks are encountered. Use of isolation material with them is essential to obtain reliable rotation data considering the intensity of shocks. Usually, each gyroscope comes with an isolator panel specific to itself. In certain situations, however, a proper isolator configuration is unavailable for the gyroscope. In this study, analyses required to use a sandwich panel isolator with a gyroscope other than its original one are presented. Isolation material is modeled as orthotropic and its characteristic properties are obtained from the comparison between the modal tests and the finite element model by using optimization. Effects of full realization of the boundary conditions on the modal data are also shown.

**Keywords** Material characterization • Orthotropic material model • Parametric optimization • Model correlation • Modal analysis

## 32.1 Introduction

In structural design, knowledge in material behavior is necessary to obtain reliable simulations. On this account, considerable amount of research is done for determining the elastic properties of materials. A great number of techniques for the identification of the elastic properties of either isotropic or orthotropic materials have been proposed. In case of isotropic materials, identification of material properties is somehow simpler whereas the same procedure for anisotropic materials requires different approaches. Most of these techniques exploit the dynamic response of a specimen made of the material. In these techniques, the response of a numerical model of the specimen is connected with its experimental behavior. Unknown material parameters in the numerical model are updated until the model behavior matches the experimental results as close as possible. The parameter values used in the finalized numerical model are the results of the identification procedure and yield the elastic properties of the material. A considerable majority of the studies of this kind used modal tests of the specimen for comparison with the numerical model. McIntyre and Woodhouse [1] identified both elastic and damping constants of thin orthotropic plates by measuring and analyzing the low modes of vibration. Deobald and Gibson [2] determined elastic constants of orthotropic plates with boundary conditions consisting of clamped and free edges. Ayorinde and Gibson [3] presented a similar approach to determine elastic behavior of orthotropic plates with free edges. In 2000, Gibson published a paper summarizing the research he and his colleagues conducted and outlining the concept of modal testing for orthotropic material identification [4]. De Visscher et al. [5] obtained the stiffness and damping properties of orthotropic composite plates by comparing experimental modal parameters and the corresponding results from a numerical model in combination with the modal strain energy method. Hongxing [6] proposed a mixed numerical/experimental technique where the experimental and modal data are correlated through a parameter optimization method. Carne et al. [7] developed a constitutive model for the elastic response of an aluminum honeycomb material using virtual testing from cell-level computational simulations and validated this model through comparison with modal test results. Similar to many of these studies, this study consists of modal testing of a structure including an unknown material and a numerical model of this structure established through

Ö. Mencek (✉) • M. Aykan
Division of Defense Systems Technologies, ASELSAN Inc., Ankara 06172, Turkey
e-mail: omencek@aselsan.com.tr
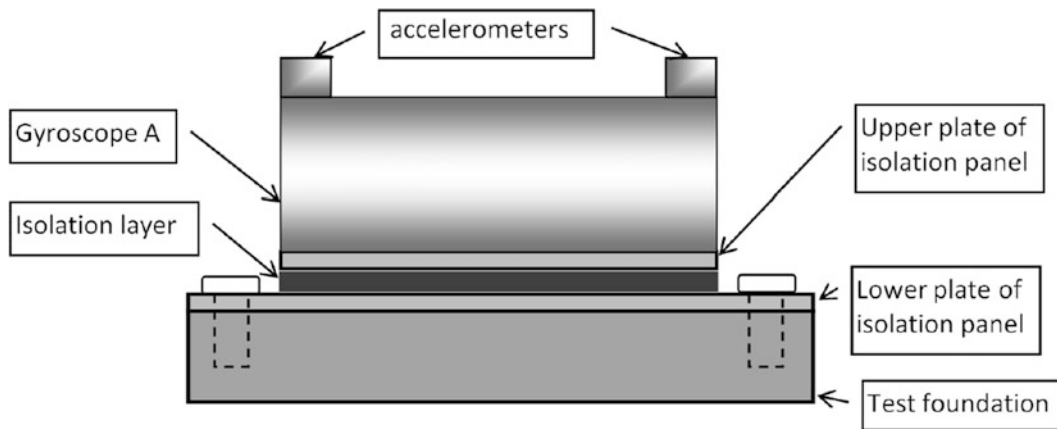
**Fig. 32.1** Representative configuration of test setup for gyroscope A

finite element method. The structure is an isolation layer within a gyroscope where the quantitative material properties of the isolation layer are to be identified. The aim is to be able to use the obtained material model in case of different gyroscope geometries.

## 32.2 Methodology

In this study two different gyroscopes, hereafter called gyroscopes A and B, are used with the same isolation panel. The isolation layer is a rubberlike material with unknown mechanical behavior. It is sandwiched between two plates of aluminum as shown in Fig. 32.1.

In order to identify the material properties of the isolation layer, a finite element model (FEM) of the gyroscope A with the isolation panel is established and modal analysis is done on this environment. Meanwhile, modal tests are performed on the gyroscope, and then the results obtained from FEM are compared to that of modal tests. Material properties of the isolation layer are set through optimization, such that the natural frequencies from the FEM match the test results. The material is taken as an orthotropic one and is modeled accordingly. Then the same isolation panel is attached to the second gyroscope (gyroscope B). Similarly, modal tests are performed and a FEM is established. Determined material properties from gyroscope A are used in the FEM of gyroscope B. Results from modal tests and finite element modal analysis are compared to observe the validity of the material model.
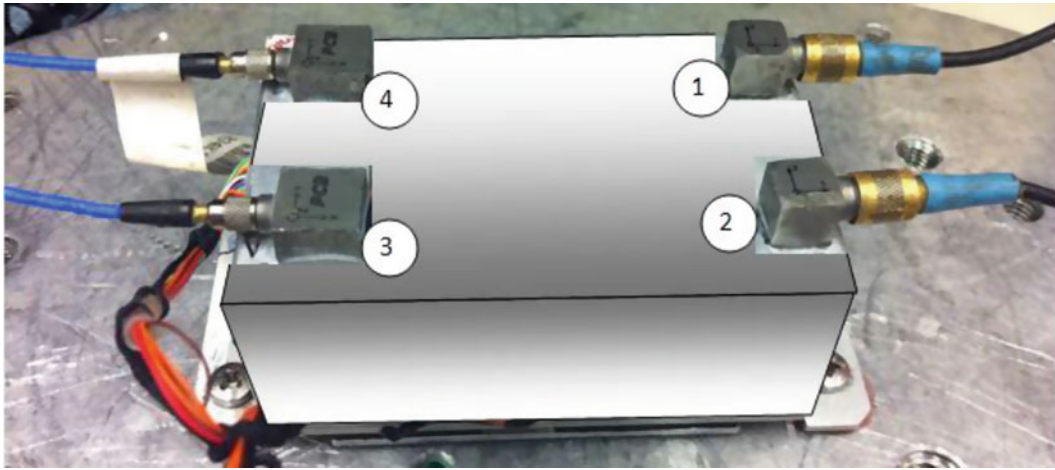
## 32.3 Gyroscope A

### 32.3.1 Preliminary Modal Tests

This gyroscope, with its isolation sandwich layer attached, is fixed to a test foundation through bolts as shown in Fig. 32.1 and the accelerometers are located as in Fig. 32.2.

Modal tests are performed with a roving hammer and fixed accelerometers. Hammer is applied on various directions (x, y and z) at each accelerometer location. Natural frequencies and mode shapes obtained through the analysis of these tests are presented in Fig. 32.3.

The rectangular area formed by the lines represents the upper face of the gyroscope, where colors blue and yellow stand for the undeformed and deformed shapes, respectively. The corners of the rectangle, marked with point numbers, represent the accelerometer locations with numbers being the same as the test setup shown in Fig. 32.2.

**Fig. 32.2** Accelerometer locations and configuration of test setup for gyroscope A

## 32.3.2 FEM Model

Gyroscope A is modeled with its isolator panel attached in ANSYS® environment and a modal analysis is performed on this model. As mentioned before, the isolation material is modeled as an orthotropic material. For an orthotropic material, nine properties are to be defined to fully characterize the mechanic behavior. These properties consist of three sets of Young's modulus, Poisson's ratio and shear modulus values; each set defined in x, y and z directions. For an orthotropic material, elasticity matrix must be positive definite. This is introduced as a constraint in the optimization procedure as follows:

$$\nu_{xy}^2 \frac{E_y}{E_x} + \nu_{yz}^2 \frac{E_z}{E_y} + \nu_{xz}^2 \frac{E_z}{E_x} + 2\nu_{xy}\nu_{yz}\nu_{xz}\frac{E_z}{E_x} < 0 \tag{32.1}$$

Natural frequencies obtained from the modal tests are set as target parameters. Initial conditions for all moduli are set as 1 MPa. On top of these, damping behavior of the material is introduced as Rayleigh damping. Since any entered damping data is ignored in modal analysis plant of ANSYS®, it was not included in the optimization procedure. Instead, the harmonic response of the model under constant force is studied over a frequency range covering first six modes. Available data sheet of the gyroscope had provided the maximum displacement of the gyroscope in the direction normal to upper surface of the gyroscope. Damping coefficient is adjusted such that the response gave the approximate displacement value at the most dominant mode in the studied range.

Preliminary results have shown that the process failed to deliver matching natural frequencies. Furthermore, the order of the corresponding mode shapes differed from that obtained from modal tests. The closest possible natural frequencies and the corresponding mode shapes are presented in Fig. 32.4.

At this point authors suspected whether the physical boundary condition is fully realized in ANSYS® environment. During the hammer test, the gyroscope is fixed to the foundation through the holes on the lower plate of the isolation sandwich as shown in Fig. 32.1. By this means there has formed a contact between the surfaces of the lower plate and the foundation. This contact allows only compression between these two surfaces. In order to realize this boundary condition in ANSYS® environment, "compression only" support is defined between these surfaces. However, this support type is nonlinear and it is disabled during the modal analysis, letting midsection of the lower plate to move freely without any compression from the bottom. Consequently, results of these modal tests are not comparable with this FEM and it is not possible to form a valid material model. In order to overcome this inconvenience and mimic the boundary condition in ANSYS® environment, a different approach is employed and the modal tests are updated. Details of this approach and the accordingly updated modal tests are presented in the next Section.
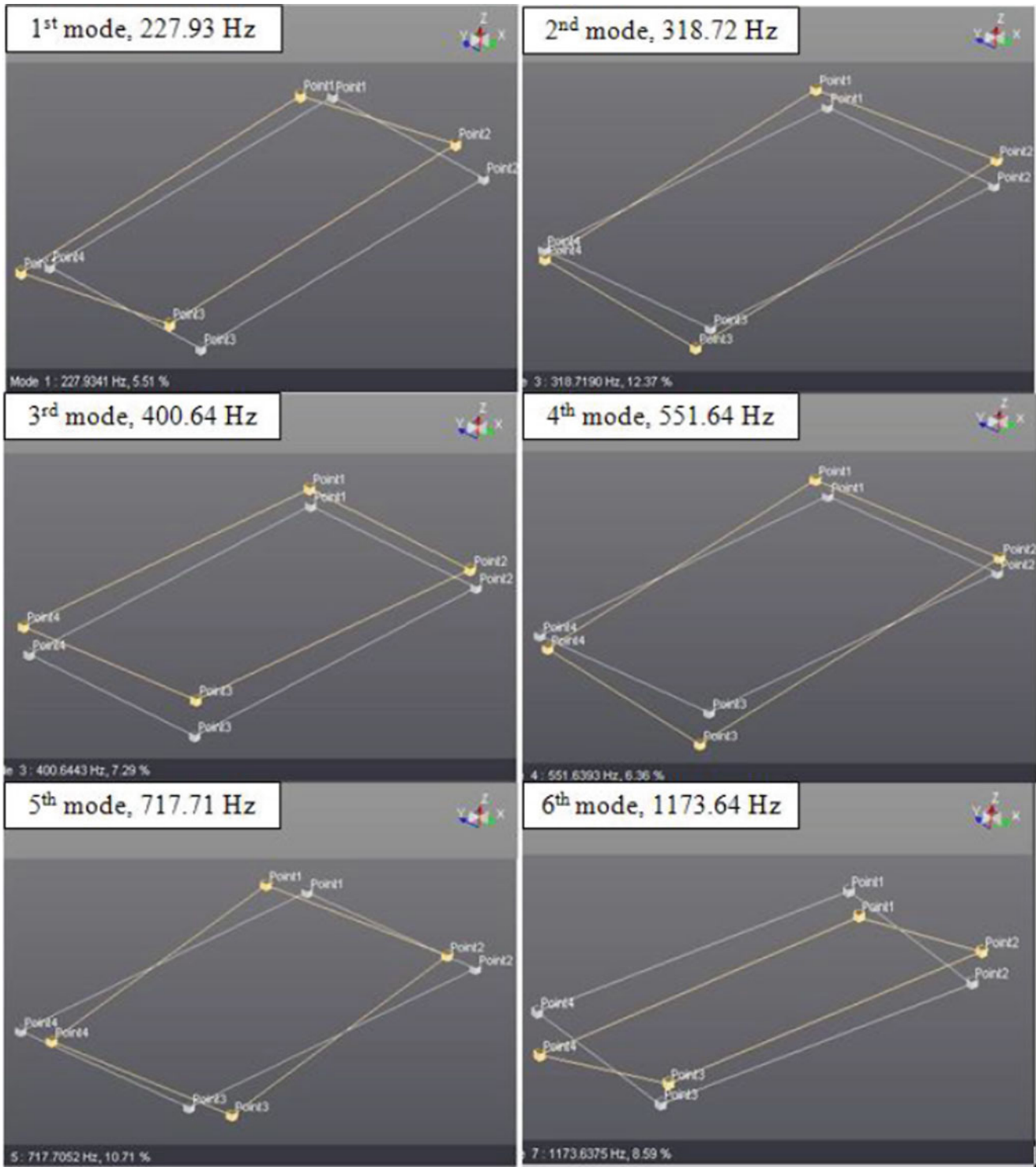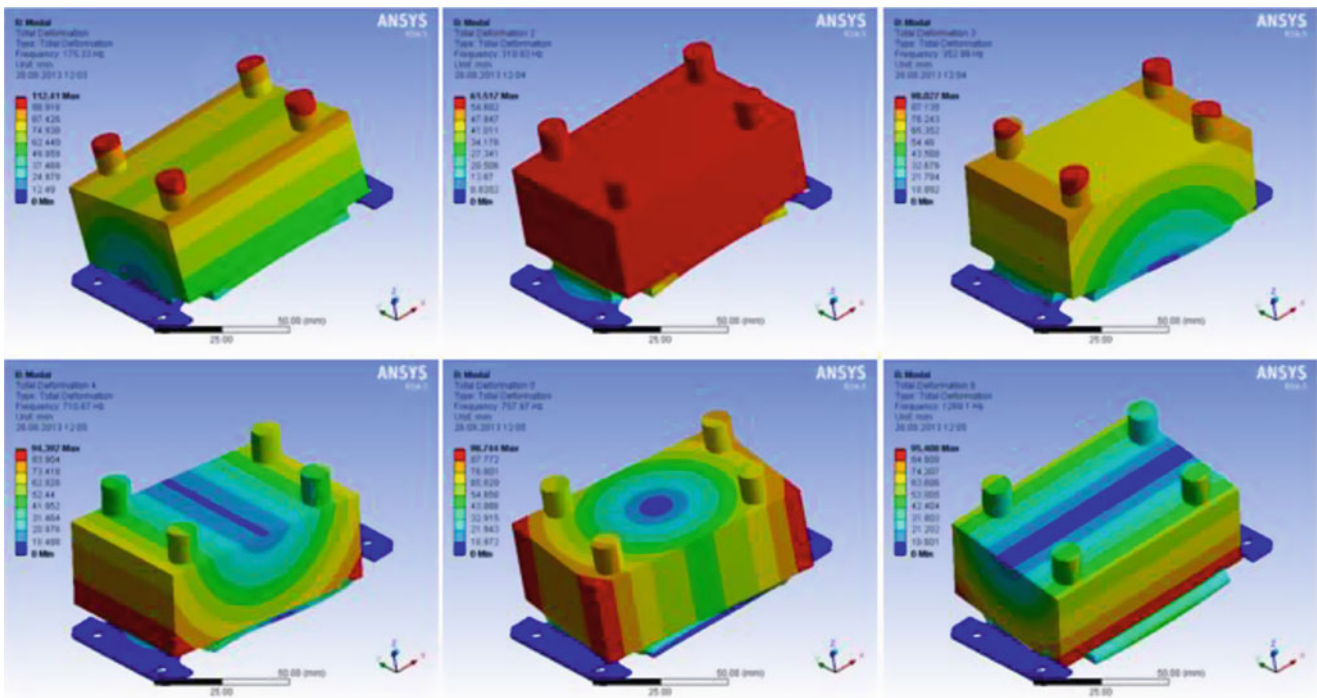
**Fig. 32.3** First six natural frequencies and corresponding mode shapes of gyroscope A from modal tests

### 32.3.3 Updated Modal Tests

In order to actualize the boundary condition forced by ANSYS®, there needs to be gap between the lower plate and the foundation while keeping the lower plate fixed through the bolts. In other words, the lower plate should be fixed through the bolt holes only, without any other contact throughout the plate surface. This is formed by adding washers through the bolts between the lower plate and the test foundation. The configuration is shown in Fig. 32.5.

**Fig. 32.4** First six natural frequencies and corresponding mode shapes of the gyroscope A from first FEM $f_1 = 175.33$ Hz, $f_2 = 319.93$ Hz, $f_3 = 352.99$ Hz, $f_4 = 710.67$ Hz, $f_5 = 757.97$ Hz, $f_6 = 1,269.1$ Hz
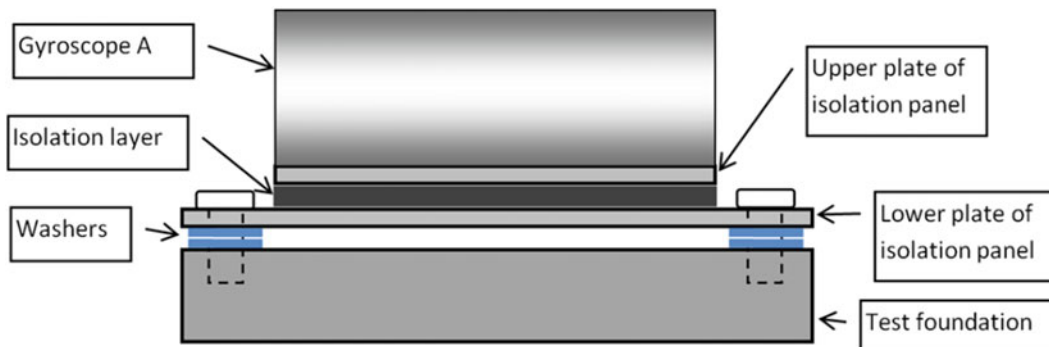


**Fig. 32.5** Representative drawing of plate-foundation connection with washers used

As can be observed, use of washers enables the fixed boundary condition at bolt locations while allowing the middle part of the lower isolation plate to swing in both up and down directions. By this means, the boundary condition between the lower isolation plate and the foundation is created at the closest possible measure to the model prepared in ANSYS®. Modal tests are repeated with this configuration and the results are given in Fig. 32.6.

When the results of each modal test are compared, the first observation is the lowered natural frequencies caused by the introduced motion flexibility. Even without updating the material properties in ANSYS® to match the natural frequencies, the order of the modes is seen to be equivalent with that of FEM. In addition, the mode shapes from the test configuration without washers include phase distortions between points due to nonlinear boundary condition. On the other hand, the mode shapes from the latter configurations have nearly no distortions.

Once the natural frequencies and mode shapes are obtained, the material properties can be set accordingly, as explained in the previous section. Obtained material properties and corresponding modal analysis results are presented in the following Section.
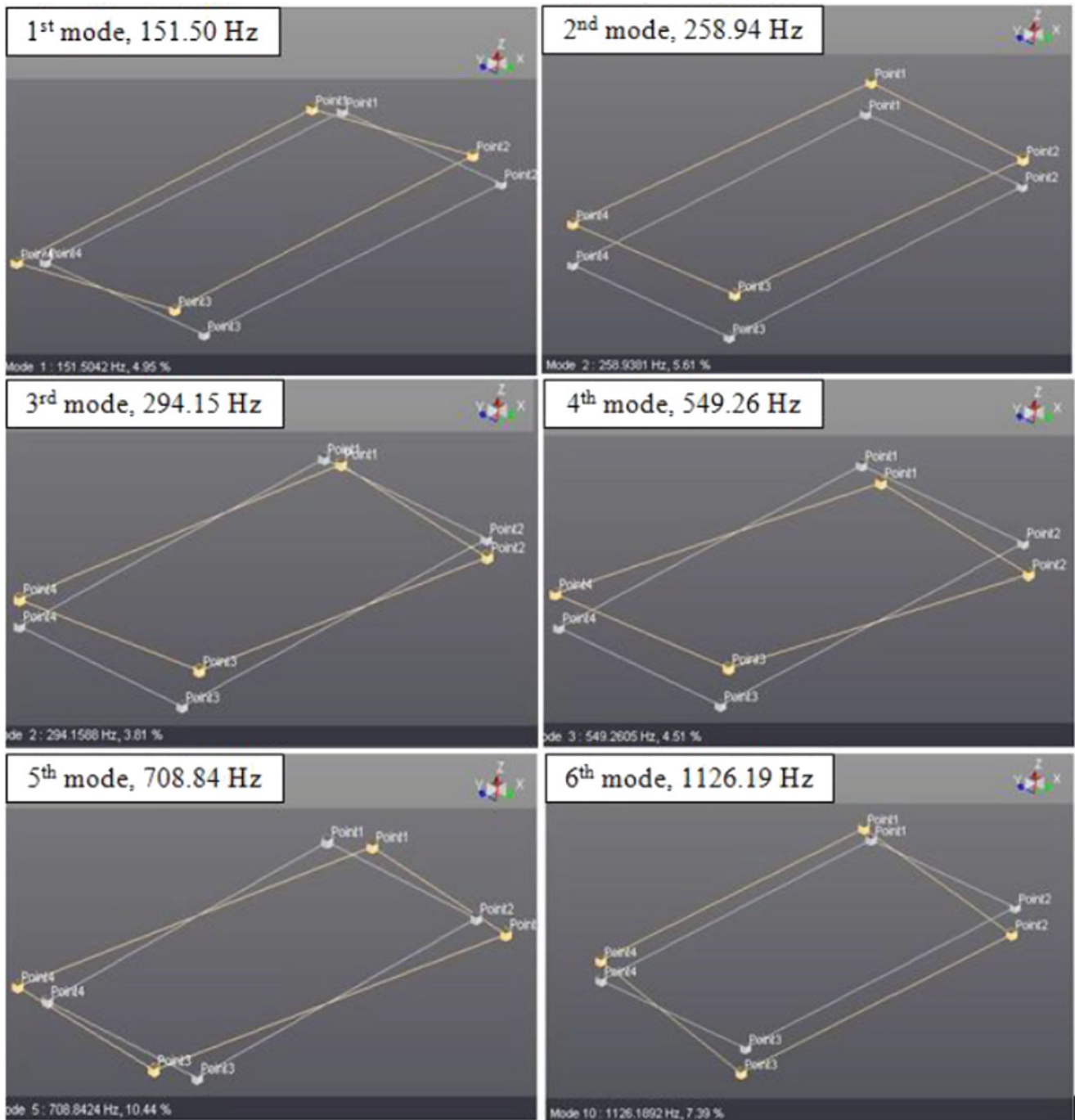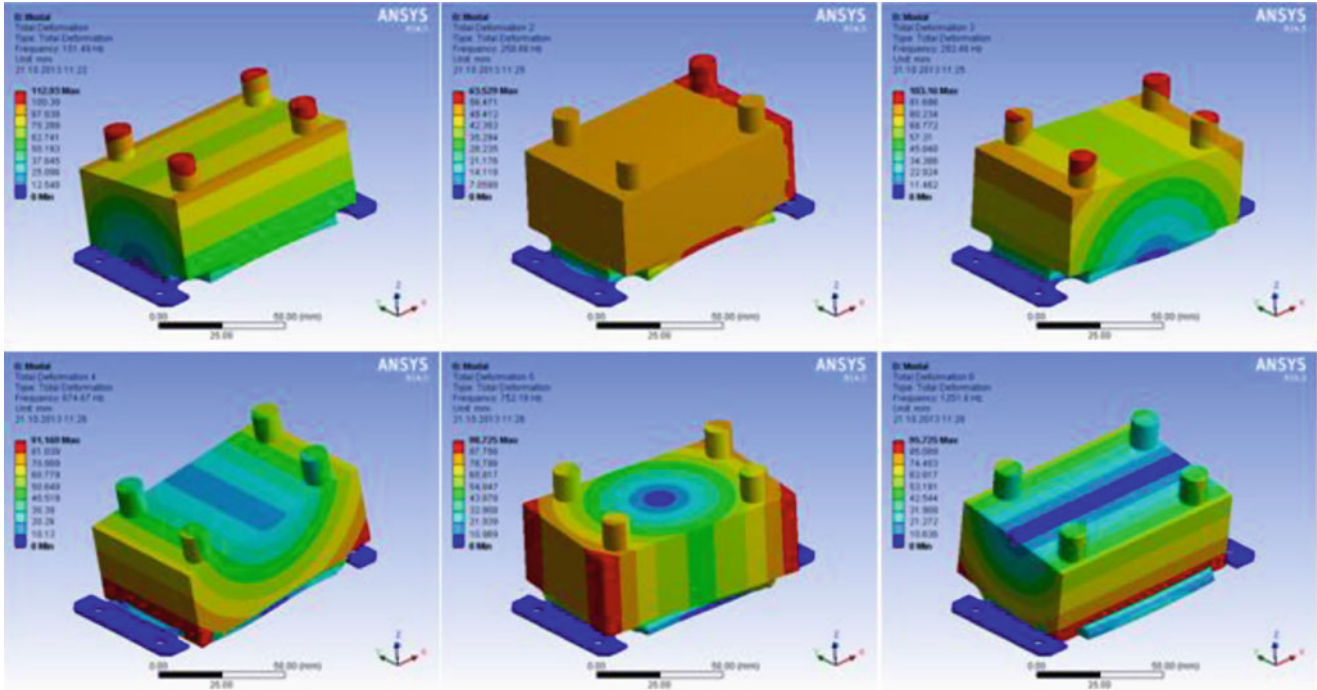
**Fig. 32.6** First six natural frequencies and corresponding mode shapes of gyroscope A from modal tests, washers used

## 32.4 Updated FEM and Material Properties

As mentioned earlier, the material properties are determined by an optimization procedure where the natural frequencies of the FEM are set to match the ones obtained from modal tests. Process revealed that a compromise was needed since all the natural frequencies did not match at the same time. Being considered as the dominant mode, manipulations are performed to match the second frequency as close as possible. In the manipulation stage, it is observed that shear moduli are actually optimized and any change in one of these properties results in notable shifts in natural frequencies and it cannot be compensated by changing another property. However; changes in Young's moduli are compensable within each other.

**Table 32.1** Sets of identified material properties

| Material properties (MPa) | First set | Second set | Third set |
|---|---|---|---|
| $E_x$ | 1.8 | 2.7 | 8 |
| $E_y$ | 2 | 2.4 | 4 |
| $E_z$ | 1 | 1.2 | 1.6 |
| $G_{xy}$ | 4.73 | 4.73 | 4.73 |
| $G_{yz}$ | 5.14 | 5.14 | 5.14 |
| $G_{xz}$ | 1.60 | 1.60 | 1.60 |
| $\nu_{xy,yz,xz}$ | 0.49 | 0.49 | 0.49 |
| $\beta$ (damping coefficient) | $6.3117 \times 10^{-7}$ | $6.2791 \times 10^{-7}$ | $6.3414 \times 10^{-7}$ |



**Fig. 32.7** First six natural frequencies and corresponding mode shapes of the gyroscope A from second FEM $f_1 = 151.49$ Hz, $f_2 = 258.66$ Hz, $f_3 = 292.46$ Hz, $f_4 = 674.67$ Hz, $f_5 = 752.16$ Hz, $f_6 = 1{,}251.6$ Hz

It is observed that increasing or decreasing all Young's moduli at the same time leaves the natural frequencies unchanged. Increase in $E_x$ and $E_y$ results in lower natural frequencies while increase in $E_z$ increases the natural frequencies. Once this observation was made, it is decided to create multiple sets of material properties to see the how the results will be affected during the tests with gyroscope B. Three different sets of material properties are extracted where Young's moduli are different in each set and shear moduli are set fixed. Modal analysis in ANSYS® is repeated with each set of material data. Note that damping coefficients are determined separately, after each moduli set is finalized. Sets of material properties are given in Table 32.1.

Results of the modal analysis performed in ANSYS with the second set of material properties are presented in Fig. 32.7.

## 32.5 Gyroscope B

In order to validate the material model obtained in previous sections, the same isolator panel is attached to another gyroscope: gyroscope B. Modal tests and FEM construction are performed on this configuration in the same manner as in gyroscope A. Obtained sets of material properties are utilized in FEM and results are compared with modal test results.
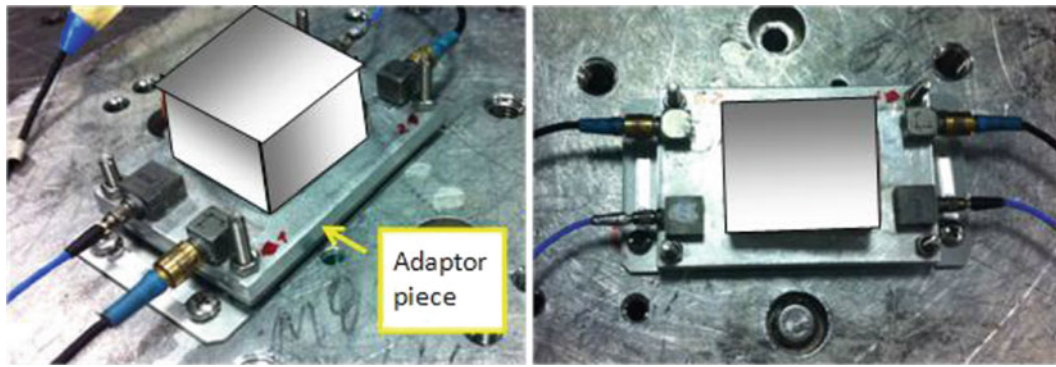
**Fig. 32.8** Configuration of test setup for gyroscope B

### 32.5.1 Modal Tests

Gyroscope B has a different geometry when compared to gyroscope A such that it sits on a smaller area. In order to be able to use this gyroscope with the gyroscope A's isolator panel, an adaptor piece is manufactured. Adaptor piece is a simple aluminum plate of 6 mm thickness with appropriately located through and counter threaded holes. As shown in Fig. 32.8, upper plate of the isolation panel is bolted all through the adaptor piece while the gyroscope is fixed to this adaptor via screws. Accelerometers are located on the adaptor piece instead of gyroscope for practical reasons. Based on the observations of modal tests with gyroscope A, vibratory motion of the system relies mostly on the deformation of isolation material while the gyroscope behaves rigid. Hence, placement of accelerometers on adaptor piece is assumed to be proper and correct.

As mentioned in previous sections, use of washers at bolt locations is essential in order to correctly compare the modal test and FEM modal analysis results. These tests are therefore performed using washers. Natural frequencies and corresponding mode shapes obtained from the analysis of these tests are given in Fig. 32.9 below. The rectangular area represents the upper surface of the adaptor piece. Yellow and blue lines represent the deformed and undeformed model, respectively.

### 32.5.2 FEM Model with Preset Material Properties

Similar to gyroscope A, a FEM model is constructed for gyroscope B. Modal analyses with each set of orthotropic properties are performed. Resulting natural frequencies and percent errors w.r.t. modal test results are given in Table 32.2.

Results show that different sets of material properties result in approximate natural frequencies. When the obtained natural frequencies are broadly observed and compared to the ones from modal test, each of them has a certain amount of error. The third natural frequency has the smallest error, where the second and first natural frequencies follow with relatively larger errors. The mode shapes corresponding to the second data set are shown in Fig. 32.10.

Despite the errors in the natural frequencies, the order of mode shapes is correct when compared to modal test results. Based on all these observations it can be concluded that the material models have a consistency between each other; however the exact natural frequencies they generate are not as close to the test results as in gyroscope A.

### 32.5.3 Sweep Tests and FRFS

Gyroscope B is also subjected to sine sweep test in order to extract the FRF characteristics. The same configuration used in the modal tests is used as shown in Fig. 32.11.

The gyroscope is subjected to harmonic acceleration loading of a unit earth acceleration for the frequency range of 20–1,500 Hz. The FRFs in Figs. 32.12 and 32.13 are obtained by dividing the acceleration response from each accelerometer at each frequency increment by 1 g, hence are dimensionless. In order to see the effect of boundary condition on dynamic response, the measurements are held both with and without washers. Figs. 32.12 and 32.13 present the transfer functions obtained from measurements with and without washers, respectively.
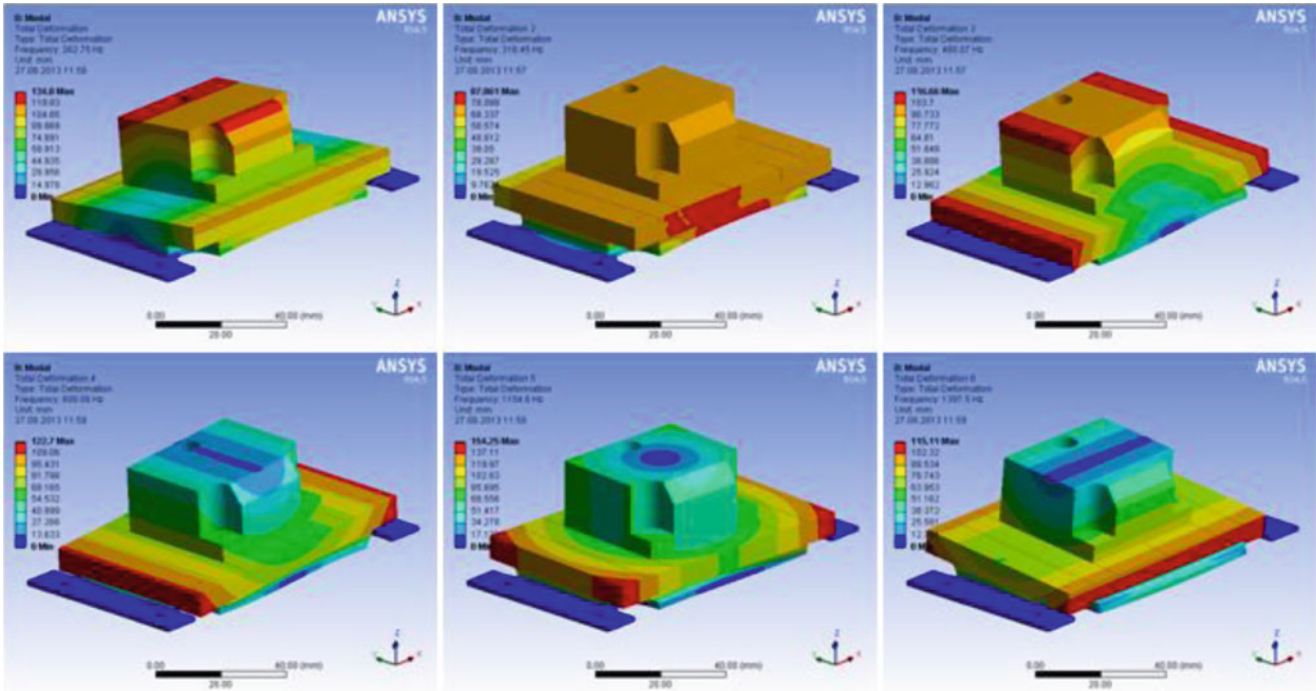
**Fig. 32.9** First six natural frequencies and corresponding mode shapes of gyroscope B from modal tests, washers used

When the FRFs of each boundary condition are assessed, significant effect of using washers is observed. Other than the notable change in the natural frequencies, response of the system at lower frequencies is considerably higher when washers are used. This shows that use of washers is essential in model correlation while it is not recommended in field use due to high response level at first visible mode.

**Table 32.2** Comparison of modal test and FEM modal analysis results

|       | Test results (Hz) | First set results (Hz) | Error (%) | First set results (Hz) | Error (%) | Third set results (Hz) | Error (%) |
|-------|-------------------|------------------------|-----------|------------------------|-----------|------------------------|-----------|
| $f_1$ | 287.65            | 262.21                 | 8.84      | 262.75                 | 8.66      | 263.92                 | 8.25      |
| $f_2$ | 345.24            | 317.91                 | 7.92      | 318.45                 | 7.76      | 319.96                 | 7.32      |
| $f_3$ | 474.69            | 484.22                 | 2.01      | 485.07                 | 2.19      | 487.32                 | 2.66      |
| $f_4$ | 520.68            | 807.51                 | 55.09     | 808.06                 | 55.19     | 809.38                 | 55.45     |
| $f_5$ | 959.74            | 1,154.3                | 20.27     | 1,154.6                | 20.30     | 1,155.1                | 20.36     |
| $f_6$ | 1,230.21          | 1,397.1                | 13.57     | 1,397.5                | 13.60     | 1,398.8                | 13.70     |



**Fig. 32.10** First six natural frequencies and corresponding mode shapes of the gyroscope B from FEM $f_1 = 262.75$ Hz, $f_2 = 318.45$ Hz, $f_3 = 485.07$ Hz, $f_4 = 808.06$ Hz, $f_5 = 1,154.6$ Hz, $f_6 = 1,397.5$ Hz
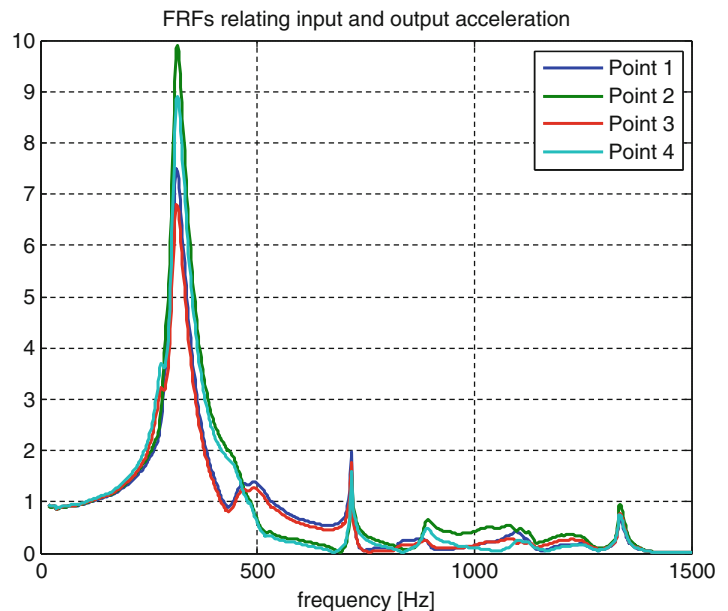
**Fig. 32.11** Location of accelerometers on gyroscope B for sweep tests
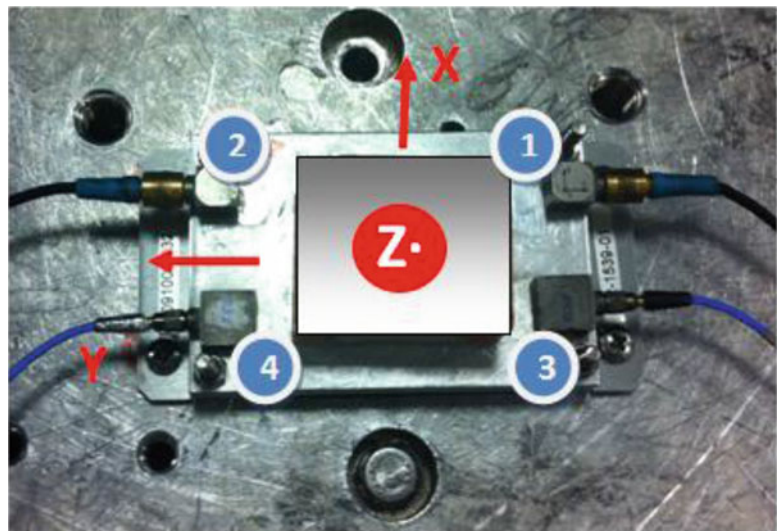
**Fig. 32.12** Transfer functions obtained from the sweep tests of gyroscope B, no washers
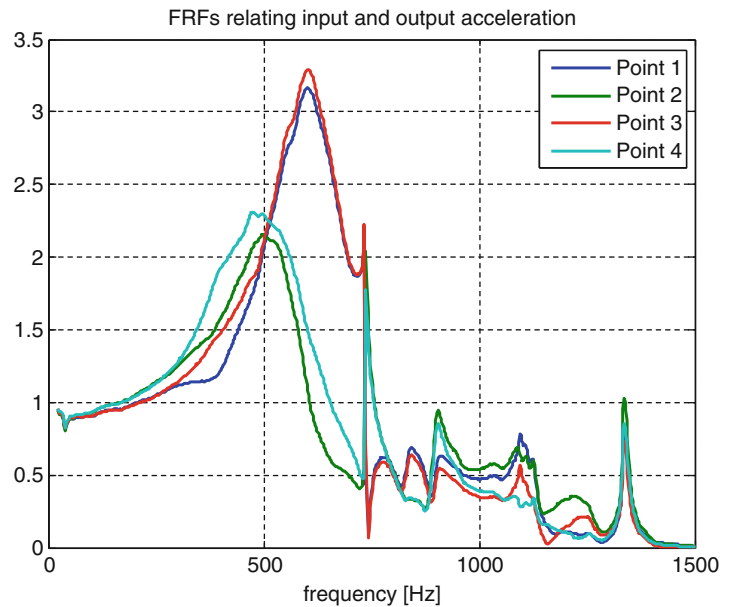


**Fig. 32.13** Transfer functions obtained from the sweep tests of gyroscope B, with washers



## 32.6   Conclusion

A study performed to obtain material characteristics of an isolation layer in a gyroscope is presented. The material is accepted to be orthotropic and modeled accordingly. Young's and shear moduli are determined through an optimization procedure so that the modal test results and FEM modal analysis results match each other. During the procedure it was observed that the boundary condition in the FEM is conceptually different than the actual test rig. In order to overcome this inconvenience, the connection of the test rig is modified and the modal tests are updated. Effect of the details of fixing a test structure to a foundation on modal test results is shown through this observation. Damping property of the material is determined by seeking the response of the structure at the dominant mode frequency. Identified material properties are employed in FEM of another gyroscope with the same isolation layer. Modal tests are performed on this gyroscope as well and the results are compared to FEM modal analysis results. The results have revealed a certain degree of error at each natural frequency, whereas the mode shapes came up in the same order. In addition, sweep tests performed of the second gyroscope are performed. Transfer functions relating the acceleration at the measuring point and the acceleration load are presented. Sweep tests are carried out with both boundary conditions and the difference between the FRF sets are observed.

# References

1. McIntyre ME, Woodhouse J (1988) On measuring the elastic and damping constants of orthotropic sheet materials. Acta Metall 36(6): 1397–1416
2. Deobald LR, Gibson RF (1988) Determination of elastic constants of orthotropic plates by a modal analysis/Rayleigh-Ritz technique. J Sound Vib 124:269–283
3. Ayorinde EO, Gibson RF (1993) Elastic constants of orthotropic composite materials using plate resonance frequencies, classical lamination theory and an optimized three-mode Rayleigh formulation. Compos Eng 3(5):395–407
4. Gibson RF (2000) Modal vibration response measurements for characterization of composite materials and structures. Compos Sci Technol 60(15):2769–2780
5. DeVisscher J, Sol H, DeWilde WP, Vantomme J (1997) Identification of the damping properties of orthotropic composite materials using a mixed numerical experimental method. Appl Comput Mater 4:13–33
6. Hongxing H, Sol H, DeWilde WP (2000) Identification of plate rigidities of a circular plate with cylindrical orthotropy using vibration data. Comput Struct 77(1):83–89
7. Lopez FP, Neilsen MK, Carne TG, O'Gorman CC (2001). Development and validation of an orthotropic constitutive model for aluminum honeycomb, Proceedings of the 2001 SEM Annual Conference, Portland, OR, USA.
8. Carne TG, Stasiunas EG (2008) Identification of full orthotropic constitutive model using measured modal data, Proceedings of the 11th International Congress and Exposition June 2–5, Orlando, FL, USA.

# Chapter 33
# Loss Factors Estimation Using FEM in Statistical Energy Analysis

**Takayuki Koizumi, Nobutaka Tsujiuchi, and Katsuyoshi Honsho**

**Abstract** Statistical energy analysis (SEA) is an effective method for predicting the noise and vibration in the high-frequency band. To predict the vibration energy in SEA, it is necessary to identify the parameters called loss factors accurately. But experiments are expensive and time consuming because many test models are necessary to examine the effects of reducing the vibration energy. So we need to estimate the changes of loss factors when the structure is modified to reduce the vibration energy. This paper describes an estimation method of loss factors using finite element method (FEM). We focus on two subsystems dismounted from structure models and modify the design by changing the number of bolts and the thickness of the panel. Furthermore we construct the accurate FE models of dismounted subsystems by comparing the prediction results with the experimental results. As a result, we confirm the utility of the loss factors estimated in FEM.

**Keywords** SEA • Coupling loss factor • Damping loss factor • FEM • Two subsystems

## 33.1 Introduction

The co-generation system (CGS) is effective for reducing gas emissions which causes global warming, and the number of the CGS installations is increasing every year. In this system, a gas engine is installed as the power source. This engine causes the large vibration to the enclosure. For this reason, the reduction of the vibration in the CGS is required. To reduce it, the modification of the enclosure would be more desirable than the improvement of the engine in view of cost performance and development period. In modification of the enclosure, it is efficient to analyze the vibration of it.

The finite element method (FEM) is effective to analyze the vibration level accurately in low frequency band, but not in high frequency. Recently the statistical energy analysis (SEA) has been widely used as the vibration analysis method in high frequency band [1]. To predict the vibration energy in the SEA, it is important to estimate accurately the parameters called loss factors. They vary when the structure is modified to reduce the vibration energy. Whenever the structure is modified, the loss factors need to be estimated again. The experiment is popular to estimate the loss factors accurately. However, experiments are expensive and time consuming because many test models are necessary to examine the effect of reducing the vibration energy. Therefore, a new method is desirable to estimate the loss factors effectively without the test model.

In this study, we develop a method to estimate the loss factor in simulation by using the FEM. It enables us to analyze the frequency response to acceleration in structure with any modification. We focus on the two subsystems dismounted from structure model and modify the design by changing the number of bolts and thickness of the panel. We construct a finite element model of dismounted subsystems to compare the experimental with the analytical data. The loss factors in two subsystems are estimated by the equivalent models on bolt joints in the FEM. We validate the utility of the estimated loss factors by predicting the vibration energy in the SEA. As a result, the vibration energy is estimated accurately by constructing the accurate FE models.

T. Koizumi • N. Tsujiuchi • K. Honsho (✉)

Department of Mechanical Engineering, Doshisha University, 1-3, Tataramiyakodani, Kyoto 610-0321, Japan
e-mail: dum0524@mail4.doshisha.ac.jp

## 33.2 Theory

SEA is a prediction method for vibration and noise that treats the vibration transmission as a power flow. The power of each subsystem is represented by the space average in the frequency band. The power flow between subsystems is described by power balance equations. The power flow equations of the subsystems shown in Fig. 33.1 are written below:

$$P_{i1} = P_{l1} + P_{12} \tag{33.1}$$

$$P_2 = P_{L2} + P_{21} \tag{33.2}$$

where $P_1$ and $P_2$ are the input power from the external energy sources to the subsystems, $P_{L1}$ and $P_{L2}$ are the internal loss power in subsystem 1 and 2, $P_{12}$ is the transmitted power from subsystems 1–2.

The internal loss power is represented as the loss factor and the subsystem's frequency and energy as follows:

$$P_{L1} = \omega \eta_{11} E_1 \tag{33.3}$$

$$P_{L2} = \omega \eta_{21} E_2 \tag{33.4}$$

where $\eta_{11}$ and $\eta_{22}$ are the damping loss factors and $\omega$ is the angular frequency. $E_1$ and $E_2$ are the space-averaged energy of the subsystem. The coupling loss power is written below:

$$P_{12} = \omega \eta_{12} E_1 - \omega \eta_{21} E_2 \tag{33.5}$$

where $\eta_{12}$ and $\eta_{21}$ are the coupling loss factors between subsystems 1 and 2. $N_1$ and $N_2$ are the modal density of the subsystems in a frequency bandwidth. Using the relationship of loss factors $\eta_{12} N_1 = \eta_{21} N_2$, Eq. 33.5 becomes the following:

$$P_{12} = \omega \eta_{12} N_1 (E_{m1} - E_{m2}) = \omega \eta_{12} N_1 \left( \frac{E_1}{N_1} - \frac{E_2}{N_2} \right) \tag{33.6}$$

Equations 33.1 and 33.2 can be written as follows:

$$P_{i1} = \omega \eta_1 E_1 + \omega \eta_{12} N_1 \left( \frac{E_1}{N_1} - \frac{E_2}{N_2} \right) \tag{33.7}$$

$$P_{i2} = \omega \eta_2 E_2 + \omega \eta_{21} N_2 \left( \frac{E_2}{N_2} - \frac{E_1}{N_1} \right) \tag{33.8}$$
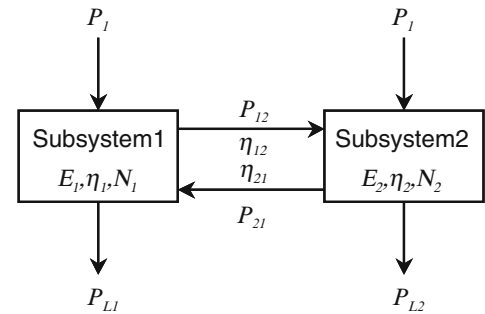


**Fig. 33.1** Power flow balance between two subsystems

For a structure with a multi-subsystem, the power flow equation in matrix form becomes [1]:

$$\omega \begin{bmatrix} \left(\eta_1 + \sum_{i \neq 1}^{N} \eta_{1i}\right) N_1 & -\eta_{12} N_1 \cdots & -\eta_{1N} N_1 \\ -\eta_{21} N_2 & \left(\eta_2 + \sum_{i \neq 2}^{N} \eta_{2i}\right) N_2 \cdots & -\eta_{2N} N_2 \\ \vdots & \cdots & \\ -\eta_{N1} N_N & \cdots \cdots & \left(\eta_N + \sum_{i \neq N}^{N-1} \eta_{Ni}\right) N_N \end{bmatrix} \begin{bmatrix} E_1/N_1 \\ E_2/N_2 \\ \vdots \\ E_N/N_N \end{bmatrix} = \begin{bmatrix} P_1 \\ P_2 \\ \vdots \\ P_N \end{bmatrix} \qquad (33.9)$$

The energy of each subsystem can be obtained by this equation if the loss factor matrix, which is the second term on the left-hand side, is given. Therefore obtaining an accurate loss factor is significant.

The structure subsystem energy is calculated by the following equation by the spatial average of vibration velocity $v$ and mass $m$:

$$E = M \langle v^2 \rangle \qquad (33.10)$$

For a sound field subsystem inside the structure, the energy is written below by mass $m$, the spatial average of sound pressure $p$, and acoustic characteristic impedance $Z_0$:

$$E = \frac{M \langle p^2 \rangle}{Z_0^2} \qquad (33.11)$$

With Eqs. 33.10 and 33.11, the subsystem's vibration and sound pressure can be calculated if energy is obtained from a power balance Eq. 33.9:

## 33.3 SEA Models

### 33.3.1 Test Object

Figure 33.2 shows a test object that is constructed of a base, a roof, four frames, and four panels. The external size of this object is $700 \times 500 \times 390$ mm, and its structural elements are fixed by bolts, nuts and spacers. We dismount two subsystems from this structure and estimate loss factors by exciting them. Figure 33.3 shows the two subsystems connected with three bolts. The details of bolt joints are shown in the Fig. 33.4.

### 33.3.2 The SEA Subsystems

The object is divided into some subsystems in SEA based on the following assumptions.

1. The bended part of the subsystems and the shin panels deal with equivalent thickness.
2. Screw holes are neglected.

Figure 33.5 shows the SEA model. Subsystem 1 is the base, subsystem 2 is the roof, subsystems 3–6 are the frames, and subsystems 7–9 are the panels. In this study, we particularly focus on the base and panel 8 as the two subsystems connected using bolts.
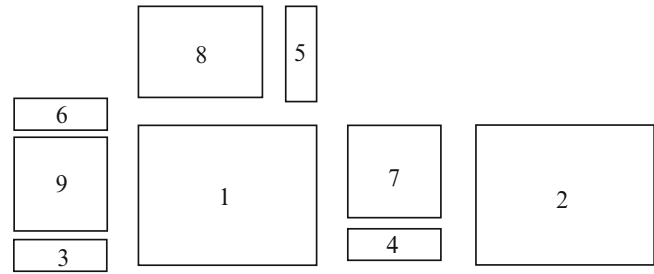
**Fig. 33.2** Outline view



**Fig. 33.3** Outline of the two
subsystems



**Fig. 33.4** The detail of the bolt
joints

**Fig. 33.5** SEA model. 1: base, 2: roof, 3–6: frame, 7–9: panel



### 33.3.3  Estimation Method of SEA Parameter

Power Injection Method (PIM) simultaneously estimates damping and coupling loss factors [2]. In this method, vibration power is injected into each subsystem to measure the vibration energy in each subsystem. Each loss factor is estimated by using these experimental data. The coupling loss factor is estimated by the following equation:

$$\eta_{ij} \cong \frac{1}{\omega} \frac{\langle E_{ji} \rangle}{\langle E_{ii} \rangle} \frac{P_j}{\langle E_{jj} \rangle} \tag{33.12}$$

where $\langle \cdot \rangle$ shows the root mean square value. This equation is constituted by the energies of the focused and conterminous subsystems. The damping loss factors are estimated using the following equation:

$$\eta_i = \frac{P_i/\omega - \left( \sum E_{ii} \eta_{ii} \right) + \left( \sum E_{ji} \eta_{ji} \right)}{E_{ii}} \tag{33.13}$$

## 33.4  Excitation of the Two Subsystems Connected Using Bolts

We excite the two subsystems connected using bolts to predict the damping and coupling loss factors. In this study, we change the thickness of the panel and the number of bolts as structural modifications. We compare the loss factors with two, three or five bolts. The two subsystems are suspended by rubber ropes for the free-free condition. The Fig. 33.6 shows the measurement and excitation points on the panel and the base. Each subsystem is excited in periodic chirp signal by using vibrator. The Figs. 33.7 and 33.8 show the predicted coupling and damping loss factors when the thickness of the panel is 2.3 mm. The Figs. 33.9 and 33.10 show the predicted coupling and damping loss factors when the thickness of the panel is 1.6 mm. According to these figures, we can find that each loss factor is approximately the same values in all frequency bands, regardless of changing the number of bolts. Therefore, if the thickness of the panel is same, we only have to consider one kind of joint condition to estimate the vibrations on all kinds of the joint conditions. So we use the results with the three bolts as the representative values. In the next chapter, we construct the FE model of the coupled two subsystems with the three bolts and compare the analytical results with the experimental results.

## 33.5  The Construction of the Finite Element Model

The analytical time depend on the amount of finite element model. Moreover, for a complicated structure, the accuracy of analysis decreases. Therefore, we construct the FE model of Panel 8 to analyze the damping loss factor. In this chapter, we describe the construction of the FE model.
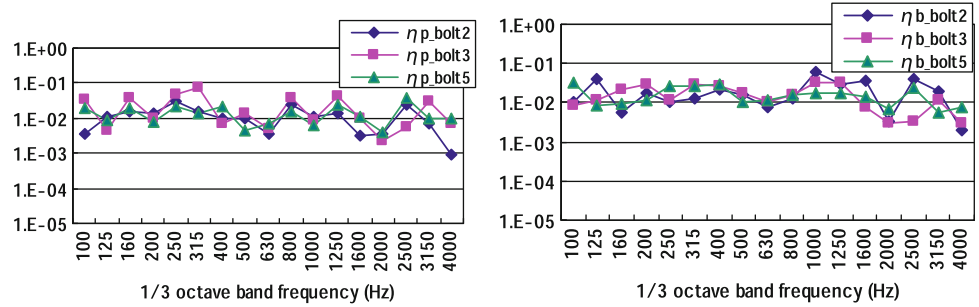
**Fig. 33.6** Measurement and excited points on each subsystem (*left*: panel, *right*: base)
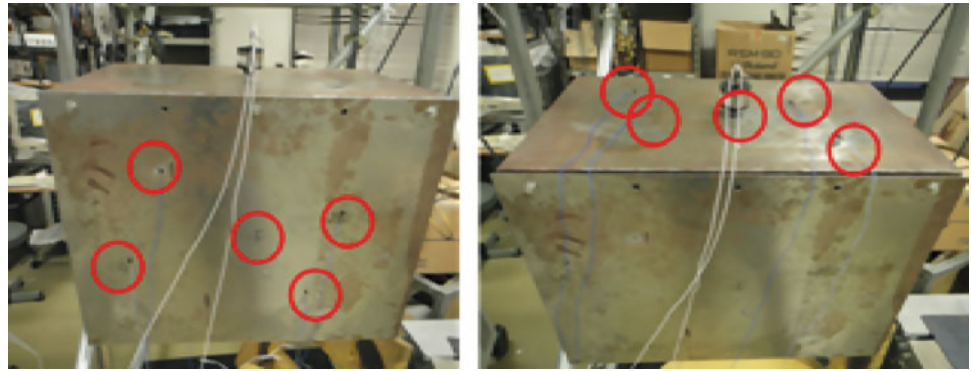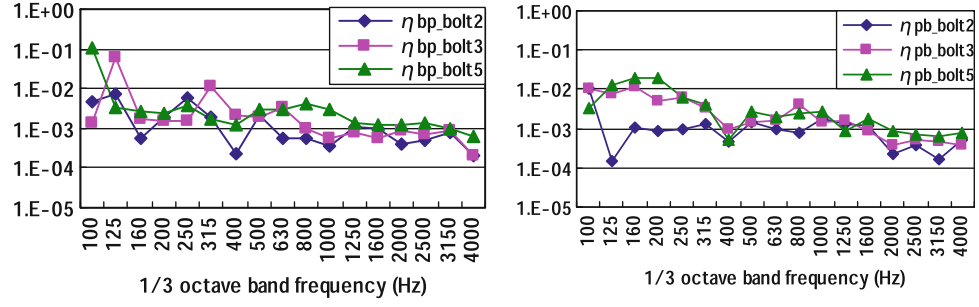


**Fig. 33.7** Coupling loss factors on jointed models (panel 2.3 mm)
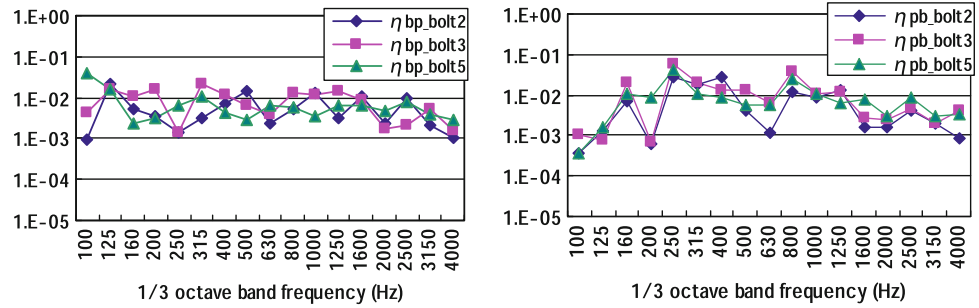


**Fig. 33.8** Damping loss factors on jointed models (panel 2.3 mm)



**Fig. 33.9** Coupling loss factors on jointed models (panel 1.6 mm)



## 33.5.1   Test Equipment

We construct the FE model to compare the analysis data with the experimental data. We measure accelerations on the panel and the base as single subsystems by hammering test. They are excited with an impact hammer, and the vibration accelerations are measured by accelerometers. Each subsystem is stringed in free-free condition. The envelope data of the vibrations are calculated by impulse responses obtained from the FRF data.
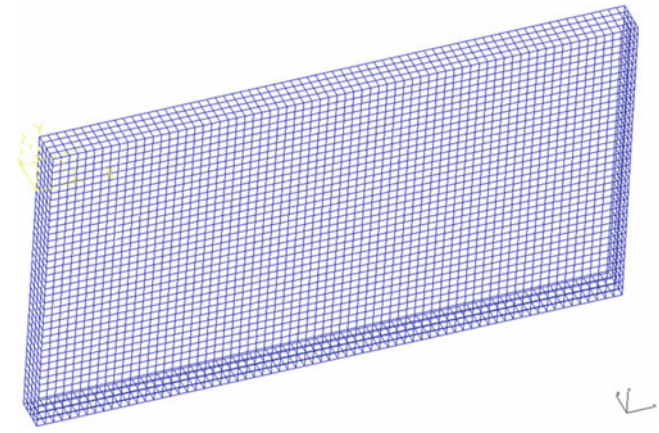
**Fig. 33.10** Damping loss factors on jointed models (panel 1.6 mm)
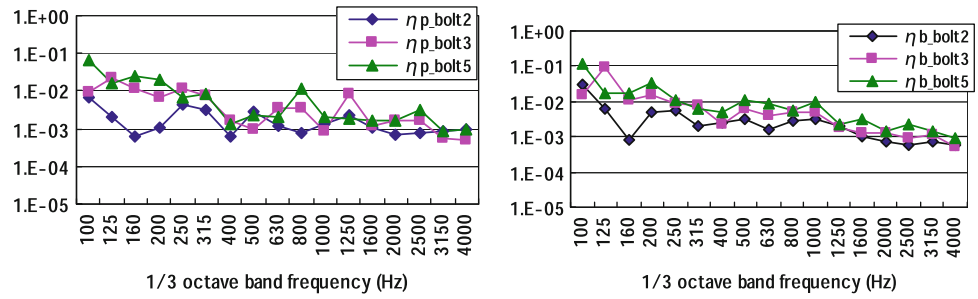


**Fig. 33.11** FE model of the panel
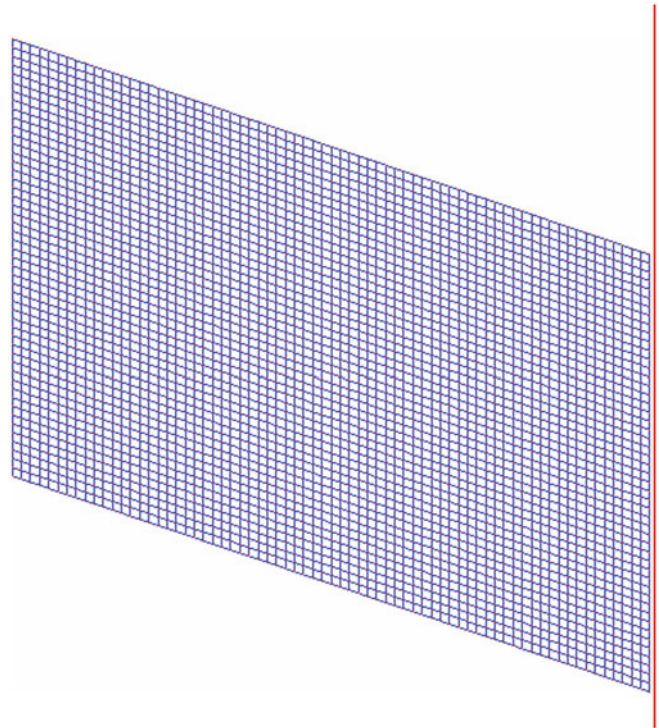


**Fig. 33.12** FE model of the base



## 33.5.2  FE Model of Panel and Base

We constructed the FE models of panel 8 and the base. Figures 33.11 and 33.12 shows FE models that were constructed by using finite element analysis software I-DEAS. The Table 33.1 shows the material properties and the Table 33.2 shows the parameters to generate the mesh model of each subsystem. Figure 33.13 shows comparison results of accelerations between FE models and measurement results. They show the analysis results give close agreement with measurement results.
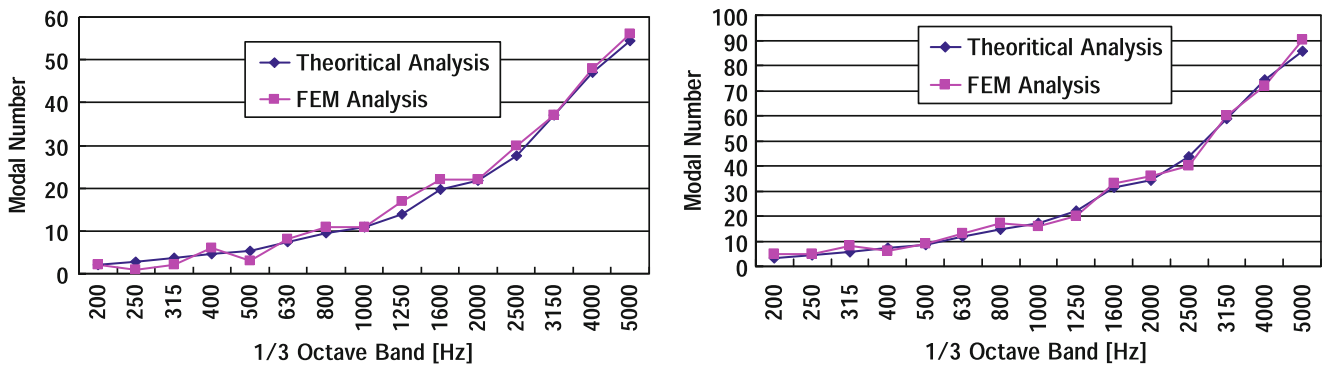
**Table 33.1** Material properties

| –          | Young's modulus [GPa] | Density [kg/m$^3$] | Poisson's ratio | Structural damping |
|------------|-----------------------|--------------------|-----------------|--------------------|
| Steel plate | 205                   | 7,500              | 0.30            | 0.01               |

**Table 33.2** The parameters to generate the mesh models

| –     | Mesh length [mm] | Node count | Element count |
|-------|------------------|------------|---------------|
| Panel | 10               | 3,692      | 3,570         |
| Base  | 10               | 3,712      | 3,602         |
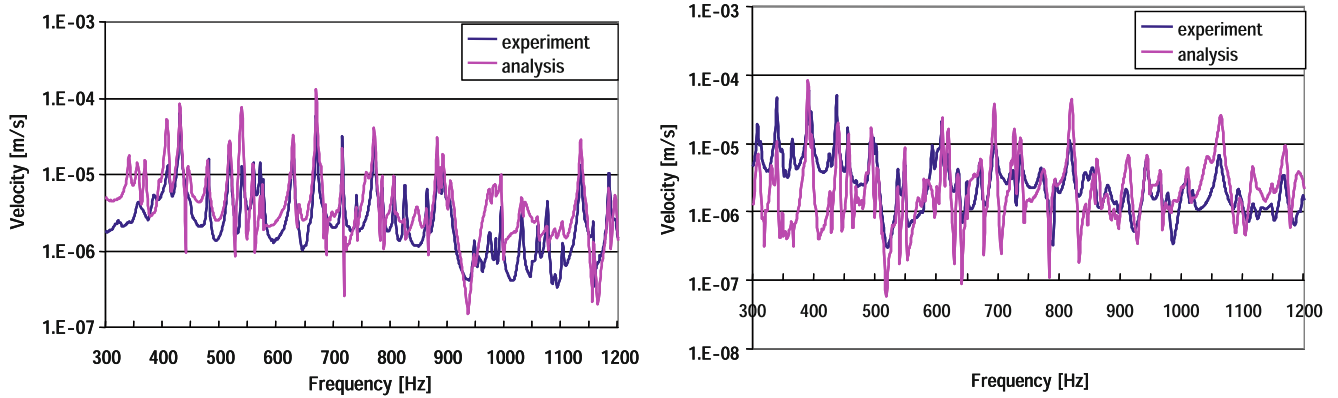


**Fig. 33.13** Comparison result of vibration response (*left*: panel, right: base)



**Fig. 33.14** Comparison of the mode number (*left*: panel, right: base)

Moreover, Fig. 33.14 shows the mode number on each subsystem in 1/3 octave band frequency. Good agreement of mode number is shown in this figure. As a result, we were able to analyze the acceleration in the same level of experiment by using this FE model.

### 33.5.3 The FE Model of the Coupled Subsystems

We constructed the FE model of the two subsystems coupled with the three bolts by using the FE models constructed in the previous section. To construct the accurate FE model of the bolts and spacers, we connected each node corresponding to the bolt position with bar elements using the TUBE type. The thickness of the panel is 1.6 mm and the distance of the gap between the panel and the base is 15 mm. To consider the equivalent stiffness of the contact surface, we connected the nodes surrounding the node corresponding to the bolt positions with RBE element. Figure 33.15 shows the constructed FE model of the coupled subsystems. By using this FE model, we estimated the coupling loss factors. Figure 33.16 shows the comparison results of the coupling loss factors between measurement and analytical result. According to this figure, we found the good agreement of the coupling loss factors. As a result, we confirm the utility of the loss factors estimated in FEM. Therefore we only have to use this FE model to predict the vibration velocity of the objects in high frequency bands even if the number of the bolts is changed.

**Fig. 33.15** The FE model jointed
by the three bolts
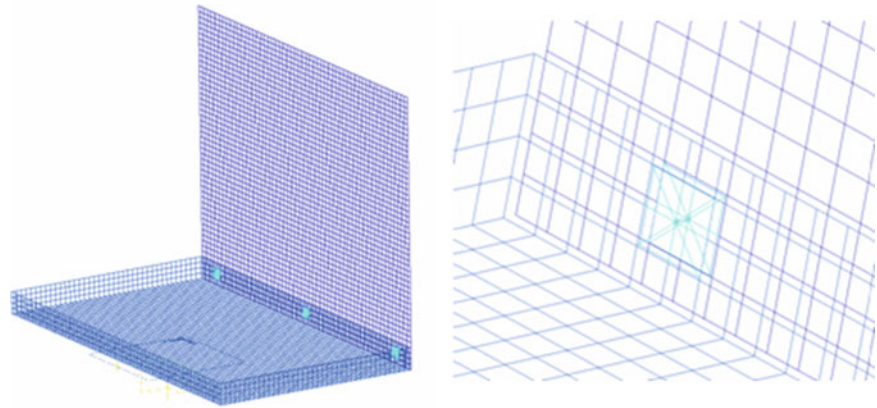


**Fig. 33.16** Comparison results
of the coupling loss factors (panel
1.6 mm)
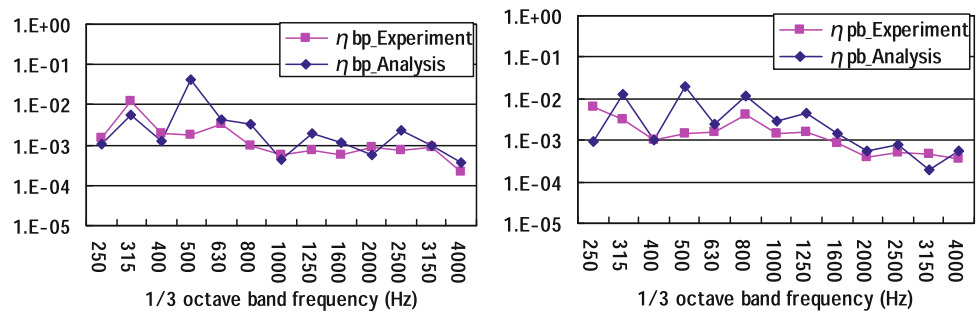


## 33.6   Conclusions

The following conclusions were drawn from this study

1. Each loss factor was approximately the same values in all frequency bands on the coupled two subsystems, regardless of changing the number of bolts.
2. When the thickness of the panel was changed from 1.6 mm to 2.3 mm, each loss factor was increased.
3. We constructed the FE model of the coupled subsystems dismounted from the structure models.

## References

1. Lyon RH, Dejong RG (1995) Theory and application of statistical energy analysis, 2nd edn. Butterworth-Heinemann, Boston, MA
2. Bies DA, Hamid S (1980) In situ determination of loss and coupling loss factors by the power injection method. J Sound Vib 70(2):187–204

# Chapter 34
# Investigation of Crossing and Veering Phenomena in an Isogeometric Analysis Framework

**Stefano Tornincasa, Elvio Bonisoli, Pierre Kerfriden, and Marco Brino**

**Abstract** The dynamic properties of crossing and veering in coupled structures have been studied both numerically and analytically, but they are difficult to investigate using Finite Element Analysis because of the change in the topological arrangement due to the different configuration.

Isogeometric Analysis, recently developed method for numerical simulation, could overcome some of the drawbacks of the change in the configuration such as remeshing, coupling between the nodes of the different models, need of a fine mesh to allow small change in the configuration to be comparable to the mesh size.

The key of this method is to avoid meshing and using the same basis functions used by the geometry, namely Non-Uniform Rational B-Splines (NURBS), to define the discretization of a Finite Element model. Other advantages are the possibility of increasing the order of the functions to obtain smooth stress field across the element interfaces.

An experimental test-rig composed by beams and masses, which allow different configuration and dynamic coupling as well, is used as test case to validate the accuracy of the results with respect to both experimental data and classical Finite Element Analysis.

**Keywords** Crossing and veering phenomena • Isogeometric analysis • Modal analysis of coupled structure • Nitsche's method

## 34.1 Introduction

In a mechanical structure, in particular those composed by different parts assembled together, the variation of a parameter, such as a dimension, the relative position between components, will cause a change in the dynamic behaviour of that structure. The parametric analysis of this change in behaviour with respect to the parameter could reveal two phenomena of interaction between the modes, namely crossing and veering [1].

The first case appears when there is no coupling between eigenspaces and then the mode trajectories will cross without any interaction while, in the latter, coupling features will cause the modes to interact showing an initial convergence and then a divergence of the trajectories. These phenomena are well known in aeroelasticity and commonly found in long-span bridges [2], bladed discs [3], and aircraft wings [4–6].

Since crossing and veering are mostly proven both analytically and numerically, some experimental analyses have been performed [7] to validate the theoretical results, where the test-rig is a frame where one of the inner bar has a screw which allows to change the stiffness of itself.

Deeper analysis on the interaction of the modes and investigation on the transition zone have been performed in [8] by Du Bois and Adhikari.

---

S. Tornincasa • E. Bonisoli
Politecnico di Torino, Corso Duca degli Abruzzi, 24-10129, Torino, Italy

P. Kerfriden • M. Brino (✉)
School of Engineering, Institute of Mechanics and Advanced Materials, Cardiff University,
Queen's Buildings, The Parade, Cardiff CF24 3AA, UK
e-mail: marco.brino@polito.it

Concerning Finite Element Analysis, widely used to perform the parametric analyses, a new technique named Isogeometric Analysis (IGA) [9] is being developed with the aim of making design (mostly Computer Aided Design) and simulation (FEM) converge to the same framework and take advantage of the integration of the two environments to manage the change in the geometrical definition to the mathematical model, by using the Non-Uniform Rational B-Splines (NURBS) function that define the geometry, directly as basis function in the FE model.

Since its first results, IGA has shown giving several advantages in structural mechanics such as smoothness across the element boundaries and the possibility of raising the order and gaining smoothness [10], better performance in the simulation of problems with contacts [11–15] having smooth interface and not gaps and overlaps, due to its tight relationship with CAD it allows to perform topological optimization directly on the geometrical model [16–19].

In the field of structural vibrations, IGA provides advantageous properties, mostly due to the gain of accuracy at high orders, with opposite behaviour compared to the high-order standard elements, and the positiveness of the entries of the mass matrix, due to the non-negative property of NURBS basis functions, which give more stability in transient dynamics problems.

NURBS-based IGA has some disadvantages which are topics for recent and future developments of the methods, such as the local or adaptive refinement and the need of using several NURBS patches for a certain complexity of the geometry.

T-Spline [20, 21] is one of the technologies that could replace NURBS and solve both the problems, but a trivariate version is not yet established in CAD software packages. For this reason a multi-patch geometry is considered for modelling components with complex shape, but it raise the problem of connecting the patches together. In case of the possibility to generate a conforming parameterization at the patch interface, a simple node-to-node master–slave relationship can be defined and the implementation is straightforward, but when this is not possible the coupling can be performing using Nitsche's method [22]. This method is known for the imposition of boundary conditions in the weak form, and an extension can perform the coupling of different domains. The method is in between the Lagrange multipliers and the penalty method, and it takes the advantage of both, namely the consistency of the Lagrange multiplier approach, and the relative ease of implementation and and parameter selection of the penalty method.

The surveys by Imregun and Visser [23], in the 1990s, show the emerging of finite element model updating. The problem of updating a numerical model by using data acquired from a physical vibration test is richly handled by Mottershead and Friswell [24]. They showed how many issues are to be addressed to produce the desired improvement. The methods are either direct or iterative. The latter are based on minimizing an objective function that is generally a non-linear function. The effect of the improvement due to including second order sensitivities was studied by Kim et al. [25]. Another type of method was proposed by Lin et al. [26] to employ both the analytical and the experimental modal data for evaluating sensitivity coefficients with the objective of improving convergence to cases where there is a higher error magnitude, which happens for complex analytical model.

Although several different approaches have been proposed and successfully applied on different structures, the authors of this paper would propose their experience on avionic equipment. The aim is to define an appropriate and updated FE model for modal analysis (FEA) and to match the numerical results with an experimental modal analysis (EMA) campaign. The inverse eigensensitivity approach [24, 27] is proposed as an iterative model updating technique with respect to an experimental modal test campaign. Its validity and quick convergence has been demonstrated in the literature, but modal truncation and experimental inaccuracy effects may represent an interesting task for model updating of this kind of structures. The principal task of this article is the comparison of two different version of the method used to reach a good matching between the modal characteristics of an avionic structure modeled with a linear FE approach and substructured in components. The mathematical bases are the same for both methods but the difference is defined in the objective functions to minimize, and this difference goes to affect the dimensions of the sensitivity matrix that are smaller for the new method than for the previous one.

In this paper an experimental test-rig already considered in [28] is used as subject to investigate its crossing and veering phenomena, focusing on the modelling of the test-rig using NURBS, in order to obtain an *analysis-suitable* geometry, with the properties suitable for running a structural modal isogeometric analysis.

In the first section, the test-rig and its aims and features are presented, in order to underline some of the characteristics to focus the attention to.

In the second section, NURBS and isogeometric analysis in general are considered, with description of the main concept and the differences with respect to standard FEA, and the NURBS model of the test-rig is presented as well, with all the details to understand how it is modelled.

In the third section it is presented the concept of Nitsche's method for domain coupling, with details of the entries of the coupling terms and matrices, with the application to the test-rig.

In the fourth section, a modal analysis of the test-rig using IGA, with comparison to the results that were previously obtained using a beam-based FE code and commercial FE software. Then a parametric modal analysis is performed to obtain the frequency loci plot, where crossing and veering phenomena reveal.

In the last section, the IGA model is updated using the experimental data obtained from the test-rig, to fit the curves with the experiments.

## 34.2 The Experimental Test-Rig

The test-rig considered for investigating crossing and veering is shown in Fig. 34.1. It represents a wing-like structure, where its components can be considered as three thin beams with different orientation and three added masses. The first and the third beam are fixed in space, and they have orthogonal orientation with respect to each other, while the second beam can have a chosen continuous orientation thanks to the rotating device between the first and the second beam.

The configuration parameter, in this case, is the angular position of the second beam, where the "0 deg" configuration is considered as the one where the second and third beams are aligned. This parameter defines a coupling condition among the different beams, with the aim of having veering among bending modes. Due to its envelope on a common axis, the ideal theoretical model of beams and lumped added masses have no coupling between bending and torsional eigenspaces, hence the expectation is to have crossing condition among them.

This structure can be easily modelled in Finite Elements with beams, used for the actual beams and for the cylindrical parts as well, considering a bulk density in order not to change the mass of those parts.

To compute the parametric analysis with the beam structure, an FE code developed by the authors named LUmped Parametric Open Source (LUPOS), is used thanks to its parametric concept. In Fig. 34.2 the model in LUPOS is shown.

On this test-rig, Experimental Modal Analysis was performed in order to identify the natural frequencies for 19 configurations, from 0 to 90° with 5° step, and they will be considered as a reference to further update the material properties modelled in all the different solutions.

The three beams are produced in Aluminium alloy, while the beam used as a clamp, and the rotating device are made by Steel. The remaining components which forms the added masses are made by Aluminium.

Figure 34.3 shows detailed view of what the three added masses are and what are their aims.
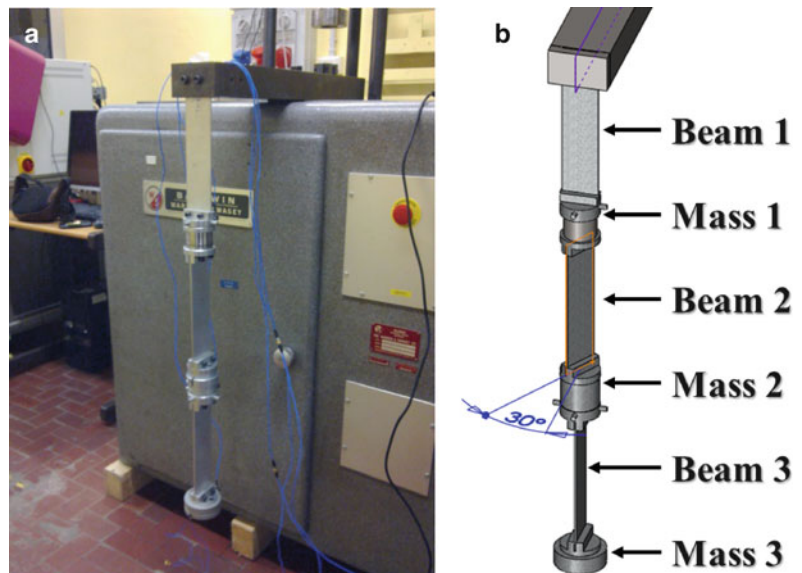


**Fig. 34.1** The experimental test-rig: (**a**) actual model with test hardware; (**b**) full CAD model with configuration parameter

**Fig. 34.2** LUPOS test-rig model
with node numbering
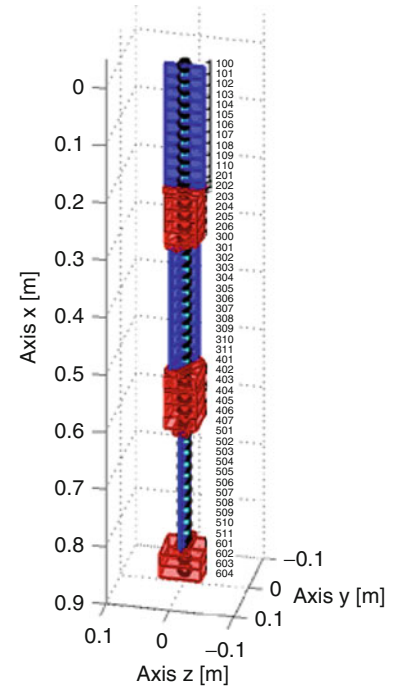




**Fig. 34.3** Details of the test-rig: (**a**) first added mass with rotating graduated device; (**b**) second added mass with fixing device; (**c**) third added mass

## 34.3 Nurbs-Based IGA and Test-Rig Model

In Isogeometric Analysis, applied to solid structural mechanics, use trivariate NURBS (all the details about are widely explained in [29]) to define the discretization in a Finite Elements environment. The basic concept is to use a set of NURBS instead of the usual Lagrange basis functions.

Being NURBS rational B-Splines, the latter is to be considered. B-Spline basis functions are defined by a *knot vector*, which is a vector of parameters in ascending order $\Xi = \{\xi_1 \, \xi_2 \cdots \xi_{n+p+1}\}$, where $n$ is the number of basis functions and $p$ is the polynomial degree. A particular case (and mostly used in CAD) of knot vector is the *open knot vector*, which is a knot vector where the first and last knots are repeated $p + 1$ times.
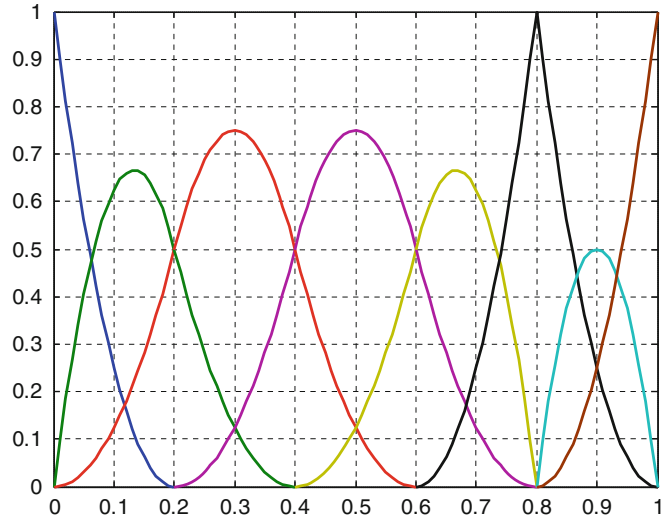
A B-Spline basis functions is defined using the following recursive formula, starting from the order $p = 0$

$$N_{i,0}(\xi) = \begin{cases} 1 & if \ \xi_i \le \xi \le \xi_{i+1} \\ 0 & otherwise \end{cases} \tag{34.1}$$

$$N_{i,p}(\xi) = \frac{\xi - \xi_i}{\xi_{i+p} - \xi_i} N_{i,p-1}(\xi) + \frac{\xi_{i+p+1} - \xi}{\xi_{i+p+1} - \xi_{i+1}} N_{i+1,p-1}(\xi) \tag{34.2}$$

In Fig. 34.4 the elements of a cubic (p = 2) B-spline generated with an open knot vector are displayed.

**Fig. 34.4** B-spline basis
functions from knot vector
{0,0,0,1,2,3,4,4,5,5,5}

NURBS, instead, are projection of entity from dimension $d+1$ to $d$, where $d$ is the number of physical spatial dimension ($d=2$ for a plane, $d=3$ for 3D) and the added dimension is a parameter called *weight*, and they are associated to the basis functions. The NURBS basis functions are then defined as

$$R_{i,p}(\xi) = \frac{N_{i,p}(\xi)\, w_i}{W(\xi)} = \frac{N_{i,p}(\xi)\, w_i}{\sum_{j=1}^{n} N_{j,p}(\xi)\, w_j} \tag{34.3}$$

where it can be noticed that if all the weights are equals, the NURBS basis function are weighted B-Splines functions.

To obtain a solid discretization, three sets of knot vectors must be defined $\Xi = \{\xi_1\ \xi_2 \cdots \xi_{n+p+1}\}$, $H = \{\eta_1\ \eta_2 \cdots \eta_{n+p+1}\}$ and $Z = \{\zeta_1\ \zeta_2 \cdots \zeta_{n+p+1}\}$. Thanks to tensor-product structure, the solid NURBS is defined as

$$R_{i,j,k}^{p,q,r}(\xi,\eta,\zeta) = \frac{N_i(\xi)\, M_j(\xi)\, L_k(\xi)\, w_{i,j,k}}{\sum_{\widehat{i}=1}^{n} \sum_{\widehat{j}=1}^{m} \sum_{\widehat{k}=1}^{l} N_{\widehat{i}}(\xi)\, M_{\widehat{j}}(\xi)\, L_{\widehat{k}}(\xi)\, w_{\widetilde{i,j,k}}} \tag{34.4}$$

$$\mathbf{V}(\xi,\eta,\zeta) = \sum_{i=1}^{n} \sum_{j=1}^{m} \sum_{k=1}^{l} \mathbf{P}_{i,j,k}\, R_{i,j,k}^{p,q,r}(\xi,\eta,\zeta) \tag{34.5}$$

where $\mathbf{P}_{i,j,k}$ are the coordinates of the *control points* in the physical space and N,M,L are the elements of the B-splines generated using knot vectors $\Xi$, $H$ and $Z$, respectively.

Taking advantage of the *isoparametric* concept in finite elements, where the basis functions used to geometrically define an element are also used to discretize the fields of interest (e.g. displacement field in solid mechanics)

$$\mathbf{u}^e(\xi,\eta,\zeta) = \sum_{a=1}^{n} \mathbf{d}_a^e\, R_a^e(\xi,\eta,\zeta) \tag{34.6}$$

where $\mathbf{u}^e$ are the displacements in the physical directions and $\mathbf{d}_a^e$ are the Degrees of Freedom to find and the elements of the solid NURBS have been attributed a unique index a.

The test-rig can be represented, with remarkable simplification, using six trivariate NURBS: three bricks and three cylinders.

In Fig. 34.5 are shown the different parameterizations of the bricks and the cylinders. For the first, parametric and physical dimensions are perfectly aligned, while for the latter instead of the usual circumferential vs. radial parameterization (common when modelling annular sections), the choice is the deformation of a bi-quadratic square, by moving the middle control points of the four edges. The obtained surfaces, the rectangle and the circle, are extruded adding the third parametric dimension and creating the control points for the new surface.

**Fig. 34.5** Two main trivariate NURBS patches with parametric directions: (**a**) brick to represent beam; (**b**) cylinder to represent added mass
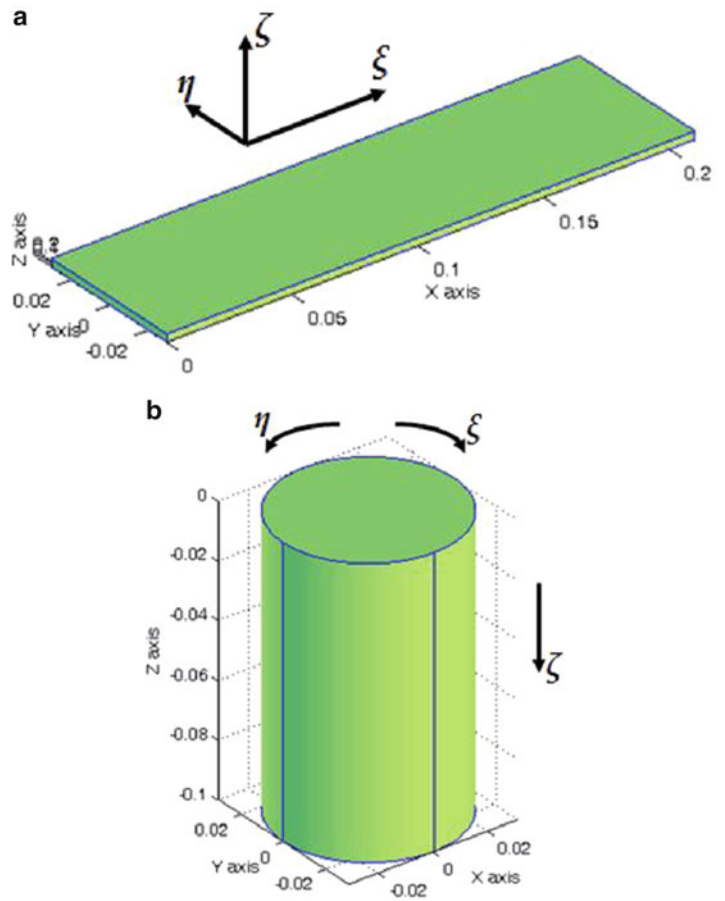
Modelling the six patches with their own dimensions to represent the beams and the added masses, rigid roto-translation of the control points allow the patches to be oriented and repositioned in order to compose the desired configuration of the assembly (Fig. 34.6). The same roto-translation process will be used to orient the second beam to represent the different parametric configurations.

In Fig. 34.7 is intended to underline the geometrical comparison among the CAD model, the LUPOS model and the IGA model, to check for geometric consistency.

## 34.4 Nitsche's Method for Domain Coupling

Considering the theoretical example in Fig. 34.8, two different domains have two surfaces at the same position (interface) and the starting statement is the continuity of the displacements and of the normal stress between the two surfaces which represent the interface.

The basic concept in the method is based on the introduction of a *jump* and *average stress* operators, at the interface

$$[\mathbf{u}] = \mathbf{u}^1 - \mathbf{u}^2 \tag{34.7}$$

$$\{\boldsymbol{\sigma}\} = \frac{1}{2}\left(\boldsymbol{\sigma}^1 - \boldsymbol{\sigma}^2\right) \tag{34.8}$$

The concepts that underline this method will not be explained in this paper, however the complete proof used in this work can be found in [22, 32].

Nitsche's method adds other terms to the weak form of the problem, allowing the introduction of coupling entries in the stiffness matrix, while the mass matrix will remain unchanged instead.

**Fig. 34.6** IGA model



Geometric input model
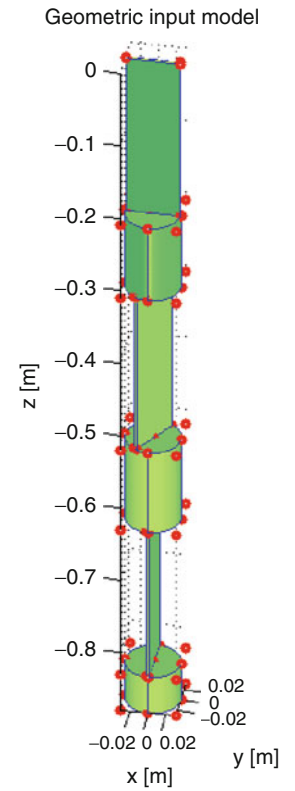
**Fig. 34.7** Comparison of the different models: (**a**) CAD; (**b**) LUPOS; (**c**) IGA
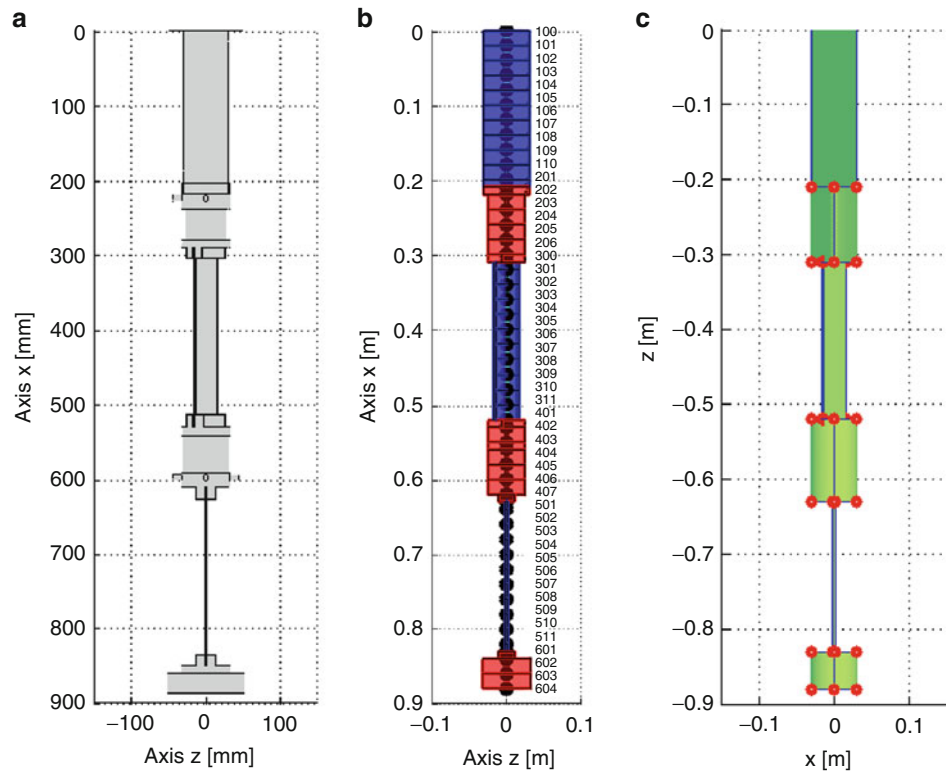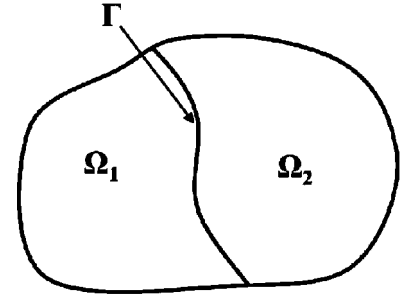


Considering a linear static case, the governing equation considering all Nitsche's terms is

$$\left[ \mathbf{K}^b + \mathbf{K}^n + \left( \mathbf{K}^n \right)^T + \mathbf{K}^s \right] \{\mathbf{x}\} = \{\mathbf{f}_{ext}\} \tag{34.9}$$

**Fig. 34.8** Domain composed by two subdomains $\Omega_1$ and $\Omega_2$, with an internal interface $\Gamma$



where $\mathbf{K}^b$ is the assembly of the stiffness matrices, without any coupling entries

$$\mathbf{K}^b = \sum_{i=1}^{2} \int_{\Omega^k} \left(\mathbf{B}^k\right)^T \mathbf{C}^k \mathbf{B}^k \, d\Omega \tag{34.10}$$

in which $\mathbf{B}$ is the *strain-displacements* matrix and $\mathbf{C}$ is the material constitutive elasticity matrix.

The Nitsche's coupling terms are

$$\mathbf{K}^n = \begin{bmatrix} -\int_\Gamma \mathbf{N}^{1T}\mathbf{n}\frac{1}{2}\mathbf{C}^1\mathbf{B}^1 d\Gamma & -\int_\Gamma \mathbf{N}^{1T}\mathbf{n}\frac{1}{2}\mathbf{C}^2\mathbf{B}^2 d\Gamma \\ \int_\Gamma \mathbf{N}^{2T}\mathbf{n}\frac{1}{2}\mathbf{C}^1\mathbf{B}^1 d\Gamma & \int_\Gamma \mathbf{N}^{2T}\mathbf{n}\frac{1}{2}\mathbf{C}^2\mathbf{B}^2 d\Gamma \end{bmatrix} \tag{34.11}$$

$$\mathbf{K}^s = \begin{bmatrix} \int_\Gamma \alpha\mathbf{N}^{1T}\mathbf{N}^1 d\Gamma & \int_\Gamma \alpha\mathbf{N}^{1T}\mathbf{N}^2 d\Gamma \\ \int_\Gamma \alpha\mathbf{N}^{2T}\mathbf{N}^1 d\Gamma & \int_\Gamma \alpha\mathbf{N}^{2T}\mathbf{N}^2 d\Gamma \end{bmatrix} \tag{34.12}$$

where $\mathbf{N}$ is the basis functions matrix, $\mathbf{n}$ is the normal vector and $\alpha$ is a *stabilization parameter*, That needs to be large enough in order to guarantee positive definitiveness of the discrete assembled operator.

In this work the authors have chosen the stabilization parameter empirically, but some studies in [30, 31] a dependency of the parameter on size of elements $h_e$ and material parameters

$$\alpha = \frac{\lambda + \mu}{2} \frac{\theta(p)}{h_e} \tag{34.13}$$

where $\lambda$ and $\mu$ are the *Lamé parameters* for linear elastic solid, and $\theta(p)$ is a function dependent by the polynomial order of the basis functions.

## 34.5 Parametric Modal Analysis and Results

For the computation of the natural frequencies an FE Modal Analysis is performed at each configuration, obtaining parametric results. Modal Analysis practically means to solve the eigenvalue problem starting from the equations of motion of the undamped system, discretized by Finite Elements

$$[\mathbf{M}]\{\ddot{\mathbf{x}}\} + [\mathbf{K}]\{\mathbf{x}\} = \{\mathbf{0}\} \tag{34.14}$$

where $\{\mathbf{x}\}$ is the vector of the Degrees of Freedom of the system, $[\mathbf{M}]$ and $[\mathbf{K}]$ are respectively the *mass* and *stiffness* matrices, both symmetric, positive and semi-positive definite respectively. In this case the stiffness matrix is the one which includes all Nitsche's coupling terms.

**Fig. 34.9** Refined model used to perform the simulation
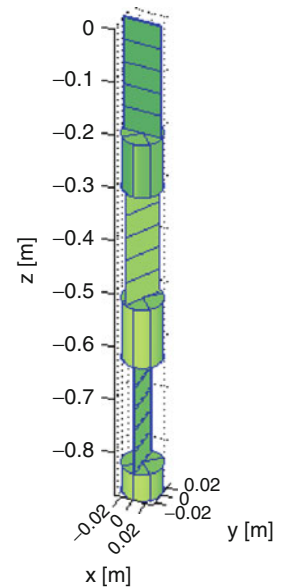


The eigenvalue problem is solved using

$$\det\left([\mathbf{K}] - \omega^2\,[\mathbf{M}]\right) = 0 \tag{34.15}$$

to find the eigenvalues $\omega^2$ and the eigenvectors $[\boldsymbol{\Phi}]$, considering only non-trivial solutions.

These values are stored for each configuration, and the eigenvalues (or the natural frequencies) are plot with respect to the configuration parameter.

The *coarsest mesh*, that is the mesh with the minimum number of elements needed to *exactly* represent the required geometry, must be refined to reach a reasonable accuracy. In terms of modal analysis, and considering that in this particular case the analysis and comparison is performed considering the first seven modeshapes, only a few numbers of elements per beam are necessary. In Fig. 34.9 it is shown the discretization used for the analysis. For the beam elements, a single element through the thickness and one element along the width are enough, while for the length five elements are the minimum number for representing with enough accuracy the bending of higher modes. The functions are cubic in all the three parametric dimensions.

For the added masses, a single element would be enough, considering that the they can be considered infinitely rigid with negligible contribution to the elasticity. Due to Nitsche coupling, a finer discretization is necessary for better let the method distribute the coupling entries on more elements. The patches have cubic functions for all the parametric dimensions.

In Fig. 34.10 it is shown the comparison of Mode 3 and Mode 6 using LUPOS, a tri-dimensional standard FEM and IGA, for the 30° configuration.

The three models have different characteristics, and the most valuable is the number of elements (and/or Degrees of Freedom) with respect to geometrical accuracy. In Table 34.1 the number of elements and Degrees of Freedom are compared among the three models.

LUPOS is a reasonable solution for this problem, due to the possibility of modelling the structure with simple beams, and using thicker beams for modelling the added masses, but is has the drawback of not taking into account the cylindrical feature of the added masses. For dimensional reasons the sides of the cross section are considered to be of the same dimensions of the diameter of the actual cylinders, therefore a bulk density must be defined, in order that the masses are equal to the actual ones. Another LUPOS drawback is that the displacement information is related to the axis of the beams and of the cylinders, and not of the external surfaces (important for comparison with Experimental Modal Analysis results) but this can be easily overcome by adding *Rigid Joint* elements to connect the axis to the desired point of the surface.

SolidWorks model is composed by second-order tetrahedra (10 nodes) therefore, due to the small thickness of the beams and the accuracy request to approximate the cylindrical feature, the number of elements and Degrees of Freedom is very high. And moreover, the geometry is not exact but approximated.

IGA model in this particular case is straightforward due to the simplicity of the geometries involved. In the coarsest mesh, only one element per patch is enough to exactly represent the model.

**Fig. 34.10** Comparison of Mode 3 (*upper*) and Mode 6 (*lower*) among the different models: (**a**) SolidWorks; (**b**) LUPOS; (**c**) IGA
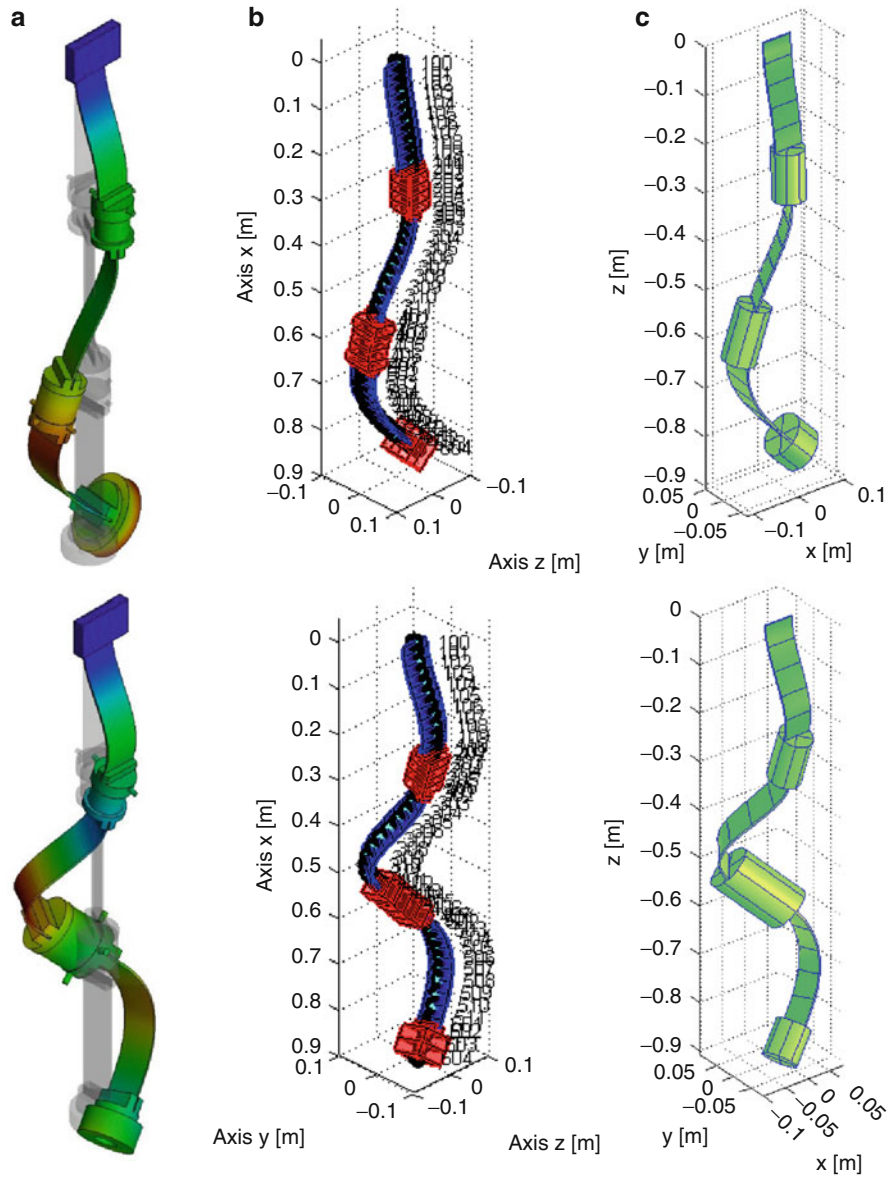


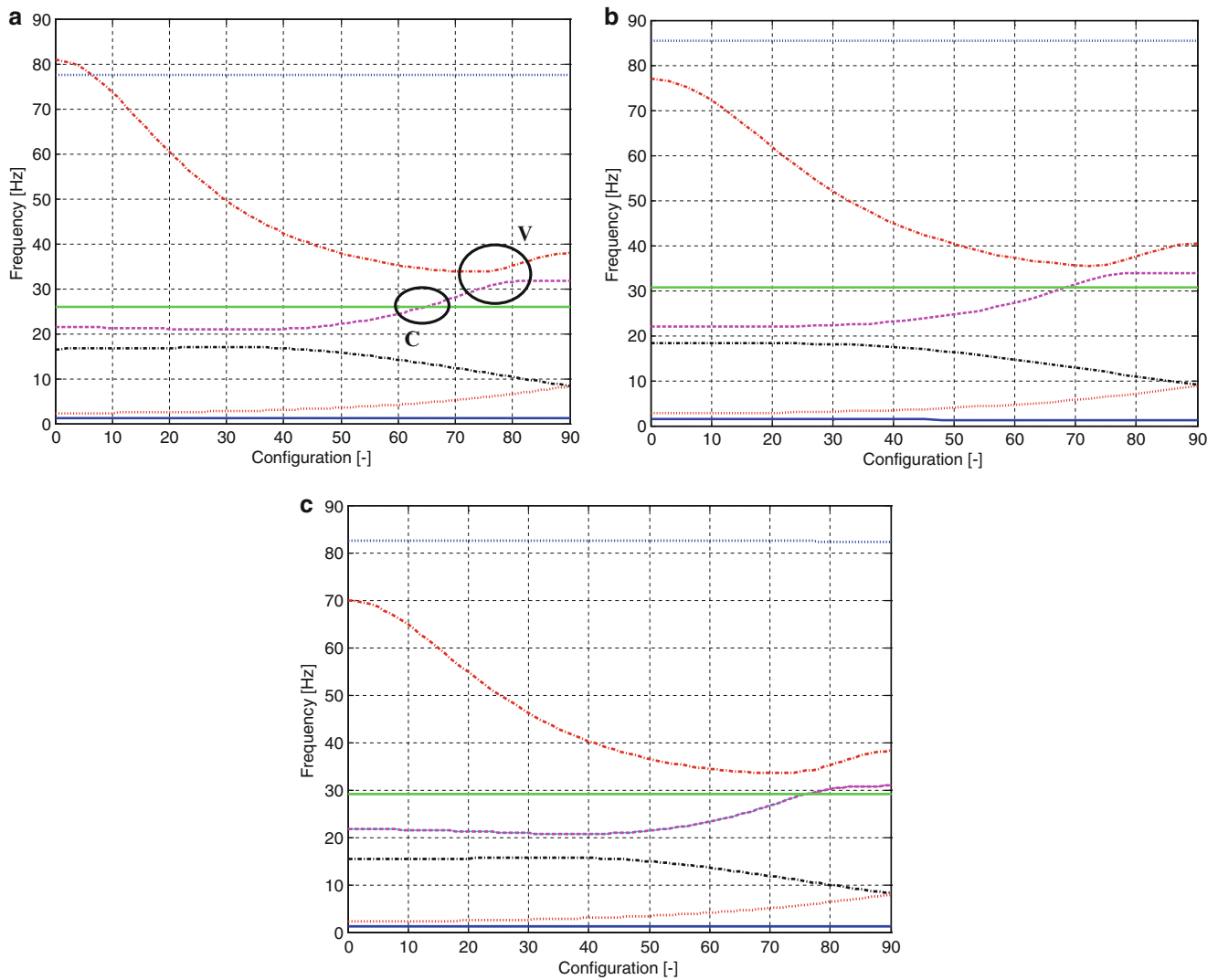**Table 34.1** Comparison of the dimensions of the three different test-rig models

| Model | No. of Elements | No. of DoFs |
|---|---|---|
| LUPOS | 49 | 294 |
| SolidWorks | 3,996 | 24,840 |
| IGA | 27 | 2,052 |

A parametric analysis is then performed from configuration 0 to 90°, with 1° of step size, obtaining 91 sets of eigenvalues and eigenvectors. The frequency loci with respect to the configuration parameter are represented in Fig. 34.11 for LUPOS, SolidWorks and IGA respectively.

The region marked with *C*, involving Mode 4 and Mode 5 at approximately 70° is a possible *crossing* region, while the region marked with *V*, involving Mode 5 and Mode 6 between 72 and 76° is a possible *veering* region.

Considering that a crossing region is when there is no interaction between the modes and the opposite in case of veering, one tool to confirm the nature of the interaction is the Modal Assurance Criterion (MAC) index

$$MAC_{i,j} = \frac{\left(\boldsymbol{\Phi}_i^T \boldsymbol{\Phi}_j\right)^2}{\left(\boldsymbol{\Phi}_i^T \boldsymbol{\Phi}_i\right)\left(\boldsymbol{\Phi}_j^T \boldsymbol{\Phi}_j\right)} = \cos^2\alpha_{i,j} \tag{34.16}$$

**Fig. 34.11** Comparison frequency loci plots: (**a**) LUPOS; (**b**) SolidWorks; (**c**) IGA

in which two eigenvectors are compare together and the index, usually inside a range from 0 to 1 (or scaled from 0 to 100 %), mathematically checks how the vectors are parallels, while the engineering interpretation is the similarity of the two modeshapes. Evaluating the MAC index for all the configurations allows following a frequency loci.

In this case, MAC comparison is performed to check the two marked regions in Fig. 34.11. In Figs. 34.12 and 34.13 the MAC matrices obtained are shown.

In the first case, even though the distance between the configurations considered is short, the MAC matrix shows a full switch between mode 4 and mode 5. The values are very close to 100 %, with negligible value on the diagonal, hence no interaction between those modes is present, hence this region can be classified as *crossing* region.

In the second case, there is not a full switch, but there are correlations between the modeshapes of the two configurations, hence the modal information are being passed from a mode to the other. The distance between the configuration is wider, and the off-diagonal terms are not negligible. For these reasons this region can be classified as *veering* region.

**Fig. 34.12** MAC index between configurations 69° and 71°
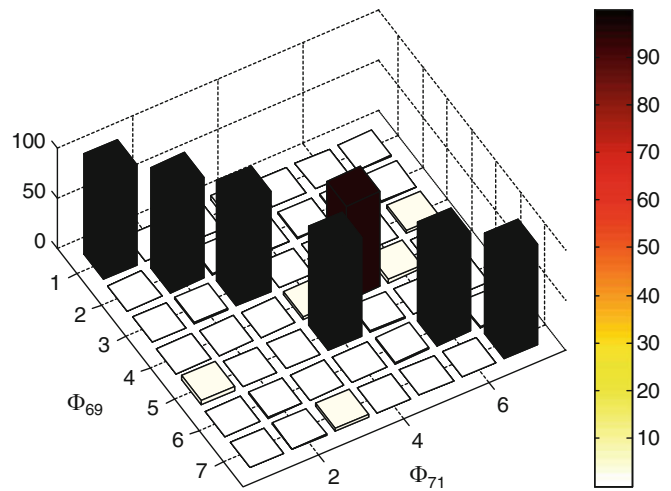


**Fig. 34.13** MAC index between configurations 72° and 76°
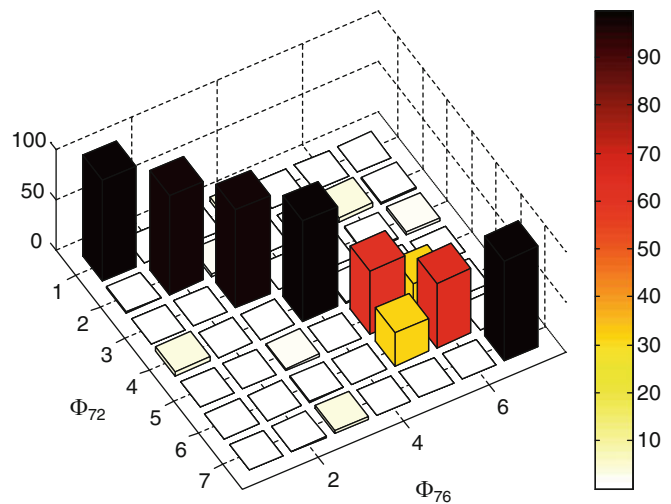


## 34.6    Updating with Inverse Eigensensitivity Approach

The IGA results obtained with parametric modal analysis can be compared to the frequencies obtained from the experimental campaign on the test-rig. The experimental modal analysis was performed with tri-axial accelerometers with hammer excitation. 19 configurations from 0 to 90°, with 5° angular step, were considered.

Figure 34.14 compares the numerical results vs. the experimental ones.

Although the path of the frequency loci is consistent, they show a shift with respect to the experimental identified points in the figure. These differences are mostly due to an incorrect estimate of the material parameters (for modal analysis Young modulus and density) with respect to the actual ones.

Even though for the density the parameter updating could be performed by weighting the actual components and finding the value of bulk density such that the total weight of the finite element component is equal to the actual one, in this work both density and elasticity modulus are considered in the computation of these parameters using the Inverse Eigensensitivity approach.

The model is split considering beams and added masses as sub-structures, hence four parameters can be considered as updating parameters:

– $E_b$ : Young modulus of the beams;
– $\rho_b$ : density of the beams;
– $E_m$ : Young modulus of the added masses;
– $\rho_m$ : density of the added masses;

**Fig. 34.14** EMA vs. IGA frequency loci comparison before updating
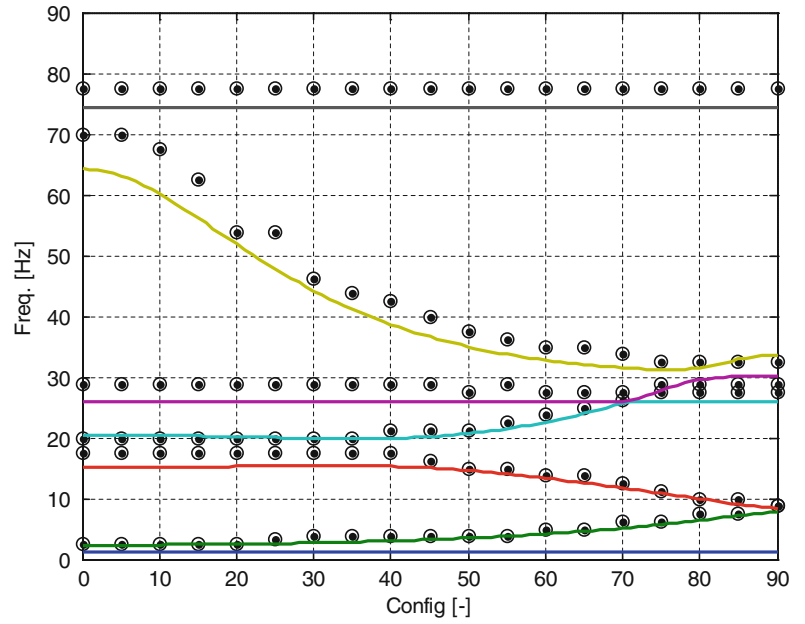
Since the contribution of the elasticity of the added masses to the lower frequencies modes is negligible, the updating of the Young modulus of this substructure can be deactivated, reducing the problem to the updating of three parameters.

The total assembled mass and stiffness matrices are obtained by summing the sub-matrices, expanded to the total degrees of freedom

$$[M] = \sum_{i=1}^{pm} a_i \, [M_i], \quad [K] = \sum_{i=1}^{pk} b_i \, [K_i] \tag{34.17}$$

which are weighted by the independent parameters $a_i$ and $b_i$.

The system involved in the iterations of the sensitivity is

$$
\left\{
\begin{array}{c}
\frac{\omega_{\exp,1}^2 - \omega_1^2}{\omega_1^2} \\[4pt]
\frac{\{\Delta\Phi^{(1)}\}^T \{\Delta\Phi^{(1)}\}}{\|\Phi^{(1)}\|^2} \\[4pt]
\vdots \\[4pt]
\frac{\omega_{\exp,r}^2 - \omega_r^2}{\omega_r^2} \\[4pt]
\frac{\{\Delta\Phi^{(r)}\}^T \{\Delta\Phi^{(r)}\}}{\|\Phi^{(r)}\|^2}
\end{array}
\right\}
=
\left[
\begin{array}{ccccccc}
\frac{\partial\omega_1^2}{\partial a_1}/\omega_1^2 & \cdots & \frac{\partial\omega_1^2}{\partial a_{pm}}/\omega_1^2 & \frac{\partial\omega_1^2}{\partial b_1}/\omega_1^2 & \cdots & \frac{\partial\omega_1^2}{\partial b_{pk}}/\omega_1^2 \\[4pt]
\frac{\{\Delta\Phi^{(1)}\}^T}{\|\Phi^{(1)}\|^2}\frac{\partial\{\Phi^{(1)}\}}{\partial a_1} & \cdots & \frac{\{\Delta\Phi^{(1)}\}^T}{\|\Phi^{(1)}\|^2}\frac{\partial\{\Phi^{(1)}\}}{\partial a_{pm}} & \frac{\{\Delta\Phi^{(1)}\}^T}{\|\Phi^{(1)}\|^2}\frac{\partial\{\Phi^{(1)}\}}{\partial b_1} & \cdots & \frac{\{\Delta\Phi^{(1)}\}^T}{\|\Phi^{(1)}\|^2}\frac{\partial\{\Phi^{(1)}\}}{\partial b_{pk}} \\[4pt]
\vdots & & \vdots & \vdots & & \vdots \\[4pt]
\frac{\partial\omega_r^2}{\partial a_1}/\omega_r^2 & \cdots & \frac{\partial\omega_r^2}{\partial a_{pm}}/\omega_r^2 & \frac{\partial\omega_r^2}{\partial b_1}/\omega_r^2 & \cdots & \frac{\partial\omega_r^2}{\partial b_{pk}}/\omega_r^2 \\[4pt]
\frac{\{\Delta\Phi^{(r)}\}^T}{\|\Phi^{(r)}\|^2}\frac{\partial\{\Phi^{(r)}\}}{\partial a_1} & \cdots & \frac{\{\Delta\Phi^{(r)}\}^T}{\|\Phi^{(r)}\|^2}\frac{\partial\{\Phi^{(r)}\}}{\partial a_{pm}} & \frac{\{\Delta\Phi^{(r)}\}^T}{\|\Phi^{(r)}\|^2}\frac{\partial\{\Phi^{(r)}\}}{\partial b_1} & \cdots & \frac{\{\Delta\Phi^{(r)}\}^T}{\|\Phi^{(r)}\|^2}\frac{\partial\{\Phi^{(r)}\}}{\partial b_{pk}}
\end{array}
\right]
\left\{
\begin{array}{c}
\Delta a_1 \\[4pt]
\vdots \\[4pt]
\Delta a_{pm} \\[4pt]
\Delta b_1 \\[4pt]
\vdots \\[4pt]
\Delta b_{pk}
\end{array}
\right\}
\tag{34.18}
$$

where $\|\Phi^{(r)}\|^2 = \{\Phi^{(r)}\}^T\{\Phi^{(r)}\}$ and the matrix is the balanced sensitivity matrix $[S]$. In order to estimate the coefficients of the sensitivity matrix $[S]$, by taking derivatives of the $M$ and $K$-orthogonality properties of eigenvectors, it results [14, 15]:

$$\frac{\partial\omega_r^2}{\partial a_i} = -\omega_r^2 \, \{\Phi^{(r)}\}^T \, [M_i] \, \{\Phi^{(r)}\}, \quad \frac{\partial\omega_r^2}{\partial b_i} = \{\Phi^{(r)}\}^T \, [K_i] \, \{\Phi^{(r)}\}. \tag{34.19}$$

$$\frac{\partial\{\Phi^{(r)}\}}{\partial a_i} = \sum_{s=1}^{N} \alpha_i^{r,s} \{\Phi^{(s)}\}, \quad \frac{\partial\{\Phi^{(r)}\}}{\partial b_i} = \sum_{s=1}^{N} \beta_i^{r,s} \{\Phi^{(s)}\} \tag{34.20}$$

**Fig. 34.15** EMA vs. IGA
frequency loci comparison after
updating
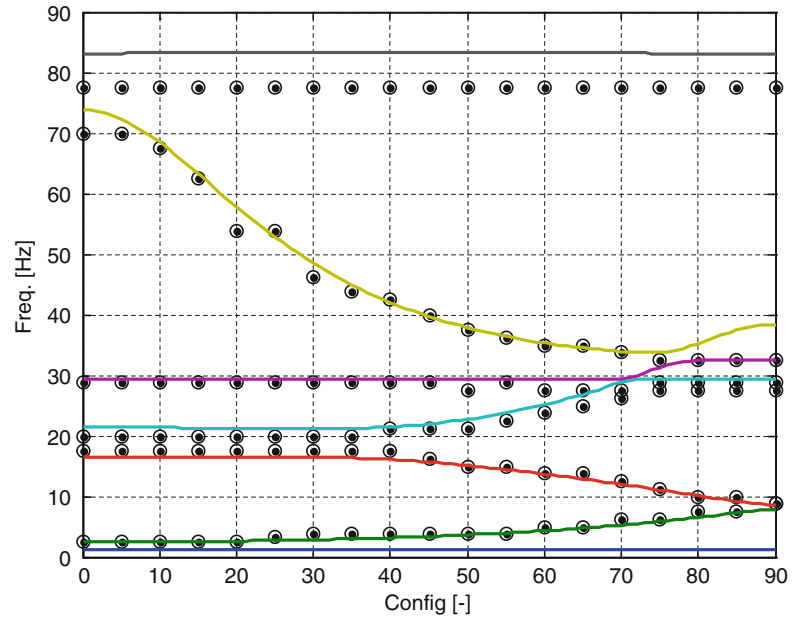


Where

$$\begin{cases} \alpha_i^{r,s} = \dfrac{-\omega_r^2 \left\{\Phi^{(s)}\right\}^T [M_i] \left\{\Phi^{(r)}\right\}}{\omega_r^2 - \omega_s^2} \ , \ r \neq s \\ \alpha_i^{r,s} = -\frac{1}{2} \left\{\Phi^{(s)}\right\}^T [M_i] \left\{\Phi^{(r)}\right\} \ , \ r = s \end{cases} \ , \ \begin{cases} \beta_i^{r,s} = \dfrac{\left\{\Phi^{(s)}\right\}^T [K_i] \left\{\Phi^{(r)}\right\}}{\omega_r^2 - \omega_s^2} \ , \ r \neq s \\ \beta_i^{r,s} = 0 \ , \ r = s \end{cases} \tag{34.21}$$

hence the eigenvectors derivative are expressed by using the expansion theorem and considering eigenvectors as a base to describe those terms.

The updating procedure has been achieved solving the following linear system:

$$\{\Delta \ Eig\} = [S] \ \{\Delta \ Par\} = [U] \ [\Sigma] \ [V]^T \ \{\Delta \ Par\}, \tag{34.22}$$

where the number of updating parameters are usually much smaller than the number of modal residual equations in the original inverse eigensensitivity method, while $[S]$ is more similar to a square matrix in the proposed modification.

Therefore the updating parameters are obtained in a least square sense, by a Singular Value Decomposition technique

$$\{\Delta \ Par\} = [V] \ [\Sigma]^+ [U]^T \ \{\Delta \ EigenV\}, \tag{34.23}$$

where $[\Sigma]^+$ is the Moore-Penrose generalized inverse matrix of $[\Sigma]$.

The results of Eq. 34.23 are used to update the material parameter at each iteration, which results in

$$[M] = \sum_{i=1}^{pm} (a_i + \Delta a_i) \ [M_i], \quad [K] = \sum_{i=1}^{pk} (b_i + \Delta b_i) \ [K_i] \tag{34.24}$$

The procedure is necessarily iterative, but engineering experience is suitable for avoiding not physical solutions. Therefore the iterative algorithm is not automatic. Furthermore two degree of freedom for piloting the iterations is available at each iteration: the number of modes to control and how many parameters can be accepted or neglected in the updating parameters. In fact in this first test the first six modes are always taken into account for all iterations, but for the first five iterations only the more important four parameters are updated to tune the modal characteristic (density $\rho$ and Young's modulus $E$ of the upper and bottom plates).

In Fig. 34.15 it is presented the results of the frequency loci compared to the experimental data, which now fits better the actual values. Seven iterations were necessary to reach this result.

It is noticed that the seventh mode was not considered for the updating.

## 34.7   Conclusions

In the previous sections, the consistency of an IGA parametric modal analysis for investigating crossing and veering phenomena in a test structure is presented.

The method was compared with the solutions obtained with beam-based open-source FE code named LUPOS, and with commercial CAD-CAE software.

The advantages of an IGA model with Nitsche's method for coupling the different patches were presented, giving more values to the other advantages that are already present in literature.

A consistency of the results with respect to experimental data was shown using the method of the inverse eigensensitivity approach.

For future developments, improvement can be taken into account in both numerical and experimental parts. For the latter, a deeper investigation with modal testing for smaller configuration resolution around the crossing and veering region can be performed, to check the consistency of the experimental modeshapes with the numerical ones, in the transition zones.

In the numerical part, a geometrical model closer to the CAD original geometry can be built, in order of better model the joints and the added masses.

More generally, in the IGA field, a more direct relationship to a CAD model built in a commercial software and the trivariate analysis-suitable model to be used for the simulation is to be developed.

## References

1. Leissa W (1974) On a curve veering aberration. J Appl Math Phys (ZAMP) 25:99–111
2. Chen X, Kareem A, Matsumoto M (2001) Multimode coupled flutter and buffeting analysis of long span bridges. J Wind Eng Ind Aerod 89:649–664
3. Chan Y, Inman DJ (2010) Management of the variability of vibration response levels in mistuned bladed discs using robust design concepts. Part 1. Parameter design. Mech Syst Signal Pr 24:2777–2791
4. Bae JS, Inman DJ, Lee I (2004) Effects of structural nonlinearity on subsonic aeroelastic characteristics of an aircraft wing with control surface. J Fluid Struct 19:747–763
5. Khodaparast H, Mottershead JE, Badcock K (2010) Propagation of structural uncertainty to lineat aeroelastic stability. J Fluid Struct 88: 223–236
6. Tang D, Dowell E (2010) Aeroelastic response of aircraft with freeplay structural nonlinearity. In: Proceedings of 2nd aircraft structural design conference, London
7. Maeda T, Baburaj V, Ito Y, Koga T (1998) Flexural-torsional coupling effect on vibrational characteristics of angle-ply laminates. J Sound Vib 210(3):351–365
8. du Bois JL, Adhikari S, Lieven NA (2007) Experimental and numerical investigation of mode veering in a stressed structure. In: Proceedings of 25th IMAC, Orlando, FL
9. Hughes TJR, Cottrell JA, Bazilevs Y (2005) Isogeometric analysis: CAD, finite elements, NURBS, exact geometry and mesh refinement. Comput Methods Appl Mech Eng 194(39–41):4135–4195
10. Cottrell JA, Hughes TJR, Reali A (2007) Studies of refinement and continuity in isogeometric structural analysis. Comput Methods Appl Mech Eng 196(41–44):4160–4183
11. Temizer I, Wriggers P, Hughes TJR (2011) Contact treatment in isogeometric analysis with NURBS. Comput Methods Appl Mech Eng 200 (9–12):1100–1112
12. Jia L (2011) Isogeometric contact analysis: geometric basis and formulation for frictionless contact. Comput Methods Appl Mech Eng 200 (5–8):726–741
13. Temizer I, Wriggers P, Hughes TJR (2012) Three-dimensional mortar-based frictional contact treatment in isogeometric analysis with NURBS. Comput Methods Appl Mech Eng 209–212:115–128
14. De Lorenzis L, Temizer I, Wriggers P, Zavarise G (2011) A large deformation frictional contact formulation using NURBS-based isogeometric analysis. Int J Numer Meth Eng 87(13):1278–1300
15. Matzen ME, Cichosz T, Bischoff M (2013) A point to segment contact formulation for isogeometric, NURBS-based finite elements. Comput Methods Appl Mech Eng 255:27–39
16. Wall WA, Frenzel MA, Cyron C (2008) Isogeometric structural shape optimization. Comput Methods Appl Mech Eng 197(33–40):2976–2988
17. Manh ND, Evgrafov A, Gersborg AR, Gravesen J (2011) Isogeometric shape optimization of vibrating membranes. Comput Methods Appl Mech Eng 200(13–16):1343–1353
18. Qian X, Sigmund O (2011) Isogeometric shape optimization of photonic crystals via Coons patches. Comput Methods Appl Mech Eng 200 (25–28):2237–2255
19. Qian X (2010) Full analytical sensitivities in NURBS based isogeometric shape optimization. Comput Methods Appl Mech Eng 199 (29–32):2059–2071
20. Bazilevs Y, Calo VM, Cottrell JA, Evans JA, Hughes TJR, Lipton S, Scott MA, Sederberg TW (2010) Isogeometric analysis using T-splines. Comput Methods Appl Mech Eng 199(5–8):229–263
21. Scott MA, Li X, Sederberg TW, Hughes TJR (2012) Local refinement of analysis-suitable T-splines. Comput Methods Appl Mech Eng 213–216:206–222

22. Nitsche J (1971) Uber ein variationsprinzip zur losung von dirichlet-problemen bei verwendung von teilraumen, die keinen randbedingungen unterworfen sind. Abh Math Sem Univ Hamburg 36:9–15
23. Imregun M, Visser WJ (1991) A review of model updating techniques. Shock Vib Digest 23(1):9–20
24. Mottershead JE, Friswell MI (1993) Model updating in structural dynamics: a survey. J Sound Vibr 167(2):347–375
25. Kim KO, Anderson WJ, Sandstorm RE (1983) Non-linear inverse perturbation method in dynamic analysis. AIAA J 21(9):1310–1316
26. Lin RM, Lim MK, Du H (1995) Improved inverse eigensensitivity method for structural analytical model updating. Trans ASME J Vibr Acoust 117:192–198
27. Bonisoli E, Fasana A, Garibaldi L, Marchesiello S (2002) Sensitivity analysis and damage location over the Z24 bridge. In: ONERA, Structural health monitoring, Paris, pp. 1007–1015
28. Bonisoli E, Delprete C, Esposito M, Mottershead JE (2011) Structural dynamics with coincident eigenvalues: modelling and testing. In: Proceedings of the 29th IMAC, vol 3(6). Detroit, MI, pp. 325–337
29. Piegl LA, Tiller W (1996) The NURBS book. Springer, Berlin
30. Fritz A, Hüeber S, Wohlmuth BI (2004) A comparison of mortar and Nitsche techniques for linear elasticity. CALCOLO 41(3):115–137
31. Bazilevs Y, Hughes TJR (2007) Weak imposition of Dirichlet boundary conditions in fluid mechanics. Comput Fluids 36(1):12–16
32. Nguyen VP, Kerfriden P, Bordas S (2013) Isogeometric cohesive elements for two and three dimensional composite delamination analysis. Compos Sci Technol http://arxiv.org/abs/1305.2738

# Chapter 35
# Influence of Fan Balancing in Vibration Reduction of a Braking Resistor

F. Braghin, M. Portentoso, and E. Sabbioni

**Abstract** This paper presents an application of modal analysis, focused on the estimation of the impedance function of a mechanical system. In particular, the analyses aim to evaluate the forces transmission of a railway braking resistor to be mounted on the floor of a train carbody. The breaking resistor contains two cooling fans which force the air flow through the electrical resistances that dissipate the breaking energy by Joule effect: the high speed rotation of these fans represents a remarkable source of excitation which affects the system and passengers' comfort. Previous tests showed that the structure were not adequate to filter the vibrations, thus the transmitted forces to the train carbody were not negligible. A proper reduction of the fans mechanical imbalance, achieved by new technology, leads to extremely good results which are now reported in this paper.

**Keywords** Modal analysis • Structure borne noise • Braking resistor • Mechanical impedance • Mechanical imbalance

## 35.1  Introduction

Electric braking is frequently used in high speed trains to support or substitute traditional friction brakes. During electric braking, when the speed of an inverter-controlled AC motor is reduced, the motor acts as a generator and feeds back energy to the frequency converter. As a result, voltage in the intermediate circuit of the inverter increases. When a specific threshold is exceeded, the energy must flow to an external braking system in order to avoid drive failures. Braking resistors are designed to absorb such energy and to dissipate it into heating. The use of brake resistors allows drives to fulfil the requirements of particularly severe duty cycles, for example those featured by frequent braking, long lasting braking or impulsive braking.

Due to the conversion of electrical energy into heat, braking resistors are usually ventilated. The coupling of the rotating speed of the cooling fan with some of the eigenfrequencies of the braking resistor may generate vibrations and noise. Of course, these issues can be worsened if a mechanical imbalance of the fan is present [1, 2].

The influence of fan balancing on the vibrations transmitted by a braking resistor is discussed in this paper. In [1], the results of experimental tests carried out on a braking resistor prototype were shown. During the tests, emerged that the prototype was not able to reach the required comfort standard, i.e. it was not able to adequately damp the vibrations produced by the rotation of the fun. A new prototype was thus designed. Specifically, to address vibration issues, a new technology was used to reduce fan mechanical imbalance.

Experimental tests were carried fixing the braking resistors to a supporting structure previously developed by the authors [1]. The structure was built to allow braking resistors certification. At a design stage, in fact, the train the braking resistor has to be mounted on is not available. Thus a supporting structure having the same mechanical mobility/impedance of the final installation is needed for certification.

F. Braghin (✉) • M. Portentoso • E. Sabbioni
Department of Mechanical Engineering, Politecnico di Milano, Via La Masa 1, 20156 Milano (MI), Italy
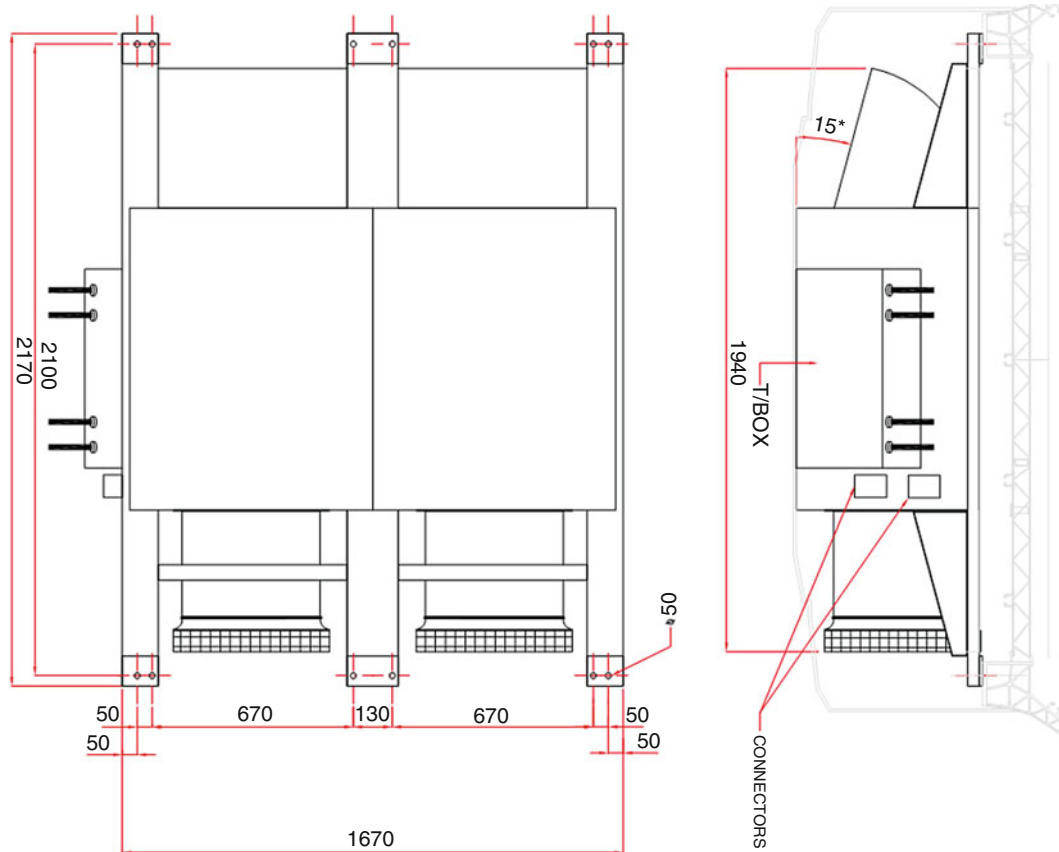e-mail: francesco.braghin@polimi.it

**Fig. 35.1** Tested braking resistor

## 35.2 Tested Braking Resistors

The tested braking resistor prototype is constituted of:

- resistor banks/elements (active part);
- cooling fan;
- resistor enclosure.

As it can be seen in Fig. 35.1, all these parts are fixed to a frame made of two beams of stainless steel linked by two crossbars. The resistor enclosure is 2 mm thick in stainless steel and presents two openings on the lateral sides for intaking and the exhausting cooling air. In particular the intake conduct presents a protruding structure making the breaking resistor asymmetric. Rivets joint all the components.

The prototype is exactly alike the braking resistor tested in [1], except for the cooling fan. Since the braking resistor tested in [1] was not able to reach the required comfort standard (i.e. it was not able to adequately damp the vibrations produced by the rotation of the fun), a new technology was adopted to reduce the mechanical unbalance of the fans (i.e. rotor mass reduction by 37%, rotor and blades are a single element instead of blades bolded to the rotor, aluminium die casting instead of standard carpentery). In the following, results concerned with the new braking resistor prototype will be shown and compared with the ones presented in [1].

## 35.3 Modal Analysis of the Braking Resistor

Experimental modal analysis was applied to identify the modes of vibration of the structure of the braking resistor prototype [1].

Experimental tests were performed exciting the structure of the braking resistor along the vertical axis using a dynamometric hammer PCB 086D50. The dynamic response was measured with several mono-axial piezo-accelerometers [1].

**Table 35.1** Modal parameters of the identified modes

| Mode | $f$ (Hz) | $h$ |
|------|----------|-------|
| 1 | 14.66 | 0.057 |
| 2 | 21.42 | 0.041 |
| 3 | 23.27 | 0.027 |
| 4 | 27.83 | 0.048 |
| 5 | 31.11 | 0.010 |
| 6 | 31.42 | 0.053 |
| 7 | 32.61 | 0.005 |
| 8 | 33.31 | 0.006 |
| 9 | 34.76 | 0.012 |
| 10 | 36.22 | 0.015 |
| 11 | 49.28 | 0.084 |
| 12 | 57.18 | 0.014 |
| 13 | 61.18 | 0.083 |

To identify the frequency response of the braking resistor structure, measures were processed according to the following procedure [3]:

- computation of the spectra applying the FFT algorithm,
- calculation of auto-spectra and cross-spectra averaging 20 tests,
- estimation of the coherence functions and the frequency response functions with the $H_3$ estimator.

Then modal parameters of the braking resistor structure were identified. On the purpose, the frequency response of the braking resistor structure was modeled according to [4]:

$$H_{num}(\Omega) = \sum_{j=1}^{N} \frac{-\Omega^2 A_j}{-\Omega^2 + i 2 h_j \omega_j \Omega + \omega_j^2} \tag{35.1}$$

where $N$ is the number of considered modes, $A_j$ is the complex modal parameter, $h_j$ is the viscous damping factor, $\omega_j$ is the natural frequency and $i$ is the imaginary unit.

The identification process was performed minimizing an objective function $J$ that is composed by the sum of square errors between the numerical and experimental frequency response functions in the frequency range between 10 and 65 Hz. In order to take into account that the measures reliability is not constant, the square errors are weighted with the experimental coherence, $C$.

Therefore the expression of the objective function $J$ is

$$J = \sum_{f_j \in [10;65] Hz} C(f_j) |H(f_j) - H_{num}(f_j)|^2 \tag{35.2}$$

where $\Omega_j = 2\pi f_j$, while $H$ and $H_{num}$ are the experimental and the estimated frequency response functions, respectively.

The Gauss–Newton algorithm [5] has been adopted for the nonlinear minimization.

The modal parameters of the first 13 identified modes are summarized in Table 35.1. Since the rated rotational frequency of the resistor fan is 49.2 Hz, it excites the 11th mode of the structure near its resonance.

## 35.4   Experimental Tests and Set-Up

To evaluate forces and vibrations transmitted by the braking resistor, a supporting structure was designed having the same mechanical impendence of the final installation of the prototype.

To verify the impedance of the supporting structure, impulsive tests were carried out. Figure 35.2 shows the test rig for impedance assessment. In Fig. 35.2 the six mounting points of the braking resistor are evidenced through red circles as well as the reference axis for the impulsive excitation. At each of the six mounting points, three single axis PCB Model 333B30 piezo-accelerometers having sensitivity equal to 100 mV/g have been placed (Fig. 35.3), oriented according to the reference axis shown above.

**Fig. 35.2** Test rig for the braking resistor
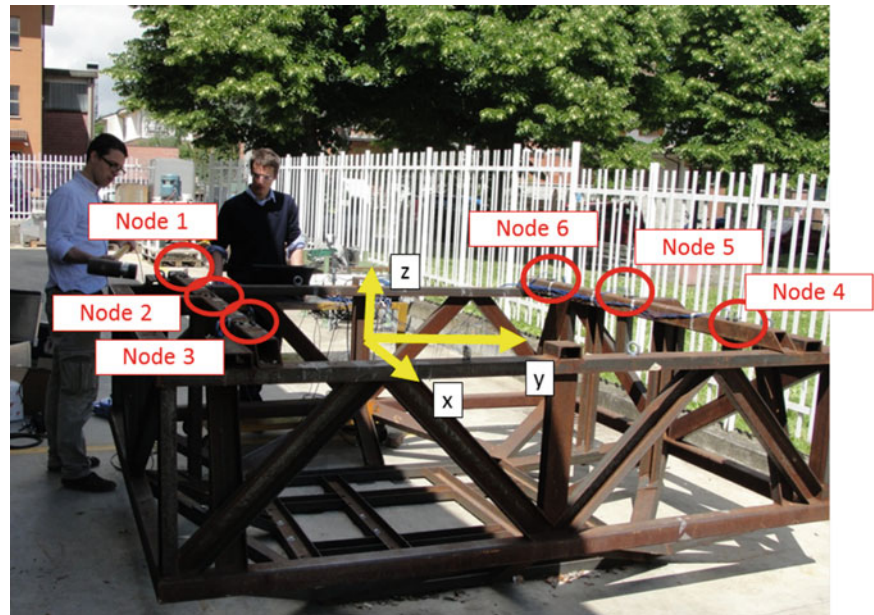


**Fig. 35.3** Three single axis piezo-accelerometer (at mounting point 5, see Fig. 35.2)
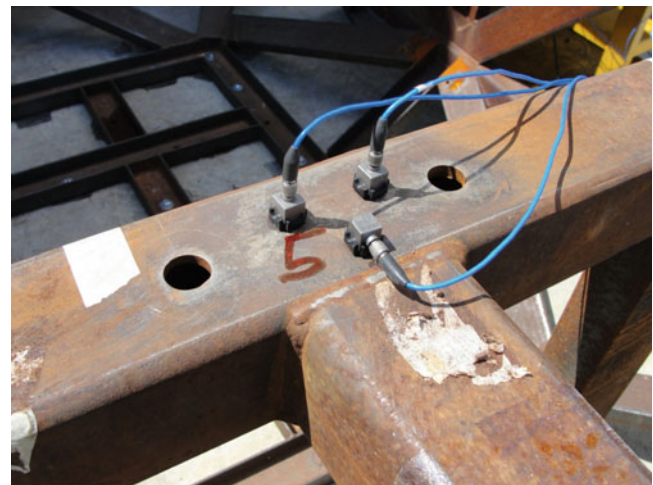


The mechanical impedance of the test frame (Fig. 35.2) was assessed through impulsive tests carried out using a 5.5 kg PCB Model 086D50 dynamometric hammer with hard plastic tip (084A32) and a 0.32 kg PCB Model 086D05 dynamometric hammer with medium plastic tip (084B0) both having a sensitivity of 0.23 mV/N.

The impact has been applied as close as possible to the mounting point (where the accelerometers were placed).

Impacts were repeated at least 10 times to be able to filter out random noise and acquired through NI CompactDAQ chassis equipped with one NI9205 module and PCB Model 482C Series signal conditioners. The sampling frequency was set equal to 10 kHz.

## 35.5   Mechanical Impedance of the Supporting Structure

As anticipated, mechanical impedance of the supporting structure the braking resistor is fixed on was identified through impact tests. The acquired signals were triggered using the force as a trigger signal, a pre-trigger of 0.5 s and a window length of 4 s, in order to avoid leakage. Then the direct mechanical impedance of the test rig at each mounting point and along each direction in one-third octave bands was evaluated according to [6]:
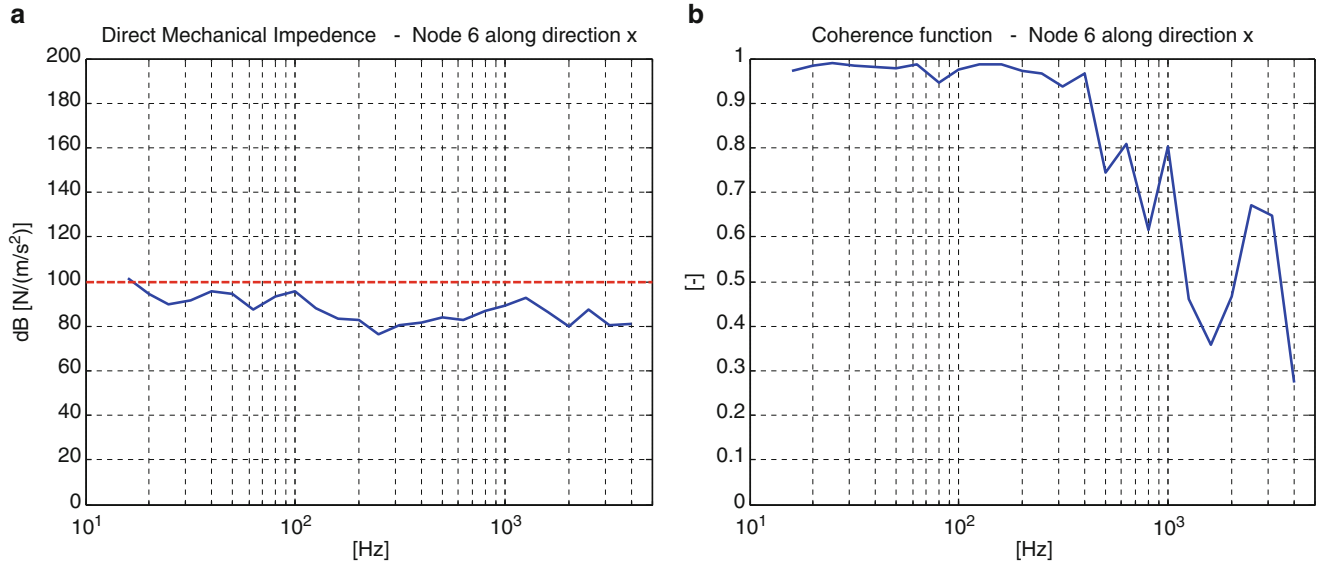
**Fig. 35.4** Mechanical impedance of the fixture at node 6 along direction $x$ (**a**) and corresponding coherence function (**b**). The limit valuie of 100dB is imposed by the train manufacturer

$$Z_{jk}^{R}(\omega) = \frac{1}{n_p}\sum_{p=1}^{n_p}\frac{S_{v_{jk}-f_{jk},p}(\omega)}{S_{v_{jk}-v_{jk},p}(\omega)} = \frac{1}{n_p}\sum_{p=1}^{n_p}i\omega\frac{S_{a_{jk}-f_{jk},p}(\omega)}{S_{a_{jk}-a_{jk},p}(\omega)} \tag{35.3}$$

being $j$ the point of application of the force, $k$ the direction of excitation and of measurement, $f_{j\_k}$ the impulsive force applied at point j along direction $k$, $v_{j\_k}$ the velocity at point $j$ along direction $k$, $a_{j\_k}$ the measured acceleration at point $j$ along direction $k$, $n_p$ the number of impacts, the cross-spectral density function between $v_{j\_k}$ and $f_{j\_k}$ for impact $p$, $S_{v_{jk}-v_{jk},p}$ the autospectral density function of $v_{j\_k}$ for history $p$, $S_{a_{jk}-f_{jk},p}$ the cross-spectral density function between $a_{j\_k}$ and $f_{j\_k}$ for impact p and $S_{a_{jk}-a_{jk},p}$ the autospectral density function of $a_{j\_k}$ for impact $p$. Note that the evaluated mechanical impedance $S_{v_{jk}-f_{jk},p}(\omega)/S_{v_{jk}-v_{jk},p}(\omega)$, is used in case of uncorrelated input and output noise as in the considered case.

As an example of obtained results, Fig. 35.4 shows the mechanical impedance of the fixture at node 6 along direction x as well as the corresponding coherence function. It can be seen that the coherence function tends to drop at frequencies higher than 500 Hz due to the adopted hammer tip.

## 35.6  Assessment of the Constraint Forces at the Mounting Points of the Braking Resistor

The constraint forces at the mounting points of the braking resistor were assessed through experimental tests carried mounting the braking resistor inside the previously described supporting structure. The same measurement set-up used to assess the mechanical impedance of the supporting structure was adopted (see Figs. 35.2, 35.5 and 35.6). Figure 35.5 shows the braking resistor inside the test frame and highlights the mounting points with a red circle.

In must be underlined that the attachments of the braking resistor with the supporting structure are exactly alike the ones with the train (Fig. 35.6).

Two working conditions were analysed during the tests:

- half rated speed (1,455 rpm);
- rated speed (2,910 rpm).

Each test lasted 300 s and the collected time histories have been divided into sub-histories of 10 s in order to achieve statistical significance through an averaging operation on the results. Sampling frequency was set to 13 kHz.

The average spectrum of the speed at the mounting points was calculated according to:

**Fig. 35.5** Mounting points (*red circles*) and local reference system of the braking resistor
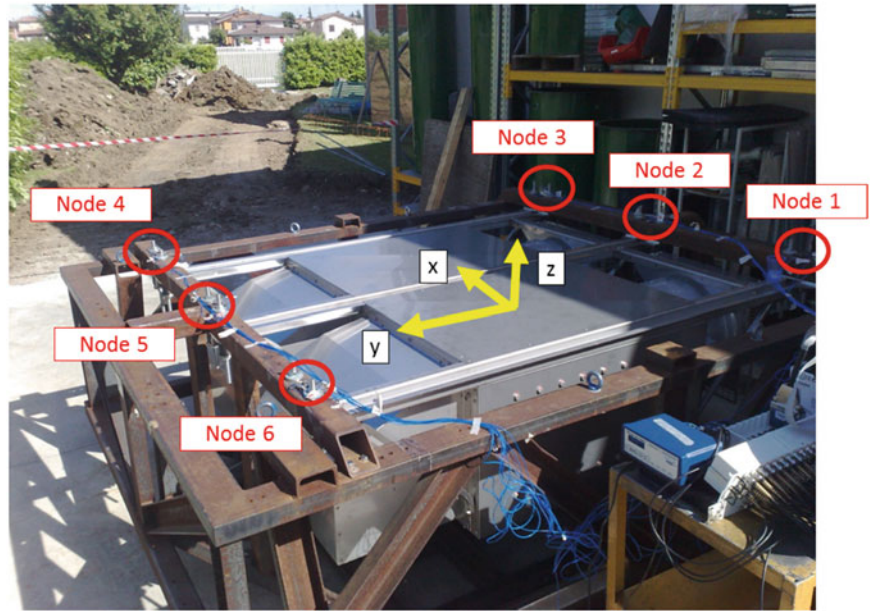


**Fig. 35.6** Detail of the mounting point 4 showing the rigid fixing and the three single axis piezo accelerometers
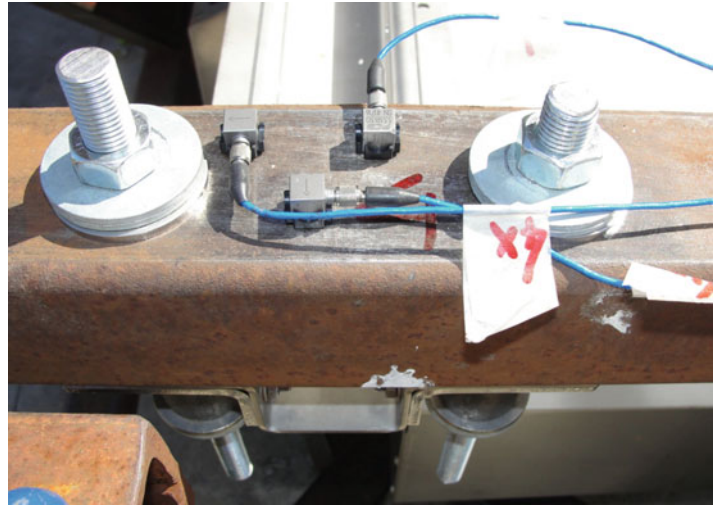


$$S_{v_{jk}}(\omega) = \frac{1}{i\omega}\sqrt{\frac{1}{n_p}\sum_{p=1}^{n_p} S_{a_{jk}-a_{jk,p}}(\omega)} \qquad (35.4)$$

being $j$ the point of application of the force, $k$ the direction of excitation and of measurement, $v_{j\_k}$ the velocity at point $j$ along direction $k$, $a_{j\_k}$ the measured acceleration at point $j$ along direction $k$, $n_p$ the number of impacts, the cross-spectral density function between $v_{j\_k}$ and $f_{j\_k}$ for impact $p$, $S_{a_{jk}-a_{jk,p}}$ the autospectral density function of $a_{j\_k}$ for history $p$, $S_{v_{jk}-f_{jk,p}}$ the spectrum of $v_{j\_k}$.
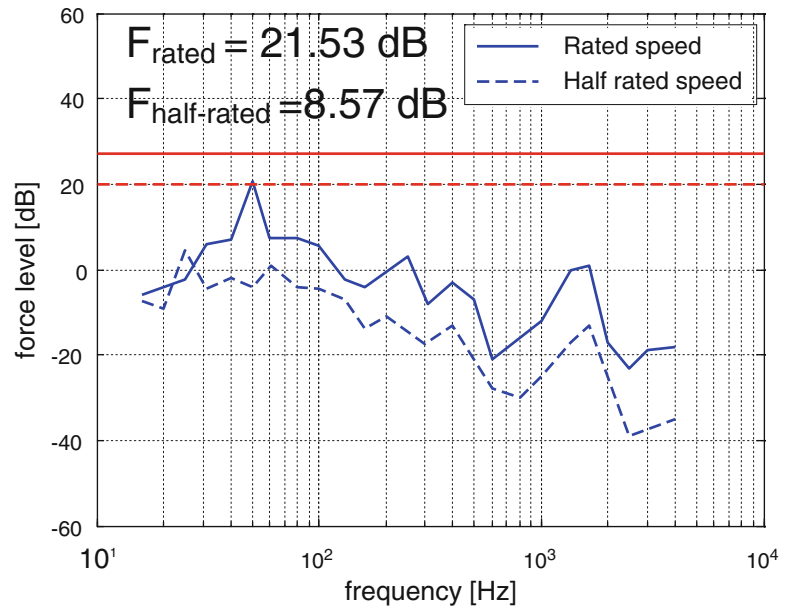
The resulting spectrum of the constraint force was obtained as the product of the experimental mechanical impedance times the average spectrum of speed:

$$S_{f_{jk}}(\omega) = Z_{jk}^R(\omega) S_{v_{jk}}(\omega) \qquad (35.5)$$

where $S_{f_{jk}}$ is spectrum of the force at the mounting point $j$ indirection $k$, while $Z_{jk}^R$ is the experimental mechanical impedance of the mounting point $j$ in direction $k$ (assessed from previous tests).

Finally the one third octave band levels and the wideband force level was evaluated according to the "time-averaged sound pressure level" (standard ISO 3744, [7]).

**Fig. 35.7** Force level along $z$ direction at rated and half rated speed working conditions for node 1. New prototype



**Fig. 35.8** Force level along $z$ direction at rated and half rated speed working conditions for node 1. Braking resistor tested in [1]
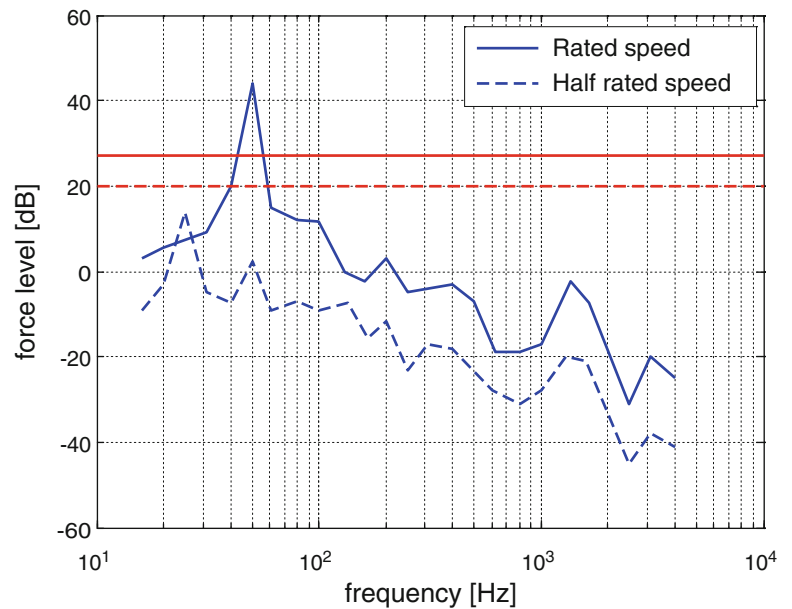


Figure 35.7 shows the spectrum of the constraint forces in one third octave bands for rated speed and half-rated working conditions at node 1 along z direction for the braking resistor prototype test. On the left bottom corner of the figure the wideband force level for the two tested conditions is reported.

As it can be seen, a dynamic amplification at approximately 50 Hz is present, due to the coupling between the rotational speed of the fan and the 11th mode of vibration of the braking resistor. The reduction of mechanical imbalances of the fan however allowed to significantly reduce the amplitude of the resonance peak with respect to the prototype tested in [1], whose spectrum is reported for the same working conditions in Fig. 35.8. Specifically the fan of the new prototype allows a reduction of about 20 dB of the constraint forces in correspondence of the resonance peaks. This allows to fulfil comfort requirements.

## 35.7 Concluding Remarks

In the present paper, an experimental approach for assessing structure borne noise generated by a braking resistor was presented. The supporting structure was tested to verify that its mechanical impedance is equivalent to that of the final installation of the braking resistor. The supporting structure was then used to test a prototype of a braking resistor. A first series of tests carried out considering half rated and fully rated working speed showed that a mechanical imbalance of the cooling fan could produce significant vibrations, which could jeopardize comfort. The braking resistor was then modified. Specifically a new production process was applied to reduce the mechanical imbalances of the cooling fan. Experimental tests on the new prototype showed a significant reduction of vibrations, which can guarantee satisfactory comfort levels.

## References

1. Braghin F, Cheli F, Galli G (2013) Experimental assessment of structure borne noise generated by a braking resistor. In: Conference proceedings of the society for experimental mechanics series, vol 39(4), pp 495–501
2. Braghin F, Galli G, Sabbioni E (2009) Modal analysis of a railway braking resistor. In: Conference proceedings of the society for experimental mechanics series
3. Bendat JS, Piersol AG (1993) Engineering applications of correlation and spectral analysis. Wiley, London
4. Ewins JD (2001) Modal testing: theory and practice. Wiley, London
5. Björck A (1996) Numerical methods for least squares problems. SIAM, Philadelphia
6. IEC 60068-3-3 (1991) Environmental testing—part 3: guidance—seismic test methods for equipment
7. ISO 3744 (2010) Acoustics-determination of sound power levels and sound energy levels of noise sources using sound pressure—engineering methods for an essentially free field over a reflecting plane

# Chapter 36
# Vibrations of Discretely Layered Structures Using a Continuous Variation Model

**Arnaldo J. Mazzei and Richard A. Scott**

**Abstract** Recently, there has been a large body of work directed towards the use of non-homogeneous materials in controlling waves and vibrations in elastic media. Two broad categories have been studied, namely, media with continuous variation of properties and those with discrete layers (cells). Structures with both a finite and infinite number of cells (periodic layout) have been examined. For the former, direct numerical simulation or transfer matrix methods have been used. The current work focuses on one-dimensional cases, in particular a two-layer cell. Transfer matrix methods require writing solutions for each layer of the basic cell and then matching them across the interface, a process that can be quite lengthy. Here an alternate strategy is explored in which the discrete cell properties are modeled by continuously varying functions (here logistic functions), which has the advantage of working with a single differential equation. Natural frequencies have been obtained using a forced motion method and are in excellent agreement with those found using a transfer matrix approach. Mode shapes for the continuous variation model have been obtained using a finite difference scheme and compare well with those obtained via the transfer matrix approach.

**Keywords** Waves in non-homogeneous media • Layered structures vibrations

## Nomenclature

| | |
|---|---|
| $B_i$ | Constants of integration |
| $c_i$ | Wave speed, $c_i = \sqrt{E/\rho_i}$ |
| $c_r$ | Numerical parameter, $c_r = c_1/c_2$ |
| $E$ | Young's modulus ($E_i$, Young's modulus for i-th material) |
| $f_1, f_2$ | Non-dimensional material functions |
| $H(x)$ | Logistic function |
| $Heaviside(x)$ | Step function |
| $L$ | Length of rod, $L = L_1 + L_2$ |
| $m_r$ | Numerical parameter, $m_r = \rho_1/\rho_2$ |
| $S_i$ | Shape function (i-th) |
| $t$ | Time |
| $u$ | Longitudinal displacement of the rod |
| $w$ | Non-dimensional longitudinal displacement of the rod |
| $x$ | Longitudinal coordinate |
| $x_d$ | Non-dimensional longitudinal coordinate |

A.J. Mazzei (✉)
Department of Mechanical Engineering, C. S. Mott Engineering and Science Center, Kettering University,
1700 University Avenue, Flint, MI 48504, USA
e-mail: amazzei@kettering.edu

R.A. Scott
Department of Mechanical Engineering, G044 W. E. Lay Automotive Laboratory, University of Michigan,
1231 Beal Avenue, Ann Arbor, MI 48109, USA

| $\alpha$ | Numerical parameter for length of individual cell components of the layered rod |
| --- | --- |
| $\rho$ | Mass density ($\rho_i$, density value for i-th material) |
| $\tau$ | Non-dimensional time |
| $\omega$ | Natural frequency of longitudinal vibrations for the rod |
| $\omega_d$ | Non dimensional natural frequency of longitudinal vibrations for the rod |

## 36.1 Introduction

There has been an explosion of interest in the past few years in the use and analysis, both theoretical and numerical, of layered solids for vibration and wave control. Media with continuous variation of properties, such as Functionally Graded Materials (FGM), and those with discrete layering (specific example of which is infinite periodic array of cells, in the study of block waves). For studies on discrete layers see references [1–4]. Numerical approaches to waves in non-homogeneous media can be found in reference [5]. The current work treats a one-dimensional uniaxial problem involving two layers bonded together with the preliminary goal of determining the natural frequencies and mode shapes. They can be found using a transfer matrix method which requires determining the solutions for each layer and matching them across the interface, a procedure that can be quite lengthy and cumbersome. A main thrust of the current work is an exploration of using an alternate method in which the two-layered cell is modeled by continuously varying functions (here use is made of logistic functions), which has the considerable advantage of working with a single differential equation. This differential equation does not possess analytic solution and is not readily amenable to direct numerical analysis using MAPLE® software (the software of choice here). The natural frequencies are obtained using a forced-motion strategy, detailed below, and are found to be in excellent agreement with those obtained using the transfer matrix method approach for both fixed-fixed and free-fixed boundary conditions. Mode shapes in the single differential equation are obtained by a finite difference scheme and are found to be in good agreement with those from the transfer matrix method.

## 36.2 Basic Problem

Shown in Fig. 36.1 is a two-layer elastic rod with properties as indicated. Consider this layered structure in which **E** and **ρ** vary in a discontinuous fashion.

In the following some methods for obtaining the natural frequencies and mode shapes of the rod are explored.

## 36.3 Transfer Matrix Approach

For a thorough discussion of the transfer matrix approach see references [6, 7]. In general the axial displacement $u(x,t)$ of a segment must satisfy the equation:

$$\frac{\partial}{\partial x}\left(E(x)\frac{\partial u(x,t)}{\partial x}\right) - \rho(x)\frac{\partial^2 u(x,t)}{\partial t^2} = 0 \tag{36.1}$$

where $E(x)$ and $\rho(x)$ are functions describing the longitudinal variations of Young's modulus and mass density, respectively.

For constant properties, the equation of motion for the "i-th" segment is:

$$\left(\frac{\partial^2 u_i(x,t)}{\partial x^2}\right) = \frac{1}{c_i^2}\left(\frac{\partial^2 u_i(x,t)}{\partial t^2}\right), \quad i = 1, 2 \ldots \tag{36.2}$$
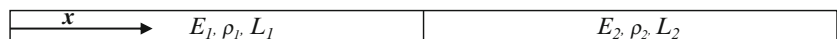
where $c_i = \sqrt{\frac{E_i}{\rho_i}}$.

**Fig. 36.1** Layered material

| $x \longrightarrow$ $E_1, \rho_1, L_1$ | $E_2, \rho_2, L_2$ |
| --- | --- |

### 36.3.1  Frequencies

Assuming a vibration form $u_i = S_i(x)\sin(\omega t)$ leads to:

$$\frac{\partial^2 S_i}{\partial x^2} + \frac{\omega^2}{c_i^2}S_i = 0, i = 1, 2\dots \tag{36.3}$$

The solutions of which are

$$S_1 = B_1 \cos\left(\frac{\omega}{c_1}x\right) + B_2 \sin\left(\frac{\omega}{c_1}x\right)$$

$$S_2 = B_3 \cos\left(\frac{\omega}{c_2}x\right) + B_4 \sin\left(\frac{\omega}{c_2}x\right) \tag{36.4}$$

Two sets of boundary conditions are investigated, namely, fixed-fixed and free-fixed. Fixed-fixed conditions and interface continuity gives:

$$S_1 = 0, x = 0; \, S_2 = 0, x = L \, (L = L_1 + L_2); \quad S_1 = S_2, x = L_1; \tag{36.5}$$

Whereas, force continuity leads to:

$$E_1 \frac{\partial S_1}{\partial x} = E_2 \frac{\partial S_2}{\partial x}, x = L_1 \tag{36.6}$$

These four conditions lead to a system of algebraic equations in $B_1$, $B_2$, $B_3$ and $B_4$:

$$B_1 = 0$$

$$B_3 \cos\left(\frac{\omega}{c_2}L\right) + B_4 \sin\left(\frac{\omega}{c_2}L\right) = 0$$

$$B_2 \sin\left(\frac{\omega}{c_1}L_1\right) = B_3 \cos\left(\frac{\omega}{c_2}L_1\right) + B_4 \sin\left(\frac{\omega}{c_2}L_1\right)$$

$$\frac{E_1 c_2}{E_2 c_1} B_2 \cos\left(\frac{\omega}{c_1}L_1\right) = -B_3 \sin\left(\frac{\omega}{c_2}L_1\right) + B_4 \cos\left(\frac{\omega}{c_2}L_1\right) \tag{36.7}$$

The natural frequencies are found on setting the determinant of the coefficients to zero. After some lengthy manipulations, one finds:

$$\det \begin{bmatrix} 0 & \cos\left(c_r \omega_d\right) & \sin\left(c_r \omega_d\right) \\ \sin\left(\frac{\omega_d}{1+\alpha}\right) & -\cos\left(c_r \frac{\omega_d}{1+\alpha}\right) & -\sin\left(c_r \frac{\omega_d}{1+\alpha}\right) \\ m_r c_r \cos\left(\frac{\omega_d}{1+\alpha}\right) & \sin\left(c_r \frac{\omega_d}{1+\alpha}\right) & -\cos\left(c_r \frac{\omega_d}{1+\alpha}\right) \end{bmatrix} = 0 \tag{36.8}$$

where $L_2 = \alpha L_1$, $\omega_d = \frac{\omega}{c_1}L$, $c_r = \frac{c_1}{c_2}$ and $m_r = \frac{\rho_1}{\rho_2}$, with $L = (1 + \alpha)L_1$ and $\frac{E_1 c_2}{E_2 c_1} = m_r c_r$.

For free-fixed boundary conditions and interface continuity:

$$\left.\frac{dS_1}{dx}\right|_{x=0} = 0; \, S_2 = 0, x = L \, (L = L_1 + L_2); \quad S_1 = S_2, x = L_1; \tag{36.9}$$

Note that force continuity, Eq. 36.6, still applies. Then the corresponding system of algebraic equations is:

$$B_2 = 0$$

$$B_3 \cos\left(\frac{\omega}{c_2}L\right) + B_4 \sin\left(\frac{\omega}{c_2}L\right) = 0$$

$$B_1 cos\left(\frac{\omega}{c_1}L_1\right) = B_3 \cos\left(\frac{\omega}{c_2}L_1\right) + B_4 \sin\left(\frac{\omega}{c_2}L_1\right)$$

$$\frac{E_1 c_2}{E_2 c_1} B_1 \sin\left(\frac{\omega}{c_1}L_1\right) = B_3 \sin\left(\frac{\omega}{c_2}L_1\right) - B_4 \cos\left(\frac{\omega}{c_2}L_1\right) \tag{36.10}$$

For this case the natural frequencies can be found from:

$$\det \begin{bmatrix} 0 & \cos(c_r\omega_d) & \sin(c_r\omega_d) \\ \cos\left(\frac{\omega_d}{1+\alpha}\right) & -\cos\left(c_r\frac{\omega_d}{1+\alpha}\right) & -\sin\left(c_r\frac{\omega_d}{1+\alpha}\right) \\ m_r c_r \sin\left(\frac{\omega_d}{1+\alpha}\right) & -\sin\left(c_r\frac{\omega_d}{1+\alpha}\right) & \cos\left(c_r\frac{\omega_d}{1+\alpha}\right) \end{bmatrix} = 0 \tag{36.11}$$

### 36.3.2 Mode Shapes

Note that in the fixed-fixed case on setting the determinant to zero (Eq. 36.8) only two of Eq. 36.7 are independent. Also, the amplitude scale is arbitrary. Then setting $B_2 = 1$, leads to:

$$B_3 \cos(c_r\omega_d) + B_4 \sin(c_r\omega_d) = 0$$

$$\sin\left(\frac{\omega_d}{1+\alpha}\right) = B_3 \cos\left(c_r\frac{\omega_d}{1+\alpha}\right) + B_4 \sin\left(c_r\frac{\omega_d}{1+\alpha}\right) \tag{36.12}$$

which, with $r_d = c_r\omega_d$, gives:

$$B_4 = -B_3\frac{\cos(r_d)}{\sin(r_d)} \tag{36.13}$$

and

$$B_3 = \frac{\sin\left(\frac{\omega_d}{1+\alpha}\right)}{\left[\cos\left(c_r\frac{\omega_d}{1+\alpha}\right) - \frac{\cos(r_d)}{\sin(r_d)}\sin\left(c_r\frac{\omega_d}{1+\alpha}\right)\right]} \tag{36.14}$$

Then, the mode shapes for the fixed-fixed case are:

$$S_1 = \sin(\omega_d x_d), 0 \le x_d \le 0.5$$

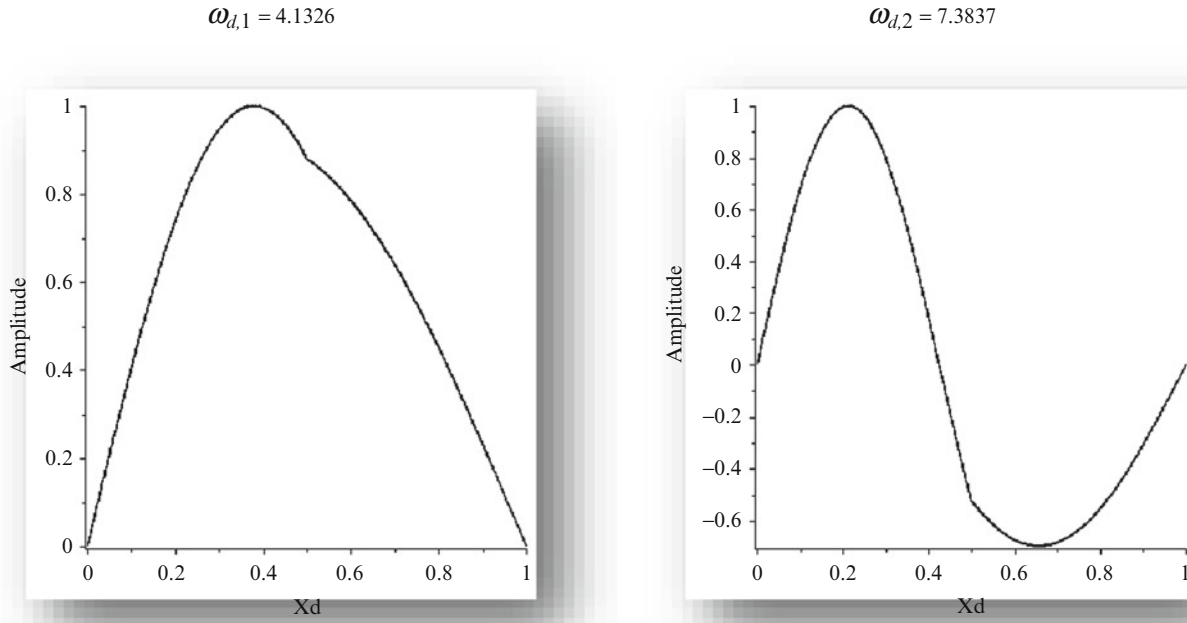$$S_2 = B_3 \cos(c_r\omega_d x_d) + B_4 \sin(c_r\omega_d x_d), 0.5 \le x_d \le 1.0 \tag{36.15}$$

where $x_d = \frac{x}{L}$.

In a similar manner, for the free-fixed case, setting $B_1 = 1$, leads to:

$$B_4 = -B_3\frac{\cos(r_d)}{\sin(r_d)}$$

(same as Eq. 36.13) and

$$B_3 = \frac{\cos\left(\frac{\omega_d}{1+\alpha}\right)}{\left[\cos\left(c_r\frac{\omega_d}{1+\alpha}\right) - \frac{\cos(r_d)}{\sin(r_d)}\sin\left(c_r\frac{\omega_d}{1+\alpha}\right)\right]} \tag{36.16}$$

$$\omega_{d,1} = 4.1326 \qquad\qquad\qquad\qquad\qquad\qquad \omega_{d,2} = 7.3837$$



**Fig. 36.2** First and second mode shapes for layered rod (fixed-fixed)

Then, the mode shapes are:

$$S_1 = \cos\left(\omega_d x_d\right), 0 \le x_d \le 0.5$$

$$S_2 = B_3 \cos\left(c_r \omega_d x_d\right) + B_4 \sin\left(c_r \omega_d x_d\right), 0.5 \le x_d \le 1.0 \qquad (36.17)$$

### 36.3.3 Numerical Example

Consider the rod shown in Fig. 36.1 and assume the following materials: Aluminum ($E_1 = 71$ GPa, $\rho_1 = 2{,}710$ kg/m$^3$) and Silicon Carbide ($E_2 = 210$ GPa, $\rho_2 = 3{,}100$ Kg/m$^3$).

For the fixed-fixed case, taking $\alpha = 1$, Eq. 36.8 leads to the following values for the first two non-dimensional natural frequencies: $\omega_{d,1} = 4.1326$ and $\omega_{d,2} = 7.3837$. The mode shapes corresponding to these frequencies can be found via equations (36.15). They are shown in Fig. 36.2.

For the free-fixed case (and $\alpha = 1$), Eq. 36.11 leads to the following values for the first two non-dimensional frequencies: $\omega_{d,1} = 2.2725$ and $\omega_{d,2} = 5.6338$. The mode shapes can be found via Eq. 36.17 and are shown in Fig. 36.3.

## 36.4  Continuous Variation Model

In Eq. 36.1 substituting the following non-dimensional variables: $x_d = x/L$, $w = u/L$ and $\tau = \omega t$, gives:

$$\frac{\partial}{\partial x_d}\left[ f_1\left(x_d\right)\frac{\partial w\left(x_d, \tau\right)}{\partial x_d}\right] - \frac{\rho_1 L^2}{E_1}\omega^2 f_2\left(x_d\right)\frac{\partial^2 w\left(x_d, \tau\right)}{\partial \tau^2} = 0 \qquad (36.18)$$

$$\omega_{d,1} = 2.2725 \qquad\qquad\qquad \omega_{d,2} = 5.6338$$
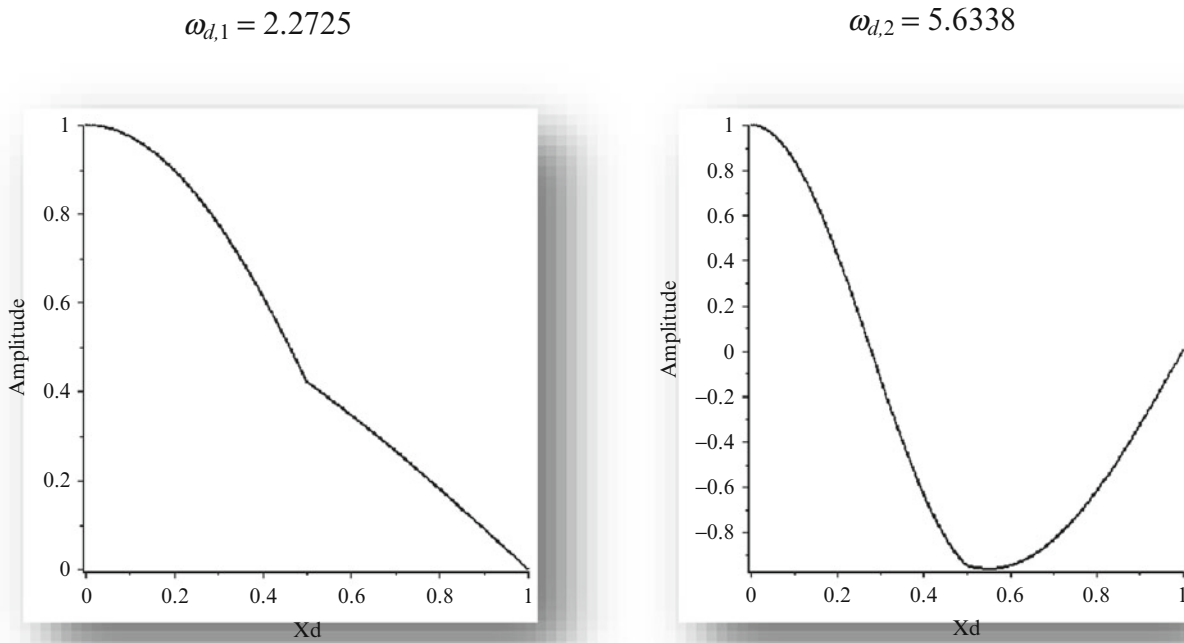


**Fig. 36.3** First and second mode shapes for layered rod (free-fixed)

Assuming $w(x_d, \tau) = S(x_d)\sin(\omega_d\tau)$ leads to:

$$\frac{d}{dx_d}\left[f_1(x_d)\frac{dS(x_d)}{dx_d}\right] + f_2(x_d)\omega_d{}^2 S(x_d) = 0 \tag{36.19}$$

where the non-dimensional functions $f_1(x_d)$ and $f_2(x_d)$ describe the material properties variation. They are given by: $E = E_1 f_1(x_d)$, $\rho = \rho_1 f_2(x_d)$. Also, $L = L_1 + L_2$ and $\omega = \omega_d \sqrt{E_1/(\rho_1 L^2)}$ where $\omega$ is the natural frequency of vibration (rad/s).

### 36.4.1 Finite Difference Approach

Next a finite difference method (FDM) is used for calculating the natural frequencies of the layered structure. As discussed above, the structure is assumed to be a single cell composed by one metallic phase and one ceramic phase (Aluminum and Silicon Carbide).

For the FDM, transitions from one material to another (step functions) are approximated via logistic functions:

$$H(x) \approx \frac{1}{2} + \frac{1}{2}\tanh(Kx) = \frac{1}{1 + e^{-2Kx}} \tag{36.20}$$

where a larger $K$ corresponds to a sharper transition at (in the above equation) $x = 0$.

Here the approach uses a second-order central difference scheme for the internal nodes. The boundary node values are calculated via the boundary conditions (either fixed-fixed or free-fixed). The partial differential equations are discretized in space leading to a system of ordinary differential equations in time.

Note that, in the FDM approach, a transition that is not very sharp from one material to another is desirable in order to produce a reasonable number of nodes in the "transition zone". This is shown in Fig. 36.4. The figure also shows Heaviside functions which represent sharp transitions. For this case they are given by ($x_d = 0.5$ locates the transition zone at the center of the cell):
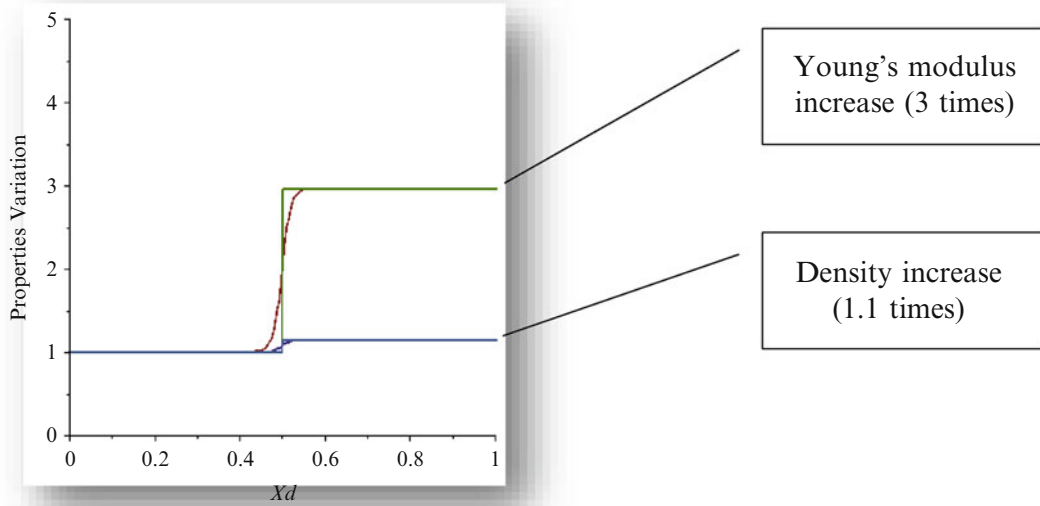
**Fig. 36.4** Properties transition for a single cell layered rod

$$f_1(x_d) = 1 + 1.9577\,Heaviside\,(x_d - 0.5)$$

$$f_2(x_d) = 1 + 0.1439\,Heaviside\,(x_d - 0.5) \tag{36.21}$$

The logistic function approximations are:

$$f_1(x_d) \approx 1.9789 + 0.9789 \tanh(50x_d - 25)$$

$$f_2(x_d) \approx 1.0720 + 0.0720 \tanh(50x_d - 25) \tag{36.22}$$

Subdividing the cell into ten elements, the FDM gives the results shown in Fig. 36.5, for the first two frequencies and mode shapes of the fixed-fixed case. Increasing the number of elements to 30 produces $\omega_{d,1} = 3.9845$, $\omega_{d,2} = 6.7176$ (accuracy is increased, as seen via a comparison with values given above).

With ten elements the results for the first two frequencies and mode shapes of the free-fixed case are shown in Fig. 36.6. In this case a first-order forward difference scheme was used for the leftmost point calculation. Increasing the number of elements to 30 produces $\omega_{d,1} = 1.8093$, $\omega_{d,2} = 5.4604$.

### 36.4.2  Forced Motion Approach

Note that, in general, the problem posed by Eq. 36.19 subjected to a specific set of boundary conditions does not have analytic solutions. In principle solutions can be obtained (numerically) by solving an eigenvalue problem. However a problem arises in that MAPLE®'s off-the-shelf solver (the software utilized here) only gives the trivial solution. The strategy employed next is similar to one described in reference [8] and consists of using MAPLE®'s two-point boundary value solver to solve a forced motion problem. In this case an axial non-dimensional forcing function $F^* = F\sin(\omega_d \tau)$ is introduced into Eq. 36.18, which leads to the following form for Eq. 36.19:
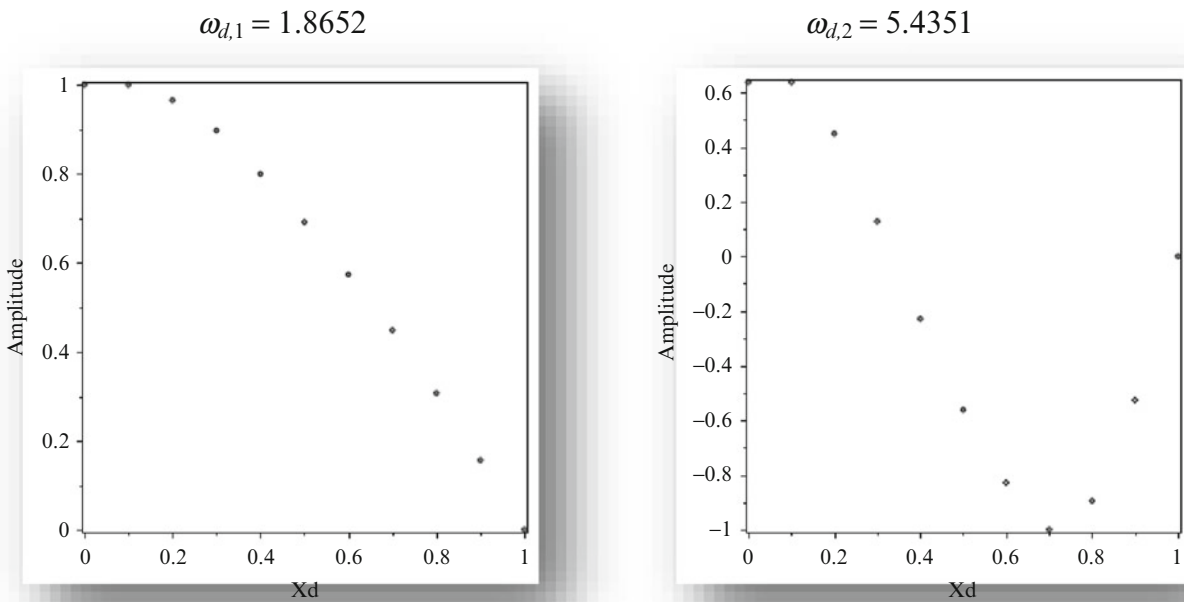
$$\frac{d}{dx_d}\left[f_1(x_d)\,\frac{dS(x_d)}{dx_d}\right] + f_2(x_d)\,\omega_d{}^2 S(x_d) = F \tag{36.23}$$

Then $F$ is taken to be equal to 1. By varying the frequency $\omega_d$ and observing the mid-span deflection of the rod, resonant frequencies can be found on noting where abrupt changes in the sign of the deflection occurs.

$$\omega_{d,1} = 3.8660 \qquad\qquad \omega_{d,2} = 6.4939$$
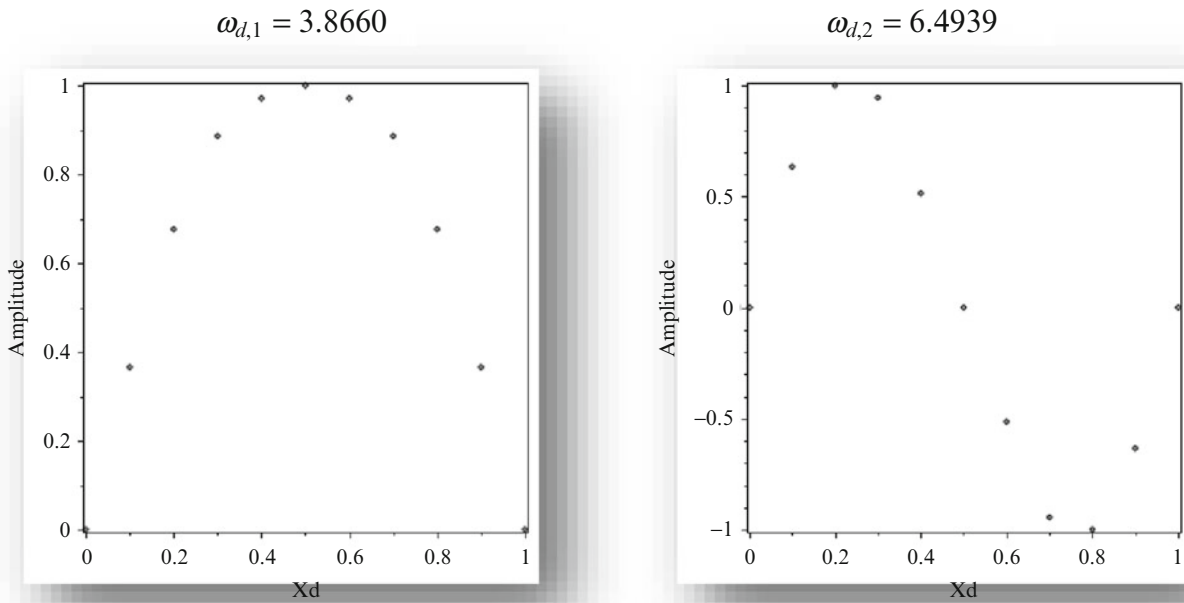


**Fig. 36.5** Frequencies and mode shapes via FDM approach (fixed-fixed, ten elements)

$$\omega_{d,1} = 1.8652 \qquad\qquad \omega_{d,2} = 5.4351$$



**Fig. 36.6** Frequencies and mode shapes via FDM approach (free-fixed, ten elements)

Using this approach the first and second frequencies, for the fixed-fixed case, are approximately $\omega_{d,1} = 4.14$ and $\omega_{d,2} = 7.44$, respectively. The changes in the sign of the deflections can be seen in Fig. 36.7 (first frequency) and Fig. 36.8 (second frequency). They show the deflections before and after going through a resonance.

The first and second frequencies for the free-fixed case are approximately $\omega_{d,1} = 2.29$ and $\omega_{d,2} = 5.65$. The changes in the sign of the deflections can be seen in Fig. 36.9 (first frequency) and Fig. 36.10 (second frequency).

Note that the mode shapes cannot be readily obtained using this method (here the previously discussed FDM is used for that).

$$\omega_{d,1} = 4.13$$

$$\omega_{d,1} = 4.14$$
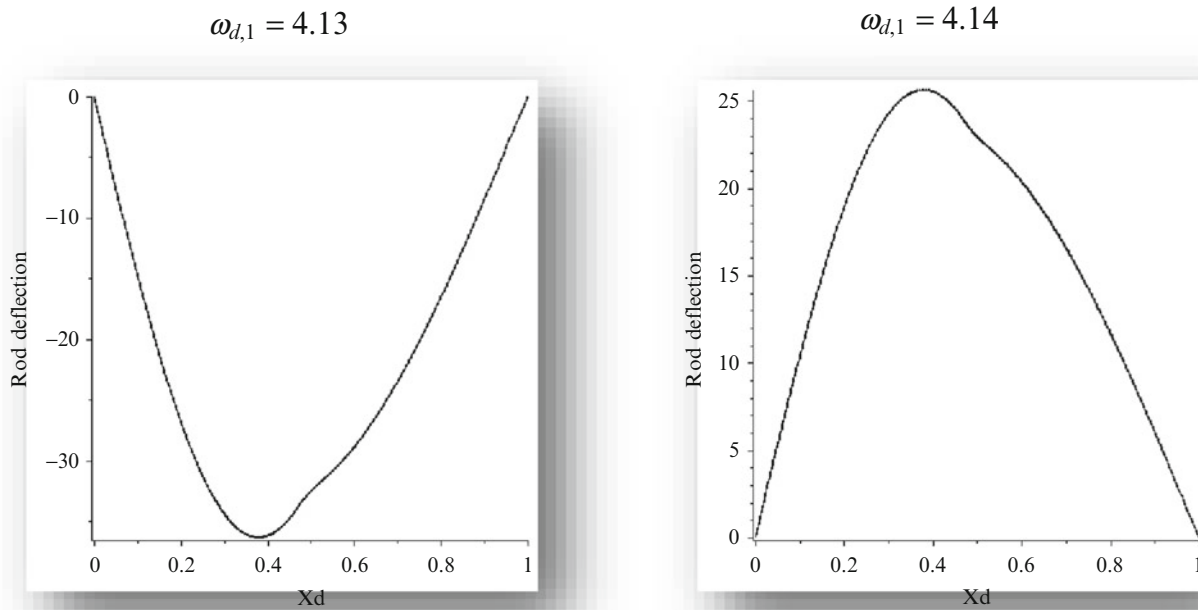
**Fig. 36.7** First frequency via forced-motion approach (fixed-fixed)

$$\omega_{d,2} = 7.43$$

$$\omega_{d,2} = 7.44$$
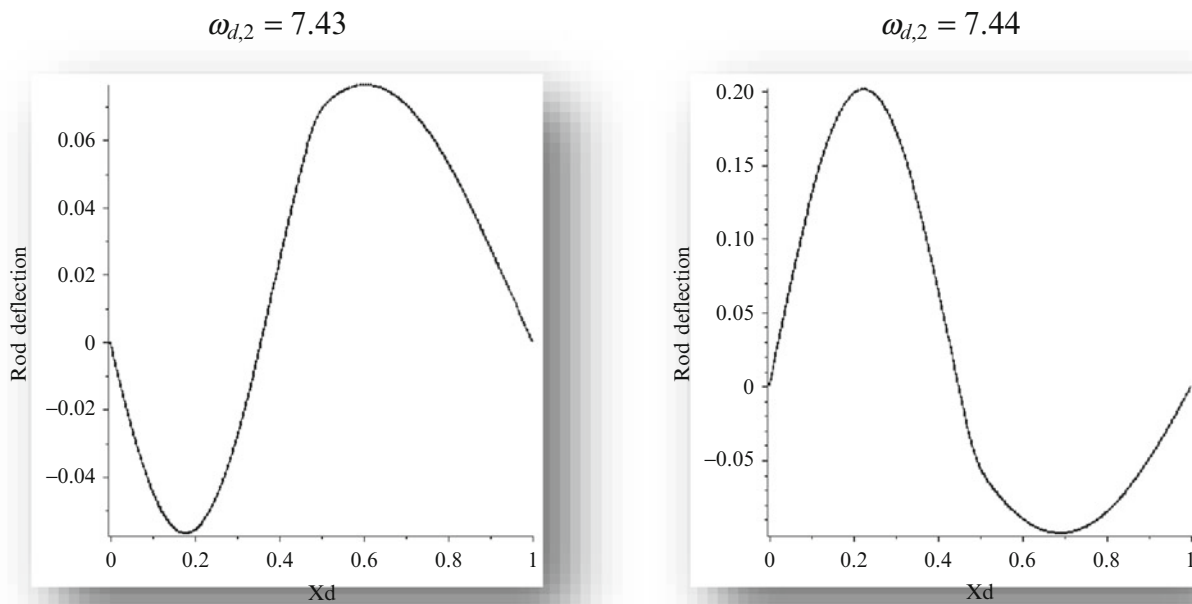
**Fig. 36.8** Second frequency via forced-motion approach (fixed-fixed)

## 36.5  Comparisons

In the following the results produced by the numerical approaches utilized above are compared to the values obtained using the transfer matrix method. These are summarized in Table 36.1.

Note that the forced-motion approach produces very accurate results when compared to the transfer matrix method. It can be utilized with confidence as an alternate method when the matrix approach becomes mathematically complex.
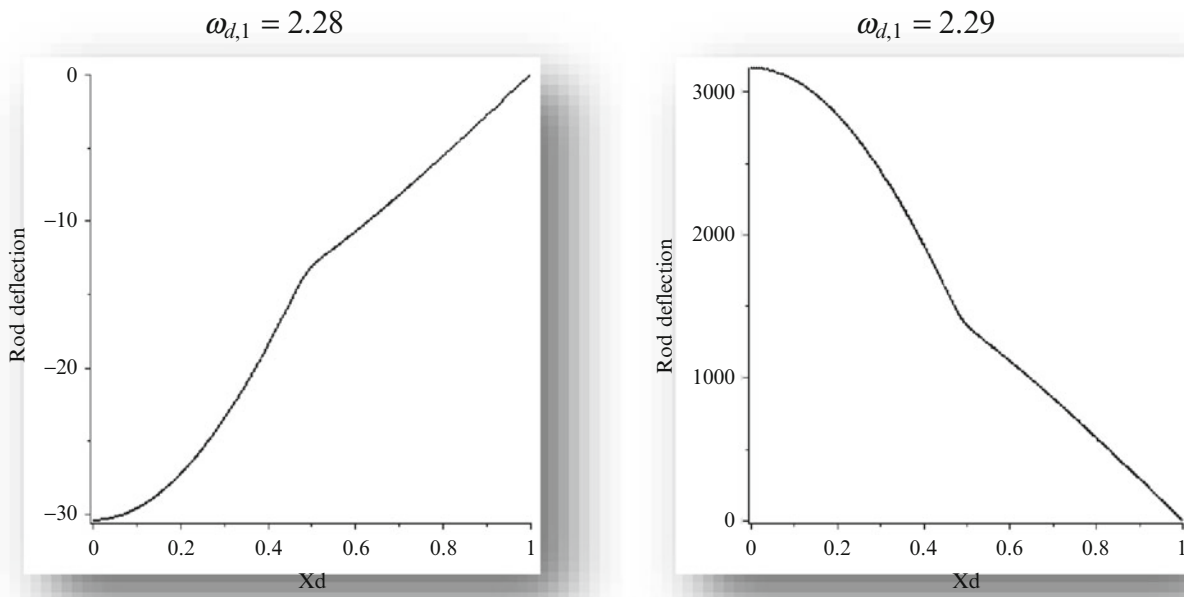
The FDM produces reasonable results.

$$\omega_{d,1} = 2.28 \qquad \qquad \omega_{d,1} = 2.29$$



**Fig. 36.9** First frequency via forced-motion approach (free-fixed)

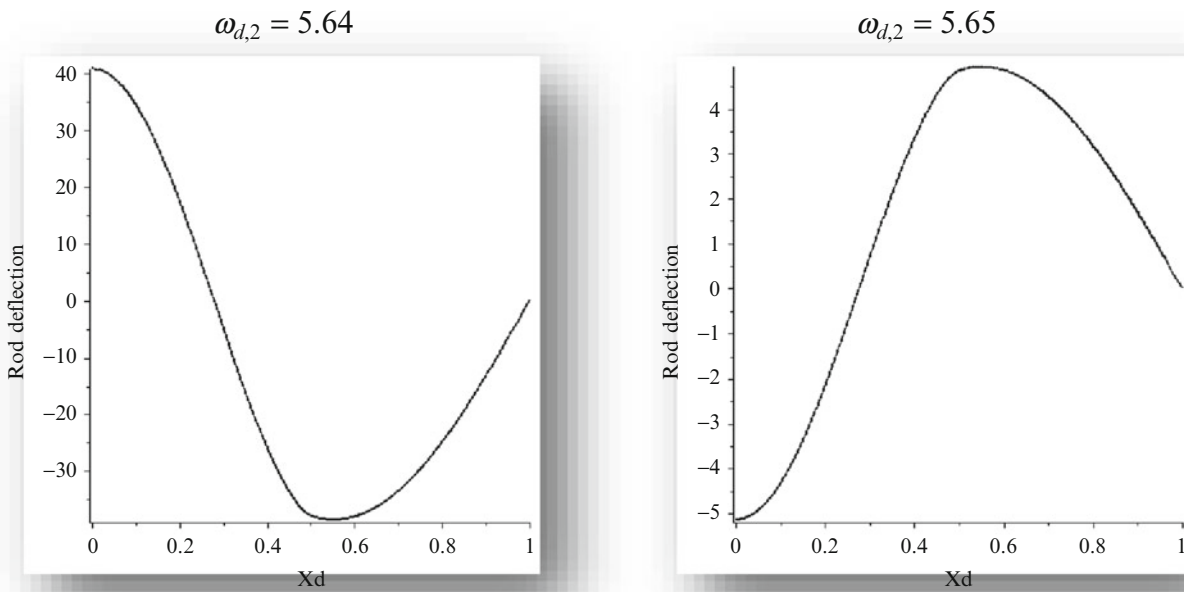$$\omega_{d,2} = 5.64 \qquad \qquad \omega_{d,2} = 5.65$$



**Fig. 36.10** Second frequency via forced-motion approach (free-fixed)

**Table 36.1** Results comparison using transfer matrix method as baseline

|  | Transfer matrix | FDM | Differences (%) | Forced motion | Differences (%) |
|---|---|---|---|---|---|
| Fixed-fixed first frequency | 4.1326 | 3.9845 | 3.58 | 4.14 | 1.08 |
| Fixed-fixed second frequency | 7.3837 | 6.4939 | 12.05 | 7.44 | 0.76 |
| Free-fixed first frequency | 2.2725 | 1.8093 | 20.38 | 2.29 | 0.77 |
| Free-fixed second frequency | 5.6338 | 5.4604 | 3.08 | 5.65 | 0.25 |
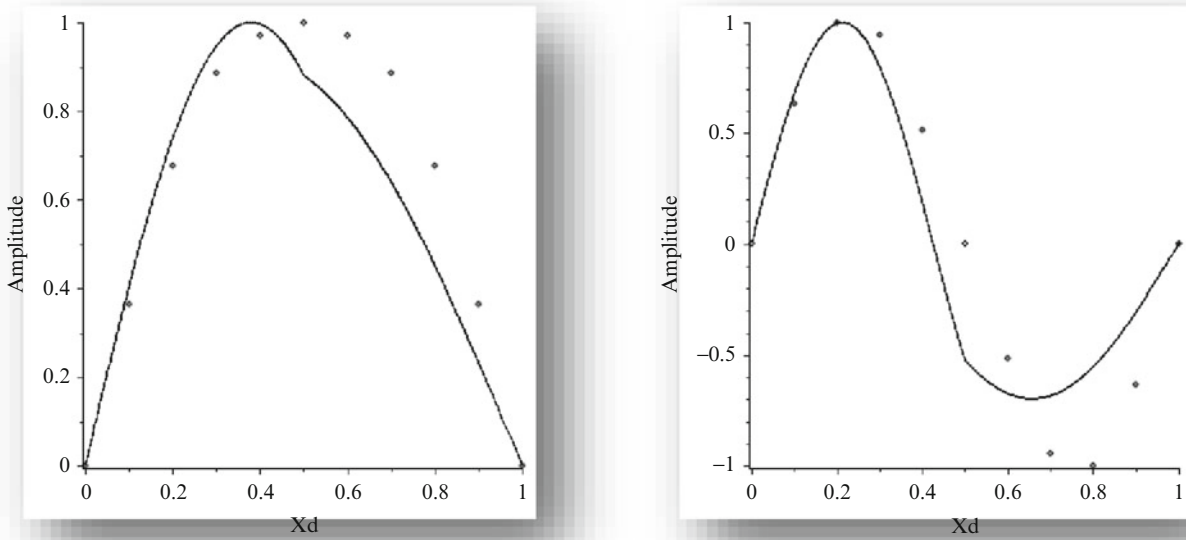
**Fig. 36.11** Mode shapes comparison: transfer matrix versus FDM approaches (fixed-fixed)
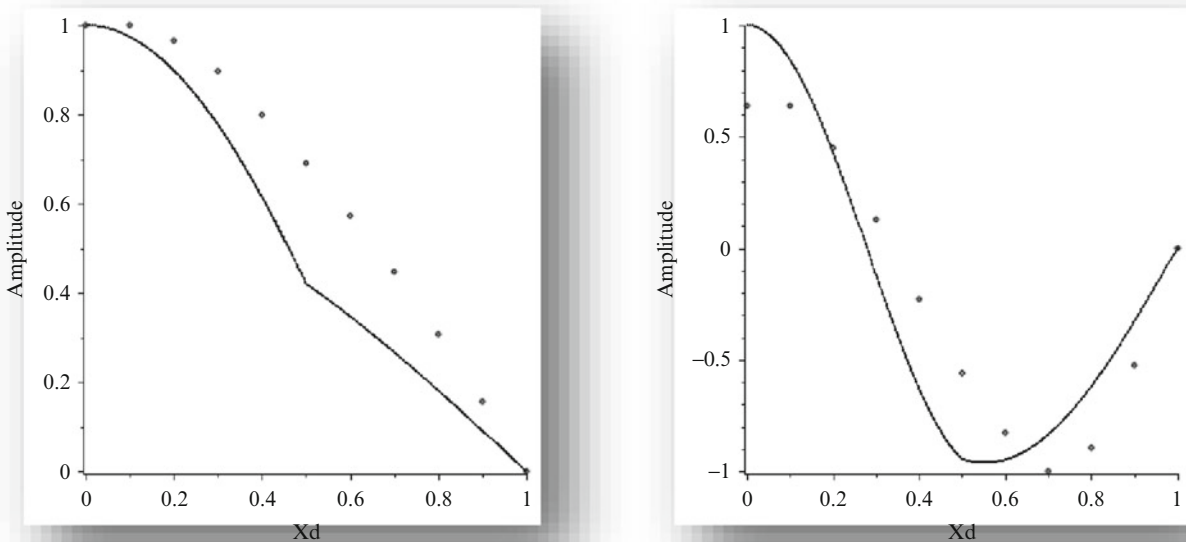


**Fig. 36.12** Mode shapes comparison: transfer matrix versus FDM approaches (free-fixed)

In relation to the mode shapes, comparisons for the fixed-fixed and free-fixed cases are given in Figs. 36.11 and 36.12, respectively. One can see that the FDM can produce a somewhat reasonable representation of the shapes. In order to capture the transition zone effect (seen in the transfer matrix generated modes) it is necessary to use more elements.

Based on the previous results it is seen that the continuous variation model is a promising alternative to transfer matrix methods.

## 36.6  Conclusions

Longitudinal motions of a two-layer elastic rod were treated. Exact natural frequencies (lowest two) and associated mode shapes were found using a transfer matrix approach, for both fixed-fixed and free-fixed boundary conditions.

Then a single differential equation model was developed using continuous approximations to the actual discontinuous material properties. Natural frequencies were found from this model using a forced motion method and they were in excellent agreement with the exact values (for an Aluminum/Silicon Carbide rod).

Mode shapes were obtained using a finite difference scheme and were in reasonable agreement with the exact ones for a relatively course mesh.

## References

1. Lee EH, Yang WH (1973) On waves in composite materials with periodic structure. SIAM J Appl Math 25(3):492–499
2. Hussein MI, Hulbert GM, Scott RA (2006) Dispersive elastodynamics of 1D banded materials and structures: analysis. J Sound Vib 289 (4–5):779–806
3. Hussein MI, Hulbert GM, Scott RA (2007) Dispersive elastodynamics of 1D banded materials and structures: design. J Sound Vib 307 (3–5):865–893
4. Vasseur JO, Deymier P, Sukhovich A, Merheb B, Hladky-Hennion AC, Hussein MI (2013) Phononic band structures and transmission coefficients: methods and approaches. In: Deymier PA (ed) Acoustic metamaterials and phononic crystals, vol 173. Springer, Berlin, pp 329–372
5. Berezovski A, Engelbrecht J, Maugin GA (2008) Numerical simulation of waves and fronts in inhomogeneous solids. World Scientific Publishing Co. Pte. Ltd., Singapore
6. Velo A, Gazonas G, Bruder E, Rodriguez N (2008) Recursive dispersion relations in one-dimensional periodic elastic media. SIAM J Appl Math 69(3):670–689
7. Shen M, Cao W (2000) Acoustic bandgap formation in a periodic structure with multilayer unit cells. J Phys D Appl Phys 33(10):1150–1154
8. Mazzei AJ, Scott RA (2013) Resonances of compact tapered inhomogeneous axially loaded shafts. In: Allemang R, De Clerck J, Niezrecki C, Wicks A (eds) Special topics in structural dynamics, vol 6. Springer, New York, pp 535–542

# Chapter 37
# Next-Generation Random Vibration Tests

**P.M. Daborn, C. Roberts, D.J. Ewins, and P.R. Ind**

**Abstract** This paper describes a radically new approach to the vibration testing of structures in order to demonstrate their endurance under simulated service conditions. The excitation mechanisms of structures in-service typically fall into one of three configurations; (i) excitation from a parent structure through mechanical connections (e.g. during transportation), (ii) excitation from aerodynamic forces distributed over the outer surface of the structure (e.g. aircraft and rockets in flight), or (iii) A combination of (i) and (ii). In nearly all cases, the in-service excitation is multi-directional, yet it is standard practice to replicate these environments with three orthogonal single-axis vibration tests. In addition, a considerable mismatch of the boundary conditions between the in-service and laboratory configurations is common, especially when replicating aerodynamic environments. This paper presents quantitative evidence of limitations with the status quo and demonstrates a superior method; Impedance Matched Multi-Axis Testing (IMMAT). Three noteworthy improvements of the new method are; (i) enhanced replication of the in-service environment, (ii) much shorter test durations, and (iii) a significant reduction in costs associated with random vibration tests.

**Keywords** Random vibration • Multi-axis testing • Missile • MIMO • Mechanical impedance

## 37.1 Introduction

Ground-based vibration tests are widely undertaken to replicate the damaging effects of vibration measured in-service. To carry out random vibration tests, environmental test houses typically use procedures developed in the 1960s and 1970s [1–3]. The status quo is to attach the structure-under-test to a high mechanical impedance shaker and to sequentially test the structure in three orthogonal axes. Typically, the direction of the test axis is selected to line up with the principal axis of the structure and is not based on scientific reasoning. This single axis testing methodology arose in the early days of vibration testing due to the technology available and was adequate for the expectations of that time. Some important advancements have been made in some areas; for example the development of Multi-Input-Multi-Output (MIMO) random control has enabled single-axis twin-shaker vibration tests to be undertaken on missile systems, although issues within the test configuration and the requirement for three separate single-axis tests still remains. Other notable advancements in the field of environmental testing are force-limiting techniques and multi-axis testing facilities [4–6], although these are not commonplace by any means.

---

P.M. Daborn • P.R. Ind
Structural Dynamics, AWE Aldermaston, Reading RG7 4PR, UK

P.M. Daborn (✉) • C. Roberts • D.J. Ewins
Bristol Laboratory for Advanced Dynamics Engineering (BLADE), Aerospace Engineering, University of Bristol,
Queen's Building, University Walk, Bristol BS8 1TR, UK
e-mail: philip.daborn@awe.co.uk; aepmd@bristol.ac.uk

C. Roberts
DES Wpns DOSG ST4b1, MOD Abbey Wood, Bristol BS34 8JH, UK

There is much literature which demonstrates that traditional vibration tests are overly severe [7–10]. This is to be expected; commercial and military establishments are comfortable with the notion that they are overtesting and therefore ensuring that their structures are robust, safe and serviceable. There is less published material demonstrating that traditional methods can lead to undertesting at some spectral regions [11–13].

The configuration of in-service structures comes in many varieties with the excitation mechanisms typically falling into three broad categories:

  (i)  Excitation from a parent structure through mechanical connections (e.g. during transportation).
 (ii)  Excitation from aerodynamic forces distributed over the outer surface of the structure (e.g. aircraft and rockets in flight).
(iii)  A combination of (i) and (ii).

One of the critical features of the vibration experienced by a structure is the local mechanical impedance of the excitation medium and/or the parent structure. The impedance of a large shaker system rarely matches the impedance of the parent structure in (i) and is vastly different from the free-flight aerodynamic conditions in (ii). In addition, in-service structures typically experience multi-directional excitation whereas the laboratory test is usually carried out in one axis with the location/region of the excitation location(s) being entirely different from the in-service excitation locations. The compounded mismatches between the laboratory and in-service configurations lead to unrealistic random vibration tests.

This paper quantifies the deficiencies of some current state-of-the-art random vibration tests and proposes considerable improvements using a case study which falls into category (iii), though most of the paper is relevant for any structure which experiences random vibration.

## 37.2  Objectives

The objectives of the research were as follows:

  (i)  To quantify the limitations with current methods of random vibration tests.
 (ii)  To propose a technique that can yield significant improvements.
(iii)  To quantify the improvements of the new technique over current methods.

In order to meet the above objectives, a case study was carried out—replicating the induced vibration of an underwing missile during captive air carriage. Many of the methods described in this paper, and the subsequent conclusions, can be applied to most structures and are not specific to underwing missiles. In fact, they are applicable wherever random vibration tests are carried out.

## 37.3  Case Study: Underwing Missile

An underwing missile falls into category (iii) stated in the introduction and an example of an underwing missile is shown in Fig. 37.1. In flight, the missile is excited by two mechanisms—aerodynamic forces distributed over the outer surface of the missile and from the parent structure through mechanical connections. The nature of the vibration response is heavily dependent on the local impedance of the parent structure; in this case the launcher rail and the wing at the attachment region. To allow greater freedom within this research, a dummy 1/3rd scale model of the missile was manufactured out of aluminium and nylon and is shown in Fig. 37.2. The approximate dimensions of the 1/3rd scale model are: length = 1,200 mm, outer diameter (cylindrical section) = 60 mm and inner diameter (cylindrical section) = 54 mm. The mass was approximately 3 kg.

The case study was designed to mimic a real-world missile vibration test program by executing the following procedure:

  (i)  Carrying out a flight trial.
 (ii)  Generating a test specification based upon the data in (i).
(iii)  Carrying out a vibration test in accordance to the test specification from (ii).

Activities (ii) and (iii) from the above procedure were carried out according to the current state-of-the-art technique for missile vibration testing; the twin-shaker single-axis MIMO random vibration test. Activities (ii) and (iii) were then repeated using a new method proposed here; the Impedance Matched Multi-Axis Test (IMMAT) which will be described fully in Sect. 6.

**Fig. 37.1** Underwing missile (*picture courtesy of the Federation of American Scientists*)



**Fig. 37.2** Scale model (1/3rd) of underwing missile



**Fig. 37.3** Wind tunnel facility at the University of Bristol



## 37.4 The Flight Trial

In order to understand the anticipated service environment for a missile system, it is necessary to measure the dynamic response during flight trials. This will give the specification writer the information required to generate a test specification. The test specification will then be used to control the laboratory test for that particular missile system.

For this case study, it was not practical to carry out an actual flight trial with the dummy missile so the aerodynamic environment was provided by a wind tunnel facility within the Aerospace Department at the University of Bristol (Figs. 37.3 and 37.4). The missile was subjected to multiple wind speeds and orientated at various yaw angles (Fig. 37.5). For simplicity, only data from the maximum wind speed (88 m/s) and at 0° yaw angle is used in this research.

During the wind tunnel testing, thirteen accelerometers were attached to the missile, some of which are shown in Fig. 37.6 along with the axis definition. The accelerometers were distributed over the outer surface of the missile at six locations (1–6)

**Fig. 37.4** Wind tunnel facility
with dummy missile attached



**Fig. 37.5** Missile inside the
wind tunnel at some specified
yaw angle



**Fig. 37.6** Dummy missile
showing some of the attached
accelerometers, the launcher rail
and the axis definition



along the X axis. At the tail end of the missile (position 1) a tri-axial accelerometer sensed in all axes (X, Y and Z). At
positions 2–6, single-axis accelerometers sensed in Y and Z only. The duration of the wind tunnel testing was 50 seconds to
allow a suitable number of averages to be taken. The acceleration time histories were converted to frequency domain power
spectral densities (PSDs) and Fig. 37.7 shows some examples of the PSDs obtained during the wind tunnel testing. It should
be noted at this stage that only random vibration is considered during this case study and no attention has be given to other
forms of dynamic motion such as mechanical shock.

## 37.5 The Twin-Shaker Single-Axis Vibration Test

The twin-shaker single-axis vibration test is the current state-of-the-art for missile testing and it was felt that it should be
investigated as part of this case study. In a twin-shaker test it is possible to excite one axis only. To certify a system fully
in all axes, it is necessary to carry out three individual tests in three orthogonal directions. For simplicity, only Z direction
excitation is considered in this case study (Fig. 37.8).

**Fig. 37.7** Example PSDs obtained during wind tunnel testing
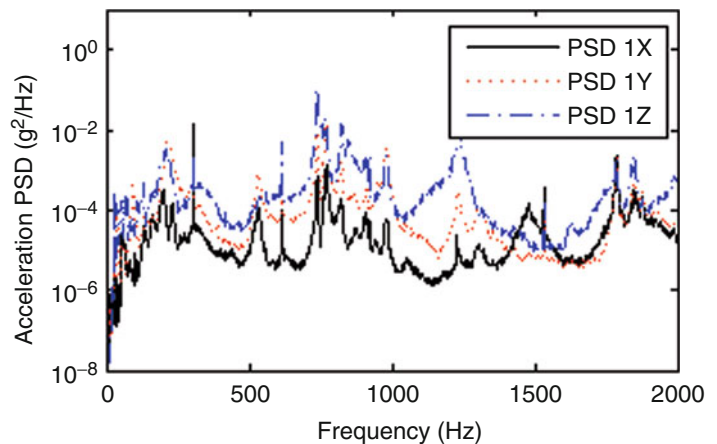


**Fig. 37.8** Twin-shaker single-axis vibration test
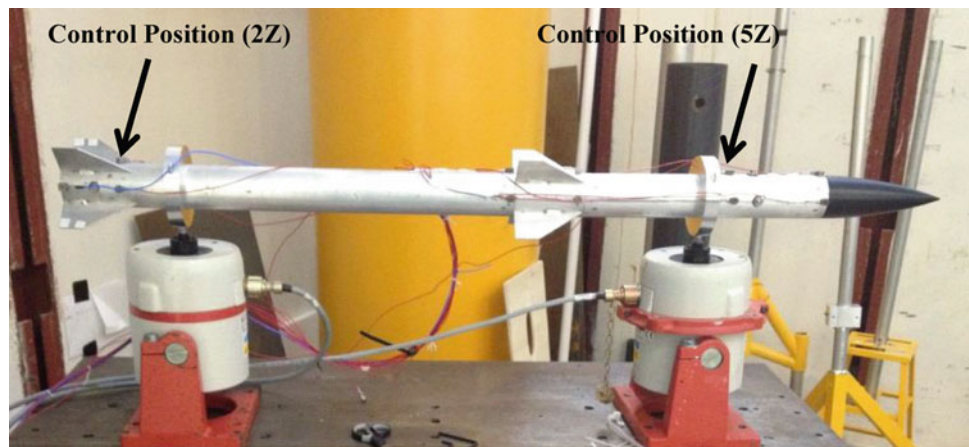


Prior to carrying out the vibration test, it was necessary to generate a test specification. As the vibration test involved two shakers (Fig. 37.8), the test specification must be suitable for MIMO random control. It order to replicate current practice, two response positions (2 and 5) were selected to control the test and were situated close to the two excitation locations (Fig. 37.8). The test specification consisted of two PSDs and one cross spectral density (CSD). The PSDs and CSD in the test specification were obtained directly from the wind tunnel environment at the control accelerometer positions and are shown in Fig. 37.9. It should be noted that harmonics, beginning at 307 Hz, can clearly be seen in the spectral density curves in Fig. 37.9. These harmonics are from the wind tunnel fan and excite the missile via the roof of the wind tunnel. They have been included in this case study to simulate the vibration that a missile might experience from its parent structure, e.g. the vibration induced by the engine through the aircraft wing.

The two electrodynamic shakers were rigidly connected to the missile via fixtures. This fixturing arrangement is typical of current practice and significantly alters the dynamics of the missile by stiffening and mass loading the local region, preventing it from bending freely and restricting cross-axis excitation. The shakers provided random excitation to the missile for 50 seconds with the test being controlled and recorded using the Leuven Measurement Systems (LMS) MIMO Random Control software and the Supervisory Control and Data Acquisition System (SCADAS) hardware.

The control curves from the twin-shaker test are shown in Fig. 37.10 and indicate good agreement between the test specification and the vibration test. This demonstrates that at the two control positions the vibration test is providing a good simulation of the aerodynamic environment from the wind tunnel. In addition, there is good agreement between the CSD from the wind tunnel and that of the twin-shaker test and of particular importance is the relative phase between the two control positions. The twin-shaker vibration test was able to go some way to replicating the harmonics of the wind tunnel fan, but it could not achieve the amplitude of the peaks.

As with the wind tunnel measurements, all thirteen accelerometers were used to measure the vibration in the twin-shaker test. Of these, two were control accelerometers used to control the vibration test with the remaining eleven being uncontrolled response measurements. The PSDs from the twin-shaker test are shown in the appendices (Fig. 37.13), with only twelve of the thirteen shown for convenience. The plots show that the vibration at the uncontrolled positions is a relatively poor simulation of the complete aerodynamic environment. In particular, there is evidence of considerable overtesting, undertesting and cross-axis overtesting (Fig. 37.13). Similar results were observed for the CSDs from the twin-shaker test (Fig. 37.14). There were

**Fig. 37.9** Test specification used in the twin-shaker vibration test
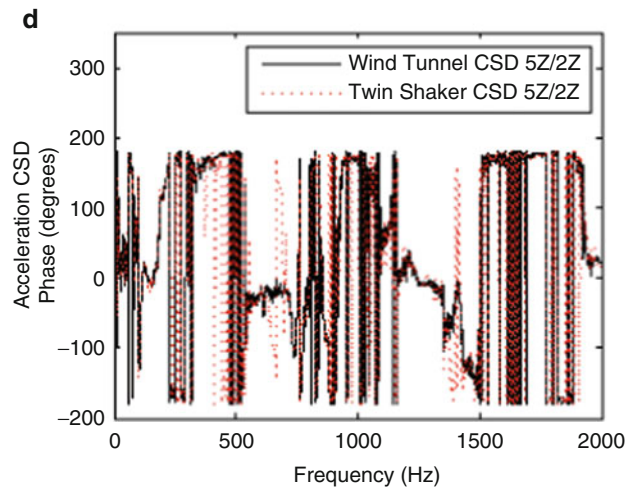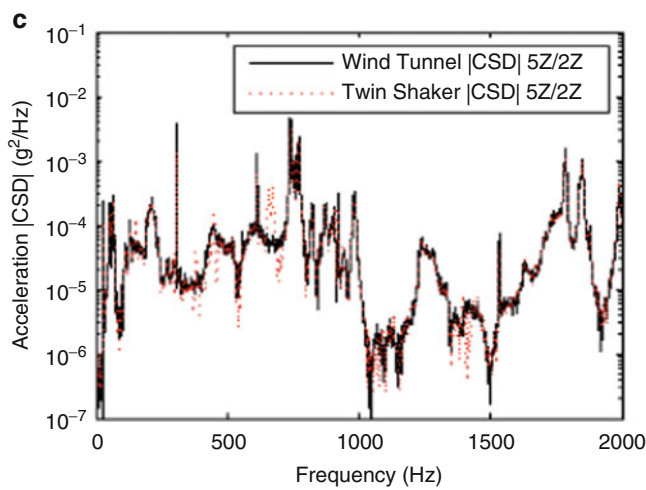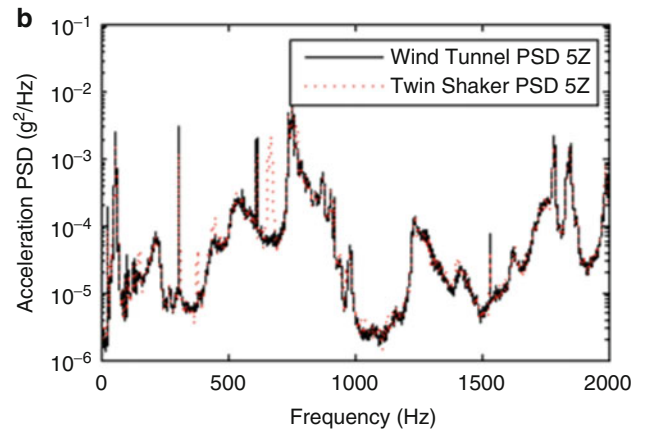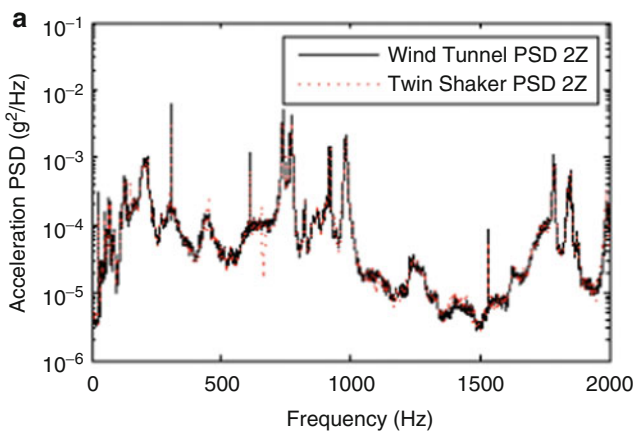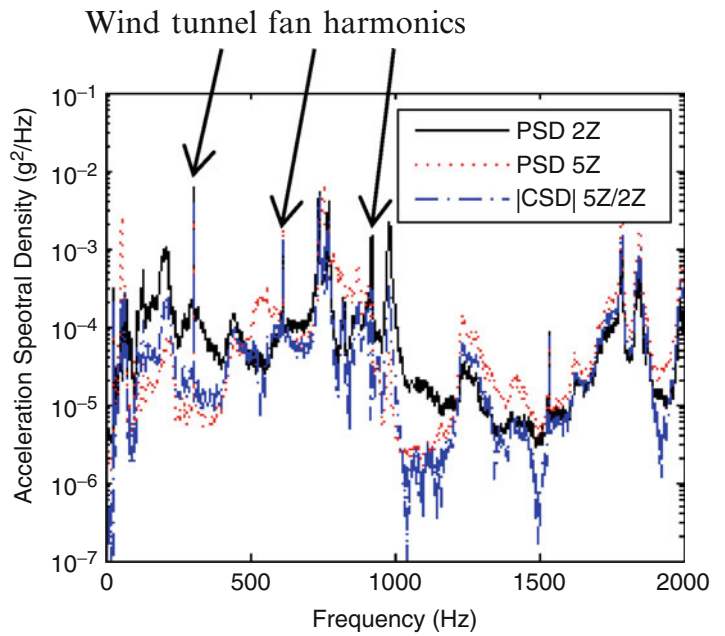


**Fig. 37.10** MIMO random control curves from twin-shaker test. (**a**) PSD 2Z. (**b**) PSD 5Z. (**c**) |CSD| 5Z/2Z. (**d**) Phase (CSD) 5Z/2Z

**Fig. 37.11** Example of phase
plot from twin-shaker test
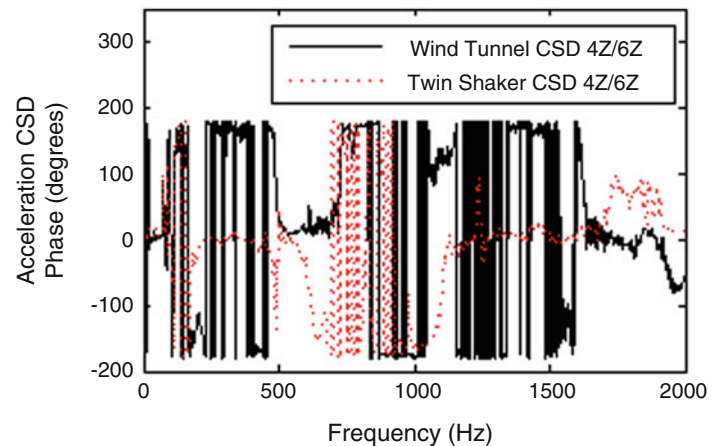


many CSDs from the twin-shaker test; it is not necessary to present them all in this paper and the plots in Fig. 37.14 are representative of the full data set. A noteworthy result is the phase of the CSDs and a representative curve is shown in Fig. 37.11. These plots show that the twin-shaker test was poor at replicating the relative phase between some of the locations when compared to the original aerodynamic environment. This has significant consequences as it means that the operating deflection shapes in the laboratory test, and the associated stress patterns are very different to the aerodynamic environments it is attempting to replicate.

## 37.6 Impedance Matched Multi-Axis Test (IMMAT)

A new approach to vibration testing has been developed and can offer significant enhancements over traditional vibration testing methods. This new approach is called Impedance Matched Multi-Axis Testing (IMMAT) and has the following critical characteristics:

 (i) The local impedance from the parent structure is included in the vibration test.
 (ii) The structure is excited in all axes simultaneously.
(iii) The attachment of the exciters has minimal influence on the dynamics of the structure.
(iv) The vibration test is controlled at many response locations using MIMO control.

The IMMAT approach was applied to the missile and is shown in Fig. 37.12. The local impedance from the wind tunnel environment was simulated by including the launcher rail and a section of wood with the same thickness as the wooden ceiling of the wind tunnel. The missile was excited in three orthogonal axes simultaneously using electrodynamic shakers attached via flexible drive rods. The vibration response of the IMMAT was controlled at the thirteen accelerometers using the Leuven Measurement Systems (LMS) MIMO Random Control software and the Supervisory Control and Data Acquisition System (SCADAS) hardware.

The test specification consisted of **all** of the PSD and CSD measurements from the wind tunnel environment and was comprised of thirteen PSDs and 78 CSDs. This resulted in a test specification with approximately 60,000 breakpoints; a breakpoint is a frequency/amplitude data point, a set of which defines the outline of the test specification and typically consists of only tens of breakpoints in traditional vibration tests.

The PSDs from the IMMAT are shown in the appendices (Fig. 37.15), with only twelve of the thirteen shown for convenience. A representative selection of |CSD| plots and CSD phase plots are displayed in the appendices (Figs. 37.16 and 37.17). The plots demonstrate that the IMMAT was able to accurately simulate the wind tunnel environment, including the wind tunnel fan harmonics.

## 37.7 Discussion and Conclusions

A case study has been presented which demonstrates some of the limitations with the conventional twin-shaker, single-axis, vibration test for underwing missiles, in particular, the poor simulation of the aerodynamic environment at uncontrolled locations during the vibration test. This was apparent in the severity of the overtest at some locations and for portions of the

**Fig. 37.12** Impedance Matched Multi-Axis Test for dummy missile. (**a**) IMMAT—view from above test setup. (**b**) IMMAT—view from tail of the missile. (**c**) IMMAT—view from below test setup

frequency bandwidth. Of more concern was the observed undertest at some uncontrolled locations. In addition, the evidence of this may not be discovered during typical qualification programs as often only the control locations are considered. Furthermore, there was evidence of cross-axis overtesting which means that any subsequent testing in orthogonal axes would subject the structure to unrealistically high stresses at the relevant frequencies. Other limitations of the twin-shaker test include the need to carry out three orthogonal tests sequentially to adequately excite all directions. In addition the fixture arrangement is likely to significantly alter the dynamics of the structure in terms of natural frequencies, modeshapes and damping. The twin-shaker test is a significant improvement compared to traditional large shaker, single-axis tests which are still commonplace today for many qualification programs on a variety of structures. The limitations described above could be considerably exaggerated for vibration tests that involve these large shaker systems.

The new Impedance Matched Multi-Axis Testing (IMMAT) technique potentially offers considerable improvements. IMMAT includes enhancements such as matching the local impedance of the parent structure and controlling the response of the structure at many locations using Multi-Input-Multi-Output control and has been successfully demonstrated in this paper.

A noteworthy improvement of IMMAT over current methods includes the excitation of all axes simultaneously with a considerable reduction in test time and the elimination of problems such as cross-axis excitation. Another major benefit of the IMMAT approach is the simulation of the original aerodynamic environment, including the power spectral densities, the cross spectral densities and the relative phase between locations. This ensures that the operating deflection shape of the structure in the IMMAT is very similar to the aerodynamic environment, leading to similar stress patterns. Finally, test houses could make substantial long-term cost savings by replacing some of their large shaker systems with a few smaller shaker systems for random vibration tests.

## A.1   Appendix 1: Twin-Shaker Vibration Test Results

See Figs. 37.13 and 37.14.

## A.2   Appendix 2: IMMAT Results
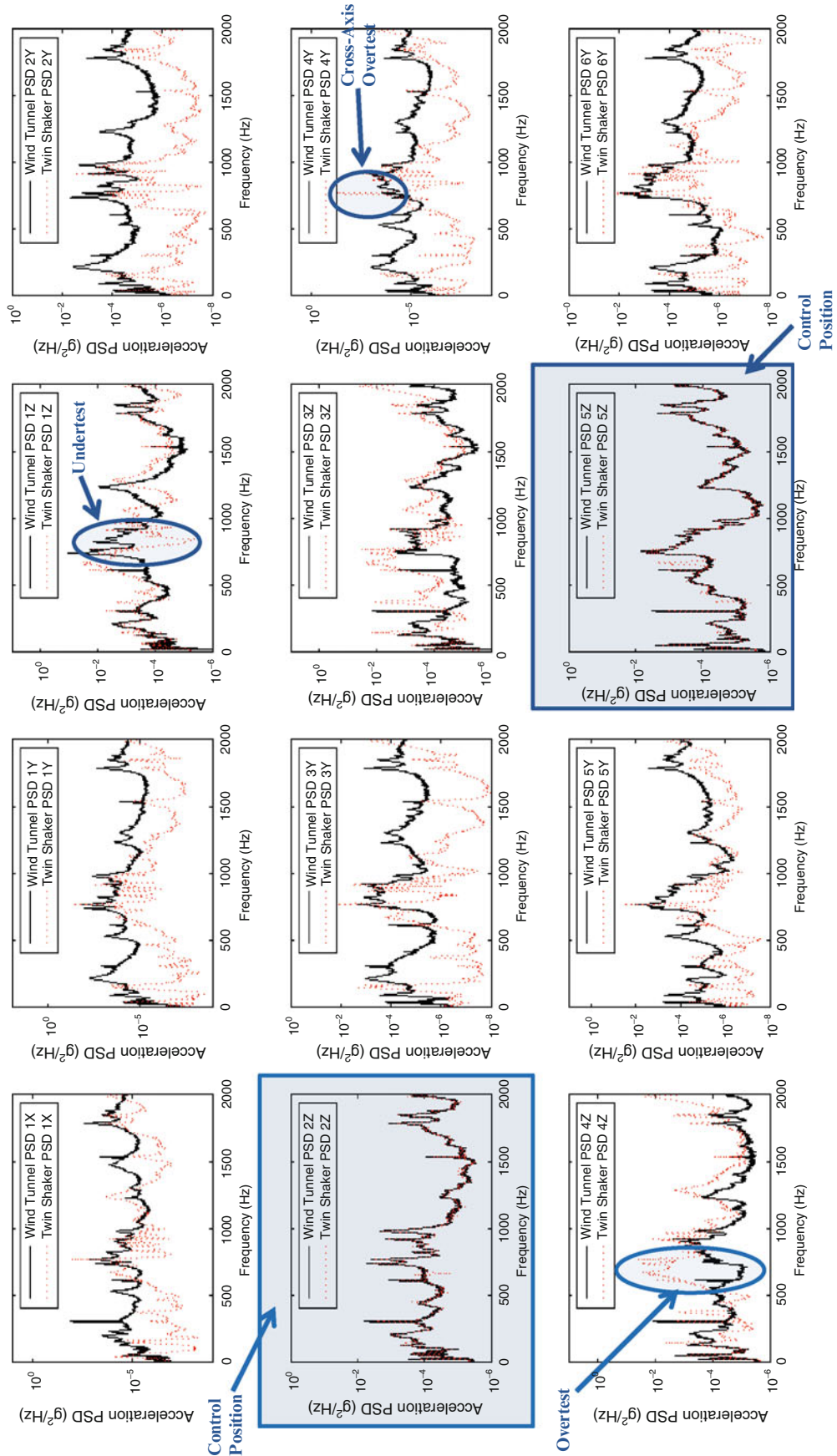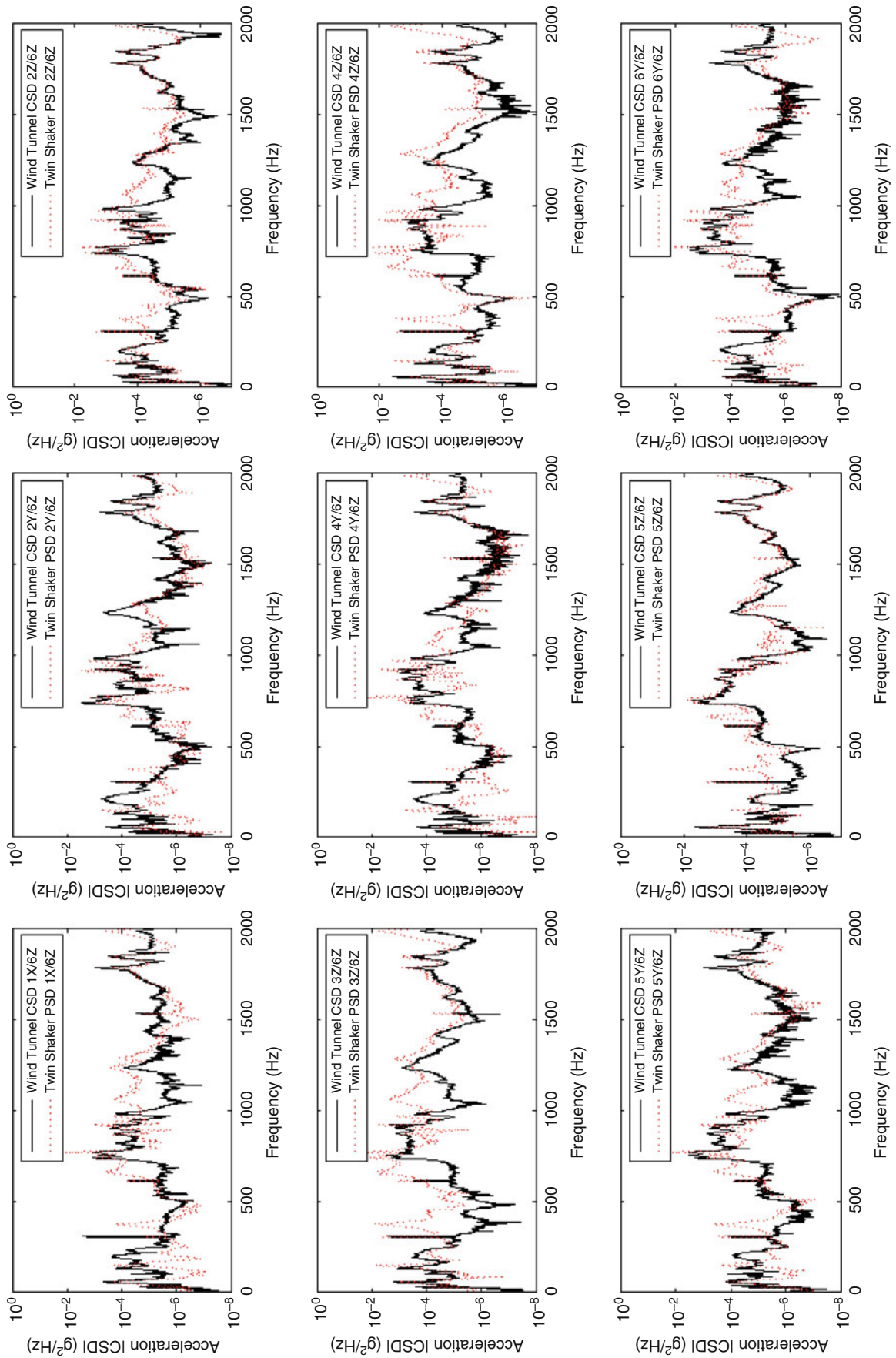
See Figs. 37.15, 37.16, and 37.17.

**Fig. 37.13** PSD response plots from twin-shaker test (Z-axis excitation)

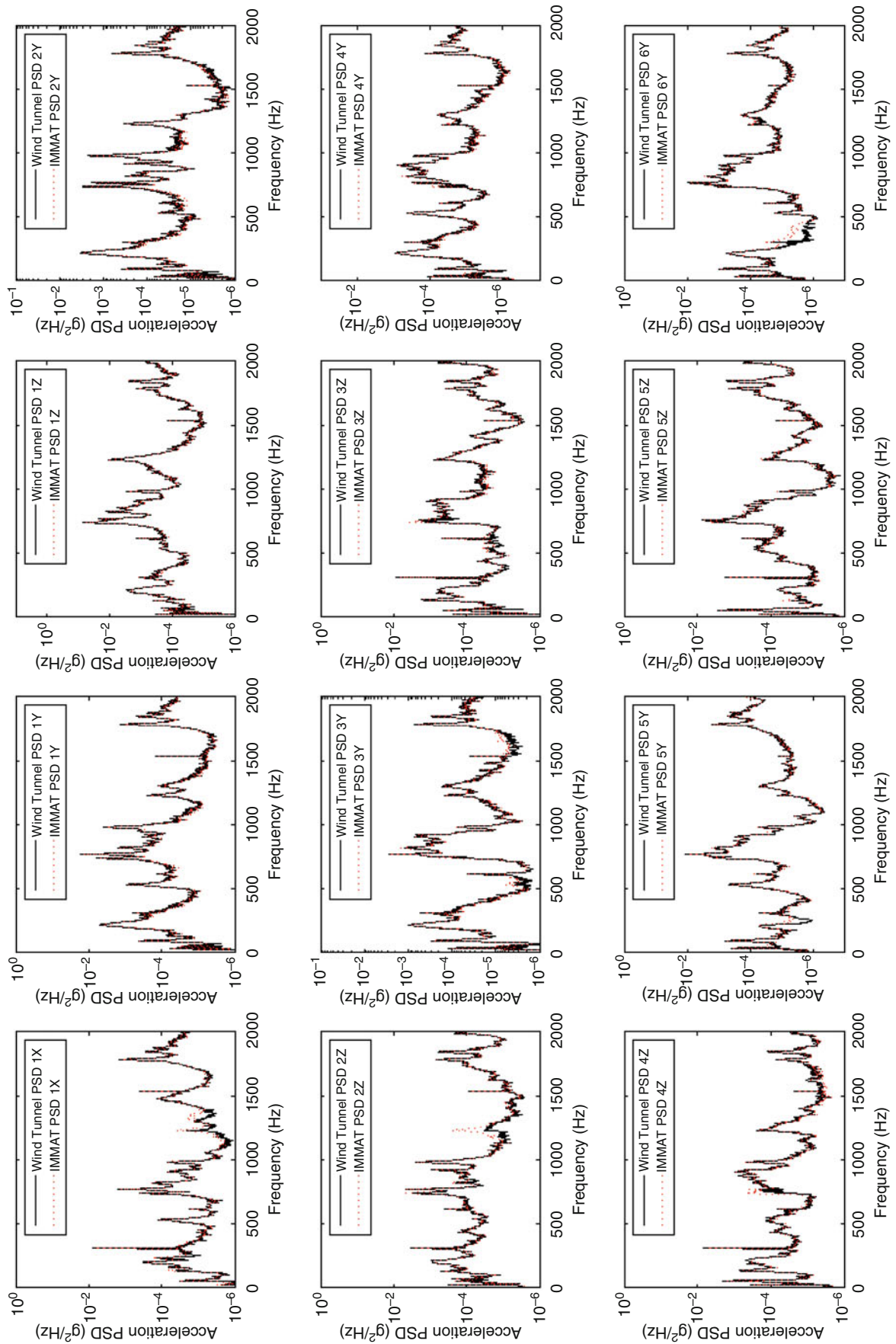**Fig. 37.14** |CSD| response plots from twin-shaker vibration test (Z-axis excitation)

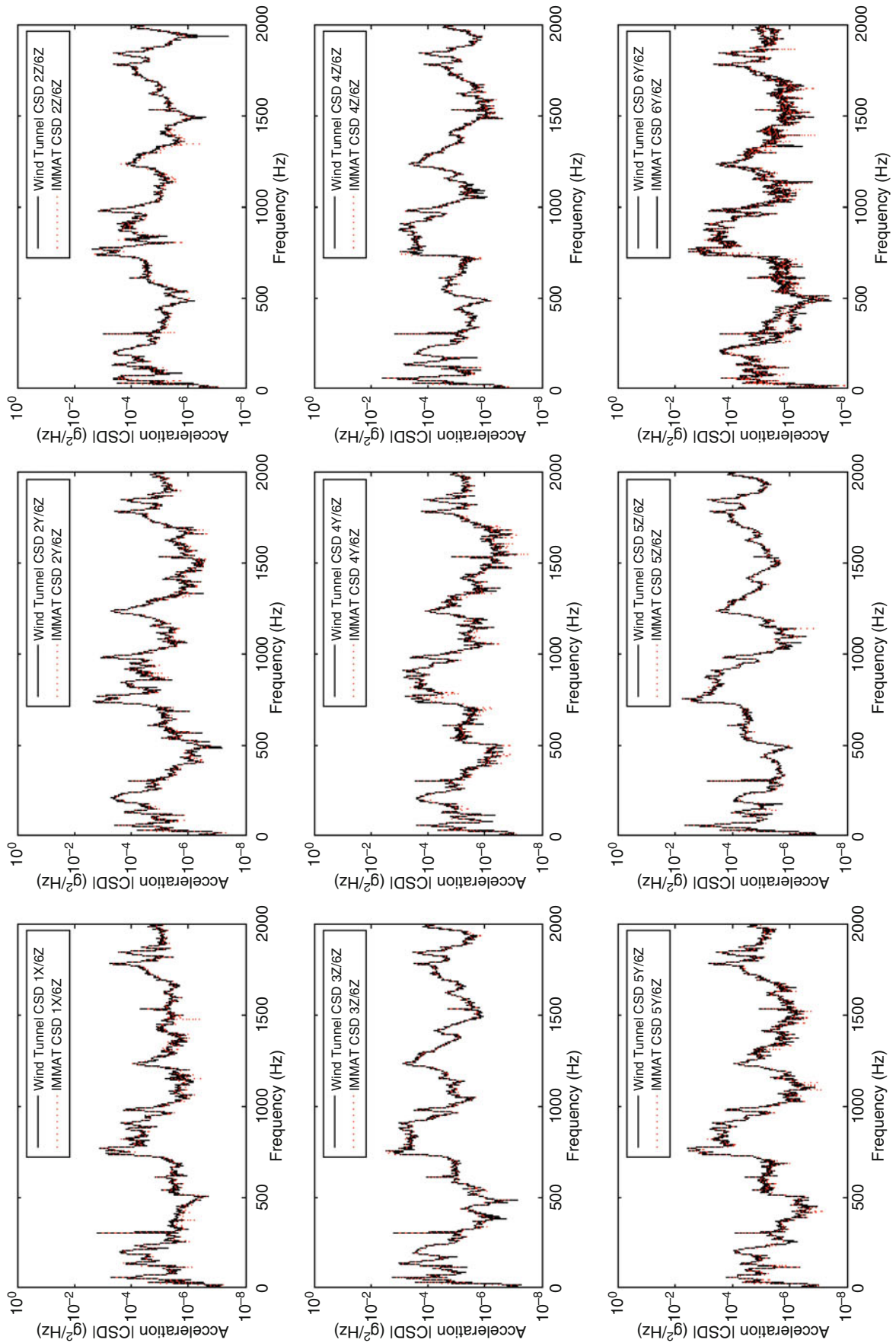**Fig. 37.15** PSD response plots from IMMAT

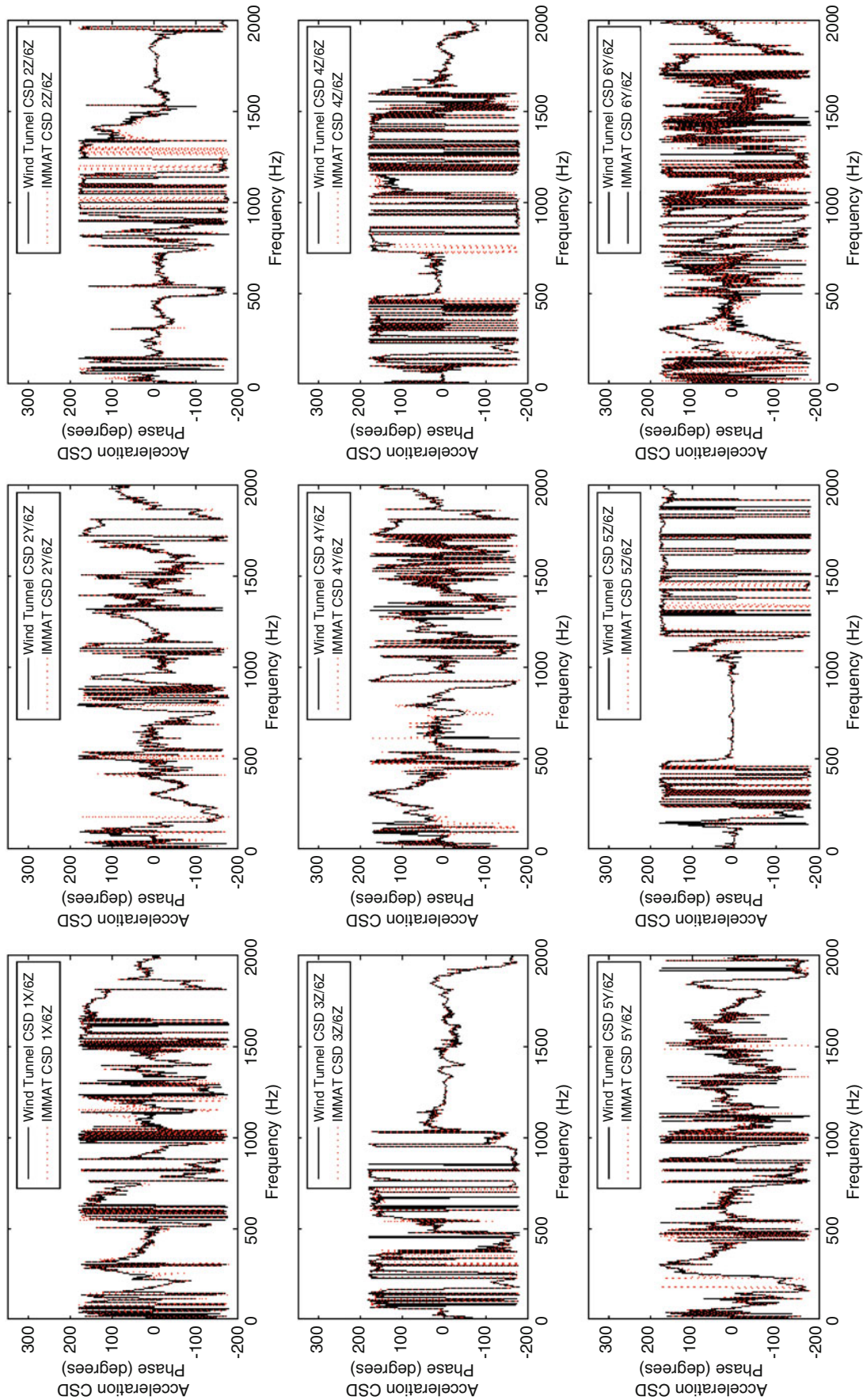**Fig. 37.16** |CSD| response plots from IMMAT

**Fig. 37.17**  CSD phase plots from IMMAT

# References

1. Kroeger RC, Hasslacher GJ III (1965) Relationship of measured vibration data to specification criteria. Acoust Soc Am 37(1):43–53
2. Piersol AG (1966) The development of vibration test specifications for flight vehicle components. J Sound Vibr 4(1):88–115
3. Piersol AG (1974) Criteria for the optimal selection of aerospace component vibration test levels. In: Proceedings of institute of environmental sciences, pp. 88–94
4. Scharton TD (1997) Force limited vibration testing. NASA Reference Publication RP-1403, Pasadena, CA
5. Osterholt DJ, Napolitano KL (2007) Six degree of freedom vibration testing. In: Proceedings of IMAC XXV, Orlando, FL
6. Smallwood DO, Gregory DL (2008) Evaluation of a 6-DOF electrodynamic shaker system. In: Proceedings of the 79th shock and vibration symposium, Orlando, FL
7. Salter JP (1964) Taming the general-purpose vibration test. Environ Eng 33(2–4):211–217
8. Witte AF, Sandia National Laboratories, Albuquerque (1970) Realistic vibration tests. Instrum Technol. 45–48
9. Soucy Y, Cote A (2002) Reduction of overtesting during vibration tests of space hardware. Can Aeronaut Space J 48(1):77–86
10. Scharton TD (1995) Vibration-test force limits derived from frequency-shift method. J Spacecraft Rockets 32:312–316
11. Daborn PM (2013) Replicating aerodynamic excitation in the laboratory. In: Proceedings of IMAC XXXI, Garden Grove, CA
12. French RM, Handy R, Cooper HL (2006) A comparison of simultaneous and sequential single-axis durability testing. Exp Techniques 30(5):32–37
13. Whiteman WE, Berman M (2005) Inedaquacies in uniaxial stress screen vibration testing. J IEST 44(4):20–23

# Chapter 38
# Optimal Phasing Combinations for Multiple Input Source Excitation

**Kevin L. Napolitano and Nathanael C. Yoder**

**Abstract** Multiple input random source excitation has proven to be an excellent method for measuring high-quality frequency response functions. Multiple-reference deterministic source excitation methods, such as multiple-reference sine sweeps, have been developed as well. The key to these deterministic methods is ensuring that the reference auto spectral matrix is invertible. This is achieved by (1) sweeping through each frequency at least as many times as there are numbers of active references and (2) changing the relative phasing or magnitude between the sources with each pass. This paper presents a method of defining an optimal set of source phasing combinations for a given the number of sources and a given number of desired phasing combinations. Assuming each source is fully activated during testing, this set of phasing combinations will produce a perfectly conditioned source auto spectral matrix.

**Keywords** Modal testing • Source excitation • Sine sweep • Multiple input • Sine dwell

## 38.1 Introduction

Multiple input random source excitation has proven to be an excellent method for measuring high-quality frequency response functions. Deterministic sinusoidal excitation techniques such as (single or multiple) discrete sine wave inputs, or sine sweeps, are often used when the random signals are not strong enough to overcome the noise floor of the test article [1]. As with random source excitation, allowing all the sources to be active simultaneously helps spread energy throughout a structure while also reducing overall testing time.

The key to ensuring that any excitation method can produce multiple-input frequency response functions is to ensure that the reference auto spectrum matrix, $[S_{XX}]$, is well conditioned so that it can be inverted [2, 3]. This is achieved by (1) stepping or sweeping through each frequency at least as many times as the number of source signals and (2) changing the relative phasing between the sources with each pass.

This paper defines a method for generating optimal relative phase combinations for a given "M" number of sources, for a given "N" number of phase cases. Each phase case will be associated with one frame of test data. The optimal solution is defined as all sources being fully engaged during each phase case and the resulting source auto spectrum matrix $[S_{XX}]$ being perfectly conditioned, i.e., proportional to the identity matrix.

First the special case where the number of sources matches the number of phasing cases is discussed. The method is then expanded to an arbitrary number of sources and phase cases, and methods for varying the phasing are discussed. After discussing how to apply these techniques to two different deterministic signal types, fixed sine and sinusoidal sweep, an example of the method using multiple-reference burst chirp excitation is presented.

K.L. Napolitano (✉) • N.C. Yoder
ATA Engineering, Inc., 11995 El Camino Real, Suite 200, San Diego, CA 92130, USA
e-mail: kevin.napolitano@ata-e.com

## 38.2   Number of Sources Equal to Number of Phase Cases

One way to generate optimal phasing combinations is to first define the baseline set of phases by equally spacing the number of sources around the unit circle in the complex plane, such that

$$\Theta_{0i} = \left(\frac{i}{M}\right) 2\pi \tag{38.1}$$

where "M" is the number of sources and the subscript "i" corresponds to the ith entry in the initial reference angle vector $\{\Theta_0\}$. An example for a three-source initial angle is presented in Fig. 38.1.

Note that the magnitude of each complex number is equal to 1, which ensures that each source is fully activated. Assuming that the numbers of phasing cases are equal to the number of independent sources, the optimal source phasing combination for the Jth frame of data can then be calculated as

$$\{\varphi_J\} = e^{iJ\{\Theta_0\}}. \tag{38.2}$$

A matrix of phasing combinations for an equivalent "M" number of sources and frames of data can be assembled as

$$[\Phi] = \left[ \{\varphi_1\} \{\varphi_2\} \bullet \bullet \bullet \{\varphi_M\} \right] = \left[ e^{i\{\Theta_0\}} \ e^{i2\{\Theta_0\}} \bullet \bullet \bullet e^{iM\{\Theta_0\}} \right] \tag{38.3}$$

Each row in this matrix corresponds to the phase assigned to a given source. Each column in this matrix corresponds to a separate phase case. For the example shown above with three sources (rows) and three frames (columns), the matrix of phasing combinations will be

$$[\Phi] = \begin{bmatrix} -\frac{1}{2} + i\frac{\sqrt{3}}{2} & -\frac{1}{2} - i\frac{\sqrt{3}}{2} & 1 \\ -\frac{1}{2} - i\frac{\sqrt{3}}{2} & -\frac{1}{2} + i\frac{\sqrt{3}}{2} & 1 \\ 1 & 1 & 1 \end{bmatrix} \tag{38.4}$$

First, note that the rows of $[\Phi]$ are perpendicular to each other such that

$$[\Phi][\Phi]^* = N[I] \tag{38.5}$$
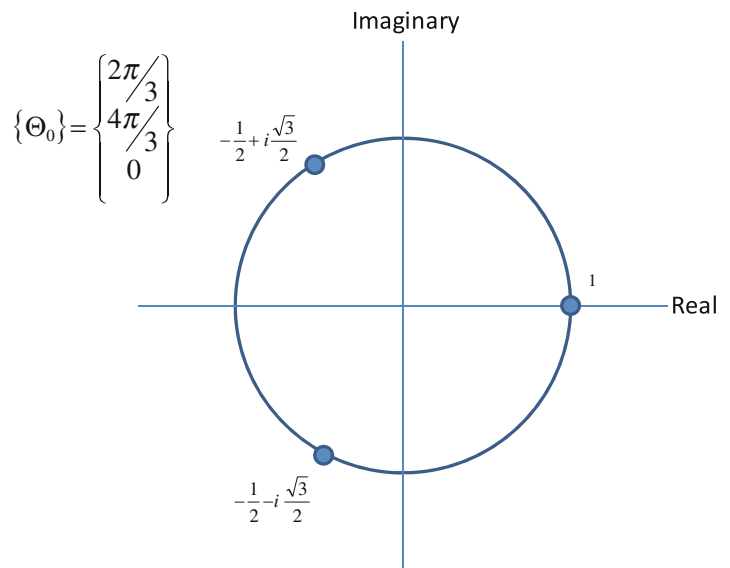


Fig. 38.1  Example of three evenly spaced locations along the unit circle

where "N" is the number of phasing cases. This equation can be expanded by representing it as a summation of the phase vectors multiplied by their Hermitian.

$$[\Phi][\Phi]^* = N[I] = \sum_{J=1}^{N} \{\varphi_J\}\{\varphi_J\}^* \tag{38.6}$$

If the source input is sinusoidal with the phasing combinations specified, then the reference auto spectrum matrix would also be defined as a summation of the phase vectors multiplied by their Hermitian.

$$[S_{XX}] = \sum_{i=1}^{N} \{\varphi_i\}\{\varphi_i\}^* \tag{38.7}$$

Thus, the reference auto spectrum matrix is perfectly conditioned; in other words, it is a diagonal matrix in which each of the diagonals has the same magnitude.

A set of optimal phase combinations for a given number of sources with the same number of phasing cases can also be calculated as the inverse fast Fourier transform of the identity matrix:

$$[\Phi] = M * IFFT([I]) \tag{38.8}$$

For the three-source, three-phase case, the phasing matrix using the inverse fast Fourier transform is

$$[\Phi] = \begin{bmatrix} 1 & 1 & 1 \\ 1 & -\frac{1}{2}+i\frac{\sqrt{3}}{2} & -\frac{1}{2}-i\frac{\sqrt{3}}{2} \\ 1 & -\frac{1}{2}-i\frac{\sqrt{3}}{2} & -\frac{1}{2}+i\frac{\sqrt{3}}{2} \end{bmatrix} \tag{38.9}$$

The matrices in Eqs. 38.4 and 38.9 are essentially equivalent, though the phasing case in which each answer assigns a given phasing combination is different, and the source assigned a given phasing case is different as well: in this example, phasing cases (i.e., the columns) 1, 2, and 3 in Eq. 38.4 are mapped to phasing cases 2, 3, and 1 in Eq. 38.9. Likewise, the sources (i.e., the rows) 1, 2, and 3 in Eq. 38.4 are mapped to sources 2, 3, and 1 in Eq. 38.9.

## 38.3   Number of Sources Less than Number of Phase Cases

While the inverse fast Fourier transform may provide a simple method of generating optimal phasing combinations, it does not lend insight into how to generate optimal phasing combinations when the number of phasing cases is greater than the number of sources. To generate an optimal set of phasing combinations for "N" phasing cases, the formula can be expanded to

$$\{\varphi_J\} = e^{iJ\{\Theta_0\}(M/N)} \tag{38.10}$$

where "M" is the number of sources and "N" is the number of phasing cases. For example, the three-source case with six phase cases, or six frames of data, will have a phasing matrix of

$$[\Phi] = \begin{bmatrix} \frac{1}{2}+i\frac{\sqrt{3}}{2} & -\frac{1}{2}+i\frac{\sqrt{3}}{2} & -1 & -\frac{1}{2}-i\frac{\sqrt{3}}{2} & \frac{1}{2}-i\frac{\sqrt{3}}{2} & 1 \\ -\frac{1}{2}+i\frac{\sqrt{3}}{2} & -\frac{1}{2}-i\frac{\sqrt{3}}{2} & 1 & -\frac{1}{2}+i\frac{\sqrt{3}}{2} & -\frac{1}{2}-i\frac{\sqrt{3}}{2} & 1 \\ -1 & 1 & -1 & 1 & -1 & 1 \end{bmatrix} \tag{38.11}$$

Again, the rows of $[\Phi]$ are perpendicular to each other, and therefore the reference auto spectral matrix, $[S_{XX}]$, will be diagonal.

## 38.4 Phase Variation

There are two ways the phasing matrix [Φ] can be modified and still produce an ideal source auto spectral matrix. The first is to provide an arbitrary rotation to the baseline shaker angle vector $\{\Theta_0\}$. This makes physical sense because only the relative phase between the different sources matters. Thus, the general form of the baseline angle is

$$\Theta_{0i} = \alpha + \left(\frac{i}{M}\right) 2\pi \tag{38.12}$$

The second way to modify the phasing matrix [Φ] is to provide an arbitrary rotation to its rows. Again, this makes physical sense in that it should not matter if a basis row vector is initially rotated—it should still be perpendicular to the other row vectors in the matrix. Thus,

$$\left[\overline{\Phi}\right] = [\Phi][R] \tag{38.13}$$

where the matrix [R] is a diagonal matrix whose Kth diagonal entry is a rotation of a designated angle $b_K$, $e^{ib_K}$.

The variables, $\alpha$ and $b_K$, are designated angles from 0 to $2\pi$. These variables can be randomly generated or selected to meet some criterion with regard to the source signal.

The optimal phasing algorithm can be applied to sine-sweep testing and steady-state sinusoidal testing. Sine-sweep testing includes both multiple-reference sine chirp and long sweeps. Steady-state sinusoidal testing includes single- or multiple-frequency sine dwell, of which periodic random excitation is a subset.

## 38.5 Examples

The algorithm defined above was implemented into two functions using ATA's IMAT toolbox. These two functions are pseudorandom and burst_chirp. The first function is used to generate multiple sine-dwell inputs at the analysis frequencies defined by the desired block size and the sampling frequency of the time-history function. The phasing combinations between the different sine waves at each frequency are varied with each frame to produce a diagonal $[S_{XX}]$ matrix at each frequency. The second function is used to generate sine sweeps. Depending on how the user defines the length of each sweep, these can be fast (burst chirp) sweeps completed within each frame of data, or they can be slow sweeps where it takes several frames of data to capture a single sweep.

### 38.5.1 Pseudo Random

An example of a digitally produced pseudo-random excitation is presented below in Fig. 38.2. The key to processing pseudo-random data is to perform signal processing on the parts of the test data that are at steady state. In this example, sixty frames of data were produced. A total of twenty phase cases were used, with each phase case used to generate three frames of data.
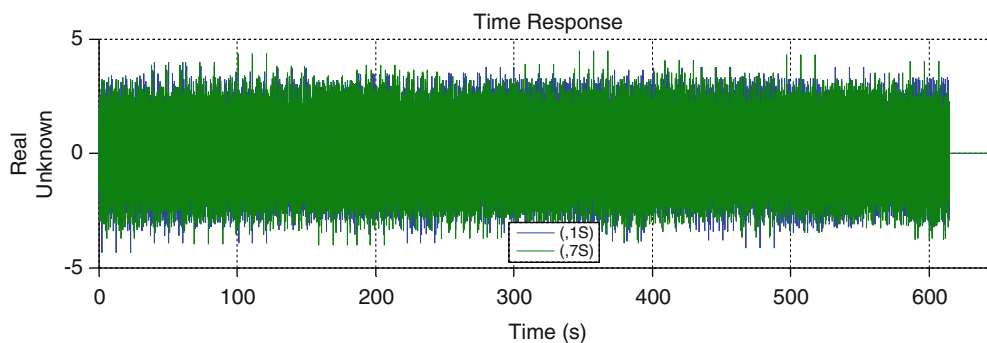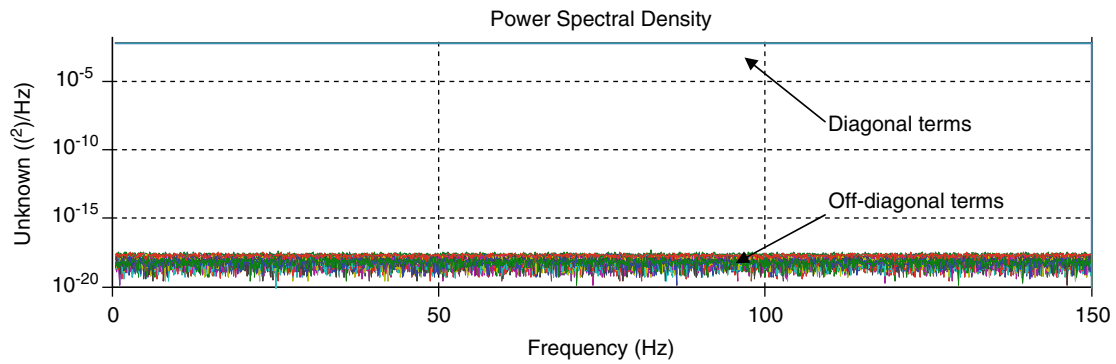


**Fig. 38.2** Example periodic random time history signal: Source 1 and Source 7

**Fig. 38.3** Reference signal auto spectrum matrix

**Table 38.1** Normalized RMS auto spectrum matrix for nine source signals

|  | Source 1 | Source 2 | Source 3 | Source 4 | Source 5 | Source 6 | Source 7 | Source 8 | Source 9 |
|---|---|---|---|---|---|---|---|---|---|
| Source 1 | $1.00E+00$ | $1.55E-08$ | $1.04E-08$ | $1.13E-08$ | $1.01E-08$ | $9.88E-09$ | $1.10E-08$ | $1.05E-08$ | $1.05E-08$ |
| Source 2 | $1.55E-08$ | $1.00E+00$ | $1.17E-08$ | $1.02E-08$ | $9.87E-09$ | $9.91E-09$ | $9.56E-09$ | $1.13E-08$ | $1.01E-08$ |
| Source 3 | $1.04E-08$ | $1.17E-08$ | $1.00E+00$ | $1.87E-08$ | $1.06E-08$ | $1.22E-08$ | $1.21E-08$ | $1.04E-08$ | $1.19E-08$ |
| Source 4 | $1.13E-08$ | $1.02E-08$ | $1.87E-08$ | $1.00E+00$ | $1.19E-08$ | $1.31E-08$ | $1.23E-08$ | $1.01E-08$ | $1.15E-08$ |
| Source 5 | $1.01E-08$ | $9.87E-09$ | $1.06E-08$ | $1.19E-08$ | $1.00E+00$ | $1.46E-08$ | $1.27E-08$ | $1.15E-08$ | $1.11E-08$ |
| Source 6 | $9.88E-09$ | $9.91E-09$ | $1.22E-08$ | $1.31E-08$ | $1.46E-08$ | $1.00E+00$ | $1.29E-08$ | $1.13E-08$ | $1.04E-08$ |
| Source 7 | $1.10E-08$ | $9.56E-09$ | $1.21E-08$ | $1.23E-08$ | $1.27E-08$ | $1.29E-08$ | $1.00E+00$ | $1.37E-08$ | $1.04E-08$ |
| Source 8 | $1.05E-08$ | $1.13E-08$ | $1.04E-08$ | $1.01E-08$ | $1.15E-08$ | $1.13E-08$ | $1.37E-08$ | $1.00E+00$ | $1.76E-08$ |
| Source 9 | $1.05E-08$ | $1.01E-08$ | $1.19E-08$ | $1.15E-08$ | $1.11E-08$ | $1.04E-08$ | $1.04E-08$ | $1.76E-08$ | $1.00E+00$ |

Condition number $= 1$

To protect the exciter from shock-type inputs, the function automatically inserts a "ramp-up" and "ramp-down" time for each phase case; therefore, the second frame in each set was used to perform signal processing because the time history function was at steady state during those frames. Signal processing was performed to determine the amount of coupling between nine source signals by calculating the full reference auto spectrum matrix, $[S_{XX}]$, which is presented in Fig. 38.3. All of the off-diagonal terms are several orders of magnitude lower than the on-diagonal terms. The RMS value for each term in the reference auto spectrum matrix is presented in Table 38.1. The condition number of the matrix of RMS values is 1.

### 38.5.2   Burst Chirp (Fast Sweep)

The optimal phase source method was also used to create burst chirp voltage input source signals for a hypothetical ground vibration test. The burst chirp input consisted of a logarithmic sweep from 1 to 40 Hz. There were nine source signals and thirty phase cases (or thirty frames of data). An example plot of one frame for two of the source signals is presented in Fig. 38.4. The summation of the magnitude of the source signal auto spectrum matrix over all frequencies (normalized by the peak maximum value) is presented in Table 38.2. The slightly different magnitudes on the diagonals are likely due to the ramp-up and ramp-down filters applied to the time-history signals. Even so, the condition number is very good at 1.0035.

## 38.6   Summary

A method for determining optimal phase angle combinations for multiple-reference sinusoidal testing (sweep or steady state) has been presented in this paper. The key to the method is to select an initial set of phase angles that are equally spaced along the unit circle in the complex plane; the phase angles are then calculated as fractional powers of these initial angles. Rotations of the initial angle or rows of the final phasing angle matrix can be used to modify the phasing angle matrix.
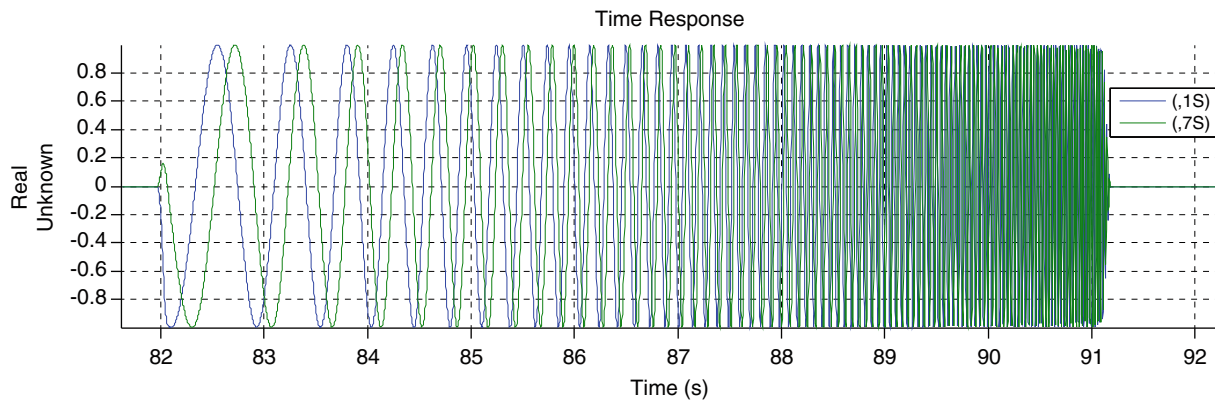
**Fig. 38.4** Example burst chirp frame of data with constant relative phase between Source 1 and Source 7

**Table 38.2** Normalized and summed auto spectrum matrix for nine source signals

|          | Source 1   | Source 2   | Source 3   | Source 4   | Source 5   | Source 6   | Source 7   | Source 8   | Source 9   |
|----------|------------|------------|------------|------------|------------|------------|------------|------------|------------|
| Source 1 | 1.00E + 00 | 4.09E − 08 | 5.82E − 08 | 4.63E − 08 | 4.63E − 08 | 4.22E − 08 | 5.38E − 08 | 4.15E − 08 | 4.48E − 08 |
| Source 2 | 4.09E − 08 | 9.97E − 01 | 4.07E − 08 | 3.31E − 08 | 3.33E − 08 | 3.81E − 08 | 3.11E − 08 | 3.57E − 08 | 2.86E − 08 |
| Source 3 | 5.82E − 08 | 4.07E − 08 | 9.97E − 01 | 8.61E − 09 | 6.41E − 08 | 2.76E − 08 | 3.99E − 08 | 2.97E − 08 | 3.22E − 08 |
| Source 4 | 4.63E − 08 | 3.31E − 08 | 8.61E − 09 | 9.97E − 01 | 9.12E − 09 | 2.67E − 08 | 4.72E − 08 | 3.58E − 08 | 2.59E − 08 |
| Source 5 | 4.63E − 08 | 3.33E − 08 | 6.41E − 08 | 9.12E − 09 | 9.97E − 01 | 3.42E − 08 | 4.10E − 08 | 2.87E − 08 | 5.20E − 08 |
| Source 6 | 4.22E − 08 | 3.81E − 08 | 2.76E − 08 | 2.67E − 08 | 3.42E − 08 | 9.97E − 01 | 3.40E − 08 | 3.22E − 08 | 3.47E − 08 |
| Source 7 | 5.38E − 08 | 3.11E − 08 | 3.99E − 08 | 4.72E − 08 | 4.10E − 08 | 3.40E − 08 | 9.97E − 01 | 4.04E − 08 | 2.75E − 08 |
| Source 8 | 4.15E − 08 | 3.57E − 08 | 2.97E − 08 | 3.58E − 08 | 2.87E − 08 | 3.22E − 08 | 4.04E − 08 | 9.97E − 01 | 3.70E − 08 |
| Source 9 | 4.48E − 08 | 2.86E − 08 | 3.22E − 08 | 2.59E − 08 | 5.20E − 08 | 3.47E − 08 | 2.75E − 08 | 3.70E − 08 | 9.97E − 01 |

Condition number = 1.0035

# References

1. Avitable P (2009) Shaker excitation. In: Presentation, 27th international modal analysis conference, Orlando, FL, February 2009. http://www.sem.org/PDF/Avitabile_shaker_excitation.pdf
2. Napolitano K, Linehan D (2009) Multiple sine sweep excitation for ground vibration tests. In: 27th international modal analysis conference, Orlando, FL, February 2009
3. Napolitano KL, Yoder NC, Brillhart RD (2012) A comparison of multiple impact testing methods. In: 30th international modal analysis conference: conference and exposition on structural dynamics, Jacksonville, FL, January 30–February 2, 2012